

BULGARIAN CHEMICAL COMMUNICATIONS

2017 Volume 49 / Number 1

*Journal of the Chemical Institutes
of the Bulgarian Academy of Sciences
and of the Union of Chemists in Bulgaria*

The Institute of Chemical Engineering at the Bulgarian Academy of Sciences – 30 years recap



As scientific and applied discipline chemical engineering is known since the beginning of the last century. Its onset is based on the demands of oil

processing, chemical industry, metallurgy, etc. being the engine of the economic development for the period. Chemical Engineering comprises scientific and applied activity for the implementation of chemical sciences in industry. Therefore its methodology comprises knowledge and theory either of chemistry or of applied physics, applied mathematics, theoretical mechanics, heat engineering, etc.

The Institute of Chemical Engineering (IChE) started as a Department of Mass Transfer processes in the Institute of General and Inorganic Chemistry at the Bulgarian Academy of Sciences. Later, in 1972 it was transformed in autonomous Central Laboratory of Chemical Engineering (CLCE) and finally it was promoted to institute in 1986 by act of the Government. Last year the Institute celebrated its 30th anniversary.

Founder of CLCE and IChE was Prof. DSc Dimiter Elenkov (Corresponding Member of BAS), also founder of the Chair of Processes and Apparatuses in the Chemical and Technological Institute in Sofia (the present Department of Chemical Engineering at the University of Chemical Technology & Metallurgy).

The mission of IChE is to contribute to the environmentally sustainable development with its scientific methodology, scientific capacity and broad experience and applied research in chemical technologies, energy saving and industrial biotechnologies. The following world-wide priorities are assumed:

- Green and waste-free technologies for reduction of industrial waste and exclusion of hazardous waste.
- Methods and processes for integrated waste management (household, industrial,

hazardous) combined by their secondary use as renewable raw materials and energy sources.

- Processes, equipment and entire technologies for enhancement of material and energy efficiency of running and new enterprises.
- Process engineering for chemical technologies and industrial biotechnologies with thermodynamic modelling.
- Training of students and post-docs in the area of competence. During the period 2009/2016 in the Institute 16 PhD theses and two - for DSc were defended. For the same period the institute had trained 43 Bachelor and Master Students.

The Institute publishes about 50 scientific articles with 40% of them in international journals with impact-factor. There are also published monographs, chapters in collections on certain subjects, review articles, etc.

In its applied activity the Institute follows the logics of the chemical technology development in Bulgaria. There are many applied technologies and units developed in the Institute throughout the years. The following has got practical application, namely: sulfur dioxide and fine particulates capturing (1967); nitrobenzene removal from aniline in distillation columns (1977); removal of hydrogen sulfide in absorption columns (1978); extraction of essential oils from plants (1980s); liquid extraction of residual copper from waste streams (1988); advanced method for sulfur dioxide oxidation for sulfuric acid production (1990); contact economizers for energy saving in thermal power plants (1990/93).

In the new century the efforts were concentrated in the field of renewable fuel technologies and waste recycling, like: methanol regeneration in biodiesel production (2007); eight equipments for bioethanol distillation (2002/2008); one for biogas

production (2009); one for pyrolysis of organic compounds, e.g. used tires (2015/16).

Various algorithms and software are developed for optimal design and management of batch and semi-continuous manufacturing.

During the last years new project on hydrogen sulfide conversion, contained in the Black sea waters, into energy was developed.

The Institute develops and maintain various connections with partners from the country and

abroad. There are joint projects with partners from the European Union (Germany, The United Kingdom, Austria, The Netherlands, etc.), the United States, Turkey, India, etc. Many projects supported by the European Frameworks Programs, by bi-lateral agreements with the U.K, Turkey, Belgium, etc. have been running for decades.

Prof. DSc Venko Beschkov

70th Anniversary for Professor Venko Beschkov, DSc



With this issue of the Bulgarian Chemical Communications we celebrate the 70th birthday of Professor Venko Beschkov and mark his considerable contributions to the chemical and biochemical engineering in Bulgaria. Many are the

important benchmarks of Prof. Beschkov's outstanding career and the results of his scientific endeavors are varied and it is difficult to select the most worthy of note in this brief overview.

Venko graduated from Sofia University with an MSc in Inorganic Chemistry with first class honors and since 1969 he has been affiliated with the Institute of Chemical Engineering, Bulgarian Academy of Sciences whose Director he was from 1993 till his retirement.

In 1978 Venko was awarded a PhD for the successful defence of his thesis: "Influence of some surface phenomena on mass transfer in liquid film flows". In 1996 he presented and defended his Doctor of Science Thesis "Kinetics and importance of mass transfer in some fermentation processes by free and immobilized biocatalysts", which summarized his research in the field of biochemical kinetics and biochemical reactors.

Venko has authored and co-authored two monographs, seven chapters in books (and encyclopedia) and 187 scientific articles published in international journals which have been cited more than 1200 times. His research achievements are highly recognized abroad and he has established, supported and actively participated in several efficient international collaborations with colleagues from Belgium, The United Kingdom, The Netherlands, Germany, Portugal, Italy, Hungary, Romania, Georgia, etc. which have spawned further networking.

In the years 1991/1992 Prof. Beschkov was appointed Deputy to the Minister of Environment of the Bulgarian Government. Besides the many duties and obligations during this period, the everyday administration of that challenging Ministry helped him to further expand his overview on the combination of science and environmental issues and gave him new ideas for modern scientific research.

We should, of course, not omit the fact that, as well as being an excellent researcher, Prof. Beschkov is a first-rate teacher and advisor - 29 MSc students and 13 PhD students have benefitted from his utter professionalism and dedicated work ethic, and are now pursuing a scientific carrier in Bulgaria and abroad.

Beschkov has been invited to deliver lectures at the universities in Louvain, Montreal, Hamburg-Harburg, Pretoria, etc., and as a plenary and key-note speaker in different congresses and conferences as well. Furthermore, he has presented different university courses in his area of expertise in the Faculties of Chemistry and Biology of the Sofia University and the University of Chemical Technology and Metallurgy in Sofia for more than thirty years.

Because of his scientific curiosity and open mind Venko has never been short of new ideas and shy of their practical application. His patents were recently recognized at the 9th International Invention Fair in the Middle East, Kuwait (2017), where they were awarded a silver and a bronze medal, respectively. His name is in the list of Honorable Inventors of the Bulgarian Patent Office Golden Book, and in 2014 Venko was awarded with the "Golden Coin of Letters" for science issued by the Club of the Bulgarian Scientific and Cultural Élite.

In 1996 Venko was elected an Editor in Chief of the Bulgarian Chemical Communications. Some of his characteristics that have shaped him as an outstanding scientist – perseverance, precision, practicality, action, tolerance to even the most outrageous views of colleagues and co-workers, and a wonderful sense of humor helped him immensely in turning the modest at that time "national" journal to the nowadays well recognized international journal with an Impact Factor.

Venko is also very actively involved in shaping the new avenues in chemical engineering in Bulgaria by participating in different National and international councils, committees, etc., and last but not least as serving as a Head of the Union of Chemists of Bulgaria for more than 8 years. His achievements, demonstrated strategic and leadership qualities are acknowledged and recognized by the Bulgarian Academy of Science and he was recently awarded the Honorary Sign "Marin Drinov" on ribbon.

Dear Venko, seventy years of age are just the present fifty... they mark a new beginning. So, enjoy

life, rock-and-roll and classical music, vacations and sight-seeing with your wonderful family and many other pursuits! Moreover that now you have some real quality time for research which you so much appreciate.

Many happy returns, and we, your former students, present colleagues and collaborators will be following and looking towards your new explorations and adventures in science – needless to say it will be worth it!

Prof. Dragomir Yankov

Prof. Roumiana Stateva

Professor Christo Boyadjiev's 80 years anniversary, 60 years in science



Professor Christo Boyadjiev was born on August 17, 1936. He graduated Higher Institute of Chemical Technology (Sofia) in 1960.

His overall inventive career is inextricably linked with the Institute of Chemical Engineering and its predecessors – the Mass Transfer Processes Department in the Institute of General and Inorganic Chemistry at the Bulgarian Academy of Sciences (1963-1972) and the Central Laboratory of Theoretical Foundations of Chemical Engineering (1972-1986).

In 1962 the young then Christo Boyadjiev after a competition starts working as a research associate in the Mass Transfer Processes Department at the Institute of General and Inorganic Chemistry. In 1963 he passed specialization in the Institute of Electrochemistry in the Soviet Academy of Sciences at the famous professor Benjamin Levich. He was highly motivated by his contact with such world-renowned scientist as Professor Levich from the school of Nobel laureate Academic Lev Landau and conducted researches on "The Effect of the Surfactants on the Hydrodynamics and Mass Transfer". In 1968 he defended his PhD dissertation entitled "The Influence of Surfactants on the Hydrodynamics and Mass Transfer in Laminar Films" at the Moscow Institute of Chemical Machinery Constructions.

The laid foundations for joint theoretical and experimental research with Prof. Levich and later with Prof. Krylov on "Hydrodynamics and mass transfer in liquid film flows" puts strong reflections on Prof. Boyadjiev's scientific researches. He continues them with his Ph.D. students. In 1978 he defended a dissertation on the same topic and received Doctor of Technical Sciences degree. The results are summarized in 39 scientific publications and two monographies "Mass Transfer in Liquid Film Flows", (Chr. Boyadjiev, V. Beschkov, Publ. House Bulg. Acad. Sci., Sofia, 1984) and "Массоперенос в движущихся пленках жидкости" (Хр. Бояджиев, В. Бешков, Изд. "Мир", Москва, 1988).

Along with these studies Prof. Boyadjiev, along with Prof. Krylov began intensive research on non-linear effects in mass transfer and became one of the

founders of the non-linear mass transfer theory. This theory is an outstanding contribution to the development of the mass transfer theory. It gives response of the nature of the observed deviations of the experimental data from the predictions of the linear mass transfer theory and explains their mechanism through the induction of secondary flows which are violating the hydrodynamic stability on the phase boundaries in gases and liquids and are changing the mass transfer kinetics. Unfortunately the early death of Professor Krylov, interrupts their joint work, but the results were published in a joint monography "Non-linear Mass Transfer", (Novosibirsk, 1996, in russian). Those studies however are continued by Prof. Boyadjiev and lead to the creation of a comprehensive non-linear mass transfer and hydrodynamic stability theory, presented in the monography "Non-Linear Mass Transfer and Hydrodynamic Stability", (Chr. B. Boyadjiev, V. N. Babak, ELSEVIER, 2000).

With the creation of the Central Laboratory on Theoretical Basis of Chemical Engineering and later the Institute of Chemical Engineering are created laboratories "Modeling and Optimization" and "Chemical Process System Engineering", whose longtime leader was Prof. Boyadjiev. This new "Processes systems engineering" research field begin to develop in Bulgaria almost parallel with his development in such leading countries like USA, UK, Switzerland and others. Methods for optimal design and / or management for modeling and simulation of chemical-technological systems, methods for energy integration and reconstruction of technological systems with continuous and batch processes, methods for multi-product and multi-process systems optimization are developed by collaborators of the laboratory, under the guidance of prof. Boyadjiev. Under his guidance are published over 40 scientific works. These basic studies are summarized in the monography "Основи на моделирането и симулирането в инженерната химия и химичната технология", (Хр. Бояджиев, ИИХ-БАН, София, 1993). Prof. Boyadjiev is a pioneer of Chemical Process Systems Engineering in Bulgaria. He set up his own school and his students taken their own path, to this day, are continuing the oriented research activities and are training the next generations young scientists.

In his 60 years creative path, Prof. Boyadjiev strived to use a new scientific method or approach

every 4-5 years. Thus in his publications a wide range of theoretical methods for modeling and simulation of processes and systems in the chemical industry are used. An overview of these methods and their application is presented in the monography, "Theoretical Chemical Engineering. Modeling and simulation ", (Christo Boyadjiev, SPRINGER - Verlag, Berlin Heidelberg, 2010). That monography presents methods for simple and complex processes modeling, methods of theoretical quantitative and qualitative models analysis, methods for analysis the stability of the models, methods for parameters identification in models and more.

His latest monography "Modeling of Column Apparatus Processes" presenting new methods for modeling of column apparatus is published in 2016,

(Christo Boyadjiev, Maria Doichinova, Boyan Boyadjiev, Petya Popova-Krumova,, SPRINGER - Verlag, Berlin Heidelberg , 2016).

For his overall contribution to the development of the chemical engineering science in Bulgaria, Professor Christo Boyadjiev was awarded with the Medal of Cyril and Methodius I class and for its contribution to the development of scientific research between Bulgaria and Russia was awarded with the Medal Mikhailo Lomonosov by the Russian Federation.

Of course much more can be said about the scientific achievements of Professor Christo Boyadjiev, but we will finish with the words:

Happy anniversary!

Prof. Natasha Bancheva

In vitro investigation of the antioxidant properties of *Cancer pagurus* hemocyanin

M. Mileva¹, Y. Raynova², I. Kindekov³, D. Krastev⁴, K. Idakieva^{2*}

¹The Stephan Angeloff Institute of Microbiology, Bulgarian Academy of Sciences, Acad. G. Bonchev Str. 26, Sofia 1113, Bulgaria

²Institute of Organic Chemistry with Centre of Phytochemistry, Bulgarian Academy of Sciences, Acad. G. Bonchev Str., Bl. 9, Sofia 1113, Bulgaria

³Scientific Laboratory of Radiation Protection, Radiobiology and Cell Radiobiology, Military Medical Academy, Sv. Georgi Sofijski Str. 3, Sofia 1606, Bulgaria

⁴Department of Anatomy and Histology, College of Medicine "Yordanka Filaretova", Yordanka Filaretova Str. 1, Sofia 1660, Bulgaria

Received May 17, 2016; Accepted June 2, 2016

Hemocyanins are copper-containing proteins in the hemolymph of many arthropods and mollusks, whose biological function is mainly related with the oxygen transport to the tissues. As components of marine food that is traditionally associated with a healthy diet, they are an interesting object for examination of their biological activity and pharmacological potential.

In the present study, the hemocyanin from the marine crab *Cancer pagurus* (CpH) was isolated and purified, and its antioxidant properties were *in vitro* investigated in prooxidant systems. Three radicals were used – superoxide, hydroxyl and 2,2-diphenyl-1-picrylhydrazyl (DPPH). The protection by CpH against oxidative damages of two model lipid membranes - rat liver supernatant and liposomal suspension in conditions of iron-induced lipid peroxidation was tested. CpH exhibited good DPPH and hydroxyl radicals scavenging activities in a concentration-dependent manner and a lower ability to capture superoxide radicals at a physiological value of pH. CpH showed very good capacity to inhibit Fe²⁺-induced lipid peroxidation in the examined systems, and chelating activity toward iron ions.

This study reveals that CpH has the ability to act as an iron chelating protein, and may provide protection against oxidative stress and decline in this way the risk of destruction of biomolecules, caused by initiation of harmful free radical-mediated chain reactions.

Keywords: *Cancer pagurus* hemocyanin, antioxidant properties, iron chelating activity

INTRODUCTION

In recent years researchers have investigated the potential of compounds in natural products, including sea food, that may possess bioactive properties, in particular, an antioxidant activity [1]. In conditions of rapid growth of the aquacultures industry, it is a challenge for scientists to utilize those valuable natural products and find novel substances, with leading biological function connected to their potential for antioxidant prevention and therapeutic applications. In particular, marine proteins have attracted a great deal of attention due to their potential effects in promoting health and reducing disease risk [1, 2]. A number of marine-derived compounds have been isolated and identified, and their therapeutic effects and pharmacological profiles characterized [3].

Hemocyanins (Hcs) are copper-containing proteins which act as oxygen carriers in the hemolymph of many molluscs and arthropods. In the latter, they exist as hexamers or multihexamers of subunits, e.g., 1×6, 2×6, 4×6, 6×6 or 8×6, depending on the species [4]. The subunits are ~75 kDa

polypeptides containing a copper pair active site, capable of binding an O₂ molecule. The increasing interest in Hcs is due to their important functions in hemolymph connected with the oxygen transport, and with the possibility for practical application in immunology. There are data showing that Hcs have good ability to modulate immune defense [5-7]. Hcs have been used for therapy of superficial bladder cancer and murine melanoma models [8, 9]. Recently, a potential anti-cancer effect of Hcs on a murine model of colon carcinoma was demonstrated, suggesting their use for immunotherapy of different types of cancer [10]. Many physiological and pharmacological functions have been reported for a variety of Hcs, but little is known about their antioxidant activity. Quite often good immunomodulators exhibit good antiradical and antioxidant properties. Thus, it was suggested that the radical-scavenging properties of Hc from marine snails *Rapana thomasiana* are the basis of its radioprotective effect in gamma induced acute radiation syndrome [11]. Very recently, for the first time, a detailed investigation on the antioxidant activity of molluscan Hc, namely the Hc of terrestrial snails *Helix aspersa* maxima, was published [12].

* To whom all correspondence should be sent:
E-mail: idakieva@orgchm.bas.bg

The only scientific report concerning the antioxidant activity of arthropodan Hc is that of Queinnec *et al.* [13]. In order to determine the antioxidant activity of Hc isolated from scorpion *Androctonus australis*, the authors have investigated the kinetics of superoxide anion decays using pulse radiolysis.

The marine crab *Cancer pagurus* (Linnaeus, 1758) (Crustacea, Decapoda, Brachyura), commonly known as an edible crab or brown crab, is the commercially most important crab species in Western Europe. The molecule of Hc isolated from *Cancer pagurus* (CpH) is composed of four immunologically distinct ~75 kDa subunits forming 2-hexameric structures [14]. It has been reported that the CpH possesses intrinsic and inducible *o*-diphenoloxidase activity [15, 16].

In the present study, the Hc from the marine crab *Cancer pagurus*, originating from the Black Sea, was isolated and purified, and its antioxidant properties were *in vitro* investigated in some prooxidant model systems.

EXPERIMENTAL

Reagents

Sephacryl S-300 was purchased from Fluka AG. Superoxide dismutase (SOD) from bovine erythrocytes and nitro blue tetrazolium (NBT) were supplied by Sigma–Aldrich Chemie GmbH. All other chemicals used were of analytical grade.

Isolation and purification of hemocyanin

The CpH was isolated according to the procedure described in [15]. Briefly, the native CpH was obtained from the hemolymph, collected from the species *Cancer pagurus* by ultracentrifugation at 180 000 g (ultracentrifuge Beckman LM-80, rotor Ti 45) for 4 h at 4 °C. The pellets were resuspended in stabilized buffer (50 mM Tris-HCl, containing 10 mM CaCl₂, 10 mM MgCl₂, and 100 mM NaCl, pH 7.2) and CpH was purified by gel filtration chromatography on a Sephacryl S-300 column (80 × 1.6 cm), equilibrated and eluted with the stabilized buffer. The purity of the isolated CpH was controlled by 7.5 % SDS-PAGE. The concentration of protein was determined spectrophotometrically using the specific absorption coefficient $A_{278}^{0.1\%} = 1.265 \text{ ml}\cdot\text{mg}^{-1}\cdot\text{cm}^{-1}$ for CpH.

Extraction of liposomes and preparation of liver supernatant

Liposomal suspension was obtained from phospholipids of egg yolk as described in [17]. After evaporation under vacuum, the chloroform fraction was dissolved in 50 mM K-Na phosphate buffer, pH 7.4, to a final concentration of 2 mg lipid·ml⁻¹.

Wistar rats (180-200 g) were used for preparation of the liver supernatant. Livers were washed *in situ* with ice-cold 1.15% KCl. After homogenization in PBS at a ratio tissue: PBS = 1:3 (w/v) and centrifugation (10 min, 5000 rpm) the supernatant was used as a working medium, containing 2 mg·ml⁻¹ protein.

Estimation of antioxidant activity

Antioxidant activity in the liposomal suspension and in the liver supernatant was determined by formation of endogenous lipid peroxidation products, reacting with 2-thiobarbituric acid (TBARS), and detected spectrophotometrically ($\lambda_{\text{max}} = 532 \text{ nm}$) according to [18]. The induction of lipid peroxidation was initiated by adding 50 μl Fe²⁺ to a final concentration of 1 mmol·l⁻¹. Each sample contained 1 ml supernatant and 0.8 ml PBS to a final concentration of 2 mg·l⁻¹ protein (or 1.8 ml liposomal suspension with concentration of 1 mg lipid·l⁻¹), 50 μl of 2.1 mmol·l⁻¹ ascorbate and 100 μl solution of CpH to achieve concentrations of 10⁻³ – 10⁻⁵ mol·l⁻¹. The amount of TBARS generated in the system was determined after incubation for 30 min at 37 °C. The activity of CpH was compared to the activity of Trolox as a hydrosoluble analogue of tocopherol, known as chain breaking antioxidant, at the same concentrations. The ratio of the absorption at 560 nm for the sample containing the tested substances in different concentrations and the same absorption for the controls (without CpH or Trolox) in percentage is called antioxidant activity (AOA, %). The experiments were performed in triplicate.

Superoxide - scavenging assay

The generation of reactive oxygen species (ROS) in the model system xanthine-xanthine oxidase (XO) and the changes occurring upon the CpH were investigated photometrically by the NBT test. The detailed procedure has been described elsewhere [18]. Briefly, spectrophotometric registration of O₂^{•-} was carried out by measuring the amount of formazan which is generated upon O₂^{•-} induced reduction of NBT. The decrease of absorbance in presence of antioxidants indicates the consumption of superoxide anion in the reaction mixture. Data are calculated in percentage as spectrophotometric scavenger index (SpSI) - the ratio of the absorption at 560 nm for the sample with CpH, and the same absorption for the control (without CpH).

DPPH - scavenging assay

The antioxidant activity using the DPPH assay was measured by modifying the method of Blois [19]. An ethanolic solution of DPPH (100 mM) was

incubated with CpH in the applied concentrations, and the optical density (OD) was monitored spectrophotometrically at $\lambda 517$ nm, after 30 min of incubation. Inhibition of DPPH in percentage (I, %) was calculated as given below:

$$I, \% = [(OD \text{ control} - OD \text{ sample}) / (OD \text{ control})] \times 100$$

Hydroxyl radical scavenging assay

Scavenging of the hydroxyl radicals ($HO\bullet$) generated by the ascorbic acid/ Fe^{3+}/H_2O_2 system was used. The reaction mixture contained 0.3 mM 2-deoxy D-ribose, 0.5 mM H_2O_2 , 50 μM Fe^{3+} and 52 μM EDTA without or with CpH in PBS, pH 7.4. The reaction was triggered by the addition of 50 μM ascorbate and the mixture was incubated at 37 °C for 30 min. Solutions of $FeCl_3$, ascorbate and H_2O_2 were made up in ultra pure water immediately before use. The extent of deoxyribose degradation by $HO\bullet$ was measured with the TBA test [20]. Percentage inhibition of deoxyribose degradation was calculated as DI, %.

Metal chelation ability

Iron chelation ability was determined by adding 200 μM of $FeCl_2$ to CpH in PBS, pH 7.4 (protein concentration 5 mg/ml). After incubation at room temperature for 10 min, absorption spectra were recorded. The chelation of iron ions by CpH was evaluated by monitoring the spectral shift after incubation [21].

Statistics

The results were expressed as mean \pm SE. Data were analyzed by the program Statistica for Windows and using Student's t-test. The results were accepted as statistically significant when $p < 0.05$.

RESULTS

The isolation and purification of Hc from the hemolymph of *Cancer pagurus* yielded a pure protein preparation, as assessed by gel filtration chromatography and SDS-PAGE (Fig. 1A). SDS-PAGE confirmed the presence of Hc subunits with a molecular mass of ~ 75 kDa (Fig. 1B). The ratio OD 340 nm/OD 280 nm = 0.2, found for the peak fractions of CpH is typical for fully oxygenated Hc and indicates that the protein is isolated with preserved active sites.

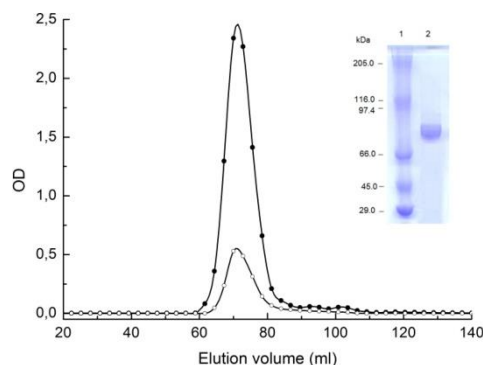


Fig. 1. A. Gel filtration chromatography of CpH, isolated from the hemolymph of *Cancer pagurus*, on a Sephacryl S-300 column (80 \times 1.6 cm), equilibrated and eluted with the stabilized buffer, at a flow rate of 0.3 ml/min. (—) OD at 280 nm, (---) OD at 345 nm. B. SDS-PAGE on 7.5% running gel: lane 1, protein markers (from the top): myosin (205.0 kDa), β -galactosidase (116.0 kDa), phosphorylase b (97.4 kDa), albumin (66.0kDa), ovalbumin (45.0 kDa), carbonic anhydrase (29.0 kDa) (Merck); lane 2, purified CpH (subunit).

The effect of CpH on Fe^{2+} -induced lipid peroxidation in liposomal system, as well as in liver supernatant, was measured by the TBARS test. Results are expressed as percentage of inhibition of the oxidation process in comparison to the control sample (without CpH or Trolox) in which the oxidation is assumed to proceed as much as possible. Lower AOA value means higher AOA. Figure 2A shows the results of Fe^{2+} -induced oxidation of an aqueous emulsion system of egg liposomes as an AOA test. On Figure 2B the results of the AOA of CpH in terms of Fe^{2+} -induced oxidation, in a system of mice liver supernatant, are shown. In both systems CpH showed an efficient dose-dependent inhibition of lipid peroxidation. Control experiments indicated that CpH did not affect the level of TBARS without creating of prooxidant conditions (data not shown). The results obtained reveal that the CpH has a potential to inhibit the oxidative processes in a slightly lower degree than Trolox.

Metal-mediated formation of free radicals may cause various modifications to DNA bases, as well as enhance lipid peroxidation. Because elemental species, such as the ferrous ion (Fe^{2+}), can facilitate the production of ROS, the ability of substances to chelate iron can be a valuable antioxidant property. Bound to CpH, iron is less susceptible to participation in the Fenton reaction. Our results demonstrated that CpH possesses ability to chelate iron ions. The absorption spectrum of CpH showed characteristic for Hcs bands at 280 and 340 nm, corresponding to aromatic residues and $Cu^{II}-O_2^{2-}$ -

Cu^{II} complexes at the active sites, respectively. Metal ions caused a spectral shift and absorbance change at 340 nm (Fig. 3). Data shown on Fig. 3 reveal that the ability of CpH to act as a peroxidation inhibitor may be related to its iron binding capacity.

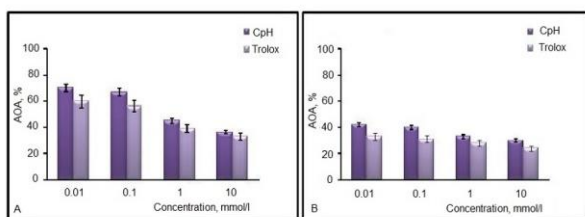


Fig. 2. Lipid peroxidation inhibitor ability of CpH in systems of egg liposomes (2A) and rat liver supernatant (2B). The ratio of the absorption at 560 nm for samples containing CpH in different concentrations and the same absorption for the controls (without CpH or Trolox) in percentage expresses the antioxidant activity (AOA).

The DPPH radical was one of the few stable radical sources and was widely used to test the free radical-scavenging ability of various samples. A freshly prepared DPPH solution exhibited a deep purple color with a maximum absorption at 517 nm. This purple color disappears when an antioxidant is present in the medium. Our results showed that CpH can quench DPPH free radicals and convert them to a colorless product, resulting in a decrease of absorbance at 517 nm. The scavenging activity of CpH was expressed as I (%). Based on the results in Table 1, there is a significant decrease ($p < 0.01$) in the concentration of DPPH radicals due to the scavenging ability of CpH.

Superoxide is an oxygen-centered radical which can generate more dangerous species and promote oxidative reactions due to its ability to reduce transition metals, release protein-bound metals and form perhydroxyl radicals which initiate lipid oxidation [20]. The generation of superoxide in the model system xanthine-xanthine oxidase and the changes occurring upon CpH were investigated spectrophotometrically by the NBT test. The decrease of absorbance in presence of CpH indicated the consumption of superoxide anion in the reaction mixture. Data were calculated in percentage as

Table 1. Antioxidant capacity of different concentrations of CpH (0.01 – 10 nmol.l⁻¹). The ability of CpH to scavenge DPPH radicals is presented in percentage (I, %). Data for the superoxide scavenging activity are presented as spectrophotometric scavenger index (SpSI). Percentage inhibition of deoxyribose degradation was calculated as DI, %.

CpH, [mmol.l ⁻¹]	I, [%]	SpSI, [%]	DI, [%]
0	100	100	100
0.01	68.2 ± 10.1**	96.6 ± 6.6	94.36 ± 8.12*
0.1	52.8 ± 9.1*	94.7 ± 5.4	93.02 ± 7.33
1.0	45.3 ± 8.7*	91.5 ± 7.1*	62.66 ± 6.37**
10	31.5 ± 7.2*	88.3 ± 7.5**	53.18 ± 4.24**

**p < 0.001 versus control; *p < 0.05 versus control

spectrophotometric scavenger index (SpSI) - the ratio of the absorption at 560 nm for the sample with CpH, and the same absorption for the controls (without CpH). From the results given in Table 1 it can be seen that CpH slightly inhibits the generation of superoxide anions in the system applied.

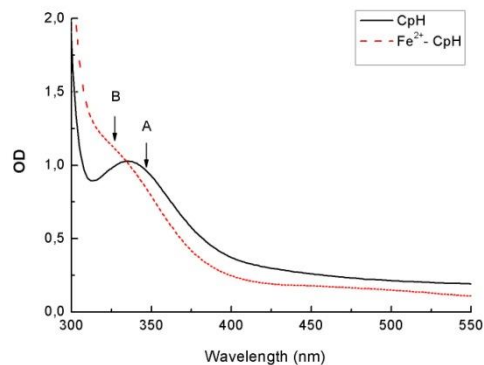


Fig. 3. Absorption spectra of CpH (A) and Fe²⁺-CpH complex (B) in PBS buffer, pH 7.4.

Hydroxyl radical (OH•) is the most reactive among oxygen species. The statistically treated results for the scavenging activity of OH• radicals of CpH are shown in Table 1. The results are expressed in percentage of inhibition of hydroxyl radical-induced deoxyribose degradation (DI). They reveal that the OH• radical scavenging activity of the tested compound increases in a concentration-dependent manner.

DISCUSSION

In this work we investigated the antioxidative profile of the copper-containing protein CpH in some model systems. In general, antioxidant compounds can interact with free radicals, to scavenge them, removing catalytic metal ions, and inhibit or retard the process of lipid peroxidation [22]. Antioxidant power of natural products can manifest itself through prevention the degradation of biomembranes by oxidants in different ways, including the possibility to express capacity of defense from the action of the free radicals [23-26].

Although peroxidation in model membranes may be very different from peroxidation in cell membranes, the results obtained in model membranes may be used to advance understanding of peroxidation in biological membranes [26].

Lipids such as free and ester forms of polyunsaturated fatty acids are vulnerable targets of free radicals. Liposomal system and rat liver homogenate are usually used as model systems to evaluate the antioxidant activities of compounds on lipid peroxidation. It is known that transition metal ions are involved in both initiation and propagation of lipid peroxidation. In this system, we found that CpH effectively inhibited ferrous ion-induced lipid peroxidation (Figures 2A, B). Ferrous chelation may render important antioxidative effects by retarding metal-catalysed oxidation [20].

The DPPH radical scavenging test is a sensitive antioxidant assay and depends of substrate polarity. CpH shows good ability to reduce the stable radical DPPH (Table 1). Undoubtedly, the DPPH test provides very important evidence of the antioxidant profile of the tested substances, but often this radical has little relevance to be present in biological systems [25, 26].

Hydroxyl radicals can be formed from superoxide anion and hydrogen peroxide in the presence of metal ions, such as iron or copper. Hydroxyl radicals could damage important biomolecules such as proteins, DNA, polyunsaturated fatty acids, nucleic acids and almost all biological membranes. Therefore, removal of hydroxyl radicals is one of the most effective defenses of a living body against various diseases. Our studies showed that CpH is a good scavenger of hydroxyl radicals (Table 1).

The fact that CpH possesses some antioxidant activities could be connected with the biological protective role of this protein. Reactive oxygen components are often generated under aerobic conditions. Hypoxia is known as a condition for generation of superoxide radicals [20]. Aquatic organisms routinely experience fluctuations in oxygen levels. In response to hypoxia exposure of *Cancer magister*, the concentration of respiratory pigment Hc significantly increased in hypoxic crabs. On the other hand, total oxy-Hc was significantly higher in crabs that had been exposed to hypoxic conditions [27]. Due to the high affinity to oxygen, several Hcs subunits play an important role as a regulator for oxidative homeostasis [11]. The beneficial effects of antioxidant marine bioactive peptides are well known in scavenging ROS and free radicals or in preventing oxidative damage. It is not surprising that proteins, such as CpH, can inhibit the

lipid oxidation by biologically designed mechanisms (e.g. antioxidant enzymes and iron-binding proteins) or by nonspecific mechanisms [1, 2].

Proteins have excellent potential as antioxidant additives in foods because they can inhibit lipid oxidation through multiple pathways including inactivation of ROS, scavenging free radicals, chelation of prooxidative transition metals [24]. A protein's overall antioxidant activity can probably occur by disruption of its tertiary structure to increase the solvent accessibility of amino acid residues so that they can scavenge free radicals and chelate prooxidative metals [28]. Considering the destructive effect of lipid peroxidation processes in several disease conditions, the ability of CpH to inhibit peroxidation could perhaps partly constitute the basis for the pharmacological reasons for its implementing.

In conclusion, the present study elucidates the antioxidant activity of CpH. This work verifies that CpH is a natural antioxidant against lipid peroxidation in rat liver supernatant, as well as in the liposomal system. Its antioxidant activities are primarily attributed not only to its free radical scavenging actions, but also to iron ion chelation ability. It will be interesting to further investigate the effect of CpH on various radical-mediated injury models *in vivo*. CpH can be incorporated into lipid-containing foods as an antioxidant to minimize free radical-mediated lipid peroxidation. It can also be used as an alternative to conventional drugs for treating human diseases associated with free radical-mediated tissue damage. However, such usage must be adequately justified by animal and clinical studies, creating a need for further research.

REFERENCES

1. D. H. Ngo, T. Vo, D. N. Ngo, I. Wijesekara, S. Kim, *Int. J. Biol. Macromol.*, **51**, 378 (2012).
2. D. Nair, R. Weiskirchen, S. Al-Musharafi, *Acta Pharmacol. Sin.*, **36**, 158 (2015).
3. I. Sheih, T. Wub, T. Fang, *Bioresearch Technologies*, **100**, 3419 (2009).
4. K. E. van Holde, K.I. Miller, *Adv. Protein Chem.*, **47**, 1 (1995).
5. J. R. Harris, J. Markl, *Micron*, **30**, 597 (1999).
6. A. Tchorbanov, K. Idakieva, N. Mihaylova, L. Doumanova, *Int. Immunopharmacol.*, **8**, 1033 (2008).
7. V. Gesheva, S. Chausheva, N. Stefanova, N. Mihaylova, L. Doumanova, K. Idakieva, A. Tchorbanov, *Int. Immunopharmacol.*, **26**, 162 (2015).
8. C. D. Jurincic, U. Engelmann, J. Gasch, K. F. Klippel, *J. Urol.*, **139**, 723 (1988).
9. D. Rizvi, R. Riggs, B. J. Jackson, D. W. McFadden, *Am. J. Surg.* **194**, 628 (2007).

10. V. Gesheva, S. Chausheva, N. Mihaylova, I. Manoylov, Doumanova, K. Idakieva, A. Tchorbakov, *BMC Immunol.*, **15**, 33 (2014).
11. Kindekov, M. Mileva, D. Krastev, V. Vassilieva, Y. Raynova, L. Doumanova, M. Aljakov, K. Idakieva, *Biotechnol. Biotec. Eq.*, **28**, 533(2014).
12. Y. Raynova, A. Marchev, L. Doumanova, A. Pavlov, K. Idakieva, *Acta Microbiol. Bulgarica*, **31**, 127 (2015).
13. E. Queinnec, M. Gardès-Albert, M. Goyffon, C. Ferradini, M. Vuillaume, *Biochim. Biophys. Acta*, **1041**, 153 (1999).
14. D. Rochu, J. M. Fine, *Comp. Biochem. Physiol. B*, **77**, 333 (1984).
15. Y. Raynova, K. Idakieva, L. Doumanova, *Compt. Rend. Acad. Bulg. Sci.*, **65**, 347 (2012).
16. K. Idakieva, Y. Raynova, F. Meersman, C. Gielen, *Comp. Biochem. Physiol. B*, **164**, 201 (2013).
17. J. Folch, M. Lees, C. Shoane-Stoaley, *J. Biol. Chem.*, **226**, 497 (1957).
18. M. Mileva, V. Hadjimitova, L. Tantcheva, T. Traykov, A. S. Galabov, V. Savov, St. Ribarov, *Z. Naturforsch.*, **55**, 824 (2000).
19. M. Blois, *Nature*, **181**, 1199 (1958).
20. B. Halliwell, J. Gutteridge, *J. FEBS Letter*, **128**, 347 (1981).
21. A. Rahman, S. Shahabuddin, J. Parish, *Carcinogenesis*, **11**, 2001 (1990).
22. B. Halliwell, J. Gutteridge, in: *Free Radicals in Biology and Medicine*, 4th edition, Oxford University Press, 2007.
23. E. Schnitzer, I. Pinchuk, D. Lichtenberg, *Eur. Biophys. J.*, **36**, 499 (2007).
24. S. Sakanaka, Y. Tachibana, *Food Chem.*, **95**, 343 (2006).
25. N. Deighton, R. Brennan, Ch. Finn, H. Davies, *J. Sci. Food Agricult.*, **80**, 1307 (2000).
26. M. Sherrya, C. Charcosset, H. Fessib, H. Greige-Gerges, *J. Liposome Res.*, **23**, 268 (2013).
27. M. Brouwer, P. Larkin, N. Brown-Peterson, C. King, S. Manning, N. Denslow, *J. Exp. Marine Biol. Ecol.*, **386**, 77 (2010).
28. I. Sheikh, T. Wub, T. Fang, *Biores. Technol.*, **100**, 3419 (2009).

ИН ВИТРО ИЗСЛЕДВАНЕ НА АНТИОКСИДАНТНИТЕ СВОЙСТВА НА ХЕМОЦИАНИН ОТ РАК CANCER PAGURUS

М. Милева¹, Ю. Райнова², Ив. Киндеков³, Д. Кръстев⁴, К. Идакиева²

¹Институт по микробиология „Стефан Ангелов“, Българска академия на науките, ул. Акад. Г. Бончев 26, 1113 София, България

²Институт по органична химия с Център по фитохимия, Българска академия на науките, ул. Акад. Г. Бончев, бл. 9, 1113 София, България

³Научна лаборатория по радиационна защита, радиобиология и клетъчна радиобиология, Военно-медицинска академия, ул. Георги Софийски 3, 1606 София, България

⁴Департамент по анатомия и хистология, Медицински колеж „Йорданка Филаретова“, ул. Йорданка Филаретова 1, 1660 София, България

Постъпила на 17 май, 2016 г.; приета на 2 юни, 2016 г.

(Резюме)

Хемоцианините са мед-съдържащи протеини в хемолимфата на много членестоноги и мекотели, чиято биологична функция е основно свързана с транспортирането на кислород до тъканите. Като компонент на морската храна, която традиционно се свързва със здравословна диета, те са интересен обект за изследване на тяхната биологична активност и фармакологичен потенциал.

В настоящото изследване, хемоцианин от морски рак *Cancer pagurus* (СрН) е изолиран и пречистен, и са изследвани неговите антиоксидантни свойства ин витро. Използвани са три радикала - супероксиден, хидроксилен и 2,2-diphenyl-1-picrylhydrazyl (DPPH). Тестван е защитния ефект на СрН срещу окислително увреждане при две моделни липидни мембрани – чернодробен супернатант от плъх и липозомна суспензия, в условията на желязо-индуцирана липидна пероксидация. СрН показват добра радикал улавяща активност по отношение на DPPH и хидроксилни радикали и по-ниска способност за улавяне на супероксидни радикали, при физиологична стойност на рН. СрН показва много добра способност да инхибира Fe²⁺-индуцирана липидна пероксидация в приложените системи, и хелатираща активност към желязни йони.

Това изследване показва, че СрН има способността да хелатира метални йони, както и да осигури защита срещу оксидативен стрес и по този начин да намали риска от разрушаване на биомолекули, причинено от свободните радикали.

Study on the synthesis of 2,3,4,6-*O*-tetraacetyl- α -D-glucopyranosyl bromide

G.L. Huang*, H. Gao, C. Yi, D. Huang, J. Han

College of Chemistry, Chongqing Normal University, Chongqing, 401331, China

Received April 8, 2016; Revised July 17, 2016

2, 3, 4, 6-*O*-Tetraacetyl- α -D-glucopyranosyl bromide **3** is widely used as an intermediate for the synthesis of sugar esters. Red phosphorus and bromine were reacted in glacial acetic acid to generate phosphorus tribromide. Then glucose pentaacetate and phosphorus tribromide were reacted to provide compound **3**. The yield of product obtained was 83.5%. ^1H NMR and ^{13}C NMR were used to confirm the structure of 2, 3, 4, 6-*O*-tetraacetyl- α -D-glucopyranosyl bromide **3**.

Keywords: 2,3,4,6-*O*-tetraacetyl- α -D-glucopyranosyl bromide, synthesis, optimization.

INTRODUCTION

Studies on the modification of sugars and their derivatives to leading drugs have become an active field in the research and development of new drugs. The brominated derivatives of sugars are important intermediates, which can be used to synthesize sugar-containing drugs and biochemical reagents of sugars. Based on the intermediates of sugar-brominated derivatives, other carbohydrate derivatives with biological and pharmacological functions can be further synthesized [1,2]. Herein, the synthesis of 2,3,4,6-*O*-tetraacetyl- α -D-glucopyranosyl bromide **3** was investigated.

RESULTS AND DISCUSSION

In order to prepare α -D-glucose pentaacetate, the catalysts mainly used are proton acids, Lewis acids, solid acids, and enzymes. The traditional homogeneous catalysts have low phase diffusion resistance, are easy to control and conveniently operated in the catalytic process, but the selectivity of the reactions and the yields of the products need to be further improved. Moreover, the homogeneous catalysts are not easy to reuse. In heterogeneous catalysis, solid acid catalysts have high selectivity and yields, but the preparation process of catalysts is complex. So, it is of very high importance to develop simple and effective catalysts with high catalytic activity and selectivity, to improve the yield of a single configuration, and to reduce the production costs [3]. Herein, glucose pentaacetate **2** was synthesized by esterification of glucose **1** and acetic anhydride, using pyridine as a catalyst (Fig. 1). The molar ratio of glucose and acetic anhydride was 1:26, the dosage of catalyst was 13 times the glucose mass, the reaction time was 20 h at room temperature, the esterification yield of glucose and acetic anhydride was up to 98%. The molar ratio of

α -glucose pentaacetate and β -glucose pentaacetate was 3:1.

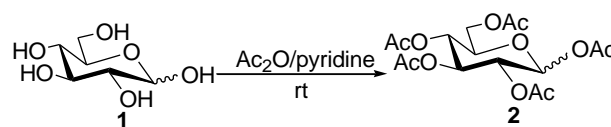


Fig. 1. Synthesis of glucose pentaacetate **2**.

The system temperature is too high to be easily reached by the decomposition of 2,3,4,6-*O*-tetraacetyl- α -D-glucopyranosyl bromide **3**, which affects the final yield and purity of product. The bromination reaction is carried out at room temperature.

The reaction time has a great influence on the product yield. Short reaction time greatly reduced the yield of product. But long reaction time also caused the yield to decrease. This is due to the fact that the stability of 2,3,4,6-*O*-tetraacetyl- α -D-glucopyranosyl bromide **3** is not high: the bromide **3** is easily decomposed by light or heat. It was proven that the optimum reaction time is 3 h.

1,2,3,4,6-Penta-*O*-acetyl-(α,β)-D-glucopyranose **2** was reacted with phosphorus tribromide. After stirring for 3 h at room temperature, 2,3,4,6-*O*-tetraacetyl- α -D-glucopyranosyl bromide **3** was obtained in a yield of 83.5% (Fig. 2).

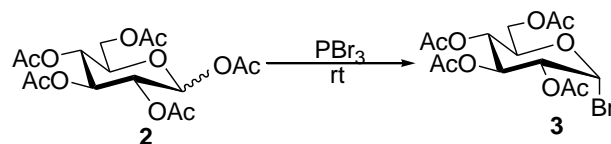


Fig. 2. Synthesis of 2,3,4,6-*O*-tetraacetyl- α -D-glucopyranosyl bromide **3**.

* To whom all correspondence should be sent:
E-mai: huangdoctor226@163.com

EXPERIMENTAL

General

^{13}C and ^1H NMR spectra were recorded using a Bruker DPX-300 spectrometer at 75 and 300 MHz, respectively. Mass spectra were recorded with a VG PLATFORM mass spectrometer using the ESI mode. TLC was performed on silica gel plates (GF₂₅₄) with detection by UV light or by charring with 10% H₂SO₄ in EtOH.

Synthesis of D-glucose pentaacetate 2

70 mL of acetic anhydride was added to a flask and was carefully mixed with 5 g of D-glucose **1**. While stirring with a magnetic stirrer, anhydrous pyridine (70 mL) was added. This mixture was kept at room temperature under stirring for 20 h. When the reaction was completed, the solution was mixed with ice and was stirred until all ice melted. The filtered product was recrystallized in a solution of water/methanol (v/v=1/2). Yield: 98%; ^{13}C NMR (75 MHz, CDCl₃): δ 170.7, 170.5, 170.2, 169.3, 167.3 (5 \times C=O), 92.0 (C-1 β), 89.8 (C-1 α), 68.8 (C-5), 67.6 (C-3 and C-4), 66.7 (C-2), 61.5 (C-6), 21.2, 21.0, 20.9, 20.8, 20.7 (5 \times C(O)CH₃); ^1H NMR (300 MHz, CDCl₃): δ 6.33 (d, 1H α , $J_{1,2}$ 1.5 Hz, H-1 α), 5.64 (d, 1H β , $J_{1,2}$ 1.5 Hz, H-1 β), 5.45 (dd, 1H, $J_{3,4}$ < 1.0 Hz, $J_{4,5}$ 1.3 Hz, H-4), 5.34-5.28 (m, 2H, H-2, H-3), 4.30 (dt, 1H, $J_{5,6}$ 6.5 Hz, H-5), 4.16-4.01 (m, 2H, H-6a, H-6b), 2.13, 2.09, 2.00, 1.99, 1.97, 1.96 (all s, 15H, 10 \times C(O)CH₃); ESI-MS: m/z =413.3 [M+Na]⁺.

Preparation of phosphorus tribromide

1.5 g of red phosphorus was suspended in 15 mL of glacial acetic acid, mixed and cooled in ice water bath to 4 °C. 3 mL of bromine was dropwise added to the above solution. After dropping, the temperature was maintained at 20 °C and the reaction mixture was stirred for 1 h, then the insoluble solid was filtered out. The filtrate was phosphorus tribromide, which was sealed for storage at low temperature.

Synthesis of 2,3,4,6-O-tetraacetyl- α -D-glucopyranosyl bromide 3

1.75 g (4.5mmol) of D-glucose pentaacetate **2** and 5 mL of phosphorus tribromide were added into a 25 mL flask, and the reaction mixture was stirred at room temperature for 3 h. Then 25 mL of chloroform was added, and washed with ice water (100 mL \times 2), saturated sodium hydrogen carbonate solution, and water. The liquid was separated, and the chloroform layer was dried with anhydrous magnesium sulfate. After filtering, the filtrate was

decompressed and concentrated, giving a light yellow syrup. The syrup was dissolved in diethyl ether under heating, then iced for 24 h. After filtering, 1.5 g of white solid was obtained. The yield was 83.5%. ^{13}C NMR (75 MHz, CDCl₃): δ 167.1 (4 \times C=O), 88.1 (C-1), 70.9 (C-5), 67.8, 67.1 (C-3/C-4), 66.8 (C-2), 60.9 (C-6), 21.0, 20.7 (4 \times C(O)CH₃); ^1H NMR (300 MHz, CDCl₃): δ 6.68 (d, 1H, $J_{1,2}$ 3.5 Hz, H-1), 5.49 (dd, 1H, $J_{3,4}$ 3.1 Hz, $J_{4,5}$ 1.1 Hz, H-4), 5.38 (dd, 1H, $J_{2,3}$ 10.2 Hz, H-3), 5.02 (dd, 1H, H-2), 4.46 (m, 1H, H-5), 4.17 (dd, 1H, $J_{6a,6b}$ 11.3 Hz, $J_{5,6}$ 5.8 Hz, H-6a), 4.01 (dd, 1H, $J_{5,6b}$ 6.6 Hz, H-6b), 2.14, 2.11, 2.05, 2.01 (all s, 12H, 4 \times C(O)CH₃).

CONCLUSIONS

2,3,4,6-O-Tetraacetyl- α -D-glucopyranosyl bromide **3** is easily removed the hydroxyl protection. It is often used for structure modification of drugs to increase the polarity of drug, reduce the toxic effects, and improve drug activity [1]. So, compound **3** has been widely used as an intermediate to modify drugs. However, due to the instability of 2,3,4,6-O-tetraacetyl- α -D-glucopyranosyl bromide **3**, its application has been limited. Therefore, the development of a more rapid, more concise, and more effective synthesis method for improving the application of compound **3** is of great importance. Herein, using phosphorus tribromide as bromide reagent, 2,3,4,6-O-tetraacetyl- α -D-glucopyranosyl bromide **3** was obtained by reaction at room temperature for 3 h with high yield (83.5%).

Acknowledgements: The Project Sponsored by the Scientific Research Foundation for the Returned Overseas Chinese Scholars, State Education Ministry. The work was also supported by Foundation Project of Chongqing Normal University (No. 14XYY020), Chongqing Research Program of Basic Research and Frontier Technology (No. cstc2015jcyjA10054), Chongqing Postgraduate's Research and Innovation Project (No. CYS15153), Open Foundation Project of Engineering Research Center for Bioactive Substances (No. AS201614), and Chongqing University Students' Training Project of Innovation & Undertaking (No. 201610637076), China.

REFERENCES

1. G. Huang, X. Mei, *Current Drug Targets*, **15**(8), 780 (2014).
2. G. Huang, X. Zhang, M. Li, P. Li, D. Luo, Z. Liu *Current Organic Synthesis*, **11**(6), 874 (2014).
3. G. Huang, Q. Tang, D. Li, Y. Huang, D. Zhang, *Current Organic Synthesis*, **13**(1), 82 (2016).

ИЗСЛЕДВАНЕ НА СИНТЕЗАТА НА 2,3,4,6-О-ТЕТРААЦЕТИЛ- α -D-ГЛЮКОПИРАНОЗИЛ БРОМИД

Г. Л. Хуанг, Х. Гао, С. Йи, Д. Хуанг, Дж. Хан

Колеж по химия, Университет Чонгкин, Чонгкин, 401331, Китай

Постъпила на 8 април, 2016 г.; коригирана на 17 юли, 2016 г.

(Резюме)

Съединението 2, 3, 4, 6-О-тетраацетил- α -D-глюкопиранозил бромид **3** се използва широко като междинно съединение при синтезата на захарни естери. Червен фосфор и бром реагират в ледена оцетна киселина за получаването на фосфорен трибромид. След това глюкозо-пентаацетат реагира с фосфорния бромид за получаването на съединението **3**. Добивът на получения продукт бе 83.5%. Използвани са ЯМР-методите ^1H NMR и ^{13}C NMR за да се потвърди структурата 2, 3, 4, 6-О-тетраацетил- α -D-глюкопиранозил бромид **3**.

Sorptive removal of Direct Blue-15 dye from water using *Camellia sinensis* and *Carica papaya* leaves

R. Rehman¹, T. Mahmud¹, R. Ejaz¹, A. Rauf¹, L. Mitu^{2*}

¹Institute of Chemistry, University of the Punjab, Lahore-54590, Pakistan

²Department of Chemistry, University of Pitesti, Pitesti-110040, Romania

Received February 2, 2016; Accepted May 4, 2016

Water treatment by an adsorption method is being evolved in recent years. In this work, the effectiveness of removing direct blue 15 dye from aqueous medium by two adsorbents, viz., *Camellia sinensis* (tea) and *Carica papaya* (papaya) leaves was evaluated and compared on a batch scale. Various parameters affecting the biosorption efficiency were optimized and then applied for Langmuir isothermal modeling of equilibrium data. Characterization of *Camellia sinensis* and *Carica papaya* was done by using FT-IR. The results showed that the *Camellia sinensis* waste was more effective and removed 90.9 mg/g of Direct Blue 15 as compared to *Carica papaya* leaves, which removed only 3.98 mg/g of this dye under optimized operational conditions. Hence, *Camellia sinensis* waste was superior to *Carica papaya* leaves for removing Direct Blue 15 dye from waste water.

Keywords: *Camellia sinensis*, *Carica papaya* leaves, Direct Blue-15 dye, Adsorption, Langmuir isotherm.

INTRODUCTION

Water pollution caused by dyes and other organic pollutants is severely increasing due to rapid flourishing of industrialization and advancement in research, which develops toxic dyeing agents [1]. Waste water coming from leather, printing, dyeing, textile, cosmetics, food coloring and paper-making industries contains a large amount of such hazardous pollutants [2-4]. They can be accumulated in surface water leading to pollution of drinking water sources. The present research work describes the removal of direct blue 15 dye from water. It is an anionic diazo direct dye. It exists as deep purple to dark blue microcrystalline powder and decomposes in air. It is soluble in water (60 g/l at 85°C) and insoluble in most organic solvents. It is also called direct sky blue A and direct sky blue 5B. Its structural formula is given in Fig. (1) [5].

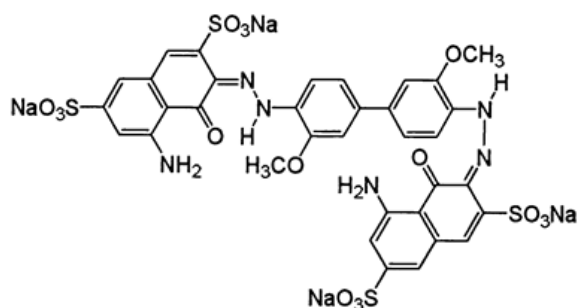


Fig. 1. Direct blue 15 dye

It has strong affinity to cellulose fibers and is thus employed in textile industries. When heated, it emits poisonous fumes of SO_x, NO_x and CO_x which are dangerous to health [6-8].

In dye containing waste water, colloidal matter increases the turbidity of water and gives it bad aroma. It prevents the penetration of sunlight essential for photosynthesis. These effluents clog the pores of soil, decrease soil fertility and prevent penetration to roots [9-11]. Several methods, such as reverse osmosis, chemical oxidation, coagulation, flocculation, sonolysis, ozonation, etc., were used for removing dyes [12]. In last decades, biosorption is becoming popular in water treatment [13]. Increase in search of low-cost biosorbents was more emphasized due to the high cost of activated carbon [14-16]. Several novel biomaterials have been used as adsorbents [17,18]. Numerous adsorbents have been reported for the elimination of direct blue-15 dye from waste water like: activated carbon, palm ash, tea waste, papaya leaves, white rot fungus, coconut, orange peels and *Loofa egyptiaca* [19-25].

In the present research work *Carica papaya* (papaya) leaves and *Camellia sinensis* (tea) waste are used as novel adsorbents for the biosorption of direct blue-15 dye. The leaves and leaf buds of this plant are used for producing tea beverage [26]. *Camellia sinensis* is useful for the treatment of tumors, bladder ailments, lethargy and abscesses [27]. The anti-microbial activity of tea is manifested against the *vibrio cholerae* bacterium which causes cholera [28]. Total cholesterol level can be reduced by consuming green tea. Body fat can also be reduced by green tea, which is supported by randomized control trials [29]. Green tea affects the

* To whom all correspondence should be sent:
E-mail: ktm7ro@yahoo.com

lining of blood vessels. It keeps them relaxed and helps to regulate changes in blood pressure. It prevents the formation of blood clots which are the main cause of heart attacks. The risk of esophageal cancer can be reduced by consuming green tea. It can kill cancer cells without damaging the healthy tissue around them [30-33].

Papaya leaves are large with a diameter of 50-70 cm. The leaf has seven lobes and is palmately lobed [34]. Low platelet counts can be cured by using papaya leaf tea which also helps against clotting. Tea made of papaya leaves acts as a laxative for the treatment of constipation [35].

EXPERIMENTAL

Chemicals used

Direct blue-15 dye (C.I.=24400, mol. wt=992.85 g/mol), HCl and NaOH were purchased from Merck (Germany) and used as such.

Preparation of adsorbents

The *Camellia sinensis* waste was taken from local markets of Lahore, Pakistan. The *Carica papaya* leaves were collected from the gardens of the home institute. Tea waste was placed in acetone for 3 h for removing color and after filtration, was dried in an oven at 110°C for 3-4 h. Papaya leaves were kept in sunlight for 3-4 days to completely remove moisture, followed by oven drying at 110°C. After that the materials were ground. Their FT-IR spectra were recorded and resulting peaks are summarized in Table 1.

Adsorption experiments

They were carried out in batch mode at 25°C. pH was maintained by 0.01 N HCl and 0.01 N NaOH. All factors were studied using a 25 ppm dye solution. After adsorption, dye concentration was checked in the filtrate on a UV-Vis spectrometer at 601 nm. The % removal of dye at any time was determined by the following equation:

$$\% \text{ Removal of dye} = (C_o - C_e / C_o) \times 100, \quad (1)$$

where C_o and C_e are the concentrations of dye before and after adsorption, respectively. Each experiment was repeated three times for increasing accuracy of the data and average values were used for calculations.

Study of adsorption isotherm

Optimized conditions of all operational parameters were applied on dye solutions with various concentrations (15-90 ppm) for studying the adsorption isotherm. After that the solutions were filtered and dye concentration was checked in the filtrate as described above. Then, applying eq. 2, Langmuir isotherms were plotted for *Camellia sinensis* waste (TW) and *Carica papaya* leaves (PL).

$$1/q = 1/bq_m C_e + 1/q_m, \quad (2)$$

The value of 'q' is calculated by formula 3:

$$q = (C_o - C_e)V/m, \quad (3)$$

where 'q' (mg.g⁻¹) is the amount of dye adsorbed, 'C_e' (ppm) is the remaining concentration of dye after adsorption, 'q_m' (mg.g⁻¹) and 'b' (L.g⁻¹) are Langmuir isotherm parameters which were calculated from the slope and intercept values of the graph of '1/q' versus '1/C_e'. 'V'(l) is the volume of dye solution, 'm' is the mass of adsorbent used. Separation factor 'R_L' and 'ΔG°' (thermodynamic parameter) were calculated using equations 4 and 5, respectively:

$$R_L = 1/(1+bC_o), \quad (4)$$

$$\Delta G^\circ = -RT \ln K, \quad (5)$$

Here 'C_o' is 25 ppm and K is the inverse of Langmuir constant 'b' [24].

RESULTS AND DISCUSSION

Characterization of adsorbents surface

Characterization of adsorbents surface was done by FT-IR to confirm the presence of functional groups that can be used for bonding with direct blue 15 dye during biosorption. The resulting characteristic vibration frequencies are listed in Table 1. It was found that carboxylic groups are present in the biosorbent samples, as indicated by the -OH group stretching frequencies at 2923.25, 2954.11, 2954.11, 2625.53 and 2923.25 cm⁻¹. Alkane group -CH₂ peaks were found at 2725.53, 1458.25, 1457.28 and 721.41 cm⁻¹. Aromatic amine peaks were found at 1304.90 and 1306.83 cm⁻¹ [36]. These functional groups can chelate dye molecules.

Table 1. Specific FT-IR absorption frequencies of leaf samples.

Adsorbents	Band frequencies (cm ⁻¹)
<i>Camellia sinensis</i>	2923.25, 2853.81, 2725.53, 1458.25, 1304.90, 721.41
<i>Carica papaya</i>	2954.11, 2923.25, 2625.53, 1457.28, 1306.83, 721.41

Adsorbent dose effect

The adsorbent dose effect was followed by varying adsorbent dose from 0.1 to 1.0 g. The maximum removal of dye occurred at adsorbent dose of 0.7 g using *Camellia sinensis* and 0.5 g using *Carica papaya*, as shown in Fig. 2. It was found that the adsorption initially increases due to the presence of a large number of adsorption sites on the surface of the adsorbents but when equilibrium is established the adsorption capacity of the biosorbent decreases. The reason is that after establishment of equilibrium, further increase in leaf sample dose leads to increased interference between the active sites, so removal of dye decreases [37-39].

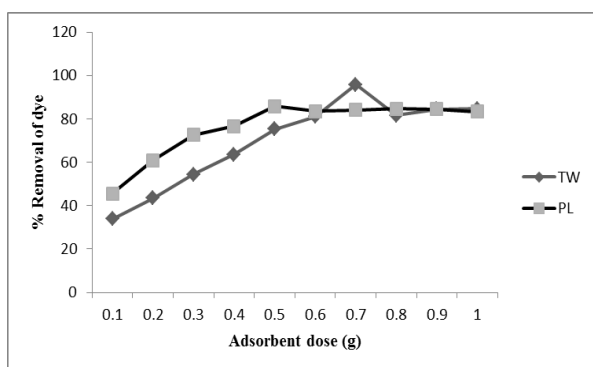


Fig. 2. Effect of adsorbent dose of *Camellia sinensis* waste (TW) and *Carica papaya* leaves (PL) on the elimination of direct blue-15 dye from water.

Effect of contact time

The effect of contact time was studied in the range from 5 to 60 min. The results are shown in Fig. 3 which indicates that the maximum removal of dye occurs in 40 and 45 min using *Camellia sinensis* and *Carica papaya* leaves, respectively.

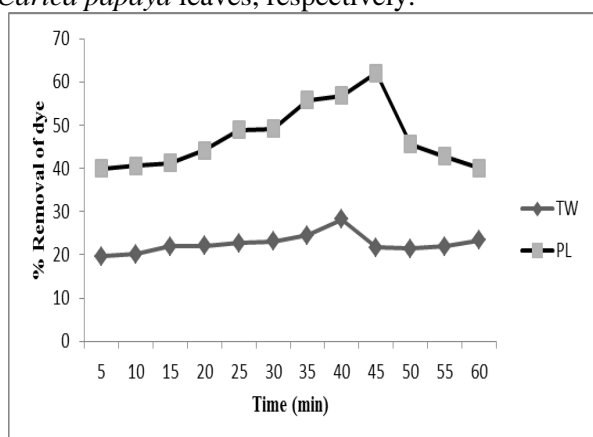


Fig. 3. Effect of contact time of *Camellia sinensis* waste (TW) and *Carica papaya* leaves (PL) on the biosorption of direct blue-15 dye from water.

In the beginning, dye adsorption was rapid due to the availability of a large number of vacant binding

sites but after the optimum time, decrease in adsorption capacity was observed due to covering of the available binding sites by dye molecules, which repel incoming molecules of dye lowering biosorption.

Effect of initial pH

The effect of initial pH is shown in Fig. 4 which indicates that dye removal is maximal at pH 3.0 using *Camellia sinensis* waste (TW) and at pH 7.0 by *Carica papaya* leaves (PL).

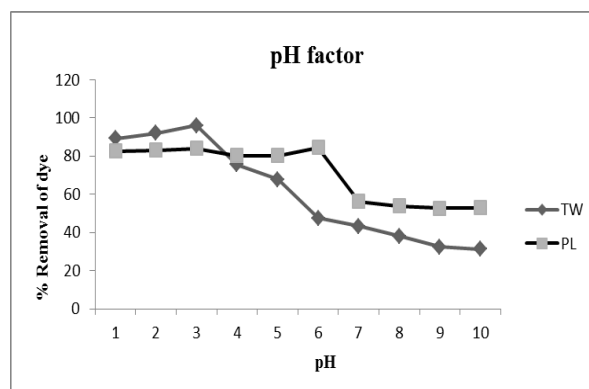


Fig. 4. pH effect on the removal of direct blue 15 dye from water using *Camellia sinensis* waste (TW) and *Carica papaya* leaves (PL).

In acidic conditions, leaves surface becomes protonated, which helps in attracting the anionic type dye, thus the removal of dye increases. But in the case of basic conditions, biosorption decreases due to the presence of negative charge on leaves surface, which repels anionic dye species, resulting in poor biosorption [39].

Effect of agitation speed

The effect of agitation speed is graphically presented in Fig. 5.

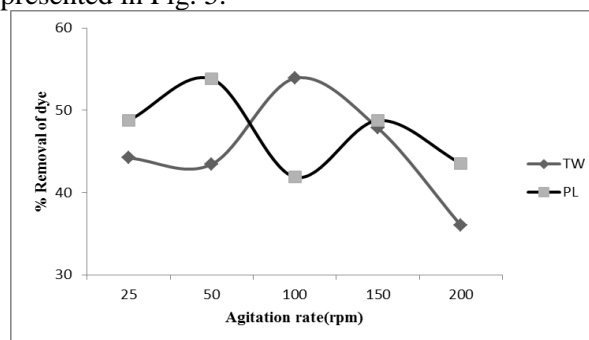


Fig. 5. Influence of agitation rate on the biosorption of direct blue 15 dye from water using *Camellia sinensis* waste (TW) and *Carica papaya* leaves (PL).

The maximum removal of dye occurred at 100 and 50 rpm using *Camellia sinensis* waste and *Carica papaya* leaves as adsorbent, respectively. Agitation of dye solution helps for better interaction

between leaf waste and dye molecules, so that these molecules penetrate to deeper layers of the adsorbent. When agitation speed surpassed the optimum level, less interaction occurred between dye molecules and adsorbent, so biosorption decreased at higher speed [39].

Effect of temperature

The effect of temperature is shown in Fig. 6. The maximum biosorption of dye occurs at 40 and 30°C using *Camellia sinensis* waste and *Carica papaya* leaves, respectively. It indicates that this process is exothermic, which was further confirmed by isothermal modeling of equilibrium data.

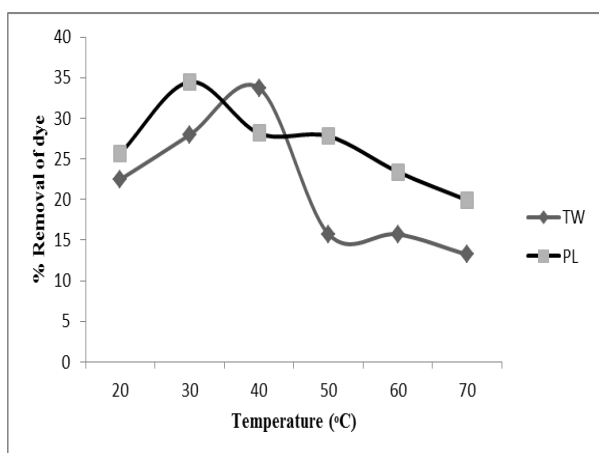


Fig. 6. Temperature effect on direct blue 15 dye adsorption from water by *Camellia sinensis* waste (TW) and *Carica papaya* leaves (PL).

Isothermal studies

The Langmuir isotherms for direct blue-15 dye adsorption using *Camellia sinensis* and *Carica papaya* are shown in Fig. 7 and the results are summarized in Table 2.

Maximum removal of dye - q_m value was 90.9 and 3.98 mg/g for *Camellia sinensis* waste (TW) and *Carica papaya* leaves (PL), respectively. The constant 'b' value for direct blue 15 dye was 2.2 and 1.65 L/g for *Camellia sinensis* waste (TW) and *Carica papaya* leaves (PL), respectively. It was

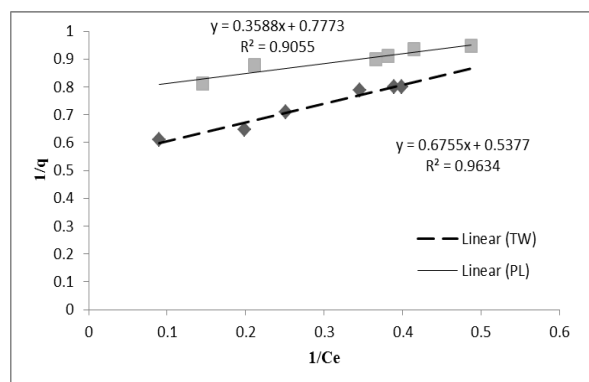


Fig. 7. Langmuir isotherm for direct blue 15 dye adsorption from water using *Camellia sinensis* waste (TW) and *Carica papaya* leaves (PL).

used to calculate ΔG° and separation factor ' R_L ' values. The correlation coefficient ' R^2 ' values indicated that the Langmuir model was suitable to explain the adsorption of direct blue 15 dye on *Camellia sinensis* waste and *Carica papaya* leaves. This indicates that adsorption sites are arranged in monolayer fashion and homogeneously distributed on the biosorbent surface.

ΔG° value indicated that these processes are exothermic in nature and separation factor ' R_L ' value less than unity indicated the favorability of these adsorbents for removing direct blue 15 dye from water on a bulk scale.

CONCLUSIONS

In the present work low-cost adsorbents such as *Camellia sinensis* waste and *Carica papaya* leaves were used for the removal of direct blue 15 dye from water. It was observed that *Camellia sinensis* waste can remove 90.9 mg.g⁻¹ of dye, which is 23 times greater than *Carica papaya* leaves' capacity of 3.98 mg.g⁻¹. The process is exothermic in nature and favorable under optimized conditions, as indicated by thermodynamic data. So these adsorbents can be used on a bulk scale for removing direct blue 15 from waste water streams.

Table 2. Results of isothermal studies for adsorption of direct blue 15 dye

Sample	R ²	b (L.g ⁻¹)	q _m (mg.g ⁻¹)	ΔG° (kJ/mol)	R _L
<i>Camellia sinensis</i> waste (TW)	0.963	2.2	90.9	-1.953	0.017
<i>Carica papaya</i> leaves (PL)	0.905	1.65	3.98	-1.238	0.024

REFERENCES

1. M. Akhtar, M.I. Bhangar, S. Iqbal, S.M. Hasany, *Journal of Hazardous Materials*, **128**, 44 (2006).
2. B. Acemioglu, *Journal of Colloid and Interface Science*, **274**, 371 (2004).
3. B. Noroozi, G.A. Sorial, H. Bahrami, M. Arami, *Dyes and Pigments*, **76**, 784 (2008).
4. G. Moussavi and M. Mahmoudi, *Journal of Hazardous Materials*, **168**, 806 (2009).
5. V.J. Odgegba, N.M. Bangbose, *Journal of Environmental Science and Technology*, **6**, 438 (2012).
6. Y. Yang, G. Wang, B. Wang, Z. Li, X. Jia, Q. Zhou, Y. Zhao, *Bioresource Technology*, **102**, 828 (2011).
7. A. Mittal, J. Mittal, A. Malviya, V.K. Gupta, *Journal of Colloid and Interface Science*, **340**, 16 (2009).
8. C. Pelekania, V.L. Snoeyink, *Carbon*, **39**, 25 (2001).
9. R. Sivaraj, C. Namasivayam, K. Kadirvelu, *Journal of Waste Management*, **21**, 105 (2001).
10. H.N. Bhatti, U. Kalsoom, A. Habib, *Journal of the Chemical Society of Pakistan*, **34**, 257 (2012).
11. S. Thirumalisamy and M. Subbian, *BioResources*, **5**, 419 (2010).
12. S. Elhami, H. Faraji, M. Tahheri, *Journal of the Chemical Society of Pakistan*, **34**, 269 (2012).
13. N.K. Lazaridis, T.D. Karapantsios, D. Georgantas, *Water Research*, **37**, 3023 (2003).
14. M. Rachakornkij, S. Ruangchuay, S. Teachakulwiroj, *Journal of Science and Technology*, **26**, 13 (2004).
15. S. Chatterjee, D.S. Lee, M.W. Lee, S.H. Woo, *Bioresource Technology*, **100**, 3862 (2009).
16. M.P. Elizalde-Gonzalez, J. Mattusch, A.A. Pelaez-Cid, R. Wennrich, *Journal of Analytical and Applied Pyrolysis*, **78**, 185 (2007).
17. R. Rehman, T. Mahmud, *Asian Journal of Chemistry*, **25**, 5351 (2013).
18. E.L. Grabowska, G. Gryglewicz, *Dyes and Pigments*, **74**, 34 (2007).
19. A. Demirbas, *Journal of Hazardous Materials*, **167**, 1 (2009).
20. A.A. Ahmad, B.H. Hameed, N. Aziz, *Journal of Hazardous Materials*, **141**, 70 (2007).
21. G. Bayramoglu, M.Y. Arica, *Journal of Hazardous Materials*, **143**, 135 (2007).
22. B.H. Hameed, D.K. Mahmoud, A.L. Ahmad, *Journal of Hazardous Materials*, **158**, 65 (2008).
23. A. Khaled, A.E. Nemr, A. El-Sikaily, O. Abdelwahab, *Journal of Hazardous Materials*, **165**, 100 (2009).
24. E. Sayad, Z. Ashtoukhy, *Journal of Environmental Management*, **90**, 2755 (2009).
25. A. Tabak, E. Eren, B. Afsin and B. Caglar, *Bioresource Technology*, **161**, 1087(2009).
26. C. Karthika, N. Vennilamani, S. Patabhi, *Chemosphere*, **60**, 1009 (2005).
27. N.H. Woodward, D.A. Balentine, M.A. Harbowy, H.N. Graham, *Chemistry and Consumption of Beverage in Caffeine*, chapter 3 (1998).
28. B.M. Lund, A.C. Baird-Parker, G.W. Gould, *Microbiological Safety and Quality of Food*, 960 (2000).
29. R. Johnson, S. Bryant, A.L. Huntley, *Maturitas*, **73**, 280 (2012).
30. M. Jain, V.K. Garg, K. Kadirvelu, *Journal of Hazardous Materials*, **162**, 365 (2009).
31. K.F. Fung, M.H. Wong, *Journal of the Science of Food and Agriculture*, **84**, 1469 (2004).
32. J. Ruan, M.H. Wong, *Environmental Geochemistry and Health*, **23**, 53 (2001).
33. M. Liebman, S. Marphy, *Nutrition Research*, **27**, 273 (2007).
34. P. Alvira, E.T. Pejo, M. Ballesteros, M.J. Negro, *Journal of Hazardous Materials*, **101**, 4851 (2010).
35. P. Simmons, J. Farrar, B. Wills, *Journal of Medical Sciences*, **366**, 1423 (2012).
36. J. Coates, *Encyclopedia of Analytical Chemistry*, John Wiley and Sons Ltd, Chichester, 2000.
37. M. Karkmaz, E. Puzenat, C. Guillard, J.M. Herrmann, *Applied Catalysis B: Environmental*, **51**, 183 (2004).
38. E. Brilas, B. Boye, I. Sires, J.A. Garrido, R.M. Rodriguez, C. Arias, P.L. Cabot, C. Comninellis, *Electrochimica Acta*, **49**, 4487 (2004).
39. M. Achaka, A. Hafidib, N. Ouazzania, S. Sayadic, L. Mandia, *Journal of Hazardous Materials*, **166**, 117 (2009).

СОРБЦИОННО ОТСТРАНЯВАНЕ НА БАГРИЛОТО ДИРЕКТНО СИНЬО-15 ОТ ВОДА ИЗПОЛЗВАЙКИ ЛИСТА ОТ *Camellia sinensis* И *Carica papaya*

Р. Рехман¹, Т. Махмуд¹, Р. Риаз¹, А. Рауф¹, Л. Миту^{2*}

¹Институт по химия, Университет в Пунджаб, Лахор -54590, Пакистан

²Департамент по химия, Университет в Питец, Питец-110040, Румъния

Постъпила на 2 февруари, 2016 г.; приета на 4 май, 2016 г.

(Резюме)

Пречистването на води по адсорбционни методи се развива бързо през последните години. В настоящата работа се изследва ефективността на отстраняване на багрилото Директно синьо-15 чрез два адсорбента, а именно листа от *Camellia sinensis* (чай) и *Carica papaya* (папая), като адсорбционната им способност е сравнена по стандартна скала. Оптимизирани са различни параметри, влияещи на биосорбционната ефективност и е приложена адсорбционната изотерма за моделиране на равновесните данни. Охарактеризирането на *Camellia sinensis* и *Carica papaya* е извършено чрез FT-IR. Резултатите показват, че отпадъците от *Camellia sinensis* са по-ефикасни и отстраняват 90.9 mg/g от багрилото в сравнение с листата от *Carica papaya*, които отстраняват само 3.98 mg/g при оптимизирани работни условия. Затова остатъците от *Camellia sinensis* превъзхождат листата от *Carica papaya* при отстраняването на багрилото Директно синьо-15 от отпадъчни води.

Optimization of process conditions and characterization of ethylene-propylene-diene rubber with bismaleimide

M. Vadivel^{1,*}, S. Shobana², S.A. Narayan³, L. Mitu⁴, J. Dhavethu Raja¹, M. Sankarganesh¹

¹Department of Chemistry & Research Centre, Mohamed Sathak Engineering College, Kilakarai - 623 806, Ramanathapuram, Tamilnadu, India.

²Department of Chemistry and Research Centre, Aditanar College of Arts and Science, Virapandianpatnam, Tiruchendur-628 216, Thoothukudi, Tamilnadu, India.

³Department of Science and Humanities, Rohini College of Engineering & Technology, Anjugramam, Kanyakumari-629 851, Tamilnadu, India.

⁴ Department of Physics and Chemistry, University of Pitesti, Pitesti-110040, Romania

Received January 18, 2016; Revised May 18, 2016

The thermal and morphological properties of ethylene-propylene-diene rubber with bismaleimide (EPDM-g-BMI) were investigated. The effects of EPDM concentration, BMI concentration, reaction time and reaction temperature in terms of grafting efficiency (%) were examined. As the BMI concentration increases, the grafting efficiency increases. The FT-IR spectroscopy analysis of EPDM-g-BMI reveals that the C=C double bond in EPDM reacts with the maleimide double bond through a nucleophilic addition reaction. The SEM image of EPDM-g-BMI reveals a rough surface due to the formation of inter-crosslinked network between EPDM and BMI.

Keywords: Thermal properties, Ethylene-propylene-diene rubber, EPDM-g-BMI, DSC, SEM.

INTRODUCTION

Ethylene-propylene-diene (EPDM) has excellent wear strength and superior mechanical resistance. It also has excellent tribological properties after chemical coupling [1]. Crosslinked EPDM is one of the major compounds commonly used as industrial polymers because of its marvelous resistance to wearing out and swelling, its thermal and flame retardant properties [2–4]. A number of graft copolymers, such as PS [5, 6], (POE)-graft-PS [7], EPDM-graft-POE [8] and (PE)-graft-PS [9–11] have been formed. These copolymers play an important role as compatibilizer at the interface of blends and decrease the interfacial tension between polymer phases.

Bismaleimides (BMI) are widely used as elevated performance composite matrices in aerospace industry. As compared with extra thermosetting polyimides, bismaleimides show both outstanding high performance and cost effectivity; thus they have been chosen as attractive candidates for advanced composite matrices [12]. Bismaleimides have outstanding solubility in the majority of the solvents like ethylene chloride, cyclohexanone, methylene chloride, etc. With the characteristics of both rigid rings and network forming ability, the final Tg of such systems can reach 400 °C [13]. Therefore, the main challenges concerning the use of

bismaleimides for composite applications are the improved processability and the crack toughness [14]. EPDM rubber has considerable marketable and technological importance and high research value. Though earlier investigations present a lot of useful information, however, no effort has been made to develop EPDM grafted bismaleimide.

EXPERIMENTAL

Materials

The EPDM (ENB type diene) terpolymer used in this study of a commercial grade Nordel IP 4750R was supplied by DuPont Dow elastomers, USA. (Ethylene/propylene/5-ethylidene-2-norbornene: 71/20/9 by wt. % and specific gravity 0.88). Dibutyltin dilaurate (DBTDL, Merck, Germany, density = 1.066 g.cm³, freezing point >110 °C, mw = 631.56). Maleic anhydride 99% (Otto Kemi, India, mw = 98.06, melting point = 53 °C). Nickel acetate (HiMedia Laboratories Pvt Ltd, India, mw = 248.86). Triethyl amine (Fisher Chemic Ltd, India, mw = 101.19). Analytical grade toluene and n-hexane were used as received. Synthesis of bismaleimide (BMI) was already reported [15].

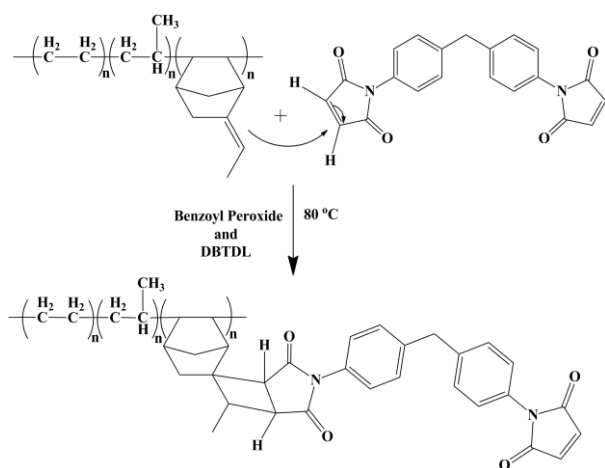
Methods

The FT-IR spectra of the samples were measured in KBr disks on a Shimadzu-1800S spectrometer. The samples were scanned from 4000 to 400 cm⁻¹. DSC (differential scanning calorimetry) was performed with a NETZSCH DSC 200 instrument. The sample (2 to 6 mg) was put in a sealed aluminum

* To whom all correspondence should be sent:
E-mail: vadivelche@gmail.com

pan and was heated at 10 °C/min in the range of 0 - 500 °C using an empty sealed pan as a reference. SEM (scanning electron microscope) micrographs of the composite materials were recorded using a Quanta-200, FEG scanning electron microscope (The Netherlands), and micrographs were taken at the required magnification. A working distance of 9.8 mm was maintained and the acceleration voltage used was 20.00 kV with the minor electron image as the detector.

Preparation of epdm grafted bismaleimide (EPDM-g-BMI)



Scheme 1. Schematic presentation of EPDM-g-BMI preparation

EPDM (10 g/5 mM) was dissolved in 200 mL of toluene. Bismaleimide (0.025g/0.5 mM) was dissolved in 20 mL of toluene. The above two solutions were mixed in a 250 mL three-necked flask fitted with a condenser and nitrogen inlet. Benzoyl peroxide (0.05 g/0.01 mM) and DBTDL (0.005 g/0.0015 mM) were added to the above mixture and heated at 80 °C for 5 h. The EPDM-g-BMI was precipitated by pouring the homogeneous mixture in excess amount of acetone where the unreacted BMI was removed. The precipitate was dried at 50 °C for 48 h (Scheme 1).

Isolation of graft terpolymer

After the synthesis, ungrafted EPDM, BMI and EPDM-g-BMI are present in the medium. The EPDM was separated from settled down products by extraction using n-hexane. The bismaleimide grafted EPDM (EPDM-g-BMI) was separated from BMI using DMF where the former is soluble and the latter is insoluble. The total conversion was calculated from the ratio of the total weight of crude products to the weight of EPDM charged. The grafting ratio and grafting efficiency were determined on the basis of the changes in polymer weight during the reaction development and the total amount of EPDM-g-BMI

formed, respectively. The grafting ratio and grafting efficiency were calculated by the following equations:

$$\text{Total conversion (\%)} = \frac{\text{The weight of polymers formed}}{\text{Weight of EPDM charged}} \times 100$$

$$\text{Grafting ratio (\%)} = \frac{\text{Weight of EPDM - g - BMI}}{\text{Weight of EPDM charged}} \times 100$$

$$\text{Grafting efficiency (\%)} = \frac{\text{Weight of EPDM - g - BMI}}{\text{Total weight of polymers formed}} \times 100$$

The best grafting efficiency of BMI onto EPDM was achieved by the solution (grafting) polymerization method. All samples were dissolved in toluene followed by intense stirring for 10 min, till the mixture became homogeneous. Then, the solution was transferred into a glass mold and closed with Para film to permit the removal of small molecules of both the solvents, and those produced in the hydrolysis. Upon gradual ventilation over 10 days, translucent samples of hybrids were obtained without cracks. All samples are listed in Table 1.

Table 1. Conditions of graft copolymerization

Conditions	Description				
EPDM concentration (%)	5.0	10	15	20	25
BMI concentration (%)	1.0	1.5	2.0	2.5	3.0
Reaction time (h)	2.0	4.0	6.0	8.0	–
Reaction temperature (°C)	50	60	70	80	–

RESULTS AND DISCUSSION

FT-IR spectroscopy

The IR spectra of EPDM and EPDM-g-BMI exhibit $\nu(\text{C-H})$ stretching, $\nu(\text{CH}_2)$ rocking $\nu(\text{CH}_3)$ symmetric bending (aliphatic) and $\nu(\text{CH}_2)_n$ wagging vibrations at 2911, 1451, 1367 & 721 cm^{-1} and 2918, 1464, 1375 & 719.15 cm^{-1} , respectively (Fig. 1).

In addition, EPDM shows vibrations at 2851 cm^{-1} and 811 cm^{-1} for $\nu(\text{C-C})$ and $\nu(>\text{C}=\text{CH}-)$ stretching due to the presence of ENB. However, $\nu(\text{C-H})$ stretching vibration at 3090 cm^{-1} is observed while $\nu(\text{C}=\text{C})$ stretching vibration at 1627.99 cm^{-1} of BMI has disappeared [15] due to the grafting reaction by a free radical mechanism which involves the allylic position of the ENB unit of the EPDM with addition across the α,β -unsaturated linkage [16] in the bismaleimide resin. Similar observations are made for bismaleimide toughened reactive rubbers [16]. A decrease in band intensity due to unsaturated $\nu(\text{C}=\text{H})$ present in the side chain of ENB at 815 cm^{-1} is observed which indicates that $\nu(\text{C}=\text{C})$ is utilized for new chemical bond formation with BMI.

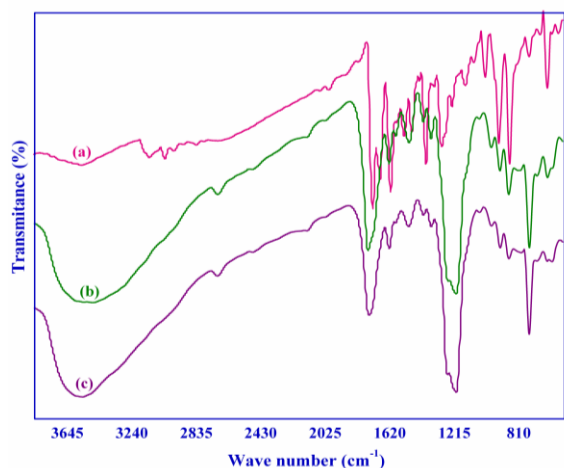


Fig. 1. FT-IR spectra of (a) EPDM, (b) BMI and (c) EPDM-g-BMI

Effect of reaction conditions on grafting

Effect of EPDM content

The effect of EPDM content on the graft copolymerization is presented in Fig. 2(a). The grafting reaction was carried out at 80 °C for 4 h with 2.5 wt% of BMI. The grafting efficiency increases linearly with the increase in concentration of EPDM, due to the availability of a double bond present in EPDM. The grafting efficiency for 10 wt% EPDM is 20% and that for 30 wt% is 30%. At higher

concentrations of EPDM, additional active sites are created and thus the grafting efficiency increases. However, a smaller number of active sites are generated in the case of lower concentration of EPDM resulting in a decrease in grafting efficiency, which favors the enhanced homopolymerization of BMI.

Effect of BMI concentration

The effect of BMI on the grafting efficiency is presented in Fig. 2(b). The grafting reactions were carried out at 80 °C for 4 h with 1, 1.5, 2, 2.5 and 3% of BMI on EPDM. The grafting efficiency increases with the increase in BMI concentration. The grafting efficiency for 2 wt% of BMI is 24.67, whereas the highest grafting efficiency of 28.01 is observed for 2.5 wt% of BMI. There is a sharp increase in grafting efficiency up to 2.5 wt% of BMI. Above 2.5 wt% of BMI no significant increase in grafting is observed. The higher concentration of BMI favors the formation of a larger number of active sites in the amine part of BMI, which favors the homopolymerization rather than grafting.

Effect of reaction time

The efficiency of grafting of BMI onto EPDM as a function of reaction time is given in Fig. 2(c). The reactions were carried out at 80°C with 0.1wt% of

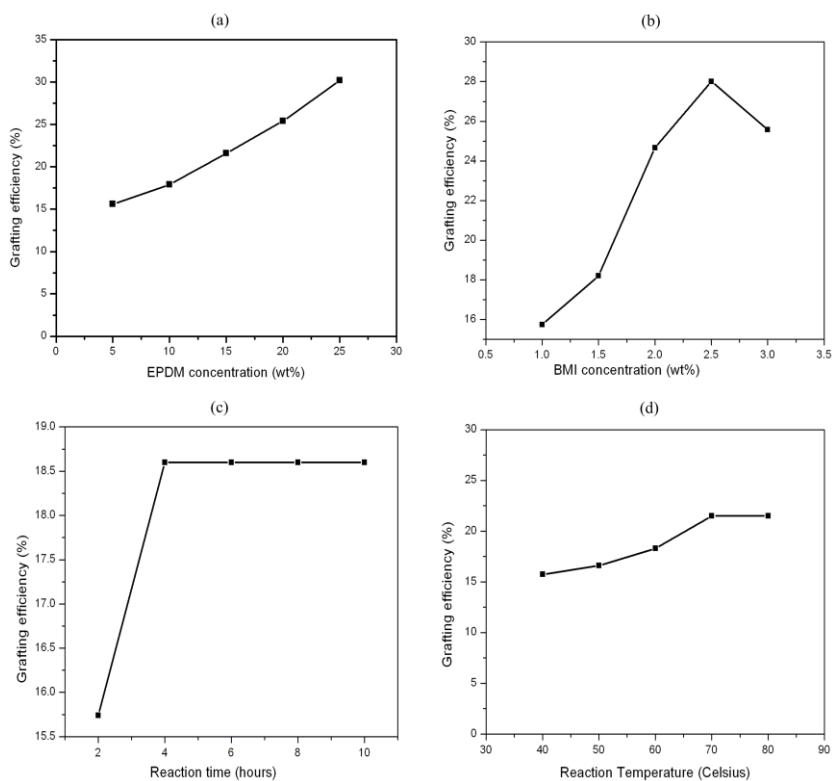


Fig. 2. Plot of grafting efficiency against (a) EPDM concentration; (b) BMI concentration; (c) reaction time; (d) reaction temperature.

benzoyl peroxide for periods of 2, 4, 6, 8 and 10 h. It was observed that the grafting efficiency increases with increase in reaction time up to 2 h, and beyond 4 h there was no appreciable effect on the grafting efficiency. However, the total conversion increases with increase in reaction time due to the formation of the homopolymer.

Effect of reaction temperature

The influence of temperature on the grafting is presented in Fig. 2(d). The reaction was carried out with 2.5 wt% of BMI and 0.1 wt% of benzoyl peroxide at different temperatures, namely, 40, 50, 60, 70 and 80 °C. The grafting efficiency increases with increasing reaction temperature from 40 to 80 °C. However, beyond 80 °C, there was no significant change in the grafting efficiency which indicates the end of the reaction.

Calorimetric analysis

A sharp endothermic peak at -52.1 °C indicates the simultaneous occurring of dehydrogenation and disproportionation of EPDM. DSC scans also show a sharp endothermic peak at 489 °C due to the curing of EPDM-g-BMI (Fig. 3).

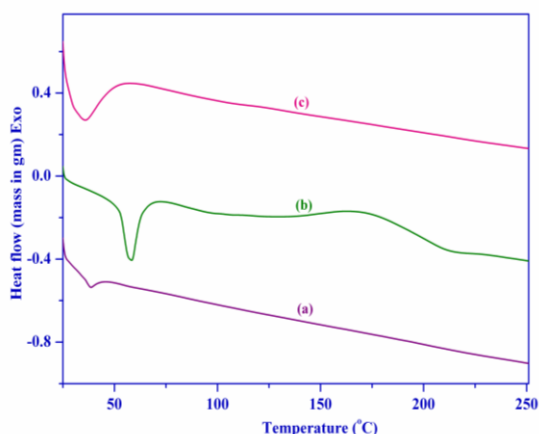


Fig. 3. DSC curves of (a) EPDM, (b) BMI and (c) EPDM-g-BMI.

The complex molecular structure of the grafted copolymer of bismaleimide and EPDM hinders the contribution of reactive sites for the curing reaction, which in turn increases the curing temperature of the system. The increase in endothermic peak temperature was also due to the steric hindrance produced by the EPDM particles between the two reacting sites, which necessitated a higher temperature to increase the reactivity of the crosslinking sites [17].

SEM analysis

The SEM images of the EPDM, BMI and EPDM-g-BMI are shown in Figs. 4(a) to 4(c). The SEM micrograph of EPDM shows a smooth surface

morphology. The SEM micrograph of the unmodified BMI reveals that crystallites with micropores are representative of the brittle phase.

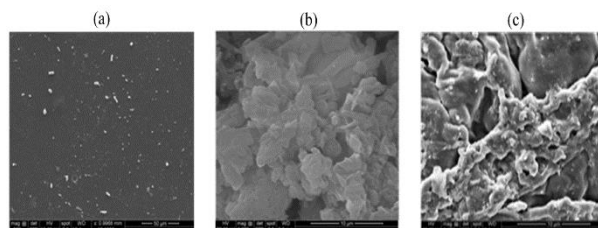


Fig. 4. SEM micrograph of (a) EPDM; (b) BMI; (c) EPDM-g-BMI.

The SEM micrograph of the EPDM-g-BMI system reveals that the minor component (BMI) is dispersed within a range of the major component (EPDM) with continuous morphology [18, 19]. Fig. 4a of pulled out traces of micrographic morphology depicts the poor adhesive nature of EPDM. Fig. 4b also shows a chunk of BMI agglomerate-like morphology. Figs. 4a and 4b explain their lower stiffness value / storage modulus. From Fig. 4c, a high interfacial tension between BMI and EPDM phases follows which leads to a bigger size of dispersed rubber phase (3.3 μm), which means enhanced stress transfer and higher impact on strength and supports the rubber wear concept by the process of plowing. It is obvious that it is a stratification phenomenon, if no segregation of the core and periphery exists, due to the configuration of inter-crosslinked network indicated by the active and rough surface. Moreover, Fig 4c implies that there is an influence on storage modulus and loss factor, separately.

CONCLUSIONS

EPDM-g-BMI graft terpolymer was synthesized by a solution polymerization method. The following conclusions are made based on the data resulting from different experimental studies. The grafting of BMI onto EPDM reveals that the C=C double bond in EPDM reacts with the maleimide double bond through a nucleophilic (Michael) addition reaction which is confirmed by FTIR spectra. It was ascertained that the threshold grafting efficiency was maximum at 2.5 mol% of BMI. The grafting efficiency increases with the increase in temperature and EPDM content. The grafting of BMI onto EPDM increases Tg values. Hence the EPDM-g-BMI rubber may be used in cable insulation application for better performance. The morphology proved that EPDM-g-BMI rubber shows improved adhesion, better stress transfer, superior impact on strength and protective rubber wear.

REFERENCES

1. M.S. Khan, D. Lehmann, G. Heinrich, U. Gohs, R. Franke, *Express. Polym. Letters*, **3**, 39 (2009).
2. J. He, X. Zhang, X. Li, R. Yang, *Plast. Rubber Compos.*, **44**, 206 (2015).
3. R. Chen, S. Lu, C. Li, M. Li, S. Lo, *J. Therm. Anal. Calorim.*, **122**, 449 (2015).
4. H. Ismail, S. Ishak, Z. A. A. Hamid, *J. Vinyl. Addit. Technol.*, **21**, 1 (2014).
5. M. F. Diaz, S. E. Barbosa, N. J. Capiati, *Polymer*, **46**, 6096 (2005).
6. M. F. Diaz, S. E. Barbosa, N. J. Capiati, *Polym. Eng. Sci.*, **46**, 329 (2006).
7. Z. H. Guo, L. F. Tong, Z. P. Fang, *Polym. Int.*, **54**, 1647 (2005).
8. J. Su, J. Zhang, *J. Elastomers Plast.*, **46**, 368 (2013).
9. G. Zhang, Y. Wang, H. Xing, J. Qiu, J. Gong, K. Yao, H. Tan, Z. Jiang, T. Tang, *RSC. Advances*, **5**, 27181 (2015).
10. Y. Gao, H. Huang, Z. Yao, D. A. Shi, Z. K
11. M. F. Diaz, S. E. Barbosa, N. J. Capiati, *Polymer*, **48**, 1058 (2007).
12. R. Rajasekaran, M. Alagar, *J. Compos. Mater.*, **42**, 1031 (2008).
13. M.R. Tant, J.W. Connell, H.L.N. McManus, *High-Temperature Properties and Applications of Polymeric Materials*. American Chemical Society, Washington DC, 1995.
14. X.J. Hu, C.Y. Fan, G.Z. Yue, Liang. *J. Mater. Process. Technol.*, **89**, 544 (1999).
15. M. Vadivel, M. Suresh Chandra Kumar, V. Selvam, S. Shobana, S. Arvindnarayan, *Asian J. Chem.*, **26**, 7160 (2014).
16. S. Takeda, H. Akiyama, H. Kakiuchi, *J. Appl. Polym. Sci.*, **35**, 1341 (1988).
17. Halimatuddahlia, H. Ismail, *Polymer Plast. Tech. Eng.*, **48**, 25 (2008).
18. S.S. Ray, M. Okamoto, *Prog. Polym. Sci.*, **28**, 1539 (2003).
19. K. Rajkumar, P. Thavamani, P. Jeyanthi, P. Pazhanisamy, *Chem. Sci. Trans.*, **2**, 1042 (2013).

ОПТИМИЗАЦИЯ НА УСЛОВИЯТА НА ПРОЦЕСА И ОХАРАКТЕРИЗИРАНЕ НА КАУЧУК ОТ ЕТИЛЕН-ПРОПИЛЕН-ДИЕН С БИС-МАЛЕИНИМИД

М. Вадивел^{1*}, С. Шобана², С.А. Нараян³, Л. Миту⁴, Дж. Дхавеетху Раджа¹, М. Санкарганеш¹

¹Департамент по химия & Изследователски център, Колеж по инженерство „Мохамед Сатхак“, Килараи 623 806, Раматхапурам, Тамилнаду, Индия.

²Департамент по химия & Изследователски център, Колеж по изкуства и наука „Адинатар“, Вирандианпатхам, Тиручендур-628 216, Тхоотхукуди, Тамилнаду, Индия

³Департамент по наука и хуманитарни знания, Колеж по инженерство и технология „Рохини“, Анджурамам, Канякумари-629 851, Тамилнаду, Индия

⁴Департамент по физика и химия, Университет в Питещ, Питещ-110040, Румъния

Постъпила на 18 януари, 2016 г.; коригирана на 18 май, 2016 г.

(Резюме)

Изследвани са термичните и морфологичните свойства на каучук от етилен-пропилен-диен с бис-малеимид (EPDM-g-BMI). Изучени са ефектите на концентрациите на EPDM и BMI, времето за реакцията и температурата в параметрите на графт-ефективността (%). С нарастване на концентрацията на BMI нараства и графт-ефективността. FT-IR спектроскопският анализ на EPDM-g-BMI показва, че C=C двойната връзка в EPDM реагира с двойната връзка в молекулата на малеинимида чрез нуклеофилна присъединителен механизъм. SEM-образите на полимера EPDM-g-BMI показват грапава повърхност поради образуването на вътрешни мрежи между EPDM и BMI.

Antioxidant potential of black pepper extract for the stabilization of sunflower oil

A. Firdos¹, A.R. Tariq¹, M. Imran¹, I. Niamat¹, F. Kanwal¹, L. Mitu^{2*}

¹*Institute of Chemistry, University of the Punjab, Lahore-54890, Pakistan*

²*Department of Chemistry, University of Pitesti, Pitesti-110040, Romania*

Received January 15, 2016; Revised May 4, 2016

Variable concentrations (500 ppm and 1000 ppm) of methanolic extract of black pepper were used for the stabilization of sunflower oil during ambient storage. Antioxidant potential of black pepper extract was evaluated by FFA (free fatty acid), PV (peroxide value) and IV (iodine value) parameters. The efficacy of the extract towards sunflower oil samples increased with increase in concentration. 500 ppm of black pepper extract added to control showed comparable values of FFA, PV and IV to that of 200 ppm of BHA or BHT added to control. However, stabilized sample of black pepper extract showed less increase in the PV and FFA values. The current study reveals that black pepper is a potent source of natural antioxidants that can be safely used to suppress peroxidation of lipids and to prevent them from getting rancid.

Keywords: Sunflower oil, Antioxidant potential, Stabilization, BHA, BHT, Black pepper.

INTRODUCTION

Since long time, synthetic antioxidants such as butyl hydroxytoluene (BHT) and butyl hydroxyanisole (BHA) are being used to prevent oils and fats from deterioration. But there are several safety and economic concerns associated with their usage [1]. In spite of their safety and other concerns, these antioxidants are widely needed for preventing deterioration of other oxidizable substances such as cosmetics, pharmaceuticals, plastics etc. [2]. These concerns, however, can be addressed and resolved by the introduction of natural antioxidants extracted from different spices which are used as food flavors. Some important contributions regarding the evaluation of the antioxidant potential of various herbs, spices and other natural substances in the literature are: Marja *et al.* (1999) [3], Esam *et al.* (2000) [4], Sharma *et al.* (2000) [5], Yu *et al.* (2002) [6], Javid *et al.* (2003) [7], Naz *et al.* (2004) [8], Zia *et al.* (2004) [9], Hinneburg *et al.* (2006) [10], Nedyalka *et al.* (2006) [11], Jinyoung *et al.* (2008) [12] and Kandlakunta *et al.* (2008) [13]. In this study a natural herb extract was used instead of synthetic antioxidants to check its efficacy to edible oils in comparison with synthetic ones.

We have selected black pepper, a common spice consumed on a daily basis in almost every part of the world. The purpose was to evaluate its antioxidant potential for the stabilization of refined, bleached and deodorized sunflower oil.

EXPERIMENTAL

Materials and instruments

Chemicals such as BHA, n-hexane, acetic acid, BHT, potassium iodide, iodine monochloride,

sodium thiosulfate, chloroform, carbon tetrachloride, ethanol, phenolphthalein and HCl were of analytical grade and were used without further purification. The Pyrex made glass ware was immersed in 0.5% w/v EDTA overnight, rinsed with deionized water and finally dried at 150°C as per previous report [14].

Black pepper

Black pepper was purchased from a local market of Lahore. It is a cheap and easily obtainable spice that is used in many Pakistani and Indian dishes not only because of its nice flavor but also for its medicinal value.

Preparation of black pepper extract

The extract of finely ground black pepper was obtained in 80% methanol at room temperature [14]. The extract was evaporated to dryness under reduced pressure at 40-45°C in a rotary evaporator and was stored at -18°C for further analyses [14].

Stabilization of sunflower oil and antioxidant activity testing

Five 250 ml glass-stoppered flasks were taken. In each flask 5 g of the sunflower oil was added. One was labeled as control and in the other four 200 ppm BHA, 200 ppm BHT, 500 and 1000 ppm black pepper extracts, respectively, were added. Antioxidant potential of the control was measured immediately, while portions of the four samples were analyzed after intervals of 15, 30 and 45 days. IUPAC standard methods [15, 16] were used for the determination of free fatty acids (FFA), peroxide (PV) and iodine (IV) values during ambient storage of sunflower oil.

* To whom all correspondence should be sent:
E-mail: ktm7ro@yahoo.com

RESULTS AND DISCUSSION

Effect of synthetic antioxidants and black pepper extracts on FFA

It is established in the literature that an increase in free fatty acid value will take place as fat deterioration proceeds; hence FFA is the best indicator of deterioration [17]. FFA was reduced from 0.214% to 0.188% with BHA and from 0.214% to 0.193% with BHT during 45 days of storage, Fig. (1). Similar findings have been reported by Kiyomi [17].

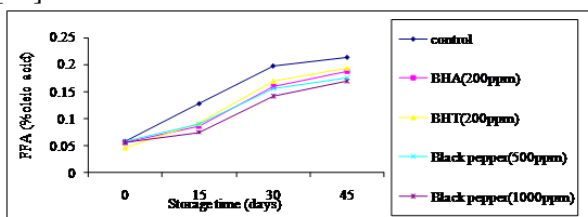


Fig. 1. Comparison of free fatty acid values with time.

Addition of 1000 ppm black pepper extract showed significant reduction in the FFA value of sunflower oil during 45 days of storage, as compared to BHA or BHT. Reduction of FFA by 500 ppm black pepper extract was comparable to BHA and BHT as it showed 0.176% FFA value at the 45th day of storage while 1000 ppm black pepper extract showed 0.170% FFA value at the same day of storage. These findings are comparable with related results of Frega *et al.* [18].

Effect of synthetic antioxidants and black pepper extracts on peroxide values

The gradual increase in PVs of synthetic and 500 ppm & 1000 ppm black pepper extracts is shown in Fig.(2).

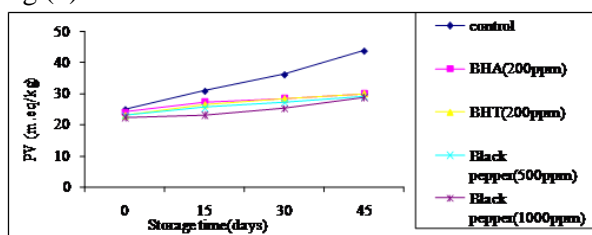


Fig. 2. Comparison of PV values with storage time.

Control showed a PV value of 43.8 m.e.q/kg at 45th day of storage while the sample with added BHA showed a value of 29.88 m.e.q/kg. Similarly, the sample with added BHT showed a PV value of 30.0 m.e.q/kg at the 45th day of storage. The samples with added 500 ppm and 1000 ppm black pepper extracts appreciably controlled the peroxide value and a regular increase in PV as a function of storage time was observed for all samples at all intervals.

The control sample showed a tremendous increase in PV as compared to the other samples. Stabilized samples showed a slower increase in PV as compared to control. PV of 500 ppm black pepper was comparable with that of the synthetic antioxidants BHA and BHT.

Effect of synthetic antioxidants and black pepper extracts on iodine values

Along with the increase in free fatty acid and peroxide values, a marked decrease in the iodine value was observed during storage of sunflower oil. Results are shown in Fig. (3).

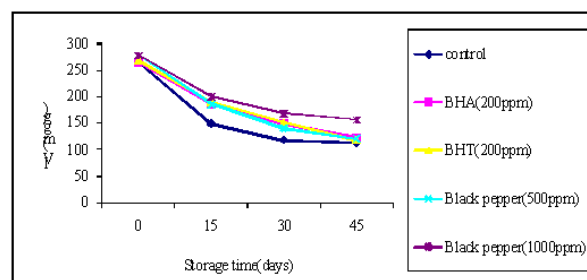


Fig. 3. Comparison of iodine values with time

These results showed that the addition of synthetic and natural antioxidants (BHA & BHT and black pepper extracts) retarded the decreasing trend of the iodine value in sunflower oil samples relative to control during storage for 45 days. The iodine value of the control oil sample at the 45th day of storage was 114.01 mg/g. Addition of BHA and BHT to sunflower oil resulted in iodine values of 123.22 mg/g and 117.99 mg/g, respectively, at the 45th day of storage. While the IV of 500 ppm black pepper stabilized extract was 120.85 mg/g at the 45th day of storage and for 1000 ppm black pepper stabilized extract was 155.98 mg/g at the same day of storage. Therefore, the iodine values of stored sunflower oil treated with synthetic antioxidant and black pepper extracts were distinctly higher than that of the control oil sample.

The gradual decrease of IV can be attributed to breaking of double bonds of unsaturated fatty acids of lipids that is consistent with the findings of Noor and Augustin [19].

CONCLUSIONS

The antioxidant activity of a methanolic extract of black pepper for the stabilization of sunflower oil is comparable with that of synthetic antioxidants such as butyl hydroxyanisole (BHA) and butyl hydroxytoluene (BHT). Rancidity of oil can safely be controlled using high levels of black pepper extract as compared to synthetic antioxidants (BHA & BHT) and thus can increase stability of oils and fats.

REFERENCES

1. H.L. Madsen, G. Bertelsen, *J. Trends Food Sci. Tech.*, **6**, 271 (1995).
2. L.O. Demirezer, A.K. Bergere, H.J. Schiewe, A. Zeeck, *J. Phyto.*, **58**, 1213 (2001).
3. P. Marja, A.I. Hopia, J.V. Hikki, J.P. Raugha, S. Tytti, M. Heinonen, *J. Agric. Food Chem.*, **47**, 3954 (1999).
4. H.M. Esam, H.A. Khalil, *J. Food Chem.*, **69**, 135 (2000).
5. A. Sharma, S. Gautam, S.S. Jadhav, *J. Agric. Food Chem.*, **48**, 1340 (2000).
6. L. Yu, S. Haley, M. Harris, *J. Food Chem.*, **78**, 457 (2002).
7. J. Ullah, M. Hamayoun, T. Ahmad, M. Ayub, M. Zafarullah, *Asian J. Plant Sci.*, **2**, 1192 (2003).
8. S. Naz, H. Sheikh, R. Siddiqi, S.A. Sayeed, *J. Food Chem.*, **88**, 253 (2004).
9. Z.U. Rehman, F. Habib and W.H. Shah, *J. Food Chem.*, **85**, 215 (2004).
10. I. Hinneburg, H.J.D. Dorman, R. Hiltunen, *J. Food Chem.*, **97**, 122 (2006).
11. V.Y. Nedyalka, E. Marinova, J. Pookorny, *Eur. J. Lipid Sci. Tech.*, **108**, 776 (2006).
12. L. Jinyoung, L. Yoosung, C. Eunok, *LWT–Food Sci. Tech.*, **4**, 11871 (2008).
13. B. Kandlakunta, A. Rajendran, L. Thingnganing, *J. Food Chem.*, **106**, 85 (2008).
14. M.I. Bhanger, S. Iqbal, F. Anwar, M. Imran, M.Z. Haq, *Int. J. Food Sci. Tech.*, **43**, 779 (2008).
15. C. Paquot, A. Hautfenne, (eds.), Standard methods for the analysis of oils, fats and derivatives, 7th revised and enlarged ed., International Union of Pure and Applied Chemistry (IUPAC), London: Blackwell Scientific Publications, 1987.
16. IUPAC, Standard methods for the analysis of oils, fats and derivatives (7th ed.), Oxford: Blackwell Scientific Publication, London, 1987.
17. K. Kiyomi, S. Yasuko, K. Kassigeku, *J. Sci. Food Agric.*, **41**, 91 (1995).
18. N. Frega, M. Mozzon, G. Lercker, *J. Am. Oil Chem. Soc.*, **76**, 325 (1999).
19. N. Noor, M.A. Augustin, *J. Sci. Food Agric.*, **35**, 805 (1984).

АНТИОКСИДАНТЕН ПОТЕНЦИАЛ НА ЕКСТРАКТ ОТ ЧЕРЕН ПИПЕР ЗА
СТАБИЛИЗИРАНЕТО НА СЛЪНЧОГЛЕДОВО МАСЛО

А. Фирдос¹, А.Р. Тарик¹, М. Имран¹, И. Ниамат¹, Ф. Канвал¹, Л. Миту^{2*}

¹Институт по химия, Университет в Пунджаб, Лахор -54890, Пакистан

²Департамент по химия, Университет в Питещ, Питещ-110040, Румъния

Постъпила на 15 януари, 2016 г.; коригирана на 4 май, 2016 г.

(Резюме)

Използван е метанолов екстракт от черен пипер в различни концентрации (500 ppm и 1000 ppm) за стабилизирането на слънчогледово масло при съхранение при обикновени условия. Антиоксидантният потенциал на черния пипер е оценен чрез анализа на свободните мастни киселини (FFA), пероксидното число (PV) и йодното число (IV). Ефикасността на екстракта спрямо пробите от слънчогледово масло нараства с нарастването на концентрацията му. Добавянето на 500 ppm от екстракта показват съпоставими стойности за FFA, PV и IV с тези при 200 ppm добавки от ВНА или ВНТ. Обаче стабилизираните проби с екстракт от черен пипер показват по-слабо повишение на стойностите на PV и FFA. Настоящата работа показва, че черният пипер е потенциален източник на природни антиоксиданти, които може да се използват безопасно за подтискането на окислението на липидите и да се предотвратява гранияването им.

Pyrolysis of animal bone, characterization of the obtained char and tar and application of bone tar for crosslinking of epoxy resin

B. Purevsuren¹, Ya. Davaajav¹, J. Namkhainorov¹, Z. I. Glavcheva-Laleva², V. Genadiev³,
I. K. Glavchev^{4*}

¹*Institute of Chemistry and Chemical Technology, Mongolian Academy of Sciences, Ulaanbaatar-51, Mongolia.*

²*Institute of Organic Chemistry with Centre of Phytochemistry, Bulgarian Academy of Sciences, Acad. G. Bonchev Str., Building 9, 1113 Sofia, Bulgaria*

³*Research Institute of Building Materials, 1, Ilia Beshkov Str., 1528 Sofia, Bulgaria*

^{4*}*University of Chemical Technology and Metallurgy, 8, Kl. Ohridski Blvd, 1756 Sofia, Bulgaria*

Received October 19, 2015; Revised May 27, 2016

In this investigation the technical characteristics and elemental composition of animal bones were determined and their pyrolysis, production of bone char, tar, water and gases and application of bone tar as a curing agent of epoxy resin were studied. It was found that animal bone has a higher quantity of mineral components - (A^a -63.5%) than organic matter - (V^a - 31.30%) and also has less organic carbon - (C^{daf} -32.90%) than oxygen and other elements - (O^{daf} + others - 55.9%). Pyrolysis experiments of animal bone were carried out at different heating temperatures and the yields of obtained solid (char), liquid (tar and pyrolysis water) and gas products were determined. A temperature around 600°C was determined as the optimal heating temperature of pyrolysis and the obtained products were approximately 66.35% char, 4.33% tar, 18.02% pyrolysis water and 11.29% gas. The bone char has a higher ash content – 84.8% compared to initial bone (A^a - 63.5%) and significantly lower contents of carbon, hydrogen, nitrogen and oxygen. For tar the contents of carbon, hydrogen and nitrogen increased almost 10 times compared to char while the content of oxygen was the same in both products. The pyrolysis of the animal bone samples was carried out in a laboratory reactor. In the present work a curing agent- tar was obtained from animal bone by pyrolysis. The product contains 18.95% of pyrolysis water with 76.05% degree of curing reaction for epoxide resin ED – 20. We prepared a new curing agent for epoxide resin by mixing bone tar and diethylenetriamine at a mass ratio of 1:1 (homogeneous mixture), which has 96% degree of curing reaction.

Keywords: animal bone, bone pyrolysis, bone char and tar, application of tar as a crosslinking agent of epoxy resin.

INTRODUCTION

Animal bones are very important bio-organic source of Ca and P [1] and are also used for obtaining bone powder, glue and fat. About 40-50 thousand tons of animal bones per year are produced in Mongolia. Unfortunately, animal bone is almost considered as a waste material in Mongolia, except the production of small amount of bone powder for export. The production of cheap animal glue was, however, closed. The same is the situation in Bulgaria, only the quantity of animal bones is smaller.

An alternative method of animal bone processing is the thermal treatment (pyrolysis) for producing bone char and tar [2]. Bone char is a cheap and effective filtering and adsorbent material after its activation [3]. Usually pyrolysis of a mixture of animal bones and meat is carried out [4]. The first experiments of pyrolysis of pure animal bone have been carried out in a laboratory of the Mongolian Academy of Sciences and the yields of bone char, tar and gas products were determined [5, 6]. The bone

char was processed by activation with preheated water steam to produce activated carbon material with porous structure [7]. In this work a more detailed investigation of the pyrolysis process was performed.

EXPERIMENTAL

The applied cattle bones were crushed into pieces of 3-6 mm size and rinsed three times with deionized water. After that the bones were boiled at least 3 times in distilled water for 4 h. to remove meat residues, fat and finally the samples were dried at 105°C and allowed to cool in a desiccator. The analytical samples were prepared by powdering to a particle size < 0.2 mm in a steel mill. These processes are described in the Mongolian National Standards: 2719.2001 (analytical sample preparation), 656-79 (moisture content), 652-79 (ash yield), 654-79 (volatile matter yield) and 669-87 (gross calorific value). The apparatus used for elemental analysis was 5E C 2000 model CNH – analyzer. FTIR spectra were recorded on a Nicolet 20-PC FTIR spectrometer with CsI optics and DTGS detector with KBr pellets with 0.5% sample content. Thermogravimetric analyses were made with TG/DTA7200 Hitachi, Japan model equipment in

* To whom all correspondence should be sent:
E-mail: ivgl@uctm.edu

the temperature range of 20 – 1150 °C, with heating rate of 40°C/min, carrier gas nitrogen p.a. and a Pt-Rh thermocouple for temperature measurement. All pyrolysis experiments of animal bone samples were performed in a laboratory quartz retort (tube) which could contain dry air. All samples (1 g) were powdered to a particle size < 0.2 mm. The retort was placed in a horizontal electric tube furnace with a maximum heating temperature of 950°C. The actual heating temperature in the tube furnace was measured by a chromel-alumel thermocouple. The pyrolysis experiments were carried out at different heating temperatures in the range of 200-700°C with a constant heating rate of 20°C/min. Firstly, the quartz retort with the bone sample was heated to 600°C with a heating rate of 20°C/min and was kept at 700°C for 80 min. The retort was connected with a thermostated glass tube also heated in a tube furnace at 80°C for collecting tar. This tube was connected with an air-cooled glass vessel for collecting pyrolysis water. The glass vessel for pyrolysis water was also connected with a thin glass tube for collecting non-condensable gases. The yields of pyrolysis products including solid residue (coal char), tar (condensed liquid product) and pyrolysis water (condensed liquid product) were determined by weighing and the yield of gases was determined by difference as the average value of 3 replicates.

The preparative-scale pyrolysis experiments of animal bone samples were performed in a laboratory vertical cylindrical retort made of stainless steel which could contain 1000 g. of sample. The retort was placed in an electric furnace (model SNOL) with a maximum temperature of 950°C. The actual heating temperature was measured using a chromel-alumel thermocouple immersed in the bone bed, equipped with a potentiometer for temperature control. The retort was connected with an air-cooled iron tube, a water-cooled laboratory glass condenser and a collection vessel for the condensate of liquid products (tar and pyrolysis water). The non-condensable gases after the water-cooled condenser left the system through a thin glass tube. The experiments were carried out at a temperature of 900°C at a heating rate of 20 °Cmin⁻¹. The yields of products including solid residue (char), tar and pyrolysis water were determined by weighing and the yield of gases - by difference.

Method for separation of tar and pyrolysis water

The liquid condensed products of bone pyrolysis consist of tar and pyrolysis water. They form two

immiscible layers which can be easily separated by means of a separatory glass funnel. The upper layer is tar (a viscous liquid) with black-brown color and unpleasant smell. The bottom layer is pyrolysis water (not viscous liquid) with bad smell and brown color. The final cleaning of tar from pyrolysis water residues takes place by mixing with thermally treated CaCl₂ and separating (filtering or centrifuging). The mass ratio of tar and pyrolysis water is approximately 1:4.

The pyrolysis water can be concentrated by vacuum distillation. The distillation starts at 45 °C by foaming and forming colorless water drops and continues until 85 °C. In our experiments 63% concentrated pyrolysis water with black-brown color and some precipitates, 27% colorless distilled water and 14% uncondensed gas was obtained.

Method for curing of epoxy resin with tar and concentrated pyrolysis water

A sample of 1.0 g. of technical grade epoxy resin ED-20, made in Russia, was mixed with 15-20% tar or 20-25% concentrated pyrolysis water in a small glass vessel to form a homogeneous mixture. When this mixture was kept for 24 h. at room temperature, no curing of the epoxy resin took place. Therefore, this mixture was transferred to a small glass vessel and was kept for 2h. in an oven at 120°C. In this case there was curing of the epoxy resin resulting in a hard glassy product. The cured epoxy resin was powdered in a steel mill and 1.0 g. of the sample was packed in a pre-weighed filter paper and was extracted with technical grade acetone, product of Merck on a Soxhlet apparatus. After finishing the extraction, the sample and filter paper were dried at 105 °C in an oven until constant weight and the fraction insoluble in acetone (gel fraction or degree of curing reaction of epoxy resin in %) was determined. The accuracy of weighing was 0.0001 g. To increase the curing ability of bone tar, a homogeneous mixture of bone tar and technical grade diethylenetriamine, CAS N 111-40-0, product of DOW, was made by mixing the liquids (mass ratio 1:1) in a glass vessel. Diethylenetriamine (DETA) is a standard curing agent of epoxy resin.

RESULTS AND DISCUSSION

The average results of the pyrolysis of animal bones are given in tables 1 and 2.

Animal bone is a bio-organic material characterized with a higher mineral content such as 63,35% ash and for this reason has comparatively

Table 1. Analytical results for the pyrolysis of animal bone samples

№	Sample	Moisture, %	Ash, %		Volatile matter, %		Caloric value,
		W ^a	A ^a	A ^d	V ^a	V ^{daf}	Q ^{daf} , kcal/kg
1.	Animal bone	5.68	63.35	67.17	31.30	86.06	3604

daf = dry, a = ash-free;

Table 2. Results of the analysis of animal bones.

№	Sample	C ^{daf} , %	H ^{daf} , %	N ^{daf} , %	H/C	O ^{daf} + others %
1.	Animal bone	32.90	8.00	3.20	2.91	55.90

(N+O)^{daf}- by difference

Table 3. Yield of pyrolysis products at different heating temperatures of animal bone samples.

№	Heating temperature, T°C	Time of heating, min.	Char, %	Condensed liquid products, %		Uncondensed gas, %
				Tar	Pyrolysis water	
1.	200	80	93.20	1.30	2.98	2.52
2.	300	80	83.02	2.63	7.53	6.82
3.	400	80	75.12	4.84	13.10	6.94
4.	500	80	70.86	6.55	13.27	9.32
5.	600	80	69.71	7.21	12.57	10.51
6.	700	80	68.60	7.20	12.10	12.00

Table 4. Yield of pyrolysis products in a large-scale retort at 600°C

№	Char, %	Condensed liquid products, %		Uncondensed gas, %
		Tar	Pyrolysis water	
1.	67.25	4.31	17.60	10.84
2.	65.89	4.45	18.66	11.00
3.	65.92	4.24	17.80	12.04
4.	66.35	4.33	18.02	11.29

Table 5. Elemental composition of the bone pyrolysis char and tar and main technical specifications.

№	Elemental composition and specifications	Char	Tar
1.	Carbon (C), wt %	8.4	73.3
2.	Hydrogen (H), wt %	0.5	10.1
3.	Nitrogen (N), wt %	1.1	11.3
4.	Oxygen (O), wt % (by difference)	5.1	5.3
5.	H/C atomic ratio	0.71	1.65
6.	Ash, wt %	84.8	-
7.	Volatile matter, wt % (daf)	7.7	-
8.	Caloric value, kcal/kg	560.33	-

Table 6. Conditions of curing tests and determined degree of curing reaction of epoxide resin with bone pyrolysis tar and pyrolysis water

№	Samples: Epoxy resin(ER), Tar (T), Pyrolysis Water(PW), Diethylenetriamine (DETA)	Added amount of curing agent, %	Weight of cured sample for extraction in acetone, g	Weight of cured sample after extraction in acetone, g	Acetone soluble fraction, %	Acetone insoluble fraction(degree of curing reaction), %
1	ER+T	15.00	1.2626	0.2393	81.05	18.95
2	ER+PW	20.00	0.6477	0.4077	37.05	62.95
3	ER +PW	60.00	0.7243	0.5509	23.94	76.05
4	ER+PW(concentrated)	20.00	0.9952	0.7282	26.81	73.12
5	ER+(T+DETA)(50:50wt.%)	15.00	1.0231	0.9812	4.00	96.00

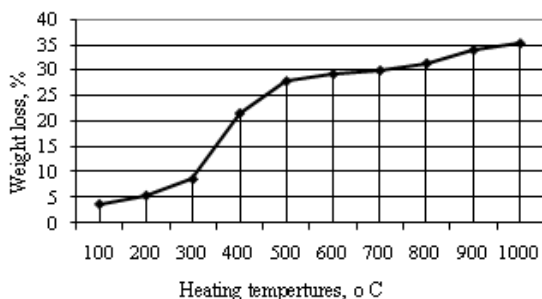


Fig.1. Results of the thermogravimetric analysis of animal bone.

lower volatile organic matters and calorific value. The elemental composition of bone (Table 2) shows that the contents of organic C,H and N are lower and the contents of O and other elements are higher, which is an evidence for the higher mineral content of animal bone (Table 1).

The results of the thermogravimetric analysis of animal bone are shown in Figure 1.

The heating of the bone sample at temperatures in the range of 25-1000 °C in nitrogen atmosphere shows that the thermal decomposition of bone ends with a 35% weight loss and 65% hard residue at 1000 °C (Figure 1). The TG curve in Figure 1 consists of different temperature intervals (steps) such as 25-200°C; 200-500°C; 500-700°C; 700-1000°C. In the first step (25-200°C) the weight lost is due to the release of some absorbed gas and moisture from the bone sample. In the second step (200-500°C) intensive thermal decomposition of the organic matter of the bone samples starts forming liquid (tar and pyrolysis water) and gas products. In the third step (500-700°C) the weight loss strongly decreases, which is an indication for ending thermal decomposition and starting carbonization of the bone sample. In the fourth step (700-1000°C) the weight loss slowly increases, which is related with the release of gas, e.g., CO₂, H₂, P₂O₅ from the mineral bone contents.

The further experiments focused on the pyrolysis of the bone samples at different heating temperatures in a standard quartz retort and the yields of obtained hard residue (char), condensed liquid (tar and pyrolysis water) and gas products after pyrolysis were determined (Table 3).

Table 3 shows that the yield of char decreases and the yields of tar, pyrolysis water, gas slowly increase by increasing the heating temperature. The yields of pyrolysis products are comparatively higher in the temperature range of 500-700 °C, which is the optimal heating temperature. The results of the thermogravimetric analysis (Figure 1) and the results of the pyrolysis experiments (Table 3) are very

similar and confirm each other. 600°C was chosen as the optimal heating temperature and the further experiments of pyrolysis were carried out in a large-scale retort at this temperature for collecting more char and tar for their characterization. The yields of pyrolysis products in the large-scale retort (for 3 replicate experiments) are shown in Table 4.

The FT-IR spectrum of bone char is shown in Fig. 2.

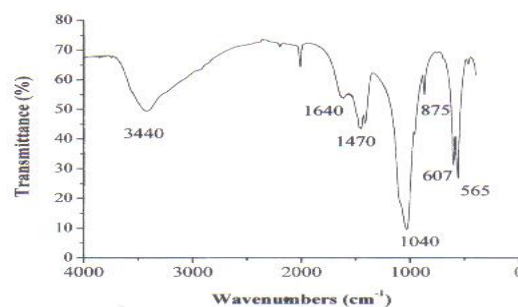


Fig. 2. FT-IR spectrum of bone char

The FT-IR spectrum of bone char in Figure 2 shows that the bands observed at 1640 and 3440 cm⁻¹ indicate adsorbed H₂O in the char. The bands appearing at 875 and 1470 cm⁻¹ are indicative of carbonate. Bands located around 1040, 607 and 560 cm⁻¹ are related with phosphate group absorption. The FT-IR spectrum of bone tar is presented in Figure 3.

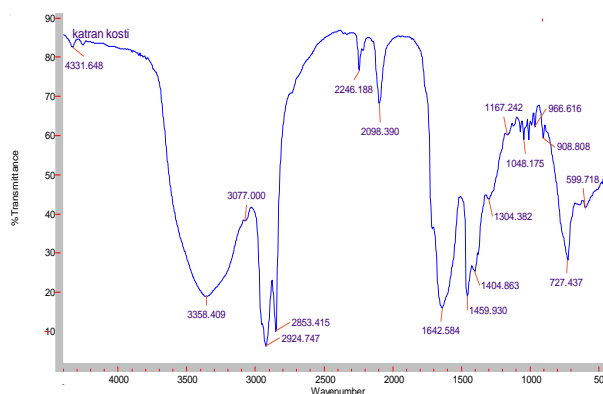


Fig. 3. FT-IR spectrum of bone tar

The FT-IR spectrum of bone tar in Figure 3 shows weak absorption bands for H of aromatic -CH group at 1000-1300, 700-800 cm⁻¹ and strong bands for H of aliphatic -CH₃, -CH₂ and -CH groups at 2853-2924 cm⁻¹ and also for H of -OH and -NH, -NH₂ groups at 3358 cm⁻¹. There are strong bands at 1400-1642 cm⁻¹ for skeletal vibrations of >C=O groups in ketones, aldehydes, esters and quinines. Therefore the bone tar is a multicomponent mixture mainly consisting of organic substances with aliphatic chains and aromatic structures with oxygen and nitrogen functionalities.

The separated bone tar and pyrolysis water were tested as curing agents for epoxide resin, because the oxygen and nitrogen functionalities in them can react with the epoxy ring of the resin. Epoxy resin, tar and pyrolysis water are soluble in acetone. In case of curing reactions between them, the product should not be soluble in acetone, because of crosslinking reactions between the epoxide chain molecules. The primary results obtained and the conditions of curing reactions are presented in Table 6.

The data in Table 6 show that T and PW both display some curing ability for ER, but the curing ability of PW is over 3.3 times higher than that of T. By increasing the amount of PW 3 times, the degree of curing increased to 76.05%, but such large amount of the curing agent is not suitable. Therefore, as mentioned in the experimental part, the PW was concentrated and used as a curing agent. In this case almost the same result was achieved (73.12%) compared with that of unconcentrated PW (76.05%). This result shows that T and PW originate from the bio-organic material – bone, containing 3.2% N. Therefore T and PW have a certain amount of oxygen (-OH; -COOH) and nitrogen (-NH; -NH₂; -CN) functionalities, H atoms from which are able to react with the epoxy groups of ER in crosslinking reactions. PW has more functionalities than T.

To increase the curing ability of bone tar a homogeneous mixture of tar and diethylenetriamine was prepared at a mass ratio of 1:1; the determined degree of curing reaction was 96%. The results of this experiment show that this is a reasonable way for increasing the curing ability of bone tar for epoxy resin (Table 6).

In our previous work a curing agent (casein tar from milk casein, having higher nitrogen content (15.75%) than bone (3.2%)), has been obtained with 94.00-96.00% degree of curing reaction for ER [9]. In our present work a curing agent with 18.95% (T) and 76.05% (PW) degree of curing reaction for ER was obtained from animal bones by pyrolysis. The lower degree of curing reaction of bone T and PW in comparison with that of milk casein is due to the lower content of N in bones.

CONCLUSIONS

1. For the first time the technical characteristics and elemental composition of pure animal bones were determined. Animal bones contain a larger amount of mineral components (A^a-63.5%) than organic matter (V^a-31.30%) and also have less organic carbon (C^{daf}-32.90%) than oxygen and other elements (O^{daf} + others -55.9%).

2. Heating of bone samples in the temperature range of 25-1000 °C in nitrogen atmosphere shows

that the thermal decomposition ends with 35% weight loss and 65% hard residue. The TG curve consists of different temperature intervals (steps) such as 25-200°C; 200-500°C; 500-700°C and 700-1000°C. In the first step (25-200°C) the weight loss is due to the release of absorbed gas and moisture from the bone samples. In the second step (200-500°C) intensive thermal decomposition of the organic matter of the bone sample starts, forming liquid (tar and pyrolysis water) and gas products. In the third step (500-700°C) the weight loss strongly decreases, which is an indication for ending thermal decomposition and starting carbonization of the bone sample. In the fourth step (700-1000°C) the weight loss slowly increases, which is related with the release of gas, e.g., CO₂, H₂, P₂O₅ from the mineral content of the bone.

3. The bone char has a higher content of ash-84.8% than initial bone (A^a- 63.5%) and strongly decreased content of carbon, hydrogen, nitrogen and oxygen. The caloric value of the char is 6.4 times lower than that of initial bone, which confirms the lower content (8.4%) of C in the char.

4. In the case of tar, the content of carbon, hydrogen and nitrogen increased almost 10 times in comparison with the char, except the content of oxygen, which remains the same in both cases. Increasing of the content of C, H and N in the tar indicates that these elements come from the bone organic matter released during the thermal decomposition of bone. The pyrolysis tar is a viscous liquid with black-brown color and unpleasant smell.

5. The FT-IR spectrum of bone char shows that the bands observed at 1640 and 3440 cm⁻¹ indicate adsorbed H₂O in the char. The bands appearing at 875 and 1470 cm⁻¹ are indicative of carbonate. The bands located around 1040, 607 and 560 cm⁻¹ were related with phosphate group absorption.

6. The FT-IR spectra of bone tar in Figure 3 show weak absorption bands for H of aromatic -CH group at 1000-1300, 700-800 cm⁻¹ and strong bands for H of aliphatic -CH₃; -CH₂ and -CH groups at 2853-2924 cm⁻¹ and also for H of -OH and -NH and -NH₂ groups at 3358 cm⁻¹. There are strong bands at 1400-1642 cm⁻¹ for skeletal vibrations of >C=O groups in ketones, aldehydes, esters and quinines. Therefore, the bone tar is a multicomponent mixture consisting mainly of organic substances with aliphatic chains and aromatic structures with oxygen and nitrogen functionalities.

7. Curing agents - tar and pyrolysis water were obtained from pyrolyzed animal bone with 18.95% and 76.05% degree of curing reaction for low molecular epoxy resin, respectively.

8. A new curing agent for the same epoxy resin was prepared by mixing bone tar and diethylenetriamine at a mass ratio of 1:1 (homogeneous mixture), displaying 96% degree of curing reaction.

REFERENCES

1. B. Kramer, M. J. Shear, *J. Biol. Chem.*, **79**, 147 (1928).
2. W. I. Abdel-Fattan, T. M. Ghazy, M. M. Selim, *Thermochimica Acta*, **51**, 287 (1981).
3. F. Cecen, O. Aktas, Activated carbon for water and wastewater treatment, WILEY-VCH Verlag GmbH & Co. KGaA, 2012.
4. www.engconf.org/staging/wp-content/uploads/2014/08/11-AA_Oral
5. B. Purevsuren, T. Gerelmaa, S. Enkhtuul, *Proceedings of the Mongolian Academy of Sciences*, **1**, 13 (2001).
6. B. Purevsuren, B. Avid, J. Narangerel, T. Gerelmaa, Y. Davaajav, *Journal of Materials Science*, **39**, 737 (2004).
7. B. Purevsuren, Mongolian Patent No 3024 (2008).
8. B. Purevsuren, B. Avid, T. Gerelmaa, Y. Davaajav, T. J. Morgan, A. Herod, R. Kandiyoti, *Fuel*, **83**, 799 (2004).
9. B. Purevsuren, Y. Davaajav, V. Genadiev, H. Kotsev, I. Glavchev, *Bulgarian Chemical Communications*, **45**(2), 157 (2013).

ПИРОЛИЗА НА ЖИВОТИНСКИ КОСТИ, ХАРАКТЕРИЗИРАНЕ НА ПОЛУЧЕНИТЕ ВЪГЛЕН И КАТРАН И ПРИЛАГАНЕТО НА КОСТЕН КАТРАН ЗА ОМРЕЖВАНЕ НА ЕПОКСИДНА СМОЛА.

Б. Пуревсурен¹, Я. Давааджав¹, Дж. Намхайноров¹, З. И. Главчева-Лалева², В. Генадиев³,
И. К. Главчев⁴

¹ *Институт по химия и химични технологии, Монголски академия на науките, Улан Батор-51, Монголия.*

² *Институт по органична химия, Българска академия на науките, акад. Г. Бончев Street, Сграда 9, 1113 София, България;*

³ *Изследователски институт по строителни материали, ул. Илия Бешков 1, 1528 София, България*

⁴ *Химикотехнологичен и металургичен университет, 8 Кл. Охридски, 1756 София, България*

Получена на 19 октомври, 2015 г.; преработена на 27 май, 2016 г.

(Резюме)

В това изследване са определени техническите характеристики и елементният състав на животински кости, тяхната пиролиза, производството на твърд, течен и газообразни продукти и приложението на течния продукт като втвърдител на епоксидна смола. Животинските кости се характеризират с по-голямо съдържание на минерални компоненти - (A^a -63,5%), отколкото на органични - (V^a - 31,30%), а също и с по-малко съдържание на органичен въглерод- (C^{daf} -32,90%) отколкото на кислород и други елементи (O^{daf} + други -55,9%). Пиролизните опити на животински кости са проведени при различни температури на нагряване и са определени добивите на твърд (пиролизен въглен), течен (катран и пиролизна вода) и на газообразни продукти. Температурата около 600°C бе определена като оптимална температура на нагряване и са получени около 66,35% пиролизен въглен, 4,34% катран, 18,02% пиролизна вода и 11,29% газове са получени при пиролизата. Пиролизният костен въглен има високо съдържание на пепел -84,8% в сравнение с костите (A^a -63,5%) и със интензивно намаление на съдържанието на въглерод, водород азот и кислород. В случая на катрана, съдържанието на въглерод, водород и азот нараства около 10 пъти в сравнение със съответното съдържание в костите. Пиролизата на проби от животински кости е проведена в лабораторен реактор. Във предишна наша работа бе получено втвърдяване на епоксидна смола ЭД – 20 със костния катран 18,95% и с пиролизна вода 76,05%. Ние приготвихме нов втвърдител на същата смола чрез смесване на костния катран с диетилентриамин в масово съотношение 1:1 (хомогенна смес), която дава 96% на омрежващата реакция.

Monomeric phenolic compounds from hydrolyzed waste lignocellulosic materials

T. Hr. Radoykova,* S. K. Nenkova, I. V. Valchev

University of Chemical Technology and Metallurgy, 8 Kl. Ohridski Blvd., 1756 Sofia, Bulgaria

Received November 23, 2015; Revised July 1, 2016

Alkaline treatment (4 and 6 hours) of hydrolyzed waste lignocellulosic materials was carried out. Monomeric phenolic compounds: 2-methoxyphenol, 3-ethylphenol, 4-ethyl-2-methoxyphenol, 2,6-dimethoxyphenol, 4-hydroxy-3-methoxybenzaldehyde, 4-hydroxy-3,5-dimethoxybenzaldehyde, 1-(4-hydroxy-3-methoxyphenyl) ethanone, 1-(4-hydroxy-3,5-dimethoxyphenyl) ethanone, etc. were obtained. Toluene and ethyl acetate were used for extraction of the monomeric products.

Keywords: Waste hydrolyzed lignocellulosic materials; Alkaline treatment; Phenolic compounds; Extraction.

INTRODUCTION

The chemical treatment of wood to produce cellulose and monosaccharides is accompanied by the production of about one third of its mass of lignin-rich residue. The production of bioethanol from raw materials has been increasing, and hence, the utilization of lignin has started to attract significant interest.

The alkaline hydrolysis of lignin results in its depolymerization through the rupture of ether and C-C bonds connecting the phenylpropane units. The method leads to the production of low-molecular weight monomeric phenols (2,6-dimethoxyphenol, 3,6-dimethoxy-4-hydroxy acetophenone, 4-ethylguaiacol, 2-methoxyphenol, 4-ethyl-2-methoxyphenol, 2-methoxy-4-propylphenol, 4-methylcatechol, phenol, 4-hydroxy-3,5-dimethoxybenzaldehyde, and 4-hydroxy-3-methoxybenzaldehyde [1]. Waste lignocellulosic biomass has been shown to be a suitable source of monomeric phenolic compounds [2]. The monomeric and oligomeric lignin-derived products have been produced by supercritical water treatment of softwood and hardwood [3-5] and might be useful for substituting the aromatic chemicals from fossil resources.

In our earlier investigations, the antioxidation effect of methoxyphenols produced from lignin was demonstrated by the oxygen absorption of liquid paraffin in a laboratory manometric installation [6] and by determining the gasoline induction period [7]. Furthermore, alkaline treatment is widely applied in hydrolyzed residual lignin activation aiming its utilization [8]. In the cited paper it was found that the treatment with 5.0 % NaOH leads to

the production of lignin products with the highest hydrophilicity and the best porosity.

The aim of the present study was to investigate the nature of the low-molecular products extracted with a polar and a non-polar solvent from the liquid phase after the alkaline treatment, from hydrolyzed waste lignocellulosic materials. Steam explosion and dilute acid hydrolysis were used as pretreatment methods. Their application was followed by enzymatic hydrolysis with cellulase enzyme complex combined with β -glucosidase [9].

EXPERIMENTAL

The process conditions were determined based on the results of our earlier investigations [10, 11]. The determination of lignin was carried out according to TAPPI standard test method T 222 om-11.

The alkaline treatment of hydrolyzed waste lignocellulosic materials was carried out in stirred autoclaves made of stainless steel, heated in a bath of polyethylene glycol at 180 °C for 4 and 6 hours. An aqueous solution of NaOH (5%) was used as a depolymerization agent, at a ratio of waste materials to aqueous NaOH solution of 1:8. The principal scheme for the production of low-molecular compounds from hydrolyzed waste lignocellulosic materials is shown on Fig.1. The destructed lignin suspension obtained by alkaline treatment was filtered, and the quantity of solid residue was determined. The dissolved part was precipitated by acidification with HCl (2 mol/L) to pH 1 - 2. The volume of the liquid part separated by filtration was reduced by rota evaporation. A triple extraction was carried out at a toluene to water ratio of 1:5. The toluene extract was dried up with anhydrous Na₂SO₄ and then filtered. The liquid phase separated after the toluene extraction was subjected to a double extraction with ethyl acetate at an organic to water ratio of 1:5. The amounts of obtained extracts,

* To whom all correspondence should be sent:
E-mail: nusha_v@uctm.edu

insoluble residue, precipitated and non-precipitated lignin were determined.

The compounds were identified by GC-MS analysis with a KONIK gas chromatography unit, model HRGC 5000B, equipped with a mass selective detector, MS Q 12. A 15 m × 0.25 mm i.d. capillary column KNK 5 with a film thickness of 0.25 μm was used. The GC oven temperature was held at 40 °C for 5 min and then programmed to attain a temperature of 270 °C at a 10 °C/min ramping rate. The injector temperature was 280 °C with 20:1 split ratio. Helium was used as the carrier gas at a constant flow rate of 1.3 mL/min. Typical mass spectrometry operating conditions were as follows: temperature of transfer line, 250 °C; temperature of ion source, 245 °C; electron energy, 70 eV.

RESULTS AND DISCUSSION

The lignin content determined in the hydrolyzed waste lignocellulosic materials is shown in Table 1. The yield of products from the alkaline treatment of hydrolyzed waste lignocellulosic materials is shown in Table 2. During alkaline treatment, 55 to 75% of the starting material became soluble (Table 2). These values include both solubilized lignin and hydrolyzed polysaccharides. Some cellulose and lignin remained as insoluble residue. The main portion of lignin was destructed and dissolved in the alkaline solution. From the solution, after acidification, alkaline activated lignin was separated; the liquid phase contained low-molecular phenol compounds (LMPC) from the decomposed lignin.

It was found that by increasing the process duration, enhanced yield of monomeric compounds was obtained.

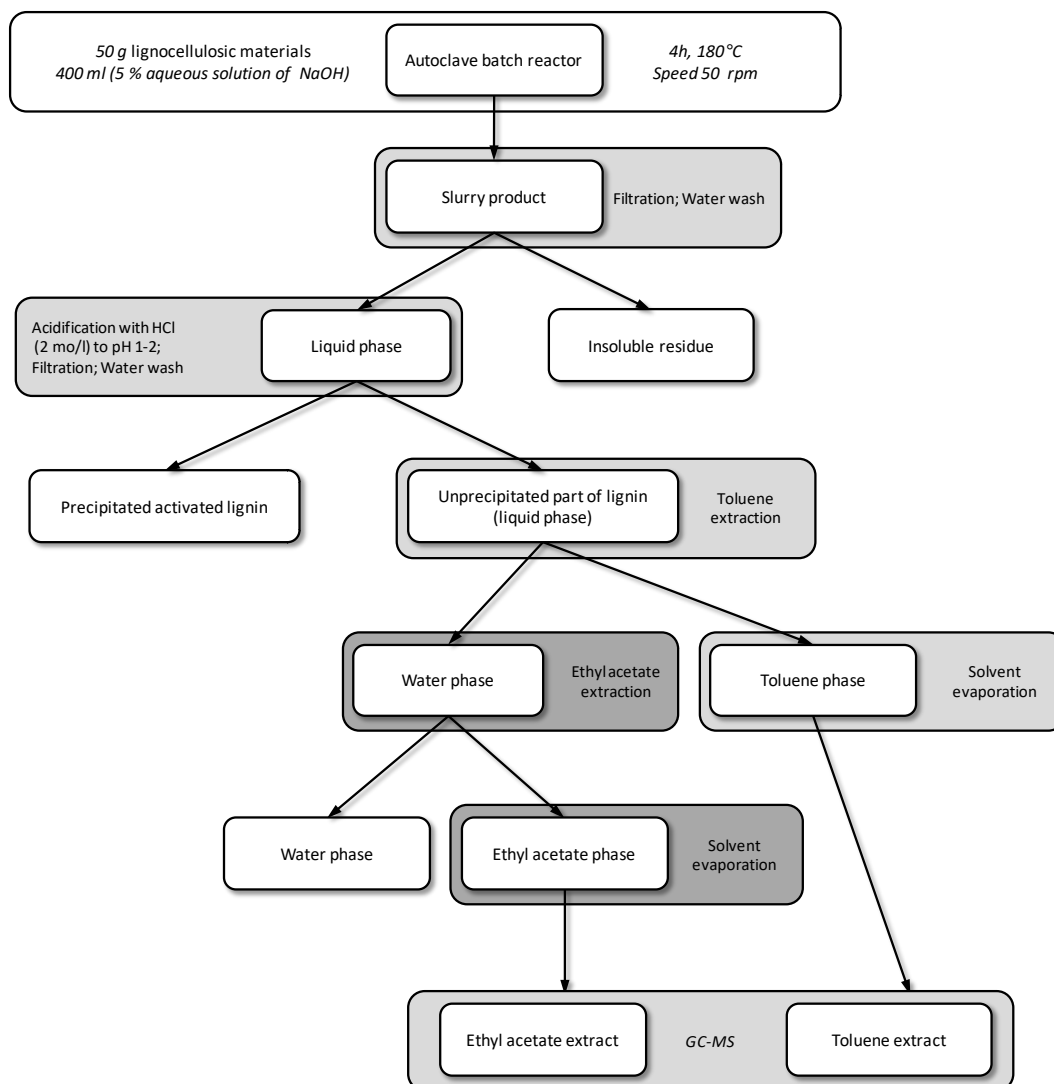


Fig. 1. Scheme for production of low-molecular compounds from hydrolyzed waste lignocellulosic materials.

Table 1. Lignin content in hydrolyzed waste lignocellulosic materials

Waste materials from	Lignin content [%]
Acid (130°C) and enzymatic hydrolysis of wheat straw	40.2
Steam explosion (190°C) and enzymatic hydrolysis of wheat straw	36.6
Acid (130°C) and enzymatic hydrolysis of maize stalks	42.7
Steam explosion (190°C) and enzymatic hydrolysis of maize stalks	38.3
Steam explosion (190°C) and enzymatic hydrolysis of paulownia	37.4

Table 2. Yield of products from the alkaline treatment of hydrolyzed waste lignocellulosic materials

Waste materials	Duration of treatment [h]	Undissolved residue [%*]	Dissolved part				Total yield of monomeric compounds [% of lignin content]
			Precipitated lignin [%*]	Unprecipitated part in the aqueous phase [%*]	Toluene extract [%*]	Ethyl acetate extract [%*]	
Wheat straw Acid pretreatment	4	29.64	22.46	47.90	1.64	1.50	7.81
	6	28.75	28.43	42.82	3.00	3.77	18.50
Wheat straw Steam explosion pretreatment	4	44.53	25.14	30.33	1.88	3.68	15.19
	6	28.75	28.43	42.82	3.00	3.77	18.50
Maize stalks Acid pretreatment	4	36.44	16.48	47.08	0.87	2.13	7.02
	6	27.83	26.49	45.68	3.97	3.30	17.02
Maize stalks Steam explosion pretreatment	6	29.26	21.60	49.14	3.27	3.74	18.28
Paulownia Steam explosion pretreatment	6	24.34	19.40	56.26	3.93	2.22	16.45

Note: * mass percentage of initial material.

With 4 h of alkaline treatment, the highest yield of low molecular compounds was obtained by steam explosion of enzymatic hydrolyzed straw (15.19% mass of lignin). The highest yield of soluble and precipitated lignin was obtained by this process. It was found that the total yield of low-molecular compounds with acid pretreatment is considerably lower than the yield obtained with steam explosion pretreatment. (7.81% mass of lignin for wheat straw and 7.02% mass of lignin for maize stalks). Probably, the acid pretreatment leads to some condensation in the chemical structure of the lignin.

With 6 h of alkaline treatment, the highest yield of low molecular compounds was obtained again by steam explosion of enzymatic hydrolyzed straw (18.50% mass of lignin). The yield obtained from steam explosion of maize stalks was 18.28%, followed by the yield from acid pretreatment of

maize stalks (17.02%) and the yield from steam explosion of paulownia (16.45 %).

Tables 3 and 4 present the low-molecular compounds and their contents identified in the toluene extracts and in the ethyl acetate extracts.

The following compounds were identified in both extracts, but in different quantities: 2-methoxyphenol, 3-ethylphenol, 4-ethyl-2-methoxyphenol, 2,6-dimethoxyphenol, 4-hydroxy-3-methoxybenzaldehyde, 4-hydroxy-3,5-dimethoxybenzaldehyde, 1-(4-hydroxy-3-methoxyphenyl) ethanone, 1-(4-hydroxy-3,5-dimethoxyphenyl) ethanone, etc. The polar solvent ethyl acetate extracts mainly carbonyl compounds, such as ketones, aldehydes, and carbonic acids, which are not extracted by toluene.

The main compounds extracted with toluene are: 2,6-dimethoxyphenol (from 13.7 to 46.4 Area %); 1-(4-hydroxy-3,5-dimethoxyphenyl) ethanone (from

Table 3. Compounds identified in the toluene extracts

Compounds	Retention time, [min]	Wheat straw (Acid)	Wheat straw (Steam explosion)		Maize stalks (Acid)		Maize stalks (Steam explosion)	Paulownia (Steam explosion)
		[Area,%]	[Area,%]		[Area,%]		[Area,%]	[Area,%]
		4h	4h	6h	4h	6h	6h	6h
Unidentified compound	5.20	1.2	0.8	-	-	-	-	-
Benzaldehyde	5.91	9.1	2.9	-	3.4	-	-	-
Phenol	6.71	5.7	1.5	-	1.8	-	-	-
Unidentified compound	7.67	8.9	4.2	-	4.7	-	-	-
Unidentified compound	7.80	1.3	-	-	-	-	-	-
Unidentified compound	7.93	1.0	1.0	-	3.2	-	-	-
1,3-cyclopetanedione	8.33	2.6	2.4	-	1.8	-	4.0	-
2-methoxyphenol	8.85	22.8	24.2	23.2	15.9	14.6	16.2	11.6
Unidentified compound	9.43	-	1.2	-	1.2	6.6	3.9	11.7
3-Ethylphenol	9.92	1.8	3.8	-	3.8	-	-	-
4-Ethyl-2-methoxyphenol	11.91	-	1.2	10.8	1.7	10.9	3.7	-
Unidentified compound	11.96	-	-	-	-	-	3.4	-
Unidentified compound	12.01	-	-	-	-	-	5.5	-
2,6-Dimethoxyphenol	12.89	13.7	16.5	29.2	23.2	29.8	40.6	46.4
4-Hydroxy-3-methoxybenzaldehyde	13.52	2.9	9.1	-	2.7	-	-	-
1-(4-Hydroxy-3-methoxyphenyl) ethanone	14.62	3.1	6.5	-	2.9	4.3	-	-
Unidentified compound	15.12	-	0.7	-	-	-	-	-
4-Hydroxy-3,5-dimethoxybenzaldehyde	16.63	1.1	1.4	-	1.8	4.4	-	-
1-(4-Hydroxy-3,5-dimethoxyphenyl) ethanone	17.43	24.8	22.6	36.8	27.1	29.4	22.7	30.3
Unidentified compound	17.76	-	-	-	1.1	-	-	-
Unidentified compound	20.23	-	-	-	2.6	-	-	-
Unidentified compound	24.39	-	-	-	1.1	-	-	-

22.6 to 36.8 Area %) and 2-methoxyphenol (from 11.6 to 24.2 Area %).

CONCLUSIONS

By extraction with two solvents, the following lignin degradation products were isolated: 2-methoxyphenol, 3-ethylphenol, 4-ethyl-2-methoxyphenol, 2,6-dimethoxyphenol, 4-hydroxy-3-methoxybenzaldehyde, 4-hydroxy-3,5-dimethoxybenzaldehyde, 1-(4-hydroxy-3-methoxyphenyl)

ethanone, 1-(4-hydroxy-3,5-dimethoxyphenyl) ethanone, etc.

The total yield of extracted monomeric compounds after 6 h of alkaline treatment is from 16.45% mass of lignin (paulownia, steam explosion) to 18.50% mass of lignin (straw, steam explosion followed by enzymatic hydrolysis). It was found that the highest total yield of low-molecular compounds from the waste was obtained with steam explosion pretreatment. The acid pretreatment may lead to lignin condensation.

Table 4. Compounds identified in the ethyl acetate extracts

Compounds	Retention time, min	Wheat straw	Wheat straw (Steam explosion)		Maize stalks (Acid)		Maize stalks (Steam explosion)	Paulownia (Steam explosion)
		(Acid)	[Area,%]		[Area,%]		[Area,%]	[Area,%]
		4h	4h	6h	4h	6h	6h	6h
Unidentified compound	4.00	5.2	-	-	3.7	-	-	-
Unidentified compound	4.26	3.2	-	-	-	-	-	-
Benzaldehyde	5.84	1.3	-	-	3.6	-	-	-
Phenol	6.66	6.0	13.1	14.5	7.0	-	-	-
1,2- Cyclopentanedione-3-methyl-	7.68	3.1	-	-	1.6	-	-	-
1,3-Diethylbenzene	8.04	1.4	-	-	3.3	-	-	-
1,3-Cyclopentanedione 2,4-Dimethyl-	8.28	5.8	7.5	-	2.1	-	7.6	4.6
2-methoxyphenol	8.82	8.9	8.5	4.0	12.2	5.6	3.5	17.3
Unidentified compound	9.02	2.7	8.0	-	9.0	-	-	16.7
Unidentified compound	9.40	-	-	-	1.2	-	-	-
Unidentified compound	9.64	-	6.1	-	1.6	-	-	5.2
Unidentified compound	9.92	1.0	-	-	2.0	-	-	-
Benzoic acid	10.32	1.6	-	-	2.0	-	-	6.4
Benzenediol	10.76	3.7	-	-	3.0	-	-	10.8
3-Methoxy-1,2-benzenediol	11.62	3.3	6.0	-	-	-	-	6.8
2,6-Dimethoxyphenol	12.89	10.2	7.9	9.0	10.4	11.7	17.0	13.1
4-Hydroxybenzaldehyde	13.04	1.7	-	-	-	-	-	-
4-Hydroxy-3-methoxybenzaldehyde	13.49	5.4	5.3	25.6	3.2	13.3	14.9	4.7
1-(2-Hydroxyphenyl) ethanone	14.05	2.3	4.9	-	-	-	-	-
1-(4-Hydroxy-3-methoxyphenyl) ethanone	14.59	2.5	-	3.3	2.1	8.6	-	-
4-Hydroxy-3-methoxybenzoic acid	15.58	1.6	6.6	-	-	5.9	-	-
4-Hydroxy-3,5-dimethoxybenzaldehyde	16.61	1.8	-	-	-	10.8	4.4	-
Unidentified compound	16.80	1.0	-	-	-	-	-	-
1-(4-Hydroxy-3,5-dimethoxyphenyl) ethanone	17.43	23.6	26.1	43.6	32.0	38.6	40.1	14.4
4-Hydroxy-3,5-dimethoxybenzoic acid	18.30	1.7	-	-	-	-	-	-
Diisobutyl phthalate	18.68	-	-	-	-	-	7.8	-
Dibutyl phthalate	19.71	1.0	-	-	-	5.4	4.7	-

Acknowledgements: The authors are grateful for the support of the National Science Fund of the Ministry of Education and Science.

REFERENCES

1. R.W. Thring, E. Chornet, *J Chromatogr*, **467**, 441 (1989).
2. S. Nenkova, T. Radoykova, K. Stanulov, *J. Univ. Chem. Technol. Met. (Sofia)*, **46**(2), 109 (2011).
3. K. Ehara, D. Takada, S. Saka, *J. Wood Sci.*, **51**, 256 (2005).
4. D. Takada, K. Ehara, S. Saka, *J. Wood Sci.*, **50**, 253 (2004).
5. E. Minami, S. Saka, *J. Wood Sci.*, **51**, 395 (2005).
6. T. Vasileva, K. Stanulov, S. Nenkova, *J. Univ. Chem. Technol. Met. (Sofia)*, **43**(1), 65 (2008).

7. T. Radoykova, K. Stanulov, S. Nenкова, *Oxidation Communications*, **34**(2), 463 (2011).
8. G.N. Dalimova, *Chem. Nat. Comp.*, **42**(1), 88 (2006).
9. P. Tsekova, S. Petrin, I. Valchev, S. Nenкова, V. Blyahovski, G. Radeva, *Italic 6, Science & Technology of Biomass: Advances and Challenges*, Sept. 5-8, Viterbo, Italy, 2011, p. 311.
10. S. Nenкова, T. Vasileva, K. Stanulov, *Chem. Nat. Compd.*, **44**(2), 182 (2008).
11. T. Radoykova, S. Nenкова, K. Stanulov, *Chem. Nat. Compd.*, **46**(5), 807 (2010).

МОНОМЕРНИ ФЕНОЛНИ СЪЕДИНЕНИЯ ОТ ОТПАДЪЧНИ ХИДРОЛИЗНИ ЛИГНОЦЕЛУЗОЗНИ МАТЕРИАЛИ

Т. Х. Радойкова,* С. К. Ненкова, И. В. Вълчев

Химико-технологичен и металургичен университет, бул. Климент Охридски №8, 1756 София, България

Постъпила на 23 ноември, 2015; коригирана на 1 юли, 2016

(Резюме)

Проведена е алкална обработка (4 и 6 часа) на отпадъчни хидролизни лигноцелулозни материали. Получени са следните мономерни фенолни съединения: 2-метоксифенол, 3-етилфенол, 4-етил-2-метоксифенол, 2,6-диметоксифенол, 4-хидрокси-3-метоксибензалдеhid, 4-хидрокси-3,5-диметоксибензалдеhid, 1-(4-хидрокси-3-метоксифенил) етанон, 1-(4-хидрокси-3,5-диметоксифенил) етанон, и др. За екстрахиране на мономерните продукти са използвани толуен и етилацетат.

Received November 23, 2015; Revised July 1, 2016

Synthesis, spectroscopic characterisation and biological activity studies of Co(II), Ni(II), Cu(II) and Zn(II) metal complexes with azo dye ligand derived from 4,4'-diaminodiphenylether and 5-sulpho salicylic acid

S. N. Chaulia

P. G. Department of Chemistry, G. M. (AUTO) College, Sambalpur, Odisha (INDIA)

Received February 16, 2016; Revised May 27, 2016

A series of metal complexes of Co(II), Ni(II), Cu(II) and Zn(II) have been synthesized with a new azo dye ligand 4,4'-bis(2'-hydroxy-3'-carboxy-5'-sulphophenylazo)diphenylether derived from 4,4'-diaminodiphenyl ether and 5-sulpho salicylic acid. The metal complexes along with the ligand have been characterised by analytical, molar conductance, magnetic susceptibility measurement, IR, NMR, electronic, ESR, mass spectra and thermal study. The analytical and spectral data predicts octahedral for Co(II), Ni(II), distorted octahedral geometry for Cu(II) complexes and tetrahedral geometry for Zn(II) complex. Computational study of the ligand and the metal complexes has been made to determine the geometrical parameters and the global reactive descriptors. The XRD (powder pattern) indicates orthorhombic crystal system for the Cu(II) complex. The thermal study reveals thermal stability of the complexes and the fluorescence study predicts photoactive properties of the azo compounds. The SEM image of the Zn(II) complex provides its information about its surface morphology. The Biological study indicates the antibacterial properties and DNA binding activity of the newly synthesised compounds.

Keywords: Computational study, Biological study, Azo compounds, SEM image

INTRODUCTION

Azo compounds constitute the largest class of synthesised organic dyes and azo dyes and their metal complexes have been attracting the attention of researchers due to their versatile application in various fields. In addition to the traditional uses of dyes as dyeing agents[1], laboratory reagents[2], these compounds are also used in biomedical studies as antibacterial, antifungal, antitumor agents etc [3,4] and high technology areas including textiles, paper, leather and electro-optical devices[5,6]. The Azo compounds derived from 4,4'-diaminodiphenyl ether and its complexes have evoked great interest in recent years due to its antibacterial properties and its application in the making of thermally stable materials that can be used in the field of adsorption and catalysis[7,8], that encouraged me to prepare azo dye from 4,4'-diaminodiphenylether and 5-sulpho salicylic acid, its metal complexes, to characterise the compounds by various physico-chemical and spectral techniques and to evaluate their biological activities.

EXPERIMENTAL

Materials and Measurements

All chemical and solvents used in this investigation are analytical grade provided by

Himedia and double distilled deionised water was used during the experiments. Elemental analysis of the ligand and complexes was carried out by Perkin-Elmer elemental analyser, cobalt, nickel, copper and Zn contents were determined by Perkin-Elmer 2380 atomic absorption spectrometer and chloride content was estimated by standard procedure, Systronic conductivity bridge 30 was used to measure molar conductance of the complexes, Magnetic susceptibility of the complexes was measured by Guoy's balance using $\text{Hg}[\text{Co}(\text{NCS})_4]$ as a calibrant at room temperature, IR spectra of the ligand and metal complexes were recorded using KBr pellets by Perkin-Elmer FT-IR spectrometer within the range 4000- 450 cm^{-1} , UV-Visible spectra of the complexes were collected using a THERMO SPECTRONIC 6 HEXIOS α and fluorescence spectra were recorded in a Fluorescence spectrometer, ^1H NMR spectra of the ligand and the Zn(II) complex were obtained from 500 MHz- NMR spectrometer using TMS as reference, ESR spectrum of the Cu(II) complex was recorded on spectrum of the Cu(II) complex was recorded on JES-FA 200 ESR spectrometer, Mass spectra of the ligand and its complexes were recorded through JEOL GC-MS Mass Spectrometer, thermal study of the metal complex was done by NETZSCH STA 449 F3 JUPITOR, SEM image of the complexes were taken in JES FA 200, the XRD powder pattern of the Cu(II) complex was collected using a Philips X'Pert Pro diffractometer.

* To whom all correspondence should be sent:
E-mail: satyanarayanchaulia@gmail.com

In order to get the better picture about reactivity and geometrical parameters, computational study of the ligand and the metal complexes was performed by Gaussian 03 software package[9].

The DNA binding study of the azo compounds was made by Gel electrophoresis method [10]. 10 μL of the metal complexes was taken along with 15 μL of CT DNA solution dissolved in Tris-EDTA in centrifuge tubes. The tubes were incubated at 37°C for 1 hour. After incubation, the tubes containing solution were kept in a refrigerator at 0°C for few minutes, 5 μL gel loading buffer with tracking dye (0.25% bromo phenol) was taken in the tubes for electrophoresis. The electrophoresis was continued under constant voltage (50 V) and photographed under UV illumination.

Hydrodynamic volume change [11] was observed by Ostwald Viscometer immersed in a thermostatic bath maintained at 37°C. A digital stopwatch was used to measure the flow time, mixing of complexes under investigation with CT-DNA was carried out by bubbling nitrogen. Data were presented by plotting a graph indicating $(\eta/\eta_0)^{1/3}$ versus $[\text{complex}]/[\text{DNA}]$ where η is the viscosity of DNA in presence of complexes and η_0 represents the viscosity of DNA alone.

The antibacterial activity of the ligand and its metal complexes was studied in vitro by the cup-plate method [12] against the *Escherichia coli* (MTCC 40) and *Staphylococcus aureus* (MTCC 87) using agar nutrient as the medium. The investigated ligand and its complexes were

dissolved in DMF. The sterilised agar plates were swabbed with the bacteria culture and filled with test solutions, then incubated at 37 °C for 24 h. The activity was evaluated by measuring the zone of inhibition with respect to the standard drug Tetracycline.

Synthesis of the ligand

The ligand is synthesised by the coupling reaction between diazonium chloride solution derived from 4,4'-diaminodiphenylether and the alkaline solution of 5-sulphosalicylic acid. The diazonium chloride solution was prepared by the dissolution of 4,4'-diaminodiphenylether(0.01 mol, 2.0 gram) in hydrochloric acid and adding equivalent sodium nitrite solution at 0 – 5 °C with vigorous stirring, The ice-cooled diazonium chloride solution was added to added to alkaline solution of 5-sulphosalicylic acid(0.02 mol, 4.02 gram). The coloured azo compound produced again recrystallised from ethanol (Fig. 1.).

Preparation of metal complexes

The metal chlorides in ethanol solution were mixed with DMF solution of the ligand separately and the reaction mixture was refluxed for one hour at 60 °C. The solution is allowed to cool and concentrated Ammonia solution was added drop wise to the solution with stirring till the formation of complex compounds. The solid (Fig. 3, 4) complexes thus separated were washed with alcohol and dried in vacuum (Fig. 2).

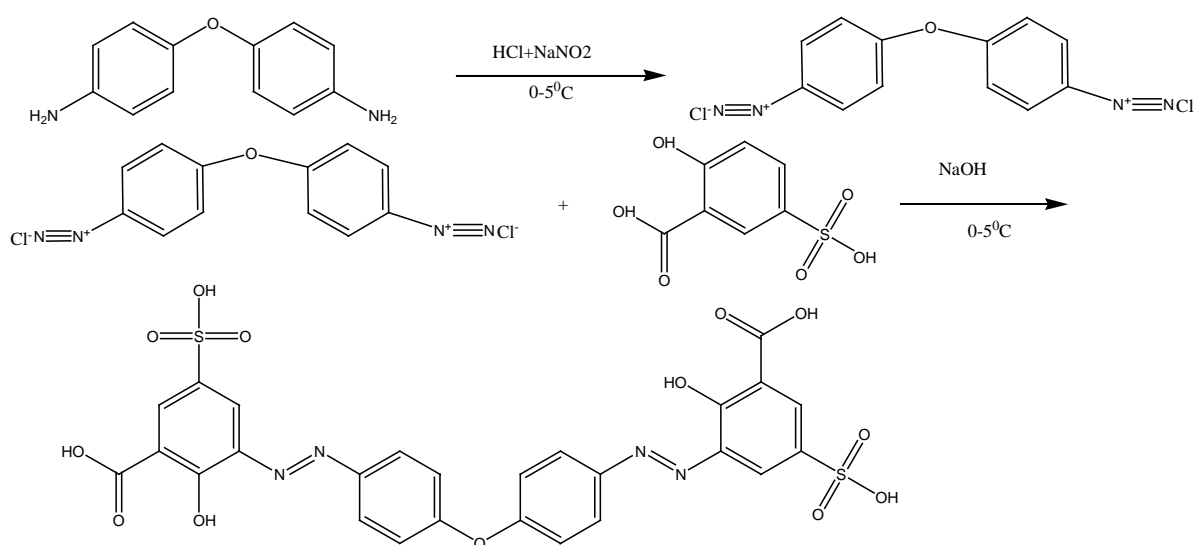


Fig. 1. Reaction scheme-1.



M= Co(II), Ni(II) and Cu(II)



M'= Zn(II)

Fig. 2. Reaction scheme-2.

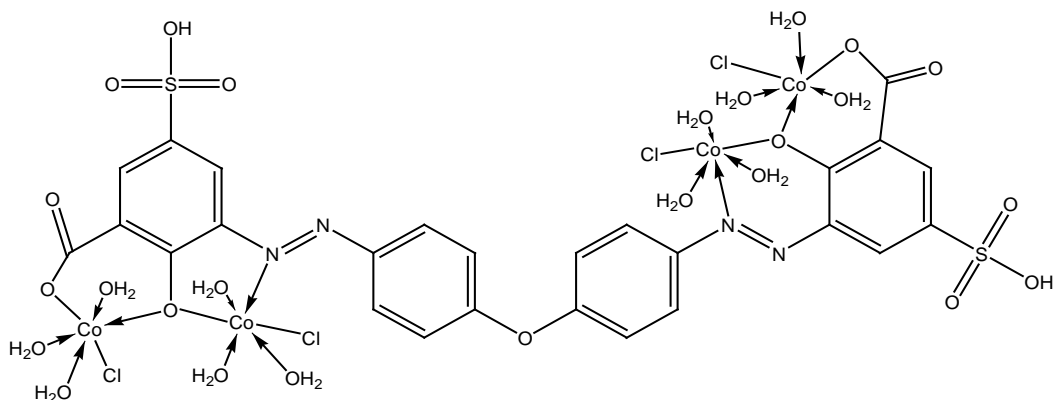


Fig. 3. Structure of Co(II) complex.

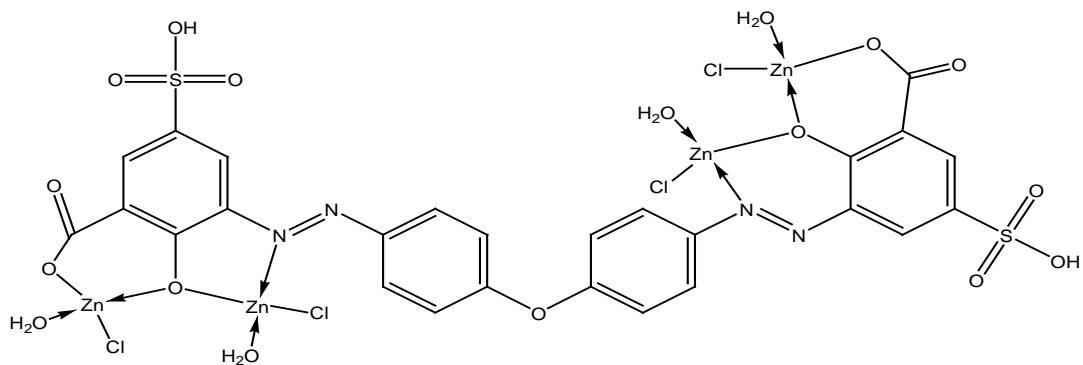


Fig. 4. Structure of Zn(II) complex.

RESULTS AND DISCUSSION

The analytical and physical properties of the Azo dye and its complexes are in good agreement with calculated values (Table 1). The analytical data of the complexes are consistent with the general formula $[M_4LCl_4(H_2O)_{12}]$ for Co(II), Ni(II), Cu(II) and $[M'_4LCl_4(H_2O)_4]$. The molar conductance of the complexes with 1×10^{-3} M DMSO solution are found to be in the range of 9.1-12.5 $\text{ohm}^{-1}\text{cm}^2\text{mol}^{-1}$ indicating non-electrolytic nature[13]. All compounds are insoluble in ethanol, methanol, acetone, ether, and chloroform but soluble in DMF and DMSO.

IR study

The IR spectrum of the ligand (Fig. 5) is compared with the spectra of metal complexes (Fig. 6) in order to examine the mode of bonding between ligand and complexes (Table 2). The IR spectrum of the ligand shows a broad band at 3422 cm^{-1} which is missing from the spectra of the metal complexes that indicates deprotonation of phenolic(-OH) and bonding of metal atoms with oxygen atom of the -OH group. The C-O frequency vibration band observed at 1268 cm^{-1} in ligand is shifted to $\sim 1235 \text{ cm}^{-1}$ in complexes confirming bonding of metal atoms with oxygen atom of -OH group[14]. Two bands appear at 1383 and 1589 cm^{-1} corresponds to ν_{sym} and ν_{asym} respectively in the spectrum of the ligand which are observed at 1279 cm^{-1} and 1581 cm^{-1} due to ν_{sym} and ν_{asym} that

indicates monodentate nature of the carboxylate group and bonding of carboxylic oxygen with metal atoms[15]. A band appears at 1491 cm^{-1} corresponds to -N=N- group in the ligand is shifted to $\sim 1489 \text{ cm}^{-1}$ in metal complexes that suggests bonding of azo nitrogen with the metal ions[16].The peak at 1657 cm^{-1} in ligand confirms the presence carbonyl group of ethanoyl group of the ligand which is shifted to 1649 cm^{-1} in metal complexes that indicates bonding of carbonyl oxygen atom with the metal ions. The spectra of

complexes reveal the presence of band at $\sim 3512 \text{ cm}^{-1}$ due to the vibrational frequency of O-H of coordinated/ lattice held water. The presence of coordinated water is further confirmed by the rocking band at $\sim 836 \text{ cm}^{-1}$ and twisting band at $\sim 780 \text{ cm}^{-1}$ [17].The vibrational frequencies of M-O and M-N bonds which appear at $\sim 589 \text{ cm}^{-1}$ and $\sim 489 \text{ cm}^{-1}$ respectively confirm the bonding between metal ions with the ligand through phenolic oxygen and azo nitrogen atoms[18].

Table 1. Analytical data of the ligand and its metal complexes

comp	Colour	M.P. (°C)	% Found(calcd)					
			M	C	H	N	Cl	S
LH ₄	Brick Red	85	-	47.15 (47.42)	2.32 (2.75)	8.29 (8.51)	-	9.43 (9.7)
	Reddish brown	>300	18.43 (18.88)	24.87 (25.02)	3.01 (3.07)	4.12 (4.49)	11.03 (11.37)	4.96 (5.14)
[Ni ₄ LCl ₄ (H ₂ O) ₁₂]	Red	>300	18.39 (18.82)	24.76 (25.04)	2.99 (3.07)	4.33 (4.49)	11.11 (11.37)	4.94 (5.14)
[Cu ₄ LCl ₄ (H ₂ O) ₁₂]	Brown	>300	19.89 (20.07)	24.53 (24.65)	2.86 (3.02)	4.21 (4.42)	11.07 (11.20)	4.65 (5.06)
[Zn ₄ LCl ₄ (H ₂ O) ₄]	Light red	>300	22.87 (23.15)	27.33 (27.64)	1.75 (1.96)	4.75 (4.96)	12.14 (12.55)	5.43 (5.68)

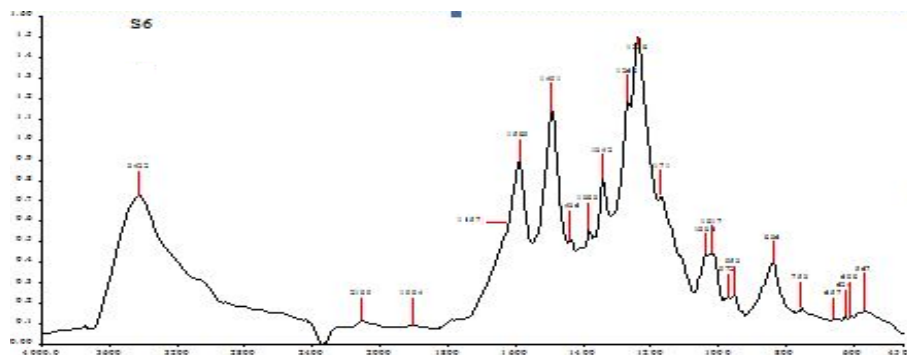


Fig. 5. IR Spectrum of the ligand.

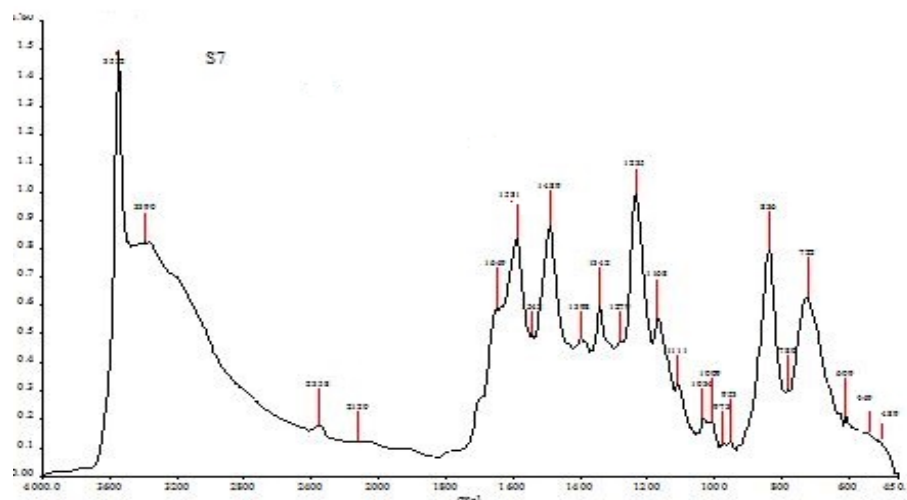


Fig. 6. IR Spectrum of the Co(II) complex

Table 2. IR data of the investigating compounds

compound	$\nu(\text{C-O})$ cm^{-1}	$\nu(\text{N=N})$ cm^{-1}	$\nu(\text{COO}^-)_{\text{sym}}$ cm^{-1}	$\nu(\text{COO}^-)_{\text{asym}}$ cm^{-1}	$\nu(\text{M-O})$ cm^{-1}	$\nu(\text{M-N})$ cm^{-1}
1	1268	1491	1383	1589	-	-
2	1235	1489	1279	1581	589	489
3	1234	1488	1278	1580	588	489
4	1235	1488	1279	1581	588	489
5	1236	1489	1278	1580	589	488

1-LH₄, 2- Co(II) complex, 3-Ni(II)complex, 3- Cu(II) complex and 4- Zn(II) complex

Electronic spectra and magnetic measurement

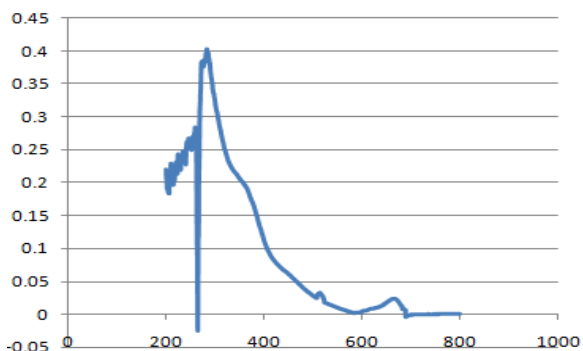
As synthesis of single crystals of the complexes has been failed, the electronic spectral and magnetic moment measurement data are used to confirm the geometry of the complexes (Table 3). Three d-d transition bands are observed in the Spectrum of Co(II) complex (Fig. 7.) at 13880, 16150, 26315 cm^{-1} corresponding to ${}^4\text{T}_{1g}(\text{F}) \rightarrow {}^4\text{T}_{2g}(\text{F}), {}^4\text{T}_{1g}(\text{F}) \rightarrow {}^4\text{A}_{2g}(\text{F}), {}^4\text{T}_{1g}(\text{F}) \rightarrow {}^4\text{T}_{2g}(\text{P})$ that indicates octahedral geometry of the complex [19]. The electronic parameters of the Co(II) complex were calculated by using the following equations.

$$Dq = \nu_2 - \nu_1/10$$

$$B = \nu_2 + \nu_3 - 3 \nu_1/15$$

$$\beta_{35} = B/971$$

$$\% \text{ of } \beta_{35} = (\beta^0) = (1 - \beta_{35})100$$

**Fig. 7.** Electronic Spectrum of the Co(II) complex.

In the Ni(II) complex (Fig. 8) also three bands are observed at 14705, 18867, 25641 cm^{-1} due to ${}^3\text{A}_{2g}(\text{F}) \rightarrow {}^3\text{T}_{2g}(\text{F}), {}^3\text{A}_{2g}(\text{F}) \rightarrow {}^3\text{T}_{1g}(\text{F}), {}^3\text{A}_{2g}(\text{F}) \rightarrow {}^3\text{T}_{1g}(\text{P})$ which arises from octahedral geometry [20]. The parameters of the complex were calculated by using the equations

$$Dq = \nu_2 - \nu_1/10$$

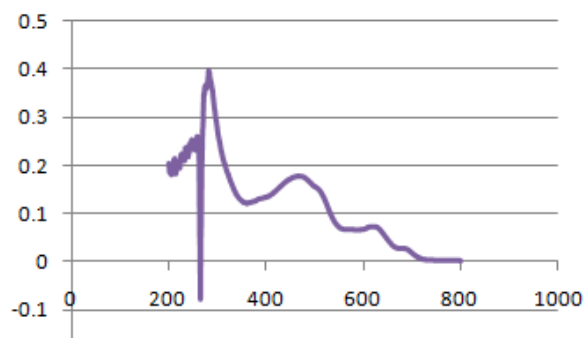
$$B = \nu_2 + \nu_3 - 3 \nu_1/15$$

$$\beta_{35} = B/1041$$

$$\% \text{ of } \beta_{35} = (\beta^0) = (1 - \beta_{35})100$$

The Racah parameter (B), Nephelauxetic effect (β), β^0 of Co(II) and Ni(II) complexes strongly indicate covalent bonding between ligand and metal ions. The value of ν_2/ν_1 for Co(II) and Ni(II) complexes was found to be 1.16 and 1.28

respectively which are close to the value expected from an octahedral geometry.

**Fig. 8.** Electronic Spectrum of the Ni(II) complex

The Cu(II) complex shows a d-d transition band at 15350 cm^{-1} which may be assigned to ${}^2\text{E}_g \rightarrow {}^2\text{T}_{2g}$ transition which favours a distorted octahedral geometry for the complex [22]. The magnetic susceptibility measurements of the metal complexes are undertaken to get information's regarding their structures. The magnetic moment of the Co(II), Ni(II) and Cu(II) complexes were found to be 1.38 B.M., 1.31 B.M. and 1.04 B.M. respectively in place of 3.87 B.M., 2.83 B.M. and 1.73 B.M. magnetic moment expected from an octahedral geometry. This sub-normality in magnetic moment of the investigating complexes may be due to interaction of electron spins of the neighbouring metal ions. This anti ferromagnetism due to pairing of electron spins may be due to super exchange through (M-O-M) [23,24]. The Zn(II) complex is found to be diamagnetic, hence tetrahedral geometry may be suggested based on the spectral and analytical data.

¹H NMR Study

The spectra of the ligand (Fig. 9) and Zn(II) complex (Fig. 10) are recorded in DMSO-d₆ solvent. The ¹H NMR spectrum of the ligand shows multiplet at δ 6.99-8.45 ppm which may be assigned to aromatic protons. The peaks at δ 10.21 ppm corresponds to phenolic (-OH) group and -CH₃ group is also confirmed by the presence of peak at δ 2.89 ppm [25].

The spectrum of Zn(II) complex is compared with the azo dye ligand and it is observed that the peak due to –OH group found in the ligand was absent in the complex. This indicates deprotonation of –OH group and formation of metal-O bond [26] in accordance with the data revealed by IR.

Mass spectra Study

As mass spectra of the compounds provides vital information for their structural elucidations,

the mass spectra of the ligand and its Co(II) (Fig. 11, 12) complexes are recorded to confirm their molecular mass and stoichiometric composition. The spectrum of the ligand shows the molecular ion peak at m/z 658.76 corresponding to the molecular mass of [C₂₆H₁₈N₄O₁₃S₂]. The spectrum of the Co(II) complex of the ligand gives molecular ion peak at m/z 1248.27 which confirms its proposed molecular formula as [M₄LCI₄(H₂O)₁₂]

Table 3. Electronic data of the metal complexes.

Compound	λ_{max} (cm ⁻¹)	Transitions	B	β_{35}	% of β_{35}	ν_2/ν_1	Geometry	μ_{eff} B.M.
1	13880	$^4T_{1g}(F) \rightarrow ^4T_{2g}(F)$	55	0.056		1.16	octahedral	1.38
	16150	$^4T_{1g}(F) \rightarrow ^4A_{2g}(F)$						
	26315	$^4T_{1g}(F) \rightarrow ^4T_{2g}(P)$						
	34482	CT						
2	14705	$^3A_{2g}(F) \rightarrow ^3T_{2g}(F)$	19.8	0.019		1.28	octahedral	1.31
	18867	$^3A_{2g}(F) \rightarrow ^3T_{1g}(F)$						
	25641	$^3A_{2g}(F) \rightarrow ^3T_{1g}(P)$						
	38461	CT						
3	15350	$^2E_g \rightarrow ^2T_{2g}$	-	-	-	-	Distorted octahedral	1.04

1-Co(II) complex, 2-Ni(II)complex, 3- Cu(II) complex

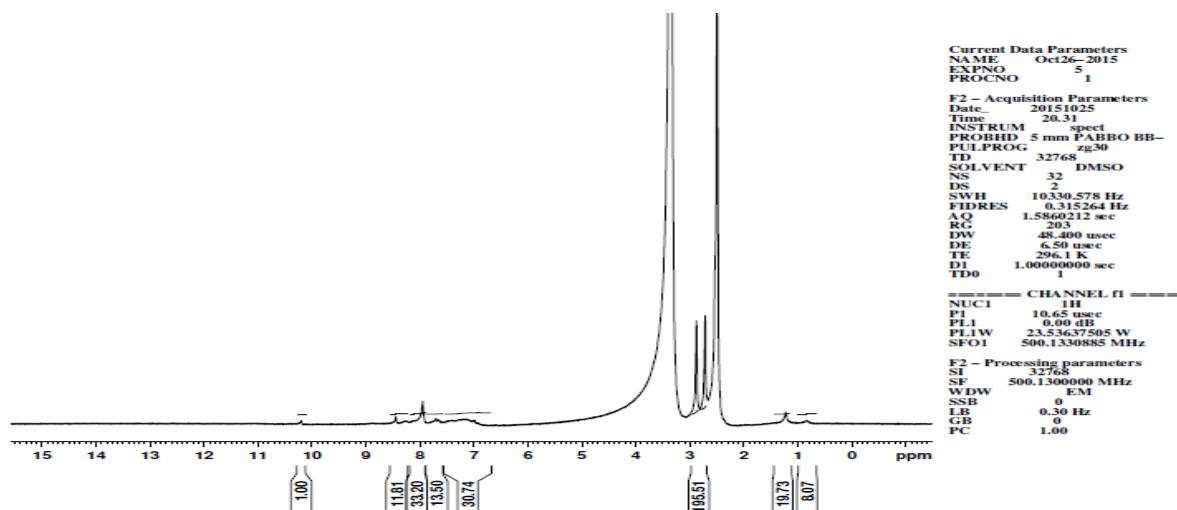


Fig. 9. ¹H Spectrum of the ligand.

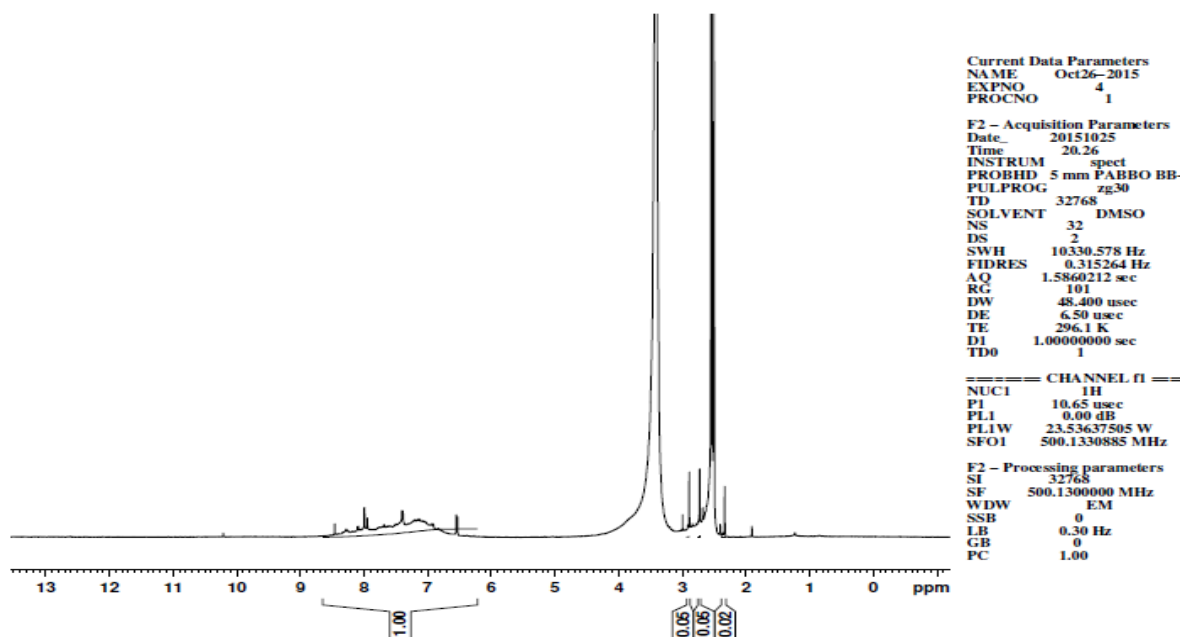


Fig. 10. ¹H Spectrum of the Zn(II) complex

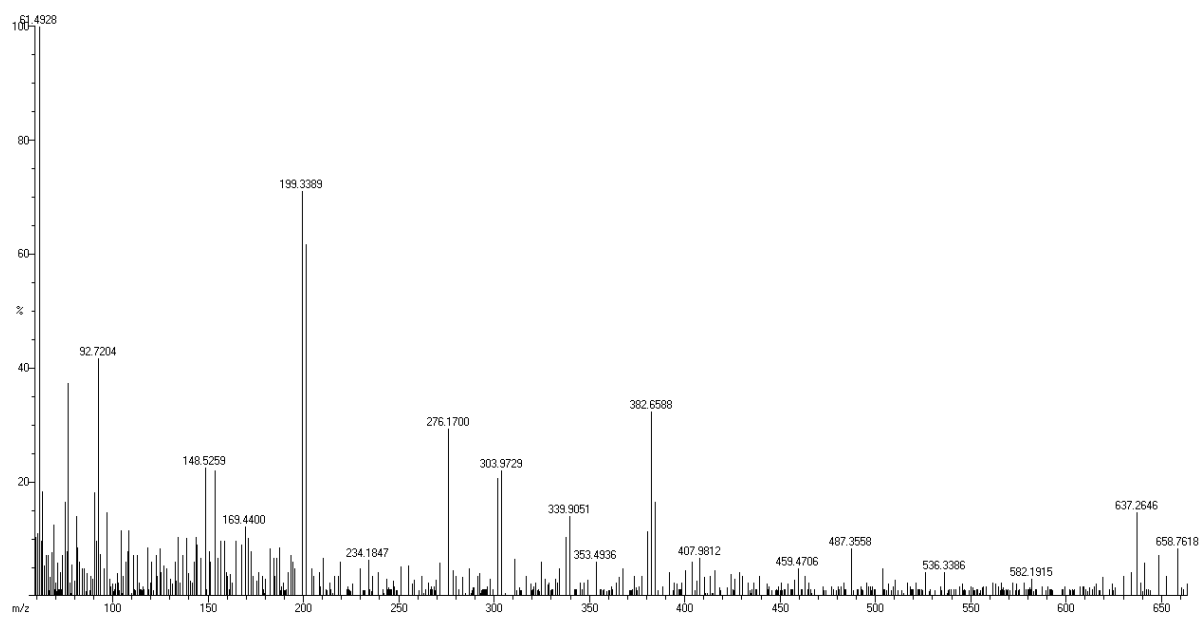


Fig. 11. Mass Spectrum of the ligand

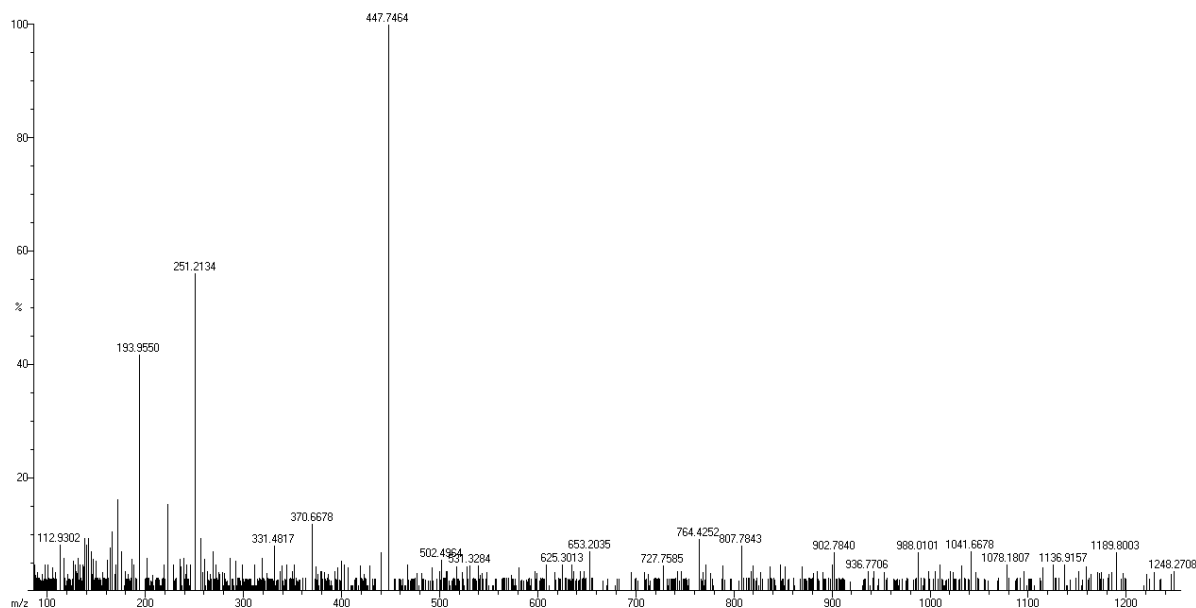


Fig. 12. Mass Spectrum of the Co(II) complex.

ESR spectra

The ESR spectrum of the Cu(II) (Fig. 13) complex was recorded at room temperature to study nature of bonding between the Cu(II) ion and donor atoms of the ligand. The spectrum shows that g_{\parallel} value is 2.16 and g_{\perp} is 2.05. As the $g_{\parallel} > g_{\perp} > 2.0023$, the unpaired electron is localised in $d_{x^2-y^2}$ orbital of the Cu(II) ion and axial symmetry tetragonal geometry of the complex is implied[27]. This is confirmed by the electronic spectrum of the complex. The observed value of G was found to be 3.2 by using the relation $G = g_{\parallel} - 2 / g_{\perp} - 2$ which suggests exchange interaction between the copper centres in a polycrystalline solids[28]. The g_{av} value of the complex is calculated as 2.086 by using the relation $g_{av} = 1/3(g_{\parallel} + 2g_{\perp})$. The spin-orbit coupling constant is also calculated by using the equation $g_{av} = 2(1 - 2\lambda/10dq)$ and it is found to be -660.05 cm^{-1} . This value is found to be less than the free ion value (-830 cm^{-1}) that indicates overlapping of metal-ligand orbitals[29]. The covalent bonding between metal ion and orbitals of the ligand is also confirmed from the g_{\parallel} value, According to Kivelson and Neiman covalent bonding can be predicted for a Cu(II) complex with g_{\parallel} value less than 2.3[30]. Hence, distorted octahedral geometry may be proposed for the Cu(II) complex.

Thermogravimetric study

The thermo gravimetric study of the Ni(II) (Fig. 14, 15) complex as a representative member of the investigating complexes was carried out by the simultaneous TG,DTG and DSC techniques in the atmosphere of nitrogen at a rate of $10 \text{ }^{\circ}\text{C}$ per minute from the ambient temperature to $1400 \text{ }^{\circ}\text{C}$. The TG /DTG curves show that the complex suffers mass loss in a number of stages. The complex loses a mass of 13.39 % at $82.2 \text{ }^{\circ}\text{C}$ in the first stage, with an endothermic peak at $85 \text{ }^{\circ}\text{C}$ in the DSC curve which corresponds to the loss of lattice held water. In the second stage, it suffers a mass of 12.60 % at $341.6 \text{ }^{\circ}\text{C}$ corresponding to the loss of coordinated water with a endothermic peak at $312 \text{ }^{\circ}\text{C}$. The complex compound loses a mass of 27.09 in the third stage which corresponds to the loss of ligand moiety and chlorine atoms at $565 \text{ }^{\circ}\text{C}$ with an endothermic peak $580 \text{ }^{\circ}\text{C}$. The complex suffers a total mass of 62.78 % and its remaining residual mass consisting of NiO as the residue is 37.22% up to $1400 \text{ }^{\circ}\text{C}$. This study indicates thermal stability of the complex.

XRD study

The XRD(powder pattern) study of the Cu(II) complex given in Fig. 16, Table 4 and Ni(II) complex given in Fig. 17, Table 5 was made to determine their crystal system. The X-ray powder diffraction diagram was collected from the X'Pert diffractometer and the recording conditions are 40 kv and 40 mA for $\text{CuK}\alpha$ with $\lambda = 1.542 \text{ \AA}$ between 20° to 80° with a step size of 0.0089° .

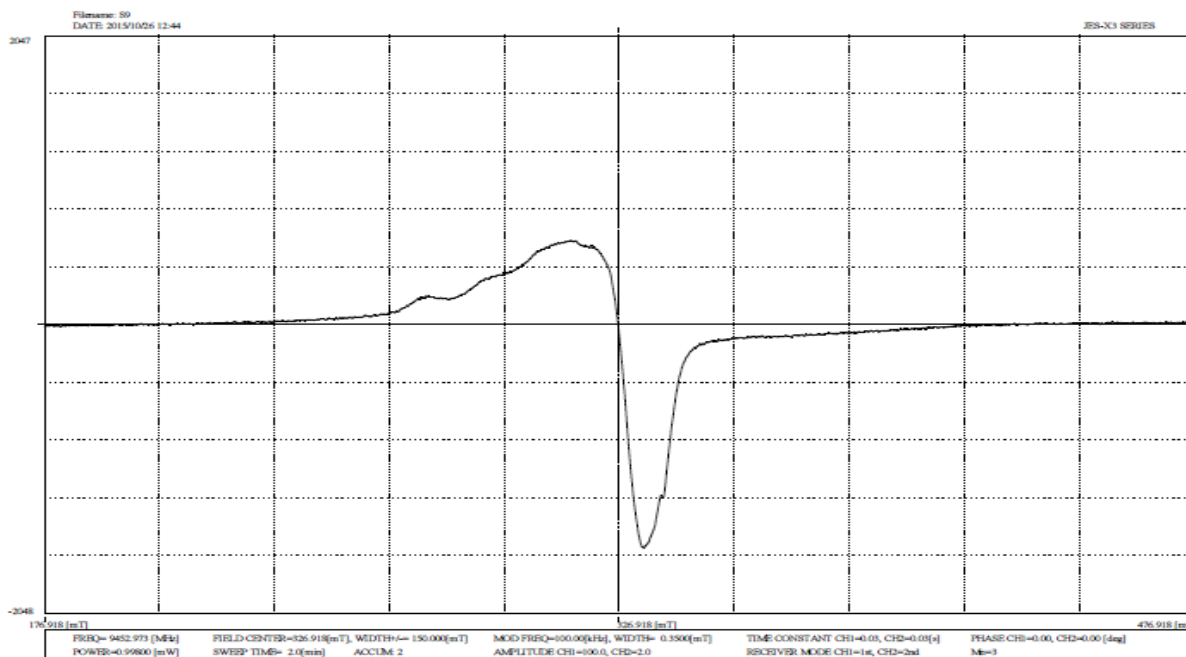


Fig. 13. ESR Spectrum of the Cu(II) complex.

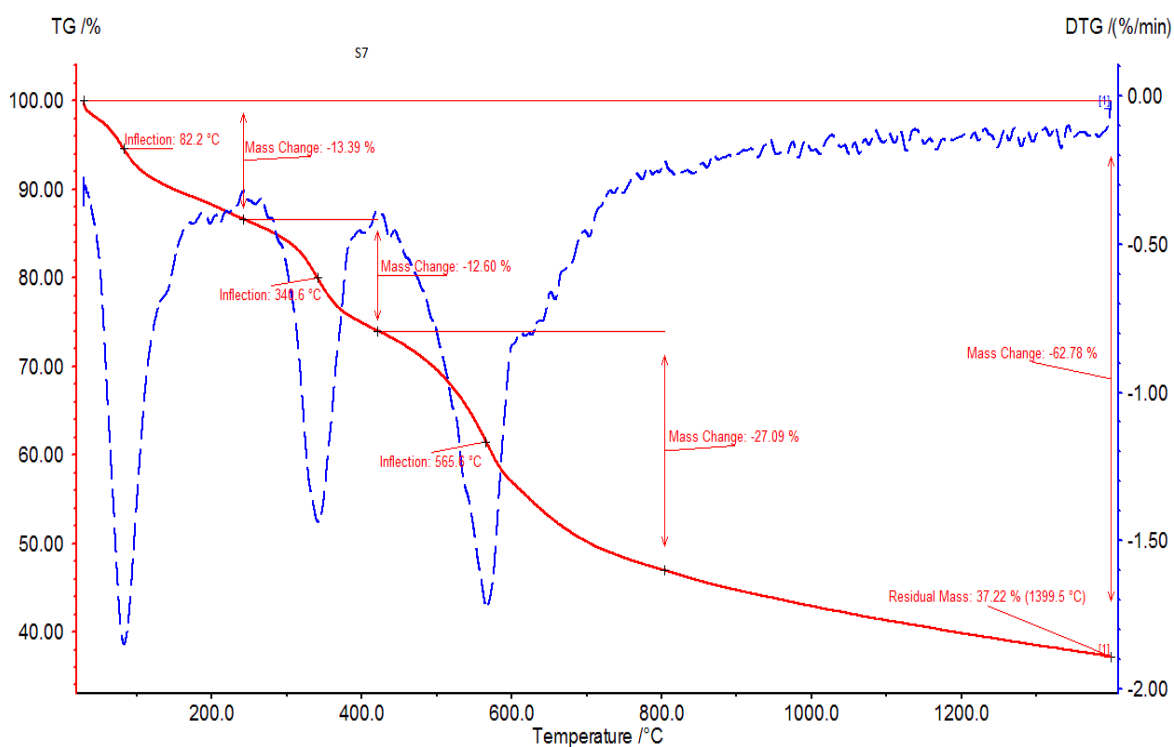


Fig. 14. TG/DTG Graph of Ni(II) complex.

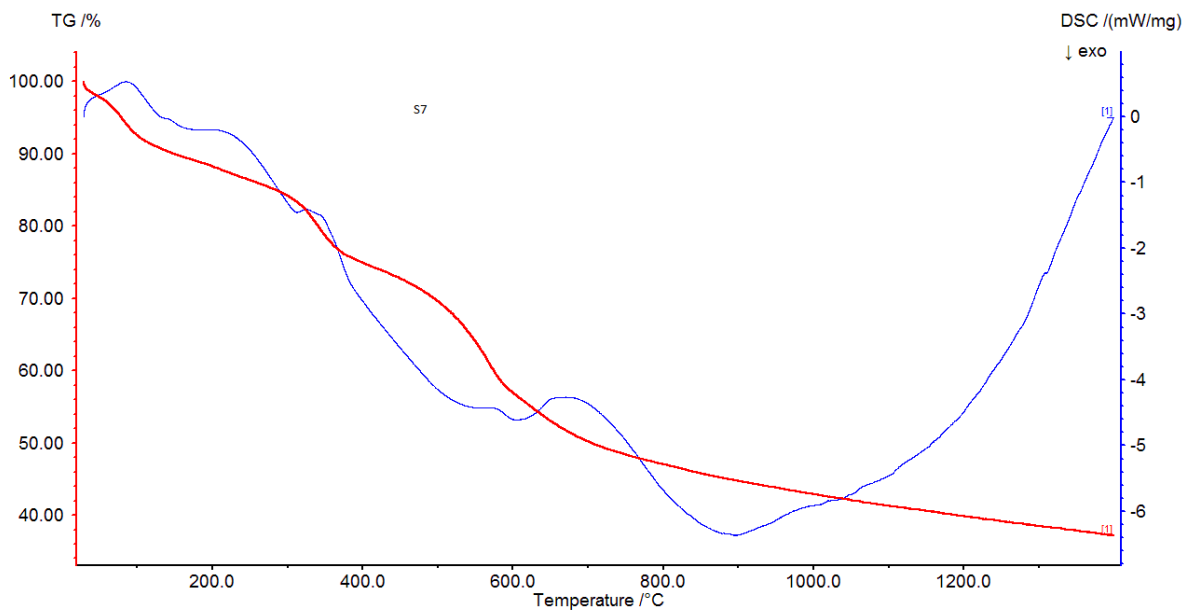


Fig. 15. DSC Graph of Ni(II) complex.

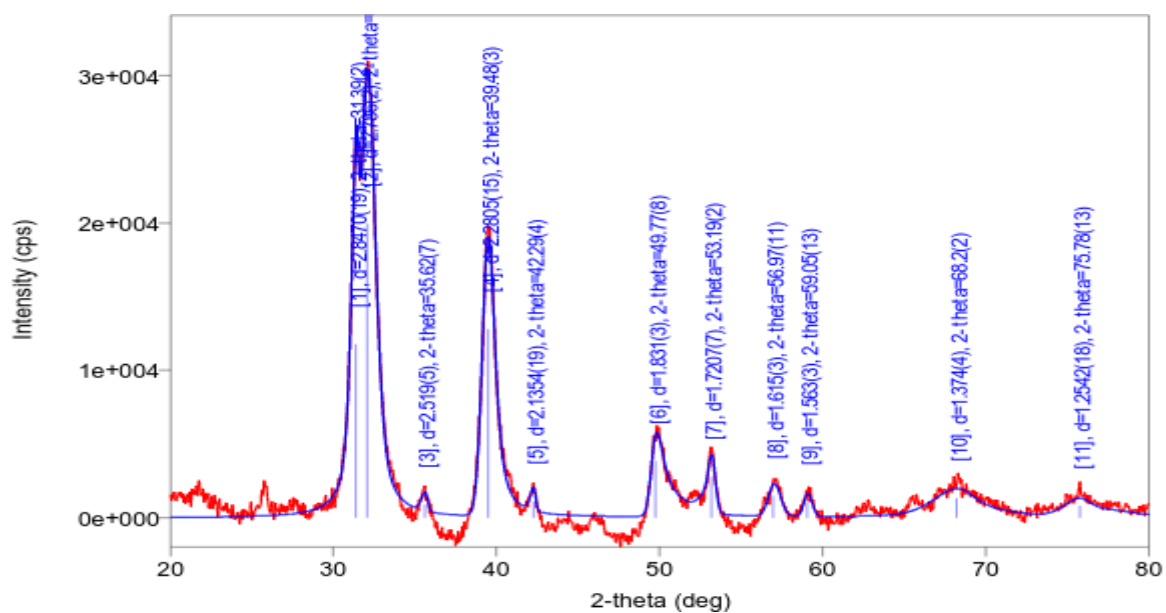


Fig. 16. XRD Powder pattern of the Cu(II) complex.

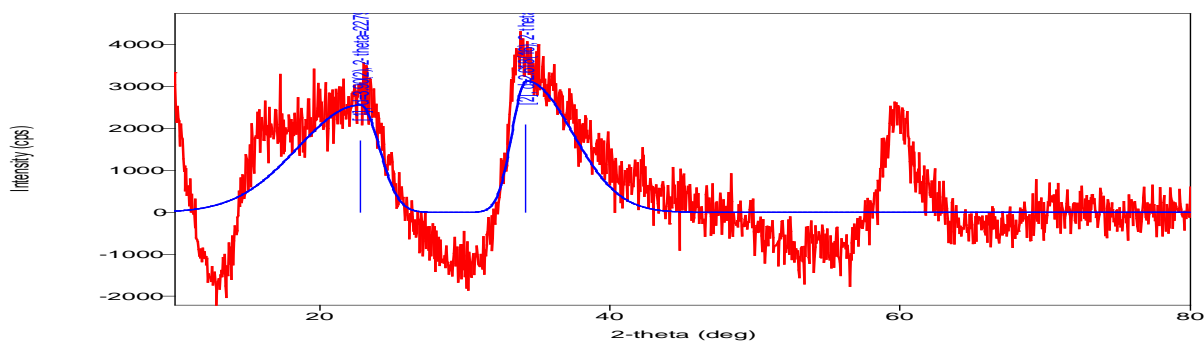


Fig. 17. XRD Powder pattern of the Ni(II) complex.

Table 4. XRD data of the Cu(II) complex at room temperature.

Sl no	2 θ (degree)	d	FWHM(degree)	Intensity(cps degree)
1	31.39(2)	2.8470(19)	0.56(4)	8980(1850)
2	32.10(2)	2.786(2)	1.06(8)	28678(1957)
3	35.62(7)	2.519(5)	0.4(2)	418(254)
4	39.48(3)	2.2805(15)	0.94(3)	15078(384)
5	42.29(4)	2.1354(19)	0.37(12)	463(177)
6	49.77(8)	1.831(3)	1.01(12)	5850(399)
7	53.19(2)	1.7207(7)	0.57(9)	2385(214)
8	56.97(11)	1.615(3)	0.86(10)	1386(178)
9	59.05(13)	1.563(3)	0.57(11)	699(108)
10	68.2(2)	1.374(4)	3.3(3)	6740(334)
11	75.78(13)	1.2542(18)	2.31(18)	3094(231)

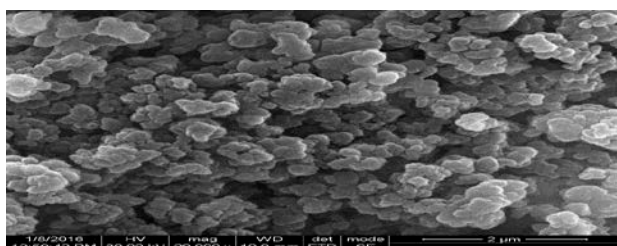
Table 5. XRD data of the Ni(II) complex at room temperature.

Sl no	2 θ (degree)	d	FWHM(degree)	Intensity(cps degree)
1	22.79(15)	3.90(2)	6.6(4)	11979(788)
2	34.2(2)	2.618(16)	4.49(2)	10912(742)

The XRD powder pattern was processed in X'pert high score software package. The search matching procedure was adopted for the PXRD pattern for the Cu(II) complex and revealed a match with a copper compound corresponding JCPDS powder diffraction file with PDF No 751765 . The pattern can be indexed to be a orthorhombic crystal system with $a=14.25$, $b=22.68$, $c=13.50$, $\alpha=\beta=\gamma=90^\circ$, lattice-primitive and space group is $Ccca$. Similarly, the search matching procedure is repeated for Ni(II) complex that provided a match with a Nickel compound corresponding JCPDS powder diffraction file with PDF No 451027 and the pattern is indexed to be a Hexagonal crystal system with lattice primitive and space group $P6_3/mmc$.

Surface morphology study

The surface morphology study of the Zn(II) complex of the ligand as a representative of all complexes was undertaken to evaluate its morphology and particle size. It is seen from the SEM image of the complex as given in Fig. 18 that the size of the particles is 2 μm with the formation single phase morphology. It is also noticed that there is a uniform matrix of the synthesized complex and the complex shows a flower like shape consisting of particles with nanosized grain.

**Fig. 18.** SEM image of Zn(II) complex

Fluorescence study

The fluorescence study of the ligand (Fig. 19) and its Cu(II) complex (Fig. 20) were carried out to study the photoconductive nature of the investigated compounds and the emission spectra of the compounds were given here. The ligand shows a emission maximum wavelength at 400 nm but the Cu(II) complex depicts the emission maximum wavelength at 420 nm. The red shift of the λ_{max} value of the complexes may be due to the deprotonation of the (-OH) group. The fluorescence intensity of the complex is more than the ligand due to complexation as it enhances conformational rigidity and non-radiative energy loss[31]. The emission in the complexes may be due to intraligand $\pi - \pi^*$ transition. These findings suggest that both the ligand and its complex are fluorescent in nature[32].

Computational study

A computational study of the investigating compounds was made to examine their reactivities and to evaluate geometrical parameters. Gauss view 4.1[33] and chemcraft software are used to draw the structures. The structures of the ligand and its all metal complexes are optimised at B3LYP[34] level of theory using 6-311++G(d,p) basis set. 6-311++G(d,p) is a large basis set which include diffused and polarised wave functions to take in to account the characteristics associated with ionic species having heavy atoms like N. The harmonic frequency calculation is also carried out at the same level of theory to ensure that the structures are true minima. Optimised was performed without any symmetry constraint using the default convergence criteria provided in the software.

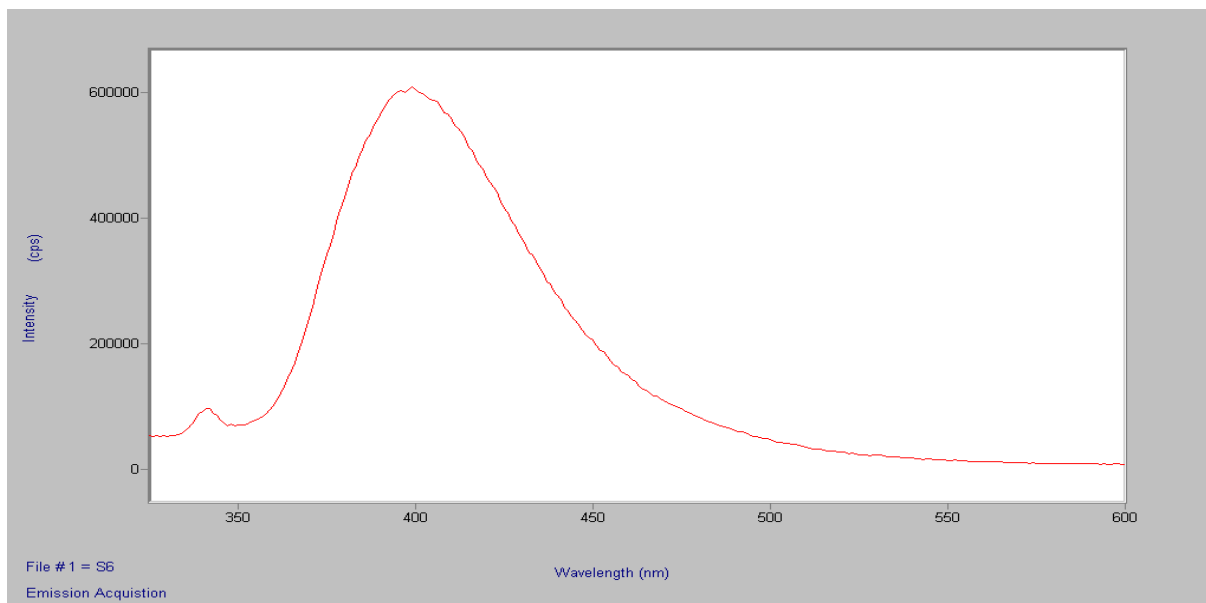


Fig. 19. Emission Graph of ligand.

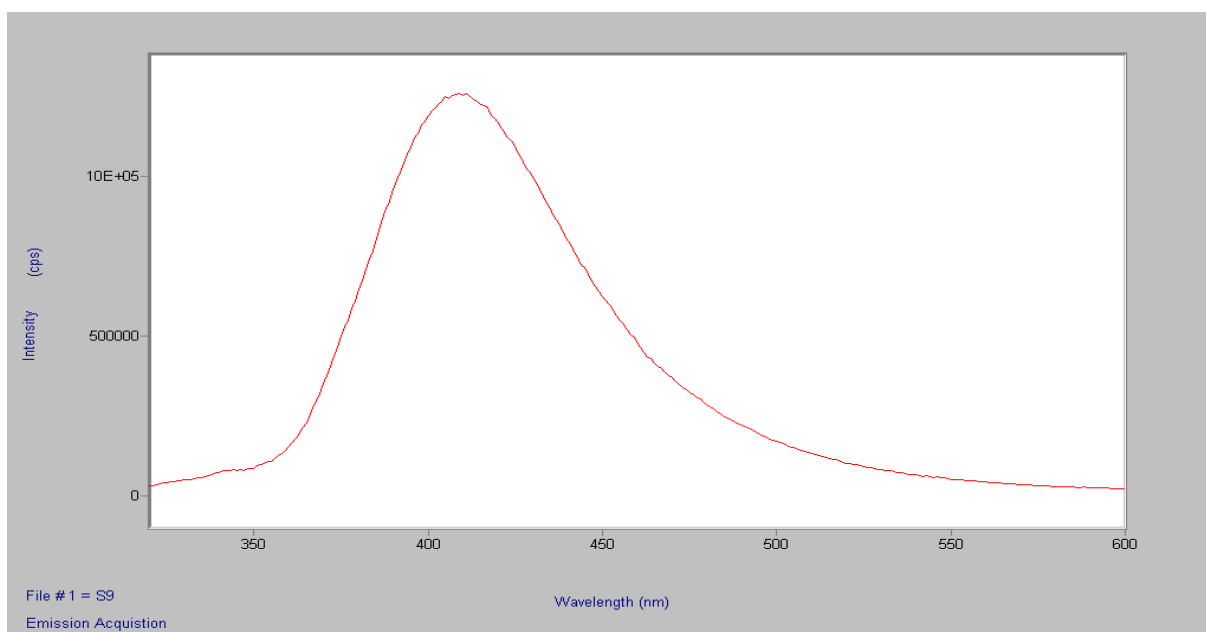


Fig. 20. Emission Graph of Cu(II) complex.

Conceptual DFT defines chemical potential μ as the first derivative of energy with respect to number of electrons

$\mu = \left(\frac{\partial E}{\partial N}\right) \vartheta(r)$ where E= energy, N= number of electrons of the system at constant external pressure $\vartheta(r)$.

and chemical hardness n as the half of the second derivative of energy with respect to number of electrons, so chemical hardness will be the first derivative of energy with respect to number of electrons

$$n = \frac{1}{2} \left(\frac{\partial \mu}{\partial N}\right) \vartheta(r)$$

But chemical potential(μ) and chemical hardness(n) were also calculated in most cases in

terms ionisation potential(IP) and electron affinity(EA) and therefore

$$\mu = -\left(\frac{IP+EA}{2}\right) \text{ and } n = \left(\frac{IP-EA}{2}\right)$$

According Koopman's theorem, IP and EA are related to energies of the Highest occupied molecular orbital(E_{HOMO}) and Lowest occupied molecular orbital(E_{LUMO}) in this way

$$IP = -E_{HOMO} \text{ and } EA = -E_{LUMO}$$

$$n = \left(\frac{E_{LUMO}-E_{HOMO}}{2}\right) \text{ and } \mu = \left(\frac{E_{LUMO}+E_{HOMO}}{2}\right)$$

and Parr and co-workers proposed electrophilicity[35] as a measure of electrophilic

power of a compound the electrophilicity can be represented as

$$\omega = \frac{\mu^2}{2n}$$

The chemical potential(μ) and chemical hardness(n), electrophilicity and dipole moment of the ligand and complexes are given in the table-6. The reactivity of the ligand and its metal complexes can be predicted by considering the minimum electrophilicity principle. According to minimum electrophilicity principle, compound having minimum electrophilicity will have maximum stability. The chemical potential(μ), chemical hardness(n), electrophilicity(ω) were calculated from the HOMO and LUMO value of the ligand and its complexes (Fig. 21) and presented in the table 6.

The geometrical parameters of the investigating compounds were also collected from their optimised geometry (Fig. 22, 23) and presented in the table 7. It is seen from the table that the bond angles around the metal ion in case of Co(II), Ni(II) and Cu(II) complexes are close to 90° and in case of Zn(II), it is close to 109°. Therefore, distorted octahedral geometry for Co(II), Ni(II) and Cu(II) complexes and distorted tetrahedral geometry may be suggested for the Zn(II) complex.

Non-linear optical properties

The electronic properties of chemical compounds are related to their non-linear optical activities. Easy electron transition between molecular orbitals is the basic requirement for good nonlinear optical materials. It is seen from the Table-6 that all metal complexes except Zn(II) complex have higher dipole moment than the free ligand. The energy gap between the HOMO and LUMO of the ligand is found to be higher than the complexes. All these findings indicate that complexes have better nonlinear optical properties[36] than the free organic ligand. The Cu(II) complex will be the good nonlinear optical material due to small energy gap between its HOMO and LUMO and high dipole moment.

BIOLOGICAL EVALUATIONS

Antibacterial studies

All the test compounds were screened against the gram-positive and gram negative bacterial (Table 8, Fig. 24). The ligand and some complexes have moderate effect on the growth of the microorganism. The complexes have more antibacterial abilities than the free ligand and the enhanced ability of the complexes may be explained by considering overtone's concept and chelation theory [37].

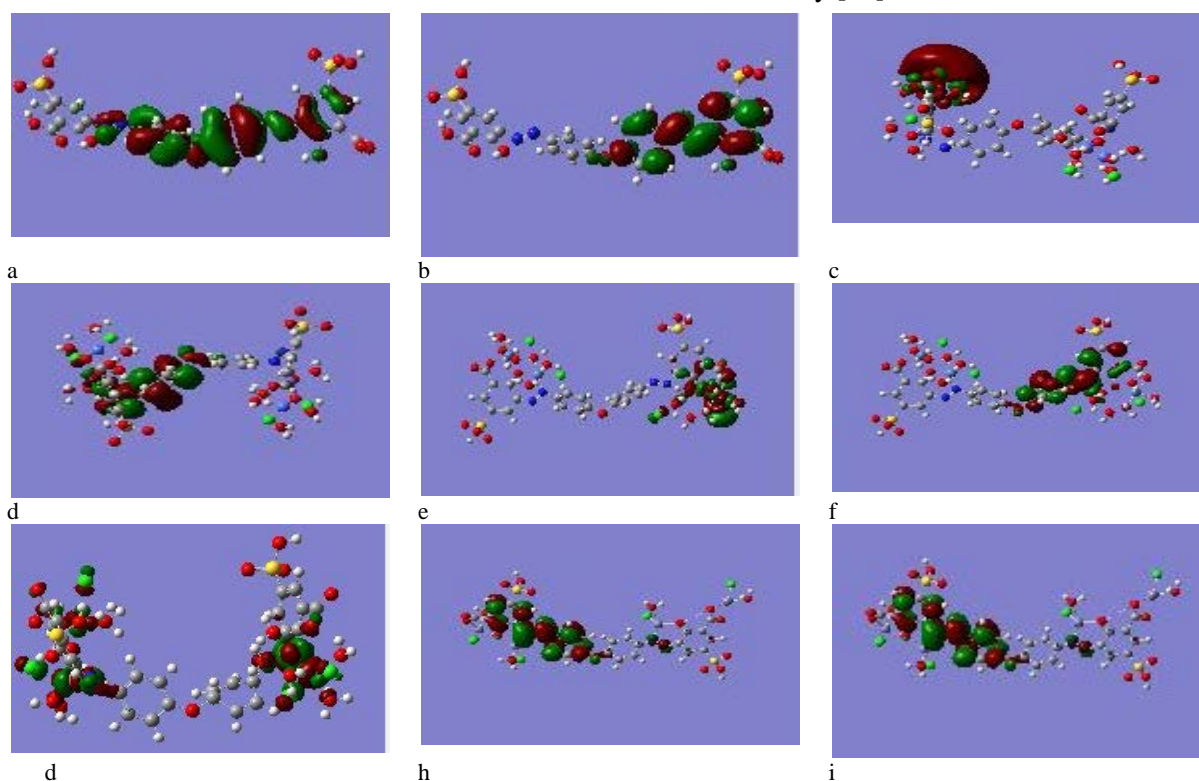


Fig. 21. HOMO and LUMO of the ligand a) HOMO of the ligand; b) LUMO of the ligand; c) LUMO of the Co(II) complex; d) HOMO of the Co(II) complex; e) HOMO of the Ni(II) complex; f) LUMO of the Ni(II) complex; g) HOMO of the Cu(II) complex; h) HOMO of the Zn(II) complex; i) LUMO of the Zn(II) complex.



Fig. 22. Optimised geometry of the Ni(II) complex

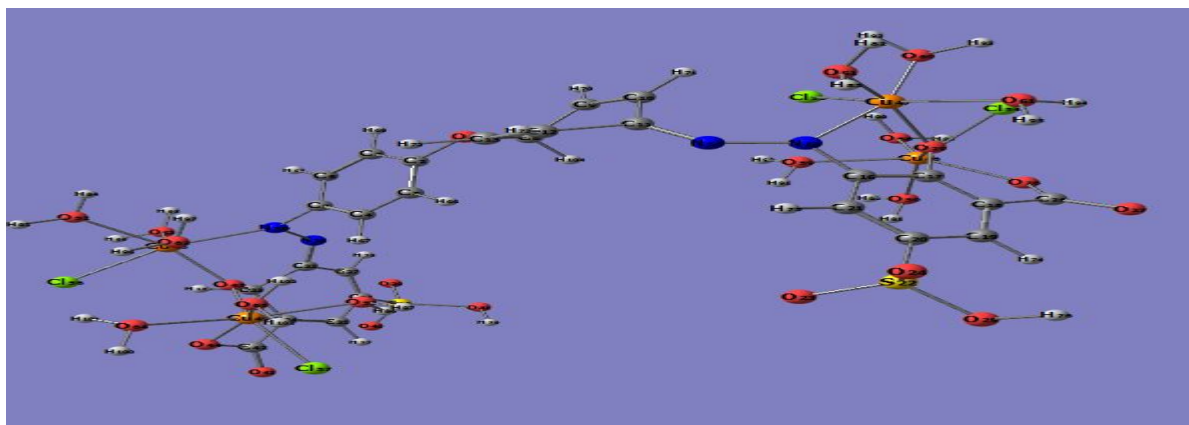


Fig. 23. Optimised geometry of the Cu(II) complex

Table 6. Reactive descriptors of the ligand and its complexes.

Compound	E _{HOMO} (eV)	E _{LUMO} (eV)	μ(eV)	n(eV)	η(eV)	Dipole moment(B.M.)
LH ₄	-0.33549	0.01561	-0.1599	0.1755	0.072	8.194
[Co ₄ LCl ₄ (H ₂ O) ₁₂]	-0.17651	0.00380	-0.086	0.090	0.041	14.592
[Ni ₄ LCl ₄ (H ₂ O) ₁₂]	-0.30137	-0.01775	-0.1595	0.1418	0.089	25.544
[Cu ₄ LCl ₄ (H ₂ O) ₁₂]	-0.11799	-0.07763	-0.097	0.0201	0.234	29.54
[Zn ₄ LCl ₄ (H ₂ O) ₄]	-0.34638	-0.02249	-0.1844	0.1619	0.1050	4.9775

Table 7. Selected bond length and bond angle

comp	Bondlength(A ⁰)				Bondangle(°)	
	N(14)-N(15)	N(15)-C(16)	O(28)-C(27)	N(15)-M(47)-O(29)	N(15)-M(47)-O(60)	N(15)-M(47)-Cl(55)
1	1.232	1.445	1.352	-	-	-
2	1.273	1.483	1.351	87.779	96.927	84.565
3	1.273	1.481	1.350	87.769	96.926	84.561
4	1.274	1.416	1.373	75.431	91.848	96.578
5	1.244	1.462	1.347	86.938	107.854	101.008

1.LH₂, 2.[Ni₄LCl₄(H₂O)₁₂], 3.[Cu₄LCl₄(H₂O)₁₂], 4. [Zn₄LCl₄(H₂O)₄]

Table 8. Antibacterial Screening of the investigating compounds.

compound	Concentration	<i>E. coli</i>	<i>S. aureus</i>
1.LH ₄	500 μg/ml	9	12
2.[Co ₄ LCl ₄ (H ₂ O) ₁₂]	500 μg/ml	14	13
3.[Ni ₄ LCl ₄ (H ₂ O) ₁₂]	500 μg/ml	10	14
4.[Cu ₄ LCl ₄ (H ₂ O) ₁₂]	500 μg/ml	12	12
5.[Zn ₄ LCl ₄ (H ₂ O) ₄]	500 μg/ml	10	11
6.Tetracycline	500 μg/ml	30	30

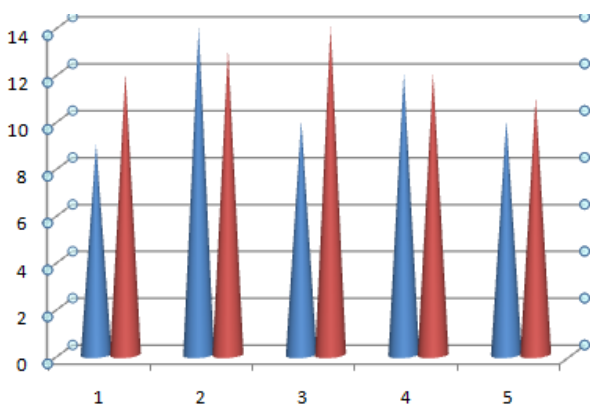


Fig. 24. Antibacterial Screening of the investigating compounds

Gel electrophoresis

The interaction between complex and metal complexes was also studied by gel electrophoresis as given in Fig. 25. The electrophoresis study shows that intensity of the DNA-complex bands are less than the DNA control and the intensity decreases in the order of $[\text{Cu}_4\text{LCl}_4(\text{H}_2\text{O})_{12}] > [\text{Ni}_4\text{LCl}_4(\text{H}_2\text{O})_{12}] > [\text{Co}_4\text{LCl}_4(\text{H}_2\text{O})_{12}]$ (lane 2- Co(II) complex, lane 3 – Ni(II) complex, lane 4- Cu(II) complex and lane 1- DNA CONTROL . Due to the intercalation of the metal complexes in to the DNA base pairs, intensity decreases

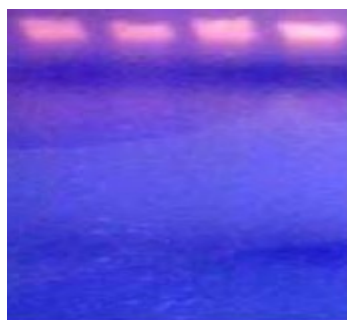


Fig. 25. Intensity of the DNA-complex: from left - 1. $[\text{Cu}_4\text{LCl}_4(\text{H}_2\text{O})_{12}]$, 2. $[\text{Ni}_4\text{LCl}_4(\text{H}_2\text{O})_{12}]$, 3. $[\text{Co}_4\text{LCl}_4(\text{H}_2\text{O})_{12}]$, 4. DNA control

Viscosity measurement test

All the metal complexes are subjected to viscosity measurement study to confirm the DNA binding abilities of the metal complexes with the CT DNA. The increase in viscosity of DNA occurs when the complexes intercalate between the base pairs due to extension in the helix[38]. The effects of all the synthesised complexes on the viscosity of DNA are shown in Fig.26. The graph shows that viscosity of DNA increases with increase in the concentration of complexes and the order of increase of viscosity is $[\text{Cu}_4\text{LCl}_4(\text{H}_2\text{O})_{12}] > [\text{Ni}_4\text{LCl}_4(\text{H}_2\text{O})_{12}] > [\text{Zn}_4\text{LCl}_4(\text{H}_2\text{O})_4] > [\text{Co}_4\text{LCl}_4(\text{H}_2\text{O})_{12}]$.

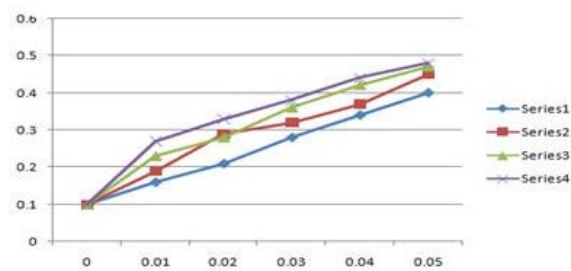


Fig. 26. $(\eta/\eta_0)^{1/3}$ verses $[\text{complex}]/[\text{DNA}]$ Series: 1- $[\text{Cu}_4\text{LCl}_4(\text{H}_2\text{O})_{12}]$, 2- $[\text{Ni}_4\text{LCl}_4(\text{H}_2\text{O})_{12}]$, 3- $[\text{Zn}_4\text{LCl}_4(\text{H}_2\text{O})_4]$, 4- $[\text{Co}_4\text{LCl}_4(\text{H}_2\text{O})_{12}]$.

CONCLUSION

On the basis various physico-chemical and spectral data presented and discussed, the ligand acted as a hexa dentate ligand as it coordinated with the metal atoms through OON-NOO donor atoms. Distorted octahedral geometry for the Co(II), Ni(II), Cu(II) and distorted tetrahedral geometry for Zn(II) is proposed on the basis of analytical, spectral data and computational study. Thermal study of the metal complex indicates thermal stability of the complexes, the fluorescence studies reveals that both ligand and its metal complexes have fluorescent properties and can be used for making photo conducting materials. The ligand and its complexes are known to have antibacterial properties and DNA binding abilities as indicated from their biological studies.

Acknowledgements: Author acknowledges UGC for financial support in the form of Minor Research Project(F.PSO-4/13-14(ERO) and SAIF, IIT ,CHENNAI for providing spectral data.

REFERENCES

1. A.T. Peters, H.S. Freeman, Colour chemistry, the design and synthesis of organic dye and pigments, Elsevier App. Sci. Publications, 1991.
2. A.M. Khedr, M. Gaber, R.M. Issa, H. Erten, *Dyes Pigm.*, **67**, 117 (2005).
3. F. Arjmand, M. Muddasir, *J. of Photochem. Photobiol. B Biol.*, **101**,37 (2010).
4. F. Arjmand, B. Mohani, S. Ahmed, *Eur. J. Med. Chem.*, **40**, 1103 (2005)
5. K. Nejati, Z. Rezvani, B. Massoumi, *Dyes Pigm.*, **75**, 653 (2007)
6. M. Tumer, D. Ekinci, F. Tumer, A. Bulut, *Spectrochim. Acta Part A Mol. Biomol. Spectroscopy*, **67**, 916 (2007).
7. S. Rai, A. Bajpai, S. Lokhandwala, *Adv. Mat. Lett*, **5**(4), 206 (2014).
8. C. Selvi, D. Nartop, *Spectrochim Acta A Mol. Biomol. Spectroscopy*, **95**, 165 (2012).

9. F. Frisch, G. Trucks, H. Schlegel, G. Scuseria, M. Robb, J. Cheeseman, J. Montgomery, T. Ureven, K. Kudin, J. Burant, Gaussian 03 Rev B. 03, Gaussian Inc, Pittsburg, PA, 2003.
10. D. Sobolova, M. Kozurkova, T. Plichta, Ondrusova, Z. Simkovic, M.H. Paulikova, A. Valent, *International Journal of Biological Macromolecules*, **48**, 319 (2011).
11. L. H. Abdel-Rahman, R. M. El-Khatib, L.A. E. Nassr, A.M. Abu-Dief, F. El-Din Lashin, *Spectrochimica Acta Part A: Molecular Biomolecular Spectroscopy*, **111**, 266 (2013).
12. R.S. Brant, E.R. Miller, *J. Bacteriol.*, **38**(5), 525 (1939).
13. W.J. Geary, *Coord. Chem. Rev.*, **7**, 81 (1971).
14. A. Saxena, J.P. Tondon, *Polyhedron*, **3**, 681 (1984).
15. S.D. Robinson, M.F. Uttley, *J. Chem. Soc.*, **2**, 1912 (1973).
16. R.B. King, *Inorganic Chemistry*, **5**, 300 (1961).
17. V. Stefov, V. M. Petrusevski, V. M. Soptrajanov, *B. J. Mol. Structure*, **97**, 2939 (1961).
18. K. Nakamoto, *Infrared and Raman Spectra of Inorganic and Coordination compounds*, Wiley and sons, 2009.
19. A.B.P. Lever, *Coord. Chem. Rev.*, **3**, 119 (1968).
20. M. Shakir, A.K. Mahammed, O.S.M. Nasman, *Polyhedron*, **15**, 3487 (1996).
21. P.P. Dholakiya, M.N. Patel, *React. Inorg. Met. Org. Nano-Met. Chem.*, **32**, 819 (2002).
22. S. Yamada, *Coord. Chem. Rev.*, **1**, 445 (1966).
23. A.B.P. Lever, E.I. Solomon, *Inorganic Electronic Structure and Spectroscopy*, Wiley and sons, 2014.
24. M.K.S. Abou, H. Faruk, *J. of Iran Chem. Soc.*, **5**, 122 (2008).
25. D.H. Williams, I. Fleming, *Spectroscopic methods in organic chemistry*, Tata McGraw Hill, 1994.
26. A.E. Ahmed, Taha, M.A. E. *Spectrochimica Acta Part A: Molecular Biomolecular Spectroscopy*, **56**, 2775 (2011).
27. A.F.M. Benial, V. Ramakrishan, R. Murugesan, *Spectrochimica Acta Part A: Molecular Biomolecular Spectroscopy*, **79**, 1803 (2000).
28. B.J. Hathaway, D.E. Billing, *Coord. Chem. Rev.*, **5**, 143 (1970).
29. R.L. Dutta, A. Syamal, *Elements of Magnetochemistry*, East-West Press PVT LTD, 2010.
30. D. Kivelson, R.R. Neiman, *J. Chem. Phys.*, **35**, 159 (1970).
31. C. Anita, C.D. Sheela, P. Tharmaraj, S. Sumati, *Spectrochimica Acta Part A: Molecular Biomolecular Spectroscopy*, **96**, 493 (2012).
32. A. Majumdar, G.M. Rosair, A. Mallick, N. Chattopadhyaya, S. Mitra, *Polyhedron*, **25**(8), 1753 (2006).
33. R. Dennington, T. Keith, J. Milliam, *Gauss View Version 4.1*, 2007.
34. A.D. Beckel, *J. Chem. Phys.*, **98**, 564 (1993).
35. R.J. Parr, R.J. Pearson, *J. Am. Chem. Soc.*, **75****12**, 105 (1983).
36. S.M. Soliman, M. A.M. Abu-Youssef, J. Albering, A. El-Faham, *J. Chem. Sci.*, **12**, 2137 (2015).
37. A.B.P. Lever, *Journal of Molecular Structure*, **129**, 180 (1985).
38. P.R. Hertzberg, P.B. Dervan, *J. Am. Chem. Soc.*, **104**, 313 (1982).

СИНТЕЗА, СПЕКТРОСКОПСКО ОХАРАКТЕРИЗИРАНЕ И БИОЛОГИЧНА АКТИВНОСТ НА Co(II), Ni(II), Cu(II) И Zn(II) МЕТАЛНИ КОМПЛЕКСИ С ЛИГАНДИ ОТ АЗО-БАГРИЛО, ПОЛУЧЕНО ОТ 4,4'-ДИАМИНОДИФЕНИЛЕТЕР И 5-СУЛФОСАЛИЦИЛОВА КИСЕЛИНА

С.Н. Чаулия

Департамент по химия, Г.М. Колеж, Самбалтур, Одиша, Индия

Постъпила на 16 февруари, 2016 г.; коригирана на 27 май, 2016 г.

(Резюме)

Синтезирани са серия от метални комплекси на Co(II), Ni(II), Cu(II) и Zn(II) с нови лиганди от азо-багрило 4,4'-bis(2'-хидрокси-3'-карбокси-5'-сулфофенил-азо)дифенил етер и 5-сулфосалицилова киселина. Металните комплекси и лигандите са охарактеризирани чрез аналитични методи (ИЧ- и ЯМР-спектроскопия, мас-спектрометрия, електронни спектри) и измервания на моларната проводимост, магнитна чувствителност и термични измервания. Аналитичните и спектралните данни предсказват октаедрична геометрия за комплексите на Co(II) и Ni(II), деформирана октаедрична геометрия за комплекса на Cu(II) и тетраедрична геометрия на комплекса на Zn(II). Проведени са числени изследвания на лигандите и металните комплекси за определянето на геометричните параметри и на общите реактивни дескриптори. Рентгено-структурният анализ на прахови образци показва орто-ромбична кристална система за комплекса на Cu(II). Термичните изследвания разкриват термична стабилност на комплексите, а флуоресцентните изследвания предвиждат фотоактивни свойства на азо-съединенията. Снимките на Zn(II)-комплексите от сканираща електронна микроскопия дават информация за тяхната повърхностна морфология. Биологичното изследване разкрива анти-бактериални свойства и ДНК-свързваща активност на синтезираните съединения.

Improved hydrogen storage capacity of CNTs synthesized in presence of iron catalyst using arc discharge method in air atmosphere

N. Ismail^{1*}, R. Joshi², J. Engstler², J. J. Schneider²

¹Physical Chemistry Department, National Research Centre, Dokki 12311, Cairo, Egypt

²Department of Chemistry, Inorganic Chemistry, Darmstadt University of Technology, Darmstadt, Germany

Received January 15, 2016; Revised November 4, 2016

Arc discharge method is used to prepare carbon nanotubes (CNTs) in air atmosphere with high yield. Multiwall-CNTs are produced in absence of catalyst. When 10wt% of Fe and amorphous FeB are used as catalysts during the synthesis process, the quality of produced CNTs is improved and the number of walls tends to decrease. The XRD structural study records the graphite 002 pattern accompanied with the main peaks of Fe structure. Scanning electron microscopy showed high yield of CNTs distributed all over the soot when catalysts are used. High transmission electron microscopy is utilized to investigate the local microstructure of the CNTs. The growth mechanism of CNTs in presence of amorphous FeB is discussed. After removal of the catalyst, the hydrogen storage capacity is measured at 80K under applied hydrogen pressure up to 20 bar. The storage capacity is improved to 3.25 wt% when CNTs are prepared in presence of catalysts.

Key words: Hydrogen storage, Carbon nanotubes, Catalyst

INTRODUCTION

Since their discovery in 1991 [1], CNTs draw the attention of the researchers, as they possess unique mechanical, electronic, thermal, chemical and optical properties. Scientists classified them according to the number of walls as single-walled nanotubes (SWNTs), double-walled nanotubes (DWNTs) and multi-walled nanotubes (MWNTs). The most popular methods of CNTs preparation are arc discharge, chemical vapor deposition and laser ablation [2-7]. Other methods have been reported, e.g., electrolysis [8,9], hydrothermal [10] and ball milling [11,12]. Arc discharge is considered as the most successful preparation method for quantitative production. However, the atmosphere used is mostly hydrogen [13], noble gas like argon or helium [14] or a mixture of hydrogen with noble gas [15]. Carbon nanotubes have been found promising for several applications like hydrogen energy storage. This is due to their interesting rolling graphene sheets. The tube hollow cavity is considered a possible site for hydrogen to occupy along with its possible adsorption on the outer surface as a result of Van der Waals forces. Several publications reported the adsorption of hydrogen by CNTs either electrochemically [16-18] or from the gas phase [19-21]. Additionally, CNTs were used as a catalyst to overcome the slow kinetics of Mg hydride. Chen *et al.* [22] added CNTs to Mg hydride during ball milling which enhanced the formation of Mg hydride

nanoparticles. They detected remarkable improvements of kinetics of Mg hydride absorption/desorption cycling. When TiO₂-Co nanoparticles decorated the CNTs using electrophoretic deposition, Bordbar *et al.* [23] recorded a two-fold increase in the hydrogen discharge capacity (305 mAh/g) compared to CNT alone. Another study claimed an enhancement in hydrogen storage capacity of Ag-CNTs when CNTs have been deposited on Ag microporous foam by electrophoretic deposition [24]. The researchers believed that the interconnections between the CNTs and the Ag increased and became more stable, and in return, the charge transfer process through the electrode was facilitated. This was believed to be the reason for the remarkable increase in the hydrogen storage capacity to reach 5.2 wt%. When 10 mol% of CNTs were mixed with NaAlH₄ the hydrogen storage capacity reported was 3.3 wt% [25], a further increase up to 4.2 wt% was achieved by rehydrogenation.

In this work we report a convenient method of preparation of CNTs by arc discharge method in air atmosphere. Fe and amorphous FeB alloy were used as catalysts for the synthesis process and the hydrogen storage capacity was enhanced in case of CNTs prepared using a catalyst.

EXPERIMENTAL

Preparation of amorphous FeB

Intermetallic iron boride alloy of 99% purity was purchased from CHEMPUR, Poland. Mechanical alloying was performed using a planetary ball mill

* To whom all correspondence should be sent:
E-mail: nahlaismail24@yahoo.com

Fritsch Pulverisettein order to convert it from crystalline to amorphous state. A mass of 20 g of FeB alloy was transferred to a stainless steel vial. The ball to powder ratio was kept 10:1 in argon atmosphere. The powder was milled for 50 h at a constant rotation speed of 700 rpm. Figure 1 shows the XRD pattern of the amorphous structure of FeB alloy after ball milling.

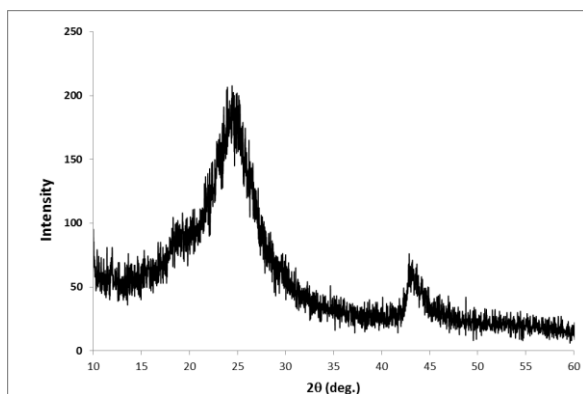


Fig. 1. XRD pattern of FeB alloy after ball milling

Setup of arc discharger

To synthesize CNTs the power was adjusted at 40V constant potential using M30-TP305E DC power supply. The two electrodes used for arc discharge are of graphite of 99.7% purity. The anode is a hollow rod of 11 mm diameter facing the cathode disc of 2.5 cm diameter mounted on a rotating copper plate. The hollow space is centered in the middle with 6 mm diameter and 6 cm depth filled with the catalyst. Filling the anode with Fe and amorphous FeB catalyst is performed in a glove box in argon atmosphere. A schematic diagram of the experimental setup is shown in ref. [26]. The copper disc rotates at a slow speed adjusted at 5 rpm and is cooled during the experiment by water running through a tube coil surrounding the cathode. All experiments were carried out in air atmosphere. Soot deposited on the cathode disc was removed using a thin blade during rotation.

Phase identification was performed by X-ray diffraction (XRD) EMPY REAN diffractometer operated at 30 mA and 45 KV, using Cu K α radiation. Phillips XL30 FEG scanning electron microscope (SEM) was utilized to study the soot morphology and Phillips CM 20 FEG transmission electron microscope (TEM) was used with an acceleration voltage of 200 KV for local microstructure investigations of the nanotubes. A volumetric Sieverts method was used to estimate the weight percentage of the amount of hydrogen adsorbed by the CNTs, as previously mentioned in [2, 28].

RESULTS AND DISCUSSION

The anode was filled with 10wt% of Fe in argon atmosphere, then arc discharge was operated for few minutes in air and the chamber was left to cool down before repeating the process. The soot deposited on the cathode disc was collected. Its physical properties are: hard grey from the outside and black from inside where bundles of CNTs exist. The SEM image of the soot (Fig. 2) reveals its hard, brittle properties.

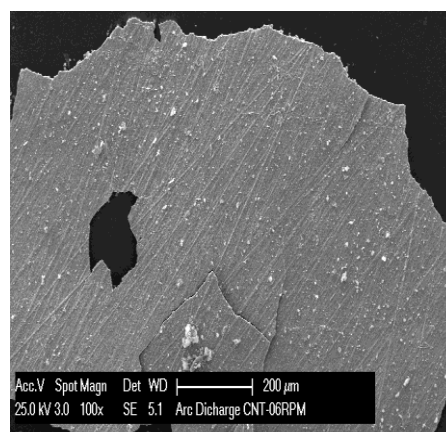


Fig 2. SEM image of the soot

The soot was purified from undesired carbonaceous materials by calcination in an oven at 550°C for 1 h. After that, the soot was re-weighed and the difference in weight was considered as undesired carbonaceous materials which became oxidized to CO₂. The remaining product was CNTs. In absence of a catalyst, the undesired carbonaceous materials were found to be 7wt. % of the soot. When Fe and amorphous FeB were used as catalysts, the undesired carbonaceous materials were reduced to 1.3 wt. % and 1.7 wt. %, respectively.

The SEM image of the CNTs synthesized without a catalyst is shown in Fig 3a. Long nanotubes which look like needles are observed in different areas of the image, their lengths are in micrometers. The image shows the graphitized materials covering the major parts of the image. Figs.3b and c present the image of the crushed soot formed in presence of Fe and amorphous FeB, respectively. These images justify the high yield of CNTs calculated in presence of catalyst. The formation of bundles of CNTs is seen all over the soot samples and few graphitized materials are observed. The length of CNTs observed is in micrometers. The rotating cathode disc promoted the formation of μm long CNTs both in presence and absence of the catalyst. Certainly, the presence of Fe and amorphous FeB remarkably promotes the CNTs yield and the distribution of the CNTs all over the soot, and also minimizes the formation of graphitized materials.

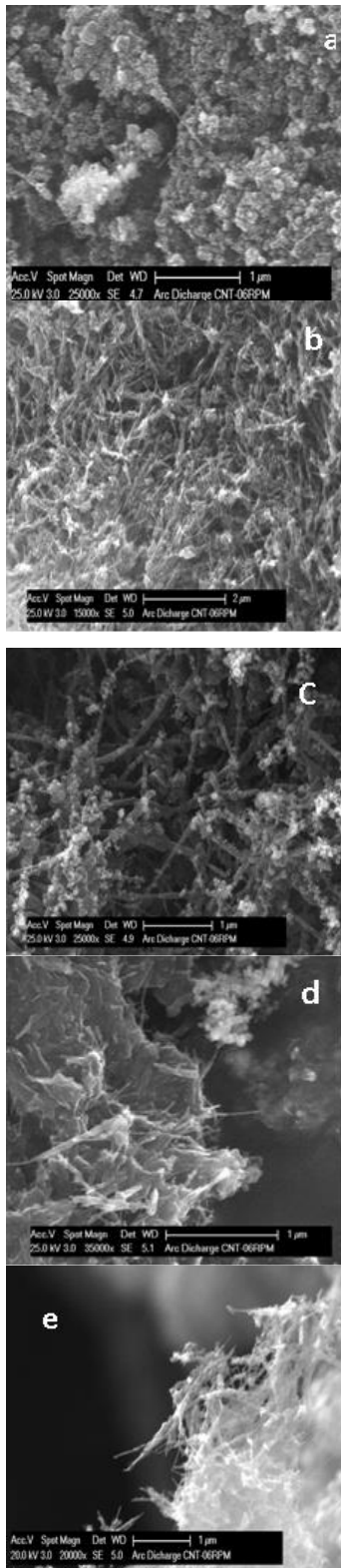


Fig 3. SEM images of the prepared CNTs

The soot formed in presence of Fe and FeB was purified by stirring in boiling 6M HCl for 2 h, then ultrasonicated in ethanol for 10 min. The SEM images of purified CNTs are presented in Figs 3 d and e. The images illustrate the formation of lumps of CNTs.

For local microstructure investigations to identify the type and size of CNTs, HR-TEM was utilized. The images of CNTs synthesized without a catalyst and in presence of Fe and amorphous FeB as catalysts, are shown in Fig 4.

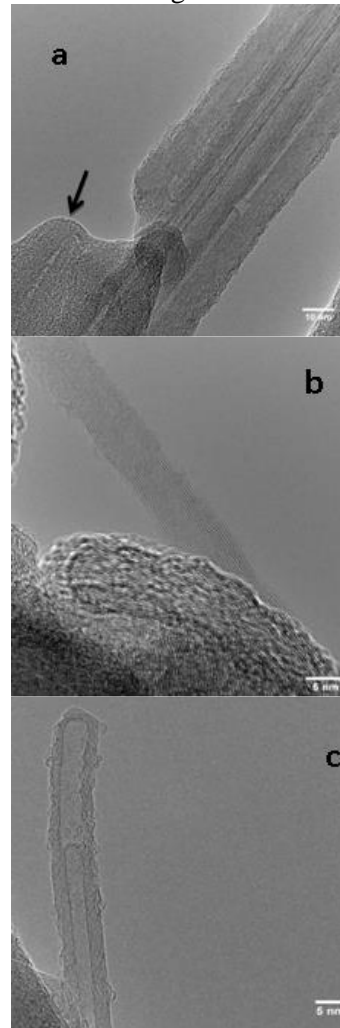


Fig 4. SEM images of CNTs formed a) without a catalyst, b) in presence of Fe, c) in presence of amorphous FeB.

Image (a) shows the CNTs synthesized without a catalyst - MWCNTs with a large number of walls, outer diameter larger than 10 nm and inner diameter about 2.5 nm. They coexist with ellipsoidal polyhedral particles (see the arrow) which are considered as embryonic state of CNTs which may grow under constant ion supply [29]. Figs. 4b and c present the local microstructure of the CNTs grown in presence of Fe and amorphous FeB, respectively. From image 4b it is seen that the synthesized CNTs inner diameter is 2.5 nm and the outer diameter is 6.3 nm, the number of walls is 5-7. Image 4c shows that the CNTs inner diameter is 3.9 nm, the outer diameter is 6.7 nm and the same number of walls is observed in the case of Fe. The statistical error of the measurement is ± 0.2 . From these results we deduce

that the presence of the catalyst tends to reduce the number of walls and this agrees with another conformation [30] that the catalyst favors the growth of single- and double-wall CNTs rather than MWCNTs. During arc plasma discharge the catalyst metal atoms vaporize along with the carbon atoms and at the cathode the metal liquid redistributes its temperature in a way that it suppresses the formation of multi-walls during the nucleation of the carbon nanotubes. For the binary catalyst FeB the nonmetal is added as a promotor, during plasma arc discharge, the difference between the metal and nonmetal melting points leads to the formation of a core/shell on the cathode [31, 32]. It forms active sites on the catalyst surface so that CNTs nucleation occurs at these sites. Thus, the type of catalyst controls the number of walls and the diameter of the nanotubes. In case of metallic Fe as a catalyst, the tube diameters were relatively smaller than those of the tubes formed in presence of amorphous FeB; in both cases of catalysts the number of walls was almost the same. This observation confirms the suggestion that core/shell active sites (of logically larger diameter) are formed and that nucleation occurs on these sites.

The structural investigation of the soot was carried out using XRD (Fig. 5). The plots show the 002 graphitic reflections of pyrolytic graphite [33, 34], which indicates a high degree of crystallinity. The CNTs formed in presence of Fe as a catalyst, record additional peaks of Fe pattern.

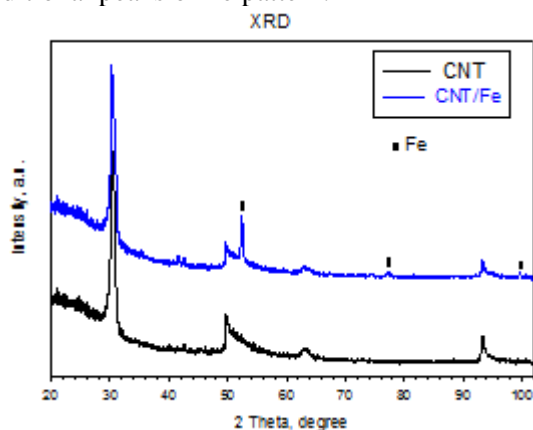


Fig 5. XRD patterns of the CNTs soot in presence of Fe as a catalyst and without a catalyst.

The hydrogen sorption capacity in weight percentage was estimated by the computer programmed volumetric Sieverts device. At 80K, the pressure composition isotherm (PCI) of CNTs formed in absence of the catalyst is shown in Fig.6. The plot displays type II isotherm so that at relatively low applied hydrogen pressure (up to 13 bar), the CNTs adsorb hydrogen linearly, then the rate of adsorption decreases by increasing the applied

hydrogen pressure. At 20 bar, the amount of sorbed hydrogen is 2.5 wt%.

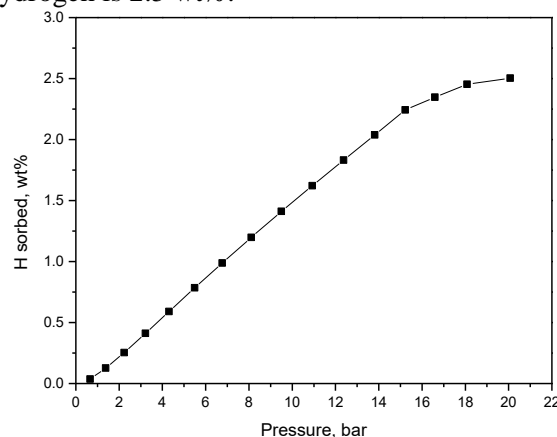


Fig 6. PCT isotherm of the CNTs prepared in absence of a catalyst.

At the same temperature, the hydrogen sorption plots of the CNTs prepared in presence of Fe and amorphous FeB are shown in Figs. 7 and 8, respectively. Both diagrams display linear first order plots so that the rate of hydrogen sorption is almost constant all over the range of the applied hydrogen pressure.

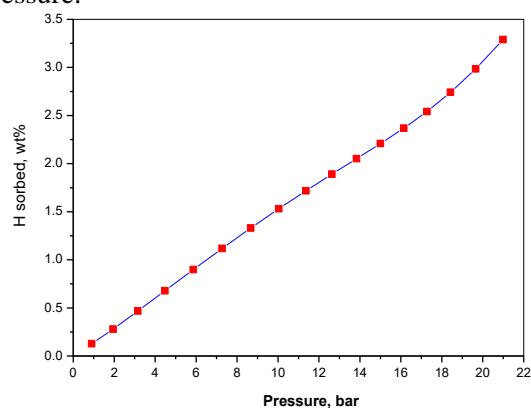


Fig 7. PCT isotherm of the CNTs prepared in presence of Fe.

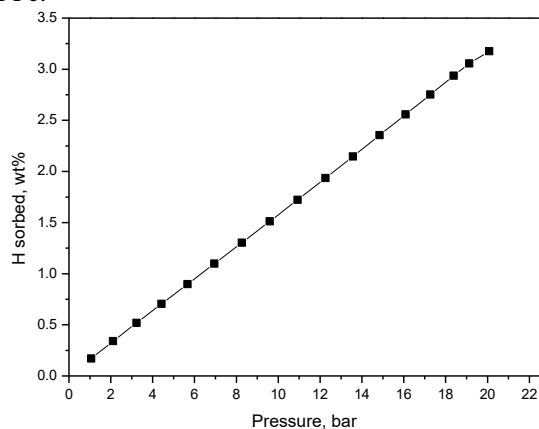


Fig 8. PCT isotherm of the CNTs prepared in presence of amorphous FeB.

The amounts of hydrogen stored by the CNTs at 20 bar are 3.25 and 3.2 wt % respectively. The

enhancement of the amount of hydrogen sorbed by the CNTs prepared in presence of the Fe catalysts is related to the quality of CNTs produced in presence of the catalysts. The regularity of the produced CNTs and the reduction of the number of walls may have increased the possibility of the CNTs to uptake more hydrogen.

CONCLUSIONS

Carbon nanotubes were prepared by arc discharge in an air atmosphere. Contrary to other research reports [35], CNTs can be prepared without a catalyst, but the presence of the catalyst, in our case Fe and amorphous FeB, improved the quality of the CNTs. Regular tubes were produced. In addition, the presence of Fe and FeB tended to reduce the number of walls to reach penta to hepta walls. The improved quality of the CNTs in presence of the catalysts had enhanced, on its turn, the hydrogen sorption capacity under the same conditions.

Acknowledgement: *Deutscher Akademischer Austauschdienst (DAAD) is acknowledged for funding the scholarship of Dr. Nahla Ismail in TU-Darmstadt as part of this work.*

REFERENCES

1. S. Iijima, *Nature*, **354**, 56 (1991).
2. F. Danafar, A. Fakhru'l-Razi, M.A.M. Salleh, D.R.A. Biak, *Chem. Eng. J.*, **155**, 37 (2009).
3. M. Kumar, Y. Ando, *J. Nanosci. Nanotechnol.*, **10**, 3739 (2010).
4. J.-P. Tessonier, D.S. Su, *Chem. Sus. Chem.*, **4**, 824 (2011).
5. J. Prasek, J. Drbohlavova, J. Chomoucka, J. Hubalek, O. Jasek, V. Adam, R. Kizek, *J. Mater. Chem.*, **21**, 15872 (2011).
6. D.B. Geohegan, A.A. Puretzky, X. Fan, M.A. Guillorn, M.L. Simpson, V.I. Merkulov, S.J. Pennycook, *MRS Proc.*, **593**, 3 (2011).
7. M. Lubej, I. Plazl, *Chem. Biochem. Eng. Q.*, **26**, 277 (2012).
8. W.K. Hsu, J.P. Hare, M. Terrones, H.W. Kroto, D.R.M. Walton, P.J.F. Harris, *Nature*, **377**, 678 (1995).
9. J.B. Bai, *Chem. Phys. Lett.*, **365**, 184 (2002).
10. Y. Gogotsi, J.A. Libera, M. Yoshimura, *J. Mater. Res.*, **15**, 2591 (2011).
11. N. Pierard, A. Fonseca, Z. Konya, I. Willems, G. Van Tendeloo, *Chemical Physics Lett.*, **335**, 1(2001).
12. F. Liu, X. Zhang, J. Cheng, J. Tu, F. Kong, W. Huang, C. Chen, *Carbon*, **41**, 2527 (2003).
13. X. Zhao, S. Inoue, M. Jinno, T. Suzuki, Y. Ando, *Chem. Phys. Lett.*, **373**, 266(2003).
14. Y. Liu, S. Xiaolong, Z. Tingkai, Z. Jiewu, M. Hirscher, F. Philipp, *Carbon*, **42**, 1852 (2004).
15. D. Tang, S. Xie, W. Liu, B. Chang, L. Sun, Z. Liu, G. Wan, W. Zhou, *Carbon*, **38**, 480 (2000).
16. Y. Sun, L. Ma, B. Zhou, P. Gao, *Intern. J. Hydrogen Energy*, **37**, 2336(2012).
17. A.K.M. FazelKibria, Y.H. Mo, K.S. Park, K.S. Nahm, M.H. Yun, *Intern. J. Hydrogen Energy*, **26**, 823 (2001).
18. G.P. Dai, C. Liu, M. Liu, M.Z. Wang, H.M. Cheng, *Nano Lett.*, **2**, 503(2002).
19. Young-Jung Heo, Soo-Jin Park, *J. Ind. Eng. Chem*, **31**, 330(2015).
20. T. Ramesh, N. Rajalakshmi, K.S. Dhathathreyan, *J. Energy Storage*, **4**, 89(2015).
21. R. Mohtadi, P. K. Sivasubramanian, S.-J. Hwang, A. Stowe, J. Gray, T. Matsunaga, R. Zidan, *Intern. J. Hydrogen Energy*, **37**, 2388 (2012).
22. B.-H. Chen, C.-H. Kuo, J.-R. Ku, P.-S. Yan, C.-J. Huang, M. -S. Jeng, F. -H. Tsau, *J. Alloys Compd.*, **568**, 78(2013).
23. M. Bordbar, T. Alimohammadi, B. Khoshnevisan, B. Khodadadi, A. Yeganeh-Faal, *Intern. J. Hydrogen Energy*, **40**, 9613(2015).
24. B. Khoshnevisan, M. Behpour, S. Shoaie, *Intern. J. Hydrogen Energy*, **37**, 2298(2012).
25. D. Pukazhselvan, B. K. Gupta, A. Srivastava, O.N. Srivastava, *J. Alloys Compd.*, **403**, 312(2005).
26. R. Joshi, J. Engstler, P. K. Nair, P. Haridoss, J. J. Schneider, *Diam. Relat. Mater.*, **17**, 913(2008).
27. N. Ismail, M. Madian, M.S. El-Shall, *J. Ind. Eng. Chem.*, **30**, 328(2015).
28. N. Ismail, I.H. Abd El-Maksod, H. Ezzat, *Intern. J. Hydrogen Energy*, **35**, 10359(2010).
29. Y. Satio, T. Yoshikawa, M. Inagaki, *Chem. Rev. Lett.*, **204**, 277 (1993).
30. X. Lin, X.K. Wang, V.P. Dravid, R.P.H. Chang, J.B. Ketterson, *Appl. Phys. Lett.*, **64**, 181 (1994).
31. J.B. Donnet, H. Oulanti, T. Le Huu, *Diam. Relat. Mater.*, **17**, 1506(2008).
32. Z. Wang, Z. Zhao, J. Qiu, *Carbon*, **44**, 1845 (2006).
33. M. Meyyappan, CRC Press, Boca Raton, 70 (2004).
34. T. Belin, F. Epron, *Mater. Sci. Eng. B*, **119**, 105(2005).
35. T. Zhao, Y. Liu, J. Zhu, *Carbon*, **43**, 2907 (2005).

ПОДОБРЕН КАПАЦИТЕТ НА ВЪГЛЕРОДНИ НАНОТРЪБИ (CNT) ЗА СКЛАДИРАНЕ НА ВОДОРОД ПРИ ДЪГОВО ИЗПРАЗВАНЕ ВЪВ ВЪЗДУХ В ПРИСЪСТВИЕ НА ЖЕЛЕЗЕН КАТАЛИЗАТОР

Н. Исмаил¹, Р. Джоши², Й. Енгстлер², Й.Й. Шнайдер²

¹Департамент по физикохимия, Национален изследователски център, Докки 12311, Кайро, Египет

²Департамент по химия, Неорганична химия, Технологичен университет в Дармщадт, Германия

Постъпила на 15 януари, 2016 г.; коригирана на 4 ноември, 2016 г.

(Резюме)

Използване е метод на дъгово изпразване във въздушна атмосфера за изготвянето на въглеродни нанотръби (CNTs) с висок добив. Многостенните CNTs се получават в отсъствие на катализатор. Когато се добавят 10 % (тегловни) желязо и аморфен FeV като катализатор по време на синтезата качеството на получените CNTs се подобрява и броят на стените намалява. Рентгено-структурният анализ показва наличието на графит 002, придружени от главни пикове на желязна структура. Сканиращата електронна микроскопия показва висок добив на CNTs, разпределени по целите сажди когато се използва катализатор. Високо-трансмисионна електронна микроскопия е използвана за изследването на локалната микроструктура на CNTs. Обсъден е механизма на израстване на CNTs в присъствие на FeV. След отстраняването на катализатора е измерен капацитета за складиране на водород при 80 K при налягане на газа до 20 бара. Капацитетът на складиране се подобрява до 3.25 % (тегловни), когато CNTs се изготвят в присъствие на катализатор.

Studies of the physico-chemical characteristics and fatty acid composition of commercially available Algerian frying edible oils

R. Sadoudi*, D Ali Ahmed, M. Trache, A Kecili

Agriculture Department, Faculty of Biology and Agriculture, Mouloud Mammeri University of Tizi-Ouzou, 15000, Algeria

Received January 22, 2015; Revised February 2, 2016

In the present study various physical and chemical characteristics have been studied and may be used for quality control of the main edible vegetable oil brands sold on the Algerian market, namely: Afia, elio, fleurial, La Belle, Oleor. The result obtained indicate that all the oils were consistent with the norms established indicative of edible oils with a good quality: Free Fatty Acid ranged from 0.044 to 0.054 %, the peroxide value varied from 1.61 to 2, the iodine value ranged from 124.07 to 129.91, the saponification value (189.01 to 192.21), the density at 20°C (0.917-0.921) and the refractive index at 40°C (1.4663-1.4670). However, the oils recorded a high PUFA content (mean 60%) suggesting that our oils are highly unsaturated and may be susceptible to rancidity. "Fleurial" oil can be more sensitive to oxidation and thermal alteration when compared with the others; this oil had the lowest induction period (8.27h), the lowest activation energy (438.16KJ/mol) and the highest PUFA content (mean 65%); however, at the factory, this oil was enriched by vitamins A and D, which makes it suitable for use as a salad oil.

Keywords: frying vegetable oils, Algeria, characterization

INTRODUCTION

Vegetable oils are substances derived from oil plants; they are composed of triglycerides which contain primarily polyunsaturated and monounsaturated fatty acids. Oil is extracted primarily from seeds. However, the crude oil obtained needs to be refined in order to transform it into a range of useful products for industry and consumers.

Oils improve the flavor, lubricity, texture, and satiety to foods. They have also been found to have a major role in human nutrition. Oils and fats have the highest energy in comparison to carbohydrates and proteins, carriers of oil soluble vitamins and many contain fatty acids essential for health, that are not manufactured by the human body [1].

Algeria has a large deficit in edible oils. The main oil produced is olive oil. But production hardly covers the needs and that makes it highly dependent on imports to supply the market. Thus, high quantities of crude oil are imported. After refining, the oil is sold under different brands. Some oils are pure and others are a blend of two oils. These oils are sold at different prices and used in cooking, notably for frying.

The main objective of this study was to characterize the refined vegetable oils used for

frying commercialized in Algeria and improve the understanding as regards the oil quality, stability and applicability.

MATERIALS AND METHODS

Samples for examination represent all (five) Algerian manufacturers, i. e. Cevital Bejaïa (two oils: Fleurial and elio), C.O.G.B/La Belle Bejaïa (one oil: La Belle) and Afia International Oran (two oils: Oleor and Afia). The five refined edible vegetable oils analyzed in this study were acquired from a supermarket, Tizi-Ouzou, Algeria. These oils were submitted to the following tests: Free Fatty Acid, peroxide value, iodine value, saponification value, fatty acid composition, density, UV absorbance, Rancimat test, activation energy and refractive index assessment using the methods given in Table 1. The Data obtained was statistically analyzed using analysis of variance (ANOVA).

Free Fatty Acids content (FFA)

FFA content is a conventional expression of the percentage mass-fraction of the oil total. In view of the results shown in Table 2, the percentages of FFA (calculated as oleic acid) of the vegetable oils sold on the Algerian market were very low. The results obtained were in the range of 0.044%±0.003 ("elio" oil), 0.050±0.001 ("Afia" oil), 0.051±0.003 ("Oleor" oil), 0.051±0.005 ("fleurial" oil) and 0.054±0.003 ("La Belle" oil). These values were under the value of 0.2%, which is the maximum established by the

* To whom all correspondence should be sent:
E-mail: Sadoudirab@yahoo.fr

Algerian standard 1169 (1990) for refined oils. The values were lower than those reported for Slovene sunflower oils (0.043) by Tasic and Klofutar [2]. The low values can be attributed to the efficient removal of the FFA during the refining of crude oil.

Table 1. Methods of analyses

<i>Chemical analysis</i>	
Free Fatty Acids (AFNOR NF T60-204, 1988).	
Peroxide value (AFNOR NF T60-220, 1988).	
Iodine value (AFNOR – NFT60 – 203, 1968).	
Saponification value (AFNOR T60-206, 1968)	
<i>Physical analysis</i>	
Refraction index (ISO 6320, 2000),	
Density « DMA 4500 » densimeter,	
Ultraviolet spectrophotometry (AFNOR T60-223, 1968),	
Fatty acid composition (AFNOR ISO 5509, 1978),	
Rancimate test (ISO 6886) «Rancimat 743»,	
Activation energy « NETZSCH STA 449C »	

RESULTS AND DISCUSSION

Chemical properties

The mentioned chemical and physical characteristics of refined oils in our country are shown in Table 2. As shown, significant differences were found between these edible oils.

Iodine value

The iodine value (IV) is an indicator of the degree of unsaturation of fats and oils. The IV is the mass of iodine in grams that is consumed by 100 grams of oil. The IV provides an overall status of the unsaturation of the oils. The iodine value increases with the increase of unsaturation of oil. As in the measurement of the FFA %, our oils have acceptable values of IV in comparison with the range established by the Algerian Official Journal (120-143gI₂/100g oil) and Codex STAN 210, 1999 (118-141). In addition, these values are in agreement with those suggested by Pocklington [3] for edible oils of good quality.

Nevertheless, frying vegetable oils in our country are more unsaturated than those commercialized in Romania; Chira et al. [4] obtained the values of 113, 122 and 128 for canola oil, sunflower and soybean oil respectively. Our results were also higher than those of Tasic and Klofutar [2] for oils commercialized in Slovenia. The high IV indicates a high degree of unsaturation of our oils. From the oils studied, “fleural” oil is characterized by the greatest

IV; this may result from the fact that this oil has a higher content of polyunsaturated fatty acids. Its established unsaturated character affects the stability of the oils and as a result, leads to the appearance of degradation effects during storage.

Peroxide value

The peroxide value of an oil or fat is used as a measurement of the extent to which rancidity reactions have occurred during storage. This parameter expresses the oxidation in its early stages. The values obtained were low (mean 1.826) compared to the maximum acceptable value of 10meq KOH/g by the Codex Alimentarius Commission for oleaginous seed. The oils under investigation were purchased the same day these were received by the supermarket, which explains the lowest peroxide value. The low values of PV are indicative of the low levels of oxidative rancidity of the oils.

Otherwise, our fresh oils are less peroxidized than those commercialized in Bulgaria; Marinova et al. [5], that report values of 8.8 and 4 meq for sunflower and soybean oil, respectively. Bazlul Mobin et al. [6] report the values of 2.5 and 5 meq for our oils in Malaysia. Tasic and Klofutar [2] determined that the average of the peroxide values for four brands of our sunflower oil in Slovenia was 2.090.

Saponification value

The saponification value (SV) is an indicator of the average molecular weight and hence chain length. It is inversely proportional to the molecular weight of the lipid [7]. The results for the SV of the refined oils analyzed in this study were similar. These values were in agreement with the Algerian Official Journal (189-195) and Codex STAN 210, 1999 (188-194).

It was established that a high SV (>194) for the fats and oils is due to the predominantly high proportion of shorter carbon chain lengths of the fatty acids [8]. Our oils contain fatty acids with the same number of carbon atoms; four fatty acids are present in significant quantities: palmitic, stearic, oleic and linoleic acids which are all basically medium chain fatty acids and account for the high SV values.

The SV of the “fleural” oil is lower than the result of Chira et al. [4] for sunflower oil in Romania (mean 204), but higher than that found by Tasic and Klofutar [2] for sunflower oils commercialized in Slovenia (192.077).

Table 2. Physical and chemical properties of the refined oils studied.

	Oil brands :				
	La Belle	Oleor	elio	Afia	Fleurial
Free fatty acids (%)	0.054±0.003	0.051±0.003	0.044±0.003	0.050±0.001	0.051±0.005
Peroxide value (meq kg ⁻¹)	2.00±0.20	1.97±0.12	1.70±0.20	1.85±0.10	1.61±0.21
Iodine value (g 100g ⁻¹)	127.05±2.07	124.07±4.10	125.14±4.82	126.25±4.03	129.91±2.78
Saponification value (mg g ⁻¹)	191.06±1.41	189.32±0.77	192.21±1.49	189.22±0.96	189.01±0.62
Refractive index at 40°C	1.4664	1.4664	1.4667	1.4663	1.4670
Densities at 20°C	0.921	0.920	0.917	0.920	0.920
A _{232nm} (1%)	3.03	2.93	3.07	2.93	2.52
A _{270nm} (1%)	1.74	2.00	2.34	1.75	2.06
A ₂₃₂ /A ₂₇₀	1.74	1.46	1.30	1.67	1.22

Table 3. Saturated fatty acid composition of different types of vegetable oils (% w/w).

Type of Oil	C14	C16	C18	C20	C24
La Belle	0.080±0.000 ^a	10.611±0.016 ^d	3.984±0.0016 ^c	0.423±0.003 ^b	0.201±0.001 ^c
Fleurial	0.070±0.000 ^e	6.472±0.008 ^f	3.857±0.004 ^e	0.273±0.001 ^f	0.245±0.005 ^a
Oleor	0.080±0.000 ^b	10.637±0.003 ^c	3.919±0.000 ^d	0.432±0.002 ^a	0.202±0.003 ^c
Afia	0.070±0.000 ^c	10.749±0.012 ^b	4.493±0.003 ^b	0.358±0.000 ^d	0.124±0.002 ^e
Elio	0.070±0.000 ^d	8.050±0.001 ^e	3.517±0.000 ^f	0.288±0.002 ^e	0.213±0.002 ^b

Means ± SD (standard deviation) within a column with the same lower case letters are not significantly different at P < 0.05; C14, myristic acid; C16, palmitic acid; C18, stearic acid; C20, behenic acid; C24, lignoceric acid

Table 4. Unsaturated fatty acid composition of different types of vegetable oils (% w/w).

Type of Oil	C18:1 n-9	C18:1 n-7	C18:2 n-6	C18:3 n-3	C20:1 n-9
La Belle	28.055±0.030 ^a	1.458±0.002 ^a	49.366±0.020 ^f	5.199±0.003 ^d	0.250±0.001 ^b
Fleurial	23.266±0.004 ^d	0.699±0.002 ^f	64.442±0.043 ^a	0.327±0.001 ^f	0.152±0.001 ^f
Oleor	27.184±0.012 ^b	1.441±0.006 ^b	50.240±0.027 ^e	5.297±0.001 ^c	0.266±0.006 ^a
Afia	20.977±0.003 ^e	1.335±0.001 ^c	55.063±0.007 ^c	6.376±0.000 ^b	0.183±0.001 ^d
Elio	23.537±0.002 ^c	1.059±0.003 ^e	60.475±0.002 ^b	2.320±0.000 ^e	0.173±0.003 ^e

Means ± SD (standard deviation) within a column with the same lower case letters are not significantly different at P < 0.05; C18:1, oleic acid; C18:2, linoleic acid; C18:3, linolenic acid; C20:1, paullinic acid

Table 5. The content of SFA, MUFA, PUFA (% w/w) and the values of P/S indexes in different types of vegetable oils.

Type of Oil	Total SFA	Total MUFA	Total PUFA	P / S	n-6 / n-3
La Belle	15.331±0.023 ^c	29.763±0.033 ^a	54.565±0.023 ^f	3.560±0.006 ^f	9.494±0.004 ^c
Fleurial	10.959±0.016 ^f	24.117±0.005 ^d	64.769±0.042 ^a	5.909±0.013 ^a	195.271±0.121 ^a
Oleor	15.281±0.013 ^d	28.891±0.012 ^b	55.537±0.028 ^e	3.633±0.004 ^e	9.474±0.005 ^c
Afia	15.797±0.010 ^b	22.495±0.003 ^e	61.439±0.007 ^c	3.890±0.004 ^c	8.630±0.000 ^d
elio	12.188±0.000 ^e	24.769±0.002 ^c	62.795±0.003 ^b	5.150±0.001 ^b	26.060±0.000 ^b

Table 6. Densities, UV absorption, induction period and activation energies of refined edibles vegetables oils analyzed.

Oils	Densities at :				A _{232nm} / A _{270nm}	IP (h)	Activation energies (KJ / mol)
	283.17K (10°C)	293.14K (20°C)	303.14K (30°C)	313.14K (40°C)			
M1	0.926	0.921	0.916	0.913	1.741	10.15	550.09
M2	0.926	0.920	0.916	0.912	1.465	14.05	581.52
M3	0.922	0.917	0.912	0.909	1.311	13.46	570.50
M4	0.926	0.920	0.916	0.912	1.674	13.25	570.03
M5	0.926	0.920	0.916	0.912	1.223	08.27	438.16

M1: La Belle; M2: Oleor; M3: elio; M4: Afia and M5: fleurial

Physical properties

The physical properties of vegetable oils depend primarily on the composition (and hence the biological origin) and temperature [9]. They can be used to assess the purity or quality of lipid material with reference to the known standards or preferred characteristics [10].

Fatty acid composition

FA contents (as % of total FA) of all oils were significantly different. The percentage of the total saturated fatty acid (SFA) contents changed from $10.959 \pm 0.016\%$ (“fleurial” oil) to $15.797 \pm 0.010\%$ (“Afia” oil) (Table 3). These results are logical considering the nature of these oils. “Fleurial” oil is constituted only of sunflower oil, while “Afia” oil is 100% soybean oil. It seems that soybean oils contain the highest percentage of SFA from sunflower oils. Indeed, Kostik et al. [11]; Tazan et al. [12]; Zambiazzi et al. [13] reported that soybean oils were more saturated when they were compared to sunflower oils; the values obtained were respectively 13.5% *v.s* 8.8%, 14.24% *v.s* 9.45% and 15.10 *v.s* 12.36%; consequently, soybean oil may be more resistant to oxidation spoilage in comparison to sunflower oil. Otherwise, these values were lower than those found by Asgary et al. [14] for edible Iranian frying oils (18.9%). In consideration of SFA content, our oils are not suitable for frying. It has been indicated that only saturated oils are considered good sources for cooking and short term frying processing, due to their relatively higher SFA content and consequently higher stability [15, 16]. In addition, palmitic acid (C16:0) was the major SFA for all our oils, followed by stearic acid (C18:0). The values of our oils are lower than those of Iranian frying oils; these common SFAs that jointly constitute 21.8% in Iranian frying oils, but only 10.329% in our “fleurial” oil. The distribution patterns of myristic (C14:0) and behenic (C22:0) are almost the same for all vegetable oils and are independent of the oil origin, only traces were found. However, arachidic (C20:0) and lignoceric (C24:0) were found in considerable amounts in all our oils. Besides, our vegetable commercialized oils don't contain lauric acid (C12:0). This result is in line with Gregorio [17] and Gopala et al. [18]; these authors reported that only coconut oil is a major source of lauric acid.

The mean values of total unsaturated FAs (UFAs) of our oils varied from 83.934% (“Afia” oil) to 88.886% (“fleurial” oil) of the total FAs for all refined vegetable oils used in our study. Oleic (C18:1, ω 9) and linoleic (C18:2) acids were the major UFA present in all studied oils (Table 4).

“fleurial” oil and pure sunflower oil, contain a low proportion of palmitic acid as well as a considerable quantity of oleic acid and very high content of linoleic acid which give it a higher UFA content than other oils. This result is in accordance with Kostik et al. [11]; Tazan et al. [12] and Zambiazzi et al. [13]. Hence, our commercialized oils are much unsaturated than those used in Iran: frying (72.3%), cooking (83.4%) and hydrogenated oils (34.9%). The oleic acid content of our oils was the lowest in comparison to Iranian edible oils: cooking (41.7%) and frying oils (40.2%). However, considering the linoleic acid content, our oils appears to be superior; whereas frying, cooking and hydrogenated Iranian oils contain only 28.4%, 37.5% and 7.3% respectively.

The relationship between SFA and PUFA content is expressed as the P/S index. All the vegetable oils analyzed present a total PUFA higher than the SFA content (Table 5); these oils had a P/S ratio which varied from 3.560 (“La Belle” oil) to 5.909 (“fleurial” oil); these values were higher compared to Iranian frying oil (1.66), but similar to the cooking oils used in this country (4.351). All the refined vegetable oils used in our country are highly unsaturated. The refined oils have a higher total PUFAs content than the oils used in Iran (60.07% *v.s* 31.5% for frying oils), which make our oils suitable for use as a salad oil. Our commercialized vegetable oils, despite containing significantly higher amounts of PUFA, were used in frying. “Fleurial” oil showed a high PUFA (C18:2 + C18:3) content (64.769%) with linoleic acid being the major FA (64.442%) and α -linolenic acid the minor one, when compared with all other oils; consequently, this oil presented the highest n-6/n-3 ratio (195.271%). It is obvious, that due to the high content of PUFAs our oils are more prone to oxidation. Thus, none of these oils is suitable for frying.

Refractive index

Both the iodine value and refractive index (RI) are important characteristics which determine the degree of saturation or unsaturation of fats and oils. The RI of oils depends on their molecular weight, fatty acid chain length, degree of unsaturation and degree of conjugation [10]. The mean (1.466), obtained at 40°C, for the oils under investigation was within the range established by Codex alimentarius (1992) (1.466-1.470). As for the iodine value, “fleurial” oil showed a high value for the RI (1.467) in comparison to other oils.

Density

Density is one of the important characteristics of a vegetable oil. This parameter is dependent on their PUFA content, oxidation and polymerization level [19]. In this study, the density was determined for temperatures ranging from 283.17K (10.17°C) to 313.14K (40.14°C). The density variation with temperature for the studied oils was presented in Table 6. It can be observed that blindedoil ("elio") has a lower density than the others which have similar densities.

Otherwise, it was observed from this study that the densities of pure sunflower oil ("fleural" oil) and pure soybean oil ("La Belle" and "Oleor" oils) are comparable to those of pure soybean oils. These values are within the range established by Codex STAN 210 (1999) at 20°C (0.918-0.923 for sunflower oil and 0.919-0.925 for soybean oil). From Table 6, it can be seen that the density of all oils decline with the rise in temperature. These values are lower than those obtained by Bazlul Mobinet al.[6] for our sunflower oil (0.932) and soybean oil (0.931) in Malaysia.

Rancimate test and activation energy

The oil stability index directly relates to the oxidative resistance of oil. This quality is proportional to the induction period. This latter represents the time needed for decomposition of hydroperoxides produced by oil oxidation [20]. The Rancimat induction time at 98°C for oils under investigation varied from 8.27 h to 14.05 h (Table 6); the minimum and maximum of the oxidative stability belongs to "fleural" and "Oleor" oils, respectively.

It can also be seen that pure soybean oil is more stable than pure sunflower oil. "Oleor" oil, with a higher induction time, was probably more stable in comparison to others. "Fleural" oil recorded a low induction period and a high iodine value suggesting that this oil may be particularly sensitive to oxidation. The sensibility of this oil ("fleural" oil) is most likely due to its FA composition which contains a high proportion of PUFA (nearly 65%) (Table 5).

However, the induction times of our oils were found to be higher than those in most countries. Marinova et al. [5] noted a value of 6.7h and 11.5h respectively for sunflower and soybean oils sold in Bulgaria.

The activation energy represents the minimum energy required to start a chemical reaction. It is expressed, in this study, in units of kilojoules per mole (kJ/mol). The two parameters (activation energy and Rancimat test) showed a good agreement

when the results were compared. From Table 6 it is seen that the energies values ranged from 438.16 KJ/mol ("fleural" oil) to 581.52 KJ/mol ("Oleor" oil). The results reveal that the minimum energy required for "fleural" oil to undergo deterioration reactions when compared to other oils is an indication of the bad oxidative stability of this oil. The energy activation of "fleural" oil has a direct relationship with the Rancimat test and the high degree of unsaturation of this oil.

CONCLUSIONS

The quality and properties of freshly refined vegetable oils sold in Algeria were evaluated through this study using different parameters. The results obtained indicate that there are significant differences in all the physical and chemical parameters analyzed of these oils. All the refined vegetable oils had a very high IV. This is an indication of high unsaturation in these oils and thus they become more vulnerable to oxidation, making these oils unsuitable for deep-fat frying purposes notably "fleural" oil. This oil had the highest PUFA content, mainly represented by linoleic acid, which makes it particularly sensitive to oxidation. In addition, its induction time and energy activation were very low; this is also another reason to make this oil more vulnerable to oxidation and thermal processing such as frying. However, this oil ("fleural" oil) has nutritional advantages; indeed, during its refining, vitamins A and D were incorporated, which makes this oil suitable for use as a salad oil.

REFERENCES

1. R.D. O'Brien, *Fats and Oils*, 3rd ed., CRC Press, Taylor and Francis Group, 2009, p. 2.
2. D.R. Tasic, C. Klofutar, *Acta. Chim. Slov.*, **46**, 511 (1999).
3. W.D. Pocklington, *Pure and Appl. Chem.*, **62**, 2339 (1990).
4. N. Chira, C. Todașcă, A. Nicolescu, G. Păunescu, S. Roșca, *U.P.B. Sci. Bull B*, **71**, 4, (2009).
5. E. M. Marinova, K.A. Seizova, I.R. Totseva, S.S. Panayotova, N.I. Marekov, S.M. Momchilova, *Bulgarian Chemical Communications*, **44**, 57 (2012).
6. M.S. Bazlul, A. Anees, H.I. Mohamad, H. Sufia, R. Mohd, A.K. Mohd Omar, *Grasas Y Aceites*, **61**, 423 (2010).
7. A.A Gohari, R. Farhoosh, K.M.H. Haddad, *J. Agr. Sci. Tech*, **13**, 1053 (2011).
8. R. Kirk, R. Sawyer, *Pearson's composition and analysis of foods*. 9th edition, Addison Wesley longman Ltd. England, 1991, p.9, p.608.
9. J.N. Coupland, D.J. McClements, *Journal of the American Oil Chemists' Society*, **74**, 1559 (1997).

10. D.S. Nichols, K. Sanderson, In *Chemical and Functional Properties of Food Lipids* (Z. E. Sikorski and A. Kolakowska, (Eds), CRC Press, 2003, p. 29.
11. V. Kostik, S. Memeti, B. Bauer, *Journal of Hygienic Engineering and Design*, **3**, 112 (2013).
12. M. Tasan, U. Gecgel, M. Demirci, *Grasas y Aceites*, **62**, 284 (2011).
13. R.C. Zambiasi, R. Przybylski, M.W. Zambiasi, C.B. Mendonca, *Curitiba*, **25**, 111 (2007).
14. S. Asgary, B. Nazari, N. Sarrafzadegan, S. Saberi, L. Azadbakht, A. Esmailzadeh, *J Res Med Sci.*, **14**, 211 (2009).
15. W.L. Clark, G.W. Serbia, *Food Technology*, **45**, 84 (1991).
16. S. McKenzie, D.C. Taylor, Seed oils: a new age. *Plant Biotechnology*, **1**, 1 (1996).
17. C.G. Gregorio, Fatty Acids and Derivatives from Coconut Oil. Bailey's Industrial Oil and Fat Products, 6th Ed, John Wiley & Sons, Inc. 2005.
18. <http://coconutboard.nic.in/English-Article-Gopalakrishna-CFTRI.pdf>.
19. J. P. Wolff, Manuel des corps gras. Edition, Tec & Doc, Lavoisier, Paris. 1968, p.551.
20. M.V. Läubli, P.A. Bruttel, *Journal of the American Oil Chemists' Society*, **63**, 792 (1986).

ИЗСЛЕДВАНЕ НА ФИЗИКО-ХИМИЧНИТЕ ХАРАКТЕРИСТИКИ И СЪСТАВА ОТ МАСТНИ КИСЕЛИНИ НА ТЪРГОВСКИ АЛЖИРСКИ ХРАНИТЕЛНИ РАСТИТЕЛНИ МАСЛА

Р. Садуди*, Д. Али Ахмед, М. Траче, А. Кецили

Департамент по земеделие, Факултет по биология, Университет „Мулуд Мамери“, Тизи-Узу, 15000, Алжир

Постъпила на 22 януари, 2015 г.; коригирана на 2 февруари, 2016 г.

(Резюме)

В настоящата работа са изследвани различни физични и химични характеристики на главните хранителни растителни масла и смеси, предлагани на алжирския пазар: Afia, elio, fleurial, La Belle, Oleor. Тези характеристики може да послужат за качествен контрол на маслата.

Получените резултати показват, че всички масла отговарят на нормите за хранителни масла с добро качество: съдържанието на свободни мастни киселини е в границите от 0.044 до 0.054 %, пероксидното число варира от 1.61 to 2, йодното число е в интервала от 124.07 до 129.91, числото на осапунване е от 189.01 до 192.21), плътността при 20°C е между 0.917 и 0.921, а индекса на пречупване при 40°C е между 1.4663-1.4670. Обаче, съдържанието на поли-ненаситени мастни (PUFA) достига средно 60%, което показва, че маслата са склонни към гранясване. Маслото “fleurial” е най-чувствително спрямо окисление и термични въздействия; то има най-кратък индукционен период (8.27 часа), най-ниска активизираща енергия (438.16 kJ/mol) и най-високо съдържание на PUFA (средно 65%). Но то е богато на витамините А и D, което го прави подходящо за консумация.

Synthesis of a new five-coordinate ternary copper (II) complex: crystal structure and spectral studies

A.R. Rezvani¹, H. Janani¹, F. Rostami-Charati^{2*}, B.W. Skelton³

¹Department of Chemistry, University of Sistan and Baluchestan, PO Box 98135-674, Zahedan, Iran,

²Department of Chemistry, Faculty of Science, Gonbad Kavous University, P.O. Box 163, Gonbad, Iran

³Chemistry, School of Biomedical, Biomolecular & Chemical Sciences, The University of Western Australia, 35 Stirling Highway, Crawley, Perth, Western Australia 6009, Australia

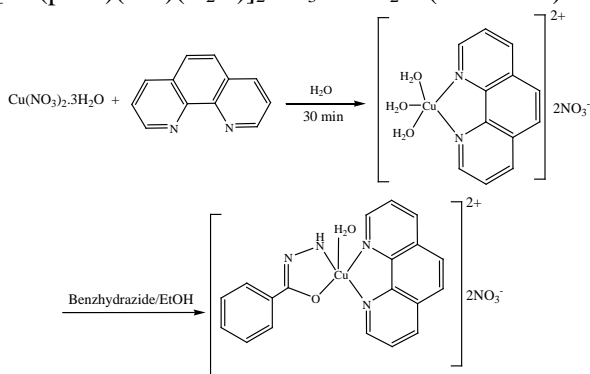
Received February 26, 2016; Revised May 28, 2016

A new ternary complex of benzhydrazide-phenanthroline-H₂O ligands with copper (II) was synthesized and characterized by elemental analysis, infrared spectroscopy and UV-Vis electronic absorption spectroscopy. The crystal and molecular structure of [Cu(BH)(Phen)(H₂O)]₂NO₃·1.5 H₂O was determined by the single crystal diffraction method which confirmed that the complex has square pyramidal geometry and contains a bidentate heterocyclic ligand on one side and a bidentate benzhydrazide (BH) ligand on the other side. This coordination takes place through the nitrogen and oxygen atoms from benzhydrazide and two nitrogen atoms from 1,10-phenanthroline. The apical position is occupied by an oxygen atom from a water molecule as a third ligand.

Keywords: Copper (II) complex, Mixed ligand, X-ray crystal structure, Square pyramidal.

INTRODUCTION

Investigation on mixed ligand systems reveals that ternary complexes are often more stable than expected from statistical reasons [1-3]. They are known for their high stability, and are multifunctional in many fields of chemistry. The mixed chelate complexes of Cu(II) have general formulas such as [Cu(NN)(NO)]⁺ and [Cu(NN)(OO)]⁺ that are extremely stable. In addition, they attracted the attention of the scientific community because of their peculiar spectroscopic, photochemical and electrochemical features [4-8]. They also have useful pharmacological benefits. In this set of formulas, two nitrogen atoms (N,N) from the phenanthroline molecule represent a di-imine ligand [9]. Herein, we report the synthesis, structure and spectral properties of [Cu(phen)(BH)(H₂O)]₂NO₃·1.5 H₂O (Scheme 1).



Scheme 1. Synthesis of [Cu(phen)(BH)(H₂O)]₂NO₃·1.5H₂O.

EXPERIMENTAL

Material and methods

All chemicals used were of reagent grade and used without any purification. The IR spectra were recorded in KBr pellets on an FT/IR JASCO 460 spectrophotometer in the range of 4000-400 cm⁻¹. Elemental analysis for C, H and N was performed on a Heraeus CHN-O-Rapid elemental analyzer. Electronic spectral measurements were performed using a JASCO 7850 spectrophotometer.

General procedure for the synthesis of [Cu(phen)(BH)(H₂O)]₂NO₃·1.5 H₂O

Magnetically stirred solution of Cu(NO₃)₂·3H₂O (1 mmol, 0.2416 g) and 1,10-phenanthroline (1mmol, 0.198g) in water (10 mL) immediately produced a blue colored solution. After that, ethanolic solution of benzhydrazide (1 mmol, 0.136 g) was slowly added. Then, the resulting solution was filtered and allowed to evaporate slowly at room temperature. After one week, blue crystals of the complex were formed.

RESULTS AND DISCUSSION

The procedure was simple and easy to handle. The structure of the compound [Cu(phen)(BH)(H₂O)]₂NO₃·1.5 H₂O was characterized by single crystal X-ray diffraction. The single crystals of the complex, obtained by slow evaporation from its aqueous ethanolic solution, were suitable for X-ray diffraction study (Figure 1).

* To whom all correspondence should be sent:

E-mail: f_rostami_ch@yahoo.com

X-ray crystallography

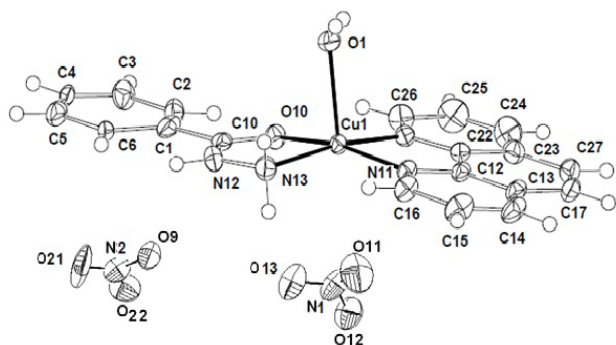


Fig.1 Molecular structure of the complex $[\text{Cu}(\text{phen})(\text{BH})(\text{H}_2\text{O})]2\text{NO}_3 \cdot 1.5 \text{H}_2\text{O}$ projected oblique the coordination plane. Only one component of the disordered atoms is shown.

Infrared spectral study

The IR spectrum of the complex displays an absorption band at 1552 cm^{-1} that is related to the C=N moiety of Phen [10]. The basal positions are occupied by the nitrogen atoms of the heterocyclic base that represents the absorption of Cu-N, which is seen in the range of $400\text{--}4000 \text{ cm}^{-1}$. This phenomenon is due to the heterocyclic ring [11-12]. Besides, Cu-O vibration was observed at 455 cm^{-1} in the IR spectrum. The spectrum of the water molecule was observed at 3422 cm^{-1} [13]. When this complex was heated for 15-20 min at 100°C , the Cu-O bond did not disappear from the IR spectrum. This observation indicates that the water molecule in this complex is a coordinated ligand with the copper (II) ion. The band observed at 1764 cm^{-1} is related to the nitrate group in the crystal lattice of the complex [14].

Electronic spectrum

The electronic spectrum of the complex in solution was recorded in various solvents (MeOH, EtOH and DMF) and their maximum parameter was approximately the same in all solvents. The spectrum exhibited a d-d transition as a broad band centered at 675 nm. The $\pi \rightarrow \pi^*$ intraligand transitions in the phenyl group were observed in the 220-270 nm region [15,16]. The electronic spectral data of the complex in ethanol solution are listed in Table 1.

Table 1. Electronic absorption solution data [10^{-4} M]

Solution (EtOH)	Assignments
λ_{max} (nm)	
675	d-d
272	$\pi \rightarrow \pi^*$
224	$\pi \rightarrow \pi^*$

Single crystal structure of the complex was established from X-ray diffraction. The extracted crystal data of the complex are summarized in Table 2 and the structure of the complex is depicted in Fig. 1. Herein, by considering the structure of X-rays, we could explain that ellipsoid atoms have been drawn at the 50% probability level. Selected coordination geometries are shown in Table 3.

Crystallographic data for the structures were collected at 100(2) K on an Oxford Diffraction Gemini diffractometer fitted with graphite-monochromated Mo $K\alpha$ radiation yielding N_{total} reflections, these merging to N unique after analytical absorption correction (R_{int} cited), with N_{o} reflections having $I > 2\sigma(I)$. The structure was refined against F^2 with full-matrix least-squares using the program SHELXL-97 [17]. The phenyl ring of the benzohydrazine ligand is disordered over two sites with equal occupancies. Anions were modeled as being NO_3^- on the basis of refinement. Two of these, NO_3 (2) and NO_3 (3), were disordered about crystallographic inversion centres. Two solvent water molecules, O (2) and O (3), were located with site occupancies for O (3) fixed at 0.5 after trial refinement. Hydrogen atoms of water molecule for O (1) and O (2) were included at located positions and refined with restrained geometries. Those for O (3) were not located. All remaining H-atoms were added at calculated positions and refined by use of a riding model with isotropic displacement parameters based on those of the parent atom. Anisotropic displacement parameters were employed throughout for the non-hydrogen atoms.

Structural description

The formula of the new synthesized complex is shown in Figs. 1 and 2. The copper is five-coordinate square pyramidal with the apical bond, Cu-H₂O $2.1733(16) \text{ \AA}$, longer than those in the basal plane which lie in the range $1.9572(16)\text{--}2.013(2) \text{ \AA}$. The hydrazine H atoms are all involved in H-bonding with the oxygen atom from nitrate group. The hydrogen atoms of the dd water molecule form hydrogen bonds with the oxygen atom of nitrate groups and water molecules as solvent O (2), that lead to the formation of a three-dimensional network. The geometrical details are shown in Table 4.

Table 2. Crystal data and structure refinement for the complex

Empirical formula	C ₁₉ H ₂₁ CuN ₆ O _{9.50}
Formula weight	548.96
Temperature	100(2) K
Wavelength	0.71073 Å
Crystal system	Triclinic
Space group	$P\bar{1}$
Unit cell dimensions	a = 9.0342(9) Å b = 9.6415(5) Å c = 13.8100(9) Å α = 88.668(5)° β = 73.969(7)° γ = 78.467(6)°
Volume	1132.12(15) Å ³
Z	2
Density (calculated)	1.610 Mg/m ³
Absorption coefficient	1.031 mm ⁻¹
F(000)	564
Crystal size	0.50 × 0.43 × 0.15 mm ³
θ range for data collection	3.69 to 34.89°
Index ranges	-14 ≤ h ≤ 12, -13 ≤ k ≤ 14, -22 ≤ l ≤ 21
Reflections collected, N_{total}	15814
Independent reflections, N	9095 [R(int) = 0.0255]
N_o , [$I > 2\sigma(I)$]	6287
Completeness to $\theta = 33.50^\circ$	99.2 %
Absorption correction	Analytical
Max/min. transmission	0.89/0.66
Refinement method	Full-matrix least-squares on F ²
Data / restraints / parameters	9095 / 281 / 407
Goodness-of-fit on F ²	1.019
Final R indices [$I > 2\sigma(I)$]	$R_1 = 0.0654$, $wR_2 = 0.1902$
R indices (all data)	$R_1 = 0.0912$, $wR_2 = 0.2001$
Largest diff. peak and hole	2.601 and -1.574 e.Å ⁻³

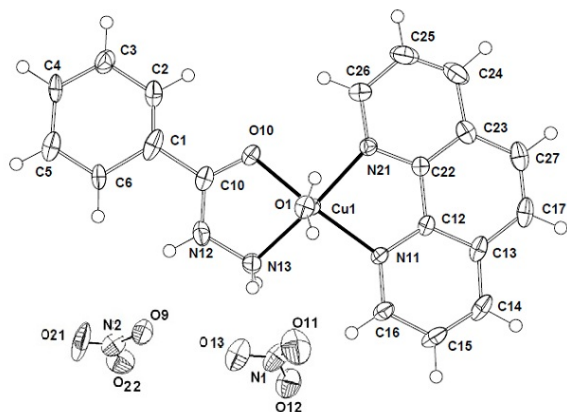
Table 3. Selected bond lengths [Å] and angles [°] for the complex

Cu(1)-O(10)	1.9572(16)
Cu(1)-N(21)	1.9813(18)
Cu(1)-N(11)	2.0047(18)
Cu(1)-N(13)	2.013(2)
Cu(1)-O(1)	2.1733(16)
O(10)-Cu(1)-N(21)	92.20(7)
O(10)-Cu(1)-N(11)	167.24(7)
N(21)-Cu(1)-N(11)	82.86(7)
O(10)-Cu(1)-N(13)	82.18(8)
N(21)-Cu(1)-N(13)	168.82(8)
N(11)-Cu(1)-N(13)	100.59(8)
O(10)-Cu(1)-O(1)	92.17(7)
N(21)-Cu(1)-O(1)	98.71(7)
N(11)-Cu(1)-O(1)	100.19(7)
N(13)-Cu(1)-O(1)	91.18(8)
C(16)-N(11)-C(12)	118.23(19)
C(16)-N(11)-Cu(1)	130.03(16)
C(12)-N(11)-Cu(1)	111.71(13)
C(10)-O(10)-Cu(1)	113.08(14)
N(12)-N(13)-Cu(1)	106.68(14)

Table 4. Hydrogen bonds for g 44 [Å and °].

D-H...A	d(D-H)	d(H...A)	d(D...A)	<(DHA)
N(12)- H(12)...O(31) ²	0.88	1.72	2.566(8)	159.5
N(12)- H(12)...O(32)	0.88	2.02	2.886(9)	169.8
N(13)- H(13A)...O(23)	0.92	2.07	2.929(4)	154.8
N(13)- H(13A)...O(22) ¹	0.92	2.16	2.876(5)	134.5
N(13)- H(13B)...O(11)	0.92	2.16	3.060(3)	167.4
O(1)- H(1BO)...O(13)	0.818(15)	1.918(15)	2.728(3)	171(3)
O(1)- H(1AO)...O(2)	0.791(13)	1.933(14)	2.720(3)	173(4)
O(2)- H(2AO)...O(3)	0.903(17)	2.26(2)	2.827(5)	120(2)
O(2)- H(2BO)...O(13) ³	0.840(16)	1.984(19)	2.783(3)	159(3)

Symmetry transformations used to generate equivalent atoms:

¹ -x,-y,-z+1; ² -x+1,-y,-z+1; ³ -x+1,-y+1,-z**Fig. 2.** Molecular structure of the complex projected onto the coordination plane. Only one component of the disordered atoms is shown.

CONCLUSION

The present paper reports the synthesis, characterization and crystal structure of a new five-coordinate ternary copper (II) complex. In the structure of the complex the copper atom has square pyramidal coordination geometry. This coordination is due to two nitrogen atoms from phenyl groups of phenanthroline and one oxygen and one nitrogen atoms from benzhydrazide in the basal plan. The water molecule occupies the axial position. Unique properties are observed for Cu²⁺ complexes containing an aromatic diimine and bidentate ligand with oxygen and nitrogen atoms [18-20]. The effective magnetic moment (μ_{eff}) of the complex was measured by the Evans method. The magnetic moment of the complex in crystalline state at 300K was found to be 1.92 B.M which is consistent with

the spin only values for mononuclear d9 copper (II) system [21-23]. The elemental analysis data are consistent with a 1:1:1 ratio of the metal ion: benzhydrazide: heterocyclic base for the synthesized complex.

Crystal data of [Cu(phen)(BH)(H₂O)]2NO₃ · 1.5 H₂O

Crystallographic data (except structure factors) for the structure have been deposited in the Cambridge Crystallographic Data Centre as a supplementary publication CCDC 1007750. Copies of the data can be obtained, free of charge, on application to CCDC, 12 Union Road, Cambridge CB2 1EZ, UK, (fax: +44-(0)1223-336033 or e-mail: deposit@ccdc.cam.ac.uk). Summary of Data CCDC 1007750; Formula: C₁₉H₂₁CuN₆O_{9.50}; Unit cell parameters: a 9.0342(9) Å, b 9.6415(5) Å, c 13.8100(9) Å; $\alpha = 88.668(5)^\circ$, $\beta = 73.969(7)^\circ$, $\gamma = 78.467(6)^\circ$; space group $P\bar{1}$.

REFERENCES

1. H. Siegel, P.R. Huber, R.F. Pasternack, *Inorg. Chem.*, **10**, 2226 (1971).
2. W.B. Schaap, D.L. McMasters, *J. Am. Chem. Soc.*, **83**, 4699 (1961).
3. P.R. Huber, R. Griesser, H. Siegel, *Inorg. Chem.*, **10**, 945 (1971).
4. I. Gracia-Mora, L. Ruiz-Ramirez, C. Gomez-Ruiz, M. Tinoco-Mendez, A. Marquez-Quinones, L.R.-D. Lira, A. Marin-Hernandez, L. Macias-Rosales, M.E. Bravo-Gomez, *Metal Based Drugs*, **8**, 19 (2001).
5. A. De Vizcaya-Ruiz, A. Rivero-Muller, L. Ruiz-Ramirez, G.E.N. Kass, L.R. Kelland, R.M. Orr, M. Dobrota, *Toxicol. in Vitro*, **14**, 1 (2000).

6. L. Ruiz-Ramirez, I. Gracia-Mora, M.E. da le Rosa, H. Sumano, C. Gomez, F. Arenas, E. Gomez, E. Pimentel, M. Cruces, *J. Inorg. Biochem.*, **51**, 406 (1993).
7. K. Shinozaki, Y. Kaizu, *Bull. Chem. Soc. Jpn.*, **67**, 2435 (1994).
8. R.M. Everly, D.R. McMillin, *J. Phys. Chem.*, **95**, 9071 (1991).
9. O.O.E. Onawumi, O.O.P. Faboya, O.A. Odunola, T.K. Prasad, M.V. Rajasekharan, *Polyhedron*, **27**, 113 (2008).
10. A.W. Addison, T.N. Rao, J. Reedijk, J. van Rijn, G.C. Verschoor, *J. Chem. Soc., Dalton Trans.*, 1984, 1349.
11. R.E. Wilde, T.K. Srinivasan, *J. Inorg. Nucl. Chem.*, **36**, 323 (1974)
12. A. Paulovicova, U. El-Ayaan, Y. Fukuda, *Inorg. Chim. Acta*, **321**, 56 (2001).
13. [13] P.B. Sreeja, M.R.P. Kurup, A. Kishore, C. Jasmin. *Polyhedron*, **23**, 575 (2004).
14. M. Gerloch, R. Mason, *J. Chem. Soc.*, 296 (1965).
15. J.P. Fackler Jr, F.A. Cotton, D.W. Barnum, *Inorg. Chem.*, **2**, 97 (1963).
16. R.H. Holm, F.A. Cotton, *J. Am. Chem. Soc.*, **80**, 5658 (1958).
17. G.M. Sheldrick, *Acta Cryst. A*, **64**, 112 (2008).
18. [G.M. Sheldrick, SHELX-97, Programs for Crystal Structure Analysis, University of Göttingen, Göttingen, Germany, 1997.
19. L.J. Farrugia, *J. Appl. Crystallogr.*, **30**, 565 (1997).
20. C.F. Macrae, P.R. Edgington, P. McCabe, E. Pidcock, G.P. Shields, R. Taylor, M. Towler, J. van de Streek, *J. Appl. Crystallogr.*, **39**, 453 (2006).
21. F.A. Cotton, G. Wilkinson, C.A. Murillo, M. Bochmann, *Advanced Inorganic Chemistry*, 6th Ed., Wiley, New York, 1999, 867.
22. D.J. Mackey, S.V. Evans, *J. Chem. Soc., Dalton Trans.* 2004(1976).
23. R.S. Drago, *Physical Methods for Chemists*, 2nd ed., Saunders, Philadelphia, (1992).

СИНТЕЗА НА НОВ ТРЕТИЧЕН МЕД (II) КОМПЛЕКС: КРИСТАЛНА СТРУКТУРА И СПЕКТРАЛНИ ИЗСЛЕДВАНИЯ

А. Реза Резвани¹, Х. Джанани¹, Ф. Ростами-Чарати^{2*}, Б.У. Скелтън²

^{1,2}Департамент по химия, Университет на Систан и Балучестан, Захедан, Иран

²Департамент по химия, Научен факултет, Университет „Гонбад Кавус“, Гонбад, Иран

³Департамент по химия, Училище за биомедицински, биомолекулни и химически науки, Университет в Западна Австралия, Пърт, Западна Австралия 6009, Австралия

Постъпила на 26 февруари, 2016 г.; коригирана на 28 май, 2016 г.

(Резюме)

Синтезиран е нов третичен комплекс на мед (II) с лиганди от бензхидразид фенантролин- H₂O и е охарактеризиран чрез елементарен анализ, инфрачервен спектър и UV-Vis електронен абсорбционен спектър. Определена е кристалната и молекулна структура на [Cu(BH)(Phen)(H₂O)]₂NO₃·1.5 H₂O по метода на единичната кристална дифракция, което потвърждава, че комплексът има квадратна пирамидална геометрия и съдържа бидендатен хетероцикъл от едната страна и би-дендатен бензхидразид (BH) от другата страна. Тази координация се осъществява чрез азотния и кислородния атом от бензхидразида и два азотни атома от 1,10-фенантролина. Противоположната позиция се заема от кислороден атом от водната молекула като трети лиганд.

A simple, efficient and scalable synthesis of substituted bis-arylchloromethanes

R. K. Bandi, A. Waghmare, R. M. Hindupur, H. N. Pati*

Process Chemistry Department, Advinus Therapeutics Ltd., 21 & 22, Phase II, Peenya Industrial Area, Bangalore-560058, India

Received April 20, 2015; Revised January 14, 2016

An efficient and scalable two-step synthesis of bis-arylchloromethanes, an important building block for the synthesis of biologically important aryl piperidine and piperazine derivatives, and its 4,4'-disubstituted analogues is described.

Keywords: Substituted bis-arylchloromethanes; scalable synthesis; biologically active compounds.

INTRODUCTION

Diphenylchloromethane and its halogen substituted analogues are important building blocks for the synthesis of aryl piperazine compounds which are important structural units for the synthesis of a variety of biological compounds [1-3]. This skeleton has also been established as a useful privileged scaffold for library synthesis and drug discovery applications. A number of diphenyl methyl piperazine derivatives are being used as pharmaceuticals for a range of different biological targets [4]. Similarly, the diphenylmethoxy skeleton is the key structural element of the widely employed anticholinergic, antihistaminic agents and dopamine reuptake inhibitors as well [5]. *Ebastine*, *benzatropine* and *vanoxerine* are the most relevant examples that constitute diphenylmethoxy as an integral unit (Figure 1).

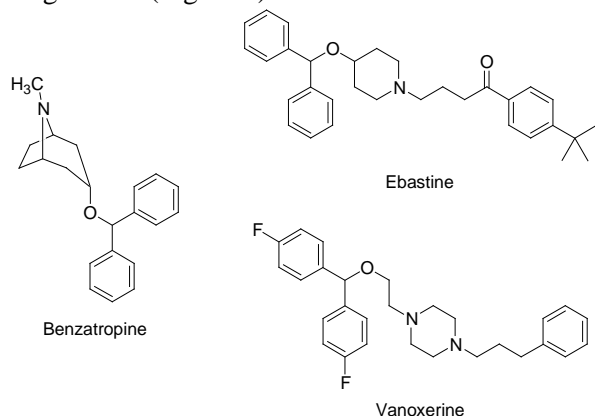


Fig. 1. Biologically important molecules possessing diarylmethane moieties

As a consequence, a number of synthetic methods have been reported for the synthesis of diphenylchloromethane and its derivatives. In particular, synthetic routes involving the use of transition metal reagents and catalysts have been described. Though a variety of synthetic protocols are reported in the literature, the use of toxic,

expensive and air-sensitive aryl metal reagents and catalysts in presence of anhydrous solvents restrict their application on a practical scale. Further, cumbersome catalyst recovery and product contamination are additional drawbacks of these methodologies. Moreover, it is difficult to ensure robustness and reproducibility on kilogram scale using these reagents. Herein we report an efficient large-scale procedure for the synthesis of diphenylchloromethane and its derivatives.

In a two-step synthetic pathway, Scheme 1, benzophenone **1a-c** is reduced to benzhydrol **2a-c** using sodium borohydride, which on nucleophilic substitution with thionyl chloride, furnishes the dichlorophenylmethane **3a-c**.

EXPERIMENTAL

All raw materials were obtained from commercial suppliers and were used as received. Melting points were determined on a Buchi B-545 digital melting point apparatus and are uncorrected. ¹H NMR spectra were recorded on a Varian-400 spectrometer using CDCl₃ as the solvent with TMS as the internal standard. The reaction was monitored and the purity of the compounds was analyzed using HPLC.

General procedures

Diarylmethanol (2a-c): To a cold solution of benzophenone **1a-c** in methanol (5 vol.) sodium borohydride (1 equiv.) was added and the mixture was stirred for 1 h at the same temperature. After complete consumption of the starting material (monitored by TLC), excess methanol was removed from the reaction mixture under reduced pressure. The reaction mixture was then quenched with water (5 vol.), extracted with ethyl acetate, dried over anhydrous sodium sulfate and filtered. The filtrate was evaporated to dryness to obtain crude diarylmethanol **2a-c** which was used in the next step.

* To whom all correspondence should be sent:
E-mail: hari.pati@advinus.com

6. S. Amlipur, N.K. Singam, S. Pombala, P. Yedla, S. Partha, S. Ganesh, C. Kumar, J.R. Vaidya, *Med. Chem. Res.* **23**, 3207 (2014).
7. P. Hassan, F. Zhong-Ping, D. Yanbing, Z. Lingyun, P. Hossein, M. Jerrie-Lynn, B. Francesco, T. Elizabeth, S. Eric, W.V. Todd, P. Frank, W. Z. Gerald, A.M. Lester, P.S. Terrance, *Bioorg. Med. Chem. Lett.*, **20**, 1378 (2010).
8. F.A. Gunther, R.C. Blinn, *J. Am. Chem. Soc.*, **72**, 4282 (1950).

ПРОСТА, ЕФЕКТИВНА И МАЩАБИРАНА СИНТЕЗА НА СУБСТИТУИРАНИ БИС-АРИЛ-ХЛОРОМЕТАНИ

Р. К. Банди, А. Вагмар, Р. М. Хиндупур, Х.Н. Пати *

Департамент по химични процеси, Адвинус Терапевтикс ООД, 21 & 22, Фаза II, Промислена зона Пееня, Бангалор-560058, Индия

Постъпила на 20 април, 2015 г.; коригирана на 14 януари, 2016 г.

(Резюме)

Описана е ефективна и мащабирана двустепенна синтеза на бис-арил-хлорометан, който е важна градивна единица за синтезата на биологично важни пиперидин- и пиперазинови производни и неговите 4,4'-двузаместени аналози.

Free radicals properties of some gamma-irradiated organic compounds

R. Şimşek¹, M.G. Gündüz¹, C. Şafak¹, Ö. Kökpınar², M. Aydın^{3*}

¹Faculty of Pharmacy, Hacettepe University, TR 06100-Ankara, Turkey

²Vocational School of Technical Sciences, Adıyaman University, Turkey

³Faculty of Education, Adıyaman University, TR 02040-Adıyaman, Turkey

Received May 15, 2015; Revised February 3, 2016

Powders of some organic compounds (compounds 1-4) were irradiated with ⁶⁰Co gamma-rays and the spectroscopic properties of the free radicals formed were investigated at ambient temperature using electron paramagnetic resonance (EPR) technique. The analysis of the EPR spectra of irradiated powder samples demonstrated that the paramagnetic species produced by the radiation damage was NCH₂. The *g* values of the radicals and the hyperfine structure constants of the free electron with nearby protons and ¹⁴N nucleus were determined. The EPR spectra show that they are of radicals remained unchanged for more than two months. The results were found to be in good agreement with earlier studies on amine radicals.

Keywords: EPR, Free radicals, Gamma-irradiation, 1,4-dihydropyridines.

INTRODUCTION

It is known that ionizing radiations produce free radicals that have unpaired electron [1]. Free radicals provoke both beneficial and harmful effects in living organisms [2]. By initiating and propagating free radical chain reactions, they can damage the cells and may be involved in the progression of a number of diseases including diabetes, hyperlipidemia, neurodegeneration, heart disease, cancer, and so on [3-5]. Qualitative and quantitative aspects of free radicals in oxidative stress can be evaluated by using different techniques [6]. The EPR spectroscopy is the most effective technique for detection of free radicals [7, 8]. Thus, the EPR method has been applied to the identification of irradiation damage centres in many substances, including amino acids, drugs and other organic compounds [9-18]. The spectroscopic splitting factor *g* and the hyperfine coupling constants (*a*) of unpaired electrons give valuable information about the structure of the radical [19]. The X-irradiated hippuric acids have been investigated at 295 K by the EPR technique and the observed paramagnetic species have been attributed to the PhCONH-CH₂ radical [20]. Furthermore, the EPR of gamma-irradiated powders of L-arginine monohydrochloride were studied by Aydın [21] at ambient temperature, and the radiation damage center was attributed to the NH₂(NH)HNĈHCH₂CH₂CH(NH₂)COOH radical. Another technique to identify the molecular structure of substances is the infrared spectroscopy.

1,4-Dihydropyridines are an important class of L-type calcium channel blockers that mainly exert their pharmacological activity by modulating Ca²⁺ influx

and are used to treat cardiovascular conditions such as hypertension and angina [22, 23]. We have previously reported the development of a series of condensed 1,4-dihydropyridine derivatives. Although the effects of these compounds on calcium and potassium channels have been elucidated [24, 25], the defects induced by gamma-irradiation have not been investigated. The purpose of this study is to investigate the defects induced by gamma-irradiation in powders of 1,4-dihydropyridine derivatives (compounds 1-4) and to determine their properties at ambient temperature.

EXPERIMENTAL

Materials

The study was performed on the following dihydropyridine derivatives differing in number, position and type of the substituents:

Compound 1: methyl 2-methyl-4-(2,3-dichlorophenyl)-5-oxo-7-phenyl-1,4,5,6,7,8-hexahydroquinoline-3-carboxylate; molecular weight (MW, g/mole): 442.34;

Compound 2: ethyl 2,7-dimethyl-4-(2,5-dichlorophenyl)-5-oxo-1,4,5,6,7,8-hexahydroquinoline-3-carboxylate; MW, g/mole: 394.30;

Compound 3: ethyl 2-methyl-4-(2,3-dichlorophenyl)-5-oxo-7-phenyl-1,4,5,6,7,8-hexahydroquinoline-3-carboxylate; MW, g/mole: 456.37;

Compound 4: ethyl 2-methyl-4-(2,5-dichlorophenyl)-5-oxo-7-phenyl-1,4,5,6,7,8-hexahydroquinoline-3-carboxylate; MW, g/mole: 456.37.

* To whom all correspondence should be sent:
E-mail: maydin@adiyaman.edu.tr

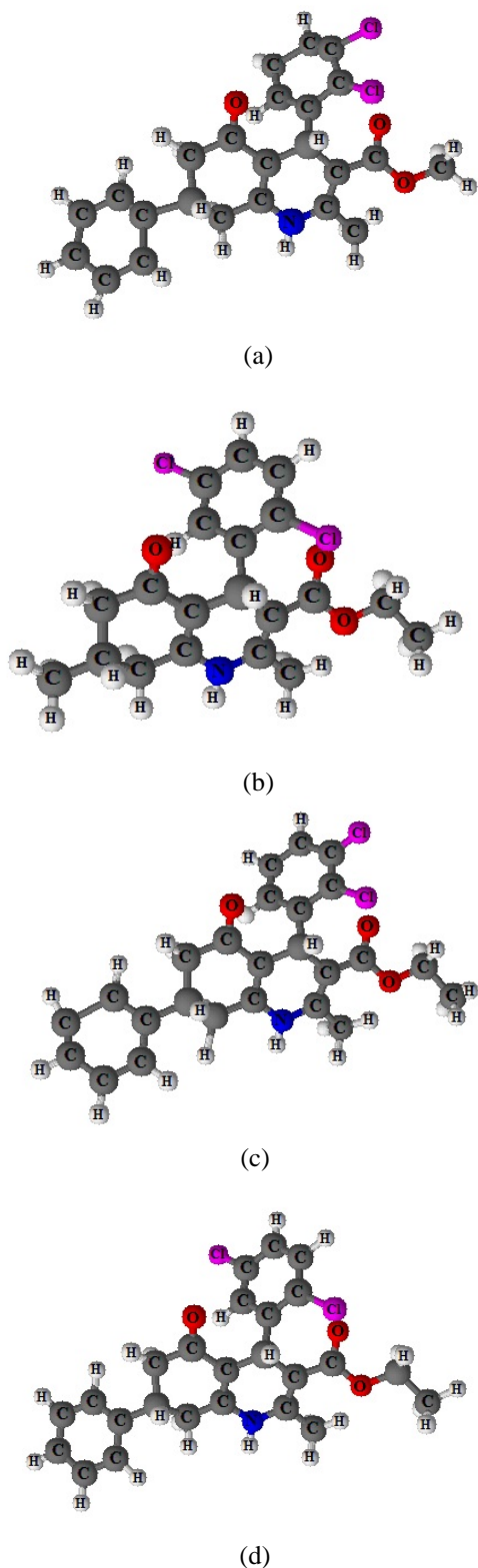


Fig. 1. Molecular structures of: (a) compound 1, (b) compound 2, (c) compound 3, (d) compound 4.

The synthetic procedure to obtain the compounds 1-4 has been described previously [24]. Briefly: 1 mmol of the appropriate 1,3-cyclohexanedione (5-methyl-1,3-cyclohexanedione /5-phenyl-1,3-cyclohexanedione), dichloro-substituted benzaldehyde (1 mmol) and methyl or ethyl

aminocrotonate (1 mmol) were refluxed for 4 h in methanol. The solvent was then evaporated and the residue was crystallized from ethanol. The molecular structures of the compounds are shown in Figs. 1a-d which are simple demonstration pictures obtained from ACD/3D Viewer (Freeware) to explain the structural properties of the compounds used in this study.

Irradiation

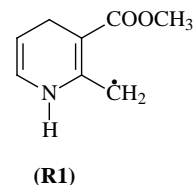
The powder samples were irradiated for 40 h using ^{60}Co gamma ray source with dose speed of 0.89 kGy/h. The irradiated samples were kept in plastic bags at ambient temperature in the dark.

EPR spectroscopy

The EPR measurements were performed with a Varian model X-band E-109C spectrometer at ambient temperature. The modulation amplitude was below 0.40 mT and the microwave power was 2 mW. The spectroscopic g factors of the radicals were determined by comparison with a diphenylpicrylhydrazyl (DPPH) sample ($g = 2.0036$) as reference [26]. Before irradiation no EPR signals were observed for all studied samples. The EPR spectra of the gamma-induced free radicals were unchanged and undiminished at ambient temperature for more than two months after irradiation.

RESULTS AND DISCUSSION

The EPR spectrum of the gamma irradiated compound 1 at ambient temperature is shown in Fig. 2a. The spectrum exhibits a triplet (1:2:1) due to the two equivalent α - protons adjacent to the carbon atom and each of the lines (1:2:1) splits into the triplet (1:1:1) because of the ^{14}N nucleus, resulting in an approximate intensity distribution of 1:1:1:2:2:2:1:1:1. Hence, the paramagnetic species can be attributed to the R1 radical which is a result of the removal of hydrogen atom from the methyl group.



The EPR parameters (g factor and hyperfine splitting) of the R1 radical were extracted from the EPR spectrum analysis as $a_{\alpha} = 1.56$ mT, $a_N = 0.42$ mT and $g = 2.0034 \pm 0.0005$. The simulation of the EPR spectrum with the above given values is shown in Fig. 2b.

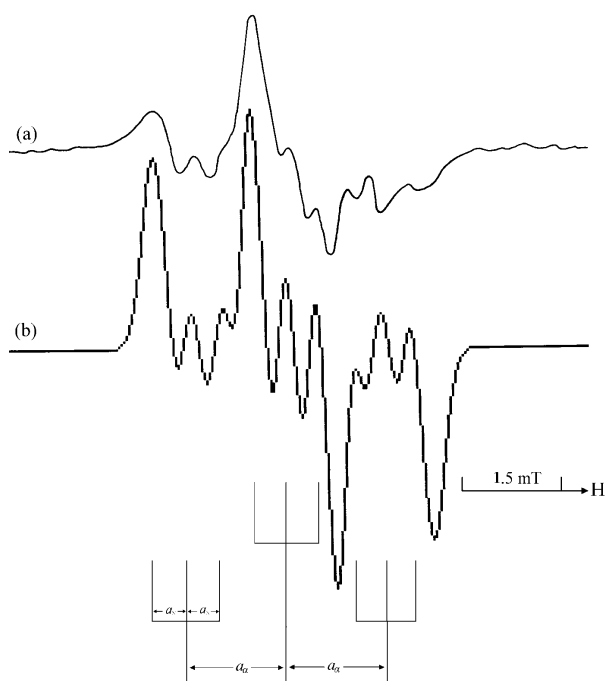


Fig. 2. (a) EPR spectrum of gamma-irradiated compound **1**, (b) simulation of the spectrum.

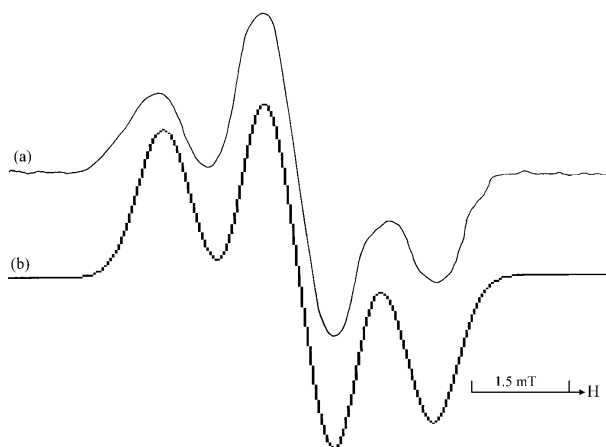
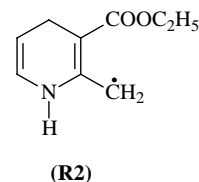


Fig. 3. (a) EPR spectrum of gamma-irradiated compound **2**, (b) simulation of the spectrum.

The radical R1 discussed here is similar to the radical which has been observed in the gamma-irradiated powders of ethyl 2-methyl-4-(2,6-dichlorophenyl)-5-oxo-7-phenyl-1,4,5,6,7,8-hexahydroquinoline-3-carboxylate at ambient temperature; the determined EPR parameters were $a_\alpha = 1.24$ mT, $a_N = 0.48$ mT and $g = 2.0029$ [27]. But the hyperfine coupling constants of the α -protons measured here are higher than the values reported in ref. [27]. Similar values of the hyperfine coupling constants of α -protons have been found in the gamma-irradiated N-glycyl-L-valine as 1.45 mT [28].

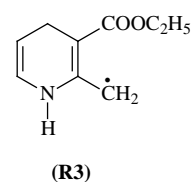
The characteristic EPR spectrum of the gamma-irradiated compound **2** at ambient temperature is shown in Fig. 3a. As can be seen, the spectrum

consists of a triplet with a spacing of 1.34 mT. The 1:2:1 triplet structure of the spectrum is obviously brought about by the interaction of the unpaired electron with two magnetically equivalent α -protons in the methylene group. Therefore, we assume that this EPR spectrum belongs to the R2 radical.



A simulation of the EPR spectrum is shown in Fig. 3b using the hyperfine coupling constants $a_\alpha = 1.34$ mT, $a_N = 0.41$ mT and linewidth (ΔH) 0.54 mT. Since the linewidth of the spectrum is larger than the hyperfine splitting of the nitrogen nuclei, the hyperfine splitting is not observed in the spectrum and was determined using the simulation program. The g value of the radical was measured as $g = 2.0029 \pm 0.0005$. The EPR spectrum of the radical R2 is similar to the EPR spectrum observed in the irradiated powders of ammonium acetate at ambient temperature [4], but the hyperfine coupling constants of α -protons were higher than the values determined for the radical R2. However, similar to the R2 radical were the hyperfine coupling constants of α -protons measured in the gamma-irradiated azocalix [4] arene ($a_\alpha = 1.28$ mT) [29].

Fig. 4a presents the EPR spectrum of the gamma-irradiated compound **3**, recorded at ambient temperature. Since this spectrum has fairly large linewidth ($\Delta H = 0.60$ mT), it is not resolvable at first view. The EPR parameters of the spectrum can be determined from the simulation of the spectrum [30, 31]. The hyperfine constants values obtained by the simulation are $a_\alpha = 1.24$ mT, $a_N = 0.46$ mT and $\Delta H = 0.60$ mT and the simulated spectrum (Fig. 4b) is in excellent agreement with the experimental spectrum. The measured g value at the center of the spectrum is 2.0032. According to these results, we can state that the R3 radical is obtained by the removal of hydrogen from the methylene group.



The EPR spectrum of the gamma-irradiated compound **4** is similar to that of the irradiated compound **3**. Thus, the observed radical of the gamma-irradiated compound **4** is similar to the radical R3. Therefore, the spectrum of compound **4**

is not shown. The g values, hyperfine coupling constants and linewidth obtained by the simulation are $a_{\alpha} = 1.24$ mT, $a_N = 0.46$ mT and $g = 2.0027 \pm 0.0005$. These results agree well with the EPR parameters of the $(\text{CH}_3)_2\text{N}\dot{\text{C}}\text{H}_2$ radical [12]. The g values of the radicals in this study, which were produced by gamma rays, are in agreement with the literature data for their analogous and various other amine radicals [15, 21, 27, 32-36].

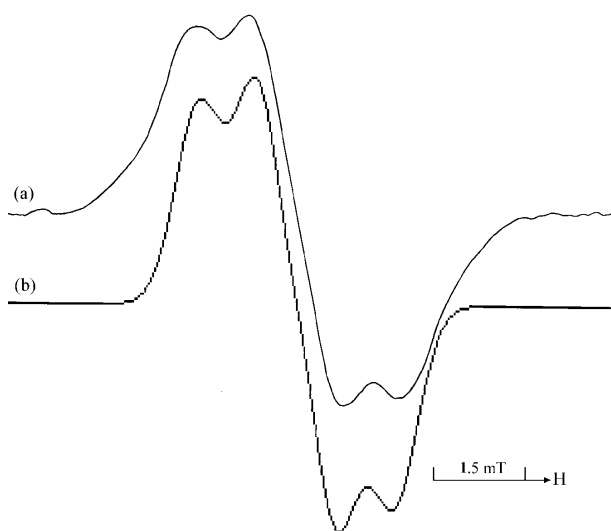


Fig. 4. (a) EPR spectrum of gamma-irradiated compound **3** and compound **4**, (b) simulation of the spectrum.

CONCLUSION

It can be concluded that gamma-irradiation produces very stable amine type free radicals of dihydropyridine derivatives. The EPR parameters and the spectroscopic properties of these radicals were determined. The values of the spectroscopic splitting factor g of these radicals were quite similar to the g -factor for a free electron. The determination of magnetic properties of the produced radicals can be helpful in the study of similar radicals found in biological systems.

REFERENCES

1. H. Tuner, M.O. Bel, M. Polat, *Radiat. Phys. Chem.*, **107**, 115 (2015).
2. S.I. Rana, R. Chawla, R. Kumar, S. Singh, A. Zheleva, Y. Dimitrova, V. Gadjeva, R. Arora, S. Sultana, R. K. Sharma, *J. Pharm. Bioallied Sci.*, **2**, 80 (2010).
3. U. Sayin, Ö. Dereli, E. Türkkän, H. Yüksel, M. Birey, *Radiat. Phys. Chem.*, **80**, 38 (2011).
4. M. H. Başkan, M. Aydın, D. Çanakçı, Ş. Osmanoğlu, *Radiat. Eff. Defect. Solids*, **169**, 226 (2014).

5. X. Guo, C. Chang, E. Y. Lam, *J. Magn. Reson.*, **204**, 26 (2010).
6. C. L. Hawkins, M. J. Davies, *Biochim. Biophys. Acta*, **1840**, 708 (2014).
7. B. Caliskan, H. Tokgoz, *Radiat. Eff. Defect. Solids*, **169**, 225 (2014).
8. B. Caliskan, *Acta Phys. Pol. A*, **125**, 135 (2014).
9. W. C. Lin, C. A. McDowell, J. R. Rowlands, *J. Chem. Phys.*, **35**, 757 (1961).
10. M. Ogawa, *Radiat. Phys. Chem.*, **16**, 281 (1977)
11. J. Stankowski, W. Kempinski, P. Byszewski, Z. Trybula, *Acta Phys. Pol. A.*, **88**, 1117 (1993).
12. R. Köseoğlu, E. Köseoğlu, F. Köksal, *Appl. Radiat. Isot.*, **58**, 63 (2003).
13. R. Mladenova, N. D. Yordanov, *Bulgarian Chem. Commun.*, **39**, 128 (2007).
14. K. Aleksieva, N.D. Yordanov, *Radiat. Eff. Defect. Solids*, **167**, 685 (2012).
15. U. Sayin, *J. Mol. Struct.*, **103**, 132 (2013).
16. B. Çalışkan, A.C. Çalışkan, R. Yerli, *J. Mol. Struct.*, **1075**, 12 (2014).
17. Y. Karakirova, N.D. Yordanov, *Radiat. Phys. Chem.*, **110**, 42 (2015).
18. Y. Karakirova, N. Yordanov, *Bulgarian Chem. Commun.*, **47**, 144 (2015).
19. F. Köksal, O. Çakır, I. Gümrükçü, M. Birey, *Z. Naturforsch.*, **40a**, 903 (1985).
20. N. A. Salih, A. Sanderud, E. Sagstuen, O. I. Eid, A. Lund, *J. Phys. Chem. A*, **10**, 8214 (1997).
21. M. Aydın, *Braz. J. Phys.*, **40**, 429 (2010).
22. D. J. Triggle, *Drug Develop. Res.*, **58**, 5 (2003).
23. N. Edraki, A.R. Mehdipour, M. Khoshneviszadeh, R. Miri, *Drug Discov Today*, **14**, 1058 (2009).
24. M. G. Gündüz, G. S. Öztürk, I. M. Vural, R. Şimşek, Y. Sarioğlu, C. Şafak, *Eur. J. Med. Chem.*, **43**, 562 (2008).
25. M. G. Gündüz, S. Celebi, B. Kaygısız, R. Şimşek, K. Erol, C. Şafak, *Lat. Am. J. Pharm.*, **28**, 922 (2009).
26. N. D. Yordanov, *Appl. Mag. Res.*, **10**, 339 (1996).
27. M. Aydın, R. Şimşek, M.G. Gündüz, C. Şafak, Y.E. Osmanoğlu, *J. Mol. Struct.*, **1035**, 378 (2013).
28. M. H. Başkan, *Radiat. Eff. Defect. Solids*, **163**, 35 (2008).
29. K. Usta, O. O. Karakus, A. Usta, H. Deligoz, *Magn. Reson. Chem.*, **51**, 671 (2013).
30. L. Ateş, Ö. Dereli, E. Türkkän, Ü. Sayın, F. Sevgi, R. Tapramaz, M. Birey, *J. Mol. Struct.*, **1005**, 8 (2011).
31. M. H. Başkan, M. Aydın, Ş. Osmanoğlu, R. Topkaya, *Radiat. Eff. Defect. Solids*, **165**, 938 (2010).
32. D. E. Wood, R. V. Lloyd, *J. Chem. Phys.*, **53**, 3932 (1970).
33. P. Neta, R. W. Fessenden, *J. Phys. Chem.*, **75**, 738 (1971).
34. F. Köksal, Ş. Osmanoğlu, I. Kartal, F. Uzun, *Radiat. Phys. Chem.*, **49**, 537 (1997).
35. E. Bešić, *J. Mol. Struct.*, **917**, 71 (2009).
36. M. Aydın, *Bulgarian Chem. Commun.*, **43**, 419 (2011).

СВОЙСТВА НА СВОБОДНИТЕ РАДИКАЛИ НА НЯКОИ ГАМА-ОБЛЪЧЕНИ ОРГАНИЧНИ СЪЕДИНЕНИЯ

Р. Шимшек¹, М. Г. Гюндюз¹, Дж. Шафак¹, Й. Кьокпинар², М. Айдын^{3*}

¹Факултет по фармация, Университет Хаджетепе, 06100-Анкара, Турция

²Професионално училище за технически науки, Университет Адъяман, Турция

³Образователен факултет, , Университет Адъяман, Турция, 02040-Адъяман, Turkey

Постъпила на 15 май, 2015 г.; коригирана на 3 февруари, 2016 г.

(Резюме)

Прахове на някои органични съединения (дихидро-пиридини, съединения 1-4) бяха облъчени с гамалъчи от ⁶⁰Со, а спектроскопските свойства на образуваните свободни радикали бяха изследвани при обикновена температура с помощта на електронен парамагнитен резонанс (EPR). Анализът на EPR-спектрите показва, че парамагнитните продукти, получени при радиационната деструкция са NĈH₂. Определени са стойностите *g* на радикалите и свръх-фините структурни константи на свободните електрони с близките протони и ядрата на ¹⁴N. EPR-спектрите показват, че те са на радикали, оставащи непроменени в продължение на повече от два месеца. Резултатите са в добро съгласие с тези от предишни изследвания на аминови радикали.

Comparison between acetic acid and propanoic acid as a solvent/catalyst in the indolenines synthesis: an approach without any indole by-product

S. Sajjadifar¹, M. A. Zolfigol², N. Javaherneshan¹, G. Chehardoli^{3*}

¹Department of Chemistry, Payame Noor University, Tehran, Iran

²Faculty of Chemistry, Bu-Ali Sina University, Hamedan, 6517838683, Iran

³Department of Medicinal Chemistry, School of Pharmacy, Hamadan University of Medical Sciences, Zip Code 65178, Hamadan, Iran

Received May 24, 2015; Revised June 7, 2016

Some indolenines (3*H*-indoles) were prepared *via* reaction of phenylhydrazine derivatives, isopropyl methyl ketone, 2-methyl cyclohexanone and diisopropyl ketone in the presence of propanoic acid or acetic acid as a catalyst/solvent under reflux conditions. We compared the obtained results with propanoic acid to those with acetic acid. In most cases, the results were similar. In some cases, however, propanoic acid provided slightly better results with respect to reaction time and yields. Under these reaction conditions, we did not observe any indole output as by-product.

Keywords: Indolenine, 3*H*-indole, Phenylhydrazine derivatives, Aliphatic ketones, Propanoic acid, Acetic acid

INTRODUCTION

Indolenine derivatives are a very important class of nitrogen-containing compounds and have been widely used in dyes and antimigraine drugs of the triptan class [1]. The first report of indolenine synthesis was announced by Fischer in 1883 [2]. Some of the Brønsted acids such as HCl, H₂SO₄, polyphosphoric acid and *p*-toluenesulfonic acid, and also Lewis acids such as boron trifluoride, zinc chloride, iron chloride, and aluminum chloride have been successfully used as catalysts [2, 3].

Robinson suggested the mechanism of Fischer indole synthetic reaction [4-6]. The methodologies for the synthesis of 3*H*-indole derivatives are very limited [7]. Therefore, a general and efficient method for the synthesis of 3*H*-indole derivatives is an attractive and formidable challenge in synthetic chemistry [8].

Miller and Neal Schinske have examined the effects of acid catalysts and temperature in the Fischer indole synthesis. Higher acidity or higher temperature during the thermal process cause cyclization toward the less substituted position. The observations are considered in terms of a refined version of the first two stages of the mechanism of the reaction [9].

A perplexing aspect of the Fischer indole synthesis has been reported in the cyclization of phenylhydrazones of unsymmetrical ketones to form two possible indoles. The early generalizations of Plancher [5] suggesting that the course of the reaction depends only on the structure

of the ketone moiety of the phenylhydrazone, have not been sustained by more recent investigations [10-12] in which the ratio of the products has been found to vary with the nature of the acid used as the catalyst, its concentration, or its absence in a thermal cyclization.

Recently, we used citric acid as an organocatalyst for the preparation of some new indolenine derivatives under reflux of ethanol [13].

In continuation of the studies on the preparation and functionalization of heterocyclic compounds [14-17], herein we report that propanoic acid can be used as a catalyst/solvent for the preparation of some indolenine derivatives without any indole output as a by-product and that the results are comparable with those using acetic acid.

EXPERIMENTAL

General

All chemicals were purchased from Merck or Fluka Chemical Companies. Progress of the reactions was monitored by TLC using silica gel SIL G/UV 254 plates. IR spectra were run on a Shimadzu FTIR-8300 spectrophotometer. The ¹H NMR (300 MHz) and ¹³C NMR (75 MHz) spectra were run on a Bruker Avance DPX spectrometer. Melting points were recorded on a Büchi B-545 apparatus in open capillary tubes.

General procedure for the indolenine synthesis

Phenylhydrazines derivatives (1 mmol) and three aliphatic ketones [isopropyl methyl ketone, 2-methyl cyclohexanone and diisopropyl ketone] (1 mmol) were added to propanoic acid (3 mL) under reflux conditions. The mixture was refluxed for the

* To whom all correspondence should be sent:

E-mail: chehardoli@umsha.ac.ir, cheh1002@gmail.com

appropriate time (see the table) under stirring. Progress of the reactions was monitored by TLC (using *n*-hexane:ethylacetate 3:1 as an eluent). The mixture was cooled and neutralized with 1 M NaOH, then diluted with water (100 mL) and extracted with CHCl₃ (3×50 mL). The organic layer was extracted and dried with Na₂SO₄, the solvent was evaporated and the residue was passed through a short silica gel column for further purification. A light brown viscous oil of indolenines was obtained in high yield.

RESULTS AND DISCUSSION

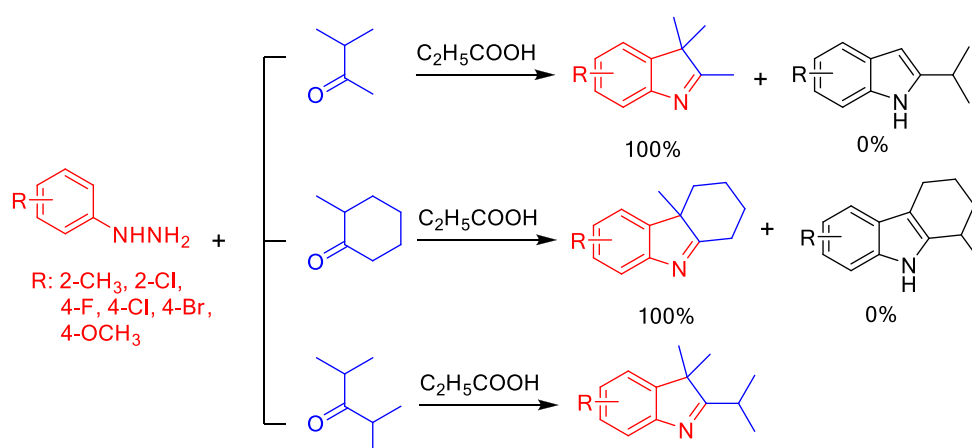
A range of indolenines derivatives was synthesized from a combination of phenylhydrazines and three aliphatic ketones in the presence of propanoic acid as a solvent/catalyst under reflux conditions. For comparing the results of propanoic acid with those of acetic acid, these reactions were also performed in the presence of acetic acid as a solvent/catalyst. In most cases, the results were similar. In some cases, however, propanoic acid provided slightly better results as regards reaction time and yields.

As mentioned in the introduction, higher temperature during the thermal process causes cyclization toward the less substituted position, i.e. indoles. Although 2-methyl cyclohexyl ketone and isopropyl methyl ketone can generate both indole and indolenine, under the present reaction conditions, no indole did not was obtained (Scheme 1). The results are summarized in the table.

Phenylhydrazine derivatives reacted with isopropyl methyl ketone and produced the corresponding indolenines (see the table, entries: **1**, **4**, **7**, **10**, **13**, **16**) in high yield (92-95%). In the ¹H NMR spectrum of these indolenines a singlet signal of two methyl groups at δ=1.1 ppm, and a singlet signal of a methyl group C-2 at δ=2.05 were noticed. The IR spectrum indicated a stretching vibration C=N at 1690 cm⁻¹.

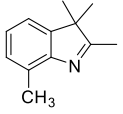
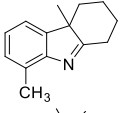
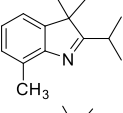
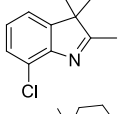
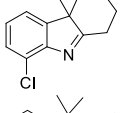
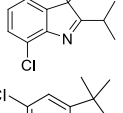
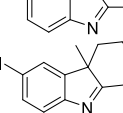
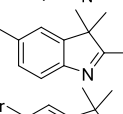
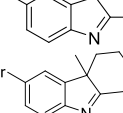
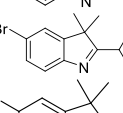
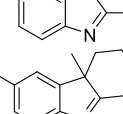
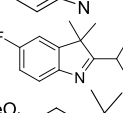
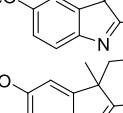
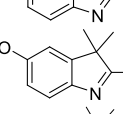
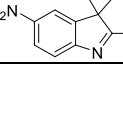
Also, phenylhydrazine derivatives reacted with 2-methyl cyclohexanone producing indolenines (see the table, entries: **2**, **5**, **8**, **11**, **14**, **17**) in high yield (86-95%). The ¹H NMR spectrum of 5,6,7,8-tetrahydro-1,4b-dimethyl-4bH-carbazole (see the table, entry 2) as a model for these indolenines showed 0.80 (t, J=11.74 HZ, 1H) 0.94 (s, 3H, CH₃) 1.10 (t, J=13.2 HZ, 1H) 1.25-1.46 (m, 2H) 1.86 (t, J=13.74 HZ, 2H) 2.19-2.30 (m, 1H) 2.36 (s, 3H, CH₃) 2.63 (d, J=12.74 HZ, 1H) 6.79 (s, 3H, Ar-H (Figure 1 as a model shows the ¹H NMR spectrum of the aliphatic cyclic region). The IR spectrum indicated a stretching vibration C=N at 1706-1716 cm⁻¹.

This reaction was carried out with diisopropyl ketone producing indolenines (see the table, entries: **3**, **6**, **9**, **12**, **15**, **18**) in good yield (71-83%). In the ¹H NMR spectrum of these products a doublet signal of two methyl groups at δ=1.52, a singlet signal of two methyl groups at δ=1.64 and a multiplet signal of CH at δ=2.17-2.29 ppm were noticed. The IR spectrum indicated a stretching vibration C=N at 1706-1716 cm⁻¹.



Scheme 1. Preparation of indolenines by the reaction of substituted phenylhydrazines with isopropyl methyl ketone, 2- methyl cyclohexanone and diisopropyl ketone.

Table. Indolenines synthesis using propanoic acid or acetic acid as a solvent/catalyst under reflux conditions

Entry	Product	Propanoic acid		Acetic acid	
		Time (h:min)	Isolated yield (%)	Time (h:min)	Isolated yield (%)
1		00:15	96	00:15	91
2		00:15	86	00:15	79
3		24:00	83	24:00	81
4		1:00	94	1:00	90
5		00:45	93	00:45	90
6		48:00	76	48:00	62
7		00:45	93	00:45	91
8		00:30	94	00:30	93
9		32:00	71	32:00	59
10		00:30	94	00:30	92
11		00:15	92	00:15	88
12		48:00	75	48:00	66
13		00:30	94	00:30	92
14		00:15	95	00:15	89
15		24:00	72	24:00	95
16		00:30	95	00:30	90
17		00:30	94	00:30	90
18		18:00	83	18:00	68
19		90:00	10	90:00	10

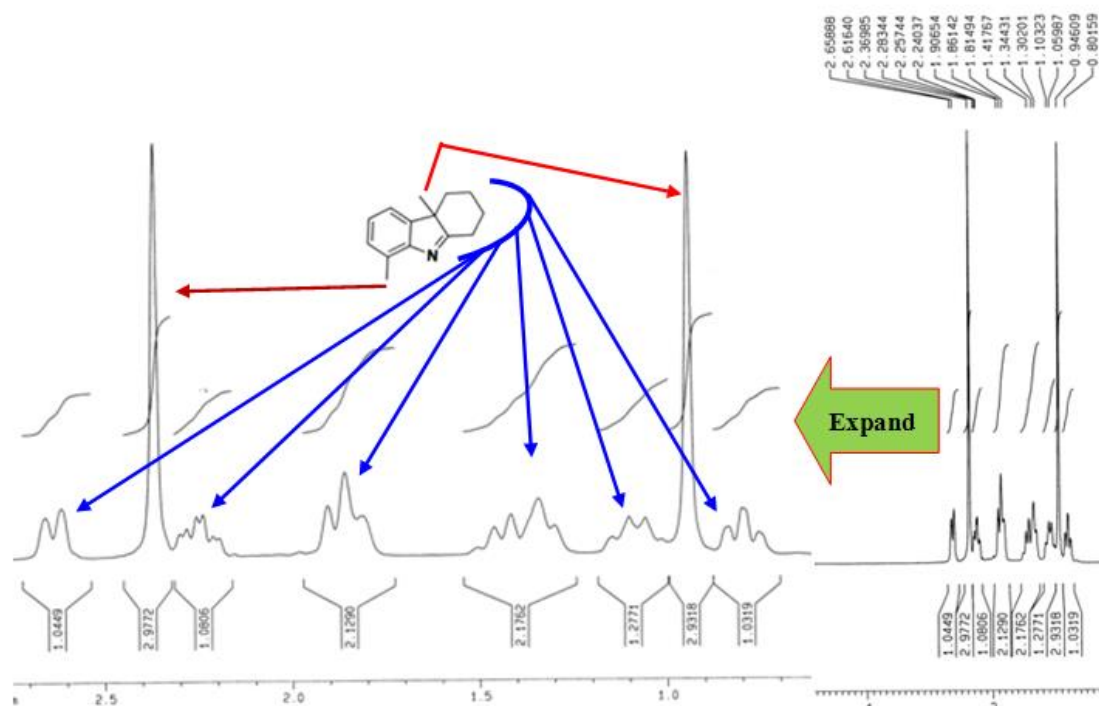


Fig. 1. ¹H NMR spectrum of the aliphatic cyclic region in 5,6,7,8-tetrahydro-1,4b-dimethyl-4bH-carbazole

CONCLUSION

As a weak organic acid, propanoic acid can act as a solvent/catalyst for the efficient indolenines (3*H*-indoles) synthesis in good to excellent yields. We compared the obtained results with propanoic acid to those with acetic acid. In most cases, the results were similar. In some cases, however, propanoic acid provided slightly better results as regards reaction time and yields. Under the present reaction conditions, we did not observe any indole output as a by-product.

Acknowledgements: The authors gratefully acknowledge partial support for this work by deputy of research, Hamadan University of Medical Sciences (Grant number 9308203950), and Center of Excellence in Development of Chemical Methods (CEDCM), Bu-ali Sina University, Hamedan, I.R. Iran.

REFERENCES

1. E. Fischer, O. Hess, *Ber.*, **17**, 559 (1884).
2. E. Fischer, F. Jourdan, *Ber.*, **16**, 2241 (1883).
3. B. Robinson, *Chem. Rev.*, **69**, 227 (1969).
4. R. B. Van Orden, H. G. Lindwell, *Chem. Rev.*, **30**, 69 (1942).
5. R. E. Lyle, L. Skarlos, *Chem. Commun.*, 644 (1966).
6. C. F. H. Allen, C. V. Wilson, *J. Am. Chem. Soc.*, **65**, 611 (1943).
7. (a) V. Boyarskikh, A. Nyong, J. D. Rainier, *Angew. Chem. Int. Ed.*, **47**, 5374 (2008), (b) B. M. Trost, J. Quancard, *J. Am. Chem. Soc.*, **128**, 6314 (2006), (c) M. Kimura, M. Futamata, R. Mukai, Y. Tamaru, *J. Am. Chem. Soc.*, **127**, 4592 (2005).
8. (a) S. Wagaw, B. H. Yang, S. L. Buchwald, *J. Am. Chem. Soc.*, **121**, 10251 (1999), (b) G. L. Glish, R. G. Cooks, *J. Am. Chem. Soc.*, **100**, 6720 (1978).
9. F. M. Miller, S. W. Neal, *J. Org. Chem.*, **43**, 3384 (1978).
10. K. H. Pausacker, *J. Chem. Soc.*, 621 (1950).
11. H. Lily, L. Funderburk, *J. Org. Chem.*, **33**, 4283 (1968).
12. M. H. Palmer, P.S. McIntyre, *J. Chem. Soc. A*, 446 (1969).
13. M. A. Zolfigol, S. Sajjadifar, G. Chehardoli, N. Javaherneshan, *Sci. Iran. C*, **21**, 2059 (2014).
14. S. Sajjadifar, H. Vahedi, A. Massoudi, O. Louie, *Molecules*, **15**, 2491 (2010).
15. G. Chehardoli, M. A. Zolfigol, *Phosphorus, Sulfur*, **185**, 193 (2010).
16. G. Chehardoli, M. A. Zolfigol, T. Faal-Rastegar, S. Mallakpour, A. Ghorbani-Choghamarani, *J. Chem. Sci.*, **121**, 441 (2009).
17. M. A. Zolfigol, G. Chehardoli, M. Shiri, *React. Funct. Polym.*, **67**, 723 (2007).

**СРАВНЕНИЕ МЕЖДУ ОЦЕТНАТА И ПРОПАНОВАТА КИСЕЛИНА КАТО
РАЗТВОРИТЕЛ/КАТАЛИЗАТОР В СИНТЕЗАТА НА ИНДОЛЕНИНИ: ПОДХОД БЕЗ
ИНДОЛОВИ СТРАНИЧНИ ПРОДУКТИ**

С. Саджадифар¹, М.А. Золфигол², Н. Джавахернешан¹, Г. Чехардоли^{3,}*

¹Департамент по химия, Университет Паяме Нур, Техеран, Иран

²Факултет по химия, Университет Бу-Али Сина, Хамедан, Иран

³Департамент по медицинска химия, Училище по фармация, Медицински университет в Хамадан, Иран

Постъпила на 24 май, 2015 г.; приета на 7 юни, 2016 г.

(Резюме)

Някои индоленини (3*H*-индоли) се получават чрез реакция на фенилхидразинови производни, изо-пропилметилкетон, 2-метил-циклохексанон и ди-изопропилкетон в присъствие на пропанова и/или оцетна киселина като катализатор или разтворител при условията на рефлукс. Ние сравнихме получените резултати при използване на двете киселини. В повечето случаи резултатите са сходни, но в някои случаи пропановата киселина дава малко по-добри резултати като време за реакцията и добиви. При тези реакционни условия отделянето на индол като страничен продукт не се наблюдава.

Thin-layer drying kinetics of nectarine slices using IR, MW and hybrid methods

O. Ismail, A. S. Kipcak*, İ. Doymaz, S. Piskin

Yildiz Technical University, Department of Chemical Engineering, 34210, Istanbul, Turkey

Received June 13, 2015; Revised January 20, 2016

In this study, slices of nectarines (*var. nucipersica* or *var. nectarine maxim*) were dried using three different drying methods: microwave (MW), infrared (IR) and hybrid (combined IR and MW). MW drying method was applied with power levels between 90–600 W, while IR drying method was applied with a power level of 125 W. For the hybrid drying, 125 W of IR and 180 W of MW were consecutively applied. Along with the aforementioned methods a pre-treatment process with citric acid was also applied. Minimum drying time of 127 min was reached using the hybrid drying method. After obtaining the experimental drying values, drying kinetics was calculated using mathematical modeling by different methods widely used in the literature. Considering the high coefficient of determination (R^2), low root mean square error (RMSE) and low chi-square (χ^2) values, the Aghbashlo *et al.* model was found to be the best one.

Keywords: MW drying, IR drying, hybrid drying, Aghbashlo *et al.* model

INTRODUCTION

Nectarines (*var. nucipersica* or *var. nectarine maxim*) and peaches (*prunuspersica*) belong to the Rosaceae family. The nectarine is a peach with recessive genes and is referred to as a "shaved peach" or "fuzzless peach", due to its lack of fuzz or short hairs. There are also some differences including fruit size, shape, firmness, external color, aroma and flavor. Nectarine fruits, which can be yellow or white fleshed, have smooth skin, a distinctive flavor and texture, and are usually smaller [1, 2]. The worldwide peaches and nectarines production in 2012 was 21 083151 tons. The major producer countries are China, Italy, USA, Greece, Spain and Turkey. The production in Turkey in 2012 was 575730 tons [3].

Dehydration operations are important steps in food processing industry. The basic objective in drying food products is the removal of water in the solids up to a certain level, at which microbial spoilage is minimized. A wide variety of dehydrated foods including dried fruits, dry mixes and soups, etc., is today available to the consumer [4]. Hot air drying has many disadvantages such as low energy efficiency and long drying times, but nevertheless, it has been widely used [5, 6].

Infrared (IR) heating has many advantages compared to hot air drying. High heat transfer coefficients, short process time and low cost of energy are the characteristic properties of IR heating. Also, the IR equipment is compact with controllable parameters permitting to control overheating and fast heating [7]. There are many studies on the IR method used for the dehydration of several foods.

Some examples are: paddy dried by Daset *et al.*, 2009, barley dried by Afzal and Abe, 2000, onion dried by Sharma *et al.*, 2005, carrots dried by Xu *et al.*, 2014 and apple slices dried by Nowak and Lewicki, 2004 [8–12].

For the last 20 years microwave drying has been of interest in the area of water removal from agricultural products. The short drying time leads to lower energy consumption and better quality of the dried food [13]. Drying time is shortened due to quick absorption of energy by the water molecules, which causes rapid evaporation of water, resulting in high drying rates of the food. However, because of non-uniform heating, uneven distribution of the microwave field can occur. Also, overheating and quality deterioration can take place. To overcome these problems, the microwave drying technique has been combined with other drying methods [14]. Several studies were conducted using the microwave method, e.g., Yongsawatdigul and Gunasekaran, 1996, dried cranberries, Bouraoui *et al.*, 1994, dried potatoes, Funebo and Ohlsson, 1998, Prothon *et al.*, 2001, Bilbao-Sainz *et al.*, 2006, dried apples and Al-Harashseh *et al.*, 2009, dried tomato pomace [15–20].

Today, efforts have been focused on developing better products in accordance with consumer preferences of the drying processes. The biggest problem encountered in fruit drying is the inner surface color change of cut fruit. Several methods were used to obviate color changes, such as: osmotic pre-drying, hot water interaction, steaming, microwave pre-drying and citric acid treatment [21, 22].

While studies exist in the literature regarding dried peaches, there are no studies on the drying of nectarines which are a subgroup of peaches. Hence,

* To whom all correspondence should be sent:
E-mail: skipcak@yildiz.edu.tr, seyhunkipcak@gmail.com

the drying time and color quality is the most important stage of this study. Two different methods of MW and IR drying were used along with the hybrid drying process (IR and MW). Lewis, Henderson and Pubis, Page and Aghbashlo *et al.* models were fitted to the experimental data for obtaining the best model for the drying kinetics of nectarine slices.

MATERIALS AND METHODS

Materials

The experiments were carried out using nectarines purchased from a local market in Istanbul, Turkey. The nectarine samples were stored in a refrigerator at 4 ± 1 °C before commencement of the experiments.

Sample preparation and pretreatment

Dry matter and moisture contents of the fresh samples were determined prior to the drying process. The moisture contents of the samples were obtained according to the Association of Official Analytical Chemists [23]. To determine the initial moisture content four sets of identical experiments were conducted. In these sets samples of 30 g were dried in an Ecocell LSIS-B2V/EC55 model incubator (MMM Medcenter Einrichtungen GmbH, Planegg, Germany) at 105 °C for 24 h. The average initial moisture content of the nectarine slices obtained from the four sets was found to be $84.0 \pm 0.1\%$ weight base.

As a pre-treatment, nectarine samples were cleaned with tap water from dust and foreign materials, then immersed into a solution of 5% citric acid and kept for 3 min at ambient temperature. Citric acid, which is known as lemon salt among the people, E330 food additive code, is used as a preservative inside the foods that reduces color conversion (becoming dark) and deterioration, also increases the shelf life of the fruits [24].

Drying equipments

Drying equipment of MW

Drying experiments were carried out in a microwave oven (Robert Bosch Hausgeräte GmbH, Germany) which has a maximum output of 800 W working at 2450 MHz. In the microwave drying process, the samples were evenly and homogeneously placed over the entire pan. The microwave oven has the capability of operating at five different microwave power levels of 90, 180, 360, 600 and 800 W.

Drying equipment of IR

Drying experiments were carried out in a moisture analyzer with one 250 W halogen lamp (Snijders Moisture Balance, Snijders bv Tilburg, Holland). During the infrared drying process, the samples were evenly and homogeneously placed over the entire pan.

Drying procedures

The MW, IR and hybrid (IR and MW) drying methods were used for the drying of nectarine slices. Before the experiments the nectarines were washed and kept in open air for 2-3 h, to become equal with the ambient temperature. Then the nectarines were cut into slices of 15 mm using a knife. These slices were used in the aforementioned drying methods.

MW drying method

The adjustment of microwave output power level and processing time was done with the aid of a digital control facility located on the microwave oven. Drying experiments were carried out using sliced nectarines of known weight of about 30 ± 2 g arranged as a thin layer on the rotatable plate fitted inside the microwave oven cabinet. The rotating plate provides equal distribution of the microwave radiation energy throughout the sample. Drying was performed at a single power level at a time. In the microwave drying method, four power levels of: 90, 180, 360 and 600 W were used. Moisture loss was measured in 60 and 30 s intervals with a digital balance (Precisa, model XB220A, Precisa Instruments AG, Dietikon, Switzerland) with an accuracy of 0.001 g. Three replicates of each experiment were performed according to a preset microwave output power level and time schedule, and the average of these results was given. Microwave drying continued till the moisture was reduced to about 0.18 g water/g dry matter. After this point the nectarine slices burned. The average values of the moisture content were used for drawing the drying curves.

IR drying method

The most convenient power level for IR drying was reported as 125 W [25, 26]. So the drying experiments were performed at an infrared power level of 125 W. Moisture loss in the samples with initial load of 32 ± 1 g was measured with a digital balance at 30 min intervals. Drying was finished when the moisture content of the samples was approximately 0.06 g water/g dry matter. The experiments were triplicated and the average values of the moisture content were used for drawing the drying curves.

Hybrid drying method

In this method, IR and MW methods were consecutively applied to the same nectarine slices. According to the results obtained from MW and IR method, the details of the hybrid drying were determined.

Firstly IR method at a power level of 125 W was applied on nectarine slices weighing 36.0 ± 1.0 g. The IR method continued until the moisture content decreased to 50%, i.e., 2.15 g water/g dry matter. Then the MW method was applied at a power level of 180 W. The second drying step was continued until the moisture content of the samples decreased to 0.10 g water / g dry matter.

Calculations of the moisture content and drying rate

During the drying process, all weighings were completed in 10 s. Samples were weighed at intervals of 30 and 2 min, for the methods of IR and MW, respectively. Three replicates were taken and the average value was calculated on dry basis by the following equation:

$$M_{initial} = \frac{W_w - W_d}{W_d} \quad (1)$$

where $M_{initial}$ is the initial moisture content of nectarine on dry matter (%), W_w is the wet weight and W_d is the dry weight of nectarine in g. The drying rate during the experiments was calculated using the following formula:

$$\frac{dM}{dt} = \frac{M_{t+dt} - M_t}{dt} \quad (2)$$

where M_t and M_{t+dt} are the moisture content at t and moisture content at $t+dt$ (g water/g dry matter), respectively, and t is the drying time (min).

Color measurements

Color analysis for MW, IR and hybrid dried nectarine samples was done on three randomly selected slices. Color measurement was done using Chromameter CR-400 (Minolta, Japan) and an image analysis system. Color tests of the nectarine

samples were replicated five times and average values were calculated. "L" represents the lightness or darkness of the sample on the scale of 0–100 where white equals 100 and dark equals 0. "a" represents redness (+) or greenness (-). "b" represents yellowness (+) or blueness (-). The color difference (ΔE), chroma (C^*) and R (a/b) were determined using the following Eqns. [27, 28]:

$$\Delta E = \sqrt{((L_o - L)^2 + (a_o - a)^2 + (b_o - b)^2)} \quad (3)$$

$$C^* = \sqrt{a^2 + b^2} \quad (4)$$

$$R = \frac{a}{b} \quad (5)$$

L_o , a_o and b_o are the parameters that are measured before drying of the fresh nectarine samples. The chroma value represents the saturation of the color, the chroma value being low for dim colors and high for vivid colors.

Mathematical modeling

In order to determine the moisture ratio as a function of drying time, four different thin-layer drying models, namely Lewis, Henderson & Pabis, Page, and Aghbashlo *et al.* models [29–32] were applied to IR and MW drying (Table 1).

The moisture ratio of the nectarines was calculated using the following Eqn.:

$$MR = \frac{M_t - M_e}{M_o - M_e} \quad (6)$$

where MR is the moisture ratio, M_t , M_o and M_e are the moisture contents (g water/g dry matter) on dry basis at any time, initial and equilibrium, respectively. The equilibrium moisture content (M_e) was assumed to be zero for microwave and infrared drying and the MR equation (Equation 6) was simplified as Eqn. 7 [33, 26]:

$$MR = \frac{M_t}{M_o} \quad (7)$$

Table 1. Thin-layer drying curve models considered

Model name	Model	Reference
Lewis	$MR = \exp(-kt)$	[29]
Henderson and Pabis	$MR = a \exp(-kt)$	[30]
Page	$MR = \exp(-kt^n)$	[31]
Aghbashlo <i>et al.</i>	$MR = \exp\left(-\frac{k_1 t}{1 + k_2 t}\right)$	[32]

Statistical analysis

The statistical analysis of experimental data was performed using Statistica 8.0.550 (StatSoft, Inc., Tulsa, OK) software package, which is based on the Levenberg–Marquardt algorithm. Three criteria of statistical analysis were used to evaluate the fitting of the experimental data to the different models: coefficient of determination (R^2), reduced chi-square (χ^2) and root-mean-square error (RMSE). These parameters can be calculated as:

$$\chi^2 = \frac{\sum_{i=1}^N \left(MR_{exp,i} - MR_{pre,i} \right)^2}{N - z}, \quad (8)$$

$$RMSE = \left[\frac{1}{N} \sum_{i=1}^N \left(MR_{pre,i} - MR_{exp,i} \right)^2 \right]^{1/2}, \quad (9)$$

where $MR_{exp,i}$ and $MR_{pre,i}$ are the experimental and predicted dimensionless MR , respectively, N is the number of data values, and z is the number of constants of the models. Higher R^2 and smaller χ^2 and $RMSE$ values indicate a better fit of the experimental data to the model [34, 35].

RESULTS AND DISCUSSION

Drying Curves

First stage (MW drying)

In the first stage the nectarines were dried in the microwave oven as natural and pre-treated. From the results of the pre-treated nectarines it can be seen that the pre-treatment process did not affect the drying time. So the pre-treatment curves are not given. The effect of microwave oven on the drying curves of natural nectarines is shown in Fig. 1.

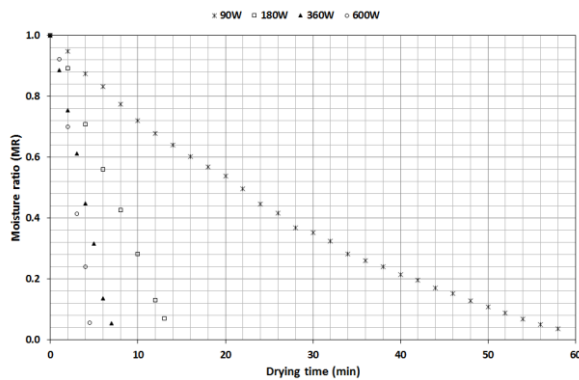


Fig. 1. Drying curves of nectarines at different microwave power level.

The final moisture content of the natural nectarines was reached for about 58 min at the microwave power level of 90 W, where at 180, 360 and 600 W, the final moisture content of the natural

nectarines was reached after 13, 7 and 5 min, respectively.

Water molecules within the nectarines are exposed to a greater number of electromagnetic waves by the increase in microwave output frequency, so the drying time was shortened by the generation of heat inside the nectarines that increased the evaporation of the water molecules (Fig. 2).

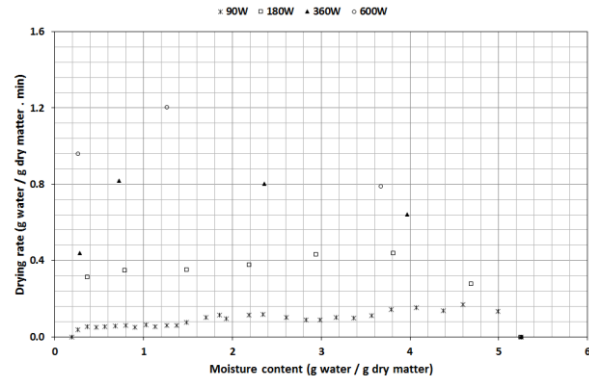


Fig. 2. Drying rate versus moisture content of nectarine slices at different microwave power levels.

In the high-moisture zone, the initial drying rates were high. Drying rates decreased over time while the moisture content of the nectarines dropped significantly.

In the microwave drying of nectarines, constant rate and falling rate periods were consecutively seen. Constant rate period was seen at the microwave power levels of 90 and 180 W in the high moisture zone, then reduced speed period was seen by the decreasing moisture content. In contrast, falling-rate period was seen at the power levels of 360 and 600 W. As a result, the microwave output power level had a crucial effect on the drying rate. Similar results were reported in previous studies [36–38].

Second stage (IR drying)

Fig. 3 shows the experimentally determined moisture ratios of natural and pre-treated nectarines versus drying time at infrared power level of 125 W. The moisture ratio of the nectarines was calculated by the simplified Eqn. 7. The moisture ratio decreased continuously with drying time. The drying curves are typical for those for similar fruits and vegetables. Drying curves were used to determine the effect of pre-treatment (citric acid) on the drying time and it can be easily seen that pre-treatment conditions very little affect the drying time. Drying was continued until the moisture content of the sample reached 0.06 g water/g dry matter and drying times were determined as 225 min and 210 min for natural and citric acid treated samples, respectively.

Similar results were reported during air-drying of citric acid treated banana by Ayim et al., 2012 [39].

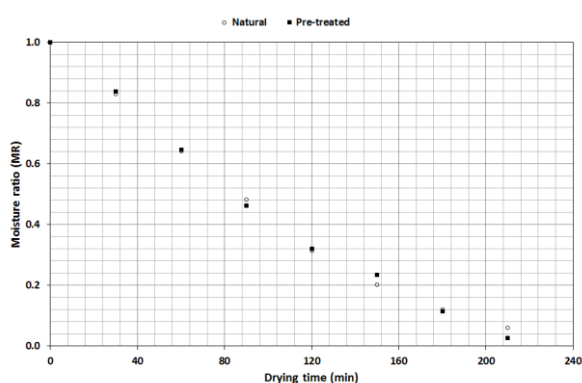


Fig. 3. Experimentally determined moisture ratios of natural and pre-treated nectarines versus drying time at infrared power level of 125 W.

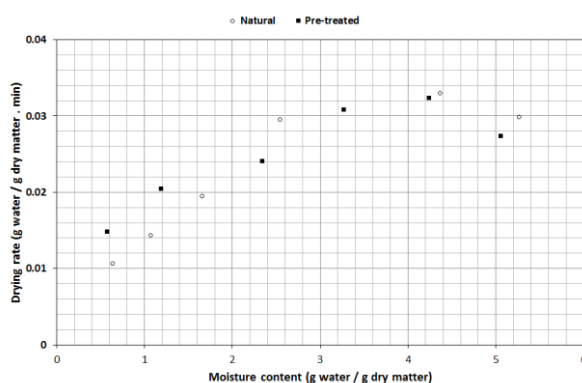


Fig. 4. Drying rate versus moisture content of nectarine slices at infrared power level of 125 W.

Curves of drying rate versus moisture content for pre-treated and natural samples are presented in Fig. 4. As can be seen, there are three drying rate periods in these curves. At the beginning of the drying process, under all drying conditions, there are short heating up periods after which the drying rates gradually decrease and two falling rate periods occur during the drying process. The results are consistent with the observations made by different authors on drying various agricultural products [40–42].

Third stage (Hybrid drying)

The hybrid drying curves of nectarines are shown in Figs. 5, 6 and 7. As seen from Fig. 5, the total moisture content reaches 50% for 120 minutes. Natural and pre-treated nectarines were dried to 0.30 and 0.27 g water/g dry matter in the falling-rate periods, respectively. The pre-treatment process had no effect on natural nectarine drying. The remaining moisture content was removed using MW at the 180 W power level (small graph inside Fig. 5) and the moisture content decreased to 0.10 g water/g dry for a period of 7 min.

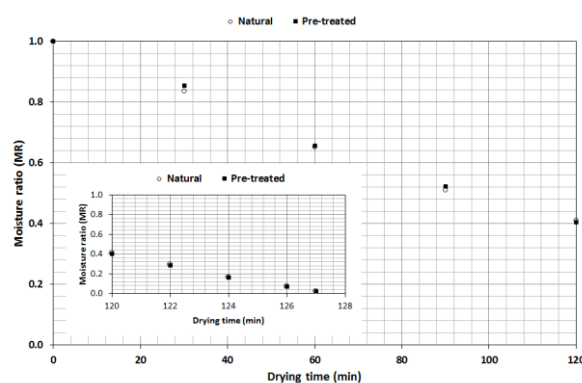


Fig. 5. Experimentally determined moisture ratio of nectarine slices versus drying time during the hybrid process.

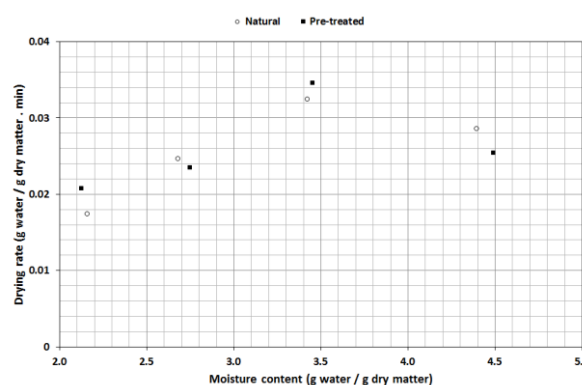


Fig. 6. Changes in drying rate with moisture content at 125 W infrared power level.

Drying rate versus moisture content of the first step of hybrid drying (IR at 125 W) is given in Fig. 6. The drying rate, although showing a short-term increase at the beginning of the drying process, shows a declining trend later for both natural and pre-treated nectarines. Constant rate drying was not observed.

The second step (MW at 180 W), of the drying rate curves for the nectarine slices is given in Fig. 7. As can be seen, in the first two minutes the drying rate increases, then decreases for both natural and pre-treated samples. As a result, the moisture content of the nectarines was very high during the initial phase of the drying process, which resulted in a higher absorption of microwave power level and higher drying rates due to the higher moisture diffusion. As the drying progressed, the loss of moisture in the product caused a decrease in the absorption of microwave power level and resulted in a fall in the drying rate. Similar findings were reported in previous studies [43, 44].

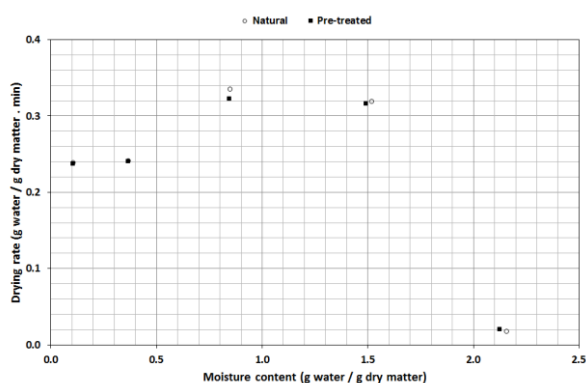


Fig. 7. Changes in drying rate with moisture content at a microwave power level of 180 W

Effect of drying and pre-treatment on the color of nectarine slices

One of the quality parameters of food and agricultural products is the color. Too big color change affects the quality of the product and leads to negative marketing conditions. For the dried products high “L” and low “R” values are preferred. In Table 2, “L”, “a”, “b”, “ΔE”, “C*” and “R” values of the control group and nectarines dried by different methods are given.

In comparison with natural nectarines, the lightness values of the pre-treated hybrid dried nectarines decreased a little; on the contrary, the redness and yellowness values increased. Citric acid pre-treatment prior to the hybrid drying process increased the lightness value. The highest values of “L”, “a”, “b” and “R” were observed for IR and hybrid dried nectarines. Similar results were obtained for various agricultural products [45, 46].

The highest and the lowest total color change (ΔE) values were found as 27.67 and 12.32 for the

MW method (600 W) and the IR method with pre-treated nectarines, respectively. The highest chroma(C*) values were obtained for the IR and hybrid methods.

The pictures of nectarines dried by different drying methods are shown in Fig. 8.

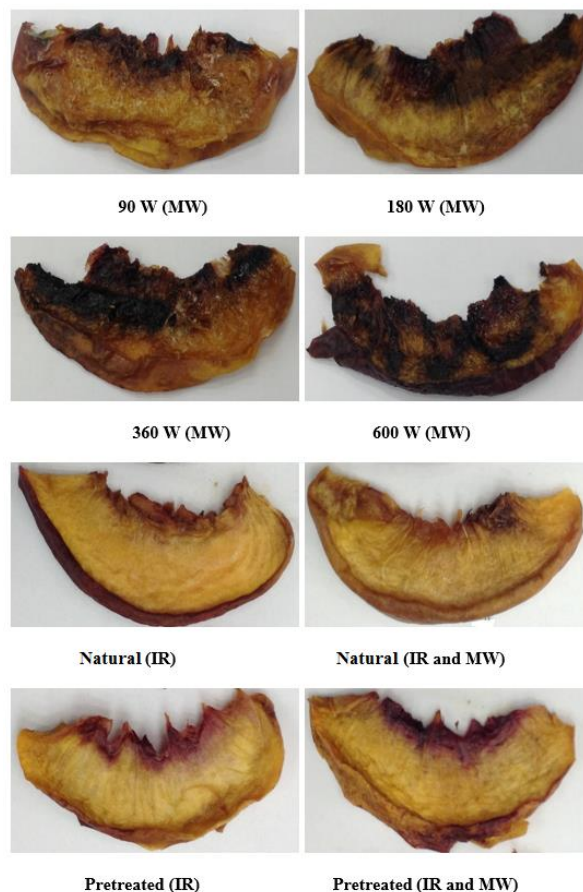


Fig. 8. Colors of dried nectarine slices

Table 2. Color parameters of fresh and dried nectarine slices

Drying Method	Power level	Nectarine	Color parameters			ΔE	C*	R
			L	a	b			
-	-	Fresh	65.10	6.00	21.56	-	22.37	0.28
MW	90 W	Natural	53.85	11.10	19.47	12.53	22.41	0.57
	180 W	Natural	51.42	13.89	20.41	15.83	24.68	0.68
	360 W	Natural	49.85	13.57	19.69	17.13	23.91	0.70
	600 W	Natural	40.68	11.90	9.97	27.67	15.52	1.19
			Natural	63.86	14.22	34.45	15.34	37.27
IR	125 W	Pre-treated	64.02	12.03	30.99	12.32	33.24	0.39
		Natural	52.15	15.14	28.43	17.28	32.21	0.53
Hybrid	125 W (IR) & 180 W (MW)	Pre-treated	63.93	15.67	30.13	12.97	33.96	0.52

As can be seen in Fig. 8, on increasing microwave output power level, excessive browning of the nectarine slices (burning) occurred. This browning decreased on lowering the microwave output power level. In the IR method, the color quality of both natural and pre-treated nectarines was found to be the best among the other methods (Table 2). During hybrid drying, the color values were close to those of the IR method, which means that the hybrid drying method leads to promising results. Another conclusion ensuing from Fig. 8 is that the pre-treatment process had a positive impact on the color quality.

RESULTS OF THE MATHEMATICAL MODELING

Mathematical modeling results of MW dried nectarines are given in Table 3.

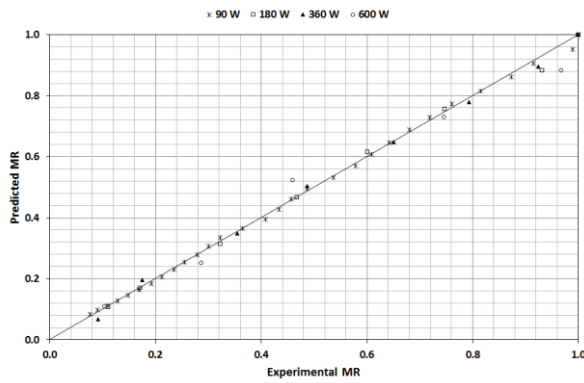


Fig. 9. Comparison of experimental and predicted moisture ratio values using the Aghbashlo *et al.* model for nectarine slices at different MW power levels

Table 3. Curve fitting criteria for the various mathematical models and parameters for nectarine slices at different MW power levels.

Power level (W)	Model	R ²	χ ²	RMSE
90	Lewis	0.9779	0.001816	0.205167
	Henderson and Pabis	0.9864	0.001147	0.145434
	Page	0.9969	0.000254	0.069229
	Aghbashlo <i>et al.</i>	0.9988	0.000098	0.037362
180	Lewis	0.9193	0.009011	0.213650
	Henderson and Pabis	0.9386	0.008041	0.200565
	Page	0.9944	0.000722	0.052846
	Aghbashlo <i>et al.</i>	0.9966	0.000444	0.029480
360	Lewis	0.9029	0.011143	0.234195
	Henderson and Pabis	0.9242	0.010146	0.217807
	Page	0.9953	0.000618	0.052454
	Aghbashlo <i>et al.</i>	0.9970	0.000389	0.039507
600	Lewis	0.8409	0.021674	0.255297
	Henderson and Pabis	0.8709	0.021981	0.258622
	Page	0.9918	0.001381	0.058116
	Aghbashlo <i>et al.</i>	0.9910	0.001928	0.062795

From the R², RMSE and χ² values obtained, the Aghbashlo *et al.* model was found as the optimum one. For the model of Aghbashlo *et al.*, the R² values were found as 0.9988, 0.9966, 0.9970 and 0.9910 for the MW power level of 90, 180, 360 and 600 W, respectively. RMSE and χ² values were calculated as 0.037362, 0.029480, 0.039507, 0.062795 and 0.000098, 0.000444, 0.000389, 0.001928 for the MW power level of 90, 180, 360 and 600 W, respectively.

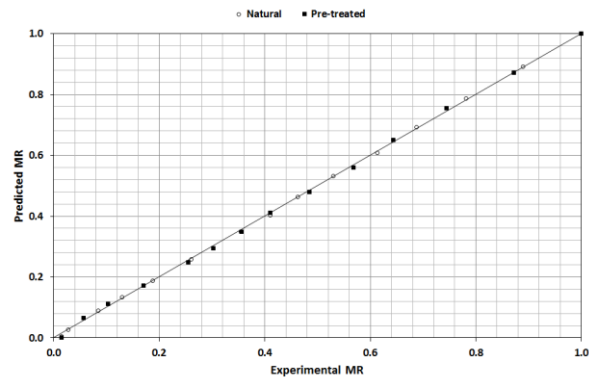


Fig. 10. Comparison of experimental and predicted moisture ratio values using the Aghbashlo *et al.* model for nectarine slices at different IR power level.

The comparison of the experimental and the predicted values is given in Fig. 9. Mathematical modeling results of the IR dried nectarines are given in Table 4.

Table 4. Curve fitting criteria for the various mathematical models and parameters for IR dried nectarine slices

Pretreatment	Model	R ²	χ^2	RMSE
Natural	Lewis	0.9632	0.004590	0.162364
	Henderson and Pabis	0.9699	0.004292	0.157089
	Page	0.9969	0.000439	0.041236
	Aghbashlo <i>et al.</i>	0.9990	0.000138	0.025463
Pre-treated	Lewis	0.9624	0.004549	0.137584
	Henderson and Pabis	0.9692	0.004341	0.133052
	Page	0.9954	0.000649	0.042771
	Aghbashlo <i>et al.</i>	0.9976	0.000329	0.035763

From the obtained results for the R², RMSE and χ^2 values, the Aghbashlo *et al.* model was again found as the optimum one. For the model of Aghbashlo *et al.*, the R² values were found as 0.9990 for natural and 0.9976 for pre-treated nectarine slices. The RMSE and χ^2 values were calculated as 0.025463, 0.000138 for natural and 0.035763, 0.000329 for pre-treated nectarines, respectively.

The comparison of the experimental and the predicted values is given in Fig. 10.

As it is seen from Figs. 9 and 10, all values are placed near the control line, meaning that the experimental and predicted values are very close.

CONCLUSIONS

Turkey has an important place in nectarine fruit production. Nectarines, mostly consumed fresh, have a significant value in terms of human nutrition. The acquisition of new products from dried nectarines, the nectarine production/ processing will increase the income and will allow the consumption of nectarines in every month of a year. Considering the described reasons, in this study, an appropriate method and conditions for drying nectarine slices was found.

In MW drying of both natural and pre-treated nectarines, the drying process was not successful because of the burning of the sugar content (7-12%) inside the nectarines. The nectarines were partly cooked. In IR drying, the drying process was successful with drying times of 210 and 225 min, for natural and pre-treated nectarines, respectively. Even if there is no significant difference in the drying time between natural and pre-treated nectarines, the color quality of pre-treated nectarines was better than that of natural dried nectarines. In the hybrid drying method, the drying time was 127 min, meaning that the drying time was reduced by 40% and 44%, for the pre-treated and natural nectarines, respectively. Likewise, in the IR method the pre-

treatment did not affect the drying time but affected the color quality.

The most suitable model for the mathematical modeling of MW and IR drying methods was that of Aghbashlo *et al.*

As a result, considering all aforementioned parameters, the best method for nectarine drying was found to be the hybrid drying method.

REFERENCES

1. W. Len-Chi, K. E. Koch, W. B. Sherman, *J. Am. Soc. Hortic. Sci.*, **120**, 101 (1995).
2. G. El-Sherief, G. B. Gado, E. M. Rizk, *J. Am. Sci.*, **8**, 139 (2012).
3. <http://faostat3.fao.org/download/Q/QC/E>.
4. M. K. Krokida, D. Marinou-Kouris, *J. Food Eng.*, **57**, 1 (2013).
5. H. Feng, J. Tang, *J. Food Sci.*, **63**, 679 (1998).
6. Z. Pan, R. Khir, L. D. Godfrey, R. Lewis, J. R. Thompson, A. Salim, *J. Food Eng.*, **84**, 469 (2008).
7. N. Sakai, T. Hanzawa, *Trends Food Sci. Technol.*, **5**, 357 (1994).
8. I. Das, S. K. Das, S. Bal, *J. Food Eng.*, **95**, 166 (2009).
9. T. M. Afzal, T. Abe, *Comput. Electron Agr.*, **26**, 137 (2000).
10. G. P. Sharma, R. C. Verma, P. B. Pathare, *J. Food Eng.*, **67**, 361 (2005).
11. C. Xu, Y. Li, H. Yu, *J. Food Eng.*, **136**, 42 (2014).
12. D. Nowak, P. P. Lewicki, *Innov. Food Sci. Emerg. Technol.*, **5**, 353 (2004).
13. E. Sanga, A. S. Mujumdar, G. S. V. Raghavan, Principles and application of microwave drying. In: Mujumdar AS. (Ed.), *Drying Technology in Agriculture and Food Sciences*. Science Publishers, Inc., Enfield, NH, 2000.
14. P. Puligundla, A. S. Abdullah, W. Choi, S. Jun, S. E. Oh, S. Ko, *J. Food Process. Technol.*, **4**, 1000278 (2013).
15. J. Yongsawatdigul, S. Gunasekaran, *J. Food Process. Pres.*, **20**, 145 (1996).
16. M. Bouraoui, P. Richard, T. Durance, *J. Food Process. Eng.*, **17**, 353 (1994).
17. T. Funebo, T. Ohlsson, *J. Food Eng.*, **38**, 353 (1998).

18. F. Prothon, L. M. Ahrne, T. Funebo, S. Kidman, M. Langton, I. Sjöholm, *LWT- Food Sci. Technol.*, **34**, 95 (2001).
19. C. Bilbao-Sáinz, A. Andrés, A. Chiralt, P. Fito, *J. Food Eng.*, **74**, 160 (2006).
20. M. Al-Harashsheh, A. H. Al-Muhtaseb, T. R. A. Magee, *Chem. Eng. Process*, **48**, 524 (2009).
21. M. K. Krokida, C. T. Kiranoudis, Z. B. Maroulis, D. Marinou-Kouris, *Drying Technol.*, **18**, 1239 (2000).
22. İ. Doymaz, B. Bilici, *Int. J. Food Eng.*, **10**, 829 (2004).
23. AOAC. Official methods of analysis. Association of Official Analytical Chemists, Arlington, USA, 1990.
24. F. H. Verhoff, Citric Acid, Ullmann's Encyclopedia of Industrial Chemistry, Weinheim, Wiley-VCH, 2005.
25. H. Kocabiyik, D. Tezer, *Int. J. Food Sci. Technol.*, **44**, 953 (2009).
26. İ. Doymaz, *J. Food Process Pres.*, **39**, 933-939.
27. F. D. Jarad, B. W. Moss, C. C. Youngson, M. D. Russell, *Dent. Mater.*, **23**, 454 (2007).
28. S. Phoungchandang, S. Saentaweek, *Food Bioprod. Process.*, **89**, 429 (2011).
29. J. S. Roberts, D. R. Kidd, O. Padilla-Zakour, *J. Food Eng.*, **89**, 460 (2009).
30. H. M. Ghodake, T. K. Goswami, A. Chakraverty, *Drying Technol.*, **24**, 159 (2006).
31. A. Kaleta, K. Górnicki, R. Winiczenko, A. Chojnacka, *Energ. Convers. Manage.*, **67**, 179 (2013).
32. M. Aghbashlo, M. H. Kianmehr, S. Khani, M. Ghasemi, *Int. Agrophys.*, **23**, 313 (2009).
33. A. Calín-Sánchez, A. Figiel, A. Wojdylo, M. Szaryez, A. A. Carbonell-Barrachina, *Food Bioprocess. Technol.*, **7**, 398 (2014).
34. A. Kaleta, K. Górnicki, *Energ. Convers. Manage.*, **51**, 2967 (2010).
35. K. O. Falade, O. S. Ogunwolu, *J. Food Process. Pres.*, **38**, 373 (2014).
36. I. Alibas, *J. Food Eng.*, **10**, 69 (2014).
37. I. Hammouda, D. Mihoubi, *Energ. Convers. Manage.*, **87**, 832 (2014).
38. N. Izli, G. Yıldız, H. Unal, E. Işık, V. Uylaşer, *Int. J. Food Sci. Technol.*, **49**, 9 (2014).
39. I. Ayim, E. A. Amankwah, K. A. Dzisi, *J. Anim. Plant Sci.*, **13**, 1771 (2012).
40. S. Mongpraneet, T. Abe, T. Tsurusaki, *Trans. Am. Soc. Agric. Eng.*, **45**, 1529 (2002).
41. J. Shi, Z. Pan, T. H. Mchugh, D. Wood, E. Hirschberg, D. Olson, *LWT- Food Sci. Technol.*, **41**, 1962 (2008).
42. E. Akhondi, A. Kazemi, V. Maghsoodi, *Sci. Iran.*, **18**, 1397 (2011).
43. Y. Soysal, *Biosyst. Eng.*, **89** (2), 167 (2004).
44. L. V. Mana, T. Orikasab, Y. Muramatsuc, A. Tagawaa, *J. Food Process. Technol.*, **3**, 1000186 (2012).
45. R. K. Toor, G. P. Savage, *Food Chem.*, **94**, 90 (2006).
46. F. H. Sahin, T. Aktas, H. Orak, P. Ulger, *Bulg. J. Agric. Sci.*, **17**, 867 (2011).

КИНЕТИКА НА СУШЕНЕ НА ТЪНКИ СЛОЕВЕ ОТ НЕКТАРИНИ ПРИ IR, MW И ХИБРИДНИ МЕТОДИ

О. Исмаил, А.С. Кипчак*, И. Доймаз, С. Пишкин

Департамент по инженерна химия, Технически университет Йълдъз, 34210, Истанбул, Турция

Постъпила на 13 юни, 2015 г.; приета на 20 януари, 2016 г.

(Резюме)

В тази работа се изследва сушенето на резени от нектарини (*var. nucipersica* или *var. nectarine maxim*) по три различни метода: микровълново (MW), инфрачервено (IR) и хибридно (комбинирано IR и MW). MW-методът е прилаган при мощности между 90 и 600 W, докато IR-методът на сушене е прилаган при мощност от 125 W. При хибридният метод последователно се прилагат IR-методът при мощност от 125 W и MW-методът при 180 W. Заедно с описаните методи се прилага и предварително третиране с лимонена киселина. Минимално време за сушене се постига при хибридният метод. Кинетиката на сушене е определена от експерименталните резултати с помощта на математично моделиране. Като най-добър кинетичен модел е определен този на Aghbashlo et al. на базата на висок коефициент на корелация (R^2), малка средно-квадратична грешка (RMSE) и ниска стойност на χ^2 -критерия.

Evaluation of persistence of gunshot residue (GSR) using graphite furnace atomic absorption spectrometry (GFAAS) method

İ. Kara^{1,2*}, Ö. Yalçinkaya³

¹Department of Engineering Physics, Faculty of Engineering, Ankara University, Ankara, Turkey

²Department of Ballistics, Ankara Criminal Police Laboratory, Ankara, Turkey

³Department of Chemistry, Faculty of Science, Gazi University, 06500 Teknikokullar, Ankara, Turkey

Received August 31, 2015; Revised February 26, 2016

In this study, the contents of Sb, Pb, and Ba in GSR collected simultaneously from the hands and clothes of the shooter and the barrel of the firearm, were determined by GFAAS in order to determine the time-dependent persistence of GSR. The most intensive GSR was found in the samples collected from the hands of the shooter, and it was observed that the persistence of GSR is longer on the barrel of firearms since this area is less prone to the effects of environmental conditions. Therefore, we were able to analyze the gunshot residues deposited on the barrel of the firearm in a longer time interval. The average half-time of the GSR particles obtained from the hands and clothes of the shooter was found to be one hour. The importance of the time factor in collecting the samples is evident from the findings. The density of the GSR detected varies depending on the type of ammunition used. Although the density of the GSR collected from the hands and clothes of the shooter depends on the type of firearm, it is evident that the surface and environmental factors are very important for the persistence of residues collected.

Keywords: Forensic Sciences, Firearm Investigation, Gunshot Residues.

INTRODUCTION

In forensic science, chemical analysis has gained importance in recent decades [1]. Identifying trace elements in gunshot residues (GSR) provides useful information helping to find the suspect and the victim. The primers of cartridges used in firearms contain lead styphnate, barium nitrate, and antimony trisulfate [2]. When a weapon is fired, the heat and pressure lead to the deposition of residual organic and inorganic substances in the gunpowder and shot shell. In addition, to reveal the shooter, firearm, and ammunition and to obtain other useful information about the shot fired, gunshot residue (GSR) analysis should be performed. There are detailed studies on the detection, identification, and analysis of the firearms that left inorganic GSR [2]. Atomic absorption spectrometry (AAS) is a common method for the analysis of trace elements [3-6]. The morphological and elemental characteristics of the GSR of the fired firearms can be analyzed using scanning electron microscopy and energy-dispersive X-ray spectroscopy (SEM/EDS) imaging techniques [7]. Analysis of the residue of the products attributable to the explosion of the shots is of great importance [6-12] to determine whether the person in question has fired a shot with that firearm [12, 13].

All of these particles can also contain abundant or trace amounts of elements such as aluminum, calcium, sulfur, and silicon; trace amounts of

chlorine, copper, iron, potassium, and zinc, as well as traces of magnesium, sodium, and phosphorus [13]. In the last three decades, the lead-free, heavy-metal-free, pollutant-reduced, or even low-emission primers are trending. The conventional pyro-system is now being replaced by “environmentally compatible” components, due to concerns about the health of shooters that contact the vapors of GSR in daily work [14]. When a firearm is fired, a cloud of various substances, which are called GSRs, leaves the muzzle along with the bullet. These particles are deposited mostly on the hands, clothes, and hair of the shooter, and on the barrel of the firearm [15]. These findings can be used to reveal the suspect and the details of the incident. If performed and interpreted correctly, such analyses distinguish between homicide and suicide [16]. In studies carried out to date, the focus was on the collection of GSR from the hand of the shooter immediately after shooting [14]. As a result of many years of experience, it was observed that GSR can be detected on the clothes and hair of the shooter after some time following the incident, despite the negative GSR-detection results in the samples collected from hands [17]. In their study conducted in 2008, Rosenberg and Dockery showed that GSR could be detected on the hands of shooters up to nine days later, according to measurements made at one-day intervals [18]. However, in practice, the swab samples are collected from the suspect a few hours after the incident.

* To whom all correspondence should be sent:
E-mail: ilkerkara06@hotmail.com

The purpose of this study is to investigate the time-dependent permanence of GSR traces obtained from three different forms of ammunition used with two different brands of pistols. This information can contribute to the routine GSR examination.

EXPERIMENTAL

Gunshot experiments

A Smith-Wesson (S&W) brand revolver and a semi-automatic Glock 17 brand pistol were used with proper Machine Chemistry Institute (MKE), Czech Republic Sellier and Bellot (S&B), and Germany (Geco) brand full-metal-jacket ammunition. GSR samples were collected from the right hand of the shooter, from a 10×10 cm area on the right sleeve of the shooter and from the interior of the barrel of the firearm used, in order to determine the time-dependent change of the persistence of GSR. All ammunition used had conventional lead-, antimony-, and barium-based primers.

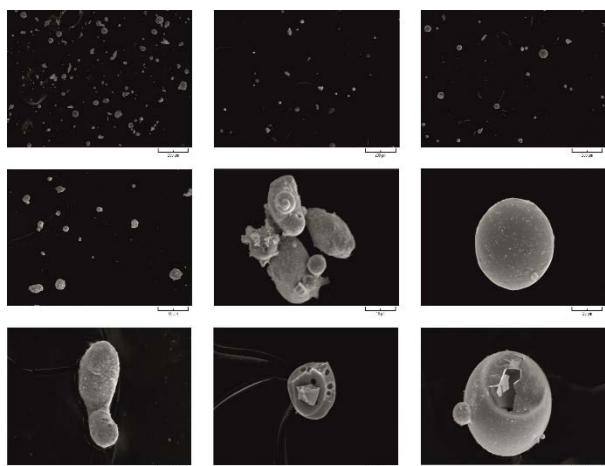


Fig.1. Backscattered electron images of chosen examples of GSR.

Each test shot took place in an indoor firing range after turning off the flow-through ventilation. Air circulation was minimal. The firearms and ammunition are listed in Table 1.

A standard solution of 5% nitric acid was prepared by diluting a 1000 mg/l stock standard solution of 50 ml, and the barrel was rinsed with this solution to obtain a solution of GSR [19]. The samples were collected immediately after each shot from the shooter's right hand and right sleeve on aluminum stubs using double-sided adhesive tape. GSR was collected by pressing the stub for 100 times to the hand skin including thumb and index finger of the right hand and the right sleeve of the shooter. To prevent any accidental contamination, the shooters did not collect any samples. For the same reason, the residues were collected by only one person, and analyzed under the same strict conditions.

Samples were collected by using different carbon tapes for each measurement, and after putting them into sterile sampling containers, 5 ml of 5% nitric acid solution was added to the containers and allowed to stay for 24 h after centrifuging for 2 h. The related samples were transferred to 5 ml vessels made for the GFAAS device. The control samples were collected from clean barrels, empty carbon tapes, empty tubes, and target areas after applying cleaning procedures.

Apparatus

A Varian (Australia) electrothermal atomic absorption spectrometer model SpectrAA 240Z equipped with a Zeeman background correction system, a thermal graphite atomizer (TGA-120), and an autosampler (PSD-120), was utilized for the determination of analytes. Integrated mode was used for the absorbance measurements throughout the studies. An antimony hollow cathode lamp (Varian), a multi-element (Co-Mo-Pb-Zn) hollow cathode lamp (Varian), and an electrothermal atomizer were used for the determination of Sb and Pb under the conditions suggested by the manufacturer. The wavelength, lamp current, and slit width were 217.6 nm, 10 mA, and 0.2 nm for Sb and 217.0 nm, 10 mA, and 1.0 nm for Pb. A Varian AA240FS was used for Ba in atomic emission (AES) mode under the conditions suggested by the manufacturer. The wavelength, slit width, and acetylene flow rate were 553.6 nm, 0.2 nm, and 2.15 L/min.

Table 1. Pistol and cartridge mark list.

Pistol Mark	Smith&Wesson			Glock 17		
Cartridge	MKE	Geco	S&B	MKE	Geco	S&B
Caliber	38 special	38 special	38 special	9 mm	9 mm	9 mm

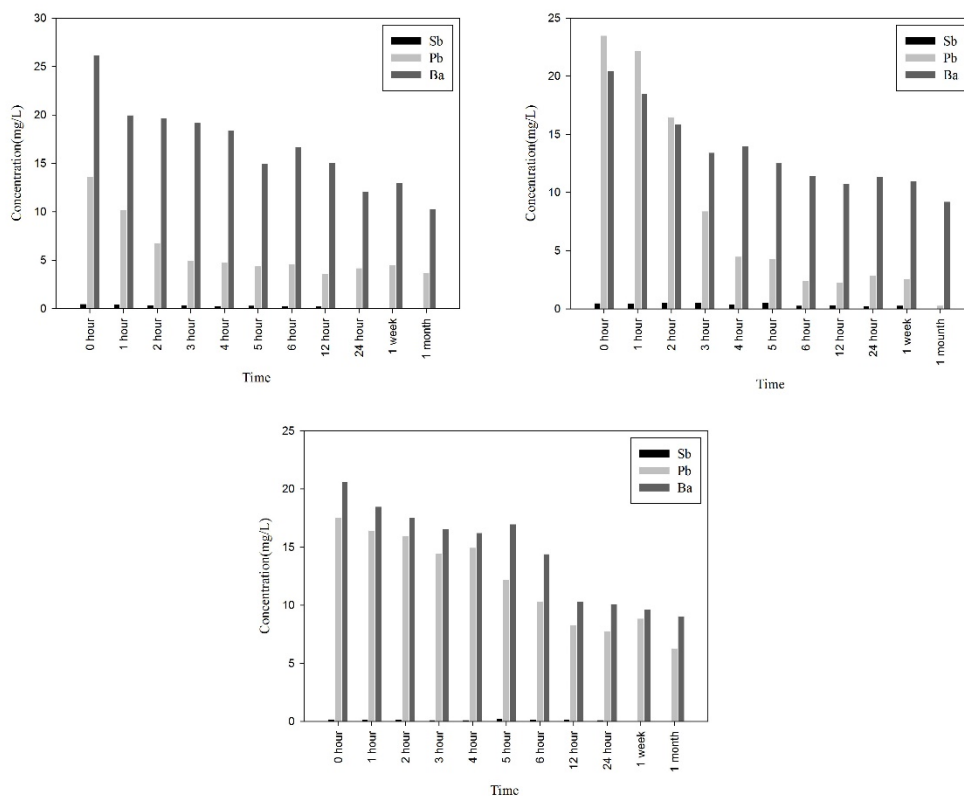


Fig. 2. Time-dependent change of the persistence of GSR particles deposited on the barrel of the S&W brand revolver for a) MKE b) Geco c) S&B brand 38 special caliber cartridges.

RESULTS AND DISCUSSION

Time-dependent amount of particles

The formation of GSR particles is a very dynamic and complex process. This process can involve numerous metal particles [20]. All of these particles can also contain abundant or trace amounts of elements such as aluminum, calcium, sulfur and silicon; trace amounts of chlorine, copper, iron, potassium, and zinc; as well as traces of magnesium, sodium, and phosphorus [15]. Quantitative analysis of antimony (Sb), barium (Ba), and lead (Pb), which are the major elemental components of most of the cartridge primers, performed on the GSR collected from the hands of a suspect, provides valuable data to be used for associating the suspect with recently discharged or contaminated firearms, or with an ammunition component. Therefore, Sb, Pb, and Ba present in the ammunition analyzed were preferred in detecting the traces of GSR. The most important factor in determining the persistence of GSR is the collection of GSR particles in a quality and steady manner. Therefore, swabs should be simultaneously taken from the same areas of the only shooter to minimize the variables, and the GSR collection method should be completely consistent.

The time-dependent persistence of the amount of

Sb, Pb, and Ba obtained from the GSR collected from the hands and clothes of the shooter, and the barrel of the firearm used is shown in figures 2-7. Naturally, GSR deposition is denser in the barrel of firearms, and it was observed that the amount deposited on the right hand of the shooter was higher than the amount collected from the clothes of the shooter.

Although the GSR density occurring after firing shots depends on the type of ammunition used, the dispersion of the particles into the environment after the explosion varied according to the type of firearm used. It is shown in figures 2-7 that the amount of particles formed significantly decreases as the distance from the barrel increases.

In Figure 2, time-dependent changes of the persistence of Sb, Pb, and Ba obtained from the particles deposited on the barrel of the S&W brand revolver were examined up to one month later. It was observed that GSR particles can be detected even after one month, since the interior of the firearm's barrel is the least affected part by environmental conditions. Of the three elements examined, the amount of Sb was found to be lower than the amounts of Pb and Ba, and its persistence was minimal. The amount of Ba was found to be significantly higher in GSR obtained from the MKE brand cartridges. In addition, they have the minimum

amount of Pb compared to other types of ammunition. Additionally, the amount of GSR particles deposited in the S&W brand revolver is expected to be lower since it has a shorter barrel than the Glock 17 brand pistol because of the design of the revolver.

In Figure 3, the time-dependent change of the persistence of Sb, Pb, and Ba obtained from the particles deposited on the barrel of the Glock 17 brand pistol were examined up to 1 month at various intervals. Although the amount of GSR deposited is approximately two times higher in a Glock 17 brand pistol due to its longer barrel in comparison with the S&W brand revolver, these two firearms had similar time-dependent persistence of GSR change.

In Figure 4, the time-dependent change of the persistence of Sb, Pb, and Ba obtained from the GSR particles collected from the right hand of the shooter after firing shots with the S&W brand revolver, examined in the range of 0-5 h, is shown. The amount of GSR dispersed was higher after the explosion in the S&W brand revolver due to the effective ballistic power of revolver ammunition and the design of the revolver [21]. Thus, the amount deposited on the hands of the shooter was higher

using a S&W brand revolver. The amount of Pb was found to be lower in GSR obtained from the MKE brand ammunition compared to other types of ammunition. GSR was detected on the hands of the shooter up to the fifth hour.

In Figure 5, the persistence of the amount of Sb, Pb, and Ba obtained from the GSR particles collected from the right hand of the shooter, using Glock 17 brand pistol, examined in the range of 0-5 h, is shown. It was observed that the amount of GSR deposited on the hands of the shooter was significantly lower compared to a revolver. This may be caused by the design of the revolver and the effective ballistic power of the ammunition used [21]. The amount of GSR collected from the shooter was maximum when the MKE brand ammunition was used.

In Figure 6, the persistence of the GSR deposited on the clothes of the shooter, using a S&W brand revolver, examined in the range of 0-5 h, is shown. Taking swabs from the shooter's clothing is a less preferred method than taking swabs from the hands of the shooter. However, GSR particles were found to stay longer on the shooter's clothes. This result is critical in evaluating cases.

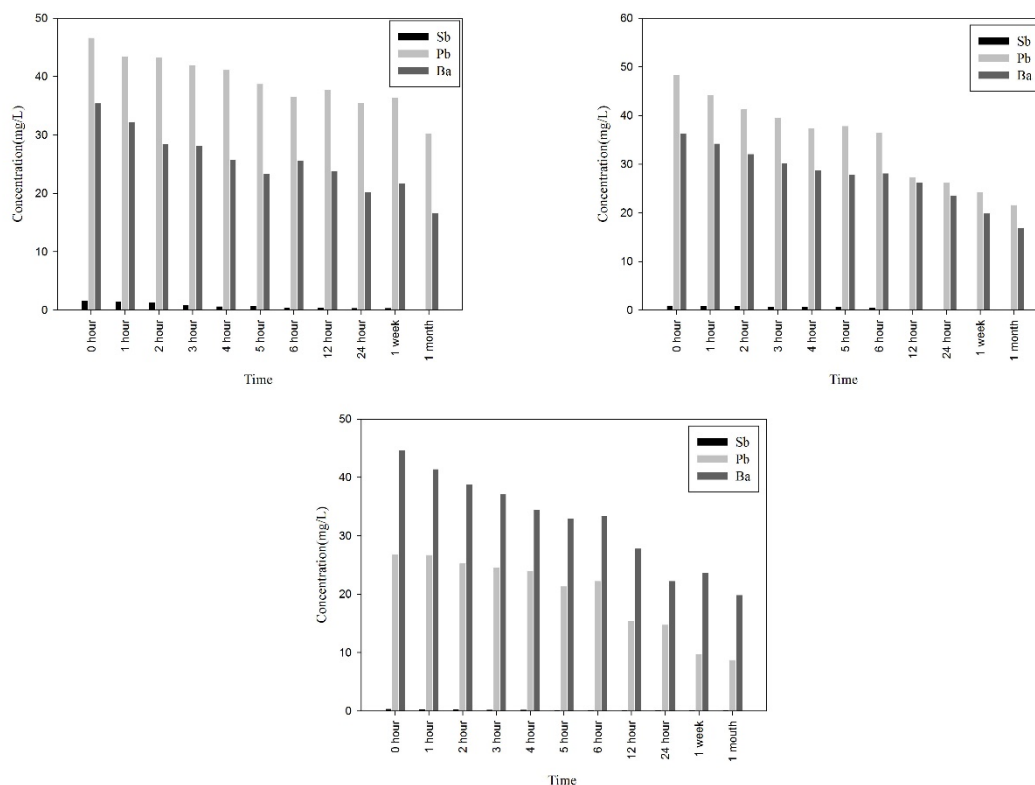


Fig. 3. Time-dependent change of the persistence of GSR particles deposited on the barrel of the Glock 17 brand pistol for a) MKE b) Geco c) S&B brand 9 mm cartridges.

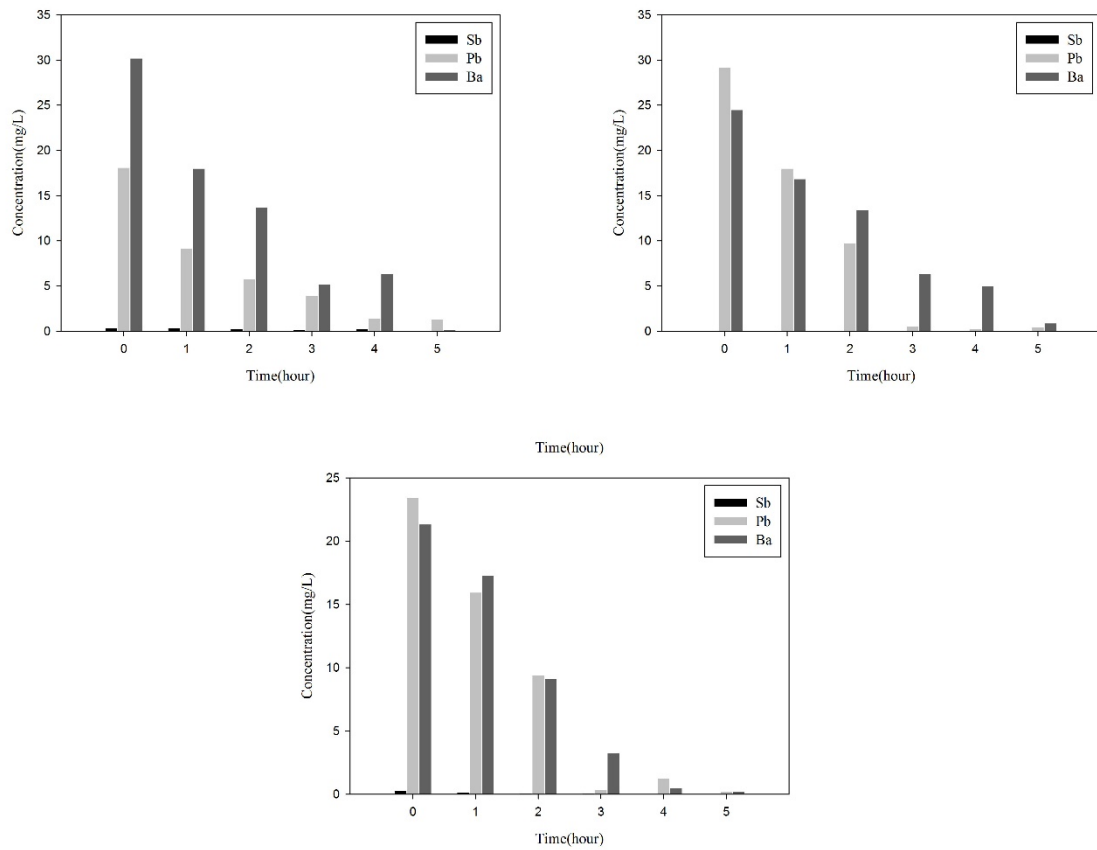


Fig. 4. Time-dependent change of persistence of GSR particles deposited on the hands of the shooter using S&W brand revolver for a) MKE b) Geco c) S&B brand 38 special caliber cartridges.

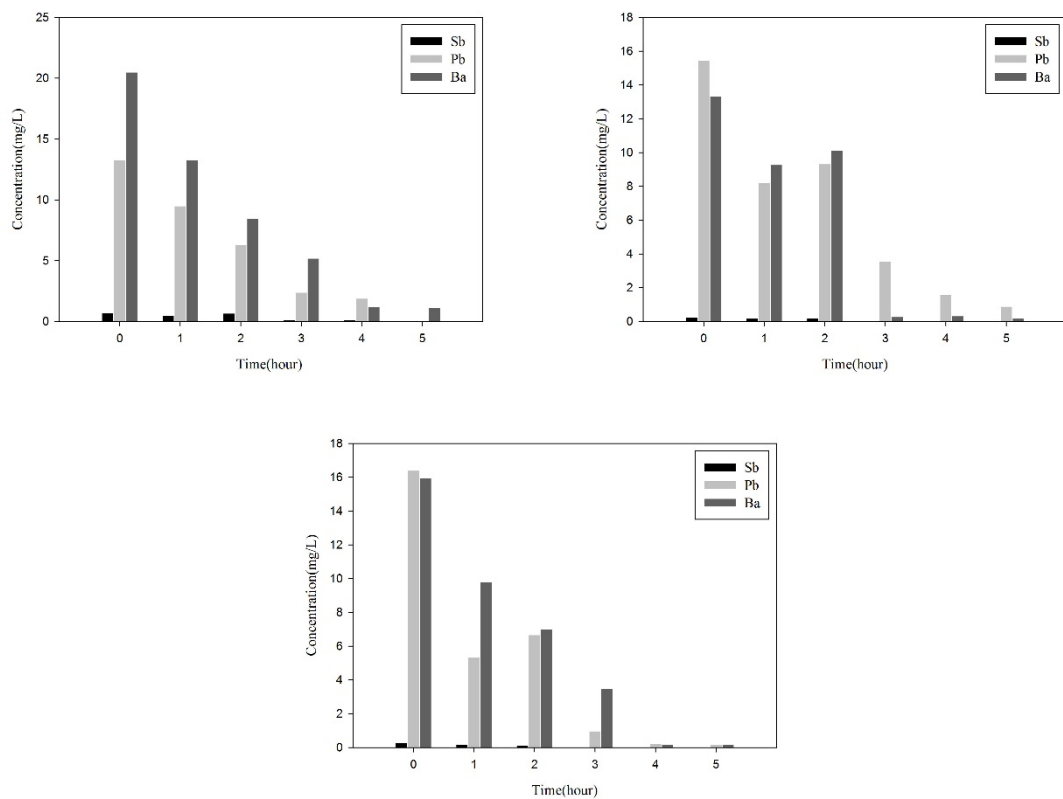


Fig. 5. Time-dependent change of persistence of GSR particles deposited on the hands of the shooter using Glock 17 brand pistol for a) MKE b) Geco c) S&B brand 9 mm cartridges.

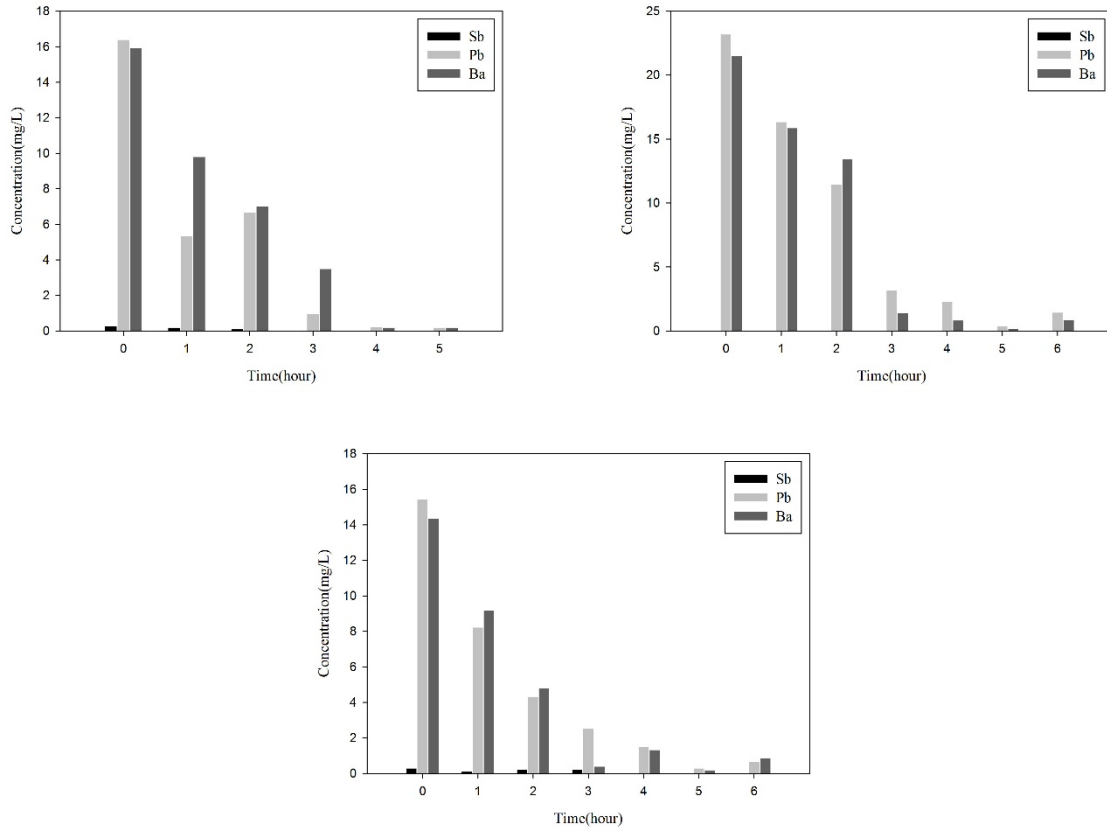


Fig. 6. Time-dependent change of persistence of GSR particles deposited on the right sleeve of the shooter using S&W brand revolver for a) MKE b) Geco c) S&B brand 38 special caliber cartridges.

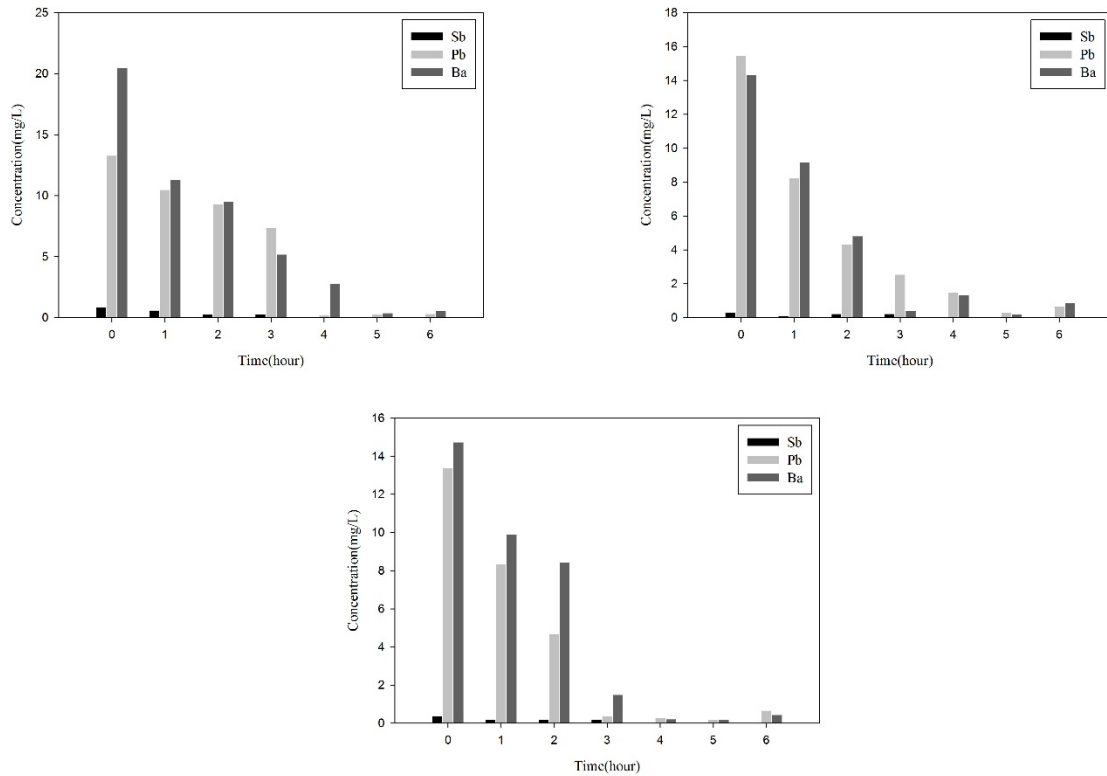


Fig. 7. Time-dependent change of persistence of GSR particles deposited on a 10x10 cm area on the right sleeve of the shooter using Glock 17 brand pistol for a) MKE b) Geco c) S&B brand 9 mm cartridges.

In Figure 7, the time-dependent persistence of GSR particles deposited on the clothes of the shooter using a Glock 17 brand pistol, examined in the range of 0-6 h, is shown. Although the GSR density was lower than that obtained with a S&W revolver, it was observed that the GSR particles could be detected up to the sixth hour later.

The persistence of GSR was found to decrease quickly after firing shots, and it was also observed that it can be detected on the hands of the shooter up to five hours later; whereas from the clothes of the shooter it can be detected up to six hours later. Hence, taking swabs from the clothes and the hands of the shooter will be beneficial for justice providers in evaluating the incident.

CONCLUSIONS

While the persistence of GSR particles is higher in the firearms' barrel, they disappear first from the hands and clothes of the shooter with time. This can be caused by the GSR particles loosely bound to the surface of the hand compared to the surface of cloth, or by the daily activities of the shooter affecting the particles on the surface of the hand. The intensity of GSR particles that occurred as a result of the explosion is highly dependent on the type of ammunition used. The intensity of GSR particles dispersed in the environment varies depending on the type of firearm. Since the barrels of firearms are less affected by the environmental conditions, the GSR particles on the barrel can be detected for a longer time. This result showed that the environmental conditions are very effective on the GSR.

This study can be considered as a recommendation for justice providers. In the detection of GSR, the type of firearm used in the incident and ammunition types were also found to be of significance. Taking swabs from the clothes and the hands of the shooter was found to be potentially advantageous. These analytical data will be beneficial in practice.

REFERENCES

1. N.F. Fidan, B. İzgi, *Bulgarian Chemical Communications*, **41**, 404 (2009).
2. K.H. Chang, P.T. Jayaprakash, C.H. Yew, A.F.L. Abdullah, *Australian Forensic Science*, **45**, 23 (2013).
3. Ö. Yalçinkaya, O. M. Kalfa, A. R. Türker. *Turkish Journal of Chemistry*, **36**, 885 (2012).
4. I. Kara., S.B. Lisesivdin, M. Kasap, E. Er, U. Uzek. *Journal of Forensic Science*, **60**, 1030 (2015).
5. A. Safavi, S. Momeni, N.J. Saghir, *Journal of Hazardous Materials*, **162**, 333 (2009).
6. I. Kara, Y. Sarikavak, S.B. Lisesivdin, M. Kasap. *Environmental Forensics*, **17**, 68 (2016).
7. D. Lepik, V. Vassiljev. *Journal of Forensic and Legal Medicine*, **17**, 412 (2010).
8. A. Zeichner, S. Ehrlich, E. Shoshani, L. Halicz. *Forensic Sci Int.*, **52**, 158 (2006).
9. L. Fanton, B. Karger. *Journal of Forensic and Legal Medicine*, **19**, 90 (2012).
10. E. Lucker. *Journal of Analytical Atomic Spectrometry*, **14**, 1731 (1999).
11. M. R. Rijnders, A. Stamouli, A. Bolck. *Journal of Forensic Science*, **55**, 616 (2010).
12. E. B. Morales, A.L. Vazquez. *Journal of Chromatography A*, **2**, 225 (2004),
13. G. Matthew, B. Mark, H. *Science & Justice*, **52**, 49 (2012).
14. Z. Brozek-Mucha, *Microsc. Microanal.*, **17**, 972 (2011).
15. H. Miyauchi, M. Kumihashi, T. Shibayama.. *Journal of Forensic Science*, **43**, 90 (1998).
16. Z. Brozek-Mucha. *Forensic Sci Int.*, **183**, 33 (2009).
17. A. Zeichner, N. Levin. *Journal of Forensic Science*, **40**, 1082 (1995).
18. M.B. Rosenberg, C.R. Dockery, *Appl. Spectrosc.*, **62**, 1238 (2008).
19. A.J. Schwoeble, D.L. Exline, *Current Methods in Forensic Gunshot Residue Analysis*, FL, CRC Press, 2000, p. 42.
20. L. Garofano, M. Capra, F. Ferrari, G.P. Bizzaro, D. DiTullio, M.A. Dell'Olio, *Forensic Sci. Int.*, **103**, 1 (1999).
21. <http://kuulapaa.com/home/highspeed/high-power.html>.

ОЦЕНЯВАНЕ НА ТРАЙНОСТТА НА ОСТАТЪЦИ ОТ ИЗСТРЕЛИ (GSR) С АТОМНО-АБСОРБЦИОННА СПЕКТРОФОТОМЕТРИЯ В ГРАФИТНА ПЕЩ (GFAAS)

И. Кара^{1,2}, О.. Ялчинкая³

¹Департамент по инженерна физика, Инженерен факултет, Университет в Анкара, Турция

²Департамент по балистика, Полицейска лаборатория по криминалистика в Анкара, Турция

³Департамент по химия, Научен факултет, Университет Гази, Анкара, Турция

Постъпила на 31 август, 2015 г.; приета на 20 май, 2016 г.

(Резюме)

В тази работа се изследва съдържанието на някои елементи (Sb, Pb и Ba) в остатъците от изстрели (GSR), събрани едновременно от ръцете и дрехите на стрелеца и от цевта на оръжието по метода GFAAS и трайността на замърсяването от остатъка (GSR). Най-интензивно замърсяване (GSR) се забелязва в пробите, взети от ръцете на стрелеца и се установява, че трайността на замърсяването е по-голяма по цевта на оръжието, тъй като тя е по-малко изложена на околна въздействие. Средното полу-време на трайност на остатъците по ръцете и дрехите на стрелеца е един час. От това се установява значението на момента на пробовзимането, Плътността на откритите GSR варира според използваните амуниции и типа на оръжието. Въпреки това се установява, че повърхността и околната среда са важни за трайността на взиманите проби.

Effect of activated carbons derived from apricot stones or polyolefin wax on hydrogen sorption properties of MgH₂

E. Grigорова^{1*}, M. Khristov¹, I. Stoycheva², B. Tsyntsarski², D. Nihtianova^{1,3}, P. Markov¹

¹ Institute of General and Inorganic Chemistry, Bulgarian Academy of Sciences, bl.11, Acad. G. Bonchev str., 1113 Sofia, Bulgaria

² Institute of Organic Chemistry with Centre of Phytochemistry, Bulgarian Academy of Sciences, bl. 9, Acad. G. Bonchev str., 1113 Sofia, Bulgaria

³ Institute of Mineralogy and Crystallography, Bulgarian Academy of Sciences, Acad. G. Bonchev Str., bl. 107, 1113 Sofia, Bulgaria

Received October 8, 2015; Revised May 16, 2016

The hydriding and dehydriding properties of 95 wt.% MgH₂ - 5 wt. % C composites, synthesized by ball milling under argon with two different carbon additives (activated carbon derived from apricot stones - AS and from polyolefin wax - POW), were studied. Both samples showed no significant difference in the hydrogen absorption kinetics and reached absorption capacity of 5.8 wt.% for 95 wt.% MgH₂ - 5 wt. % AS and 5.4 wt. % for 95 wt.% MgH₂ - 5 wt. % POW at 573K and 1MPa after 60 min of hydriding. Faster desorption rate at 623 K and 0.15 MPa was demonstrated by the composite containing activated carbon derived from apricot stones. Morphology and phase composition of the composites were investigated by TEM and XRD.

Keywords: Mg-C nanocomposites, hydriding/dehydriding, ball milling, hydrogen storage capacity

INTRODUCTION

Important factor in the use of hydrogen as a clean fuel is the development of safe and effective materials for its storage. One of the most promising hydrogen storage materials is magnesium, mostly because of its high theoretical hydrogen storage capacity (7.6 wt.%), abundance and low cost. Its practical application, however, is hindered by the slow hydrogen sorption kinetics and high hydriding/dehydriding temperatures. Improvement of the hydrogen storage properties of magnesium is achieved by the method of high-energy ball milling using different types of additives which act as a catalyst during the processes of hydriding/dehydriding. According to many authors, carbon containing additives improve the hydrogen sorption properties of magnesium [1-19]. It has been proven that carbon protects magnesium from oxidation and acts as process controlling agent during ball milling due to its anti-stacking properties [1, 4, 12-14, 19]. In addition, carbon containing additives reduce hydrogen storage temperature and improve the hydrogen sorption kinetics of magnesium based materials [2, 4, 5, 12, 13, 19].

Various carbon containing additives as graphite [1-6, 8-15, 17, 18], activated carbon [1, 6, 20-22], carbon nanomaterial [5, 16], nano diamonds [16],

diamonds [17, 18] carbon from anthracite coal [19], carbon fibers and nanofibers [1, 18], nanotubes [1, 6, 7, 14,17], carbon black [6, 14-16], amorphous carbon soot [16] and amorphous carbon [15, 17] are used as additives to magnesium and MgH₂.

All carbon materials used by Lillo-Rodenas *et al.* [1] decrease the decomposition temperature of MgH₂ and the best results are demonstrated by the mixtures with carbon nanofibres and multi-walled carbon nanotubes. Huot *et al.* [2] reported that graphite additive significantly intensifies the reactive milling synthesis of MgH₂ and improves the hydrogen desorption kinetics. Improvement of hydrogen sorption properties in ball milled MgH₂, using expanded natural graphite and compression in order to form compacted disks, has been observed by Chaise *et al.* [3]. Wu *et al.* [6, 7] found that considerable improvement of the hydrogen storage properties of Mg can be achieved upon mechanical milling of MgH₂ with carbon additives compared with non-carbon materials. Purified single-walled carbon nanotubes (SWNTs) show the most pronounced catalytic effect on the hydrogen storage properties of Mg. The hydrogen absorption capacity and hydriding kinetics of the composites are dependent on the added amount of SWNTs, as well as on the milling time [6, 7]. Several papers by Imamura *et al.* and Montone *et al.* have presented results for the Mg-graphite nanocomposites, prepared by ball milling with different organic additives [8–11]. They suggested the possibility of the formation of new sites for hydrogen storage other

* To whom all correspondence should be sent:
E-mail egeorg@svr.igic.bas.bg

than those due to the magnesium, able to reversibly store hydrogen. Materials synthesized by reactive mechanical milling of magnesium powder, a mixture of Mg-graphite flakes and MgH₂- graphite flakes for different duration, were investigated by Fuster *et al.* [12, 13]. The composite prepared from a mixture of magnesium powder and graphite shows better sorption properties in comparison with a material where graphite is added to MgH₂ already synthesized and mixed by milling. When the additive is homogeneously distributed within the bulk, graphite catalytic activity is more pronounced.

Among the composites with different carbon additives, magnesium with carbon black revealed the best hydriding properties - low temperature of hydriding and relatively fast hydriding kinetics. Spassov *et al.* [16] suggested that the improved sorption properties of this composite are due to the finer particles and the better contact between carbon and MgH₂/Mg particles compared to the other two materials studied. Hydrogen sorption by Mg-based composites with addition of different carbon additives during reactive ball milling was investigated by Rud *et al.* [17]. The use of these types of additives led to a significant increase in hydrogen sorption rate. The formation of MgH₂ during reactive ball milling has been faster for the carbon added materials than for the pure magnesium. Awad *et al.* [18] investigated the desorption reaction of MgH₂ catalyzed by different forms of carbon under microwave irradiation. Rising carbon content, microwave power and milling time resulted in enhancement of dehydrogenation rate.

Despite the numerous results published on addition of carbon to magnesium, the mechanism of carbon additive influence on hydrogen absorption/desorption properties of magnesium is not very clear. The effect of graphite and activated carbons derived from low-cost agricultural by-products on the hydrogen sorption properties of Mg and Mg₂Ni was investigated previously by us and results were published in several papers [4, 20-23]. It was established that the presence of carbon containing additives in the Mg-based composites has positive influence on their hydrogen sorption properties, leading to an enhanced hydriding rate and higher absorption capacity compared to pure magnesium. The aim of the present work was to continue the investigation of the role of carbon containing additives derived from non-expensive and waste products on the hydrogen sorption kinetics of magnesium. Activated carbons derived from apricot stones and from polyolefin wax (a waste product from polyethylene production) were used as additives to MgH₂ and the hydrogen sorption

properties of the composites obtained by ball milling under argon were studied.

EXPERIMENTAL

One of the activated carbons was prepared from apricot stones by steam pyrolysis. Detailed description of the preparation procedure of activated carbon derived from apricot stones can be found in [24]. As for the other activated carbon, it was synthesized from polyolefin wax, a waste product of low-pressure polyethylene production from Burgas petroleum plant, Bulgaria. The polyolefin wax sample was heated to 383 K until melting. Concentrated sulfuric acid was added dropwise under continuous stirring, and the temperature was increased up to 433 K. The obtained solid product was washed with water, dried at 423 K and carbonized at 873 K. POW carbonizate was subjected to water steam activation at 1073 K for 1 h to obtain activated carbon. Textural characterization was carried out by measuring the N₂ adsorption isotherms at 77 K using Quantachrome NovaWin2 porosimeter. The isotherms were used to calculate the specific surface area S_{BET} and the total pore volume V_t. The pore size distribution, micropore and mesopore volumes were obtained by applying the DFT model to the N₂ adsorption data, assuming a slit-shaped pore geometry. The carbon samples were analyzed using the FTIR spectrometer Bruker IFS 113V with resolution of 1 cm⁻¹ and 64 scans. The samples were mixed with potassium bromide (1:1000) and the mixture was pressed into pellets to be used in the analysis.

Composites of MgH₂ (98 % purity, purchased from Alfa Aesar) and 5 wt.% activated carbons, were obtained by ball milling in a planetary mono mill Fritsch Pulverisette 6. The milling was performed under Ar atmosphere using stainless steel balls (diameter 10 mm) and vial (volume ca. 75 cm³), the balls to sample weight ratio being 10:1. The rotation speed was 200 rpm and the grinding duration 30 min. Messer GmbH argon and hydrogen gases with purity of 99.998% and 99.999%, respectively, were used in the experiments. Further in the article, the composites will be denoted as: MgH₂-AS: 95 wt.% MgH₂ - 5 wt.% activated carbon derived from apricot stones; MgH₂-POW: MgH₂ - 5 wt.% activated carbon derived from POW.

The phase composition of the starting compounds, the initial, hydrided and dehydrided composites was controlled with the use of a Bruker D8 Advance X-ray diffractometer (CuK_α radiation).

Additional characterization of the samples was performed by transmission electron microscopy (TEM). The TEM studies were performed on a JEOL

2100 instrument at an accelerating voltage of 200 kV. The specimens were prepared by grinding and dispersing in ethanol followed by an ultrasonic treatment for 6 min. The suspensions were dripped on standard holey carbon/Cu grids.

The hydrogen absorption-desorption properties of the composites were determined by volumetric or Sievert's type apparatus. Hydrogen absorption proceeded at temperatures of 573 K and 473 K and a pressure $P = 1$ MPa. Desorption was carried out at 573 K and 623 K and $P = 0.15$ MPa.

RESULTS AND DISCUSSION

The XRD patterns of the composites 95 wt.% MgH_2 - 5 wt.% AS and 95 wt.% MgH_2 - 5 wt.% POW after ball milling are shown in Fig. 1.

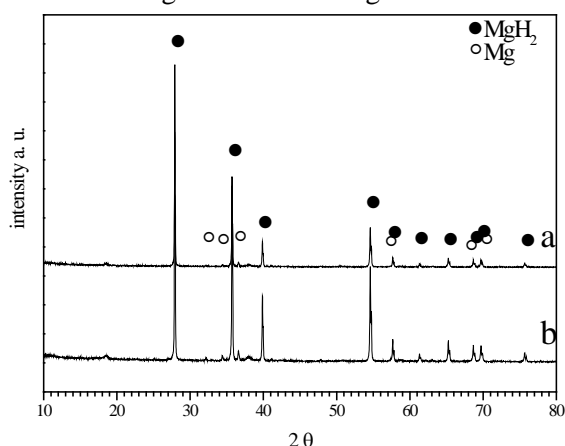


Fig. 1. X-ray diffraction pattern of the composites a) 95 wt. % MgH_2 - 5 wt. % activated carbon from apricot stones and b) 95 wt. % MgH_2 - 5 wt. % activated carbon from polyolefin wax, obtained by ball milling.

Stable β - MgH_2 was detected as the main phase. Small amount of magnesium and no MgO was detected. Probably, even after only 30 min of ball milling some part of MgH_2 was decomposed, because overpressure in the ball milling jar was observed when opened after ball milling. For such a short milling time, e.g. 30 min and at these milling parameters it is not unexpected that no metastable γ - MgH_2 was formed.

The hydrogen absorption curves at 573K and 1 MPa are presented in Fig. 2. Both composites showed very close and overlapping curves in the first 15 min of hydriding. Addition of activated carbon derived from apricot stones resulted in higher absorption capacity of 5.8 wt%. The decrease in the absorption temperature to 473 K led to a slower rate of hydriding and after 1 hour both samples reached an absorption capacity of about 1 wt.%. If we compare our previous result for the composite based on Mg and the same additive, viz. activated carbon derived from apricot stones [20, 21], it is obvious

that the 95 wt% Mg-5 wt% AS has slightly better hydrogen absorption kinetics and higher absorption capacity. Same effect on the hydrogen absorption properties was observed by Fuster et al. [13].

Obviously, the ball milling conditions of their experiments are very different from these used by us, but probably better contact with carbon containing additives can be achieved when the starting material is magnesium. With such short milling time, as applied in this study, no drastic difference in the rates of hydriding of the samples based on magnesium and magnesium hydride can be expected, as can be seen in Fig. 2.

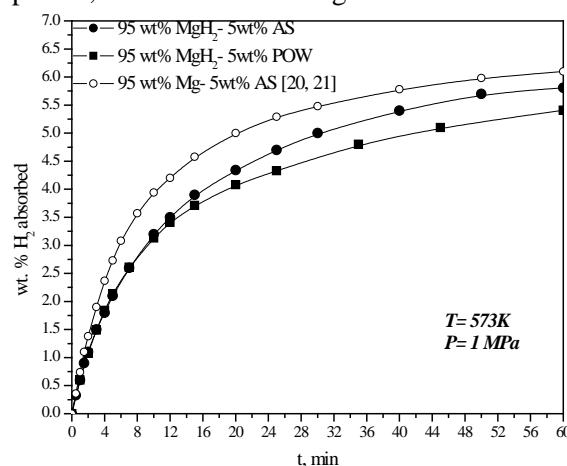


Fig. 2. Kinetic curves of hydrogen absorption by the composites 95 wt. % MgH_2 - 5 wt. % activated carbon from apricot stones and 95 wt. % MgH_2 - 5 wt. % activated carbon from polyolefin wax at $P = 1$ MPa and $T = 573$ K.

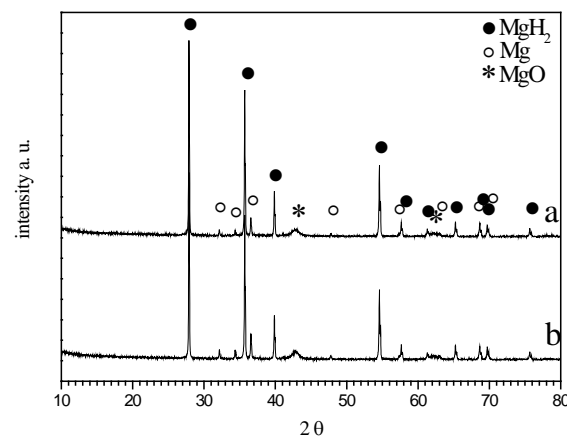


Fig. 3. X-ray diffraction pattern of the composites a) 95 wt. % MgH_2 - 5 wt. % activated carbon from apricot stones and b) 95 wt. % MgH_2 - 5 wt. % activated carbon from polyolefin wax obtained after hydriding at 573 K and 1 MPa and ten cycles.

The XRD patterns after ten cycles of hydriding/dehydriding and hydriding at 573K and 1 MPa are shown in Fig.3. β - MgH_2 was detected as the main phase and the diffraction patterns of both composites did not show substantial difference from these observed for ball milled samples (Fig. 1). Only presence of a minor quantity of MgO was registered.

The appearance of MgO could be explained by the higher surface area obtained and the sensitivity to oxidation after cycling and hydriding.

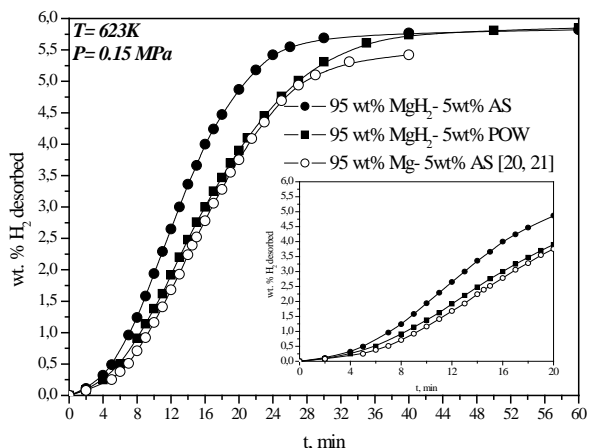


Fig. 4. Kinetic curves of hydrogen desorption from the composites 95 wt. % MgH₂ - 5 wt. % activated carbon from apricot stones and 95 wt. % MgH₂ - 5 wt. % activated carbon from polyolefin wax at P = 0.15 MPa and T = 623 K.

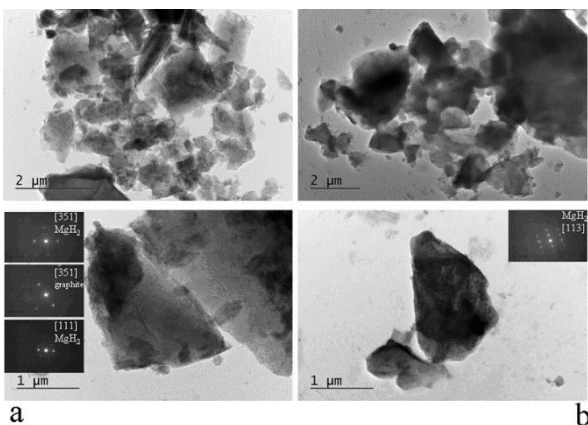


Fig. 5. TEM bright field micrograph and electron diffraction pattern of the composites a) 95 wt. % MgH₂ - 5 wt. % activated carbon from apricot stones and b) 95 wt. % MgH₂ - 5 wt. % activated carbon from polyolefin wax obtained by ball milling.

The fastest desorption rate at 623 K and 0.15 MPa was demonstrated by the composite containing activated carbon derived from apricot stones (Fig. 4). During the first few minutes of desorption all samples showed overlapping curves as it can be seen from the inset graph in Fig. 4. Desorption at a lower temperature of 573 K was not observed. The desorption rate of MgH₂-AS was faster than that published before for Mg-AS [20, 21]. This could be due to the use of MgH₂, which has a higher surface area and is more brittle material.

Table 1. Chemical characterization, BET surface area and pore volume of the activated carbons, determined by N₂ adsorption

Type of activated carbon	S _{BET} m ² /g	Ash ^{mf} wt. %	V _{tot} ^a cm ³ /g	V _{micro} ^b cm ³ /g	V _{meso} ^b cm ³ /g	C ^c wt. %	H ^c wt. %	S ^d wt. %	O ^e wt. %
--------------------------	---------------------------------------	----------------------------	---	---	--	-------------------------	-------------------------	-------------------------	-------------------------

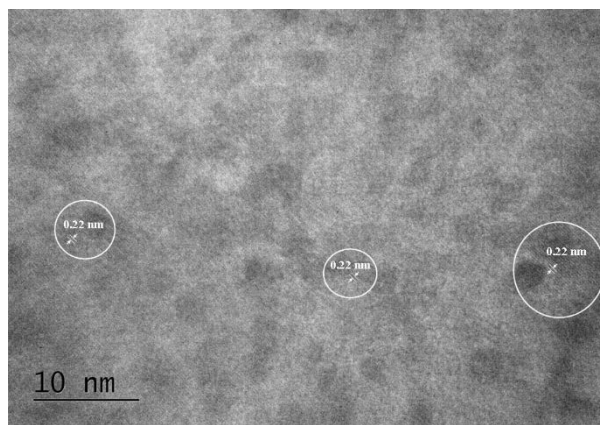


Fig. 6. HTREM image of the composite 95 wt. % MgH₂ - 5 wt. % activated carbon from polyolefin wax obtained by ball milling.

For the activated carbons derived from apricot stones and polyolefin wax the same values of specific surface area were measured, but they differ in some other characteristics. Activated carbon derived from apricot stones has a higher carbon content and a higher micropore volume than activated carbon derived from polyolefin wax (Table 1). The results from IR spectroscopy (figure not shown) demonstrated the presence of oxygen-containing surface groups for both activated carbons [20, 27]. It was shown in the literature that the electrochemical hydrogen storage is favoured in carbon materials with a well developed porosity and a low content of surface oxygen complexes [25]. The functional groups on the surface of the activated carbons, as well as the porosity have a strong effect on the adsorption properties. According to Su *et al.* [26], adsorption capacity of activated carbon for non-polar molecules such as hydrogen, increases with the increase in the amount of surface acidic groups. Additionally, Gergova *et al.* [24] established that a higher amount of surface chemical groups containing oxygen or another heteroatom in activated carbons derived from agricultural by-products, ensures higher concentrations of active sites. Both activated carbons have well developed pore structure and are suitable for the adsorption of small molecules. The activated carbon derived from apricot stones has a higher carbon content and this can probably explain the better hydrogen adsorption/desorption properties as slightly increased hydrogen absorption capacity and faster desorption for MgH₂-AS than for MgH₂-POW.

Activated carbon from apricot stones [21, 24]	800	1.10	0.50	0.36	0.04	95.1	1.3	0.7	1.9
Activated carbon from polyolefin wax	800	0.11	0.60	0.27	0.14	87.4	3.5	0.5	8.6

mf – moisture-free sample; a - evaluated at relative pressures of 0.99; b - evaluated by DFT method applied to N₂ adsorption data using slit-shaped pore model; c - data from combustion elemental analyzer; d - data from Eshka method; e - determined by difference; V_{tot} - total pore volume; V_{micro} - volume of micropores and V_{meso} - volume of mesopores; the chemical composition results are for moisture-free samples

TEM, SAED and HRTEM images of the composites after ball milling are presented in Figs. 4 a, b and Fig 5. The samples consisted of agglomerates and two principal groups of small and large particles. The particle size of the ball milled powders was varied from less than 1 μm to several μm. The composite containing activated carbon derived from apricot stones had finer particles and a separation between them was more clearly observed. MgH₂ well defined hexagonal shaped particles were not visible in contrast to the study of Chi Xue Zhou *et al.* [19]. Probable reason for that was the formation of mixed areas of magnesium hydride and carbon. The single crystal electron diffraction patterns revealed the presence of tetragonal MgH₂, Mg and graphite. The interplanar distance of the lattice fringes of about 0.22 nm belongs to (200) planes of β-MgH₂. Other lattice fringes that were observed are these of MgO - d₂₀₀ = 0.21 nm, Mg - d₁₀₀ = 0.28 nm and graphite - d₀₀₂ = 0.34 nm and d₁₀₀ = 0.21 nm. XRD patterns in Fig. 1 show no presence of MgO in both samples after ball milling, but HTREM detected this phase. Probably MgO content in ball milled composites is below the detection limits of XRD analyses. Only for the sample containing activated carbon derived from apricot stones, mixed areas on the surface containing MgH₂ and graphite were observed by SAED and HTREM. For the sample containing POW, no graphite was detected.

The influence of the carbon additive morphology on its catalytic activity concerning magnesium sorption properties was studied by Fuster *et al.* [13]. They used graphite in form of powder or flakes as an additive to Mg and MgH₂. Sorption rates were practically the same for both samples and they implied that the catalytic activity of graphite does not rely upon its initial microstructure or morphology [13]. In our experiments, as it is seen in Figs. 2 and 4, the effect of magnesium on the hydrogen absorbing properties depends on the starting material - Mg or MgH₂ and also on the type of activated carbon. It was shown that there is no substantial difference in absorption kinetics, but the effect of the additive was more pronounced in the kinetics of desorption. These two additives of activated carbon have different micropore volume,

carbon and oxygen content, which play a role in the absorption of hydrogen.

CONCLUSIONS

Hydrogen sorption properties of 95 wt% MgH₂-5 wt% activated carbon derived from apricot stones-AS or polyolefin wax-POW synthesized by high energy ball milling in argon medium were studied. Probably, because of the short time of ball milling, no formation of γMgH₂ was observed. After 60 min of hydriding at a temperature of 573 K and a pressure of 1 MPa, the composites showed no substantial difference in hydrogen absorption rate and capacity; the one containing AS reached 5.8 wt% *versus* 5.4 wt% for the second one containing activated carbon from POW.

More pronounced positive effect on the hydrogen desorption of MgH₂ was demonstrated by the activated carbon derived from apricot stones. It seems likely that for the investigated composites, after ball milling the activated carbon prepared from apricot stones had better contact with MgH₂, its addition also resulted in finer particles with less agglomerates compared to activated carbon derived from polyolefin wax. Carbon containing additive with high pore volume and higher carbon content has a more favorable effect on the hydrogen sorption characteristics of magnesium.

Acknowledgments: Financial support from the Bulgarian Academy of Sciences and Bulgarian Ministry of Education (Project DFNI-E02/2/2014) is gratefully acknowledged.

REFERENCES

1. M. A. Lillo-Ródenas, Z. X. Guo, K. F. Aguey-Zinsou, D. Cazorla-Amorós, A. Linares-Solano, *Carbon*, **46**, 126 (2008).
2. J. Huot, M.L. Tremblay, R. Schulz, *J. Alloys Compd.*, **356-357**, 603 (2003).
3. A. Chaise, P. de Rango, Ph. Marty, D. Fruchart, S. Miraglia, R. Olivès, S. Garrier, *Int. J. Hydrogen Energy*, **34**, 8589 (2009).
4. J.-L. Bobet, E. Grigorova, M. Khruassanova, M. Khristov, P. Stefanov, P. Peshev, D. Radev, *J. Alloys Compd.*, **366**, 298 (2004).
5. A. D. Rud, A. M. Lakhnik, V. G. Ivanchenko, V. N. Uvarov, A. A. Shkola, V. A. Dekhtyarenko, L. I.

- Ivaschuk, N. I. Kuskova, *Int. J. Hydrogen Energy*, **33**, 1310 (2008).
6. C. Z. Wu, P. Wang, X. Yao, C. Liu, D. M. Chen, G. Q. Lu, H. M. Cheng, *J. Alloys Compd.*, **414**, 259 (2006).
7. C. Z. Wu, P. Wang, X. D. Yao, C. Liu, D. M. Chen, G. Q. Lu, H. M. Cheng, *J. Alloys Compd.*, **420**, 278 (2006).
8. H. Imamura, S. Tabata, N. Shigetomi, Y. Takesue, Y. Sakata, *J. Alloys Compd.* **330-332**, 579 (2002).
9. H. Imamura, S. Tabata, Y. Takesue, Y. Sakata, and S. Kamazaki, *Int. J. Hydrogen Energy* **25**, 837 (2000).
10. H. Imamura, M. Kusuhara, S. Minami, M. Matsumoto, K. Masanari, Y. Sakata, K. Itoh, T. Fukunaga, *Acta Materialia* **51**, 6407 (2003).
11. A. Montone, J. Grbović, A. Bassetti, L. Mirengi, P. Rotolo, E. Bonetti, L. Pasquini, M. Vittori Antisari, *Int. J. Hydrogen Energy*, **31**, 2088 (2006).
12. V. Fuster, G. Urretavizcaya, F. J. Castro, *J. Alloys Compd.* **481**, 673 (2009).
13. V. Fuster, F. J. Castro, H. Troiani, G. Urretavizcaya C, *Int. J. Hydrogen Energy*, **36**, 9051 (2011).
14. Z. Huang, Z. Guo, A. Calka, D. Wexler, H. Liu, *J. Alloys Compd.* **427**, 94 (2007).
15. C. Milanese, A. Girella, S. Garroni, G. Bruni, V. Berbenni, P. Matteazzi, A. Marini, *Int. J. Hydrogen Energy*, **35**, 9027 (2010).
16. T. Spassov, Z. Zlatanova, M. Spassova, S. Todorova, *Int. J. Hydrogen Energy* **35**, 10396 (2010).
17. A. D. Rud, A. M. Lakhnik, *Int. J. Hydrogen Energy*, **37**, 4179 (2012).
18. A. S. Awad, T. Tayeh, M. Nakhl, M. Zakhour, B. Ourane, M. Le Troëdec, J.-L. Bobet, *J. Alloys Compd.*, **607**, 223 (2014).
19. Shixue Zhou, Haipeng Chen, Weixian Ran, Naifei Wang, Zongying Han, Qianqian Zhang, Xiaoli Zhang, Haili Niu, Hao Yu, Di Liu, *J. Alloys Compd.*, **592** 231 (2014).
20. E. Grigorova, Ts. Mandzhukova, M. Khristov, P. Tzvetkov, B. Tsyntsarski, *Bulg. Chem. Commun.*, **42**, 70 (2010).
21. E. Grigorova, Ts. Mandzhukova, B. Tsyntsarski, T. Budinova, M. Khristov, P. Tzvetkov, B. Petrova, N. Petrov, *Fuel Process. Technol.*, **92**, 1963 (2011).
22. Ts. Mandzhukova, E. Grigorova, M. Khristov, B. Tsyntsarski, *Mater. Res. Bull.*, **46**, 1772 (2011).
23. E. Grigorova, M. Spassova, M. Khristov, B. Tsyntsarski, T. Spassov, *J. Therm. Anal. Calorim.*, **116**, 265 (2014).
24. K. Gergova, N. Petrov, S. Eser, *Carbon*, **32**, 693 (1994).
25. M. J. Bleda-Martínez, J. M. Pérez, A. Linares-Solano, E. Morallón, D. Cazorla-Amorós, *Carbon*, **46**, 1053 (2008).
26. Wei Su, Ya-Ping Zhou, Liu-Fang Wei, Yan Sun, Li Zhou, *New carbon materials*, **22**, 135 (2007).
27. I. G. Racheva, B. G. Tsyntsarski, B. N. Petrova, T. K. Budinova, N. V. Petrov, B. Nagel, S. Pusz, U. Szeluga, *Bulg. Chem. Commun.*, **46**, Special Issue A, 129 (2014).

ЕФЕКТ НА АКТИВНИ ВЪГЛЕНИ, ПОЛУЧЕНИ ОТ КАЙСИЕВИ КОСТИЛКИ ИЛИ ПОЛИОЛЕФИНОВ ВОСЪК ВЪРХУ СОРБЦИОННИТЕ СВОЙСТВА ПО ОТНОШЕНИЕ НА ВОДОРОД НА MgH₂

Е. Григорова¹, М. Христов¹, Б. Цинцарски², И. Стойчева², Д. Нихтянова^{1,3}, П. Марков¹

¹ Institute of General and Inorganic Chemistry, Bulgarian Academy of Sciences, bl.11, Acad. G. Bonchev str., 1113 Sofia, Bulgaria

² Institute of Organic Chemistry, Bulgarian Academy of Sciences, bl. 9, Acad. G. Bonchev str., 1113 Sofia, Bulgaria

³ Institute of Mineralogy and Crystallography, Bulgarian Academy of Sciences, Acad. G. Bonchev Str., bl. 107, 1113 Sofia, Bulgaria

Постъпила на 8 октомври 2015 г.; коригирана на 16 май 2016 г.

(Резюме)

Свойствата на хидриране и дехидриране на композити със състав- 95 мас.% MgH₂ - 5 мас. % С, синтезирани с помощта на механоактивиране в атмосфера от аргон с две различни въглерод- съдържащи добавки са изследвани (активен въглен получен от кайсиеви костилки- AS и полиолефинов восък- POW). Двете проби не показват съществена разлика в кинетиката на абсорбция на водород и достигат абсорбиционен капацитет от 5.8 мас.% за 95 мас.% MgH₂- 5 мас. % AS и 5.4 мас. % за 95 мас.% MgH₂- 5 мас. % POW при 573 К и 1 МПа след 60 мин. хидриране. По- висока скорост на десорбция при 623 К и 0.15 МПа показва композита съдържащ активен въглен получен от кайсиеви костилки. Морфологията и фазовият състав на образците са изследвани чрез ТЕМ и XRD.

Spectrophotometric and thermodynamic study on the co-pigmentation interaction between strawberry anthocyanins and quercetin in model systems

I. Petrova¹, V. Shikov², V. Gandova^{1*}, K. Mihalev², D. I. Dimitrov¹

¹University of Food Technologies, Inorganic and Physical Chemistry Department, 4000 Plovdiv, Bulgaria

²University of Food Technologies, Department of Food Preservation and Refrigeration Technology, 4000 Plovdiv, Bulgaria

Received October 26, 2015; Revised September 26, 2016

Changes in the visible spectra of strawberry anthocyanins were studied depending on the addition of quercetin as a co-pigment. The investigations were carried out at different temperatures between 20°C and 50 °C. The solution with a molar pigment:co-pigment ratio of 1:6 exhibits absorption maxima (A_{max}) at 20 and 30 °C; in solutions with molar ratios of 1:8 and 1:10 A_{max} decreases. At temperatures of 40 and 50 °C A_{max} gradually increases with the increase in the concentrations of strawberry anthocyanin and quercetin, accompanied by bathochromic and hyperchromic effects. Experiments were performed at pH=3.4 (0.1 M McIlvaine buffer). The thermodynamic parameters of the system, ΔG , ΔH and ΔS were calculated as a function of temperature.

Keywords: Co-pigmentation, anthocyanins, quercetin, thermodynamics, equilibrium constant

INTRODUCTION

Anthocyanins represent one of the most important and most widespread groups of plant pigments of the class of flavonoids. This group of pigments is responsible for the existence of most of the red, blue, and purple colors in flowers and fruits [1]. Unfortunately, accelerated pigment degradation occurs during conventional processing and storage due to the low total content of strawberry anthocyanins [2] and their inherent heat and light sensitivity [3]. Therefore, retention of strawberry color has always been a technological challenge. Co-pigmentation is regarded today as one of the significant factors of structure stabilization and coloration of anthocyanins under *in vivo* conditions. In the last years, pigment:co-pigment couples were studied by different authors and thermodynamic parameters of the systems were determined. Marcovic *et al.* [4] investigated the process of co-pigmentation of the anthocyanin molecule malvidin with two organic acids - caffeic and ferulic acid by electronic absorption spectroscopy. Equilibrium constant, Gibbs energy and entropy of the co-pigmentation process were calculated. Color intensification of anthocyanin solutions in the presence of natural polyphenols (co-pigmentation) was re-interpreted in terms of charge transfer from the co-pigment to the anthocyanin by Da Silva *et al.* [5]. It was also demonstrated, for a large series of anthocyanin-co-pigment pairs, that the standard Gibbs free energy of complex formation linearly decreases on increasing the difference between the

electron affinity of the anthocyanin, EA(Anthoc), and the ionization potential of the co-pigment, IP(Cop). Co-pigmentation of malvin was investigated by Olivera *et al.* [6] and Baranc *et al.* [7]. The former authors studied a series of naturally occurring colorless organic molecules (co-pigments) by UV-visible absorption and determined the co-pigmentation stability constant. Co-pigment formation was defined by kinetic and thermodynamic parameters obtained by the authors of [7]. Brouillard *et al.* [8] investigated the system caffeoylquinic acid:flavylium cation of malvin chloride (1:1) using visible absorption spectrophotometry. Using UV-vis spectrophotometry, Baranac *et al.* [9] established that a process of co-pigmentation takes place between an anthocyan molecule, malvin chloride and a non-glycosidized pentahydroxyflavone. Oszianski *et al.* [10] investigated the process of co-pigmentation between isolated acylated anthocyanin and rutin. The thermodynamic parameters were related to the structure and position of the substituents in the interacting molecules. Rose petal polyphenols were found as stabilizing agents for strawberry anthocyanins in real beverage systems by Mollov *et al.* [11] and in heated model systems by Shikov *et al.* [12]. Recently, Shikov *et al.* [13-15] investigated canned and frozen fruits and strawberry anthocyanins in model solutions depending on the addition of rose petal polyphenols acting as co-pigments.

No investigation of the system strawberry anthocyanin and quercetin was found in the literature so far. The present study aimed at performing a spectrophotometric investigation on the system

* To whom all correspondence should be sent:

E-mail: gandova_71@abv.bg

pigment:co-pigment to determine its stability at different temperatures using the equilibrium constant of the transfer from the co-pigment to the anthocyanin and other thermodynamic parameters.

EXPERIMENTAL

Chemicals

The co-pigment quercetin dihydrate (97%) was from GmbH&CoAG Company, Germany. The reagents used for preparing the McIlvaine buffer of pH 3.4 - citric acid monohydrate and disodium hydrogen phosphate dodecahydrate - were from Merck (Darmstadt, Germany). The adsorbent resin Amberlite XAD 16N was purchased from Sigma Aldrich Co. (St. Louis, MO, USA). All other reagents and solvents used were of analytical grade.

Extraction, purification and determination of anthocyanins

Strawberry anthocyanins were extracted and purified as described by Shikov *et al.* [12]. Frozen strawberries (*Fragaria×ananassa* Duch. cv. Siabelle, harvest 2014) were thawed and manually squeezed in a beaker. The homogenized purée was extracted overnight at 4 °C using methanol acidified with hydrochloric acid (1%, v/v) at a solvent/solid ratio of 2.5:1 (v/w). The extraction mixture was filtered and the organic solvent was evaporated under vacuum at 30 °C. To remove sugars, salts, and amino acids from the crude extracts, the samples were purified using a column (465 × 30 mm i.d.) filled with the adsorption resin Amberlite XAD 16N. Prior to sample application, the resin was conditioned and equilibrated by rinsing with 500 ml of methanol and 1000 ml of water, and acidified with trifluoroacetic acid (TFA, pH 2). Subsequently, 250 ml of the aqueous strawberry extract were applied and the column was rinsed with 1000 ml of acidified water (pH 2). For elution of the pigments, at least 500 ml of a mixture of methanol and acidified water (TFA, pH 2) (95:5, v/v) was applied until the column was colorless. The organic solvent was evaporated from the eluate under vacuum (30 °C). To separate anthocyanins from colorless phenolics, further purification was performed by extracting the aqueous phase three times with the same volume of ethyl acetate. After evaporation and concentration under vacuum (30 °C), the residue was lyophilized for 72 h.

The total monomeric anthocyanins were assessed by the pH-differential method, as described by Shikov *et al.* [14]. The results were expressed as pelargonidin 3-glucoside equivalents.

Preparation of model solutions

Stock solutions of strawberry extract, on the basis of the total anthocyanins, and quercetin dehydrate, were prepared in McIlvaine buffer (0.1 M, pH 3.4). Model solutions of strawberry anthocyanins (1×10^{-4} M) were obtained by mixing equal volumes (5 ml) of the corresponding stock solutions and were left for equilibration (30 min at 25 °C).

Spectrophotometric measurements

Absorption spectra from 380 to 780 nm were recorded with a Helios Omega UV-Vis spectrophotometer equipped with VISIONlite software (all from Thermo Fisher Scientific, Madison, WI, USA) using 1 cm path length cuvettes.

Before measurements, the samples were thermostated (VEB MLW PRÜFGERÄTE-WERK Medingen, Sitz Freital, Germany) at 20, 30, 40 or 50 °C, respectively.

Statistical analysis

The results reported in the present study are the mean values of at least two determinations and the coefficients of variation were found to be below 2% in all cases. Linear regression analysis was performed using the statistical package of Microsoft Excel.

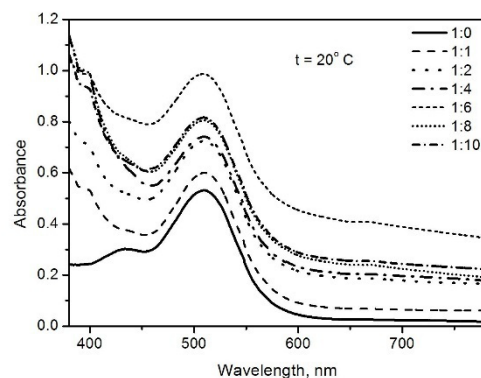
RESULTS AND DISCUSSION

Since the anthocyanin concentration in the model solutions was constant, the spectral variations (Figure 1) caused by the co-pigmentation reaction depended on the concentration of quercetin. Figure 1a presents the system at 20 °C. At this temperature some deviation from the results of co-pigmentation effect at different concentrations appeared. With an increase in co-pigment concentrations no bathochromic effect but only hyperchromic effect appeared. The results of this investigation are presented in Table 1. Da Silva *et al.* [5] studied the system malvin:ferulic acid (pigment:co-pigment) and observed similar results. At a ratio between strawberry anthocyanins and quercetin = 1:6, a large absorption maximum appeared, while with other concentrations of co-pigment and at pigment:co-pigment ratios of 1:8 and 1:10, the absorption maximum decreased. The same effect was observed in the system at a temperature of 30 °C. These results are probably connected with interactions during the co-pigmentation process which stabilized the system at this ratio (1:6). Probably a more stable complex was obtained that decomposed at a higher temperature. In Figure 1b the results of the system strawberry anthocyanins:quercetin at a temperature

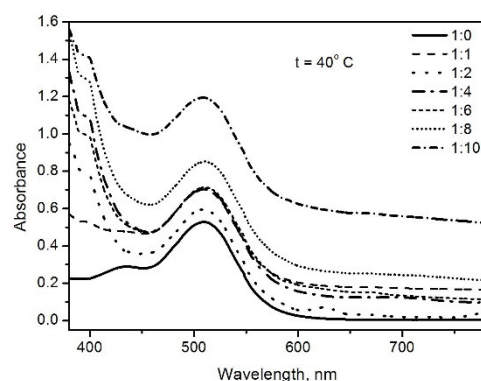
of 40 °C are shown. Co-pigmentation of these molecules at this temperature shows expected results - the absorption maximum increases with the increase inco-pigment concentration. In the studied solutions, bathochromic and hyperchromic effects on the main quercetin absorption peak at 40 and 50 °C are manifested. The respective magnitudes of the bathochromic and hyperchromic shifts at a ratio of 1:10 are observed at a higher temperature.

Table 1. Bathochromic ($\Delta\lambda_{max}$) and hyperchromic ($\Delta A\%$) effects in model solutions of strawberry anthocyanins and quercetin at different molar ratio pigment/co-pigment

Molar ratio pigment/co-pigment	$\Delta\lambda_{max}$	$\Delta A\%$
$t = 20\text{ }^{\circ}\text{C}$		
1:0	-	-
1:1	0	10.7
1:2	0	37.5
1:4	0	58.8
1:6	1	72.3
1:8	0	49.1
1:10	1	58.8
$t = 30\text{ }^{\circ}\text{C}$		
1:0	-	-
1:1	1	12.5
1:2	0	52.3
1:4	0	54.3
1:6	1	87.6
1:8	1	74.2
1:10	1	54.3
$t = 40\text{ }^{\circ}\text{C}$		
1:0	-	-
1:1	2	43.4
1:2	2	12.9
1:4	1	34.3
1:6	2	35.2
1:8	2	61.4
1:10	1	107.4
$t = 50\text{ }^{\circ}\text{C}$		
1:0	-	-
1:1	1	37.0
1:2	1	16.9
1:4	3	31.1
1:6	3	22.6
1:8	3	38.4
1:10	1	140



1 a)



1 b)

Fig.1. Absorption spectra of purified strawberry anthocyanins in model solutions with added quercetin at different pigment:co-pigment molar ratios (1:0, 1:1, 1:2, 1:4, 1:6, 1:8 and 1:10) at 20 °C (a) and 40 °C (b).

The equilibrium constant K and the thermodynamic parameters: Gibbs free energy, enthalpy and entropy for the co-pigmentation reaction, are presented in Table 2. The constant was calculated using the following equation: $\ln[(A - A_0)/A_0] = \ln[K] + n \times \ln[C]$, where A and A_0 are the absorption maximum values of the anthocyanin solution with and without added co-pigment, respectively; C is the molar co-pigment concentration; K is the equilibrium constant and n is the stoichiometric ratio of the reaction [16]. The dependence of $\ln[(A - A_0)/A_0]$ on the co-pigment concentration, $\ln[(A - A_0)/A_0] = f(\ln[C])$, is a straight line with a slope and intercept equal to n and $\ln[K]$, respectively.

The equilibrium constant exhibited different values at different temperatures.

The thermodynamic parameters: Gibbs free energy, enthalpy and entropy were calculated using the following equations [17]:

$$\Delta G = -RT \ln K_p \quad (1)$$

where R is the universal gas constant ($R = 8.314 \text{ J K}^{-1} \text{ mol}^{-1}$), T is the absolute temperature (K), ΔG is

Gibbs free energy (kJ mol^{-1}), K – equilibrium constant.

The enthalpy was calculated by the Van't-Hoff equation:

$$\frac{d \ln K}{d(1/T)} = \frac{-\Delta H}{R} \quad (2)$$

ΔH is the enthalpy for the co-pigmentation reaction (kJ mol^{-1}).

Once the Gibbs free energy and the enthalpy were obtained, the entropy was determined by the classical thermodynamic equation (3):

$$\Delta S = \frac{(\Delta H - \Delta G)}{T} \quad (3)$$

ΔS is the entropy for the co-pigmentation reaction ($\text{kJ K}^{-1} \text{mol}^{-1}$).

At 30 °C the constant showed the highest value. At the same temperature the Gibbs energy exhibited the highest value $-22.105 \text{ kJ mol}^{-1}$. This result shows that the system is most stable at 30 °C. At temperatures above 30 °C, the stability decreased and interactions between pigment and co-pigment slowed down. At all temperatures negative Gibbs energies were calculated. These results are connected with the spontaneous process of co-pigmentation leading to formation of the products. On the basis of Gibbs energy changes (Table 2) at the four temperatures it can be concluded that the process of co-pigmentation is possible only at temperatures up to 30 °C.

With temperature increase the permanent degradation of the co-pigment does not regenerate upon cooling. There is no reversibility of the co-pigmentation in the malvin-quercetin system, contrary to the malvin-rutin system [9]. In this work the same results were observed as in the malvin-quercetin system [9]. The enthalpy and entropy changes of the process were also negative at all temperatures. It can be concluded that such a dependence on temperature is a consequence of the exothermic co-pigmentation process, $\Delta H^\circ < 0$. The negative value of the entropy, ΔS , indicates that co-pigment formation establishes greater order in the system.

Figures 2-4 present the thermodynamic parameters as depending of different parameters.

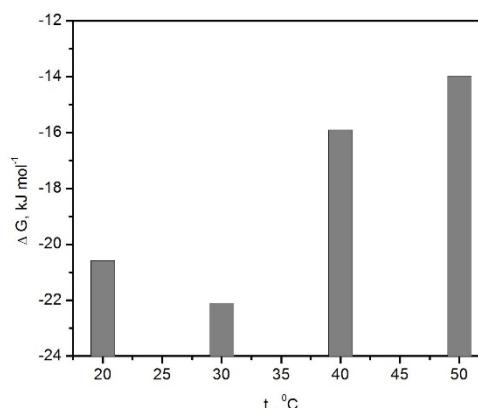


Fig. 2. Temperature dependence of Gibbs free energy for the co-pigmentation interaction between strawberry anthocyanins and quercetin.

The graphical view of Gibbs free energy dependence on the temperature is presented in Figure 2. The stability of the system is determined by the decrease in Gibbs energy to a minimal negative value. On the figure the minimal value is observed at 30 °C. The second temperature close to the first one was 20 °C. At the other two temperatures, 40 and 50 °C, the Gibbs energy increased to positive values, which is connected to the break-down of the pigment: co-pigment bond and destroying of the system.

In Figure 3 a good correlation between Ln of the equilibrium constant and different temperatures is observed. The spots exhibit linear dependence with a deviation at 30 °C due to the increase in the equilibrium constant at this temperature. According to Brouillard *et al.* [18] the temperature has a major influence on the degradation kinetic plots of $\text{Ln}(K)$ against $1/T$ (K^{-1}) for each of the Hibiscus anthocyanins. These experimental results confirm that with increase of temperature, Gibbs free energy increases to positive values too. Figure 4 presents the linear dependence between enthalpy and entropy change in the strawberry anthocyanins:quercetin system.

Table 2. Equilibrium constants and thermodynamic parameters for the co-pigmentation interaction between strawberry anthocyanins and quercetin at different temperatures and stoichiometric ratio $n=1.1:1$.

T, °C	K [M^{-1}]	ΔG [kJ mol^{-1}]	ΔH [kJ mol^{-1}]	ΔS [$\text{kJ K}^{-1} \text{mol}^{-1}$]
20	4677.351	-20.585	-25.992	-0.0184
30	6456.542	-22.105	-27.232	-0.0169
40	449.883	-15.897	-25.121	-0.0294
50	181.970	-13.974	-24.867	-0.0337

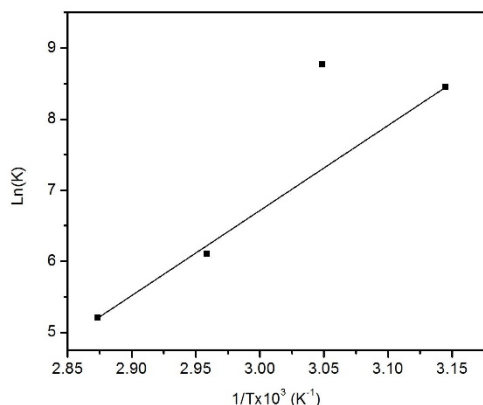


Fig.3. Plot of $\ln(K)$ for the co-pigmentation interaction between strawberry anthocyanins and quercetin as a function of reciprocal temperature.

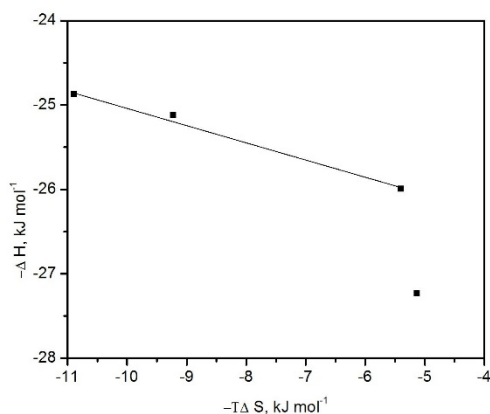


Fig.4. Plot of enthalpy-entropy compensation for the co-pigmentation interaction between strawberry anthocyanins and quercetin.

Similarly, the looser contact between pigment molecules and co-pigments, suggests enthalpy-entropy compensation. The compensation temperature was 30 °C and at this temperature the maximum value of enthalpy was observed, connected with deviation of the straight line.

CONCLUSIONS

In this study, the thermal stability of isolated strawberry anthocyanins was examined in model solutions in the presence of quercetin as a co-pigment at four temperatures. The study in the temperature range 20–50 °C revealed that the system was most stable at 30 °C. This result is connected with the Gibbs free energy determined which exhibits the lowest negative value at the same temperature. Based on the experimental and calculated results of this work, further studies would be necessary for finding out appropriate processing conditions in small temperature intervals. More

efficient utilization of this pigment is topical for food products.

Acknowledgements: We are grateful to Cima 99 Ltd. (Striama, Bulgaria) for providing the frozen strawberries.

REFERENCES

1. J.B. Harborne, *Comperative Biochemistry of the Flavonoids*, Academic Press: London, 1967, Chapter 1.
2. M.N. Clifford, *Journal of the Science of Food and Agriculture*, **80**, 1063 (2000).
3. K. Hayashi, N. Ohara, A. Tsukui, *Food Science and Technology International*, **2**, 30 (1996).
4. J. M. Markovic, N. A. Petranovic, J. M. Baranac, *J. Agric. Food Chem.*, **48**, 5530 (2000).
5. P.F. da Silva, J.C. Lima, A.A. Freitas, K. Shimizu, A. L. Macüanita, F. H. Quina, *J. Phys. Chem. A*, **109**, 7329 (2005).
6. O. Dangles, R. Brouillard, *Canadian Journal of Chemistry*, **70**(8), 2174 (1992).
7. J.M. Baranac, N. A. Petranovic, J. M. Markovic. *J. Agric. Food Chem.*, **44**, 1333 (1996).
8. R. Brouillard, G. Mazza, Z. Saad, A.M. Albrecht-Gary, A. Cheminatt, *J. Am. Chem. Soc.*, **111**(7), 2604 (1989).
9. J.M. Baranac, N.A. Petranovic, J.M. Markovic, *J. Agric. Food Chem.*, **45**(5), 1694 (1997).
10. J. Oszmianski, A. Bakowska, S. Piacente, *J. Sci. Food Agric.*, **84**, 1500 (2004).
11. P. Mollov, K. Mihalev, V. Shikov, N. Yoncheva, V. Karagyozov. *Innovative Food Science and Emerging Technologies*, **8**, 318 (2007).
12. V. Shikov, D. R. Kammerer, K. Mihalev, P. Mollov, R. Carle, *Journal of Agricultural and Food Chemistry*, **56**, 8521 (2008).
13. V. Shikov, D. R. Kammerer, K. Mihalev, P. Mollov, R. Carle, *Food Research International*, **46**, 552 (2012).
14. [14] V. Shikov, K. Mihalev, N. Yoncheva, V. Karagyozov, P. Mollov, *Journal of EcoAgriTourism*, **8**, 231 (2012).
15. V. Shikov, D. Kammerer, K. Mihalev, P. Mollov, R. Carle, *Scientific Works UFT*, **LX**, 722 (2013).
16. R. Brouillard, *Phytochemistry*, **22**, 1311 (1983).
17. S. K. Máté, K. Szabó, M. P. Nikfardjam, L. Kollár, *J. Biochem. Biophys. Methods*, **69**, 113 (2006).
18. R. Brouillard, O. Dangles, *Food Chemistry*, **51**, 365 (1994).

СПЕКТРОФОТОМЕТРИЧНО И ТЕРМОДИНАМИЧНО ИЗСЛЕДВАНЕ НА КО-ПИГМЕНТАЦИОННИ ВЗАИМОДЕЙСТВИЯ МЕЖДУ АНТОЦИАНИ ОТ ЯГОДИ И КВЕРЦЕТИН В МОДЕЛНИ СИСТЕМИ

И. Петрова¹, В. Шиков², В. Гандова^{1,*}, К. Михалев², Д. И. Димитров¹

¹ *Университет по Хранителни технологии, катедра „Неорганична химия и физикохимия”, 4000 Пловдив, България*

² *Университет по Хранителни технологии, катедра „Консервиране и хладилна технология”, 4000 Пловдив, България*

Постъпила на 26 октомври 2015 г.; коригирана на 26 септември 2016 г.

(Резюме)

Изследвана е промяната на видимите спектри на антоциани от ягоди с добавка на кверцетин, като ко-пигмент. Изследванията са проведени при различни температури от 20 до 50 °С. В разтвора приготвен с моларно съотношение 1:6 пигмент:ко-пигмент са измерени максимални абсорбции при температури 20 и 30 °С, а в другите два разтвора 1:8 и 1:10 стойностите на измерената абсорбция намаляват. При другите две температури 40 и 50 °С, измерената абсорбция се повишава с повишаване на концентрацията на разтворите, като са наблюдавани хиперхромен и батохромен ефекти. Експериментите са проведени при рН=3.4 (0.1 М Буфер на Макливайн). Пресметнати са термодинамичните параметри на системата ΔG , ΔH и ΔS като функция на температурата.

Investigation of the vapor-sensitive properties of zinc oxide layers by impedance spectroscopy

S. S. Nalimova¹, I. E. Kononova¹, V. A. Moshnikov^{1,3}, D. Tz. Dimitrov^{2*}, N. V. Kaneva²,
L. K. Krasteva², S. A. Syuleyman², A. S. Bojinova², K. I. Papazova², A. Ts. Georgieva⁴

¹*Department of Micro- and Nanoelectronics, Saint-Petersburg State Electrotechnical University, Saint-Petersburg 197376, Russia*

²*Laboratory of Nanoparticle Science and Technology, Department of General and Inorganic Chemistry, Faculty of Chemistry and Pharmacy, University of Sofia, Sofia 1164, Bulgaria*

³*Department of Integrated Electronics, Peter the Great Saint-Petersburg Polytechnic University, Saint-Petersburg 195251, Russia*

⁴*Department of Materials Science & Engineering, University of Florida, Gainesville, FL 32611, USA*

Received November 4, 2015; Revised June 27, 2016

In the field of gas sensory research, metal oxide layers are used as sensitive elements of semiconductor adsorption gas sensors. In this work samples of ZnO were prepared by the sol-gel method with variation of the annealing temperature from 100 to 500 °C. The microstructure of the surface of the obtained samples was investigated by atomic force microscopy. The sensitivity of the samples to the vapors of acetone and ethanol was investigated by the method of impedance spectroscopy. For interpretation of the obtained results an electric equivalent R-CPE circuit was used. The ZnO sample produced by annealing at 300 °C exhibited maximum sensitivity to both vapors. Addition of Fe to the ZnO sample annealed at 500 °C led to an increase in the sensitivity to the vapors of acetone and ethanol due to the increased concentration of reducing vapor adsorption sites.

Keywords: Impedance spectroscopy, zinc oxide; gas sensors; sol-gel method.

INTRODUCTION

Various metal-oxide materials as SnO₂, ZnO, Fe₂O₃, WO₃, Co₃O₄, etc., are used as sensitive materials in metal-oxide semiconductor gas sensors. Their operating principle is based on increasing the sensitive element conductivity in the surface region as a result of sorption of the analyzed gas. Depending on the composition of the sensitive layer, the sensor reacts with different vapors and gases as C₂H₅OH, CO, CH₄, H₂, O₂, etc. The operating temperature is within the range from 200 °C to 500 °C.

Sensitive layers for gas sensors are based on a significant number of materials and technologies. In modern sensor technology gas-sensitive layers are prepared using metal oxides having electron conductivity, such as SnO₂, In₂O₃, ZnO, Fe₂O₃, CuO, TiO₂, WO₃ and Co₃O₄. The principle of operation, based on metal oxide layer semiconductor gas sensors [1– 4], is the reversible change in the electrical properties during the charged oxygen species adsorption and desorption of reaction products as a result of the interaction with the molecules of reducing gases at elevated operating temperatures, usually within the range from 200 °C to 500 °C. In gas sensory research tin

dioxide is the most studied material [5]. However, ZnO is also suitable for use in this field due to the possibility to vary its resistance in a broad range, its high chemical stability, and low toxicity. Nowadays, a variety of methods is used for the preparation of nanostructured layers of ZnO, such as spray pyrolysis [6], chemical vapor deposition [7], magnetron sputtering [8], hydrothermal method [9], sol-gel technique [10–15]. The sol-gel method allows easy control over the structure of the obtained materials by varying the technological conditions of the process, such as the choice of solvent and precursor, the aging time of the sol, etc. For example, in [14], porous layers based on zinc oxide are produced by the sol-gel method and it is shown that the pore size depends on the concentration of zinc nitrate in solution.

The aim of this paper is to investigate the sensitivity of semiconductor nanomaterials based on ZnO prepared by the sol-gel method under the conditions of a gaseous medium in an alternating electric field.

EXPERIMENTAL

Four types of samples were obtained by the sol-gel method (Table 1).

* To whom all correspondence should be sent:
E-mail: dimitrov2001@yahoo.com

Table 1. Conditions of preparation of sols and corresponding samples

Type of sample	Composition of sample	Used precursors	Annealing temperature, °C
I			100
II	ZnO	Zn(CH ₃ COO) ₂ ·2H ₂ O	300
III			500
IV	ZnO-Fe	Zn(CH ₃ COO) ₂ ·2H ₂ O, Fe(NO ₃) ₃ ·9H ₂ O	500

Table 2. Parameter values of relaxators in air and in the presence of reactant gases

Type of sample	Atmosphere	f _{max} , kHz	τ, μsec	R, kOhm	R _{air} /R _{gas}	A _{air} /A _{gas}
I	Air atmosphere	11.233	14.17	434.1		
	In the presence of acetone vapor	486.26	0.33	15.7	27.6	3.1
	In the presence of ethanol vapor	46.416	3.43	125.4	3.5	1.5
II	Air atmosphere	5.094	31.24	1100		
	In the presence of acetone vapor	162.975	0.98	50.9	21.6	2.0
	In the presence of ethanol vapor	34.305	4.64	218.4	5.0	1.7
III	Air atmosphere	6.734	23.63	955		
	In the presence of acetone vapor	22.051	7.22	248	3.9	1.1
	In the presence of ethanol vapor	19.630	8.11	278	3.4	1.1
IV	Air atmosphere	2.656	59.92	1150.7		
	In the presence of acetone vapor	57.224	2.78	140.7	8.2	3.3
	In the presence of ethanol vapor	26.561	5.99	273.3	4.2	2.9

Table 3. Sensitivity of the sample in an alternating electric field to acetone and ethanol vapors

Sample type	Atmosphere	maxS _{Re}	f, Hz	maxS _{Im}	f, Hz
I		25.8	1384	536.0	2984
II	In the presence of acetone vapor	30.9	5995	9457.7	6734
III		3.8	1149.8	15.3	1385
IV		7.9	2257	126.8	1707
I	In the presence of ethanol vapor	3.3	1233	15.5	1385
II		4.7	1520	35.8	1592
III		3.2	1098	12.4	1123
IV		4.1	1707	22.2	1831

The first three types of samples were produced from sols and Zn(CH₃COO)₂·2H₂O precursor [16, 17]; for the fourth type of samples, Zn(CH₃COO)₂·2H₂O was used as a precursor and Fe(NO₃)₃·9H₂O was subsequently added [18]. Precursors were dissolved in 2-methoxyethanol. Monoethanolamine was added as a surfactant. For the fourth type of sample the mole fraction of iron nitrate in the film was chosen to be 0.5 %. All films were annealed for 1 h at fixed temperatures, as listed in Table. 1. The film thickness was kept about 1.5 μm.

The microstructure of the surface of zinc oxide layers, prepared by the sol-gel method, was investigated using atomic force microscopy (NTEGRA Thermo, NT-MDT) in semi-contact mode [19, 20].

Investigation of the electrical properties of the produced samples was performed by the method of impedance spectroscopy [21], which was a tool for investigation of electrical properties on the

interface based on the study of the influence of an electrical field with variable frequency.

Measurement of the frequency dependence of the module of complex resistivity and phase shift angle between current and voltage in the capacitor circuit was carried out in the frequency range from 100 Hz to 500 kHz. The experiment was carried out in a laboratory installation [22], providing opportunities for investigation of samples by the method of impedance spectroscopy under changing gas environment (in an air atmosphere, in the presence of vapors of ethanol and acetone at a concentration of 1000 ppm at the temperature of measurement of 300 °C).

For processing of impedance spectroscopy experimental data, the complex plane method was used. As a complex number, the impedance is represented as the dependence of the imaginary component as a function of the real one (Nyquist plot).

RESULTS

The results of the investigation of the surface morphology of the samples, produced by variation of the annealing temperature and the composition of the material, are shown in Figures 1 and 2. It was found that increasing the annealing temperature from 100 °C to 300 °C resulted in an increase in the average particle size from 10 to 100 nm and during annealing at a temperature of 500 °C aggregation of nanoparticles into larger objects of elongated shape occurred.

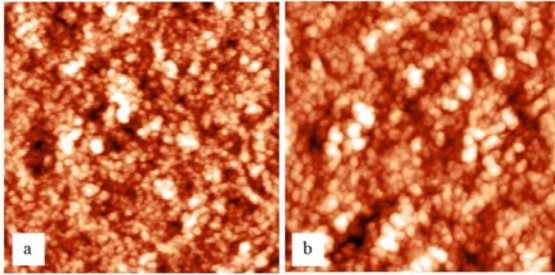


Fig. 1 a

Fig. 1 b

Fig. 1. AFM images of zinc oxide layers, prepared by the sol-gel method at various annealing temperatures: a - 100°C; b - 300°C. Scan size area of 10×10 μm².

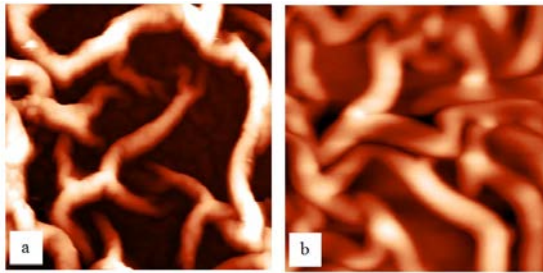


Fig. 2 a

Fig. 2 b

Fig. 2. AFM images of layers, prepared by the sol-gel method at annealing temperature of 500°C: a - ZnO; b – ZnO with the addition of Fe. Scan size area of 10×10 μm².

The investigations of the frequency dependence of the real ReZ and the imaginary ImZ components of the complex impedance were performed by plotting it in semi-logarithmic coordinates for an atmosphere of air and vapors of ethanol and acetone at a detection temperature of 300 °C. As an illustrative example, in Fig. 3 the frequency dependence of both, ReZ (Fig. 3a) and ImZ (Fig. 3b) components is shown in an air atmosphere and in the presence of vapors of acetone and ethanol for a sample of III type. On the plot of the reactive component of the complex impedance, (shown in Fig. 3b), a relaxation maximum is observed satisfying the condition $\omega\tau = 1$, where ω is the angular frequency for the maximum value of the reactive component of complex impedance (relaxation maximum point on the hodograph of the

impedance), τ is the relaxation time of polarization (characteristic charge accumulation time). The value of the characteristic charge accumulation time is inversely proportional to the angular frequency ($\tau = 1/\omega = 1/2\pi f_{\max}$, where f_{\max} - frequency corresponding to the position of the relaxation maximum).

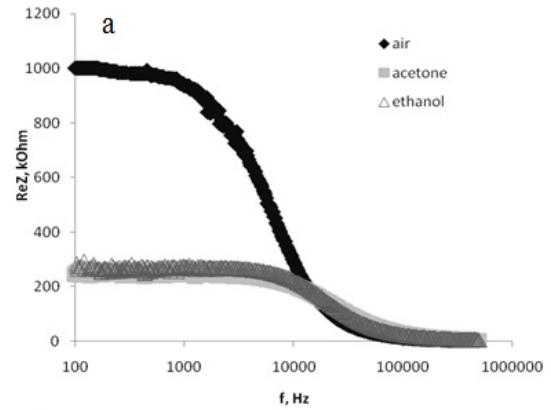


Fig. 3 a

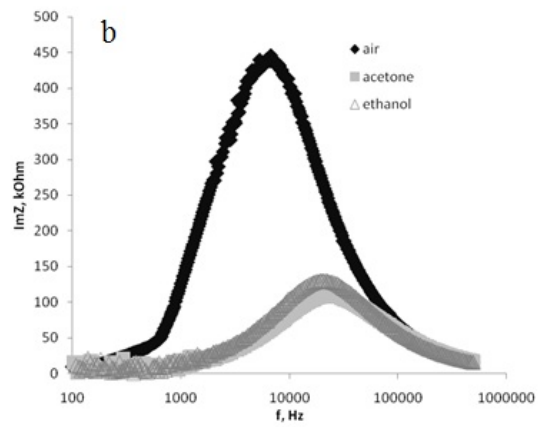


Fig. 3 b

Fig. 3. The frequency dependence of the components of the complex impedance of the sample of type III: a - real component; b - imaginary component.

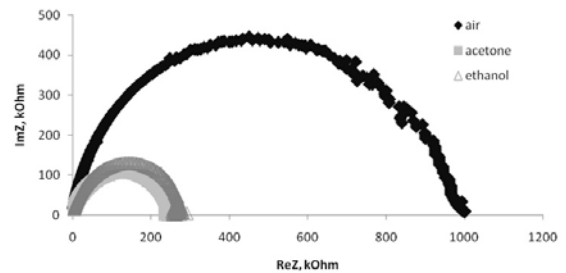


Fig. 4

Fig. 4. Nyquist diagrams for the sample of type III.

A Nyquist diagram in air and in the presence of reducing gas vapors for the sample of type III is shown in Fig. 4. It reveals that the center of the semicircle in the detection of gas shifts to higher frequencies. This is due to the shift of the relaxation maximum in the frequency dependence of the reactive component of the impedance at higher frequencies.

Impedance spectroscopy data obtained in this work are interpreted in terms of "equivalent electrical circuit". To describe the resistive-capacitive properties of the materials in the equivalent circuit the constant phase element (CPE) was used due to the fact that the centers of the semicircles on the complex plane are lying below the x-axis. The choice of the equivalent circuit elements was due to the fact that the samples are characterized by a set of relaxation times. The impedance of a constant phase element is described

by the formula: $Z = 1/A(j\omega)^n$, where A is the factor of proportionality, n is the exponential index indicating the phase deviation within the range $-1 \leq n \leq 1$, ω is the angular frequency, j is the imaginary unit. The pre-exponential frequency-independent factor has the dimension of capacitance. It was revealed that the value of the exponential index in air and in the presence of reactant gases is 0.82 – 0.99.

The spectroscopic data were interpreted by using LabVIEW media with a parallel R – CPE chain, where R is the resistance of the relaxator. The R – CPE chain is associated with the region characterizing the grain boundary of zinc oxide particles.

The value of the sensitivity toward reducing gases at a temperature of 300 °C in the detection frequency range from 100 Hz to 500 kHz was calculated in two ways: by the real component: $S_{Re} = ReZ_{air}/ReZ_{gas}$, where ReZ_{air} is the real component of the complex impedance in air, ReZ_{gas} is the real component of the impedance in the presence of reactant gas; and by the imaginary component: $S_{Im} = ImZ_{air}/ImZ_{gas}$, where ImZ_{air} is the imaginary component of the complex impedance in air, ImZ_{gas} is the imaginary component of the impedance in the presence of reactant gas.

The influence of annealing temperature and added iron to the gas sensing properties of nanomaterials is discussed in details in the next section.

DISCUSSIONS

It was revealed that the relaxation time, associated with the contact area of the particles (grain boundaries), was very sensitive to changes in the environment and resulted in a 3.4 - 42.9 fold decrease depending on the annealing temperature of the samples (Table 2). It was established that with an increase in annealing temperature of the samples from 100 °C (I type samples) to 500 °C (III type sample) the characteristic charge accumulation time increases 1.7 times in air, 21.8 times in the presence of acetone vapor, and 2.4 times in the presence of ethanol vapor (Table 2).

It is shown that on adding iron (IV type samples) to samples annealed at 500 °C (III type samples), the characteristic charge accumulation time increases 2.5 times in air, while it decreases 2.6 times and 1.4 times in the presence of vapors of acetone and ethanol, respectively (Table 2).

In this way it was revealed that for the samples, produced in the presence of reducing reactant vapors the value of the frequency-independent pre-exponential factor (the minimal and maximal values of A_{air}/A_{gas}) decreases 1.1-3.3 times, while the resistance of the grain boundaries of the particles (R_{air}/R_{gas}) - 3.1-27.6 times, calculated for all samples (Table. 2). The reasons for the decreasing values are considered to be the combined effect of the reduction of the charge depletion region at the grain boundary, the modulation of current flow channels and the recharge of surface states.

It was revealed that the maximum sensitivity is observed for type II samples annealed at 300 °C. The sensitivity of this type of samples towards acetone vapor was 30.9 at a frequency of 5995 Hz by the real component of the complex impedance and 9457.7 by the calculated imaginary component at a frequency of 6734 Hz. The sensitivity was lower towards ethanol vapor, but still significant. It was 4.7 by the real component of the complex impedance at the frequency of 1520 Hz and 35.8 by the imaginary component at a frequency of 1592 Hz (Table 3).

It was established that adding of iron (IV type samples) to the samples annealed at 500 °C (III type samples) increased the sensitivity to ethanol vapor by a factor of 1.3, evaluated by the real component of the complex impedance and by a factor of 1.8 calculated by the imaginary component. At the same time, the sensitivity to acetone vapor evaluated by the real component of the complex impedance increased by a factor of 2.1 and by a factor of 8.3 calculated by the imaginary component (Table 3). This result could be

explained by means of the model of interaction of reducing gases with metal oxides developed by our team [23].

According to our model, the increase in gas sensitivity can be achieved by using multicomponent metal oxides as sensor materials. This is done by careful selection of oxide components, taking into account their redox and acid-base properties. The effect of increasing the sensitivity of the composite materials based on ZnO-Fe₂O₃ to the vapors of acetone and ethyl alcohol in comparison with Fe₂O₃ and ZnO alone, was investigated experimentally in our work [24]. It was confirmed beyond any doubt that increasing of the concentration of reducing vapor adsorption sites (metal cations and acid OH-groups) on the surface of the composite material is responsible for the increase in sensitivity.

In summary, the observed dependence of the properties of samples of type I, II, III, based on pure zinc oxide gas-sensitive layer, as a function of annealing temperature could be explained by their specific morphological and structural characteristics. For the sample of type I the annealing temperature of 100 °C is not sufficient for the formation of the crystal structure of zinc oxide and complete evaporation of the organic components of the initial solutions. For the sample of type II the annealing temperature of 300 °C causes formation of zinc oxide particles of a size about 100 nm. For the sample of type III the annealing temperature of 500 °C causes association of the particles in micrometer-sized objects. This causes a reduction of the surface area available for surface-vapor interaction.

CONCLUSIONS

The gas-sensitive properties of samples based on zinc oxide were investigated by impedance spectroscopy at a detection temperature of 300 °C. It is revealed that during vapor detection the center of the semicircle at the Nyquist diagrams shifts to the higher frequencies region.

The data obtained by spectroscopic measurement were interpreted by using parallel R – CPE - chains. Those R – CPE - chains are associated with the region which characterizes the grain boundaries of zinc oxide particles. It was found that the values of the exponential index, the relaxation time, the pre-exponential frequency-independent factor and the resistance of the grain boundaries of the particles are very sensitive to the changes in air conditions.

It is shown that the sample of pure ZnO annealed at 300 °C has the maximum sensitivity

values to acetone and ethanol vapors. That fact is explained by the smaller particle size and structural perfection of the zinc oxide layers obtained in these synthesis conditions. It was found that the sensitivity values of ZnO samples with added Fe annealed at 500 °C to both acetone and ethanol vapors are higher than those of pure ZnO. This can be associated with complementary redox and acid-base properties of ZnO and Fe₂O₃.

Acknowledgements: Researchers from Sofia University are thankful to Beyond Everest project FP7-REGPOT-2011-1 for financial support. Russian researchers express their gratitude to the grant of Russian Science Fund (project №14-15-00324).

REFERENCES

1. S. Reiser, B. Schneider, H. Geissler, M. van Gompel, P. Wagner, M. J. Schöning, *Phys. Stat. Solidi (a)*, **210**, 898 (2013).
2. M.A. Carpenter, S. Mathur, A. Kolmakov, *Metal Oxide Nanomaterials for Chemical Sensors*, Springer Science+Business Media, New York, 2013.
3. W. Gopel, *Sens. Actuators*, **16**, 167 (1989).
4. Y.-F. Sun, S.-B. Liu, F.-L. Meng, J.-Y. Liu, Z. Jin, L.-T. Kong, J.-H. Liu, *Sensors*, **12**, 2610 (2012).
5. G. Korotcenkov, M. DiBattista, J. Schwank, V. Brinzari, *Mater. Sci. Eng.*, **77**, 33 (2000).
6. O. Dimitrov, D. Nesheva, V. Blaskov, I. Stambolova, S. Vassilev, Z. Levi, V. Tonchev, *Mater. Chem. Phys.*, **148**, 712 (2014).
7. K.H. Nam, H. Kim, H.Y. Lee, D.H. Han, J.J. Lee, *Surf. Coat. Technol.*, **202**, 5463 (2008).
8. K. Chen, K.S. Chiang, H.P. Chan, P.L. Chu, *Optic. Mater.*, **30**, 1244 (2008).
9. H. Zhou, H. Zhang, Y. Wang, Y. Miao, L. Gu, Z. Jiao, *J. Coll. Inter. Sci.*, **448**, 367 (2015).
10. C.J. Brinker, G.W. Scherer, *Sol-Gel Science. The Physics and Chemistry of Sol-Gel Processing*, Academic Press, San Diego, 1990.
11. S. Sakka (ed.), *Handbook of sol-gel science and technology: processing, characterization, and applications*, Kluwer Academic Publishers, New York, 2005.
12. I.E. Gracheva, V.A. Moshnikov, E.V. Maraeva, S.S. Karpova, O.A. Aleksandrova, N.I. Alekseyev, V.V. Kuznetsov, G. Olchowik, K.N. Semenov, A.V. Startseva, A.V. Sitnikov, J.M. Olchowik, *J. Non-Cryst. Sol.*, **358**, 433 (2012).
13. V.A. Moshnikov, I.E. Gracheva, V.V. Kuznetsov, A.I. Maximov, S.S. Karpova, A.A. Ponomareva, *J. Non-Cryst. Sol.*, **356**, 2020 (2010).
14. I. E. Gracheva, V. A. Moshnikov, S.S. Karpova, E. V. Maraeva, *J. Phys.: Conf. Series*, **291**, 012017 (2011).
15. V.A. Moshnikov, I.E. Gracheva, A.S. Lenshin, Y. M. Spivak, M. G. Anchkov, V.V. Kuznetsov, J.M. Olchowik, *J. Non-Cryst. Sol.*, **358**, 590 (2012).

16. N. Kaneva, D. Dimitrov, C. Dushkin, *Appl. Surf. Sci.*, **257**, 8113 (2011).
17. N. Kaneva, I. Stambolova, V. Blaskov, Y. Dimitriev, A. Bojinova, C. Dushkin, *Surf. Coat. Techn.*, **207**, 5 (2012).
18. N. Kaneva, A. Ponomareva, L. Krasteva, K. Papazova, G. Suchaneck, A. Bojinova, V. Moshnikov, A. Apostolov, D. Dimitrov, *Bulg. Chem. Commun.*, **45**, 635 (2013).
19. I. E. Gracheva, Y.M. Spivak, V.A. Moshnikov, AFM techniques for nanostructured materials used in optoelectronic and gas sensors, IEEE EUROCON 2009, St. Petersburg, 2009, p. 1246.
20. I.E. Gracheva, A.I. Maksimov, V.A. Moshnikov, *J. Surf. Investig. X-ray Synch. Neutr. Tech.*, **10**, 16 (2009).
21. E. Barsoukov, J.R. Macdonald, *Impedance Spectroscopy. Theory, Experiment, and Applications*, Second Edition, Wiley-Interscience, New York, 2005.
22. I.E. Gracheva, V.A. Moshnikov, M.G. An'chkov, *Instr. Experim. Tech.*, **56**, 209 (2013).
23. S.S. Karpova, V.A. Moshnikov, S.V. Mjakin, E.S. Kolovangina, *Semiconductors*, **47**, 392 (2013).
24. S.S. Karpova, V.A. Moshnikov, A.I. Maksimov, S.V. Mjakin, N.E. Kazantseva, *Semiconductors*, **47**, 1026 (2013).

ИЗСЛЕДВАНЕ НА ИЗМЕРЕНИ ПО МЕТОДА НА ИМПЕДАНСНА СПЕКТРОСКОПИЯ НА ЧУВСТВИТЕЛНИТЕ КЪМ ИЗПАРЕНИЯ СВОЙСТВА НА СЛОЕВЕ ОТ ЦИНКОВ ОКСИД

С. С. Налимова¹, И. Е. Кононова¹, В. А. Мошников^{1,3}, Д. Ц. Димитров^{2*}, Н. В. Кънева², Л. К. Кръстева², Ш. А. Сюлейман², А. С. Божинова², К. И. Папазова², А. Ц. Георгиева⁴

¹Катедра по Микро- и Наноелектроника, Санкт-Петербургски Държавен Електротехнически Университет, Санкт-Петербург 197376, Русия

²Лаборатория по Наука и Технология на Наночастици, Катедра по Обща и Неорганична Химия, Факултет по Химия и Фармация, Софийски Университет, София 1164, България

³Катедра по Интегрирана Електроника, Санкт-Петербургски Политехнически Университет на името на Петър Велики, Санкт-Петербург 195251, Русия

⁴Катедра Материалознание & Инженеринг, Университет на Флорида, Гейнсвил, ФЛ 32611, САЩ

Получена на 4 ноември, 2014 г.; ревизирана на 27 юни, 2016 г.

(Резюме)

В областта на газ-сензорните изследвания метални оксидни слоеве се използват като чувствителни елементи на полупроводниковите адсорбционни газови датчици. В тази работа проби от ZnO са получени чрез зол-гелен метод с промяна на температурата на отгряване от 100 до 500 °C. Микроструктурата на повърхността на получените проби е изследвана чрез атомно-силов микроскоп. Чувствителността на пробите към изпарения на ацетон и етанол се изследва по метода на импедансна спектроскопия. За интерпретация на получените резултати е използвана електрическа еквивалентна R-CPE схема. Пробата от ZnO, получена чрез отгряване при 300 °C проявява максимална чувствителност към изпаренията на двата органични разтворителя. Добавянето на Fe към ZnO пробата, отгрята при температура от 500 °C води до увеличаване на чувствителността към изпаренията на ацетон и етанол. Причината за това е увеличаването на концентрацията на адсорбционните центрове за редукторните газове, каквато функция изпълняват изпаренията от етанол и ацетон.

Effect of fumaric acid on the properties of alkyd resin and palm oil blend

Bl.V. Itoua^{1*}, D.S. Ogunniyi², P. Ongoka¹, L. Petrov³

¹*Ecole Normale Supérieure B.P 237, Université Marien Ngouabi, Brazzaville-Congo*

²*Department of Chemical Engineering, University of Ilorin, Ilorin, Kwara State, Nigeria.*

³*SABIC Chair of Catalysis, Chemical and Materials Engineering Department, Faculty of Engineering, King Abdulaziz University, Jeddah, Kingdom of Saudi Arabia*

Received January 27, 2016; Revised June 30, 2016

Two blends of palm oil and alkyd resins were prepared. The first blend comprises 20% palm oil while the second blend comprises 30% palm oil. These blends contained quantities of fumaric acid ranging from 2g to 10g. Also, a drying agent composed of a mixture of cobalt, calcium and lead compounds was included in each blend sample. After the preparation of the samples, their physicochemical properties such as density, viscosity, drying time, acid value, peroxide value, saponification value, and dry extract were determined following standard methods. Structural properties of prepared blends were determined by proton magnetic nuclear resonance spectroscopy. In the absence of fumaric acid, the analysis showed that the blends exhibited high drying times, low viscosity and density. However, the drying times of both alkyd blends decreased with the increase in fumaric acid content and 20% palm oil is the optimum proportion for alkyd palm oil blend. The results suggest that fumaric acid can be used in alkyd resins based on non-drying oils as a blending additive in coating formulations.

Keywords : Alkyd resin; blend; palm oil; fumaric acid; physicochemical properties; drying properties.

INTRODUCTION

Modification of polymers is one of the techniques industrially used for obtaining a large range of new products [1, 2]. Chemical and/or physical modification found large application in the industries with the aim of adjusting polymer properties to the various technical applications [3, 4]. Alkyd resins are widely used in the surface coatings industry as a binder for making industrial and offshore paints [5]. They are resinous materials synthesized by the reactions of polyol, dicarboxylic acid, and triglycerides of fatty acids derived from vegetable oils [6]. In order to enhance film properties, alkyd resins are usually modified by raw materials and/or resins by chemical incorporating [7] or physical blending [8].

The trending down of petroleum resources has resulted in an increasing demand toward vegetable oils as an inexpensive and renewable source. It is estimated that about 1 million tons of vegetable oils are used in polymeric surface coatings each year [9]. In the recent 20 years palm oil production has increased, as a result of the increasing demand toward vegetable oils as an inexpensive and renewable source. Now, compared to soybean oil, palm oil takes the second place in the list of oils produced around the world and will probably overtake soybean oil in another 10–15 years [10]. Palm oil can be considered as a useful candidate to

respond to the increasing oil consumption of organic coatings industry. Many studies are using palm oil as an alternative vegetable oil for alkyd synthesis [11, 12] and as an additive [13] for enhancing rheological properties of alkyd resins. The main problem for resins based on palm oil is that they are not able to air dry due to the low iodine value of palm oil. But the literature survey reveals that if vegetable oils are used in the blend for alkyd resin synthesis, the drying properties of alkyd resins could be improved [14]. Based on designed formulations, different types of alkyd resin were synthesized by using a mixture of oils.

Fumaric acid is a dicarboxylic acid with the same molecular weight as maleic acid. Nevertheless, they have different structural formulas. Maleic acid is *cis*-(*Z*)-2-butenedioic acid and fumaric acid is *trans*-(*E*)-2-butenedioic acid. Fumaric acid is an organic acid widely found in nature, in humans, animal feed and is an essential ingredient of plant life [15]. Fumaric acid has been used in food and beverage products since 1946 [16]. Research shows that it improves quality and reduces costs of many food products. In coating industries, fumaric acid contributes to the improvement of the properties of vegetable oils [17]. Through modification with fumaric acid in the synthesis of alkyd resins, changes are imported in their physicochemical properties [18]. In the present work the improvement of physicochemical properties of alkyd resin and palm oil blend through physical modification with different proportions of fumaric acid was investigated.

* To whom all correspondence should be sent:
E-mail: itoua_63@yahoo.fr

EXPERIMENTAL

Materials

Palm oil was obtained from Ng. Enterprise (Ng Enterprise, Edou, Oyo District, Republic of Congo). Commercial long alkyd resin was produced by MPCROKIM, 32, Rue du Mercure Z.I, Ben Arous 2013 Ben Arous, Tunisia and it was supplied by the Congolese Enterprise of Paint (COPE). The driers used were produced by DSM Coating resin, The Netherlands. The drier is a mixture of 10% of zinc-based drier, 10% of calcium-based drier, 10% of cobalt-based drier, and 10% of lead-based drier in white spirit as solvent. All materials were used as received.

*Method**Preparation of alkyd and palm oil blends*

Alkyd resins were mixed intimately with palm oil in a small aluminum box of 50ml using a spatula as a mixer. After near-perfect homogeneity of the mixture, it was left for two hours for letting air bubbles in the mixture to escape. Different samples with 10%, 20%, 30%, 40% and 50% palm oil were prepared. The same quantity of driers (0.2%) was mixed with each sample.

Preparation of alkyd and palm oil blends with fumaric acid

The samples with 20% and 30% palm oil were mixed in a small aluminium box of 50 ml to perfect homogeneity with 2g, 4g, 6g, 8g and 10g fumaric acid. The quantity of driers was increased (0,6%) to accelerate the drying time. The different samples obtained are presented in table 1.

*Testing**Viscosity*

The viscosity was measured by using a Brookfield rotary Viscometer KU-2 model DV-III according to ISO 288. It is composed of a dial with digital display and keys for the hand drive operation. The measurements were performed by using spindle n°6 posted directly on the numerical dial.

Density

The density was determined according to NF en 1097-6. The measurement was performed by using analytical scale and Pycnometer S9611826. The

Pycnometer is a metal container standardized with volume of 100 cm³. It is equipped with a bored lid of a hole to evacuate the bubbles of air and remove the excess of product.

The density was determined by the following relation:

$$D = \frac{M2-M1}{V}; \quad (1)$$

D: density of the product

M1: weight of the pycnometer empty

M2: weight of the Pycnometer filled with product

V: volume of the pycnometer

Dry extract

The quantity of dry extract was determined by using a cooking isotherm (123°C) according to ISO 3251. The dry extract was calculated from the difference of the plates, which were taken initially and lineally. The mean value of three results was reported as the percent non-volatile matter.

Drying time

The drying time (set-to-touch time) was determined according to ISO 9117. The measurement was performed by using a painting applicator of 150 microns. A thickness of 150µm is applied on the contrast paper and exposed for drying in free air. The drying time is measured when the film is not sticking to the touch any more.

¹H NMR spectra analysis

The proton nuclear magnetic resonance (¹H NMR) spectra were recorded on a Nuclear Magnetic Resonance 500 MHz (Model: FT-NMR Avance II, Bruker 500, UltraShield) instrument after dissolving the samples in deuterated chloroform CDCl₃. Each sample was dissolved in CDCl₃, and the resulting mixture was placed into a ultra-precision NMR sample tube. The probe was at room temperature. The chemical shifts are reported in ppm, using the solvent proton signal as a standard.

Acid value

Acid value was determined according to the AOAC method and the standard 969.17 1997 by titrating the mixture with a KOH solution till a pale pink coloring. The acid value (IA) was calculated as follows:

Table 1: Blend of alkyd resin and palm oil with various proportions of fumaric acid

Alkyd /Oil	80:20						70:30					
Fumaric acid [g]	0	2	4	6	8	10	0	2	4	6	8	10
Blend designation	M ₁	M ₂	M ₃	M ₄	M ₆	M ₇	M ₁	M ₂	M ₃	M ₄	M ₅	M ₆

$$IA = \frac{V \times N \times 56,1}{M}; \quad (2)$$

V: the volume of KOH (in ml) necessary to the neutralization of the free fatty acids.

N: normality of the solution of KOH

M: mass test specimen

Peroxide value

Peroxide value was determined using AOAC method and according to standard 965.33,1977 by titrating the iodine released with a thiosulfate solution.

The peroxide index (IP) was calculated as follows:

$$IP = \frac{(V-V_0) \times N \times 100}{M} = \frac{(V-V_0) \times N \times 100}{M}; \quad (3)$$

V: volume in ml of the thiosulfate solution used;

V₀: volume in ml of the thiosulfate solution used for the white test;

N: exact normality of the thiosulfate solution;

M: mass test specimen.

Saponification value

Saponification value was determined using AOAC method and according to standard 920.160,1997 by titrating the mixture with a solution of HCl. The saponification index (IS) was calculated as follows:

$$IS = \frac{56,1 \times N \times (V_0 - V)}{M}; \quad (4)$$

V₀: volume of HCl used for the white test;

V: volume of HCl used;

N: normality of KOH solution;

M: mass test specimen.

RESULTS AND DISCUSSION

Effect of fumaric acid on the drying time of the blends film

Figure 1 shows the change in drying time (set-to-touch time) with the increase in the content of fumaric acid in the blend. The drying time decreases with the increase in fumaric acid content.

The decrease in the drying time at 30% palm oil is moderate up to 10g fumaric acid content, and this decrease is clearly observed at 20%. However, the values of drying time at 30% palm oil are higher than those at 20% palm oil. Alkyd resin film dries by an autooxidation process [19], due to intake of oxygen from the atmosphere. Mechanistic studies of autooxidation revealed that the drying process of coatings based on alkyd resin is due to the presence of unsaturated bonds in the vegetable oil and results in lower drying times.

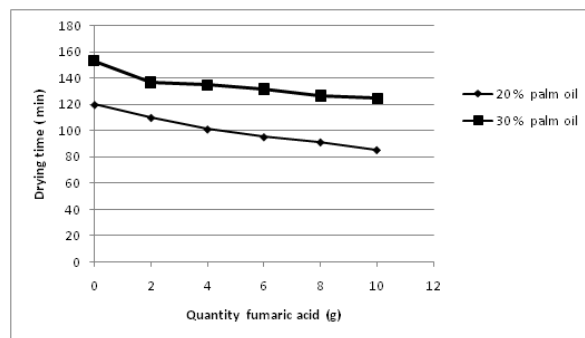


Fig.1. Drying time of alkyd resin and palm oil blend with the quantity of fumaric acid

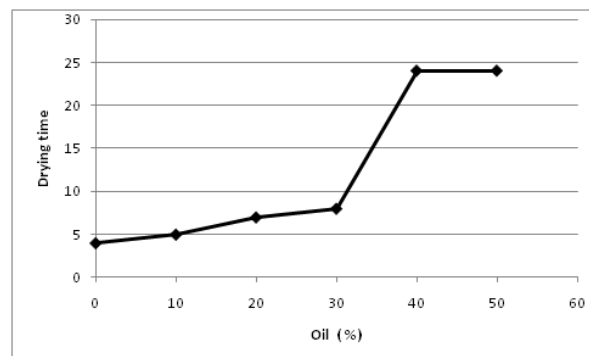


Fig. 2. Drying time of alkyd resin with the quantity of oil

Palm oil is known as a non drying oil. Its blending with alkyd resin has shown an increment of drying time (figure 2). As it is shown in figure 1, for all blends, set-to-touch (surface drying) drying time decreases on increasing the proportion of fumaric acid in the blend. This happens because of the presence of unsaturated bonds in fumaric acid which contribute to the reduction of drying times. The highest reduction of drying times in the presence of fumaric acid is for the blend with 20% palm oil content. Based on this result, it can be concluded that 20% palm oil is the optimum proportion for alkyd palm oil blend. Undoubtedly, in the presence of a more effective drying system, the oxygen activation is further accelerated and results in a shorter drying time.

Effect of fumaric acid on the dry extract of the blends film

Figure 3 shows the change of dry extract with the increase in the content of fumaric acid in the blend. The dry extract increases with the increase in fumaric acid content. The increase of dry extract is higher at 30% than at 20% palm oil content. The non-volatile material content found is 81% for the higher and 0% for the lower, indicating a relatively solid portion of blend.

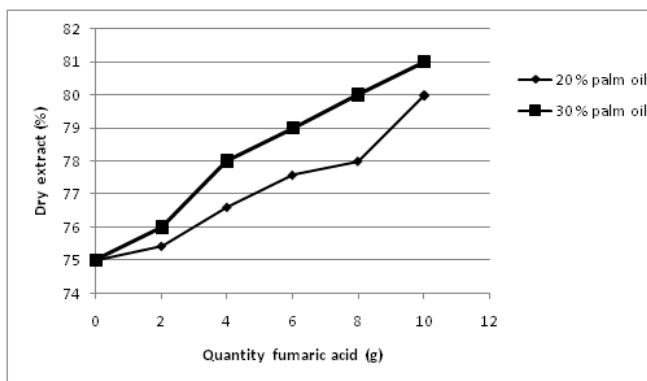


Fig. 3. Dry extract of alkyd and palm oil blend with the quantity of fumaric acid.

Characterization of palm oil and alkyd blends

Different parameters of palm oil and alkyd resin were measured and the results obtained are shown

Table 2: Physico-chemical data of alkyd resin and palm oil

Parameters	Density	Gloss (60°)	IA	IP	IS	Viscosity
Samples		[%]	[Mg KOH/g]	[mgeqO ₂ /Kg]	[mgKoH/g]	[cps]
Palm oil	0,89	-	7,29	3,29	121,2	-
Alkyd resin	0,95	86	1,68	0,28	19,63	5000

in Table 2. The density and viscosity of the alkyd was found to be 0.95 and 5000cps, respectively. The density of oil was found to be 0.89 implying freedom from any heavy metals.

Figure 2 shows the ¹H NMR spectrum of palm oil. The peaks at δ=0.85–0.90 ppm are characteristic for the proton of a terminal methyl group. The protons of all internal -CH₂ groups present in the fatty acids were confirmed by the peaks at δ= 1.60 ppm. Peaks at δ= 2.0 and δ= 2.75 ppm are characteristic for allylic and double allylic proton. The α-proton of ester group is found at δ=2.30 ppm. The -CH₂- protons of glycerol are found at δ=4.1–4.3 ppm and the protons for -CH of glycerol and unsaturated carbons appeared at δ= 5.33–5.35 ppm.

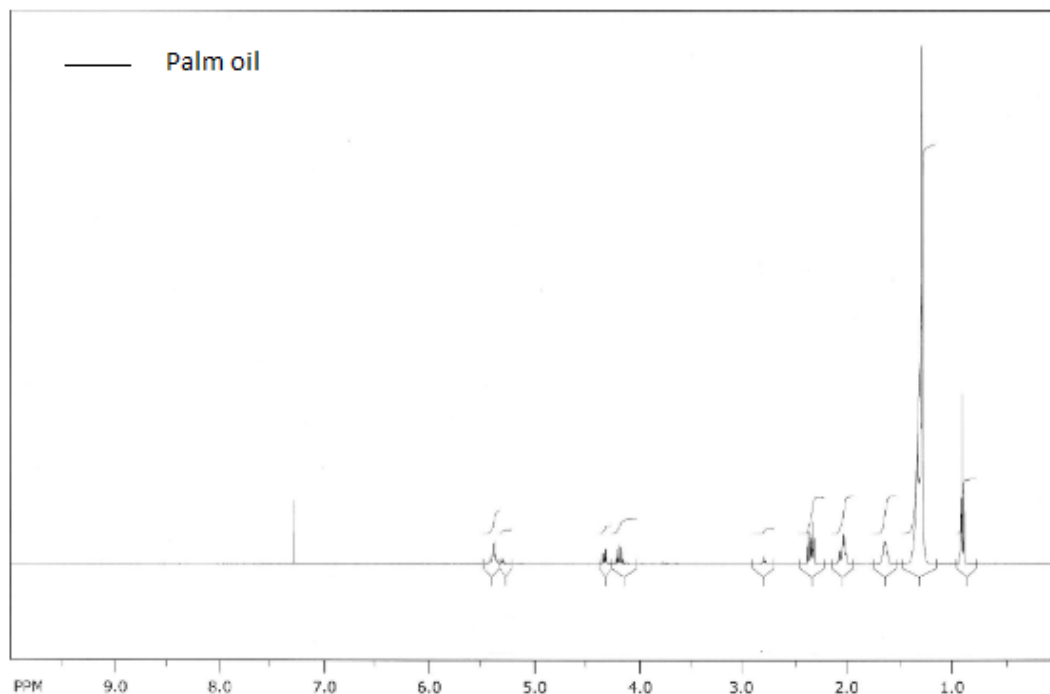


Fig .4. ¹H NMR spectrum of palm oil

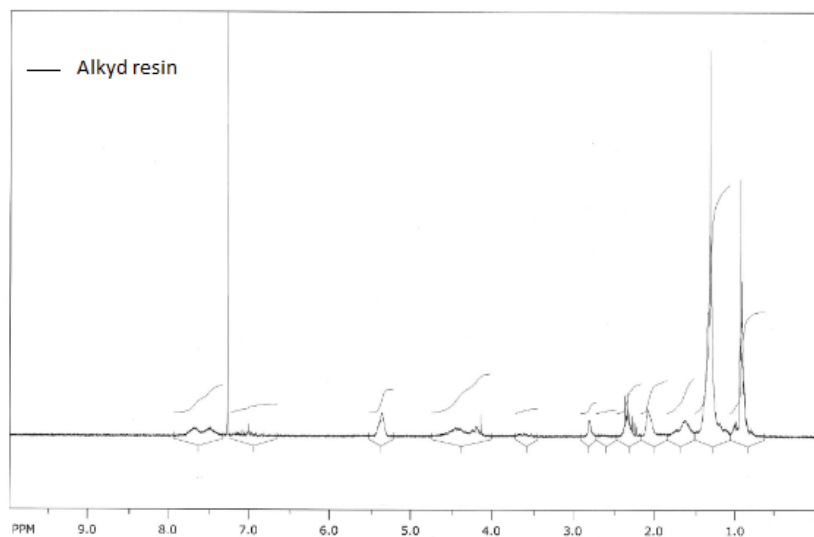


Fig.5. ¹H NMR spectrum of alkyd resin

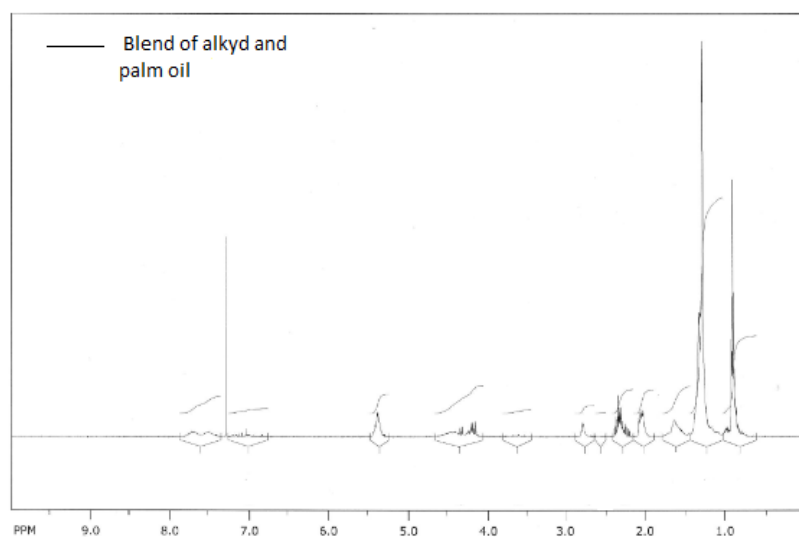


Fig. 6. ¹H NMR spectrum of alkyd and palm oil

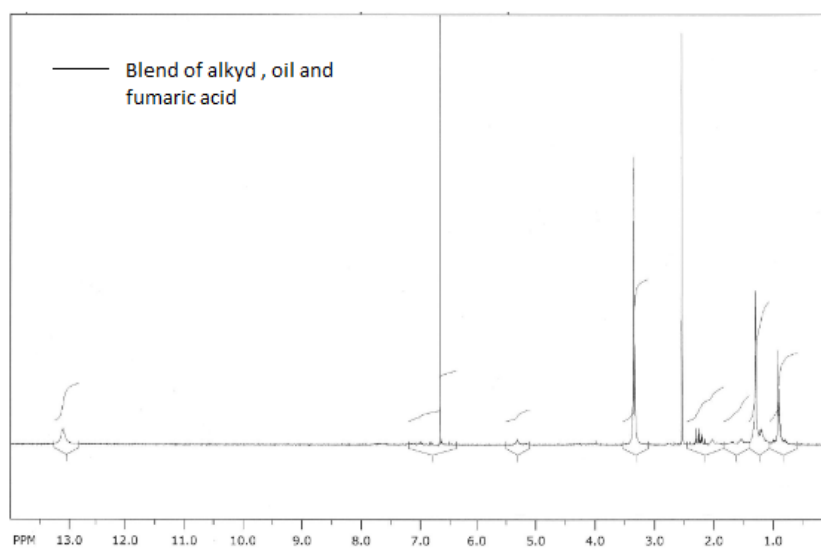


Fig. 7. ¹H NMR spectrum of a blend of alkyd, oil and fumaric acid

The information on the proton density of different alkyd samples and their blends is depicted in Figures 4, 5, 6 and 7 by ^1H NMR spectra.

The high-field region of the proton spectra ($\delta=0-3.5$) contains mainly methylene and methyl peaks from fatty acid protons. The proton for terminal methyl groups of fatty acids was confirmed by the peak at around $\delta=0.87$.

Peaks next to that in the range of $\delta=1.25$ to 3.5 are due to protons of all $-\text{CH}_2$ present in the chain.

The middle region of the proton spectra ($\delta=3.5-6.0$) contains peaks from the vinyl protons of the fatty acids (FA) incorporated in the alkyd resins and from protons of neighboring hydroxyl or ester groups [20], and thus peaks appearing at 4.2 to 4.4 can be probably attributed to the methylene protons of the glycerol molecule and those at 5.25 to 5.4 - to unsaturated carbons.

The low-field region 6.5– 8.0 contains aromatic protons originating from phthalic (PHT) and ester fragments of the polyesters. The peak appeared at 6.75 to 6.85 ppm is characteristic for the $-\text{CH}$ present in the glycerol molecule. The proton of the aromatic ring is related to the peak at $\delta=7.5-8$.

The vinyl protons of fumaric acid appear mainly at $\delta=6.53$ [21]. From figure 7 at $\delta=6.5$ to 6.56 , this peak is due to protons of $\text{CH}=\text{C}$ present in fumaric acid. The peak at $\delta=13$ can be probably attributed to the proton present in the COOH group of fumaric acid molecule.

CONCLUSIONS

The results obtained in the present work showed the easy blending of various proportions of fumaric acid with alkyd resin and palm oil. Such blending can be made for improving the generally long drying time of alkyd based palm oil. Two types of ratios of alkyd/ palm oil are reported. Blends of palm oil with long alkyd resin and palm oil were prepared and their physicochemical properties were studied. It was shown that palm oil contributed to the increase in drying time of long alkyd resin. Results indicated that 80/20 (w/w) is the optimal blend of alkyd and palm oil providing significant improvements in drying time by varying fumaric acid proportion and its incorporation in the alkyd palm oil blend. ^1H NMR technique was used for understanding the

improvements in the properties of coating film due to the presence of fumaric acid in the blend.

Acknowledgement: The authors would like to thank the Enterprise Congolaise de Peinture for technical support.

REFERENCES

1. H.S. Patel, A. M.Naji, *J. Chem. Pharm. Res.*, **3**(1),770 (2011), *IJPM*, **59**, 25, (2010)
2. M.G. Bhuvaneshwary, E.T. Thachil, *International Journal of Polymeric Materials*, **57**,543 (2008)
3. S. Jose, S. Thomas, E. Lievana, J. Karger-Kocsis, *J. Appl. Polym. Sci.*, **95**,1376 (2005)
4. V. Kalkis, R.D. Maksimov, *J. Zicans, Polymer Engineering & Science*, **39**(8), 1375 (1999)
5. R.Schwalm, *UV coatings: Basics, Recent Developments and New Applications*. Elsevier, Oxford, 2007.
6. D.S.Ogunniyi, T.E. Odetoeye, *Biores. Technol.*, **99**, 1300 (2008).
7. N. Thanamongkolit, K.R. Miller, M.D. Soucek, *Prog. Org. Coat.*, **73**(4), 425 (2012)
8. A.R.N. Azimi, R. Yahya, S.N.Gan, *Progress in Organic Coatings*, **76**, 712 (2013)
9. F.D.Gunstone, J. Alander, S.Z. Erhan, B.K. Sharma, T.A. Mc Keon, J.T. Lin, *Nonfood Uses of Oils and Fats*, Taylor and Francis Group, LLC, Boca Raton, 2007.
10. OECD-FAO, *Agricultural Outlook*, OECD Publishing, Paris, 2008.
11. A.M.Issam, C.Y. Cheun, *Malays. Polym. J.*, **4**(1), 42 (2009).
12. C.F.Uzoh, O.D. Onukwuli, R.S. Odera, S. Ofochebe, *Journal of Environment Chemical Engineering*, **1**, (2013) 777-785
13. B.V. Itoua, D.S.Ogunniyi, P.R. Ongoka, *Malays. Polym. J.*, **7**(2), 42 (2012).
14. D.H. Solomon, *The Chemistry of Organic Film Formers*, R.E. Krieger Publishing Co., New York, 1997.
15. http://www.bartek.ca/fumaric_acid.html
16. <https://www.thechemco.com/chemical/fumaric-acid/>
17. O. Ibanga, I. Isaac, N. W. Akpanudo, *International Journal of Engineering and Science (IJES)*, **3**(12), 1 (2014).
18. A.I. Aigbodion, F.E. Okieimen, E.U. Ikhuoria, I.O. Bakare, E. O. Obazee, *Journal of Applied Polymer Science*, **89**(12), 3256 (2003)
19. O.S. Privett, *J. Am. Oil Chem. Soc.*, **36**, 507 (1959).
20. A. Spyros, *Journal of Applied Polymer Science*, **88**, 1881 (2003)
21. A. J. Kirby, B. S. Souza, M. Medeiros, J. P. Priebe, A. Manfredi, F.Nome, *Chem. Commun.*, **37**, 4428 (2008).

ВЛИЯНИЕ НА ФУМАРОВАТА КИСЕЛИНА ВЪРХУ СВОЙСТВАТА НА СМЕСИ НА АЛКИДНА СМОЛА И ПАЛМОВО МАСЛО,

Бл. В. Итуа^{1*}, Д. С. Огуний², П. Онгока¹, Л. Петров³

¹*Нормално висше училище, Университет Мариен Нгуаби, Конго-Бразавил*

²*Департамент по инженерна химия, Университет в Илорин, Щат Куара, Нигерия*

³*Катедра по катализ SABIC, Департамент по инженерна химия и материалознание, Инженерен факултет, Университет „Крал Абдулазис“, Джеда, Кралство Саудитска Арабия*

Постъпила на 27 януари, 2016 г.; приета на 30 юни, 2016 г.

(Резюме)

Изследвани са две смеси от палмово масло и алкидни смоли. Първата смес съдържа 20%, а втората - 30% палмово масло. Тези смеси съдържат количества фумарова киселина в границите от 2 до 10 грама. Освен това към всяка проба се добавят съхнещи агенти, съдържащи смеси от съединения на кобалта, калция и оловото. След приготвяне на пробите се определят техните физико-химични показатели, като плътност, вискозитет, време за изсъхване, киселинно число, пероксидно число, число на осапунване по стандартни методи. Структурите на приготвените проби се определят чрез протонна ЯМР-спектроскопия. В отсъствие на фумарова киселина пробите имат по-дълго време за изсъхване, по-малки вискозитет и плътност. Времето за изсъхване на двете алкидови смеси намалява с увеличаването на съдържанието на фумарова киселина, а съдържанието на 20% палмово масло е оптимално за сместа. Резултатите показват, че фумаровата киселина може да се използва в алкидни смоли на базата на не-съхливи масла като добавка за покриващи смеси.

Density functional theory based study of the heat of polymerization of olefins

Q.-Z. Zhang^{1,2}, J.-L. Liu², F. Yang², X.-P. Hao², C.-Y. Ke², Q. Pan³, X.-L. Zhang^{2,*}

¹College of Science, Xijing University, Xi'an 710123, China

²College of Chemistry and Chemical Engineering, Xi'an Shiyou University, Xi'an 710065, China

³Department of Pharmacy, School of Medicine, Xi'an Jiaotong University, Xi'an 710061, China

Received February 15, 2016; Revised June 3, 2016

Density functional theory (DFT) at the B3LYP/6-31G level was used to compute the heat of polymerization of six olefins, namely, polypropylene (PP), 1,2-polybutadiene (1,2-LPB), poly-2-chloro-butadiene (CR), polyisoprene (IR), poly(isoprene-3,4) and poly(isoprene-1,2), by taking into account the previously determined system error. By comparing the calculated results to experimental data available in the literature for the first four polymers, the relative errors were found to be 0%, 1.66%, 2.04% and 1.20%, respectively, demonstrating that the method employed is able to calculate the heat of polymerization of olefins with reasonable accuracy and reliability. Based on the findings, the heats of polymerization for the other two polymers poly(isoprene-3,4) and poly(isoprene-1,2) were predicted to be -44.71 kJ·mol⁻¹ and -50.67 kJ·mol⁻¹, respectively.

Keywords: Heat of polymerization, Density Functional Theory (DFT), B3LYP/6-31G, Olefins

INTRODUCTION

Heat of a polymerization reaction represents the enthalpy change during the formation of the polymer from its monomer.

Such thermodynamic data are a fundamental property in chemistry, e.g., allowing feasibility studies of polymerization reactions before performing an experiment and also optimization of the polymerization processes in terms of heat transfer and other operational parameters [1]. Therefore, there has been continuous effort in determining, either experimentally or theoretically, the heat of polymerization for different polymerization reactions. Experimentally, it can be measured with a range of methods through, e.g., direct reaction calorimetry, combustion method, and thermodynamic equilibrium techniques [2]. Although there has been increasing number of reports about experimental data, there are still numerous substances for which no thermodynamic data are available, and one of the key causes is associated with the complexity of experimental setups required to obtain thermodynamic data [3]. In that respect, theoretical and computational approaches provide valuable tools as complementary or alternative methods. For example, the density functional theory (DFT), associated with Gaussian software package, has proven to be an effective approach to compute and estimate thermodynamic characteristics of a wide range of reactions [4-9], including polymerizations [10-19].

To predict the heats of formation, Keshavarz *et al.* used recently developed density functionals such as

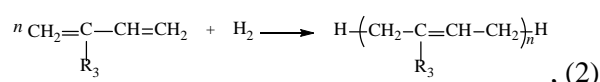
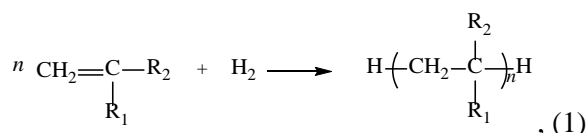
ωB97X-D and M06-2X in comparison with B3LYP for estimating the gas phase heats of formation, $\Delta_f H^\circ(g)$, and the condensed phase heat of formation, $\Delta_f H^\circ(c)$ of polycyclic saturated hydrocarbons [20]. Chi *et al.* studied the heats of formation, specific enthalpies of combustion, detonation performances, and electronic structure at B3LYP/6-311 G** level for a series of polydinitroaminocubanes [21]. Based on the computations for a series of polyisocyanoadamantanes also at the DFT-B3LYP level, Zhao *et al.* estimated the heats of formation and strengths of group interactions for 19 polyisocyanoadamantanes [22]. Lee *et al.* used DFT to calculate the thermodynamic properties of polychlorinated dibenzo-p-dioxins and also investigated the intramolecular Cl-Cl repulsion effects and their thermochemical implications [23]. In our previous work, we computed the heat of polymerization of polyethylene with DFT at the B3LYP/6-31G level and, by comparing to the experimental results, estimated the system error which was further taken into account for the calculation of the heat of polymerization of 1,3-polybutadiene [24]. Based on that, the aim of the present studies was to further study the heats of polymerization of a series of polyolefins in order to develop a reliable and efficient method for the calculation of heats of polymerization for other polymers of interest. The heats of polymerization of four polyolefins were computed and compared with published experimental data. The heats of polymerization of further two polyolefins were then predicted with the method validated.

* To whom all correspondence should be sent:

E-mail: xlzhang@xsyu.edu.cn

COMPUTATIONAL DETAILS

The computations were performed using DFT at the B3LYP/6-31G level with a Gaussian 3 program package [25]. The geometry of each molecule was optimized first, and the standard enthalpies of formation of all molecules were calculated in order to obtain the heat of polymerization. The chemical reactions of the polymerization of olefins are generally represented by equations (1) and (2).



Six polymers were examined and the corresponding side chains or groups are presented in Table 1.

The heat of polymerization of olefins is expressed as

$$\Delta H_{polymer} = \frac{1}{n} H_{polymer} - H_{monomer} - \frac{1}{n} H_H, \quad (3)$$

RESULTS AND DISCUSSION

With the Gaussian 03 program the H values of PP, 1,2-LPB, CR, IR, poly(isoprene-1,2) and poly(isoprene-3,4) with different degree of polymerization were calculated. a_n (in hartree) represents the mean of H with a degree of polymerization n . The values of a_n for different olefins polymerization are summarized in Table 2.

Further analysis on data shown in Table 2 revealed that for each polymer a can be represented by

$$a_n = a_{n-1} + a_1 - a'_0 + b_{n-1} = na_1 - (n-1)a'_0 + \sum_{i=1}^{n-1} b_i$$

when $n > 1$, (4)

where a_0 is the enthalpy of monomer, and b is a constant (in hartree). The best fitting values of b for each polymer are summarized in Table 3.

It can be seen from Table 3 that for PP the value of b_n has insignificant variation when n varies from 1 to 14, thus their mean value may be used. That also applies to the other five polymers. It indicates that n is negligible for computing their heats of polymerization if n is low ($n < 22$). When n increases ($n \gg 22$) the heat of polymerization can be determined to be the convergence value of $a_n(n \rightarrow \infty)$ taking into account the system error of $SE = -0.0004$ hartree which was obtained for computing the heat of polymerization of ethylene using the same method [24].

Thus,

$$\begin{aligned} \lim_{n \rightarrow \infty} \Delta H_{polyolefin} &= \lim_{n \rightarrow \infty} \left[\frac{1}{n} a_n - \frac{1}{n} a'_0 - a_0 \right] + SE = \\ \lim_{n \rightarrow \infty} \left\{ \frac{1}{n} [na_1 - (n-1)a'_0 + (n-1)b] - \frac{1}{n} a'_0 - a_0 \right\} + SE \\ &= \lim_{n \rightarrow \infty} \left[a_1 - a'_0 + \frac{n-1}{n} b - a_0 \right] + SE \\ &= a_1 - a'_0 + b - a_0 + SE, \quad (5) \end{aligned}$$

By inserting data from Tables 2 & 3 into equation (5), heats of polymerization for the six polymers were calculated. The results are summarized in Table 4. For comparison, experimental data for the first four polymers, obtained from the literature, are also shown.

By comparing the calculated results and experimental data available for the four polymers, absolute errors were found to be $0.00 \text{ kJ}\cdot\text{mol}^{-1}$, $1.44 \text{ kJ}\cdot\text{mol}^{-1}$, $1.62 \text{ kJ}\cdot\text{mol}^{-1}$ and $0.87 \text{ kJ}\cdot\text{mol}^{-1}$, and relative errors - 0%, 2.10%, 2.04%, and 1.20%, respectively. It was demonstrated that the use of the DFT B3LYP/6-31G method can provide good agreement between computed and experimental results with a low computational cost, which can be further applied for more complex molecular systems. Based on that, it was employed to predict the heats of polymerization for other two polymers poly(isoprene-3,4) and poly(isoprene-1,2) which were found to be $-44.71 \text{ kJ}\cdot\text{mol}^{-1}$ and $-50.67 \text{ kJ}\cdot\text{mol}^{-1}$, respectively. The prediction may be compared and validated by further experimental work.

Table 1. Six polymers with various side chain groups (R_1 , R_2 and R_3).

Polymer	R_1	R_2	R_3
Polypropylene (PP)	CH_3	H	
1,2-polybutadiene (1,2-LPB)	$\text{CH}=\text{CH}_2$	H	
Poly-2-chloro-butadiene (CR)			Cl
Polyisoprene (IR)			CH_3
Poly(isoprene-3,4)	$\text{CH}_2=\text{C}-\text{CH}_3$	H	
Poly(isoprene-1,2)	$\text{CH}=\text{CH}_2$	CH_3	

Table 2. Values of a with different degree of polymerization

	PP	1,2-LPB	CR	IR	3,4-polyisoprene	1,2-polyisoprene
a ₀	-117.794734	-155.866934	-615.452433	-195.145478	-195.145478	-195.145478
a ₁	-119.006746	-157.071514	-616.662688	-196.353608	-196.34544	-196.347412
a ₂	-236.830172	-312.960675	-1232.185366	-391.522469	-391.508378	-391.512622
a ₃	-354.653582	-468.849173	-1847.666046	-586.691365	-586.671314	-586.677827
a ₄	-472.476986	-624.737217	-2463.145597	-781.860233	-781.834251	-781.843037
a ₅	-590.300398	-780.625639	-3078.623159	-977.029127	-976.997186	-977.008238
a ₆	-708.123816	-936.514442	-3694.101793	-1172.198001	-1172.160122	-1172.173446
a ₇	-825.947223	-1092.402896	-4309.624445	-1367.366872	-1367.323056	-1367.338652
a ₈	-943.776214	-1248.291347	-4925.147118	-1562.535728	—	-1562.503856
a ₉	-1061.594052	-1404.179761	-5540.669762	—	—	-1757.669061
a ₁₀	-1179.417458	-1560.068178	-6156.192427	—	—	—
a ₁₁	-1297.24087	-1715.956593	-6771.715036	—	—	—
a ₁₂	-1415.064287	-1871.845091	—	—	—	—
a ₁₃	-1532.887702	—	—	—	—	—
a ₁₄	-1650.711114	—	—	—	—	—
a ₁₅	-1768.534528	—	—	—	—	—

Note: The heat of formation of hydrogen $a'_0 = -1.162033$ hartree.

Table 3. Best fitting of b values for different olefins

	PP	1,2-LPB	CR	IR	3,4-polyisoprene	1,2-polyisoprene
b ₁	0.021287	0.020320	0.022023	0.022714	0.020469	0.020169
b ₂	0.021303	0.020983	0.022021	0.022679	0.020471	0.020174
b ₃	0.021309	0.021437	0.022026	0.022707	0.020470	0.020169
b ₄	0.021300	0.021058	0.022019	0.022681	0.020472	0.020178
b ₅	0.021295	0.020678	0.022017	0.022701	0.020471	0.020171
b ₆	0.021306	0.021028	0.021997	0.022704	0.020473	0.020173
b ₇	0.021300	0.021030	0.022018	0.022719	—	0.020175
b ₈	0.021297	0.021066	0.021989	—	—	0.020174
b ₉	0.021307	0.021064	0.02201	—	—	—
b ₁₀	0.021301	0.021066	0.021954	—	—	—
b ₁₁	0.021295	0.020983	—	—	—	—
b ₁₂	0.021298	—	—	—	—	—
b ₁₃	0.021301	—	—	—	—	—
b ₁₄	0.021299	—	—	—	—	—
AV	0.021300	0.020974	0.022007	0.022701	0.020471	0.020172

Table 4. Comparison of calculated results with experimental data of heats of polymerization

Polymer	Calculated results		Experimental data / kJ·mol ⁻¹	Relative error / %
	hartree	kJ·mol ⁻¹		
PP	-0.032679	-85.80	-85.80 [26]	0
1,2-LPB	-0.025686	-67.44	-68.58 [27]	2.10
CR	-0.029606	-77.73	-79.35 [27]	2.04
IR	-0.026397	-71.93	-72.80 [26]	1.20
poly(isoprene-3,4)	-0.016029	-44.71		
poly(isoprene-1,2)	-0.018301	-50.67		

NB. 1 hartree = 2625.5 kJ·mol⁻¹ [28]

There is generally a range of factors which can have effects on the accuracy of the results obtained by this method, such as polarity of side chain groups, where more accurate results may be computed for determining the heat of polymerization of polymers with straight chains or small groups. Approximation is also necessary with DFT and algorithm (e.g., numerical limit analysis) in most cases. In addition, the effect of reaction conditions such as temperature, pressure and solvation can cause variation in the heat of polymerization [29] which, in turn, can result in further discrepancy between computational and experimental data.

CONCLUSIONS

In the present study, the heat of polymerization of six olefins was calculated using the DFT B3LYP/6-31G method by taking into account the previously estimated system error. The calculated heats of polymerization for four polymers, namely, polypropylene, 1,2-polybutadiene, poly-2-chlorobutadiene and polyisoprene, were compared with experimental results available in the literature, showing relative errors of 0%, 2.10%, 2.04% and 1.20%, respectively. Based on the results presented, it can be verified that the method employed was able to calculate heat of polymerization of olefins with reasonable accuracy and reliability. That method was further used to predict the heats of polymerization for the other two polymers poly(isoprene-3,4) and poly(isoprene-1,2) to be $-44.71 \text{ kJ}\cdot\text{mol}^{-1}$ and $-50.67 \text{ kJ}\cdot\text{mol}^{-1}$, respectively.

Acknowledgements: This research was financially supported by the grants of Development and Application of Supercritical Fluid Chromatography (2013YQ170525), Application Research of Supercritical Fluid Chromatography in Chinese Traditional Medicine and Its Metabolites (2013YQ17052509), and Xi'an Shiyou University Graduate Innovation & Practical Skill Training projects (YCS16212074 and 2015CX140734).

REFERENCES

1. J. H. Lii, C. H. Hu, *J. Comput. Aid. Mol. Des.*, **26**, 199 (2012).
2. S. Roy, *Polym. Bull.*, **42**, 229 (1999).
3. J. A. Sousa, P. P. Silva, A. E. H. Machado, M. H. M. Reis, L. L. Romanielo, C. E. Hori, *Braz. J. Chem. Eng.*, **30**, 83 (2013).
4. E. Zahedi, B. Xiao, *Comput. Mater. Sci.*, **101**, 301 (2015).
5. C. Cappelli, C. Duce, M. Formica, V. Fusi, L. Ghezzi, L. Giorgi, M. Micheloni, P. Paoli, P. Rossi, M. R. Tine, *Inorg. Chim. Acta*, **417**, 230 (2014).
6. S. S. Borisevich, A. V. Kovalskaya, I. P. Tsypysheva, S. L. Khursan, *J. Theor. Comput. Chem.*, **13**, 1450048 (2014).
7. I. I. Zakharov, K. Y. Kudjukov, V. V. Bondar, N. F. Tyupalo, B. F. Minaev, *Comput. Theor. Chem.*, **964**, 94 (2011).
8. A. Shiroudi, E. Zahedi, R. Zabihi, *React. Kinet. Mech. Cat.*, **102**, 21 (2011).
9. Q. Liu, Y. Bei, *Prog. React. Kinet. Mec.*, **35**, 417 (2010).
10. I. del Rosal, P. Brignou, S. M. Guillaume, J.-F. Carpentier, L. Maron, *Polym. Chem.*, **6**, 3336 (2015).
11. G. Kayik, N. S. Tuzun, *J. Mol. Graph. Model.*, **49**, 55 (2014).
12. H. Dong, T. Hou, Y. Zhao, X. Fu, Y. Li, *Comput. Theor. Chem.*, **1001**, 51 (2012).
13. I. Degirmenci, V. Aviyente, V. Van Speybroeck, M. Waroquier, *Macromolecules*, **42**, 3033 (2009).
14. N. Barros, P. Mountford, S. M. Guillaume, L. Maron, *Chem. Eur. J.*, **14**, 5507 (2008).
15. D. V. Besedin, L. Y. Ustynyuk, Y. A. Ustynyuk, V. V. Lunin, *Top. Catal.*, **32**, 47 (2005).
16. I. E. Nifant'ev, L. Y. Ustynyuk, D. V. Besedin, *Organometallics*, **22**, 2619 (2003).
17. M. Yurtsever, E. Yurtsever, *Polymer*, **43**, 6019 (2002).
18. A. V. Yakimansky, A. H. E. Muller, *J. Am. Chem. Soc.*, **123**, 4932 (2001).
19. A. Michalak, T. Ziegler, *Organometallics*, **18**, 3998 (1999).
20. M. H. Keshavarz, M. Zamani, F. Atabaki, K. H. Monjeli, *Comput. Theor. Chem.*, **1011**, 30 (2013).
21. W. Chi, X. Wang, B. Li, H. Wu, *J. Mol. Model.*, **18**, 4217 (2012).
22. H.-M. Zhao, X.-Y. Wei, Z.-Y. Wang, X.-H. Ju, *J. Mol. Struct. Theochem.*, **817**, 5 (2007).
23. [23] J. E. Lee, W. Choi, B. J. Mhin, *J. Phys. Chem. A*, **107**, 2693 (2003).
24. Q. Zhang, Z. Li, X. Li, D. Ye, X. Zheng, *Comput. Applied Chem.*, **26**, 5 (2009).
25. M. J. Frisch, G. W. Trucks, H. B. Schlegel, G. E. Scuseria, M. A. Robb, J. R. Cheeseman, J. A. Montgomery, T. Vreven, K. N. Kudin, J. C. Burant, J. M. Millam, S. S. Iyengar, J. Tomasi, V. Barone, B. Mennucci, M. Cossi, G. Scalmani, N. Rega, G. A. Petersson, H. Nakatsuji, M. Hada, M. Ehara, K. Toyota, R. Fukuda, J. Hasegawa, M. Ishida, T. Nakajima, Y. Honda, O. Kitao, H. Nakai, M. Klene, X. Li, J. E. Knox, H. P. Hratchian, J. B. Cross, V. Bakken, C. Adamo, J. Jaramillo, R. Gomperts, R. E. Stratmann, O. Yazyev, A. J. Austin, R. Cammi, C. Pomelli, J. W. Ochterski, P. Y. Ayala, K. Morokuma, G. A. Voth, P. Salvador, J. J. Dannenberg, V. G. Zakrzewski, S. Dapprich, A. D. Daniels, M. C. Strain, O. Farkas, D. K. Malick, A. D. Rabuck, K. Raghavachari, J. B. Foresman, J. V. Ortiz, Q. Cui, A. G. Baboul, S. Clifford, J. Cioslowski, B. B. Stefanov, G. Liu, A. Liashenko, P. Piskorz, I. Komaromi, R. L. Martin, D. J. Fox, T. Keith, A. Laham, C. Y. Peng, A. Nanayakkara, M. Challacombe, P. M. W. Gill, B. Johnson, W. Chen, M. W. Wong, C. Gonzalez, J. A. Pople, Gaussian, Inc., Wallingford CT, 2004.
26. C. Xiao, Y. Hu, Polymer Chemistry, Wuhan

University Press, Wuhan, China, 1998.
27. Y. Wang, Chemical Reaction Engineering, China
Petrochemical Press, Beijing, China, 2011.

28. T. J. Zielinski, R. A. Poirier, M. R. Peterson, I. G.
Csizmadia, *J. Comput. Chem.*, **3**, 477 (1982).
29. W.-D. Wang, *J. Salt Lake Res.*, **11**, 70 (2003).

ИЗСЛЕДВАНЕ НА ТОПЛИНАТА НА ПОЛИМЕРИЗАЦИЯ НА ОЛЕФИНИ С ПОМОЩТА НА ТЕОРИЯТА НА ПЛЪТНОСТНИЯ ФУНКЦИОНАЛ (DFT)

Кун-Женг Жанг¹, Джин-Лей Лю¹, Фей Янг¹, Си-Пенг Хао¹, Конг-Ю Ке¹, Синг Пан²,
Ксун-Ли Жанг^{1,*}

¹ Колеж по химия и химично инженерство, Университет Ксиан и Шю, Ксиан, Китай

² Департамент по фармация, Училище по медицина, Университет Ксиан Джиаотонг, Ксиан, Китай

Постъпила на 15 февруари, 2016 г.; коригирана на 3 юни, 2016 г.

(Резюме)

Използвана е теорията на плътностния функционал (DFT) на ниво B3LYP/6-31G за да се изчисли топлината на полимеризация на шест олефина, а именно: полипропилен (PP), 1,2-полибутадиен (1,2-LPB), поли-2-хлоробутадиен (CR), поли-изопрен (IR), поли(изопрен-3,4) и поли(изопрен-1,2), отчитайки предварително натрупаната грешка. При сравнението на изчислените резултати с достъпните експериментални данни за първите четири полимера се оказва, че относителната грешка е съответно 0%, 1.66%, 2.04% и 1.20%, което показва че методът позволява изчисляването на топлината на полимеризация на олефини с разумна точност и надежност. На тази основа топлините на полимеризация за останалите два полимера поли(изопрен-3,4) и поли(изопрен-1,2) са определени съответно на $-44.71 \text{ kJ}\cdot\text{mol}^{-1}$ и $-50.67 \text{ kJ}\cdot\text{mol}^{-1}$.

Adsorption characteristics of activated carbon obtained from residual hydrolyzed lignin

L. Raicheva¹, G. Radeva^{2*}, S. Nenkova¹, R. Nikolov³

¹Department of Pulp Paper and Printing Arts,

²Department of Physical Chemistry,

³Department of Organic Syntheses and Fuels, University of Chemical Technology and Metallurgy – Sofia, 8, St. Kliment Ohridski, Blv., 1756, Sofia, Bulgaria

Received October 5, 2015; Revised July 1, 2016

Large amounts of technical hydrolyzed lignin are a residual waste of the hydrolysis industry. Hence, there is an interest to investigate its thermal decomposition. The latter applied in this study consists in a preliminary selective thermal treatment with a subsequent activation aiming to increase the specific area and develop the porous structure. The adsorption-structural method is applied to study the behavior of the activated carbon adsorbents obtained. The main parameters of the porous structure are determined on the ground of the experimentally derived isotherms of Brunauer, Emmett and Teller. The surface thermodynamic characteristics obtained provide a comparative analysis of the samples of the initial hydrolyzed lignin and the activated carbon obtained through pyrolysis as well as through initial hydrolysis and subsequent pyrolysis of the residual hydrolyzed lignin.

Keywords: activated carbon; technical hydrolyzed lignin, BET isotherm

INTRODUCTION

Technical hydrolyzed lignin (THL) is residual waste of the hydrolysis industry. It presents a complex mixture of wood's hydrolytic decomposition including lignin, incomplete hydrolyzable polysaccharides, reducing substances, resins, mineral compounds and monosaccharides. The interest towards studying its thermal decomposition is determined by the large amounts left in the course of production [1]. THL is characterized by its capillary-porous structure determined by its initial wood capillary structure and the lignin production conditions. The porous structure developed determines the sorption properties of THL with respect to organic and inorganic products [2]. It is suitable for production of activated carbon [3] which is predominantly a microporous material with an additionally developed inner surface. Its pore distribution with respect to their dimensions depends on the type of the initial raw material, the process of activation and the conditions of its application [4]. The basic principle of activated carbon production on the ground of a carbonaceous material consists in a preliminary selective thermal treatment and subsequent activation under specific conditions. Thus, the specific surface area of the material is increased and its porous structure is additionally developed. Chemical activators can be used. KOH is one of them. It is experimentally verified that it can

split graphite microcrystals thus assuring micro-pore formation. Its application in case of activated carbon production on the ground of carbonaceous materials is also reported [5]. The basic parameters required to properly choose an activated carbon refer to its texture and mechanical parameters as well as the chemical nature of its surface. Different methods are used to study the adsorbents to be used. One finds that the adsorption-structure has the widest application in case of activated carbon adsorbents. It provides the determination of the main parameters of the porous structure only on the ground of experimentally derived adsorption isotherms [5], which is in fact its basic advantage.

The adsorption isotherm of Brunauer, Emmett and Teller (BET) is often found valid in the case of physical adsorption on highly energetic powder-like materials. The adsorption model of BET has the following characteristics: A) The adsorbent surface behaves as an energetically homogeneous one with adsorption centers of an identical capacity to adsorb; B) The adsorption layers are subsequently deposited, while each new one is identical to that previously formed; C) There are no intermolecular forces of interaction in the adsorbate itself [6, 7]. The classic form of the BET equation connects the amount of the adsorbed substance (Γ) on the surface of a solid adsorbent with the pressure of the adsorbate vapors (p). It refers to polymolecular adsorption in a pressure range from $p = 0$ to the pressure of the adsorbate saturated vapors p^0 :

* To whom all correspondence should be sent:
E-mail: grradeva@uctm.edu

$$\Gamma = \frac{\Gamma_m \theta_0 C \left(\frac{p}{p^0} \right)}{\left(1 - \left(\frac{p}{p^0} \right) \right)^2} \quad (1)$$

where Γ_m is the maximum surface concentration of the adsorbate, C is a constant (known as the BET constant C_{BET}) which depends on the temperature, while θ_0 is the accessible surface of the adsorbent. θ_0 is expressed through the following relation:

$$\theta_0 = \frac{1 - \left(\frac{p}{p^0} \right)}{1 + (C - 1) \left(\frac{p}{p^0} \right)} \quad (2)$$

The substitution of the latter into Eq. (1) leads to the following expression:

$$\Gamma = \frac{\Gamma_m C \left(\frac{p}{p^0} \right)}{\left(1 + (C - 1) \left(\frac{p}{p^0} \right) \right) \left(1 - \left(\frac{p}{p^0} \right) \right)} \quad (3)$$

Eq. (3) can be simplified through a rearrangement. This leads to:

$$\frac{1}{\Gamma \left(\left(\frac{p}{p^0} \right) - 1 \right)} = \frac{1}{\Gamma_m} + \frac{C - 1}{\Gamma_m C} \left(\frac{p}{p^0} \right) \quad (4)$$

One of the forms of the BET equation is obtained through the substitution of Γ with the volume of the adsorbed gas V corresponding to a specific value of $\left(\frac{p}{p^0} \right)$ and that of Γ_m with the maximum volume of the adsorbed gas V_m , i.e.

$$\frac{x}{V(1-x)} = \frac{1}{CV_m} + \frac{C-1}{V_m C} x \quad (5)$$

where $x = \frac{p}{p^0}$. Eq. (5) is an adequate form of the

BET isotherm because the dependence of $\frac{x}{V(1-x)}$ on x is linear and provides the determination of V_m and the constant C_{BET} . The value of V_m can be used to estimate the specific surface of the adsorbent S_{BET} :

$$S_{BET} = \frac{V_m N_A A^o}{V_0} \quad (6)$$

where N_A is the Avogadro's number, A^o is the van der Waals area of the molecule, while V_0 is the volume of a mole of a gas under normal conditions. The total area of the adsorbent's surface S_{EXT} can be calculated on the ground of:

$$S_{EXT} = S_{BET} \cdot m \quad (7)$$

where m is the sample's mass. The value of S_{BET} and S_{EXT} are used to estimate the micro-pores area S_{MI} :

$$S_{MI} = S_{BET} - S_{EXT} \quad (8)$$

The other important characteristic term, the BET constant C_{BET} , is related to the adsorption heat ΔH_1 referring to the first adsorption layer:

$$C_{BET} \approx \exp\left(\frac{\Delta H_1 - \Delta H_{cond}}{RT}\right) \quad (9)$$

ΔH_{cond} is the heat of condensation of the adsorption layers deposited on the initial one [8, 9].

The aim of the present work is to carry out a comparative thermodynamic analysis of the adsorption characteristics of highly effective carbonaceous materials (activated carbons) obtained from residual hydrolyzed lignin.

EXPERIMENTAL

The investigation was carried out with technical hydrolyzed lignin which is a residual waste obtained in the course of wood hydrolysis carried out in the course of forage yeast production. It is worth noting that it has been kept for more than 20 years on a sole.

HPLS (UltiMate 3000) was used to determine the content of residual polysaccharides with respect to that of glucose, lignin and mineral compounds. The humidity of the hydrolyzed lignin sample was determined using the Kern and Sohn apparatus at 105°C. The pH was read using a pH-meter. The characteristics of the initial material are summarized in Table 1.

Table 1. Characteristics of the initial THL.

Parameters	Values
Content of THL polysaccharides (%)	18.84
Content of mineral compounds (%)	5.18
Content of lignin (%)	65.98
pH of the aqueous suspension	3.30
Easily reduced saccharides (%)	2.00

The pyrolysis was carried out in an aluminum Fischer retort following the standard procedure. It produced semi-coke (at a final temperature of 520°C) used for the subsequent preparation of activated carbon. The liquid product obtained after THL pyrolysis was used to determine the moisture content. This was done at a pH of 5.5 using the Dean-Stark apparatus. The material balance of the pyrolyzed THL and of that subjected to hydrolysis and subsequent pyrolysis is presented in Table 2.

Table 2. Material balance of L1 and L2 samples.

Product	Yield, (%)	
	Pyrolyzed THL	Pyrolyzed THL after preliminary hydrolysis
Solid carbonaceous product	49.4	48.7
Total liquid product	29.8	31.1
- water*	67.7	70.9
- tar*	32.3	29.1
Gas and losses**	20.8	20.2

* in % on the ground of the liquid product; ** as a balance difference to 100%

The chemical activation of the samples was carried out with KOH. The samples used consisted of pyrolyzed THL (L1) and pyrolyzed THL, but were initially subjected to hydrolysis (L2). A sample of the initial THL (L0) was used as well.

A mixture of a precursor and KOH in the ratio of 1:1.2 was added to the samples described above. Then they were ground to obtain a homogeneous mass. The activation was carried out for 1 hour in a tube oven at 600 °C under vacuum. Then they were washed thoroughly to reach a neutral pH value. The subsequent process of reactivation was carried out for 2 hours in a reactor under vacuum at 300°C.

The determination of the specific surface area and the parameters of the porous structure of the treated samples were carried out using a High-Speed Surface & Pore size Analyzer System, type NOVA 1200 *e* of QUANTACHROME instruments (USA) through low temperature adsorption of nitrogen at 77.4 K.

The morphology of the initial and fabricated lignin samples was investigated by scanning electron microscopy at 20 kV using JEOL JSM 6390 with a INCA x-sight chemical analysis detector from OXFORD INSTRUMENTS.

RESULTS AND DISCUSSION

The adsorption-desorption isotherms of L0, L1 and L2 were determined through adsorption of nitrogen. They are presented in Figs.1, 2 and 3, with the corresponding SEM images.

Fig. 1 shows that the isotherm of the untreated initial THL (L0) refers to type II adsorption isotherms characteristic for nonporous solid substances or for macroporous adsorbents according to the IUPAC classification. The image presented shows that the surface of the initial lignin has a layered structure of a wavy and chaotic character which is in fact typical for most of the natural polymers.

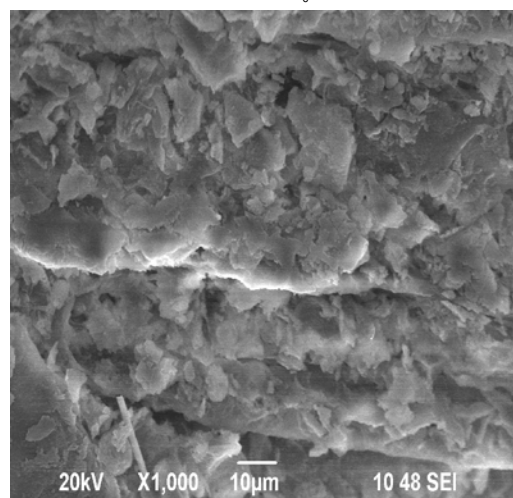
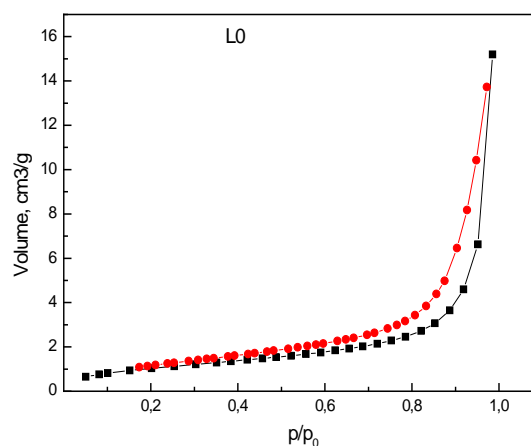


Fig.1. An adsorption-desorption isotherm of the L0 sample and the corresponding SEM image.

Fig. 2 shows that the isotherm of L1 obtained from the initial THL subjected to pyrolysis refers to a type I isotherm relevant to microporous adsorbents. There the width of the pores does not exceed the value of several adsorbate molecule diameters. The force field of the neighboring walls is overlapped by the energy of the adsorbent-adsorbate interaction. The interactions of this type are strong enough to provide complete coverage of the pores at relatively low pressures.

The pyrolysis of the initial THL does not affect the wavy character of the surface but brings about a multilayered tubular structure (Fig.2). The latter corresponds to the structure of plant cells with easily discerned pores.

Fig. 3 shows that the isotherm of L2 obtained from initial THL subjected to hydrolysis and subsequent pyrolysis refers to the mixed type (I and IV) isotherm observed in case of microporous adsorbents with a presence of mesopores. The deviation from type I behavior is observed only in the high pressure range.

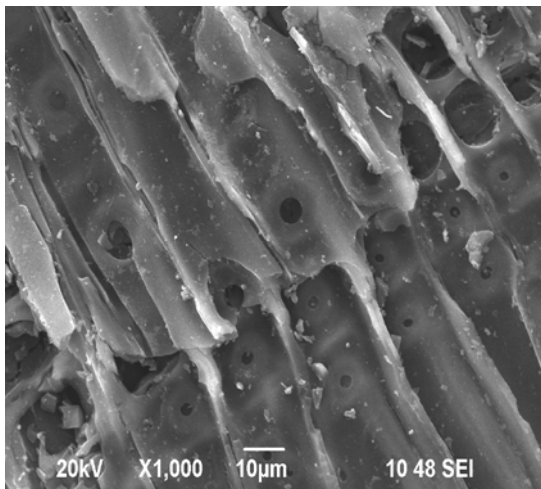
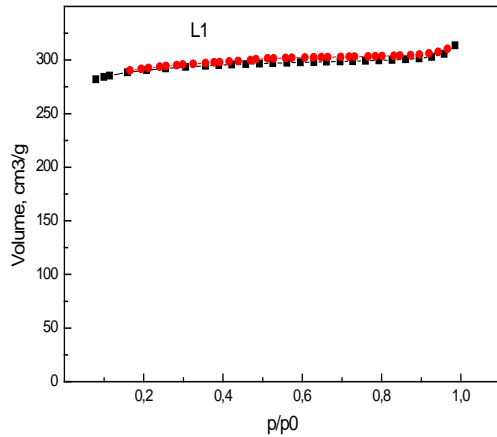


Fig.2. An adsorption-desorption isotherm of the L1 sample and the corresponding SEM image.

The surface of the L2 sample as seen in Fig. 3 is wavy with well expressed micro-pore formation. Its juxtaposition to the structure presented shows that the multilayered tubular structure is in fact preserved but the corresponding tube-like elements are sharply outlined. That is most probably due to the preliminary removal of the residual hardly hydrolysable polysaccharides.

The BET isotherm is applied to the adsorption equilibrium attained in the first monolayer. Eq. (5) is applied in the range from $0.05 \left(\frac{p}{p_0} \right)$ to $0.35 \left(\frac{p}{p_0} \right)$.

The linear dependences obtained in $\frac{x}{V(1-x)}$ vs. x

have a slope of $(B = \frac{C-1}{V_m C})$ and an intercept of $($

$A = \frac{1}{CV_m})$, i.e. they provide for the determination of

C_{BET} and the maximum volume of the adsorbed gas V_m of the samples. The values obtained are summarized in Table 3. The latter shows also the

values of the specific area of the adsorbent S_{BET} , the total area of the surface S_{EXT} and the specific area of the micropores, S_{MI} , calculated with the application of Eqns. (6), (7) and (8).

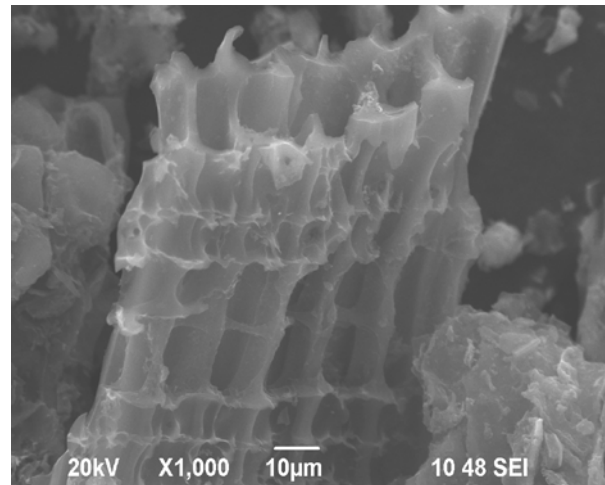
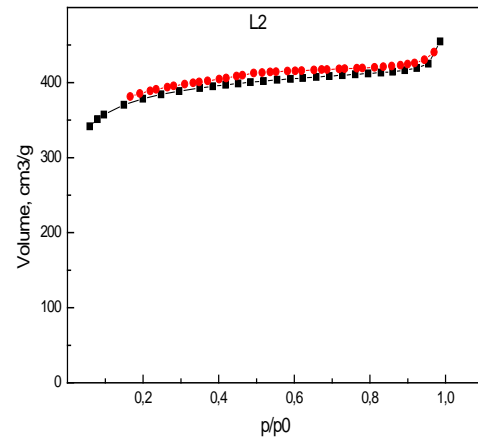


Fig.3. An adsorption-desorption isotherm of the L2 sample and the corresponding SEM image.

Table 3. Basic adsorption parameters of the initial THL and the activated carbon samples.

Sample	S_{BET} , (m^2/g)	S_{MI} , (m^2/g)	S_{EXT} , (m^2/g)	C_{BET}	V_m , (cm^3/g)	ΔH_1 , (J/mol)
L0	4	-	-	54.4	0.919	-5361.6
L1	1300	781	519	290	302.6	-6438.5
L2	1428	1259	169	527	328.3	-6822.9

As seen from Table 3 the activated carbons obtained (L1 and L2) are characterized by a large specific area S_{BET} and high values of the maximum volumes which refer to the carbonaceous materials suitable for gas adsorption. The preliminary hydrolysis and the subsequent pyrolysis and chemical activation in the case of L2 provide a dominant development of the microporous structure illustrated by the S_{MI} values obtained.

The constant C_{BET} can be used, in accordance with Eq. (9), to determine the adsorption heat (

$-\Delta H_1$) characteristic for the specific interaction of the adsorbate and the adsorbent molecules within the first adsorption layer. The Reference data shows that:

$$-\Delta H_{condN_2} = 2.79(kJ/mol).$$

The process is exothermic, while the relatively low value of the enthalpy change is an indication of the proceeding physical adsorption. But it is worth noting that the energy of the adsorbate-adsorbent interaction is greater than that of the adsorbate-adsorbate, which in turn provides polymolecular adsorption.

The values of the entropy and Gibbs function change for the first adsorption layer, ΔS and ΔG , can be evaluated with the application of Eqns. (10) and (11):

$$\Delta G = RT \ln \left(\frac{p}{p^0} \right) \quad (10)$$

$$\Delta S = \frac{\Delta H - \Delta G}{T} \quad (11)$$

Table 4 presents the values obtained for the L2 sample.

Table 4. Values of the entropy and Gibbs function change at $\left(\frac{p}{p^0}\right) = const$.

$\left(\frac{p}{p^0}\right)$	$\Delta G,$ (J/mol)	L1		L2	
		V, (cm ³ /g)	$\Delta S,$ (J/K.mol)	V, (cm ³ /g)	$\Delta S,$ (J/K.mol)
0,1	-1480.5	284.6	-102.3	361.0	-107.3
0,15	-1220.8	287.0	-98.9	371.3	-103.9
0,20	-1035.6	291.8	-96.5	385.0	-101.5
0,25	-892.1	292.0	-94.7	389.5	-99.7
0,30	-774.7	293.3	-93.2	394.1	-98.2
0,35	-675.5	294.4	-91.9	394.2	-96.9

As expected on the ground of the exothermic character of the process the values of ΔG and ΔS are negative. Furthermore they decrease with the increase of the gas adsorbed because the number of the degrees of freedom of the adsorbed species decreases with the simultaneous decrease of the forces of interaction determining the proceeding adsorption. It is worth adding that the tendency

observed in the case of L2 is also followed in L1 although the corresponding values cannot be directly juxtaposed at $V = const$.

CONCLUSION

The surface thermodynamic characteristics of the activated carbon obtained from the technical hydrolyzed lignin and of that produced from the same residual waste but through pyrolysis as well as by initial hydrolysis and subsequent pyrolysis are derived on the ground of the corresponding BET adsorption isotherms. The comparative analysis carried out shows that the additionally treated samples have a large specific area and a microporous texture. The preliminary removal of the residual non-hydrolyzable polysaccharides is a prerequisite for obtaining well outlined multilayered structures. The adsorbents' surface is energetically homogeneous and favors polymolecular adsorption. The process is a spontaneous one.

REFERENCES

1. R. J. A. Gosselink, E. de Jong, B. Guran and A. Abächerli, *Ind. Crop. Prod.*, **20**, 121 (2004).
2. C. Vasile, R. J. A. Gosselink, P. Quintus, E. G. Koukios, D.P. Koullas, E. Avgerinos, D. A. Abacherli, *Cellulose Chem. Technol.*, **40**, 421 (2006).
3. C. Hörnell, Thermochemical and Catalytic Upgrading in a Fuel Context: Peat, Biomass and Alkenes, Dissertation, Royal Institute of Technology, Department of Chemical Engineering and Technology, Stockholm, 2001.
4. G. Krüger, *Chemie in unserer Zeit*, 10, 21, (1976).
5. M. Smisek, S. Cerny, Active carbon, Elsevier Publ. Co., New York, 1970.
6. J.S. Gregg, K.S.W. Sing, Adsorption, Surface Area and Porosity, (second ed.), Academic Press, London, (1982).
7. F. Rouquerol, J. Rouquerol, K.S.W. Sing, Adsorption by Powders and Porous Solids: Principles, Methodology and Applications, Academic Press, London, (1999).
8. A. K. Ladavos, A. P. Katsoulidis, A. Iosifidis, K. S. Triantafylidis, T. J. Pinnavaia, P. J. Pomonis, *Micropor. Mesopor. Mater.*, **151**, 126, (2012).
9. K. Nakai, Y. Nakada, M. Hakuman, M. Yoshida, Y. Senda, Y. Tateishi, J. Sonda, H. Naono, *J. Coll. Int. Sci.*, **367** (1), 383, (2012).

АДСОРБЦИОННИ ХАРАКТЕРИСТИКИ НА АКТИВЕН ВЪГЛЕН ПОЛУЧЕН ОТ ОТПАДЪЧЕН ТЕХНИЧЕСКИ ХИДРОЛИЗИРАН ЛИГНИН

Л. Райчева, Г. Радева, С. Ненкова, Р. Николов

¹*Катедра „Целулоза, хартия и полиграфия”*

²*Катедра „Физикохимия”*

³*Катедра „Органичен синтез и горива,” Химикотехнологичен и металургичен университет – София, бул.
Климент Охридски 8, 1756, София, България*

Постъпила на 5 октомври 2015 г.; коригирана на 1 юли 2016 г.

(Резюме)

Големите количества отпадъчен хидролизен лигнин предизвикват силен интерес към проучванията за неговото термично разлагане. Основният принцип за получаване на активен въглен от въглеродсъдържащ материал се състои в предварителна селективна термична обработка, с последваща активация с цел увеличаване на специфичната повърхност и на порестата структура. Изследването на получените въглеродни адсорбенти е направено чрез адсорбционно-структурния метод. Главните параметри на порестата текстура са определени въз основа на опитно построените изотерми на Брунауер, Емет и Телер. На базата на получените термодинамични характеристики на повърхността е направен сравнителен термодинамичен анализ на проби от изходен хидролизен лигнин и активен въглен от пиролизиран и предварително хидролизиран и пиролизиран технически хидролизен лигнин.

Synthesis and anti-plant pathogenic fungal activity of novel benzofuran-2-carboxamide derivatives

Y. Xin*, H. Wang, F. Chen

School of Pharmacy, Chengdu Medical College, Chengdu, 610083, China

Received September 17, 2014; Revised April 28, 2016

Prompted by the various biological activities of carboxamides and benzofurans, a series of substituted benzofuran-2-carboxamide derivatives (**10a-10j** and **11a-11j**) were synthesized and evaluated for anti-plant pathogenic fungal activity. Some of the novel benzofuran-2-carboxamide derivatives exhibited good antifungal activity against four plant pathogenic fungi. Compound **10g** showed good antifungal activity at 200 mg L⁻¹ and is hoped to be a potential lead compound.

Keyword: Synthesis, anti-plant pathogenic fungal activity, benzofuran-2-carboxamide.

INTRODUCTION

Agricultural fungal diseases are a cause of major economic loss to agriculture [1,2]. At present, chemical control of fungal diseases is mainly achieved by several classes of chemicals, such as carboxamides, methoxyacrylates, pyrimidinamines, triazoles and so on [3-5]. Among them the carboxamide fungicides have played an important role in the market for fungicides [6,7]. They can inhibit the growth of pathogens and cause their eventual death by interfering with the respiration of the pathogen [8,9]. However, fungicide resistances were observed in fungal populations [10,11].

In order to overcome the threat of widespread multifungicide resistances in plant pathogenic fungi, there is ongoing demand for new fungicide agents.

Literature survey reveals that benzofurans having various amide, ester, ether and thioether derivatives with varying functional groups show antifungal activity [12-15], while little work is reported on benzofuran-2-carboxamide derivatives application in agriculture as fungicides.

Hence, we designed and synthesized (Figure 1) novel benzofuran-2-carboxamide derivatives. They were tested for antifungal activity against *Rhizoctonia solani* (*R. solani*), *Bipolaris maydis* (*B. maydis*), *Gibberella zeae* (*G.zeae*) and *Botrytis cinerea* (*B. cinerea*). To the best of our knowledge, this is the first report on benzofuran-2-carboxamide derivatives with potential controlling effect against plant pathogenic fungi.

EXPERIMENTAL

Material and Equipment

All reagents used were commercial and were used without further purification unless otherwise

indicated. Analytical thin-layer chromatography was performed with silica gel plates (60 GF254, Qingdao Haiyang Chemical Co., Ltd., Qingdao, Shandong Province, China). ¹H NMR spectra were recorded in deuteriochloroform solution on a Bruker 400 MHz spectrometer, using tetramethylsilane (TMS) as an internal standard.

Synthesis of Compounds

1. Synthesis of benzofuran-2-carboxylic acid (**4**)

1.1. Synthesis of coumarin dibromide (**2**)

A solution of Br₂ (100 mmol) in CHCl₃ (8.5 mL) was dropwise added to a well stirred solution of compound **1** (100 mmol) and CHCl₃ (20 mL) at room temperature for 3 h. Then a solution of Na₂SO₃ (20%, 20 mL) was added till the excess Br₂ was removed. The organic layer was separated, washed and dried. Finally, the solvent was removed in vacuum to give a pale yellow compound **2** in a yield of 86 % [16].

1.2. Synthesis of benzofuran-2-carboxylic acid (**4**)

KOH (800 mmol) was dissolved in absolute ethanol (70 mL) and cooled to 15°C. Then compound **2** (70 mmol) was added to the above well stirred solution in 30 min. Finally, the reaction mixture was refluxed for 30 min, and crushed ice was added. Concentrated HCl was added till the pH value of the solution was 1. The crude product was collected, washed, dried and recrystallized to give compound **4** in a yield of 79 % [16].

2. Synthesis of 3-methylbenzofuran-2-carboxylic acid (**7**).

2.1. Synthesis of compound (**6**)

A solution of compound **5** (1.36 g), K₂CO₃ (3 g), KI (1.65 g) and acetone (40 mL) was dropwise added to a well stirred solution of ethyl bromoacetate (20 mmol) at room temperature in 1 h. Then the mixture was refluxed for 2 h. Finally, the solution was cooled

* To whom all correspondence should be sent:
E-mail: tibet99@tom.com

to room temperature and filtered. The liquid was distilled and compound **6** was obtained in a yield of 84 % [17].

2.2. Synthesis of compound (7)

A solution of compound **6** (20 mmol), absolute ethanol (25 mL) and NaOC₂H₅ (3.4 g) was refluxed for 15 h. Then ethanol was removed from the reaction mixture, the resulting mixture was added to H₂O and the solution was neutralized. Finally the organic layer was separated, washed and dried. The solvent was removed in vacuum to give compound **7** in a yield of 64 % [17].

3. Synthesis of compounds (8) and (9)

Thionyl chloride (20 mL) was added to compound **4** or **7** (15 mmol) and the mixture was refluxed for 1 h. Then the excess thionyl chloride was removed in vacuum. The crude product **8** or **9** was obtained and used in the subsequent reaction without further purification [18].

4. General procedure for the preparation of the target compounds **10a-10j** and **11a-11j**.

A mixture of NaOH solution (2 mol L⁻¹, 10 mL) and arylamine (5 mmol) cooled to 0°C was added to compound **8** or **9** (5 mmol) in 10 min. Then the reaction mixture was stirred at room temperature for another 5 h. Finally, the mixture was turned into H₂O and the precipitate was collected by filtration. The pure compounds **10a-10j** and **11a-11j** were obtained by recrystallization in anhydrous ethanol in yields of 30–73%. All compounds are listed in Table 1 and the ¹H NMR spectral data are as follows [18]:

N-phenylbenzofuran-2-carboxamide (10a)

Pale brown solid, yield: 86.3 %; ¹H-NMR (400 MHz, CDCl₃): 7.17-7.19 (m,1H), 7.32-7.34 (m,1H), 7.38-7.41 (m,2H), 7.45-7.47 (m,1H), 7.56-7.57 (m,1H), 7.60 (s,1H), 7.70-7.73 (m,3H).

N-(2-chlorophenyl)benzofuran-2-carboxamide (10b)

White crystals, yield: 74.2 %; ¹H-NMR (400 MHz, CDCl₃): 7.10-7.13 (m,1H), 7.33-7.36 (m,2H), 7.44-7.49 (m,2H), 7.60-7.63 (m,2H), 7.71-7.73 (m,1H), 8.57-8.58 (m,1H), 8.97 (s,1H).

N-(3-chlorophenyl)benzofuran-2-carboxamide (10c)

Pale brown solid, yield: 70.1 %; ¹H-NMR (400 MHz, CDCl₃): 7.13-7.15 (m,1H), 7.26-7.34 (m,2H), 7.44-7.48 (m,1H), 7.53-7.59 (m,3H), 7.69 (d,1H), 7.84 (s,1H), 8.39 (s,1H).

N-(2-fluorophenyl)benzofuran-2-carboxamide (10d)

Pale brown solid, yield: 85.5 %; ¹H-NMR (400 MHz, CDCl₃): 7.11-7.20 (m,1H), 7.31-7.35 (m,1H),

7.45-7.49 (m,1H), 7.58-7.62 (m,2H), 7.71 (d,1H), 8.48-8.53 (m,1H), 8.61 (s,1H).

N-(4-fluorophenyl)benzofuran-2-carboxamide (10e)

Pale brown solid, yield: 81.3 %; ¹H-NMR (400 MHz, CDCl₃): 7.11-7.20 (m,1H), 7.31-7.35 (m,1H), 7.45-7.49 (m,1H), 7.58-7.62 (m,2H), 7.71 (d,1H), 8.48-8.53 (m,1H), 8.61 (s,1H).

N-(naphthalen-1-yl)benzofuran-2-carboxamide (10f)

Purple solid, yield: 63.9 %; ¹H-NMR (400 MHz, CDCl₃): 7.25-7.37 (m,2H), 7.42-7.65 (m,5H), 7.72-7.82 (m,2H), 7.90-7.92 (m,1H), 8.01-8.03 (m,1H), 8.17-8.19 (m,1H), 8.83 (s,1H).

N-((furan-2-yl)methyl)benzofuran-2-carboxamide (10g)

Pale brown solid, yield: 87.8 %; ¹H-NMR (400 MHz, CDCl₃): 4.68 (d,2H), 6.33-6.36 (m,2H), 6.96 (s,1H), 7.26-7.31 (m,1H), 7.36-7.43 (m,2H), 7.47-7.55 (m,2H), 7.62-7.66 (m,1H).

N-phenethylbenzofuran-2-carboxamide (10h)

Pale yellow solid, yield: 91.5 %; ¹H-NMR (400 MHz, CDCl₃): 2.96 (t,2H), 3.73-3.77 (m,2H), 6.70 (s,1H), 7.25-7.30 (m,4H), 7.33-7.35 (m,2H), 7.39-7.41 (m,1H), 7.45-7.46 (m,2H), 7.66-7.67 (m,1H).

N-(pyridin-3-yl)benzofuran-2-carboxamide (10i)

Gray solid, yield: 93.4 %; ¹H-NMR (400 MHz, CDCl₃): 7.33-7.37 (m,2H), 7.47-7.51 (m,1H), 7.57-7.59 (m,1H), 7.64 (s,1H), 7.72-7.74 (m,1H), 8.33-8.37 (m,1H), 8.42-8.48 (m,2H), 8.79 (s,1H).

N-(2-chloropyridin-3-yl)benzofuran-2-carboxamide (10j)

Pale brown crystals, yield: 78.6 %; ¹H-NMR (400 MHz, CDCl₃): 7.32-7.38 (m,2H), 7.48-7.52 (m,1H), 7.61-7.74 (m,2H), 8.18 (s,1H), 8.89-8.93 (m,2H).

3-methyl-N-phenylbenzofuran-2-carboxamide (11a)

Pale brown crystals, yield: 86.5 %; ¹H-NMR (400 MHz, CDCl₃): 2.69 (s,3H), 7.14-7.18 (m,1H), 7.31-7.35 (m,1H), 7.36-7.41 (m,2H), 7.44-7.53 (m,2H), 7.64-7.66 (m,1H), 7.70-7.73 (m,2H), 8.35 (s,1H).

N-(2-chlorophenyl)-3-methylbenzofuran-2-carboxamide (11b)

White crystals, yield: 81.7 %; ¹H-NMR (400 MHz, CDCl₃): 2.70 (s,3H), 7.09-7.11 (m,1H), 7.31-7.36 (m,2H), 7.43-7.50 (m,2H), 7.54-7.56 (m,1H), 7.65-7.67 (m,1H), 8.56-8.59 (m,1H), 8.98 (s,1H).

N-(3-chlorophenyl)-3-methylbenzofuran-2-carboxamide (11c)

White solid, yield: 76.2 %; ¹H-NMR (400 MHz, CDCl₃): 2.6 (s,3H), 7.13-7.15 (m,1H), 7.28-7.36 (m,2H), 7.45-7.56 (m,3H), 7.65-7.67 (m,1H), 7.87 (t,1H), 8.35 (s,1H).

N-(2-fluorophenyl)-3-methylbenzofuran-2-carboxamide (11d)

Pale brown crystals, yield: 88.6 %; ¹H-NMR (400 MHz, CDCl₃): 2.69 (s,3H), 7.11-7.21 (m,3H), 7.32-7.36 (m,1H), 7.45-7.49 (m,1H), 7.53-7.55 (m,1H), 7.65-7.67 (m,1H), 8.48-8.53 (m,1H), 8.61 (s,1H).

N-(4-fluorophenyl)-3-methylbenzofuran-2-carboxamide (**11e**)

Pale yellow crystals, yield: 81.5 %; ¹H-NMR (400 MHz, CDCl₃): 2.68(s,3H), 7.06-7.10(m,2H), 7.31-7.35(m,1H), 7.44-7.52(m,2H), 7.64-7.69 (m,2H), 7.65(s,1H).

3-methyl-N-(naphthalen-1-yl)benzofuran-2-carboxamide (**11f**)

White crystals, yield: 92.6 %; ¹H-NMR (400 MHz, CDCl₃): 2.72(s,3H), 7.34-7.37(m,1H), 7.47-7.62(m,5H), 7.68-7.69(m,1H), 7.74-7.76(m,1H), 7.88-7.92(m, 1H), 8.03-8.05(m,1H), 8.18-8.20(m,1H), 8.83(s,1H).

N-((furan-2-yl)methyl)-3-methylbenzofuran-2-carboxamide (**11g**)

Brown crystals, yield: 78.4 %; ¹H-NMR (400 MHz, CDCl₃): 2.64(s,3H), 4.65(d,2H), 6.32-6.36(m,2H), 6.94(s,1H), 7.26-7.30(m,1H), 7.38-7.43(m,3H), 7.59-7.61(m,1H).

3-methyl-N-phenethylbenzofuran-2-carboxamide (**11h**)

Yellow crystals, yield: 87.9 %; ¹H-NMR (400 MHz, CDCl₃): 2.64 (s,3H), 2.95 (t,2H), 3.25 (q,2H), 6.72 (s,1H), 7.25-7.30 (m,4H), 7.32-7.35 (m,2H), 7.39-7.40 (m,2H), 7.59-7.61 (m,1H).

3-methyl-N-(pyridin-3-yl)benzofuran-2-carboxamide (**11i**)

Yellow solid, yield: 88.0 %; ¹H-NMR (400 MHz, CDCl₃): 2.69 (s,3H), 7.33-7.37 (m,2H), 7.47-7.54 (m,2H), 7.66-7.68 (m,1H), 8.35-8.40 (m,3H), 8.78 (s,1H).

N-(2-chloropyridin-3-yl)-3-methylbenzofuran-2-carboxamide (**11j**)

White crystals, yield: 82.5 %; ¹H-NMR (400 MHz, CDCl₃): 2.69 (s,3H), 7.31-7.37 (m,2H), 7.48-7.52 (m,1H), 7.56-7.58 (m,1H), 7.66-7.68 (m,1H), 8.15-8.17 (m,1H), 8.91-8.93 (m,1H), 8.95 (s,1H).

In Vitro Antifungal Activity Test

For preliminary evaluation of compounds **10a-10j** and **11a-11j** the antifungal tests of *R. solani*, *B. maydis*, *G. zaeae* and *B. cirerea* were carried out using the plate growth rate method [19]. The fungi were obtained from the Institute of Pesticide and Crop Protection, Sichuan University.

The tested compounds were dissolved in acetone and added to a sterile agarized Czapek-Dox medium at 45°C. In primary screenings the compounds were used at a concentration of 200 mg L⁻¹. The control sample contained only one equivalent of acetone. The media were poured onto 8-cm Petri dishes (10

mL for each dish) and after 2 days were inoculated with 4 mm potato dextrose agar (medium) discs of overgrown mycelium. The Petri dishes were incubated at 26 °C in the dark. Two or seven days after inoculation the diameters of the cultures were measured. The percentage of inhibition of fungal growth was determined by comparison between the development of fungi colonized on media containing compounds and on the control. Carbendazim and Boscalid, commercial fungicides, were used as a positive control. Three replicates of each test were carried out and the results were statistically treated.

RESULTS AND DISCUSSION

Chemistry

The synthesis of intermediates and target compounds was performed as illustrated in Scheme 1, Scheme 2, Scheme 3 and Table 1. To synthesize target compounds **10a-10j** and **11a-11j**, the intermediates **4** and **7** were prepared in three steps. First, compound **1** was reacted with Br₂ by addition reaction to produce compound **2**. Then compound **2** was rearranged under KOH to obtain compound **3**. Finally, compound **3** was acidified by HCl to give compound **4**.

Compound **7** was prepared in two steps. First, compound **5** was reacted with ethyl bromoacetate under K₂CO₃ to produce compound **6** which was rearranged under NaOC₂H₅ to give compound **7**.

Then compound **4** or **7** was reacted with SOCl₂ to obtain compound **8** or **9**. Finally, compound **8** or **9** was reacted with various substituted aromatic amines by amidation to obtain the target compounds **10a-10j** and **11a-11j**.

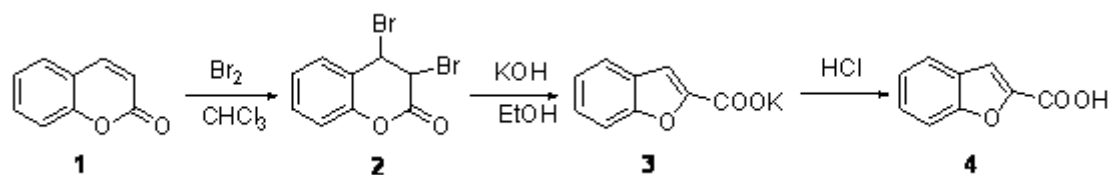
Antifungal Activity Evaluation

The results of the antifungal activity of compounds **10a-10j** and **11a-11j** against *R. solani*, *B. maydis*, *G. zaeae* and *B. cirerea* are listed in Table 2, in which the antifungal activities are expressed as inhibition of growth. We compared the growth rate of fungi on a medium containing a vehicle with the growth rate of fungi on a pure medium. The result indicated that the vehicle for compounds showed no visible antifungal activity.

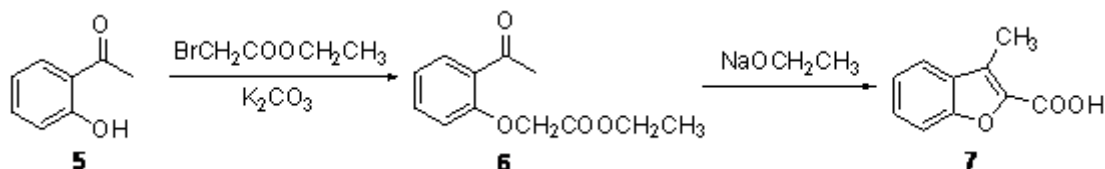
The results of Table 2 show that the target compounds **10a-10j** and **11a-11j** are active against nearly four fungi at 200 mg L⁻¹. Some of the compounds showed good antifungal activities against *R. solani*. For example, the inhibition of the growth of compounds **10f** and **10g** reached 78.68 % and 65.68 % against *R. solani* at 200 mg L⁻¹, respectively. Compounds **10g** and **10i** exhibited good antifungal activities against *B. maydis*. Their

inhibition ratios were 80.57 % and 78.36 %, respectively. Compound **10g** had good inhibition against *B. cirreia* and the inhibition ratio was 68.33

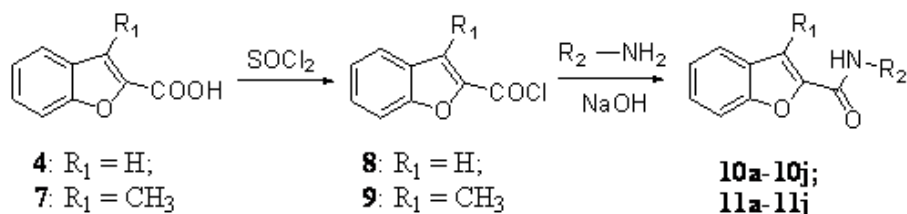
%. Compound **10g** was expected to be a potential lead compound.



Scheme 1. Synthesis of benzofuran-2-carboxylic acid (**4**).



Scheme 2. Synthesis of 3-methylbenzofuran-2-carboxylic acid (**7**).



Scheme 3. Synthesis of target compounds **10a-10j** and **11a-11j**.

Table 1. Structures of benzofuran-2-carboxamide derivatives.

Compound	R ₁	R ₂	Compound	R ₁	R ₂
10a	H	phenyl	11a	CH ₃	phenyl
10b	H	2-chlorophenyl	11b	CH ₃	2-chlorophenyl
10c	H	3-chlorophenyl	11c	CH ₃	3-chlorophenyl
10d	H	2-fluorophenyl	11d	CH ₃	2-fluorophenyl
10e	H	4-fluorophenyl	11e	CH ₃	4-fluorophenyl
10f	H	1-naphthalenyl	11f	CH ₃	1-naphthalenyl
10g	H	2-furanylmethyl	11g	CH ₃	2-furanylmethyl
10h	H	phenethyl	11h	CH ₃	phenethyl
10i	H	3-pyridinyl	11i	CH ₃	3-pyridinyl
10j	H	2-chloro-3-pyridinyl	11j	CH ₃	2-chloro-3-pyridinyl

Table 2. Antifungal activity of benzofuran-2-carboxamide derivatives at 200 mg L⁻¹.

Compound	Inhibition of growth (%)			
	<i>R. solani</i>	<i>B. maydis</i>	<i>G. zeae</i>	<i>B. cirerea</i>
10a	3.15	5.46	3.85	5.68
10b	5.23	14.26	5.39	16.34
10c	4.56	20.25	21.47	10.05
10d	25.79	6.37	2.04	24.18
10e	56.37	14.88	14.06	10.35
10f	78.68	66.41	32.64	49.88
10g	65.68	80.57	28.69	68.33
10h	4.14	39.26	14.05	18.24
10i	57.22	78.36	25.03	66.78
10j	29.29	22.12	11.66	6.28
11a	58.95	32.06	16.08	42.37
11b	18.23	32.11	4.31	11.00
11c	13.34	29.26	3.23	19.21
11d	47.26	7.78	3.69	41.06
11e	38.00	26.56	4.46	53.07
11f	15.17	20.57	34.29	46.41
11g	22.25	20.69	9.37	42.24
11h	63.87	53.35	24.06	49.45
11i	24.96	44.33	14.08	28.26
11j	12.36	12.26	8.20	5.60

CONCLUSIONS

In summary, 20 novel benzofuran-2-carboxamide derivatives **10a-10j** and **11a-11j** were synthesized and evaluated for their antifungal activity against four plant pathogenic fungi (*R. solani*, *B. maydis*, *G. zeae*, *B. cirerea*). The results showed that some of the synthesized compounds exhibited good antifungal activities at 200 mg L⁻¹ and compound **10g** is expected to be a potential lead compound. Furthermore, these preliminary results are promising and beneficial for further studies in developing new and more effective fungicides in the agrochemical field. Further structural modification and biological evaluation of these compounds are ongoing in our laboratory.

Acknowledgements: This work was supported by the Research Program of Department Education of Sichuan Province (11ZB171).

REFERENCES

1. M. J. Gilbert, C. R. Thornton, E. Gavin, G. E. Wakley, N. J. Talbot, *Nature*, **440**, 535 (2006).
2. L. P. Partida-Martinez, C. Hertweck, *Nature*, **437**, 884 (2005).
3. P. E. Russell, *J. Agric. Sci.*, **143**, 11 (2005).
4. M. T. McGrath, *Plant. Dis.*, **85**, 236 (2001).
5. C. Lamberth, S. Jeanmart, T. Luksch, A. Plant, *Science*, **341**, 742 (2013).
6. J. C. Yang, J. B. Zhang, B. S. Chai, C. L. Liu, *Agrochemicals*, **47**, 6 (2008).
7. W. Krämer, U. Schirmer, P. Jeschke, M. Witschel, 'Modern Crop Protection Compounds', Wiley-VCH Verlag & Co. KGaA, Weinheim, 2012.
8. Q. C. Huang, *World Pestic.*, **26**, 23 (2004).
9. P. Leroux, *Pestic. Sci.*, **47**, 191 (1996).
10. P. Leroux, G. Berthier, *Crop Prot.*, **71**, 6 (1988).
11. T. Veloukas, A. N. Markoglou, G. S. Karaoglanidis, *Plant Dis.*, **97**, 118 (2013).
12. M. Masubuchi, H. Ebiike, K. Kawasaki, S. Sogabe, K. Morikami, Y. Shiratori, S. Tsujii, T. Fujii, K. Sakata, M. Hayase, H. Shindoh, Y. Aoki, T. Ohtsuka, N. Shimma, *Bioorg. Med. Chem.*, **11**, 4463 (2003).
13. M. Masubuchi, K. Kawasaki, H. Ebiike, Y. Ikeda, S. Tsujii, S. Sogabe, T. Fujii, K. Sakata, Y. Shiratori, Y. Aoki, T. Ohtsuka, N. Shimma, *Bioorg. Med. Chem. Lett.*, **11**, 1833 (2001).
14. H. Ebiike, M. Masubuchi, P. Liu, K. Kawasaki, K. Morikami, S. Sogabe, M. Hayase, T. Fujii, K. Sakata, H. Shindoh, Y. Shiratori, Y. Aoki, T. Ohtsuka, N. Shimma, *Bioorg. Med. Chem. Lett.*, **12**, 607 (2002).
15. K. Kawasaki, M. Masubuchi, K. Morikami, S. Sogabe, T. Aoyama, H. Ebiike, S. Niizuma, M. Hayase, T. Fujii, K. Sakata, H. Shindoh, Y. Shiratori, Y. Aoki, T. Ohtsuka, N. Shimma, *Bioorg. Med. Chem. Lett.*, **13**, 87 (2003).
16. R. C. Fuson, J. Wayne Kneisley, E. W. Kaiser, *Org. Synth.*, **3**, 209 (1955).
17. J. C. Li, T. S. Rush, W. Li, *Bioorg. Med. Chem. Lett.*, **15**, 4961 (2005).
18. A. A. Marei, R. A. Paphael, *J. Chem. Soc.*, 2624 (1958).
19. H. Jin, Y. C. Geng, Z. Y. Yu, K. Tao, T. P. Hou, *Pestic. Biochem. Physiol.*, **93**, 133 (2009).

СИНТЕЗА НА НОВИ БЕНЗОФУРАН-2-КАРБОКСАМИДОВИ ПРОИЗВОДНИ И ТЯХНАТА АКТИВНОСТ СПРЯМО ПАТОГЕННИ ГЪБИЧКИ

Я. Син*, Х. Уанг, Ф. Чен

Фармацевтичен колеж, Медицински колеж в Ченгду, Китай

Постъпила на 17 септември, 2014 г.; коригирана на 28 април, 2016 г.

(Резюме)

Синтезирани са серия заместени бензофуран-2- карбоксамидови производни (**10a-10j** and **11a-11j**) и е оценена тяхната хербицидна и фунгицидна активност. Някои от тях проявяват добра активност срещу четири патогенни растителни фунги. Съединение **10g** показва добра фунгицидна активност при 200 mg L⁻¹ и се предполага да бъде потенциално водещо съединение.

Determination of metal ions by ultrasound-assisted hollow fiber liquid-phase microextraction technique

YuJiao Tu¹, Haizhi Wu^{2*}

¹Department of Chemical Science and Technology, Kunming University, Kunming, Yunnan Province, China;

^{2*}Faculty of Land Resources and Engineering, Kunming University of Science and Technology, Kunming, 650093, China

Received October 10, 2016; Revised February 10, 2017

A novel approach, ultrasound-assisted hollow fibre liquid-phase microextraction (UA-HF-LPME) was used for the preconcentration of Copper (Cu), cadmium (Cd) and chromium (Cr) of environmental samples by flame atomic absorption spectrometry (FAAS). The method was based on the extraction of the analytes from environmental samples (donor phase) into 15 μ L of nonanoic acid supported by a porous-walled polypropylene hollow fibre by ultrasound-mixing. Ultrasound-mixing was used as an assisted method to accelerate the mass transfer and minimize fluid loss. Under the optimal conditions, the detection limits of this method for Cr, Cu, and Cd were 0.28, 0.35, and 0.19 μ g/L, respectively. The relative standard deviations for Cr, Cu, and Cd were 2.0, 2.6 and 1.8% ($C=0.5\mu$ g/L, $n=9$). The relative recoveries of Cr, Cu, and Cd in well water and wastewater samples at the spiking level of 10 μ g/mL ranged from 80.5 to 96.4%. The method is successfully applied for these metals content evaluation in environmental samples with satisfactory results and high enrichment factors (200).

Keywords: Ultrasound-assisted hollow fibre liquid-phase microextraction, Environmental samples, Metal ions, Flame atomic absorption spectrometry.

INTRODUCTION

Environmental contamination by heavy metal ions in aquatic ecosystems has been increasing with industrial growth and development in recent years. Among all heavy metals, cadmium ion is considered as an extremely toxic metal ion when its concentration in water exceeds 0.01 mg/L which is the permissible limit for human consumption [1]. The main emissions of cadmium occur from waste incineration and fuel burning, but it is also used in foundry and metallurgic industries, batteries, plastics, fertilizers and other materials. Inhaling cigarette smoke has proven to cause exposure to cadmium [2]. Copper is an essential element for many biological systems, which plays an important role in carbohydrate and lipid metabolism. In general, copper at nearly 40 μ g L⁻¹ is required for normal metabolism of many living organisms; however, in higher levels it is considered to be toxic and severe oral intoxication will affect mainly the blood and kidneys [3]. Direct determinations of trace or ultra-trace levels of heavy metals in environmental samples are difficult because of their extremely low concentrations in interfering matrices [4]. To overcome these problems, the combination of a separation and preconcentration procedure with flame atomic absorption spectrometry (FAAS) is useful [5,6].

Therefore, a separation and preconcentration technique is extensively applied to the FAAS determination of metal ions [7], hollow fibre liquid-phase microextraction (HF-LPME) is an excellent pretreatment method that is highly compatible with FAAS and overcomes many of the disadvantages of traditional extraction techniques, such as solid-phase extraction (SPE) [8], solid-phase microextraction (SPME), co-precipitation [9], liquid-liquid extraction (LLE) [10,11] and dispersive liquid-liquid microextraction (DLLME) [12]. Hollow fibre liquid-phase microextraction (HF-LPME) technique, originally proposed by Pedersen-Bjergaard and Rasmussen [13] has gained considerable interest in the analytical area and has been widely applied to a variety of environmental and biological samples. In HF-LPME procedure, the analytes are extracted from an aqueous sample (donor phase) into an organic acceptor phase supported by a porous-walled polypropylene hollow fibre [14-16]. The volume of sample in HF-LPME can range between 5mL and greater than 1L, however, the volume of the extraction solvent (acceptor phase) is, in most cases, in the range 2-30 μ L [17], thus, the very high analyte enrichment factor can be obtained. Although classical HF-LPME procedure take long time (more than 30 min), and the repeatability is not good, the major advantages of HF-LPME are simplicity, negligible volume of solvents used, high enrichment factor, large pH tolerance range, excellent sample clean-up

* To whom all correspondence should be sent:

E-mail: 554214954@qq.com

and low cost [18]. In general, most HF-LPME reports performed using stirring to help mass transfer were very slow [19-21]. Ultrasound-assisted hollow fibre liquid-liquid-liquid microextraction was reported by Yu-Ying Chao [22] for the determination of chlorophenols in water samples. However, to the best of our knowledge, ultrasound-mixing has not yet been applied for determination metal ions in environmental samples using hollow-fibre liquid phase microextraction.

In this work, a novel approach, ultrasound-assisted hollow fibre liquid-phase microextraction (UA-HF-LPME) was used for the preconcentration of Cd, Cu, and Cr from environmental samples by FAAS. Ultrasound-mixing was used as an assisted method to accelerate the mass transfer and minimize fluid loss. The factors affecting preconcentration of the metal ions such as sample pH, eluent type and concentration, extraction solvent type and concentration, fibre length, equilibrium time and matrix effects were investigated in detail.

EXPERIMENTAL

Chemicals and reagents

All reagents used were of analytical grade. All solutions were prepared with ultra-high purity (UHP) water from a Milli-Q system (18.2 M Ω cm). Laboratory glassware was kept overnight in 10% HNO₃ solution. Standard stock solutions of metal ions (1000 mg L⁻¹) were prepared by dissolving their nitrate salts in 1 mol L⁻¹ HNO₃. The standard working solutions of metal ions were prepared by dilution of their stock solutions. Buffer solutions are CH₃COOH-CH₃COONa (pH =4-6), CH₃COONH₄ (pH=7) and NH₃/NH₄Cl (pH=8-10). 1-octanol, nonanoic acid, caprylic acid, capric acid and 1-undecanol of analytical standard were obtained from Aladdin Chemistry (Shanghai, China).

Instrumentation and materials

A ultrasound instrument was employed for experiments (Shanghai, China) and flame atomic absorption spectrometer (AA-6300C, Shimadzu, Japan) were used for the determination of the concentration of metals. A centrifuge with centrifugal vials (Shanghai surgical instrument factory, 80-2, Shanghai, China) was used for phase separation. A vortex agitator (Kylin-Bell Lab Instruments Co. Ltd., Jiangsu, China) was used for vortex-mixing. The porous hollow fibre used to support the organic phase was Q3/2 polypropylene (Wuppertal, Germany) with 600 μ m inner diameter,

200 μ m of wall thickness and pores of 0.2 μ m. A 1.0 mL microsyringe (model 702SNR) with a sharp needle tip was used for the injection of the extraction solvent into the hollow fibre lumen. Instrumental parameters were adjusted according to the manufacturer's recommendations.

Preparation of hollow fibre and UA-HF-LPME extraction procedure

The hollow fibre was cut into 5 cm length pieces. Before use them, each piece was sonicated for 5 min in acetone in order to remove any contamination in the fibre and then, dried in air. The fibre was soaked in nonanoic acid for 15 s to impregnate the pores, and the lumen of the prepared fibre piece was filled with 15 μ L nonanoic acid using a microsyringe carefully. Both open ends of the fibre were sealed by a piece of aluminium foil. Then the hollow fibre was bent to a U-shape and immersed in the 5 mL sample solution (pH 5.0, adjusted with CH₃COOH-CH₃COONa buffer solution) containing 10 μ g mL⁻¹ of each metal ion (Cu, Cd, Cr). The sample was ultrasound-mixed for 2 min at room temperature. Then, the fibre was removed from the sample solution, and its closed end was cut. The 0.5mL methanol was injected into one of its end by a microsyringe. Finally the extract was filtered by a 0.45 μ m membrane and injected into the FAAS system for analyses. A fresh hollow fibre was used for each extraction to decrease the memory effect [23].

Sample Preparation

Well water and wastewater samples were collected from Kunming, China. The samples were filtered through a 0.45 μ m membrane filter.

RESULTS AND DISCUSSION

Optimization of the UA-HF-LPME procedure

Several different experimental parameters that can influence the extraction efficiency were investigated in our experiments. The optimization procedure was done as described in UA-HF-LPME procedure.

Selection of organic extraction solvent and eluent

The type of organic solvent used in HF-LPME is an essential consideration for an efficient extraction of target analyte from aqueous solution. Firstly, it should provide high solubility for the target analytes, and should have a low solubility in water. Addition, the ideal organic extraction solvent should have a low volatility and an appropriate viscosity to prevent diffusion and volatile loss.

Compared with the other extractant, long chain alcohols and acids have those particular properties, which have special extraction efficiency for the analytes. Thus, five organic solvents (1-octanol, nonanoic acid, caprylic acid, capric acid, 1-undecanol) with different viscosities, volatilities and partition coefficients were evaluated in this work. As shown in Fig. 1, nonanoic acid was the most suitable extraction solvent as it resulted in the highest response. Nonanoic acid has larger viscosity, less volatility and better compatibility in polarity with metal ions, those characteristics attributed to lower solvent loss during extraction and higher recovery.

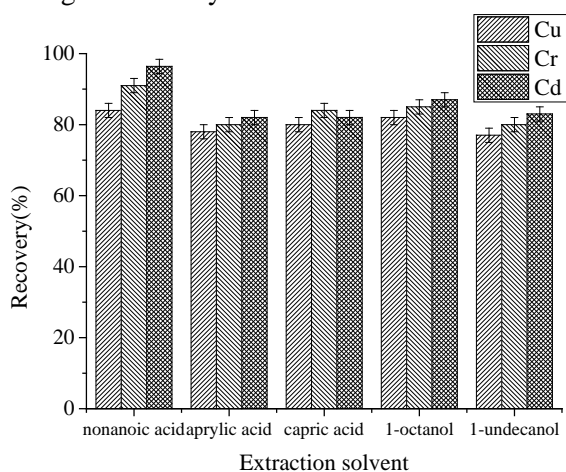


Fig. 1. Effect of extraction solvent on the recovery

The selection of eluent is critical and it affects the extraction efficiency and the enhancement factor. The elution of analytes could be inconvenient owing to irreversible binding of some elements. An appropriate eluent should desorb the metals or chelate complexes and be suitable for the subsequent determination technique. The studied eluents include methanol, ethanol and acetonitrile. The results were shown in Fig. 2, which proved methanol was the best eluent for Cu, Cr and Cd.

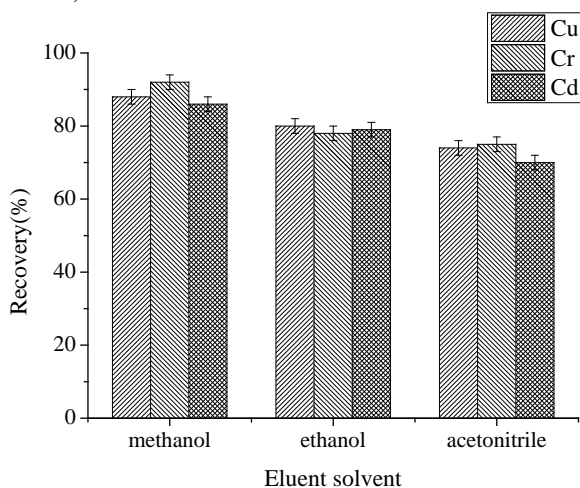


Fig. 2. Effect of eluent solvent on the recovery

Effect of fibre length

In general, a short fibre length will provide a high enrichment factor for the concentration of trace analytes in HF-LPME procedure. However, too short fibre membranes cannot provide sufficient extractant to promote analytes transport to extraction solvent. Thus, the fibre lengths of 2, 4, 5, 6, 8, and 10cm were examined. The results in Fig. 3 indicated that 5 cm was sufficient, and no significant effect was found when the fibre length ranged from 6 to 10 cm. accordingly, an HF length of 5 cm which containing approximately 20 μ L extraction solvent was selected for the subsequent experiments.

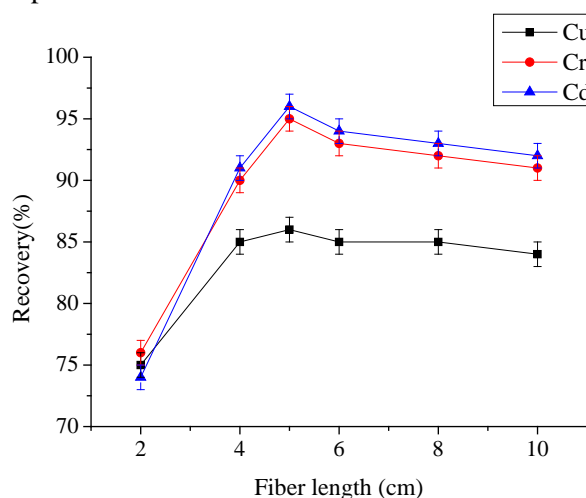


Fig. 3. Effect of fiber length

Effect of pH on UA-HF-LPME

The formation of metal complexes and its chemical stability are the two important effective factors for the HF-LPME and the pH of the sample solution plays a critical role on metal chelate formation and subsequent extraction efficiency. Thus, the effect of pH ranged from 3.0 to 9.0 using acetate buffer solutions for pH adjustment on extraction efficiency of Cr, Cu, and Cd was evaluated and the results are shown in Fig. 4. As can be seen, the optimum pH for Cr, Cu, and Cd maximum extraction efficiency was 5.0. So, in subsequent experiments, pH 5.0 was chosen as the optimum for further experiments.

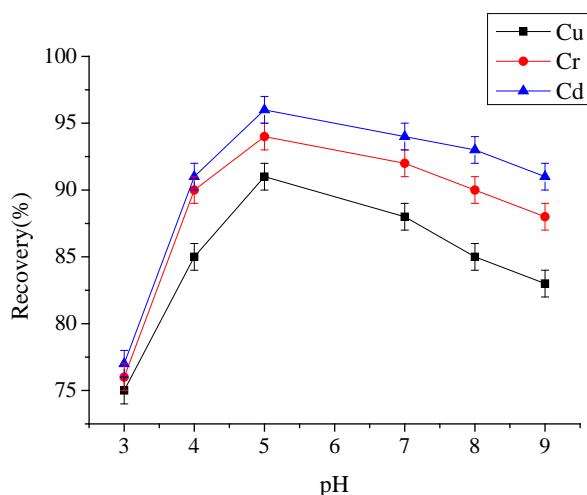


Fig. 4. Effect of pH

Effect of the ultrasound-mixing time

In our study, the extraction can be accelerated by ultrasound-mix of the sample solution. Similar results were observed with ultrasound-mixing times between 1 and 10 min (Fig. 5). Significant effect was observed on the extraction recovery when the ultrasound-mixing time was increased. This may be due to the fact that the analytes were thrown out from fibre membrane because of the high shear forces. Therefore, an ultrasound-mix time of 2 min at 3000 rpm was selected for further experiments.

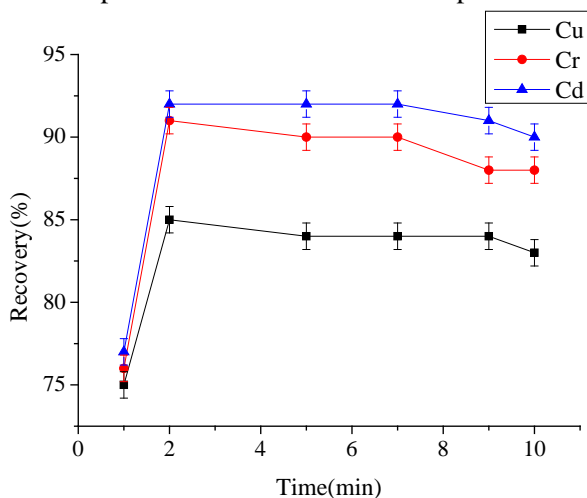


Fig. 5. Effect of the ultrasound-mixing time

Comparison of the proposed method with other reported methods

Table 1 provides a comparison between the proposed method and other reported pretreatment techniques coupled with FAAS from the viewpoint of sample preparation, recovery, extraction time, solvent amount. As listed in Table 1, the analytical performance of this novel extraction is certain advantages and feasibility.

Analytical Figures of Merits

The analytical characteristics of the method were evaluated under the optimum experimental conditions. The relative standard deviations (RSD) and the limits of detection (LOD) are effective factors to evaluate a developed analytical method. With the optimized system, the calibration graph of Cr, Cu and Cd was linear in the range of 10 to 1,000 µg/L. The calibration equation is $A=2.8 \times 10^{-2}C+0.0031$ with a correlation coefficient of 0.9997 for Cr, $A=3.6 \times 10^{-2}C+0.028$ with a correlation coefficient of 0.9968 for Cd and $A=7.9 \times 10^{-2}C+0.003$ with a correlation coefficient of 0.9999 for Cu, where A is the absorbance and C is the Cu, Cr or Cd concentration in µg/L. The detection limits, defined as the concentration equivalent to three times the standard deviation of the reagent blank, for Cr, Cu and Cd were 0.28, 0.35 and 0.19 µg/L, respectively. The relative standard deviations for Cr, Cu and Cd were 2.0, 2.6 and 1.8% ($C=0.5 \mu\text{g/L}$, $n=9$). The relative recoveries of Cr, Cu and Cd in well water and wastewater samples at the spiking level of 10 µg/mL ranged from 80.5 to 96.4%.

Analysis of Real Samples

The environmental samples which are Well water and wastewater were analyzed to evaluate the feasibility of the described preconcentration method. The obtained results are shown in Table 2. The obtained values are in good agreement with the certified values. The determination of Cr, Cu and Cd in well water and wastewater samples was made together with the recovery studies. The recoveries for spiked metal ion concentrations were found in a range of 80.5-96.4% which indicate that the method is applicable for the determination of analytes in real samples with various matrices.

CONCLUSION

A novel ultrasound-assisted hollow fibre liquid-phase microextraction (UA-HF-LPME) method has been developed for determination of three metal ions in environmental samples. The target analytes were enriched very quickly into the acceptor phase with continuous ultrasound-mixing instead of stirring. Coupled with flame atomic absorption spectrometry detection, the method has been proven to be simple, rapid, and reliable for metal ions in environmental samples. In future work, it will be extended in separation and preconcentration of different inorganic and organic species.

Table 1. Comparison of the proposed method with other reported methods

Analytes	Method	Recovery (%)	Extraction time (min)	Solvent amount	References
Pd,Ag	SPE		4		[24]
Cu,Ni,Co	SDSPE	80.7-97.5	2	0.5mL	[25]
Cu,Cr,Cd	UA-HF-LPME	80.5-96.4	2	20 μ L	This work

Table 2. Analysis of metal ions well water and wastewater

Samples	Element	Added ($\mu\text{g L}^{-1}$)	Found ($\mu\text{g L}^{-1}$)	Recovery (%)
Well water	Cu	0	ND	
		5	4.5 \pm 0.3	90
		10	8.7 \pm 0.2	87.0
	Cr	0	ND	
		5	4.8 \pm 0.2	96.0
		10	9.6 \pm 0.2	96.0
	Cd	0	ND	
		5	4.2 \pm 0.4	84
		10	8.2 \pm 0.2	82.0
Waste water	Cu	0	ND	
		5	4.2 \pm 0.4	84.0
		10	8.5 \pm 0.3	85.0
	Cr	0	ND	
		5	4.8 \pm 0.2	96.0
		10	9.6 \pm 0.2	96.0
	Cd	0	ND	
		5	4.5 \pm 0.3	90.0
		10	8.07 \pm 0.2	80.5

REFERENCES

- M.M. Saeed, M. Ahmed, *Anal. Chim. Acta.*, **2**, 525 (2004).
- T.A. Maranhao, D.L.G. Borges, M.A.M.S. da Veiga, A.J. Curtius, *Spectrochim. Acta, Part B.*, **5**, 60 (2005).
- H.B. Tabrizi, *J. Hazard. Mater. B.*, **4**, 139 (2007).
- J. Yea, S. Liu, M. Tian, W. Li, B. Hu, W. Zhou, Q. Jia, *Talanta*, **15**, 118 (2014).
- E. Yavuz, S. Tokalioğlu, H. Sahan, S. Patat, *RSC Advances*, **3**, 46 (2013).
- A. Bagheri, M. Behbahani, M.M. Amini, O. Sadeghi, A. Tootoonchi, Z. Dahaghin, *Microchim. Acta*, **3**, 178 (2012).
- A. Ballesteros-Gómez, Rubio, S. Perez-Bendito, D, *J. Chromatogr. A*, **3**, 1216 (2009).
- Q. Jia, X. Kong, W. Zhou, L. Bi, *Microchem. J.*, **1**, 89 (2008).
- M.S. Bispo, E.S.B. Morte, M.G.A. Korn, L.S.G. Teixeira, M. Korn, A.C.S. Costa, *Spectrochim. Acta, Part B*, **5**, 60 (2005).
- S.L.C. Ferreira, A.S. Queiroz, A.S.Q. Melo, J.C.R. Asis, M.G.A. Korn, A.C.S. Costa, *Anal. Lett.*, **12**, 30 (1997).
- S. Nazari, *Microchem. J.*, **2**, 90 (2008).
- C.Q. Wu, D.Y. Chen, Y.S. Feng, *Anal. Lett.*, **14**, 45 (2012).
- S. Pedersen-Bjergaard, K. Rasmussen, *Anal. Chem.*, **14**, 71 (1999).
- H. Ebrahimzadeh, N. Shekari, Z. Saharkhiz, A.A. Asgharinezhad, *Talanta*, **6**, 94 (2012).
- H. Hansson, U. Nilsson, *Talanta*, **4**, 77 (2009).
- Y.L. Wu, B. Hu, *J. Chromatogr., A*, **45**, 1216 (2009).
- S. Pedersen-Bjergaard, K.E. Rasmussen, *J. Chromatogr. A*, **1-2**, 1184 (2008).
- M. Hadjmohammadi, H. Karimiyan, V. Sharifi, *Food Chem.*, **2**, 141 (2013).
- H. Hadi, A. Makahleh, B. Saad, *J. Chromatogr., B*, **3**, 895 (2012).
- R.I. San, M.L. Alonso, L. Bartolome, R.M. Alonso, *Talanta*, **20**, 100 (2012).
- X. Xu, F.H. Liang, J.Y. Shi, X. Zhao, Z.M. Wang, *Anal. Chim. Acta.*, **15**, 790 (2013).
- Y.Y. Chao, Y.M. Tu, Z.X. Jian, H.W. Wang, Y.L. Huang, *J. Chromatogr., A*, **1**, 1271 (2103).
- M. Asadi, *Iran.J.Anal.Chem.*, **1**, 2 (2014).
- R.J. Cassella, O.I.B. Magalhaes, M.T. Couto, E.L.S. Lima, M. Neves, F.M.B. Coutinho, *Talanta*, **1**, 67 (2005).
- L. Meng, C. Chen, *Anal. Lett.*, **3**, 48(2015).

ОПРЕДЕЛЯНЕ НА МЕТАЛНИ ЙОНИ ЧРЕЗ УЛТРАЗВУК-ПОДПОМАГАНА ТЕЧНО-МИКРОЕКСТРАКЦИОННА ТЕХНИКА С КУХИ ВЛАКНА

Ю Джиао Тю¹, Хайжи Вю² *

¹Отделение по химичните науки и технологии, Университет в Кунмин, Кунмин, Провинция Юнан, Китай;

²Факултет за земни ресурси и инженерство, Университет за наука и технологии, Кунмин 650093, Китай.

Получена на 10 октомври, 2016 г.; ревизирана на 10 февруари, 2017 г.

(Резюме)

Един нов подход, ултразвук-подпомагана течно-микроекстракционна техника с кухи влакна (UA-HF-LPME) се използва за прекоцентриране на мед (Cu), кадмий (Cd) и хром (Cr) от проби от околната среда чрез атомно абсорбционна спектрометрия (FAAS). Методът се основава на екстракция на анализите от проби на околната среда (фаза донор) в 15 μL на нонанова киселина, поддържана от полипропиленови кухи влакна с порести стени, с ултразвуково смесване. Ултразвуковото смесване се използва като метод за подпомагане и ускоряване на масопеноса и свеждане до минимум на загубата на течност. При оптимални условия, границите на откриване на този метод за Cr, Cu, Cd са 0.28, 0.35 и 0.19 $\mu\text{g/L}$ съответно, относителните стандартни отклонения за Cr, Cu, Cd са 2.0, 2.6 и 1.8% ($C = 0.5 \mu\text{g/L}$, $n = 9$). Относителните нива на регенерация на Cr, Cu и Cd в проби от кладенчова вода и отпадни води в границите на 10 $\mu\text{g/L}$ варират от 80,5 до 96,4%. Методът се прилага успешно за оценка на съдържанието на тези метали в проби от околната среда със задоволителни резултати и високи фактори на обогатяване (200).

Environmental safety assessment on chlorination by-products in brine discharged from desalination plant

Jing Liu^{*}, Xingyu Zeng, Dongxing Zhou, Yunrong Zhao, Xianhui Pan

The Institute of Seawater Desalination and Multipurpose Utilization(SOA), Tianjin, China

Received October 10, 2016; Revised February 10, 2017

Concentration analysis was performed on five chlorination by-products (chloral, dichloroacetic acid, trichloroacetic acid, 2,4,6-trichlorophenol, and pentachloro-phenol) present in the brine discharged from desalination project of Dagang New Spring Co., Ltd. Moreover, toxic effects (L(E)C₅₀) analysis was performed on three basic levels of aquatic organisms, namely, *Scenedesmus vacuolatus*, *Daphnia magna*, and *Oncorhynchus mykiss*. Based on the analysis, the quotient method from the technical guidance document on safety assessment of chemical substances by the European Union was adopted to assess the ecological risks of five chlorination by-products in the brine discharged from desalination plant. The results showed that the rates of detection of five chlorination by-products were 100%. The quotients of PEC/PNEC of chloral, dichloroacetic acid, trichloroacetic acid and pentachlorophenol were higher than 1. Among the four pollutants, we must pay more attention to chloral which environmental concentration in the brine discharged from desalination plant is 17 times higher than the no effect concentrations.

Key words: by-products, brine, chlorination, desalination, discharged, safe assessment.

INTRODUCTION

The global water production by desalination will exceed 38 billion cubic meters per year, nearly twice the rate of global water production in 2008[1]. According to the 12th Five-Year (2010–2015) Plan for the scientific and technological development of seawater desalination [2], an innovative system would be established during the period, and desalination technology should reach an advanced level [3]. But brine discharge from desalination plants contains pollutants such as chemical additives and heavy metals, resulting in serious impacts on the offshore seawater environment and the ecological system. This discharge also includes anticorrosion products used in the plants and has to be treated to acceptable levels of each chemical before discharge; however, acceptable levels vary depending on certain factors such as receiving waters and state regulations. Furthermore, the extent of impact intensifies with the increasing capacity of desalination [4-6].

In order to prevent biofouling and corrosion caused by bacteria, algae, and other marine organisms during the process of desalination, bactericides such as chlorine or hypochlorite are commonly used with a regular dosage of 2–5 mg/L and a maximum of 8 mg/L [7]. These chlorine-based bactericides may react with organic compounds in seawaters to form chlorination by-products such as chloral. Although concentration of chloral declines due to continuous degradation and

dilution, even very low level could harm the aquatic organisms [8-9]. These chlorinated and halogenated organic byproducts are toxic, carcinogenic, or otherwise harmful to aquatic life. Therefore, monitoring of chlorination by-products in the discharged brine to study their environment effects has attracted significant attention which remarkably facilitates the sustainable development of the desalination industry.

In this study, concentration analysis was performed on five chlorination by-products (chloral, dichloroacetic acid (DCAA), trichloroacetic acid (TCAA), 2,4,6-trichlorophenol (2,4,6-TCP) and pentachlorophenol(PCP)) present in the brine discharged from desalination project of Dagang New Spring Co., Ltd. The vulnerability of marine ecosystems is likely to be influenced by the chlorination by-products present in brine. Therefore, preliminary environmental safety assessment on chlorination by-products in the brine discharged from desalination plant was introduced in this study.

EXPERIMENTAL

Materials Analytical methods

Nine surface water samples were collected from three sections of the hydrological station in the immediate vicinity of the brine discharge of Tianjin Dagang Newspring Co., Ltd. in July 2015 (Figure 1. Sampling points: S1-S9). Samples were collected in chemically cleaned glass sampling bottles, refrigerated, and sealed for laboratory detection. An Agilent 7890 gas chromatography system was used for analysis.

To whom all correspondence should be sent:
E-mail: g.kashi11@yahoo.com



Fig 1. Sampling locations map of 5 chlorination by-products in the brine discharged of Tianjin Dagang Newspring Co. Ltd

Analysis of chloral

The head space and gas chromatography used to determine chloral. The method has many advantages such as wide linear range, high precision, accuracy and sensitivity. The minimum detection limit can reach 0.05 $\mu\text{g/L}$, the water sample determination is simple and rapid, and the result is satisfactory. The peak with retention time of 4.28min was chloral, respectively (Fig. 2)

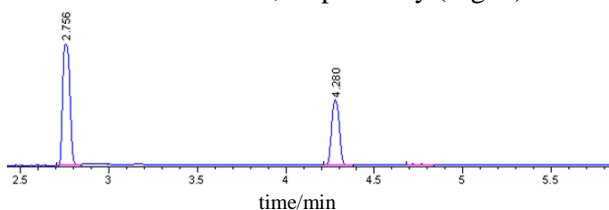


Fig.2. Chromatogram of standard solutions of chloral

Analysis of DCAA and TCAA

The purge and trap/gas chromatography used to determine DCAA and TCAA. The analyte was esterified by acidic methanol, preconcentrated by purge and trap, determined by gas chromatograph (GC) with an electron capture detector (ECD). The factors of acidic methanol were discussed. The linear correlation coefficients at concentrations ranging from 0.0 to 120.0 $\mu\text{g/L}$ were 0.998 and 0.996. The detection limits of this method were 0.15 and 0.84 $\mu\text{g/L}$.

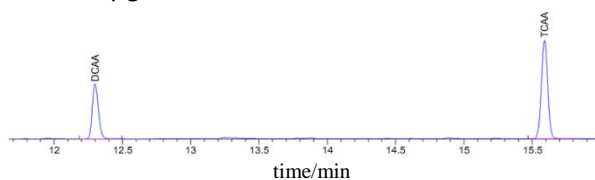


Fig. 3. Chromatograms of standard solutions of DCAA and TCAA

The relative standard deviations (RSD %) for the determination of DCAA and TCAA in water were 1.01 and 2.68%, and the recovery was 87.2-112.4%. The feasibility of this method was sensitive and precise for determination of DCAA

and TCAA. The peaks with retention time of 12.32min and 15.62min were DCAA and TCAA, respectively (Fig. 3)

Analysis of chloral

The automated headspace solid phase micro extraction (HS-SPME) and gas chromatography used to determine TCP and PCP. Through automated sample pre-treatment to improve the detection efficiency and results accuracy. The linearity in the detecting range is good (> 0.999) with the detection limits of 0.148 and 0.126 $\mu\text{g/L}$, and the RSD ($n = 7$) were 4.89 and 7.31%. Test for recovery was made by standard addition method, giving results in the range of 90.0 % - 112.8 %. The peaks with retention time of 7.65min and 9.51min were TCP and PCP, respectively (Fig. 4)

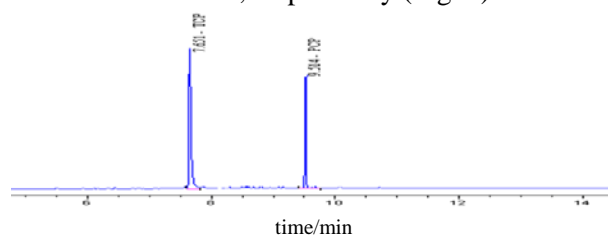


Fig. 4. Chromatograms of standard solutions of TCP and PCP

Method of Environmental Risk Assessment

An ecological risk assessment method was adopted for the environmental safety assessment, which roughly included both the qualitative and quantitative analysis. Qualitative methods were designed to assess the effects with minor quantitative information, providing the decision-making process involving deep-level information. However, quantitative methods mainly consisted of quotient methods, probability risk assessment methods, and statistical analysis methods, with quotient methods representing the most commonly and extensively used risk characterization approaches. The hazard quotient is calculated through comparison between actual environmental exposure concentrations and toxicity data characterizing the substance's harm extent, thus assessing the ecological risk of the pollutant [10-12]. Referring to Guidelines for Risk Assessment of Chemical Substances [13], the acute toxicity effects of algae, fleas, and fish could be considered as the initial assessment index in the environmental safety assessment of the pollutant, in order to preliminarily determine the range of safe concentration. Therefore, the results indicated that safety analysis and assessment could be conveniently conducted through a quotient method on five chlorination by-products in the brine discharged from desalination plant.

RESULTS AND DISCUSSION

Concentrations of chlorination by-products in the brine discharged from desalination

The statistical data of concentrations of individual chlorination by-products in the brine discharged from desalination plant are listed in Table 1. The rates of detection of five chlorination by-products were 100%.

Table 1. Concentrations of chlorination by-products in the brine discharged from desalination plant (µg/L)

	S1	S2	S3	S4	S5
Chloral	15.4	18.5	22.2	13.3	9.65
DCAA	21.9	1.37	1.37	0.36	3.3
TCAA	10.1	4.27	4.27	4.26	4.3
TCP	0.51	0.47	0.47	0.41	0.44
PCP	0.20	0.43	0.43	0.18	0.20
	S6	S7	S8	S9	
Chloral	30.6	10.7	21.0	14.6	
DCAA	3.56	0.36	0.36	2.69	
TCAA	4.26	4.26	4.26	4.47	
2,4,6-TCP	0.37	0.36	0.31	0.42	
PCP	0.08	0.07	0.06	0.20	

Safety Analysis

The Predicted No Effect Concentration (PNEC) is an estimate of the highest concentration of a chemical in a particular environment at which no adverse effects are expected and is an estimate of the sensitivity of the ecosystem to a chemical. A dose-effect assessment was adopted with the objective of determining the PNEC which could be predicted through the acute toxicity data of five chlorination by-products on algae, fleas, and fish. Dose-effect assessment primarily requires species laboratory toxicological test to obtain toxicological data before considering adequate assessment factors, which is applied to toxicological data extrapolation to calculate the PNEC, the highest concentration offering the least possible unacceptable effects. On account of several uncertainties of the extrapolation process, the assessment coefficient has been considered 1000 as extrapolating PNEC through the acute toxicity effects (L(E)C₅₀) of the three basic nutrition levels (algae, fleas, and fish) [14].

Referring to the concentrations based on aquatic life protection from Canadian Water Quality Guidelines for the Protection of Aquatic Life [15], this study provided the preliminarily prediction of the PNEC (Tab. 2).

The Predicted Environmental Concentration (PEC) represents the exposure situation of a chemical substance in the evaluated environment. PEC is obtained through model prediction or

environmental monitoring. This study conducted the exposure assessment based on the field measurement. Adhering to the “worst situation” principle in risk assessment, the highest environmental detection concentration was selected as the PEC of exposure assessment in the analysis results of different batches of samples (Tab. 2).

Risk assessment is designed to supervise the possible risks and provides the guarantee of safety. The internationally accepted hazard quotient (HQ) represents the ratio of the PEC to PNEC. In this study, quotient method was adopted to assess risk characterization and risks are quantified by using the following formula:

$$HQ = PEC/PNEC \quad (1)$$

Where, HQ represents hazard quotient; PEC is Predicted Environmental Concentration, and PNEC is the abbreviation for Predicted No Effect Concentration. Following conclusions were derived, conclusion A: for HQ <0.1, environmental risks were negligible and implementation of the management measures over target substances was not required; conclusion B: when HQ was in the range of 0.1–1.0, environment was still considered to be in the safe level, however, required long-term observation of the environmental dynamics of target substances to avoid the occurrence of high risks; conclusion C: HQ >1.0 indicated possibility of environmental risks under the existing pollution conditions; therefore, long-term monitoring was necessary and the predictability should be improved through conscientiously analyzing all links of risk assessment. The HQs of five chlorination by-products in the brine discharged from desalination plant are listed in Table 2.

Table 2. Safety assessment of chlorination by-products in the brine discharged from desalination plant

	PEC	PNEC	HQ	Conclusion
Chloral	30.6	1.8	17.0	C
DCAA	21.9	8.7	2.51	C
TCAA	10.1	8.7	1.17	C
TCP	0.51	18.0	0.03	A
PCP	0.43	0.25	1.72	C

The HQ value of chloral, DCAA, TCAA, and PCP were higher than 1.0, in particular, the HQ value of chloral reaching a peak of 17.0. The results showed that potential ecological risk from chlorination by-products was presented in the brine discharged from desalination plant. Bactericides were used in seawater desalination pretreatment, which were tended to have chlorination reaction with humus in water. The chloral was the major product, leading to a relative high level in concentrate discharge. The risk of chloral has been

proved by toxicology and biology. Based on the research, we concluded that monitoring should be conducted over chlorination by-products in brine discharged from desalination plant posing serious environmental risks. Moreover, an effective resolution program should be proposed and implemented through the study on the relationship between the ambient concentrations of chlorination by-products in concentrate and the types and amount of biocides in use.

CONCLUSION

In conducting ecological risk assessment, exposure concentration and toxicity data are represented either as single values or as distributions. Among the five chlorination by-products studied, the by-products of bactericides used in seawater desalination concentrate discharge posed serious risks on the ecology. We proposed intense monitoring of bactericide by-products, in particular, chloral. Moreover, a series of management measures should be considered to strengthen the control over concentrate discharge and the use of bactericides.

Acknowledgements: *This work was supported in part by a research grant (201305039) from the State Oceanic Administration People's Republic of China, and in part by a grant (2014BAB06B00) from the National Science Foundation. However, the manuscript has not been subjected to peer and*

policy review of the agency and therefore does not necessarily reflect its views

REFERENCES

1. M. Elimelech, W. Phillip, *Science*, **333**, 712 (2011).
2. Ministry of Science and Technology of People's Republic of China & National Development and Reform Commission, 2012.
3. T. Chen, Q. Wang, Y. Qin, X. Chen, X. Yang, *PLOS ONE*, **13**, 1 (2015).
4. Y. Wang, J. Liu, J. Lan-Ying, Q. Zhou, X.Y. Zeng *Marine environmental science*, **32**, 456 (2013).
5. J. Sathwani, J. Veza, C. Santana, *Desalination*, **185**, 1427 (2005).
6. C. Sommariva, H. Hogg, K. Callister, *Desalination* **167**, 439 (2004).
7. M.A. Xuehu, Z. Lan, S. Wang, L. Lu, *Chemical Industry and Engineering Progress*, **30**, 233 (2011).
8. A. David, L. Emma, *Water Reseach*, **44**, 5117 (2010).
9. M. Elabbar, F. Elmabrouk, *Desalination*, **185**, 31 (2005).
10. X.Y. Zeng, J. Liu, Y. Wang, X. Pan, *Journal of Safety and Environment*, **14**, 234 (2014).
11. Y. Wang, J. Liu, *The Administration and Technique of Environmental Monitoring*, **24**, 35 (2012).
12. Z. Pang, L. Feng, J. Zhou, Z. Liu, *Environmental Chemistry*, **3**, 430 (2011).
13. H. Wang, N.Y. Yang, R.Z. Yu, Z. Fang, J.L. Zhou, *Research of Environmental Sciences*, **22**, 805 (2009).
14. EU: Technical Guidance Document (TGD) on risk assessment of chemical substances following european regulations and directives, 2nd ed, Italy, 2003.
15. National Guidelines and Standards Office: Environment Canadian Water Quality Guidelines for the Protection of Aquatic Life, December 2007.

ЕКОЛОГИЧНА ОЦЕНКА НА БЕЗОПАСНОСТТА НА ВТОРИЧНИ ПРОДУКТИ НА ХЛОРИРАНЕ В САЛАМУРА, ИЗХВЪРЛЕНА ОТ ИНСТАЛАЦИЯ ЗА ОБЕЗСОЛЯВАНЕ

Джинг Лиу*, Ксингю Зенг, Донгксинг Жу, Юнронг Жао, Ксианхюй Пан

Институт за обезсоляване на морска вода и комплексно оползотворяване (SOA), Тиендзин, Китай

Получени 10 октомври 2016 г., ревизирана 10 февруари 2017 г.

(Резюме)

Извършен е анализ на концентрацията на пет вторични продукти на хлориране (хлорал, дихлорооцетна киселина, трихлорооцетна киселина, 2,4,6-трихлорофенол, и пентахлоро-фенол), намиращи се в саламурата, изхвърлена от проект за обезсоляване на Dagang New Spring Co., Ltd. Освен това, анализа на токсичните ефекти (L (E) C50) се извършва на три основни нива за водни организми, а именно, *Scenedesmus vacuolatus*, водни бълхи, и дъгова пъстърва. Въз основа на анализа, методът от документа за технически насоки за оценка на безопасността на химичните вещества на Европейския съюз е приет, за да се направи оценка на екологичните рискове от петте странични продукти на хлориране в саламура, изхвърлена от инсталация за обезсоляване. Резултатите показват, че процентът на откриване на петте продукти на хлориране е 100%. Коефициентите на PEC/PNEC на хлорал, дихлорооцетна киселина, трихлорооцетна киселина и пентахлорофенолът са по-високи от 1. Между четирите замърсители, трябва да се обърне повече внимание на хлорала, чиято концентрация в околната среда от саламурата, изхвърлена от инсталацията за обезсоляване е 17 пъти по-висока от безопасната концентрация.

Optimization of cell culture for H9N2 subtype AIV and establishment of high-yield cell strain

Yu-Jian Lu^{1,2,3}, Xin-Ming Wu⁴, Yu Guan⁴, Song-Lin Zhang⁴, Jin-Liang Wang⁴, Jiu-Xia Zhao⁵,
Wen-Yu Han², Zhi-Qiang Shen^{1,4,5*}

¹Postdoctoral Program, ⁴Shandong Binzhou Animal Science and Veterinary Medicine Academy, Binzhou, China

²Postdoctoral Program, Jilin University, Changchun, China.

³Department of Life Sciences, Binzhou University, Binzhou, China.

⁵Shandong Lvdv Biological Technology Co., Binzhou, China.

Received October 10, 2016; Revised February 10, 2017

It has become the direction and trend of influenza vaccine production by cell culture. This study aimed to establish the key technologies of the cell culture of H9N2 subtype AIV (avian influenza virus). Results showed that during the culture of the H9-4 isolate in MDCK (Madin-Darby canine kidney) cell lines, when the inoculation amount was $10^3 \sim 10^4$ with $0.5 \mu\text{g} \cdot \text{mL}^{-1}$ TPCK (tosyl phenylalanyl chloromethyl ketone)-trypsin, $40 \text{ mmol} \cdot \text{mL}^{-1}$ HEPES (hydroxyethyl piperazine ethanesulfonic acid) or $3 \text{ mmol} \cdot \text{mL}^{-1}$ Gln (glutamine) in the maintenance media, the proliferation of AIV was excellent at 96~108 hpi (hour post inoculation). Moreover, the supplement of $0.3 \mu\text{g} \cdot \text{mL}^{-1}$ TPCK-trypsin could increase the titer of the virus to a certain extent. The chicken *St3galI* gene was cloned and transfected into MDCK cell lines. By screening, 1 strain of highly-expressed *St3galI* monoclonal cell strain S8 was obtained, of which the α -2,3 linked receptor abundance was evidently increased. On S8 cells, the proliferation of H9-4 was significantly increased. The results confirmed that the infection sensitivity and replication capacity of the isolates of H9N2 subtype AIV were further improved by increasing the receptor abundance on the host cell surface.

Key words: H9N2 AIV, MDCK, TPCK-trypsin, *St3gal I* gene, α -2,3 linked receptor.

INTRODUCTION

H9N2 subtype avian influenza is a low pathogenic infectious disease of poultry caused by the AIV [1,2]. In 1966, H9N2 subtype AIV was isolated from the turkeys in the United States for the first time [3]. Since 1997, the subtype AIV has been in the epidemic in birds or poultry around the world [4-6]. H9N2 subtype AIV is a type of low pathogenic AIV (LPAIV), but it can cause the decrease of egg production rate, immune suppression, as well as the mixed infections with other viruses or bacteria, hence huge economic losses were led to the poultry industry [7,8]. In recent years, there have been world-wide incidents of human infections of H9N2 subtype AIV many times, indicating that the virus could increase its gene mutations and recombinant opportunities with other subtypes of influenza viruses because of antigenic drift and antigenic shift, which would result in continuous discoveries of new types of AIV [9-11]. Therefore, H9N2 subtype AIV is a big potential threat to human health.

According to the prevention practices of AIV in China and internationally, the vaccine is the main measure to prevent the avian influenza outbreak and to avoid huge losses. Current production of influenza vaccines for human and animals is mainly the method of embryonated eggs [8]. Despite some effective purification processing, this method still

has many disadvantages. For example, the influenza viruses isolated in embryonated eggs often happen to antigenic variations after continuous passages, this method requires high labor intensity, huge amounts of embryonated eggs, sometimes tedious purification processes, and there are also contamination problems caused by exogenous virus [12-15]. The influenza pandemic and the continuous new strains of such influenza virus call for an urgent need to establish a new method of vaccine production. With the improvement and wide application of animal cell culture techniques, the vaccine production using animal passage cells has become an inevitable trend. Compared with the method of embryonated eggs, the cell-culture-based production of influenza virus is economical, convenient and reproducible with stable quality, the mass production is easy to carry out, and the antigenicity is closer to natural strains, therefore the immune effects are quite reliable [15-19]. Currently, the establishment of the flexible and effective cell-culture-based influenza vaccine production platform has become the target of numerous producers. In the vaccine production process, the cell-culture-based production of influenza virus also has disadvantages including poor replication and low yield. In order to increase the yield, it is necessary not only to optimize the conditions for the proliferation of influenza virus, but also to thoroughly study the mechanism of the replication of influenza virus in the host cells. The

To whom all correspondence should be sent:

E-mail: bzshenzq@163.com

hemagglutinin (HA) constitutes the most important surface antigens of H9N2 subtype AIV [20,21]. Cell surface receptors and HA protein receptor binding sites are the two most important factors of the influenza viruses host specificity. There are two common influenza virus receptors: the sialic acid α -2,3 of D-Galactose (SA- α -2,3Gal), and the sialic acid α -2,6 of D-Galactose (SA- α -2,6Gal) [22-24]. Most AIV preferentially binds to the receptor of SA- α -2,3Gal receptors, while human influenza virus mainly binds to the receptor of SA- α -2,6Gal [25-27]. The infection of influenza virus is mediated by the sialic acids on the cell surface. Sialic acids usually bind with the 2nd from the bottom at the end of N terminal of the glycans, mainly Galactoses, in the way of α 2, 3 or α 2, 6 glycosidic bonds [6,28,29]. Under the effects of Sialyl transferases (STs), sialic acids then bind with the terminals of glycoproteins and glycolipids [30-32]. Therefore, it is a potential approach to increase the cell surface receptor abundance through transgenic technology to improve the effect of virus multiplication.

Given that H9N2 subtype AIV is a kind of LPAIV, it hasn't attracted much attention, hence related researches have lagged behind with very inadequate prevention methods. Although vaccination is an effective means to prevent the epidemics of the LPAIV, currently the production of such vaccine takes long preparation period, with low yields and high costs. The main reasons are that the *in vitro* proliferation of H9N2 subtype AIV is very difficult and that the cell culture technology is not mature enough. The goal of this study is optimizing of cell culture conditions of H9N2 subtype AIV, and screen the cell strains with high yields by genetic engineering technologies, so as to try and establish the key technologies and production platform for the cell culture of H9N2 subtype AIV, as well as to provide technical support for the prevention and control of the avian influenza.

MATERIALS AND METHODS

Virus strains, cell lines, bacterial strains and plasmids

H9N2 subtype AIV local isolates including H9-1, H9-2, H9-3, H9-4, H9-5, H9-6 and H9-BX, and cell lines including MDCK, Vero (Africa green monkey cell), DF-1 (a continuous cell line of chicken embryo fibroblasts), BHK (Baby hamster kidney), Vero-E and CEF (Chick embryo fibroblast) cells were all provided by Shandong Lvdu Biological Technology Co. Ltd. pCI-*neo* plasmid and DH5 α bacterial strain were preserved by Shandong Binzhou Animal Science and Veterinary Medicine Academy. And pMD18-T

plasmid was purchased from TaKaRa Biotechnology (Dalian) Co., Ltd.

Main reagents

T₄ DNA ligase and restriction endonuclease were purchased from TaKaRa Biotechnology (Dalian) Co., Ltd. Plasmid extract kit and gel extraction kit were purchased from Tiangen Biotech (Beijing) Co., Ltd. Reverse transcription kit, *Taq* DNA polymerase, DNA extraction kit, RNA extraction kit, G418, DMEM cell culture media, TPCK-trypsin, Lipofectamine 2000 Reagent were purchased from Invitrogen (Thermo Fisher Scientific), Fetal Bovine Serum (FBS) was purchased from Gibco (Thermo Fisher Scientific), the primers were produced by Shanghai Generay Biotech Co., Ltd. 1% chicken red blood cell suspension was prepared by blood collection from SPF adult male chickens.

Optimization of the conditions of AIV proliferation

The H9-1, H9-3, H9-4 and H9-5 isolated virus strains were inoculated into the embryonated eggs, the allantoic fluid was harvested after 72 hours, and used as a source of the experimental virus below. The single-layer cells grown on six-well plates (MDCK, Vero, DF-1, BHK, Vero-E and CEF cells) were washed with PBS twice, and then were inoculated with these viruses (H9-1, H9-3, H9-4, and H9-5) at different dilution levels (10^{-1} , 10^{-2} , 10^{-3} , 10^{-4} , 10^{-5} , and 10^{-6}). After different time lengths of absorption (0, 30, 60, 90 and 120 min), TPCK-trypsin at different concentrations (0, 0.125, 0.25, 0.5, 0.75, and $1.0 \mu\text{g}\cdot\text{mL}^{-1}$), trypsin at different concentrations (0, 2, 5, 8, 10, and $12 \mu\text{g}\cdot\text{mL}^{-1}$), serum at different concentrations (0, 0.2, 0.5, and 1.0%), HEPES at different concentrations (0, 5, 10, 20, 30, 40, and $50 \text{mmol}\cdot\text{L}^{-1}$), Gln at different concentrations (0, 1, 2, 3, 4, and $5 \text{mmol}\cdot\text{L}^{-1}$) or BSA at different concentrations (0, 0.1, 0.2, 0.3, 0.4, and 0.5%), were added into the maintenance media. The supernatant was harvested at different time points (24, 36, 48, 60, 72, 84, 96, 108, and 120 h), and the routine micro-hemagglutination test was conducted to measure the HA titer of the virus. At 24, 48 or 72 h after the inoculation, 0.3 or $0.5 \mu\text{g}\cdot\text{mL}^{-1}$ TPCK-trypsin could be re-added to the maintenance media [33].

Virus strain stability assay

The cells in the form of dense single layers were washed with PBS twice, and then were inoculated by 10^{-3} diluted H9-4 embryonated egg virus. After 60 min of absorption, the maintenance media containing $0.5 \mu\text{g}\cdot\text{mL}^{-1}$ TPCK-trypsin was added. And at 96 hpi the cell viruses were harvested [34]. During the 10 passages in MDCK cells, the HA titer of each passage was tested [35].

Gene cloning and vector construction

Based on the sequencing information of chicken sialyltransferase gene *St3gal I*, the primers *St3gal I* LP: 5'-GGGGAATTCATGGTCACCGTCAGGAAA-3', and *St3gal I* RP: 5'-GGGGTCGACTCATCTGCCCTTGAAAAAT-3' were designed [31]. The 5' terminals of the primers were added with restriction enzyme cutting sites *EcoR I* and *Sal I*. With the SPF embryonated egg of 12 d, RNA was extracted to produce reverse transcription cDNA. The high-fidelity *Taq* enzyme was used for the amplification of *St3gal I*, then the product was lined with pMD18-T and sequenced. The restriction enzyme cutting of pMD18-T-*St3gal I* and pCI-*neo* plasmids were performed with *Sal I*-*EcoR I*, and the extracted target segments were linked, then the eukaryotic expression vector pCI-*neo-St3gal I* was then established.

MDCK cell transinfection and cloned culture

Lipofectamine 2000 was used to transfer pCI-*neo-St3gal I* plasmids into MDCK cells, and the transgenic cell lines were acquired after 500 $\mu\text{g}\cdot\text{mL}^{-1}$ G418 (neomycin) screening (according to the specifications). The transgenic cells were diluted to the concentration of 50/100 μL . Then 2 μL cell suspension was added to 96-well plate, with the re-addition of 100 μL DMEM culture media containing G418. The single cell formed clonal clusters after 10 d culture. After the consumption of the cells, the culture was continued. With 90% confluence, the cells were transferred into 24-well plate to expand the culture [31,36].

Quantitative real time PCR

The total RNA of the stable cell strains were extracted and then used to produce cDNA by reverse transcription kit. With β -*actin* gene of MDCK cells as the internal reference, the sequences of the primers were: β -*actin* LP: 5'-CCTCTATGCCAACACAGT-3', β -*actin* RP: 5'-GTACTCCTGCTT GCTGAT-3'. The expression of *St3gal I* in transfected cells were measured by qRT-PCR (Quantitative real time PCR) assay. The primers for the amplification of *St3gal I* segment were: *St3gal I* LP: 5'-ACGAATCAGATGTTGGGAGC-3' and *St3gal I* RP: 5'-CATTACCTCATCGCATA-3'. The qRT-PCR assay was performed by LightCycler[®]480 SYBR Green Master Kit by Roche. The results and data were analyzed by LightCycler[®]480 software and Excel 2003 [37].

FCM assay

The control and the stable transfected cell strains were put into the 6-well plate evenly. At the cell

density of 90%, the cells were consumed and collected, then washed 2 times by PBS containing 10 $\text{mmol}\cdot\text{L}^{-1}$ Glycine, and then washed 1 time by Buffer 1 (50 $\text{mmol}\cdot\text{L}^{-1}$ Tris-HCl, 0.15 $\text{mol}\cdot\text{L}^{-1}$ NaCl, 1 $\text{mmol}\cdot\text{L}^{-1}$ MgCl₂, 1 $\text{mmol}\cdot\text{L}^{-1}$ MnCl₂ and 1 $\text{mmol}\cdot\text{L}^{-1}$ CaCl₂, pH 7.5). The cells were re-suspended by Blocking Solution on ice for 1 h, and then were processed with Maackia amurensisagglutinin (MAA) and blank control for incubation on ice for 1 h. The cell sedimentation was re-suspended by Rhodamine-labeled anti-digoxin secondary Ab for incubation on ice for 1 h. In the end, after 3 times wash with PBS, the products were tested by flow cytometry (FCM) [36].

TCID₅₀ and EID₅₀ assay

The control and the stable transfected cell strains were put into the 96-well plate evenly. At the cell density of 90%, the cells were inoculated with AIV which was continuous 10 times serially diluted. The CPE (cytopathic effect) were observed continuously for 72 h, then the viruses were harvested for HA test. The TCID₅₀ (tissue culture infective dose) was calculated by Reed-Muench method. The virus was diluted by saline and inoculated into the allantoic cavity of 10 d SPF chicken. The survival of embryonated eggs was observed continuously for 72 h, then the viruses were harvested for HA test. The EID₅₀ (egg infectious dose) was calculated by Reed-Muench method [38].

Data analysis

The data were analyzed by Excel 2003 and SPSS 19.0. The significance analysis of the differences among multiple groups were conducted with Duncan's Multiple Range Test. Same letter was defined as insignificant difference, while different letters indicated significant differences on 0.05 level (lowercase letters). The significance of the difference between two average numbers were tested by the t test, $p < 0.05$ was defined as significant difference, $p < 0.01$ was defined as highly significant difference, and $p < 0.001$ was defined as extremely significant difference.

RESULTS AND DISCUSSION

The establishment of the key process conditions of cell culture of H9N2 subtype AIV *Cell proliferation features of H9N2 subtype AIV*

The HA gene sequence of the isolated virus strains was compared with some international reference strains and the representative strains, which showed that these strains were divided into 3 evolved subtypes: representative strain AF156376 (Subtype I), AF156378 (Subtype II), and AF156377 (Subtype III) respectively.

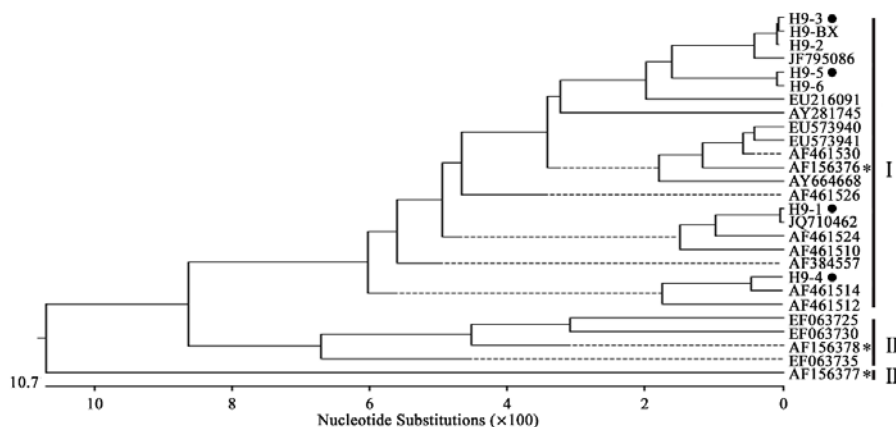


Fig. 1. The phylogenetic relationship analysis of 7 isolates compared with HA gene.

In this study, 7 strains of H9N2 subtype AIV in the comparisons (including H9-1, H9-2, H9-3, H9-4, H9-5, H9-6, and H9-BX) were all in Subtype I, with the representative strain as A/duck/Hong Kong/Y280/97 (AF156376), indicating that the 7 isolates all belonged to Eurasian strains with closed phylogenetic relationship (Figure 1). According to the locations of the isolates on the phylogenetic tree, H9-1, H9-3, H9-4, and H9-5 were selected as the candidate strains for the production of AIV vaccine.

The 4 selected strains were inoculated to MDCK cells and the hemagglutination values were tested after harvest. The results were shown in Figure 2A. With the same amount of inoculation, the proliferation of H9-4 was the best, with significant differences between the other 3 isolates. This indicated that H9-4 could proliferate easily in the cells with the potential to become a vaccine strain. H9-4 presented different sensitivities to different host cells, and that MDCK cells were the most suitable for the proliferation of H9-4 (Figure 2B). The difference of the sensitivity might be because of the better binding ability of H9-4 to cell surface receptors and the more influenza virus receptors on MDCK cells to facilitate more viruses to absorb and invade. The proliferation of H9-4 was better after 24 h cell culture with the inoculation at 10^{-3} ~ 10^{-4} (Figure 2C). Too much inoculation dose would accelerated cytopathic changes in the cells, and inhibit the proliferation of the viruses; while inadequate inoculation led to poor proliferation in the cells. During 96~108 hpi, almost all the cells presented CPE, and the titer of the virus was close to the peak value (Figure 2D). With the cell culture time, the titer decreased mainly because the constant nutrient consumption of the media and the deaths of the host cells [39]. The absorption time also influenced the proliferation of AIV: with the absorption time as 60 min, the HA titer of H9-4 was higher (Figure 2E). The HA titer was evidently increased after 2 times of freezing and thawing of cells with 10^{-3} dilution

of the viruses (Figure 2F). Higher serum concentration could present higher inhibitory effects (Figure 2G). This was because serum not only contained trypsin-resistant substance damaging the proteolysis effects of trypsin, but also had some substances that could cover virus receptors on the cell membrane, thus affecting the virus infection of the cells. Therefore, during the cell culture of H9-4, serum shouldn't be added to the maintenance media.

The influences of trypsin on the proliferation of AIV

After the inoculation of MDCK cells, trypsins with different concentrations were added into the maintenance media. The results showed that with the concentrations of TPCK-trypsin and trypsin at $0.5 \mu\text{g}\cdot\text{mL}^{-1}$ and $10 \mu\text{g}\cdot\text{mL}^{-1}$ respectively, the titer of the virus was at the peak value (Figure 3A and B). Data analysis suggested obvious improving effect of trypsin on the proliferation of AIV, and the effect of TPCK-trypsin was better than the ordinary trypsin. In addition, 24 h or 48 h after the inoculation of MDCK cells, the supplement of $0.3 \mu\text{g}\cdot\text{mL}^{-1}$ and $0.5 \mu\text{g}\cdot\text{mL}^{-1}$ TPCK-trypsin into the maintenance media could both increase the titer to a certain degree, with the better proliferation result of the addition of $0.3 \mu\text{g}\cdot\text{mL}^{-1}$ TPCK-trypsin at 48 hpi (Figure 3C).

The influenza virus HA was split by the host protease into the mature HA1 and HA2, which should be the precondition of the cell infection of AIV. However, such protease was lacking in the tissues and cells, the right amount of exogenous trypsin should be added during the proliferation period of AIV, so as to increase the splitting of HA and to enhance the infectivity of AIV [40,41]. But the excessive level of trypsin would cause the early cell shedding and the reduction of the titer, while the inadequate trypsin couldn't have the effects. After the treatment with TPCK, trypsin could present higher activity and better improving influence on the proliferation of the viruses.

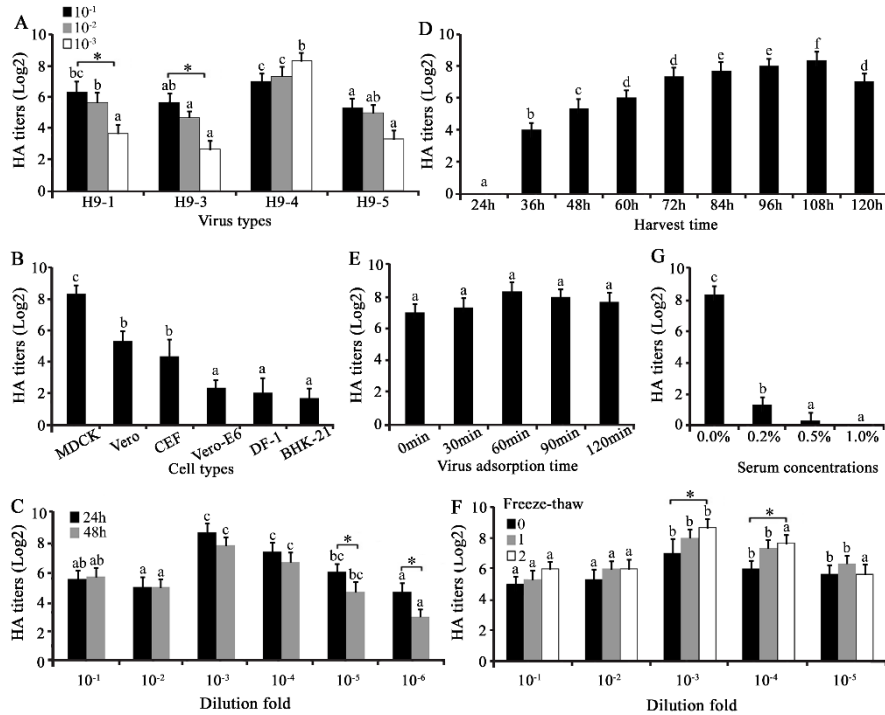


Fig. 2. Cell proliferation features of H9N2 subtype AIV. The different isolated virus strains (A), host cells (B), cell culture time and inoculation amount (C), harvest time (D), absorption time (E), freezing and thawing times (F), and serum concentration could influence the proliferation of AIV. The virus used in the other figures was H9-4 isolated strain except fig. 2A. The cell line used in the other figures was MDCK except fig. 2B. Same letter was defined as insignificant difference, while different letters indicated significant differences on 0.05 level. An asterisk (*) represented $p < 0.05$, two asterisks represented $p < 0.01$, and three asterisks represented $p < 0.001$.

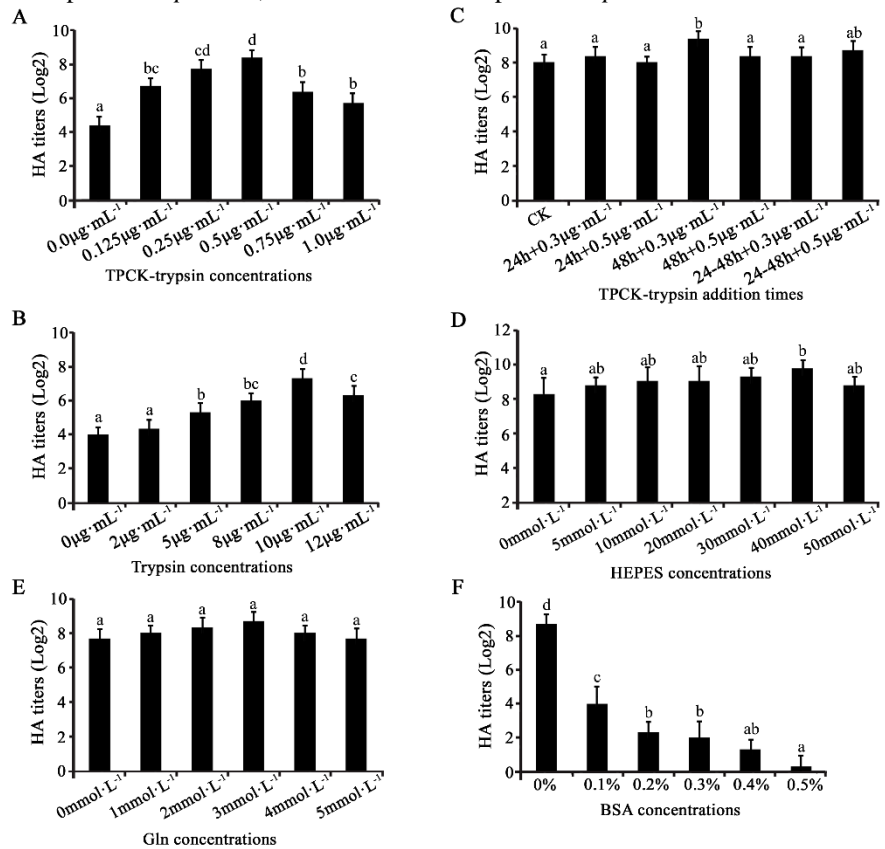


Fig. 3. Optimization of the cell culture conditions of H9N2 subtype AIV. The different TPCK-trypsin (A), Trypsin (B), TPCK-trypsin addition times (C), HEPES (D), Gln (E), and BSA (F) could influence the proliferation of AIV. The virus strain and cell line used in fig.3 were H9-4 and MDCK respectively. Same letter was defined as insignificant difference, while different letters indicated significant differences on 0.05 level.

Other factors influencing the proliferation of AIV

After the inoculation of MDCK cells, the solutions at different concentrations of HEPES, Gln or bovine serum albumin (BSA) were added into the maintenance media. The results showed that the HA titer was the highest with 40 mmol·L⁻¹ HEPES with significant differences, that the HA titer was the highest with 3 mmol·L⁻¹ Gln with non-significant differences, and that BSA inhibited the proliferation of H9-4: with higher BSA concentration, the titer was significantly lower (Figure 3D-F).

HEPES, as a hydrogen ion buffer, might maintain the long-term constant pH range; Gln, as the must-have additive in *in vitro* cell culture, was used as an energy source in the synthesis of protein and nucleic acid metabolism. Therefore, adding the right amount of HEPES and Gln in the maintenance media could help maintain normal cell growth. Just like serum, the addition of BSA also led to the obvious reduction of the titer, probably because it occupied the cell-surface receptors.

Stability of H9-4 isolates

After 11 continuous passages of H9-4 isolates from embryonated eggs in MDCK cells, the results showed that the HA titer increased gradually and achieved to the peak value at passages F4, and then began to fall (Figure 4A). This is probably because there was a gradual process of adaptation for the proliferation of AIV in the host cells. But the increased trypsin inhibitor accumulation level elevated with the passages and caused the inhibition to the proliferation, or it was also possible that the abundance of the α-2,3 linked receptors was still low on MDCK cells [39,42].

Analysis on the key factors influencing the proliferation of AIV

H9-4 isolate was inoculated into MDCK and Vero cells accordingly, with the addition of 0.5 μg·mL⁻¹ TPCK-trypsin, 40 mmol·L⁻¹ HEPES or 3 mmol·L⁻¹ Gln. It could be seen that without TPCK-trypsin, there was hardly any proliferation of virus in Vero cells whether or not with the addition of HEPES or Gln. For MDCK, it was found that without TPCK-trypsin, there was poor proliferation of AIV; and that with TPCK-trypsin, the HA titer increased significantly, and improvement of the proliferation if with the addition of HEPES or Gln (Figure 4B). The results above indicated that TPCK-trypsin was the most important factor influencing the proliferation of H9-4, and the right amount of HEPES or Gln improved the proliferation of the virus.

In order to better understand the effects of the

supplement of TPCK-trypsin, 24 h, 48 h or 72 h after the inoculation of Vero and MDCK cells, 0.3 μg·mL⁻¹ TPCK-trypsin was re-added and the HA titer was measured at 96 hpi. The results indicated the re-addition of TPCK-trypsin could improve the proliferation of the virus in both cells, but more evidently in MDCK cells (Figure 4C). The reason might be that with the elevated accumulation of trypsin inhibitor during the replication of AIV, the trypsin in the culture media was inactivated fast, and only the timely addition of TPCK-trypsin could meet the needs of effective proliferation of AIV [17,43,44].

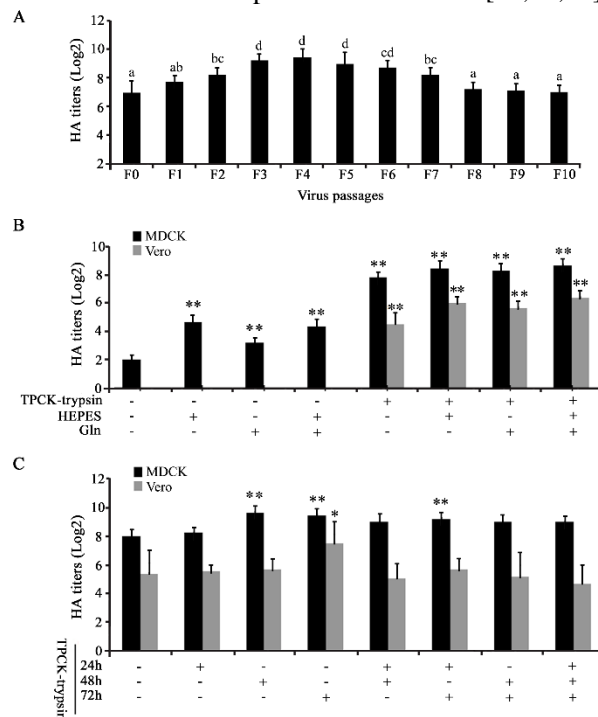


Fig. 4. Analysis on stability of H9N2 subtype AIV isolate and the key factors influencing the proliferation of AIV. (A) Stability of H9-4 isolate; (B) Effect of TPCK-trypsin, HEPES and Gln on the proliferation of H9N2 subtype AIV; (C) Effect on the proliferation of H9N2 subtype AIV supplemented with TPCK-trypsin at different time. The virus strain used in fig.4 was H9-4. The cell line used in fig. 4A was MDCK. Same letter was defined as insignificant difference, while different letters indicated significant differences on 0.05 level. An asterisk(*) represented *p* <0.05, two asterisks represented *p* <0.01, and three asterisks represented *p* <0.001.

Establishment of high-yield cell strain of H9N2 subtype AIV

Construction of pCI-neo-St3gal I vector and screening of stable transfected cell strains

In addition to optimizing the conditions of the proliferation of influenza virus, other methods could also be applied, such as reforming the cell lines for the better virus proliferation environment, the higher yield and titer. Influenza virus could

infect the host by the specific binding of HA with the host cell surface sialic acid receptor [25,45]. MDCK cells had both SA α -2,3Gal and SA α -2,6Gal receptors, while the abundance of the SA α -2,3Gal receptors were quite low and caused the low liter of AIV in MDCK cells [46]. The α -2,3-sialyltransferase I (ST3Gal I) could transfer the sialic acid to the host cell surface in the form of α -2,3 link, and formed the receptor of AIV [31]. Therefore, through the high expression of *St3gal I*, the abundance of SA α -2,3 Gal receptors on MDCK cells could be improved.

The SPF chicken *St3gal I* gene was cloned and inserted into pCI-*neo* plasmid (Figure 5A). After identification, the expression vector pCI-*neo-St3gal I* was obtained (Figure 5B). The pCI-*neo* and pCI-*neo-St3gal I* plasmids were used for the transfection of the MDCK cells. Then 30 monoclonal cell strains were selected and picked out. The PCR assay of the genomic DNA indicated only the cell strains with the target genes could present ~1 kb amplification band (Figure 5C). The total RNA of the transfected cells were extracted for RT-PCR assay. The results showed that the stable transfected cell strains could amplified proper bands (Figure 5D). 9 transfected cell strains with good amplification effect were selected for the

transcription level detection of *St3gal I* with β -*actin* gene as internal reference. The results showed that the *St3gal I* expression level in transfected cell strains were higher comparatively (Figure 5E). Combining the results of qRT-PCR, the expression level of *St3gal I* gene was the highest in S8 cell strain ($p < 0.001$), followed by S1, S3 and S4 ($p < 0.01$) (Figure 5F). The HA titer analyses showed the better proliferation of H9-4 in S8 cell strain than the control (Figure 5G).

Analysis of high-yield cell strain receptor abundance and AIV proliferation effect

Microscopic observation found that the normal MDCK cells, empty transfected and S1 cells were spindle-shaped, however S8 cells in tight arrangement appeared prismatic-shaped (Figure 6Aa-d). At 72 hpi, the growth of the control cells (uninoculated) were almost normal, with few cell masses and shedding cells (Figure 6Ae). However, the CPE were observed for the cells inoculated H9-4 virus (Figure 6Af-h). By comparison, the cytopathogenic degree of S8 cells was more severe and there were fewer adherent cells. The abundance of α -2,3 linked receptors on the stable transfected cell strains was detected by FCM assay.

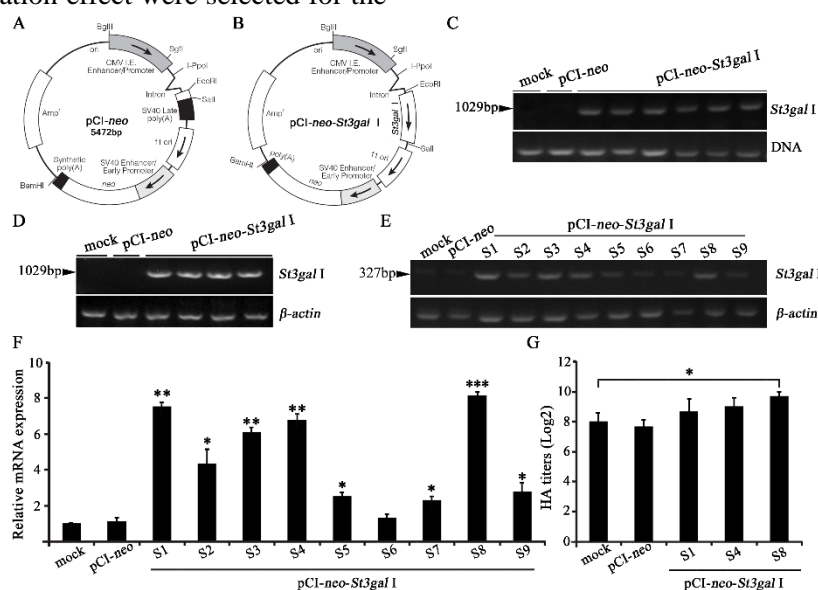


Fig. 5. Construction of eukaryotic expression vector and screening of stable transfected cell strains. (A) Schematic illustration of pCI-*neo* expression vector; (B) Schematic illustration of pCI-*neo-St3gal I* expression vector; (C) PCR assay of stable transfected cell strains; (D) RT-PCR assay of stable transfected cell strains; (E) Detection of the *St3gal I* expression level in stable transfected cell strains by RT-PCR; (F) Detection of the *St3gal I* expression level in stable transfected cell strains by qRT-PCR; (G) HA titer analyses of stable transfected cell strains by inoculation of H9N2 subtype AIV. In Fig. 5G, the culture conditions of the H9-4 isolate in different MDCK cell lines: the inoculation amount was 10^{-3} with the addition of $0.5 \mu\text{g}\cdot\text{mL}^{-1}$ TPCK-trypsin, the harvest time of AIV was at 96 hpi. An asterisk(*) represented $p < 0.05$, two asterisks represented $p < 0.01$, and three asterisks represented $p < 0.001$.

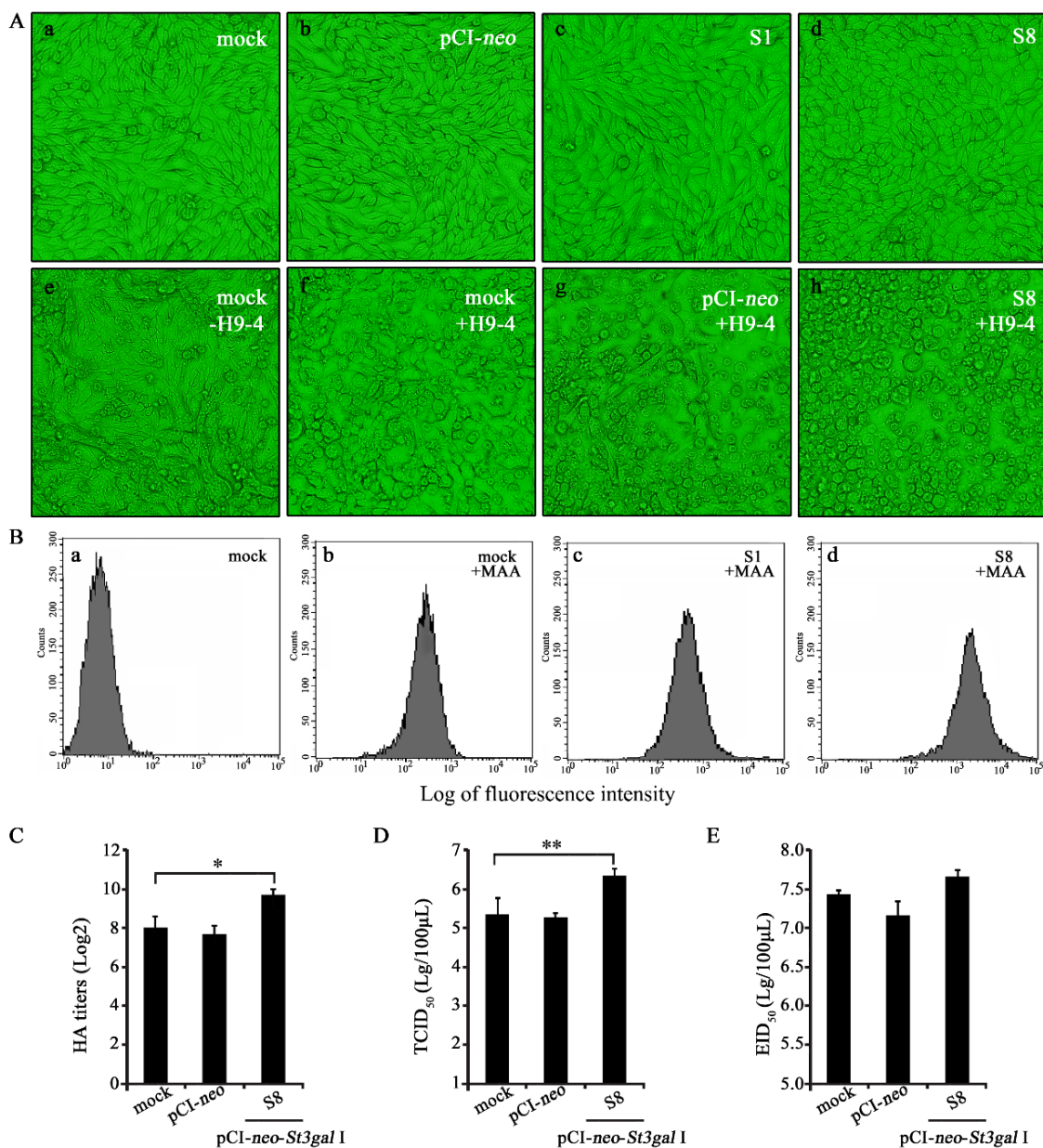


Fig. 6. Detection of receptor abundance and AIV proliferation effect. (A) The morphology of the stable transfected cell strains and CPE at 72 hpi; (B) Detection of the abundance of α -2,3 linked receptors on the stable transfected cell strains; (C-E) Detection of AIV proliferation effect by HA, TCID₅₀ and EID₅₀ assay. An asterisk(*) represented $p < 0.05$, two asterisks represented $p < 0.01$, and three asterisks represented $p < 0.001$. In Fig. 6, the culture conditions of the H9-4 isolate in different MDCK cell lines: the inoculation amount was 10^{-3} with the addition of $0.5 \mu\text{g}\cdot\text{mL}^{-1}$ TPCK-trypsin, the harvest time of AIV was at 96 hpi.

The results indicated that the fluorescence intensity of S8 cells were obviously improved, with higher content of α -2,3 linked receptors than those of the mock and S1 cells (Figure 6B). H9-4 was inoculated to S8 cells to measure the HA titer, TCID₅₀ and EID₅₀. Experimental results showed that the HA titer of H9-4 in S8 cells was significantly higher than control cells ($p < 0.05$) (Figure 6C). TCID₅₀ and EID₅₀ were also higher, including very significant differences of TCID₅₀ between S8 cells and the control ($p < 0.01$) (Figure

6D and E). Based on the above results, it concluded that S8 stable transfected cell strain created by transgenic technology could improve the cell surface α -2,3 lined receptors, the sensitivity and replication of the virus, thus it was more suitable for the proliferation of H9N2 subtype AIV. However, any physiological process in cells should often be the results of the combination of multiple genes. So the single gene transfer was also limited here. In order to increase yield of AIV in the cell culture, multiple approaches should be integrated together.

CONCLUSION

For the cell culture of the virus in some specific cell lines, the obtaining of high-titer virus depends on many factors, including the properties of the virus itself, the sensitivity of the host cells, and the ideal conditions for the biosynthesis. In this study, two strategies improving cell culture conditions, reforming cell lines were used to improve the yield of the virus. The experimental results showed that during the culture of the H9-4 isolate in MDCK cell lines, when the inoculation amount was 10^{-3} ~ 10^{-4} with the addition of $0.5 \mu\text{g}\cdot\text{mL}^{-1}$ TPCK-trypsin, the proliferation of AIV was excellent at 96~108 hpi. At different stages of AIV culture, the re-addition of $0.3 \mu\text{g}\cdot\text{mL}^{-1}$ TPCK-trypsin in the maintenance media could increase the titer of the virus to a certain extent. Also, the addition of $40 \text{ mmol}\cdot\text{mL}^{-1}$ HEPES or $3 \text{ mmol}\cdot\text{mL}^{-1}$ Gln in the maintenance media could improve the proliferation of AIV, while the addition of serum or BSA significantly inhibited the proliferation of the virus. Among them, trypsin was the key factors influencing the proliferation of H9N2 subtype AIV by optimizing the cell culture conditions. To further increase the sensitivity of H9N2 subtype AIV to the host cells, the chicken *St3gal I* gene was cloned, and was transfected into MDCK cell lines. 1 strain of highly-expressed *St3gal I*-positive monoclonal cell strain S8 was detected, of which the α -2,3 linked receptor abundance was evidently increased. After testing, it was found that the stably-expressed *St3gal I*-positive cell strain S8 could improve the infection sensitivity and replication capacity of the isolates of H9N2 subtype AIV.

Acknowledgements: This study was funded by the Postdoctoral Fund of Shandong Binzhou Animal Science and Veterinary Medicine Academy Postdoctoral Research Station (BSH2014001), the Shandong Province Natural Science Fund Project (ZR2012CL14) and the Doctor Fund of Binzhou University (2010Y08).

REFERENCES

1. D.J. Alexander, *Avian Dis.*, **51**, 161 (2007).
2. N.J. Cox, K. Subbarao, *Annu. Rev. Med.*, **51**, 407 (2000).
3. G.Y. Dong, J. Luo, H. Zhang, C. Wang, M. Duan, T.J. Deliberto, D.L. Nolte, G. Ji, H. He, *PLoS One*, **6**(2), e17212 (2011).
4. D.J. Alexander, *Avian Dis.*, **47**, 792 (2003).
5. I.H. Brown, J. Banks, R.J. Manvell, S.C. Essen, W. Shell, M. Slomka, B. Londt, D.J. Alexander, *Dev. Biol. (Basel)*, **124**, 45 (2006).
6. S. Shahsavandi, M.M. Ebrahimi, A. Mohammadi, N. Zarrin Lebas, *Cytotechnology*, **65**, 419 (2013).

7. Z.Q. Wu, J. Ji, K.J. Zuo, Q.M. Xie, H.M. Li, J. Liu, F. Chen, C.Y. Xue, J.Y. Ma, Y.Z. Bi, *Point Sci.*, **89**, 1136 (2010).
8. R. Parvin, A.A. Shehata, K. Heenemann, M. Gac, A. Rueckner, M.Y. Halami, T.W. Vahlenkamp, *Veterinary Research*, **46**, 75 (2015).
9. Y.P. Lin, M. Shaw, V. Gregory, K. Cameron, W. Lim, A. Klimov, K. Subbarao, Y. Guan, S. Krauss, K. Shortridge, R. Webster, N. Cox, A. Hay, *Proc. Natl. Acad. Sci. USA*, **97**, 9654 (2000).
10. A. Fusaro, I. Monne, A. Salviato, V. Valastro, A. Schivo, N.M. Amarin, C. Gonzalez, M.M. Ismail, A.R. Al-Ankari, M.H. Al-Blowi, O.A. Khan, A.S. Maken Ali, A. Hedayati, G.J. Garcia, G.M. Ziay, A. Shoushtari, K.N. Al Qahtani, I. Capua, E.C. Holmes, G. Cattoli, *J. Virol.*, **85**, 8413 (2011).
11. Q.Y. Teng, W. Shen, Q. Liu, G. Rong, L. Chen, X. Li, H. Chen, J. Yang, Z. Li, *J. Virol*, **12**, 143 (2015).
12. A.S. Monto, H.F. Maassab, E.R. Bryan, *J. Clin Microbiol.*, **13**, 233 (1981).
13. J.S. Robertson, C.W. Naeve, R.G. Webster, J.S. Bootman, R. Newman, G.C. Schild, *Virology*, **143**, 166 (1985).
14. E. Hoffmann, S. Krauss, D. Perez, R. Webby, R.G. Webster, *Vaccine*, **20**, 3165 (2002).
15. D. Onions, W. Egan, R. Jarrett, D. Novicki, J.P. Gregersen, *Biologicals*, **38**, 544 (2010).
16. J.P. Gregersen, H.J. Schmitt, H. Trusheim, M. Bröker, *Future Microbiol.*, **6**, 143 (2011).
17. S.Z. Feng, P.R. Jiao, W.B. Qi, H.Y. Fan, M. Liao, *Appl. Microbiol Biotechnol.*, **89**(4), 893 (2011).
18. N.A. Ilyushina, M.R. Ikizler, Y. Kawaoka, L.G. Rudenko, J.J. Treanor, K. Subbarao, P.F. Wright, *J. Virol.*, **86**, 11725 (2012).
19. V.Y. Lugovtsev, D. Melnyk, J.P. Weir, *PLoS One*, **8**(9), e75014 (2013).
20. J. Post, E.D. de Geus, L. Vervelde, J.B. Cornelissen, J.M. Rebel, *Virol J.*, **10**, 23 (2013).
21. K. Srinivasan, R. Raman, A. Jayaraman, K. Viswanathan, R. Sasisekharan, *PLoS One*, **8**, e59550 (2013).
22. S. Thongratsakul, Y. Suzuki, H. Hiramatsu, T. Sakpuaram, T. Sirinarumit, C. Poolkhet, P. Moonjit, R. Yodsheewan, T. Songserm, *Asian Pac. J. Allergy Immunol*, **28**, 294 (2010).
23. X.Y. Li, J.Z. Shi, J. Guo, G. Deng, Q. Zhang, J. Wang, X. He, K. Wang, J. Chen, Y. Li, J. Fang, H. Kong, C. Gu, Y. Guan, Y. Suzuki, Y. Kawaoka, L. Liu, Y. Jiang, G. Tian, Y. Li, Z. Bu, H. Chen, *PLoS Pathog.*, **10**, e1004508 (2014).
24. H.A. Shaib, N. Cochet, T. Ribeiro, A.M. Abdel Nour, G. Nemer, E. Azhar, A. Iyer, T. Kumosani, S. Harakeh, E.K. Barbour, *J. Infect Dev. Ctries.*, **8**(5), 570 (2014).
25. T. Ito, Y. Kawaoka, *Vet. Microbiol.*, **74**, 71 (2000).
26. R.J. Russell, D.J. Stevens, L.F. Haire, S.J. Gamblin, J.J. Skehel, *Glycoconj J.*, **23**, 85 (2006).
27. S.D. Pawar, S.S. Parkhi, S.S. Koratkar, A.C. Mishra, *J. Virol.*, **9**, 251 (2012).
28. I. Stephenson, J.M. Wood, K.G. Nicholson, M.C. Zambon, *J. Med. Virol.*, **70**(3), 391 (2003).

29. A.S. Gambaryan, A.B. Tuzikov, G.V. Pazynina, R.G. Webster, M.N. Matrosovich, N.V. Bovin, *Virology.*, **326**(2), 310 (2004).
30. H.D. Klenk, R. Wagner, D. Heuer, T. Wolff, *Virus Res.*, **82**, 73 (2002).
31. M. Matrosovich, T. Matrosovich, J. Carr, N.A. Roberts, H.D. Klenk, *Virology.*, **77**, 8418 (2003).
32. S. Ge, Z. Wang, *Critical reviews in microbiology.*, **37**, 157 (2011).
33. M. Yamoka, M. Homma, H. Hotta, *Arch. Virol.*, **140**, 937 (1995).
34. J. Baron, C. Tarnow, D. Mayoli-Nüssle, E. Schilling, D. Meyer, M. Hammami, F. Schwalm, T. Steinmetzer, Y. Guan, W. Garten, H. D. Klenk, E. Böttcher-Friebertshäuser, *J. Virol.*, 1811 (2013).
35. C.Y. Lu, J.H. Lu, W.Q. Chen, L.F. Jiang, B.Y. Tan, W.H. Ling, B.J. Zheng, H.Y. Sui, *Chin. Med. J.*, **121**(20), 2050 (2008).
36. S. Hatakeyama, Y. Sakai-Tagawa, M. Kiso, H. Goto, C. Kawakami, K. Mitamura, N. Sugaya, Y. Suzuki, Y. Kawaoka, *J. Clin. Microbiol.*, **43**(8), 4139 (2005).
37. X. Zheng, C.J. Cardona, J. Anunciacion, I. S. Adams, N. Dao, *Journal of General Virology.*, **91**, 343 (2010).
38. L.J. Reed, H. Muench, *Am. J. Hyg.*, **27**, 493 (1938).
39. Y. Genzel, U. Reichl, *Expert Rev. Vaccines.*, **8**(12), 1681 (2009).
40. J.M. Audsley, G.A. Tannock, *Drugs.*, **68**(11), 1483 (2008).
41. N.R. Hegde, *Hum. Vaccin Immunother.*, **11**(5), 1223 (2015).
42. S.H. Seo, O. Goloubeva, R. Webby, R.G. Webster, *J. Virol.*, **75**(19), 9517 (2001).
43. O. Kistner, N. Barrett, W. Mundt, M. Reiter, S. Schober-Bendixen, G. Eder, F. Dorner, *Vaccine.*, **18**(1), 50 (2001).
44. G. Kemble, H. Greenberg, *Vaccine.*, **21**(16), 1789 (2003).
45. M. Luo, *Adv. Exp. Med. Biol.*, **726**, 201 (2012).
46. T. Ito, Y. Suzuki, A. Takada, A. Kawamoto, K. Otsuki, H. Masuda, M. Yamada, T. Suzuki, H. Kida, Y. Kawaoka, *Virology.*, **71**(4), 3357 (1997); Y. Wang, J. Liu, J. Lan-Ying, Q. Zhou, X.Y. Zeng *Marine environmental science*, **32**, 456 (2013).

ОПТИМИЗАЦИЯ НА КЛЕТЪЧНА КУЛТУРА НА H9N2 ПОДТИП НА AIV И УСТАНОВЯВАНЕ НА КЛЕТЪЧЕН ЩАМ С ВИСОК ДОБИВ

Ю-Джиан Лю^{1,2,3}, Ксин-Мин Ву⁴, Ю Гуан⁴, Сонг-Лин Жанг⁴, Джин-Лиан Ван⁴, Джиу-Ксиа Жао⁵, Вен-Ю Хан², Жи-Цян Шен^{1,4,5} *

¹Постдокторска програма, ⁴ Академия за животновъдни науки и ветеринарна медицина Шандун Бинчжоу, Бинчжоу, Китай

² Постдокторска програма, Дзилин университет, Чанчун, Китай.

³Отделение на науките за живота, Университет в Бинчжоу, Бинчжоу, Китай.

⁵ Шандунски институт по биотехнология, Бинчжоу, Китай. Бинчжоу, Китай.

Получена на 10 октомври 2016 г.; ревизирана на 10 февруари 2016 г.

(Резюме)

Тенденцията в производството на противогрипна ваксина е полечаването и от клетъчни култури. Това проучване имаше за цел да установи ключовите технологии на клетъчната култура на подтип H9N2 на AIV (вируса на птичия грип). Резултатите показват, че по време на култивиране на клетъчни линии от изолат H9-4 в MDCK (Мадин-Дарби кучешки бъбрек), когато инокуломът е $10^{-3} \sim 10^{-4}$ с 0.5 мкг мл^{-1} ТРСК (тозил фенилаланил хлорметил кетон) -трипсин, 40 ммол мл^{-1} NEPES (хидроксиетилпиперазин етансулфонова киселина) или 3 ммол мл^{-1} Gln (глутамин) в средата за поддръжка, разпространението на AIV беше отлично в $96 \sim 108$ HPI (час след заразяването). Освен това, добавката на 0.3 мкг мл^{-1} ТРСК-трипсин може да увеличи титъра на вируса до известна степен. Пилешки ген St3galI бе клониран и трансфектиран в клетъчни линии MDCK. Чрез скрининг, бе получен един щам на моноклонален клетъчен щам S8, със силно изразена продукция на St3galI, от които излишъка на α -2,3 свързан рецептор очевидно се увеличава. Значително се увеличава разпространението на клетки S8 на H9-4. Резултатите потвърдиха, че инфекционната чувствителност и капацитетът на репликация на изолатите на H9N2 подтип на AIV бяха допълнително подобрени чрез увеличаване на излишъка на рецептор на повърхността на клетката гостоприемник.

Study on dust-catching and inhibiting microorganism ability of *Jacaranda mimosifolia* under the same condition of compare experiment*

LanQing Wei^{&1}, XinYan Jiang^{&1,2}, JinAn Shi^{1**},
WenZhou Zhao^{1,3}, XiaoPeng Shao^{1,4}, QiBing Chen^{1***}, Ying Sun^{1,5}

¹College of Landscape Architecture, Sichuan Agricultural University, Chengdu-611130, China

²Sichuan Shengshanshengshui Food Limited Company, Luzhou-646000, China

³College of Architecture and Design, Southwest Jiaotong University, Chengdu- 611756, China

⁴Luzhou Lao Jiao Group, Luzhou- 646000, China

⁵Department of Traditional Chinese Medicine, Shandong Drug And Food Vocational College, Weihai- 264200, China

Received October 10, 2016, Revised February 10, 2017

The study made a research on *Jacaranda mimosifolia* and other four common plant species in areas with heavy traffic in Chengdu, Zigong and Suining similarly to find an objective law aiming at the haze pollution. The results showed: the average quantity of unit leaf area's dust was *L. chinense* > *F. altissima* > *B. papyrifera* > *J. mimosifolia* > *C. pedunculatum*, which was 6.2690, 4.9561, 4.6474, 3.927, 1.0825g/m² respectively; From bacteria culture test, the bacterial colonies area of leaves dust of each plant increased over time in 24, 48, 72hrs, and the outbreak point was in 48hrs; The area also increased with the increasing temperature (10,20,25,30,37°C), but there were some differences in different levels. It was shown that there were significant differences (P < 0.05) and extreme difference (P < 0.01) between 10-20°C, especially on *L. chinense* and *C. pedunculatum*. And the relevant data of *J. mimosifolia* increased while others reduced or held steadily between 20-30°C, but the increment was much less than other plants in other times. From a general view, the bacterial colonies area of unit leaves dust-catching quantity was *C. pedunculatum* > *B. papyrifera* > *L. chinense* > *F. altissima* > *J. mimosifolia*. Thus it can be seen that *Jacaranda mimosifolia* has a certain ability of dust-catching, while there's a much stronger capability of inhibiting microorganism than other control plants. Therefore the contemporary plant configuration should be combined with the specific habitat, following the objective law. However, the specific secretion of Pythoncidere, producing by *Jacaranda mimosifolia*, as well as microorganism types need to further explore.

Keywords: *Jacaranda mimosifolia*, Pythoncidere, inhibite microorganism.

INTRODUCTION

Recent years, environmental problems have been increasing prominently while the process of urbanization was accelerating. The urban air pollution has caused API [1], PM2.5 and PM10 problems in more and more cities [2], which has seriously affected the physical and mental health of urban residents. However, the garden plants not only beautify the environment and reduce the light pollution or the noise [3], but also have a strong capacity of dust-catching and microorganism-inhibiting [4]. Dr. B.P.Toknnh has put forward the concept of *Pythoncidere* [5], the plant leaching solution to inhibit other biological growth, which mainly present in chemical materials, such as phenol and alkaloid, by changing the biofilm and protein structure of microorganism [6]. Thus it plays a significant role in improving the regional air quality.

It was reported that *Jacaranda mimosifolia*, which had the thick foliage and contains a variety of bioactive substances, could well cure the diseases on skin, gastrointestinal and cardiovascular system [7-9]. But there has not been reported [10-14] about the ability of dust-catching and inhibiting microorganism of *Jacaranda mimosifolia* in the same condition contrast other plants. Thus, the goal of this study was to explore the ability of dust-catching and inhibiting microorganism of *Jacaranda mimosifolia* under the same condition of compare experiment to heal the haze pollution in the future.

EXPERIMENTAL

Experimental material

Five common plants species, *Jacaranda mimosifolia*, *Broussonetia papyrifera*, *Ficus altissima*, *Cinnamomum pedunculatum* and *Loropetalum chinense*, at the intensive traffic places [15] in Chengdu, Zigong and Suining, which had similar habitats, were taken as research objects which had the same DBH, height and growth status [16]. Chengdu, Zigong and Suining all belong to subtropical monsoon

[&]These authors contributed equally to this work and should be considered co-first authors

* Supported by the Sichuan Science and Technology Innovation Talent Project(2015032)

** E-mail: shija5778@126.com

*** E-mail: 310023939@qq.com

humid climate of which the average annual rainfall is greater than 900mm, and the annual average temperature of 17°C, while the annual frost-free period is greater than 300 days. The bacterial culture medium (Table 1) was improved (Number 2N-5N) on the basis of Beef Extract Peptone solid medium [8, 17] in inhibiting microorganism test.

Table 1. Beef extract peptone medium with different concentrations of formula (1L distilled water, pH7.0~7.2)

number	Beef extract (g)	Peptone (g)	NaCl (g)	Agar powder (g)
1N	5.00	10.00	5.00	20.00
2N	6.00	10.00	5.00	20.00
3N	4.00	10.00	5.00	20.00
4N	5.00	8.00	5.00	20.00
5N	5.00	12.00	5.00	20.00

Treatments

The dust-catching test was performed on days with sunny and windless weather after seven days of 5mm's rainfall above [18] in two seasons, which have the biggest dust-catching ability [19], winter and spring (December 2015 to February 2016). In each season, five plant species were collected at Riyue Road in Chengdu, Dangui Road in Zigong and Heping Road in Suining, respectively.

Measurement of Leaves dust

The test sampled from the perimeter of crown leaves on the upper, middle and lower parts [20] by lopper, and the samples were carefully sealed in plastic bags. Then leaves were immersed in distilled water for 3 hours and gently brushed with a small brush, and also the plastic bag. The leaves were removed with tweezers. The test weighed the amount of leaves dust by *Weight difference method* [21]. And then, the amount of dust per unit leaf area was calculated with AutoCAD.

Bacteria culture

The inhibiting microorganism test was improved on the basis of *Natural sedimentation method* [8] with the five plant species collected from Riyue Road in Chengdu. The test cultivated bacterial colonies of the leaves dust and recorded the amount of them by setting different concentrations of medium, temperature (10, 20, 25, 30, 37°C) and time periods (24, 48, 72h). The bacterial colonies area per unit dust-catching quantity of different plant species leaves was calculated by the formula of:

$$C2 = C1 / W3 \quad (1)$$

Where, C1 is the average bacterial colonies area per dish; W3 is the average dust-catching quantity in December per dish. And the data were analyzed by Excel and DPS.

RESULTS AND DISCUSSION

Comparison of plant species dust-catching ability

The test data showed (Fig. 1) that the amount of dust-catching in December was much more than it in February. According to the survey (Fig. 2), it was known that comparison of dust-catching quantity per leaf area in December was $L. chinense > F. altissima > B. papyrifera > J. mimosifolia > C. pedunculatum$, which was 6.2690, 4.9561, 4.6474, 3.927, 1.0825 g/m² respectively. It reflected the ability of dust-catching of these five plant species.

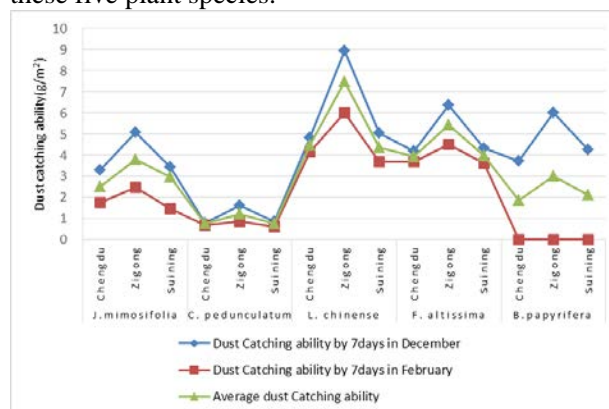


Fig. 1. Different species in December, February and average dust catching ability (experimental conditions: 25 °C, pH: 7, reaction time: 24h).

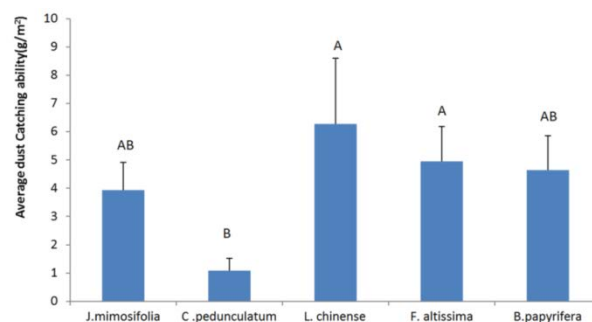


Fig. 2. The average dust catching ability of three different experimental locations in December and the letters P < 0.01 significant level (experimental conditions: 25 °C, pH: 7, reaction time: 24h)

Bacterial colonies of inhibiting microorganism test

The inhibit microorganism test showed (Fig. 3&4) the bacterial growth of leaves dust, which collected from five plant species in December at Riyue Road in Chengdu. It was visible that sterilization ability of *J. mimosifolia* was higher than others species during 0-72h.

According to the data of bacterial growth trend (Fig. 5, table 2) in different culture period (24, 48, 72h), the bacterial colonies area of leaves dust spreads with time. It was shown that, the area existed extreme differences (P < 0.01) or significant differences (P < 0.05) in 48-72h, except for *B. papyrifera*. So that, the outbreak stage of total

bacterial colonies was in 48-72h, and the point was on 48h.

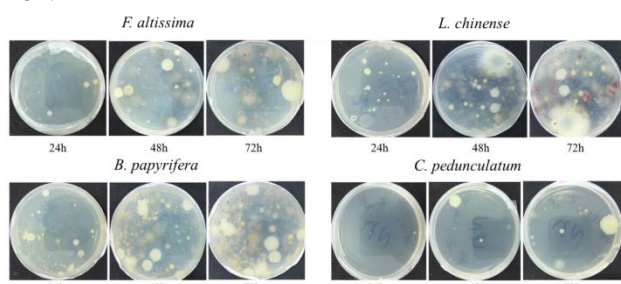


Fig. 3. Four compared plant species leaves bacteria culture growth (experimental conditions: 25 °C, pH: 7, reaction time:24-72h).

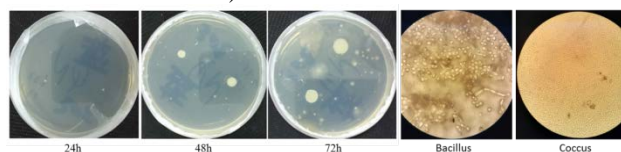


Fig. 4. *J. mimosifolia* leaves bacteria culture growth and the observation under OLYMPUS,CX21 microscope (experimental conditions: 25 °C, pH: 7, reaction time:24-72h).

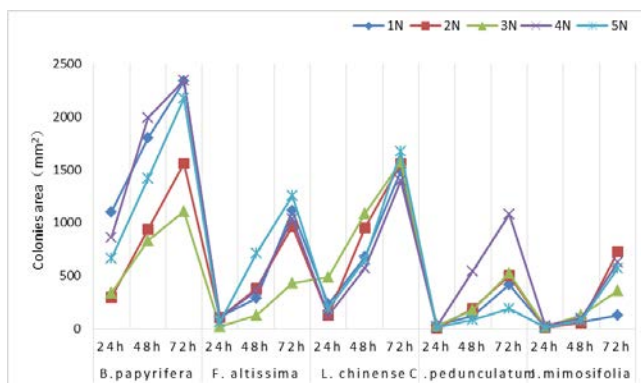


Fig. 5. Different species of different media bacterial growth trend (experimental conditions: 25 °C, pH: 7, reaction time: 24-72h, in 1N-5N medium).

According to the survey of bacterial culture at different temperatures during 72h, the maximum of each bacterial colonies area distributed at 25,30,37°C respectively, while the minimum was at 10°C(Fig. 6), which was the outdoor temperature when we collected the leaves. By analysis of variance, there were significant difference ($P < 0.05$) and extreme difference ($P < 0.01$) between 10-20°C, especially *L. chinense* and *C. pedunculatum*. The relevant data of *J. mimosifolia* increased while others reduced or hold between 20-30°C, but the increment was much less than other plant species in other period of time. So that, temperature has a great influence on the bacterial cultivate, but there was an exception on *J. mimosifolia*.

It was shown in Fig. 7 that the bacterial colonies area per dish of *J. mimosifolia* was greater than other plant species, which was $B. papyrifera > L. chinense > F. altissima > C.$

$pedunculatum > J. mimosifolia$. And the average dust-catching quantity in December in single culture dish (6358.5mm² each dish) could be calculated as 0.0300, 0.0400, 0.0315, 0.0069g and 0.0250g respectively, combined with Fig. 2.

Table 2. Bacterial colonies growth level single factor statistical analysis of different time periods about each species (species, Processing, Mean, 5% significance level and 1% significant level)

species	Processing (h)	Mean	5% signyfca nce level	1% signfica nt level
<i>B.papyrifera</i>	72	1906.5900	a	A
	48	1395.3201	a	AB
	24	649.8420	b	B
<i>F. altissima</i>	72	960.3000	a	A
	48	373.4100	b	B
	24	79.2940	b	B
<i>L. chinense</i>	72	1539.2280	a	A
	48	786.6440	b	B
	24	229.2800	c	C
<i>C.pedunculatun</i>	72	540.8340	a	A
	48	219.8780	b	AB
	24	18.9820	b	B
<i>J.mimosifolia</i>	72	482.4060	a	A
	48	82.1380	b	B
	24	14.3820	b	B

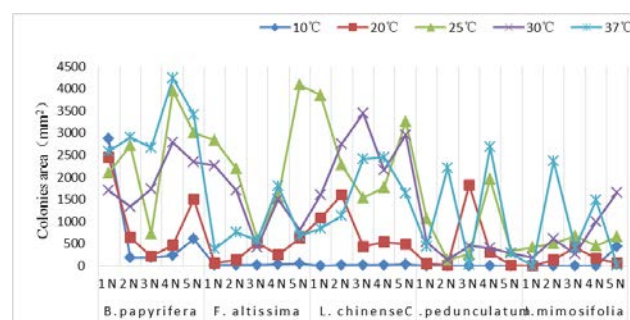


Fig. 6. The different temperatures of different species of bacterial growing line graph (experimental conditions: 10- 37°C, pH: 7, reaction time: 72h, in 1N-5N medium).

Therefore, the bacterial colonies area per unit dust-catching quantity of different plant species leaves was *C. pedunculatum* > *B. papyrifera* > *L. chinense* > *F. altissima* > *J. mimosifolia* (Fig. 8). In terms of the different formulations of the bacterial culture medium, 4N had more bacterial colonies than 3N, however, it was not particularly evident. Therefore, the demand of Beef Extract is more than Peptone in culture medium for bacteria relatively.

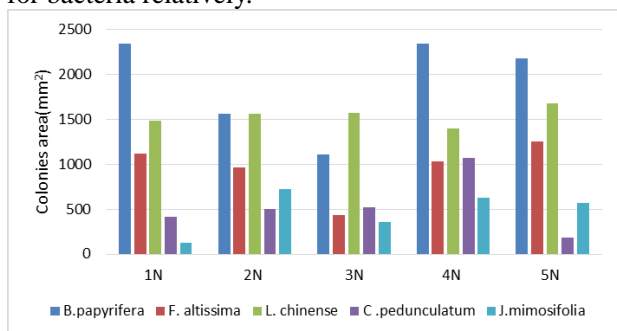


Fig.7. The average bacterial colonies area of the different plant species(experimental conditions: 10-37°C,pH: 7, reaction time:72h, in 1N-5N medium).

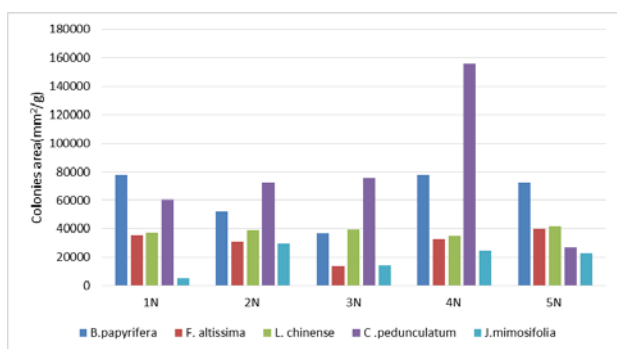


Fig.8. The average bacterial colonies area of unit dust-catching quantity(experimental conditions: 10- 37°C, pH: 7, reaction time:72h, in 1N-5N medium).

Discussion

From experimental results and analysis concluded above, the dust-catching ability of the same plant species was significantly higher in December than in February (Fig. 1). It could be seen that the dust-catching capacity of *Jacaranda mimosifolia* was affected by phenophase. The amount of dust-catching per leaf area was only 54% in February for the reason that the leaves of *Jacaranda mimosifolia* was very thin from November to February because of its dormancy [22]. So it was the same as *B. papyrifera* [23]. In addition, the ability of dust-catching of *Jacaranda mimosifolia* had a close relationship with the surface structure of leaves [24, 25]. The ability of dust-catching was weakened because of the bipinnate leaves, which reflected the positive correlation between leaf areas and dust quantity on each leaf [26], though there was fluff on the surface.

According to inhibiting microorganism test, the bacterial colonies area of each plant species' leaves dust had various trends in different times,

temperatures and media. Under the condition of the same amount of dust-catching, the smaller the bacterial area was, the stronger bactericidal ability of the plant was [27]. So, the comparison of these five plant species were *J. mimosifolia* > *F. altissima* > *L. chinense* > *B. papyrifera* > *C. pedunculatum*.

In summary, *Jacaranda mimosifolia* has a certain ability of dust-catching, while there's a much stronger capability of inhibiting microorganism than other control plants. In general, the amount of leaves dust is in proportion to the microorganism theoretically. But the result was not the case, the ability of dust-catching was *L. chinense* > *F. altissima* > *B. papyrifera* > *J. mimosifolia* > *C. pedunculatum*, while the inhibiting microorganism was *J. mimosifolia* > *F. altissima* > *L. chinense* > *B. papyrifera* > *C. pedunculatum*. The appearance of this kind of phenomenon may be related to the structure of the leaf surface and its secretion.

CONCLUSION

Therefore, the ability of inhibiting microorganism of *Jacaranda mimosifolia* is more obvious than others species while the ability of dust-catching is not that effective, which shows that different plants had different sterilization. In this case, it is urgent to do further research on the specific secretion of *Jacaranda mimosifolia* to inhibit the microorganism.

Acknowledgements: The author acknowledges the financial grant from Department of science and technology of Sichuan Province, Chengdu, China.

REFERENCES

1. L. Pei, W. Xin, C. Fahe, W. Eyi, H. Min, W. Ruibin, Y. Gang, R. Hongyan, W. Yuping, X. Yongming, *J. Environ. Sustain. Develop.*, **5**, 8 (2011).
2. R.L. Mancinelli, W.A. Shulls, *J. Appli. Environ. Micro.*, **35**(6), 1095 (1978).
3. W. Lei, W. Zhi, *J. Environ. Pollu. Contr.*, **28**(1), 51 (2006).
4. J. Shengli, J. Hexian, *J. China Fore. Scie. Tech.*, **25**(6), 5 (2011).
5. B.P. Toknnh, M. Pythoncidere, 1985.
6. X. Wu, R. Hua, Y. Yue, Y. Zhu. *J. Jour. Anhui. Agri. Univer.*, **29**, 245 (2002).
7. P. Nicasio, M. Meckes, *J.Jour. Ethnoph.*, **97**(2), 301 (2005).
8. G.H. Mahran, A.M. El-Fishawy, A.M.S. Hosny, *J. Herba Hungarica*, **30**, 98 (1991).
9. L. Qing, S. Jingan, L. Yueting, S. Ying, S. Xiaopeng, *J. Guihaia*, **3**, 360 (2015).
10. W.H. Smith, *J. New York Inc.*, 1981.
11. H. Yong, L. Lei, L. Junyi, L. Weixing, M. Liqiang, *J. Jour. Northeast Fore. Uni.*, **38**(5), 37 (2010).
12. L. Yanqing, D. Nanjing Forestry University, 2006.
13. Z. Sulan, W. Bingli, *J. Jour. Northwest Fore. Uni.*, **30**(6), 186 (2015).

14. L. Guangli, C. Qibing, *J. Jour. Sichuan Fore. Scie. Tech.*, **9**, 53 (2004).
15. G. Jinhui, W. Dongmei, Z. Liang, *J. Jour. Beijing Fore. Uni.*, **29**(2), 94 (2007).
16. D. Xiwen, C. Qiang, W. Limin, *J. Prote. Fore. Scie. Tech.*, **1**, 28 (2005).
17. L. Li, D. Chin. Academy Agri. Sci., 2008.
18. Z. Yong, L. Shuren, Y. Zhiping, *J. Jour. Huazhong Agri. Uni.*, **21**(6), 582 (2002).
19. W. Yuehan, D. Nanjing Fore. Uni., 2004.
20. Z. Jiayang, X. Jingping, Z. Man, L. Hui., *J. Jour. Henan Agri. Sci.*, **11**, 121 (2012).
21. W. Fang, X. Shangao, L. Hongyuan, L. Lanlan, Z. Qingmin, H. Mengxuan, *J. Jour. Arid Land Resour. Environ.*, **1**, 100 (2015).
22. S.D. Jingan, Sichuan Agri. Uni., 2012.
23. H. Zhen, *J. Fujian Qing Fang*, **12**, 30 (2007).
24. C. Yixin, Z. Ning, H. Huanjin, *J. Chine. Jour. Appl. Eco.*, **13**(9), 1121 (2011).
25. Z. Weikang, *J. Environ. Sci.*, **7**, 2381 (2015).
26. Z. Jiayang, X. Jingping, Z. Man, L. Hui, *J. Jour. Henan Agri. Sci.*, **11**, 121 (2012).
27. Y. M. Xihua, *People Milit. Medi. Press*, **1**, 52 (2002).

ПРОУЧВАНЕ НА ПРАХОУЛАВЯНЕТО И СПОСОБНОСТТА ЗА ИНХИБИРАНЕ НА МИКРООРГАНИЗМИ НА *Jacaranda mimosifolia* ПРИ ЕДНАКВИ УСЛОВИЯ НА ЕКСПЕРИМЕНТ ЗА СРАВНЕНИЕ

Ланцин Уей¹, Синйен Дзян^{1,2}, Дзинан Шай¹, Уънджоу Джао¹, СяоПън Шао^{1,4}, Цибин Чън¹, Ин Сун^{1,5}

¹Колеж по ландшафтна архитектура, Аграрен университет Съчуан, Ченду-611130, Китай

²Съчуанска шенианишениуи хранителна компания ООД, Луджоу-646000, Китай

³Колеж по архитектура и дизайн, Югозападна университет Цияотун, Ченду- 611756, Китай

⁴Луджоу Лао Цзяо Груп, Луджоу- 646000, Китай

⁵Департамент по традиционната китайска медицина, Професионален колеж по лекарствата и храните Шандонг, Вейхай- 264200, Китай

Получена на 10 октомври 2016 г.; коригирана на 10 февруари 2016 г.

(Резюме)

Направено е проучване на *Jacaranda mimosifolia* и други четири растителни видове в райони с интензивен трафик в Чънду, Зигон и Суйнин за да се намери обективен закон, насочен към праховото замърсяване на въздуха. Резултатите от изследването показваха: средното количество прах на единица листна площ беше *L. chinense* > *F. altissima* > *B. papyrifera* > *J. mimosifolia* > *C. pedunculatum*, съответно 6,2690, 4,9561, 4,6474, 3,927, 1,0825 г / м²; От теста на бактериални култури, площта на бактериалните колонии на прашни листа на всяко растение се увеличава с течение на времето за 24, 48, 72 часа, а най-високата точка е в 48 час; Площта също се увеличава с повишаване на температурата (10, 20, 25, 30, 37 °С), но има и някои разлики в различните нива. Показано е, че са налице значителни разлики (P < 0.05) и екстремна разлика (P < 0.01) между 10-20 °С, особено на *L. chinense* и *C. pedunculatum*. Съответните данни за *J. mimosifolia* се увеличават, докато другите намаляват или остават постоянни между 20-30 °С, но увеличението е много по-малко в сравнение с други растения по друго време. От общ поглед, реда на бактериалните колонии по уловеното количество прах на единица листна площ е *C. pedunculatum* > *B. papyrifera* > *L. chinense* > *F. altissima* > *J. mimosifolia*. Може да се види, че *Jacaranda mimosifolia* има определена способността за прахо-улавяне, докато има много по-силна способност да инхибира микроорганизмите отколкото другите контролни растения. Затова конфигурацията на съвременното растение трябва да се комбинира с конкретно местообитание, следвайки обективен закон. Въпреки това, специфичната секреция на *Pythoicidere*, произвеждани от *Jacaranda mimosifolia*, както и вида на микроорганизмите трябва да се проучат допълнително.

Study on new rural domestic sewage treatment technology based on CASS and VBF

Yonggang Zeng^{1,2}, Wenyuan Li¹, Jin Huang¹, Zhengwen Huang^{1*}, Jin Wang¹, Jin Qian^{1,3}, Ao Yuan¹, Tingting Du¹, Yaqi Hu¹, Dagang Li¹

¹. School of Architecture and Civil Engineering, Chengdu University, Chengdu, China

². Chengdu Chuanhuan Research Academy of Environmental Protection Sciences and Technology, Chengdu, China

³. School of Natural and Applied Sciences, Northwestern Polytechnical University, Xi'an, China

Received October 10, 2016, Revised February 10, 2017

The paper took the typical rural domestic sewage in the surrounding districts and counties of Chengdu as the research object, and it chose the combined process of cyclic activated sludge system (CASS) and vermibiofilter (VBF). It used computer to simulate the process and systematically analyze the process of related influencing factors, control conditions, operation mechanism of rural domestic sewage and so on. Controlled the inlet water flow Q , the concentration of the inlet water BOD S_0 (equal to 175 mg/L) and sludge age SRT (14.29 d) unchanged, respectively changed the reflux ratio R and dissolved oxygen concentration, and made the concentration of effluent BOD to reach the town sewage treatment plant pollutant discharge standard of GB18918-2002 grade B.

Key words: New rural sewage treatment, CASS, VBF, Computer dynamic simulation.

INTRODUCTION

Took into account the Chengdu belongs to the plain area, and combined with the new rural water supply and drainage system in the process of construction. It made the new rural domestic sewage in Chengdu area was easy to collect [1]. Therefore, it was obvious that developing the process of high hydraulic load, strong ability to remove nitrogen and phosphorus, simple system, convenient operation maintenance, and make the maximum use of local resources was the best choice [2]. The article selected the combination of cyclic activated sludge system (CASS) and vermibiofilter (VBF) treatment process. The wastewater was degraded by CASS technology, and then the VBF process reduced the sludge. At the same time, the paper systematically analyzed the process of related influencing factors, control conditions, operation mechanism of rural domestic sewage and so on, which provided the theoretical guidance for the practical project commissioning.

DETERMINATION OF PROCESS SCHEME

According to the specific characteristics of the new rural domestic sewage in Chengdu plain, this paper put forward the following requirements for the treatment of domestic sewage in new rural areas, 1) Low input and high efficiency. Due to the low income of rural residents, the priority should be given to the technology with low cost, low

operating cost, low energy consumption or no energy consumption, stable operation, easy maintenance and high efficiency [3]. 2) Low secondary pollution. it is easy to cause indirect pollution in the process of sewage treatment, so it is necessary to choose the treatment process without secondary pollution or low secondary pollution. 3) Strong resistance to impact load. In order to avoid the waste or paralysis of the system resources caused by the change of the sewage discharge in the domestic sewage treatment system, it is necessary to select the wastewater treatment process with strong impact load capacity [4]. 4) Easy to manage and maintain.

In conclusion, considering CASS and VBF process have the characteristics of 'three low and two little and one high', namely, low construction cost, low operation cost, low management requirements, little area, little secondary pollution, high degree of resources, and they are in line with the direction of sustainable development. Moreover, they have distinctive 'ecological balance' and 'environmental friendly' technical features. Therefore, these processes was the best choice for the treatment of rural domestic sewage [5].

RESEARCH PROGRAM

Selection of control index of sewage treatment

Collected and analyzed the main controlling parameters BOD, COD, SS, $\text{NH}_3\text{-N}$ and TP from Chengdu six urban area and Jintang, Qingbaijiang, Longquanyi, Pengzhou, Xindu, Pixian, Shuangliu, Wenjiang, Dujiangyan, Chongzhou, Dayi, Qionglai, Xinjin, Pujiang, 20 districts and counties

To whom all correspondence should be sent:
E-mail: 122054216@qq.com

(city), the concentration range of BOD, COD, SS, NH₃-N, TP and so on in sewage were shown in Table 1.

Combination of CASS and VBF process

Figure 1 presented that the process mainly included CASS and VBF two important processes. CASS pool was mainly used for the remove of BOD, COD, SS, NH₃-N, TP and so on in the sewage [6-7]. Partial supernatant fluid treated by CASS pool directly to the ultraviolet disinfection canal, and part to the adjusting tank which had the Oxygen filling function. The remaining sludge from the bottom of the CASS pool was deposited into the reservoir, and partial sludge returned to the CASS pool, and part to the adjusting tank. Entered to the adjusting tank and through water quantity and water quality regulation, the supernatant fluid and mud went into VBF pool for sludge reduction. The final drainage of VBF pool returned to CASS pool for processing, and the little sludge into the mud storage pool [8].

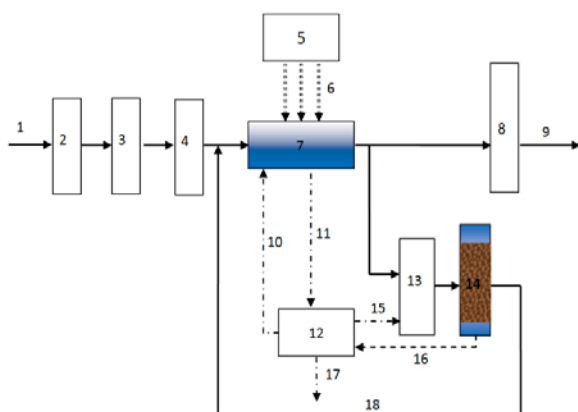


Fig. 1. Flow chart of CASS and VBF process (1.Inlet water; 2.The coarse grid; 3.Fine screen; 4.Grit chamber; 5.Ventilator room; 6.Aeration; 7.CASS pool; 8.Ultraviolet disinfection canal; 9.Effluent; 10.Return sludge; 11.Excess sludge; 12.Mud storage pool; 13.Adjusting tank; 14.VBF pool; 15.Return sludge; 16.Sludge discharging; 17.Efflux sludge; 18.Supernatant reflux.)

Computer dynamic simulate CASS technology

This paper adopted the method of computer dynamic simulation to study the influence factors which are related to organic matter removal of CASS process, controlling parameters and running mechanism. The experiment used continuous completely mixed aeration tank experiment device. The aeration tank was square, and the secondary

sedimentation tank and aeration tank were combined and they were separated by reflux baffle. The water of aeration tank entered the secondary sedimentation tank by the hole of reverse-flow baffle, and the return sludge can be realized by adjusting the height of the backflow slit. Different sludge age can be achieved by adjusting the valve of the secondary sedimentation tank. In the process of implementation, the dissolved oxygen concentration and MLSS in the aeration tank were unchanged, and the water quantity or quality was constantly changed to get different sludge load. At the same time, the sludge age was controlled by the mud discharge valve to eliminate the surplus, and the parameters of the four groups under different sludge load were measured [9]. Finally, the work of the calculation, drawing and parameter was completed [10].

VBF treatment of excess sludge

Set the VBF pool [11]: Filter was a cylinder, radius was 0.15m, height was 0.15m, volume was about 39L and the ventilation effect was good. VBF pool was divided into three parts [12-13]: watering zone, filling area and drainage area. There was a layer of elastic filler under the water distributor, and the function of it were secondary water distribution and shading and supplemental oxygen. Filling area was divided into three layers: The upper was earthworms decomposition layer, and it involved fine sawdust, rice husk and peat etc. The middle layer was added layer, and its packing was the same as the upper. Bottom layer was the retainer layer, and it was filled with the ceramic grain filters [14]. The sludge of aeration tank through water distributor and elastic packing was distributed to the filter material surface evenly. After through the packing area of 0.50m high and the hole at the bottom of the device, the sludge was collected into the tank under the vermibiofilter [15]. The experiment selected Eisenia foetida, which showed short sexual maturation period and strong adaptability and high cocoon production rate.

The ceramic filter material particle's diameter was 6.0 ~ 9.0 mm, and its solid density and bulk density respectively was 2.26g/cm³ and 0.89 ~ 1.00g/cm³, and its voids and porosity respectively was greater than 41% and 50% . In addition, its specific surface area was about 1.8×10⁴ ~5.0×10⁴cm²/g.

Table 1. The quality of input water.

Performances	BOD	COD	SS	NH ₃ -N	TP
Water Quality (mg/L)	170-200	240-300	170-200	45-52	4.0-4.5

Adjusted the sludge concentration of suspended solid (SS) to about 300mg/L in running time, the main conditions and design parameters were as follows[16]: the earthworm density was 32g/L, hydraulic load was 3.0m³/(m².d), the earthworm organic load was 35g / (kg.d), pH was about 7, and the DO was 3.5mg/L,SS was 250~350 mg/L.The concentration of volatile suspended solids (VSS) was 160 ~ 200mg/L, and COD was 350 ~ 500mg/L.

ANALYSIS OF EXPERIMENTAL RESULT

The biochemical reaction kinetic coefficient K , K_s , V_{max} , Y , K_d , a , b and so on

Without oxygen consumption rate measurement

Se as the abscissa, $(S_o - S_e)/Xt$ (sludge load) as the ordinate, the curve of substrate degradation and substrate concentration without oxygen consumption rate measurement was shown as Figure 2. According to the formula $(S_o - S_e)/Xt = K \cdot Se$ got the slope $K \approx 0.023$.

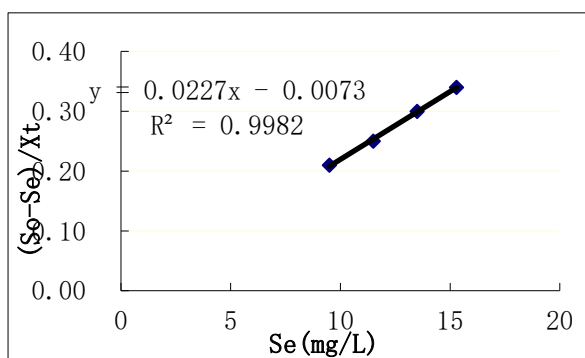


Fig. 2. Curve of substrate degradation and substrate concentration without oxygen consumption rate measurement.

$Q \cdot (S_o - S_e)/Xt \cdot V$ (sludge removal load) as the abscissa, $\Delta X/Xv \cdot V$ as the ordinate, the curve of activated sludge growth without oxygen consumption rate measurement was shown as Figure 3. According to the formula $\Delta X/Xv \cdot V = Y \cdot Q \cdot (S_o - S_e)/Xv \cdot V - K_d$, the yield coefficient of activated sludge microorganisms $Y \approx -0.300$, The self-oxidation rate of activated sludge microorganisms $K_d \approx -0.240$.

$1/Se$ as the abscissa, $(S_o - S_e)/Xt$ (sludge load) as the ordinate, the curve of substrate degradation curve without oxygen consumption rate measurement was shown as Figure 4. According to the formula $Xt/(S_o - S_e) = K_s/V_{max} \cdot 1/Se + 1/V_{max}$, $K_s/V_{max} = 40.683$, $1/V_{max} = 0.3095$. The maximum specific degradation rate of organic substrate can be obtained $V_{max} = 3.231$, Saturation constant $K_s = 12.59$.

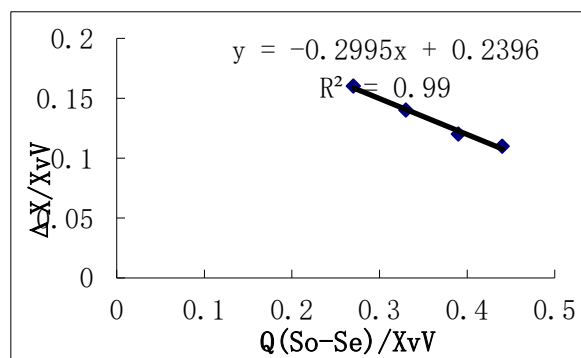


Fig. 3. Curve of activated sludge growth without oxygen consumption rate measurement.

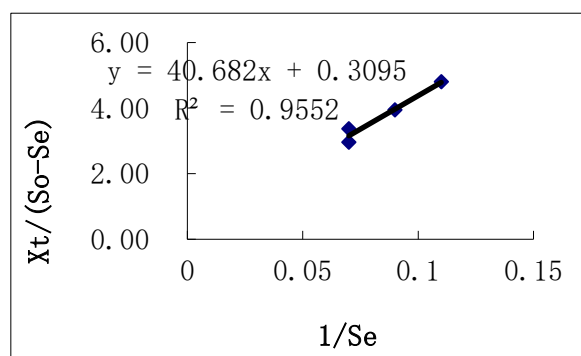


Fig. 4. Curve of substrate degradation curve without oxygen consumption rate measurement.

Therefore, without oxygen consumption rate measurement, the biochemical reaction kinetic coefficient $K = 0.023$, $Y = -0.300$, $K_d = -0.240$, $V_{max} = 3.231$, and $K_s = 12.59$.

Within oxygen consumption rate

Se as the abscissa, $(S_o - S_e)/Xt$ (sludge load) as the ordinate, the curve of substrate degradation and substrate concentration within oxygen consumption rate measurement was shown as Figure 5. According to the formula $(S_o - S_e)/Xt = K \cdot Se$ got the slope $K \approx 0.022$.

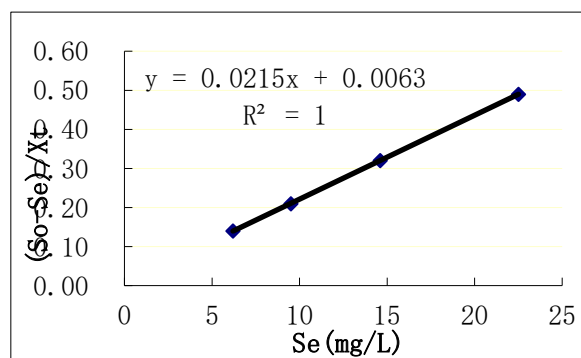


Fig. 5. Curve of substrate degradation and substrate concentration within oxygen consumption rate measurement.

$Q \cdot (So-Se)/Xv \cdot V$ (sludge removal load) as the abscissa, $\Delta X/Xv \cdot V$ as the ordinate, the curve of activated sludge growth within oxygen consumption rate measurement was shown as Figure 6. According to the formula $\Delta X/Xv \cdot V = Y \cdot Q \cdot (So-Se)/Xv \cdot V - Kd$, the microbial yield coefficient of activated sludge was $Y=0.1315$, The self oxidation rate of activated sludge microorganisms was $Kd=-0.075$.

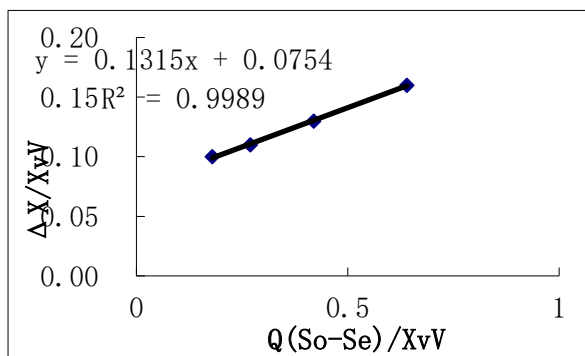


Fig. 6. Curve of activated sludge growth within oxygen consumption rate measurement.

$1/Se$ as the abscissa, $(So-Se)/Xt$ (sludge load) as the ordinate, the curve of substrate degradation curve within oxygen consumption rate measurement was shown as Figure 7. According to the formula $Xt/(So-Se) = Ks/Vmax \cdot 1/Se + 1/Vmax$, $Ks/Vmax=45.210$, $1/Vmax=0.1356$. The maximum specific degradation rate of organic substrate was obtained $Vmax=11.257$, Saturation constant $Ks=3.954$.

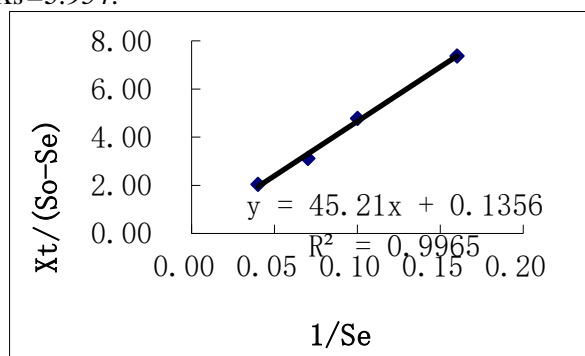


Fig. 7. Curve of substrate degradation curve within oxygen consumption rate measurement.

$Q \cdot (So-Se)/Xv \cdot V$ as the abscissa, $O_2/Xv \cdot V$ as the ordinate, the curve of oxygen consumption rate was shown as Figure 8. According to the formula $O_2/Xv \cdot V = a \cdot Q \cdot (So-Se)/Xv \cdot V + b$, $a=0.4956$, $b=0.1029$.

Therefore, within oxygen consumption rate measurement, the biochemical reaction kinetic coefficient $K=0.022$, $Y=0.1315$, $Kd=-0.075$, $Vmax=11.257$, $Ks=3.954$, $a=0.4956$, $b=0.1029$.

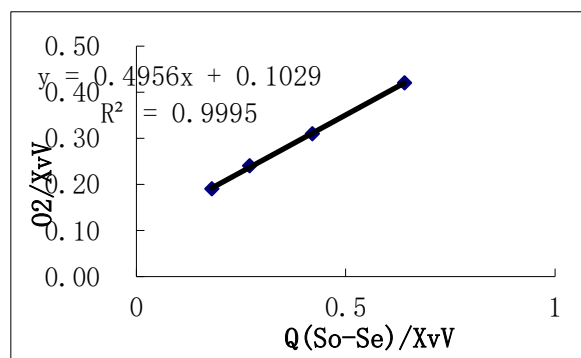


Fig. 8. Curve of oxygen consumption rate.

Discussion the relationship between substrate degradation rate and substrate concentration

In the Figure 9, without oxygen consumption rate measurement or within oxygen consumption rate measurement, the rate of substrate degradation was increased with the increase of substrate concentration. But as for the degradation rate, without oxygen consumption rate measurement was far less than within oxygen consumption rate measurement. In theory, without oxygen consumption rate measurement, the velocity should be larger. Analyzed the cause of this situation was that the MLSS sludge concentration had an influence on the organic matter degradation speed [17].

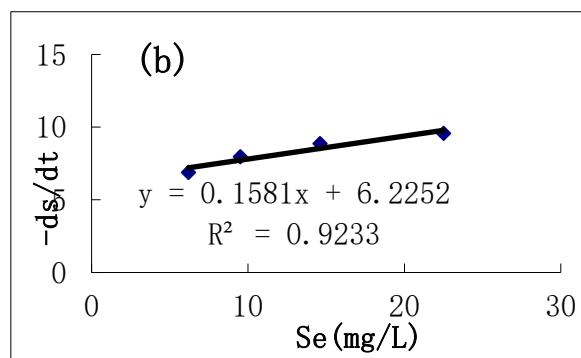
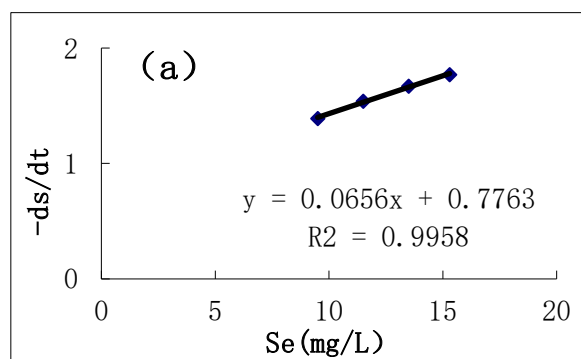


Fig. 9. The relationship between the substrate concentration and the degradation rate of the substrate without(a) and within (b) oxygen consumption rate measurement.

Discussion about the experiment from the relationship between microbial increment rate and substrate concentration

It can be seen from the Figure 10: when the oxygen consumption rate was not measured, the growth rate of activated sludge decreased with the increase of sludge removal load. But when the oxygen consumption rate was measured, the growth rate of activated sludge increased with the increase of sludge removal load. The causes of such differences was analyzed : when the concentration of organic matter in input water respectively was 100 mg/L, 125 mg/L, 150 mg/L, 175 mg/L, and the oxygen consumption rate was not measured, the sludge concentration MLSS respectively was 2481 mg/L, 2555 mg/L, 2629 mg/L, 2704 mg/L. But when the oxygen consumption rate was measured, the sludge concentration MLSS respectively was 3947 mg/L, 3145 mg/L, 2406 mg/L, 1765 mg/L. The sludge concentration was different so that the quantity of microorganism in the sludge also was different. The competition of the microorganism in the sludge to the organic matter and the dissolved oxygen had produced the above result [18].

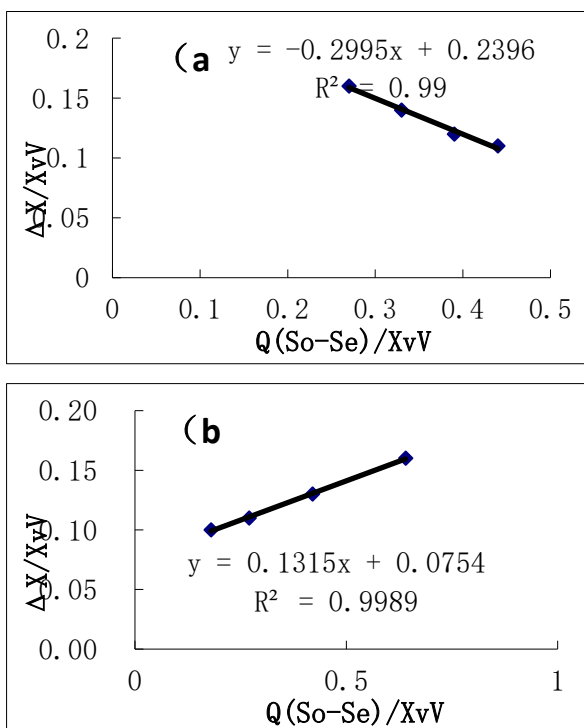


Fig. 10. Growth curves of activated sludge without(a) and within(b) oxygen consumption rate measurement.

Effect of control parameters on the system

Controlled the inlet flow rate Q, the air inflow O₂, dissolved oxygen concentration DO (2.01mg/L), the concentration of the inlet water BOD So(equal to 175mg/L) and sludge age SRT(14.29d) unchanged, and changed reflux ratio R, the relationship between reflux ratio and organic matter in water was shown in Table 2.

Table 2. The relationship between reflux ratio and organic matter in water.

Reflux ratio R(%)	20	30	40	50	60
Se (mg/L)	20.1	15.2	12.6	11.0	9.9

It can be seen from the date that the concentration of effluent BOD Se decreased with the increase of reflux ratio. Therefore, In other conditions remaining unchanged, increasing the reflux ratio can increase the degradation of organic matter [19]. The causes of the result was analyzed: Increasing the reflux ratio was equivalent to increasing the amount of sludge returned to the reactor, which increased the amount of microbes in the reactor. The amount of organic matter in the water was decreased because of the adsorption and ingestion of microorganism [20].

The inlet flow rate Q, the BOD concentration So (equal to 175mg/L) of input water and reflux ratio R (30%) were controlled to be unchanged, and the air flow was changed to change the concentration of dissolved oxygen DO. Then the following data were obtained in Table 3.

From the above data, it was concluded: increased the concentration of dissolved oxygen DO can reduce the concentration of organic matter so that the organic matter concentration can reach a higher standard, and changed the dissolved oxygen concentration DO can also make other parameters change in the treatment process. Increased O₂, the concentration of dissolved oxygen in the reaction pool increased. Increased the dissolved oxygen concentration satisfied the growth and reproduction of microorganisms for oxygen demand, made the microbial growth and reproduction have further consumption to organic matter. At the same time, it made the concentration of organic matter in water decreased gradually. Finally, higher emission standards was achieved [21].

Table 3. The relationship between dissolved oxygen and removal organic matter.

	1	2	3	4	5
Air input O ₂	9000	10000	11000	12000	13000
Dissolved oxygen concentration DO (mg/L)	0.89	1.23	1.65	2.11	2.62
Effluent BOD Se (mg/L)	29.5	22.5	17.6	14.2	11.8
MLSS X (mg/L)	1281	1762	2322	2939	3591

Sludge age SRT (d)	10.38	14.29	18.84	23.84	29.13
--------------------	-------	-------	-------	-------	-------

CONCLUSIONS

The sludge age changed with the change of other parameters, but the single change of sludge age had no effect on the concentration of organic matter in the effluent. Substrate degradation rate increased with the increase of substrate concentration. When the oxygen consumption rate was measured or not measured, the quantity of sludge increased. Not only the concentration of organic matter had an effect on the increment of microbes, sludge concentration and dissolved oxygen and so on also played an important role in the increment of microbes. In addition, the demand for O₂ increased with the increase of organic matter removal. Controlled the inlet flow rate Q, inlet water BOD so (equal to 175 mg/L) and sludge age SRT (14.29d) invariable, respectively changed reflux ratio R and the dissolved oxygen concentration DO (2.01mg/L). When the dissolved oxygen concentration DO (2.01 mg/L) was invariable, and the concentration of BOD So decreased with the increase of reflux ratio. When the reflux ratio of R (30%) was unchanged and changed the concentration of dissolved oxygen DO, and it was found that increased dissolved oxygen concentration DO can reduce the concentration of organic compounds. When reflux ratio was greater than 30% or when the concentration of DO was 1.65mg/L, the concentration of effluent BOD can reach the GB18918-2002 level B standard of 'municipal wastewater treatment plant pollutant emission standard'.

Acknowledgements: This research was financed by the National Natural Science Foundation of China (No.31600253), the Ministry of Education Comprehensive Reform Pilot Project Foundation of China (No. 201333111), the Science and Technology Department Foundation of Sichuan Province (No. 2017JY0087), the Education

Department Foundation of Sichuan Province (No. 16ZB0434), the Youth Foundation of Chengdu University (No. 2016XJZ05) and the Excellence Project Foundation of Chengdu University (No.82502).

REFERENCES

- 1.J.Q. Li, C.Y. Guo, P.H. Fei, *ESIAT.*, **1**, 70 (2012).
- 2.S.M. Dong, *Jiangsu Univ*, 1 (2011).
- 3.S.J. Rui, *Agric. Sci. Technol. Inf.*, **20**, 39 (2015).
- 4.J.R. Zhang, *Biotechnol. World.*, **12**, 19 (2015).
- 5.J. Wang, Q. Wang, J.Y. Chen, M.H. Luo, *Chin. Water. Waste Water.*, **27**(19), 17 (2011).
- 6.Y.P. He, W.Y. Gao, J.B. Chen, *Res. Econ. Environ. Prot.*, **9**, 79 (2014).
- 7.Q. Ge, S.C. Zhou, D.H. Huang, *Chin. Water. Waste Water.*, **29**(7), 101 (2013).
- 8.H. Li. *Chin. Water. Waste Water.*, **26**(20), 154 (2010).
- 9.S. Siripong, B.E. Rittmann, *Water. Res.*, **5**, 1110 (2007).
- 10.L. Ying, A.J. Guo, Z. Jing, *CESCE Part B.*, **1**, 334 (2011).
- 11.X.D. Li, J.P. Qiu, X.J. He, Y.Q. Xiao, *Water. Purif. Technol.*, **27**(4), 36 (2008).
- 12.Y.Q. Dai, *Shanghai Jiao Tong Univ*, 1 (2010).
- 13.J.Z. Jiang, M.Y. Xing, J. Yang, *Chin. Water. Waste Water.*, **30**(15), 6 (2014).
- 14.Y.D. Zheng, Y.F. Lu, A.F. Wu, *Chin. Water. Waste Water*, **32**(3), 1 (2016).
- 15.J.Z. Li, X.Z. Luo, Z. Zhen, D.H. Su, *Environ. Pollut. Control.*, **12**, 11 (2008).
- 16.Y.L. Guo, B. Meng, S. Wang, *Chin. J. Environ. Engin.*, **8**(2), 729 (2014).
- 17.M. Juan, P.C. Yao, W. Li, *Water. Sci. Technol.*, **61**(9), 2325 (2010).
- 18.Y.Y. Wang, Z.X. Zhang, M. Yan, *CAST, J. Environ. Sci. Health*, **45**(3), 370 (2010).
- 19.B.P. McNicholl, J.W. Mcgrath, J.P. Quinn. *Water. Res.*, **41**(1), 127 (2007).
- 20.T. Mino, MCMV. Loosdrecht, J.J. Heijnen, *Water. Res.*, **32**(11), 3193 (1998).
- 21.J. Yang, D.H. Yi, L.M. Zhao, *Chin. Environ. Sci.*, **28**(10), 892 (2008).

ПРОУЧВАНЕ НА НОВА ТЕХНОЛОГИЯ ЗА ОБРАБОТКА НА СЕЛСКИ БИТОВИ ОТПАДНИ ВОДИ НА БАЗАТА НА CASS И VBF

Юнган Дзън^{1,2}, Уънюан Ли¹, Дзин Хуан¹, Джануън Хуан¹, Дзин Уан¹, Дзин Циен^{1,3}, Ао Юан¹,
Тинтин Ду¹, Яци Ху¹, Даган Ли¹

¹Училище за архитектура и строителство, Чънду университет, Ченду, Китай

²Изследователска академия на науките и технологиите за опазване на околната среда, Ченду Чуанхуан
Ченду, Китай

³Училище по естествени и приложни науки, Северозападен политехнически университет, Сиан, Китай

Получена 10 октомври 2016 г.; ревизирана 10 февруари 2017 г.

(Резюме)

Статията има за изследван обект типични селски битовофекални води от околните квартали и райони на Ченду като обект. Беше избран комбиниран процес на циклична система с активна утайка (CASS) и вермибиофилтър (VBF). За да се симулира процеса и да се направи систематичен анализ на свързаните влияещи фактори, условията за контрол, операционния механизъм на селски битови отпадни води и т. н. беше използван компютър, Контролиран входящия на водния поток Q , концентрацията на БПК на входящата вода S_0 (175 мг / л) и възрастта на утайките SRT (14.29 г) са без промяна, съответно се променя съотношението рефлукс R и концентрация на разтворен кислород, и беше постигнато концентрацията на БПК на отпадъчните води да достигне стандарта за заустване на замърсители на GB18918-2002 клас В на градската станция за пречистване на отпадъчни води.

Selected papers presented at the 4th Asia-Pacific Conference on Engineering Technology (APCET 2016), February 15-18, 2016, Beijing, China.

Hydroxyl radical scavenging activity of microparticles prepared from solid fermentation by edible-medicinal fungi

Z. Yuan, P. Yan*

School of Municipal and Environment Engineering, Harbin Institute of Technology, Harbin, 150001, China

Received February 18, 2016; Revised July 26, 2016

Kelp waste is the main solid waste in the kelp processing industries. At the same time the hydroxyl •OH radical is one of the main chemical species which can damage all types of macromolecules in an organism. In this study, the possibility of incubation of popular edible-medicinal fungi producing hydroxyl radical scavenging activity polysaccharides on the kelp waste medium is discussed. Experiments were conducted to optimize the growth rate of the fungi solid fermentation. Each component of the fermentation mixture was investigated with hydroxyl radical scavenging assays respectively. Results showed that the edible-medicinal fungi could grow on this medium and produce abundant polysaccharides which have the capacity for hydroxyl radical scavenging. Assays of each component indicated the scavenging rate of the hot water extracts of these fermentation products and their polysaccharides were much higher than established by BHT control.

Keywords: Hydroxyl radical, Edible-medicinal fungi

INTRODUCTION

Kelp waste is a principle oceanic solid waste in large scale kelp cultivation and the related factories, such as the production of iodine, mannitol, sodium alginate and fucoidin [1] which contains minerals, crude fibers and proteins. With the development of these processing industries, kelp waste has been a potential source of environmental contamination that can cause water eutrophication and a potential source of red tide bloom by the draining of this industrial waste to the ocean together with the amounts of organic substance and nutritive salts [2]. Discarding this is also a great loss of natural resources. Edible-medicinal fungi fermented on kelp waste will have an excellent capacity for hydroxyl radical scavenging and polysaccharides producing with a low cost [3].

The hydroxyl •OH radical is one of the main chemical species controlling the oxidizing capacity of the global earth atmosphere. It can damage almost all types of macro molecules: nucleic acids, carbohydrates, amino acids and lipids. The hydroxyl radical has a very short in vivo half-life of approximately 10^{-9} seconds and a high reactivity [4]. This makes it a very dangerous compound for the organism [5].

It can be scavenged by antioxidants such as glutathione and melatonin and dietary antioxidants such as mannitol and vitamin E [6].

Hypsizygusmarmoreus is also called the Zhengjigu, jade mushroom, a spot jade mushroom,

in China, belonging to *Hypsizygus*, *Tricholomataceae*, *Agaricales*, *hymenomycetidae*, *Basidiomycetes*. This Edible-medicinal fungi contains 8 kinds of amino acids necessary for us humans and several kinds of polysaccharide. Its extracts drawn by hot water from the fruit body have the role of clearing away the free radicals in the human body, which suggests that the solid kelp waste fermentation may have the effects of hydroxyl radical scavenging.

MATERIALS AND METHODS

Fungi strain and Solid fermentation

The kelp waste material was obtained from factories engaged in sodium alginate production in Weihai, China. The fungi *Hypsizygusmarmoreus* was preserved in our lab and initially incubated on a potato dextrose agar PDA medium (fresh potato 20%, glucose 2% and agar 1.5%) in a Petri dish at 25°C for 10 days.

Agar plugs of 10 mm in diameter with young mycelia were punched out by a puncher and inoculated into 370 mL tissue culture bottles. It contained 50g kelp waste with addictive glucose and wheat bran.

The antioxidant BHT was used as positive control (C1). The medium without fermenting fungi was used as negative control (C2). Each treatment had three replications and each replication included three parallel tissue culture bottles.

Single factor experiments: water content, PH value, wheat bran content, temperature and glucose content were conducted to optimize the growth rate of *Hypsizygusmarmoreus*.

* To whom all correspondence should be sent:
E-mail: 43359998@qq.com

Treatment of the experimental samples

The kelp waste product after 30 day's fermentation, with mature mycelia was dried and shattered into microparticles (160~200 mesh).

The fermented powder suspension was made by the microparticles suspended in distilled water. The prepared concentration of this powder suspension is 50 mg/mL.

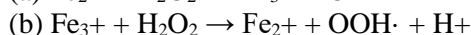
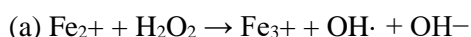
Hot water extracts were taken by bathing (100°C) of the micro particles for 2 hours, to extract the soluble part of the product which contained polysaccharides and other soluble substances. After precipitation and lyophilization, it was dissolved in distilled water with a hot water extraction of 50 mg/mL.

The polysaccharides solution was then made by four fold volumes of ethanol (95%) added to the hot water extraction. Centrifuged at 6,000 rpm for 30 min., left overnight at 4°C, the polysaccharides were then obtained after precipitation and lyophilization. The solution was then re-dissolved (50mg/mL) in distilled water as experimental samples.

All the chemicals used in the study were of analytical grade.

Assays of hydroxyl radical scavenging activity and EC_{50}

Fenton's reagent is the most common reaction producing $HO\cdot$, developed by Henry John Horstman Fenton. Ferrous Iron (II) is oxidized by hydrogen peroxide to ferric iron (III), a hydroxyl radical and a hydroxyl anion. Iron (III) is then reduced back to iron (II), a peroxide radical and a proton by the same hydrogen peroxide.



There is a maximum absorbance peak at 550 nm, adding a griess reagent to the fenton's reagent system, in a specified concentration range, the light absorption of the fenton's reagent system is positively related to the concentration of $HO\cdot$. So the light absorption OD value will be reduced when the inhibitor of $HO\cdot$ exists in the system, which can test the hydroxyl radical scavenging activity of the substance. The formula is listed below as formula (1), where ODc is the absorbance without samples and ODu is the absorbance in the presence of the samples of the fermented products.

$$\text{Hydroxyl radical scavenging activity(\%)} = \frac{ODc - ODu}{ODc} \times 100 \quad (1)$$

The EC_{50} value is the effective concentration at which hydroxyl radicals were scavenged by 50%

and was obtained by interpolation from regression analysis.

RESULTS AND DISCUSSION

Fermentation of *Hypsizygus marmoreus* on kelp waste medium

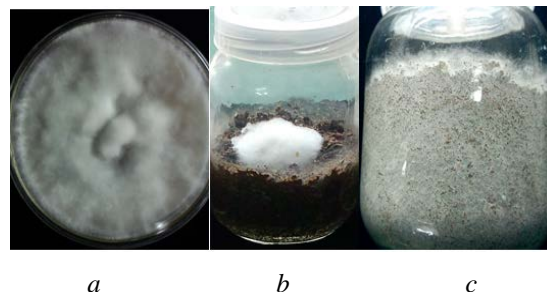


Fig. 1. *Hypsizygus marmoreus* fermented on a PDF medium (a) and a kelp waste medium (b,c)

Hypsizygus marmoreus, as shown in Figure 1 can grow on the solid medium mainly composed of kelp waste. It produced white, moderately long and dense mycelia during the fermentation, which indicated kelp waste could be employed as an alternative medium for the fermentation of *Hypsizygus marmoreus*. Experiments were conducted to optimize the growth rate of *Hypsizygus marmoreus*: water content, PH value, wheat bran content, temperature and glucose content. The results of 5 single factor experiments are shown in figure 2 and the selected optimum solid fermentation conditions for growth and achieving a maximum growth rate were shown in table 1.

Table 1. Optimum Solid Fermentation

Optimum parameters	Results
Water content (%)	70
PH value	6.5
Bran content (%)	0.25
Glucose content (%)	0.16
Temperature (°C)	22
Maximum growth rate (mm/day)	2.16±0.35

According to the single factor optimization of the growth rate for *Hypsizygus marmoreus*, the optimal solid conditions were a water content of 70%, a PH value of 6.5, bran content of 25% and glucose content of 16%. The temperature of the fermentation system was 22°C. The experiment to attain a maximum growth rate was conducted under

these conditions, which showed that the growth rate for *Hypsizygus marmoreus* was 2.16 ± 0.35 mm/d.

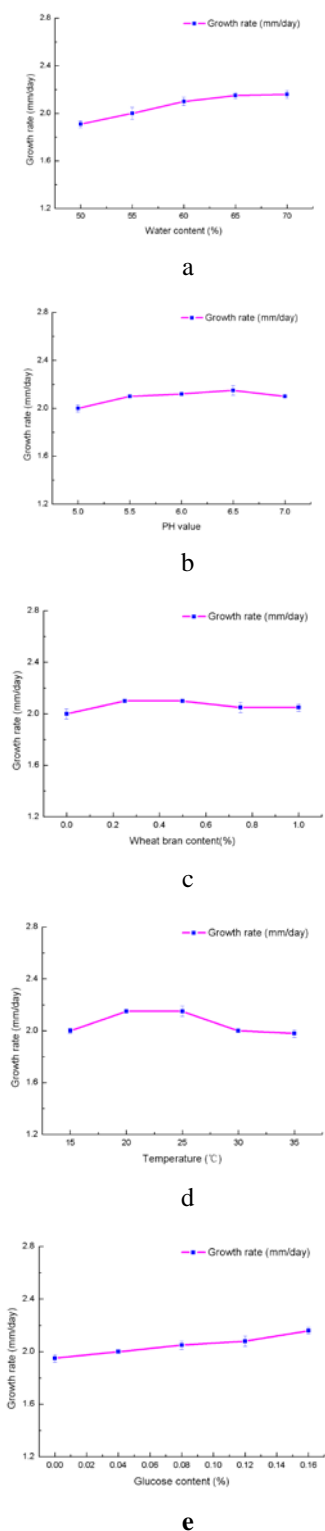


Fig. 2. Growth rate affected by the water content (a), PH value (b), wheat bran content (c), Temperature (d) and Glucose content (e)

The hot water extracts and the polysaccharides from Hypsizygus marmoreus fermentation

The dried and shattered kelp waste product was suspended in distilled water. The soluble part of the product which contained polysaccharides and other soluble substances was in hot water extracts, then the polysaccharides were drawn from hot water extracts, with the yield following these steps weighed, calculated and listed in table 2.

Table 2. Yield of the Target Product in (%).

	Hot water extracts	Polysaccharides
Yield	18.35 ± 0.62	10.58 ± 0.42

Hydroxyl radical scavenging activity

The hydroxyl radical scavenging activity of the microparticles suspension, hot water extracts and polysaccharides obtained from solid fermentation, the kelp waste medium and BHT solution are shown in Figures 3 to 5.

The Hydroxyl radical scavenging activity of the obtained samples from *Hypsizygus* incubation (T in figures 3 to 5), BHT(C1) and the seaweed waste alone (C2) as a control sample was tested. The data was presented as the mean of three independent experiments \pm SD.

The formula is listed below as formula (2), where ODc is the absorbance without samples and ODu is the absorbance in the presence of the samples of the fermented products.

$$\text{Scavenging effect} = (\text{ODc} - \text{ODu}) / \text{ODc} \quad (2)$$

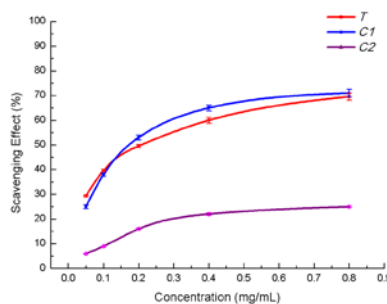


Fig. 3. Hydroxyl radical scavenging capacities of the powder suspension (T) obtained from *Hypsizygus*.

In accordance with figure 3, a dose-dependent increase of the hydroxyl radical scavenging activity of the microparticle is exhibited. The hydroxyl radical scavenging activity of the microparticles suspension was slightly less than BHT but more than the kelp waste medium without fermenting. But the hot water extracts (figure 4), especially the

polysaccharides (figure 5) drawn from the fermentation products had much more Hydroxyl radical scavenging activity than BHT and a kelp waste medium without fermenting.

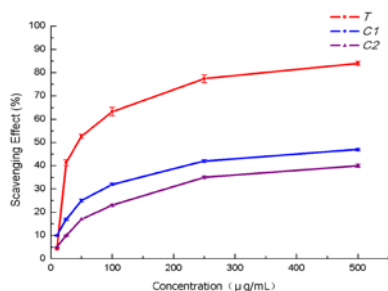


Fig. 4. Hydroxyl radical scavenging capacities of the hot water extracts (T) obtained from *Hypsizygus*.

Compared with the data for hydroxyl radical scavenging, among the fermented powder suspension, hot water extraction and polysaccharides solution and BHT solutions (as positive control), *Hypsizygus marmoreus* solid fermented products have a high hydroxyl radical scavenging activity, which also increases with the higher concentration of polysaccharides which exist in both the suspension and extracts solution at a different concentration.

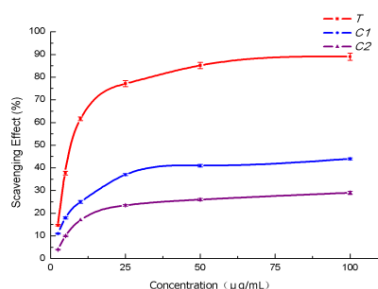


Fig. 5. Hydroxyl radical scavenging capacities of the polysaccharides (T) obtained from *Hypsizygus*

Results of EC₅₀ for each sample

The effective concentrations at which the hydroxyl radicals were scavenged by 50% (EC₅₀) were calculated according to the scavenging rate of the microparticle suspension, hot water extracts and its polysaccharides each at this 50mg/mL concentration respectively. The EC₅₀ for each sample was listed in table 3.

Table 3. EC₅₀ Value (µg/mL)

Sample	Results
Powder suspension	204±10.3
Hot water extract polysaccharides	7.44±0.51
BHT	151±13.0
Kelp waste medium	2910±32

As shown in table 3, the EC₅₀ value of the fungi sample, microparticles suspension obtained from *Hypsizygus marmoreus* fermentation was 204µg/mL, which was significantly lower than that of the kelp waste without *Hypsizygus* fermentation (2910µg/ml) as control 2, but higher than the BHT solution (151µg/ml) as control 1. The EC₅₀ for the hot water extracts obtained from *Hypsizygus marmoreus* fermentation was 7.44µg/mL, which was significantly lower than that of the kelp waste without *Hypsizygus* fermentation and the BHT solution. The EC₅₀ value for the polysaccharides obtained from fermentation was 1.73µg/mL, significantly lower than that of the kelp waste without *Hypsizygus* fermentation and the BHT solution.

According to the EC₅₀ values, the microparticle obtained from *Hypsizygus marmoreus* fermentation exhibited significantly higher hydroxyl scavenging capacity than the kelp waste medium, the hot water extracts exhibited a significantly higher hydroxyl scavenging capacity than BHT and the kelp waste medium and the polysaccharides obtained from *Hypsizygus marmoreus* fermentation exhibited a much higher hydroxyl scavenging capacity than BHT and the kelp waste medium.

CONCLUSIONS

In this study, *Hypsizygus marmoreus* was shown to grow on the solid medium mainly composed of kelp waste, which indicates that kelp waste can be employed as an alternative medium for fermentation of *Hypsizygus*.

Compared with the hydroxyl radical scavenging activity of BHT and the kelp waste medium without fermentation, the activity of the hot water extracts and polysaccharides from *Hypsizygus marmoreus* were higher than both of these, while the ferment microparticles suspension had a larger hydroxyl radical scavenging activity than the negative control but less than BHT.

Since a dose-dependent increase of the hydroxyl radical scavenging activities of the polysaccharides was exhibited and the EC₅₀ of the polysaccharides was obviously much lower than the other components from the fermentation, the polysaccharides from the *Hypsizygus marmoreus* kelp waste solid fermentation system is clearly the most effective hydroxyl radical scavenging substance in solid fermentation.

The hydroxyl radical scavenging results showed the product of the kelp waste fermentation of *Hypsizygus* have a high useful value. The efficient and high biological activity conditions of the biological conversion of kelp waste ferment of

Z. Yuan, P. Yan: Hydroxyl radical scavenging activity of microparticles prepared from solid fermentation by edible-medicinal fungi

edible-medicinal fungi has provided a potential pathway for the biological transformation of kelp waste into high value-added industrial products for application in medical and food stuffs products in natural hydroxyl radical scavenging. It is also a practical and environmentally friendly resource recycling method.

REFERENCES

1. C.L. Hurd, P.J. Harrison, K. Bischof, C.S. Lobban, *Seaweed Ecology and Physiology*, Cambridge University Press, United Kingdom, 2014.

2. J.J. Zhang, R. Duan, K. Xu, Z.L. Li, *Fisher Science (China)*, **29**, 10 (2010).

3. Y. Zhuang, P.S. Yan, T. Yang, *Journal of Computational and Theoretical Nanoscience*, **13**(4), 2531 (2016).

4. H. Sies, *European Journal of Biochemistry*, **215**(2), 213 (1993).

5. R.J. Reiter, R.C. Carneiro, C.S. Oh, *Hormon and Metabolic research*, **29**(8), 363 (1997).

6. R.J. Reiter, D. Melchiorri, E. Sewerynek, *Journal of pineal research*, **18**(1), 1 (1995).

СПОСОБНОСТ ЗА ОСТРАНЯВАНЕ НА ХИДРОКСИЛНИ РАДИКАЛИ ОТ МИКРОЧАСТИЦИ, ПОЛУЧЕНИ ПРИ ТВЪРДО-ФАЗНА ФЕРМЕНТАЦИЯ НА ЕДЛИВИ МЕДИЦИНСКИ ГЪБИ

З. Юан, П. Ян*

Училище по общинско и екологично инженерство, Харбински технологичен институт, Харбин 150001, Китай

Постъпила на 18 февруари, 2016 г.; коригирана на 26 юли, 2016 г.

(Резюме)

Отпадъците от кафявите морски водорасли са основния твърд отпадък при тяхното производство. От друга страна хидроксилните радикали •ОН са едно от главните химични вещества, които поразяват всички видове макромолекули в човешкия организъм. В настоящата работа се обсъжда възможността за ферментация на известни едливи медицински гъби с остатъци от кафяви водорасли, при което се получават полизахариди с противорадикална активност. Проведени са експерименти за оптимизиране на растежа на гъбите при твърдо-фазна ферментация. Всеки компонент на ферментационната смес е изпитан за противорадикалова активност. Резултатите показват, че едливите медицински гъби могат да растат на тази среда и да произвеждат обилно полизахариди, които имат способността да отстраняват хидроксилни радикали. Анализът на всеки компонент показва, че противорадикаловата способност в екстракти с гореща вода от ферментационните среди е много по-висока отколкото при ВНТ контрол.

Pt doped TiO₂ (Pt-TiO₂) sol gel thin films

Y.J. Jia¹, W.X. Su², Y.B. Hu², H.N. Chen^{2*}

¹School of Mechanical Engineering, Tianjin Polytechnic University, Tianjin 300387, China

²School of Computer Science and Software Engineering, Tianjin Polytechnic University, Tianjin 300387, China

Received January 3, 2016; Revised September 12, 2016

Pt was supported on a TiO₂ surface using different methods. Pt doped TiO₂ (Pt-TiO₂) sol gel thin films were successfully produced by reducing chloroplatinic acid (H₂PtCl₆). The structures of the prepared composites were investigated using X-ray diffraction (XRD). The physical morphologies of the composites were examined using transmission electron microscope (TEM). After annealing the grain size of the Pt-TiO₂ thin film was also measured by an atomic force microscope (AFM).

Keywords: TiO₂, Pt annealing, Pt-TiO₂ sol gel film.

INTRODUCTION

Recently, extensive research of titanium dioxide (TiO₂) has been carried out in efforts to develop a variety of applications including capacitors for photovoltaic cells [1], sensors [2], antireflection films [3], white pigments [4], optical coatings [5] and high density dynamic random access memory devices [6]. TiO₂ has three different crystal phases, such as anatase, rutile and brookite [7]. Rutile is the most common natural form of TiO₂. The brookite phase crystallizes in the orthorhombic system and does not exhibit any photocatalytic activity. Anatase TiO₂ has an excellent photocatalytic activity, physical and chemical stability and antimicrobial activity [8-11].

Earlier studies have revealed that the photocatalytic activity of TiO₂ can be improved significantly by doping with noble metals such as Pt, Au and Ag [12,13]. It is well known that the coverage of TiO₂ with platinum often shows a high photocatalytic activity. The doping of TiO₂ with platinum can form a Schottky diode barrier between the metal and the electronic potential barrier at the metal-semiconductor heterojunction and the TiO₂ covered with platinum traps the photogenerated electrons efficiently [14]. The deposition of Pt on the TiO₂ surface has been widely reported to improve the photocatalytic performance of the split water and the degradation of different harmful compounds [15].

In this paper, we report characteristic properties of the TiO₂ and Pt composite including the UV-visible spectra, transmission electron microscope (TEM) images, X-ray diffraction (XRD) patterns

and atomic force microscope (AFM) images.

EXPERIMENTAL DETAILS

Titanium oxide was used as a sol-gel precursor. The metal alkoxide was mixed with ethanol. The resulting solution became a milky color and white precipitation was observed. Hydrochloric acid was slowly added to the solution with vigorous stirring until the solution become transparent. Various amounts of chloroplatinic acid (H₂PtCl₆) (8 wt. % in water) was added to the TiO₂ sol-gel solution. Sodium borohydride (NaBH₄) was dispersed in ethanol and slowly added to the H₂PtCl₆/TiO₂ solution to reduce the [PtCl₆]²⁻ to zero Pt. The aged sol was spin coated on to the glass and the silicon substrate by spin-coating at 2000 RPM and heated at 200 °C for 5 minutes. UV-visible spectra were obtained with a diode array spectrophotometer (Hewlett-Packard 8452 A). The sol-gel was diluted to ethanol and dropped on to the copper TEM grid. Using this copper grid sample, TEM images were obtained with a CM200 (Philips) microscope. The TiO₂ thin films coated on to a silicon wafer were annealed in a gas environment tube furnace (EM Tech). The annealing process started from room temperature up to 750 °C in steps of 5 °C/min and then maintained the temperature for 1 h. The films naturally cooled down to room temperature. The TiO₂ thin films doped with Pt were subject to XRD analysis with an X'Pert MPD Pro diffractometer (Philips). The surface of the film was also analyzed with a NanoScope 3D (Veeco) microscope.

RESULTS AND DISCUSSION

UV-visible spectra of bare TiO₂ and Pt-TiO₂ prepared with different Pt concentrations are shown in Figure 1. The single broad intense absorption peak of Pt-TiO₂ between 300 – 350 nm can be

* To whom all correspondence should be sent:
E-mail: perfect_chn@hotmail.com

attributed to the charge-transfer from the valence band to the conduction band. The UV-visible absorption peaks also show a red shift due to the modification of TiO₂ with Pt [16].

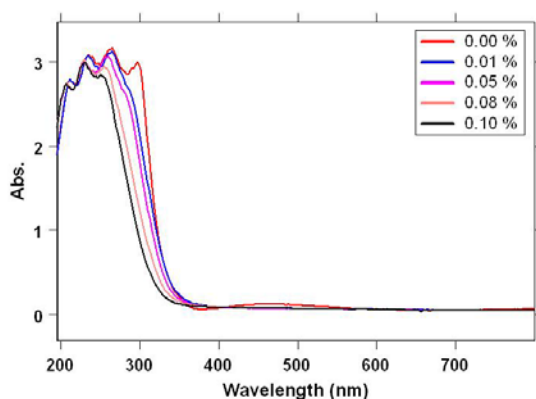


Fig. 1. UV-Visible spectra of a bare TiO₂ and Pt-TiO₂ sol-gel thin film after annealing.

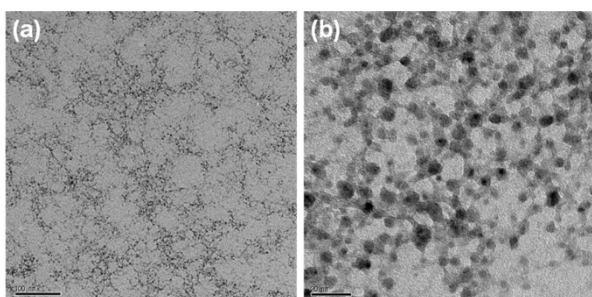


Fig. 2. TEM image of TiO₂-Pt with 0.1% Pt.

The UV-visible spectra show the possible uniform distribution of Pt-nanoparticles throughout the sol-gel films. To obtain the particle size and distribution, a TEM was employed. Figure 2 (a) shows the TEM image for the film of 0.1 % Pt-TiO₂ with a scale bar size of 100. The aggregated area

was further focused and the image obtained with a scale bar size of 20 nm is shown in Figure 2 (b). Pt-nanoparticles do not have big aggregates, distribute relatively uniformly and have particle sizes between 4–8 nm.

Figure 3 (a) shows the XRD patterns for Pt-TiO₂ films prepared by the sol-gel method with various amounts of Pt. All these samples show typical TiO₂ diffraction peaks in the form of anatase. As observed these almost coincide with the pure TiO₂ diffraction peaks and show no diffraction peaks due to the doped Pt. It can be assumed that the amount of Pt doped particles was very low, which resulted in the non-appearance of Pt crystalline peaks [17,18]. However, the diffraction intensity increased with the increase of Pt concentration. The crystalline size of the Pt-TiO₂ samples after annealing was estimated from line broadening using the Scherrer equation based on the (101) peak of anatase TiO₂ [19].

$$D = 0.9\lambda / \beta \cos \theta$$

where λ is the X-ray wavelength of Copper K α radiation, θ is the Bragg's angle and β is the pure full width of the diffraction line at half of the maximum intensity (Figure 3(b)). The calculated grain sizes are 15 nm (0.01%), 20 nm (0.05%), 35 nm (0.08%) and 40 nm (0.1%), respectively. The results refer to Pt doping and also retard the grain growth of the TiO₂ thin film.

AFM images of the Pt-TiO₂ surface were used to monitor the grain size of the sol-gel thin film that depends on the Pt concentration. 1 $\mu\text{m} \times 1 \mu\text{m}$ scans revealed it is clear that the grain size of Pt-TiO₂ gradually increased with Pt loading.

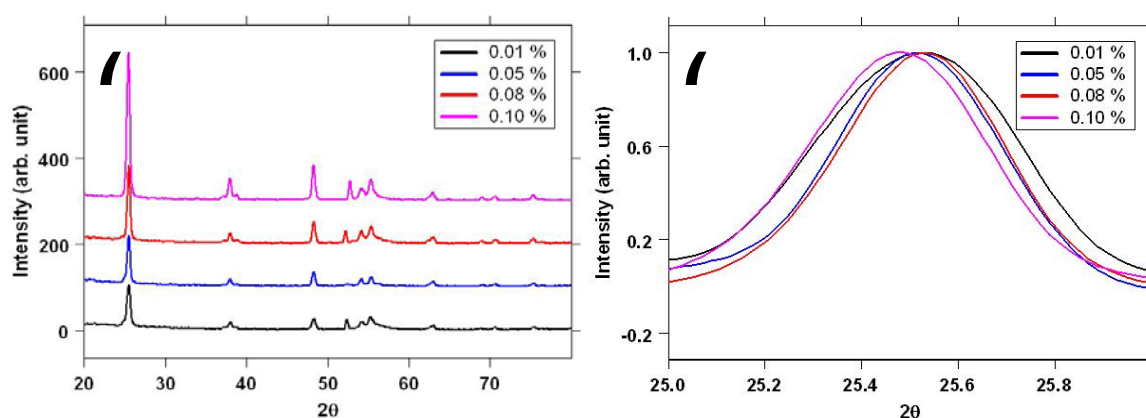


Fig. 3. XRD pattern of the TiO₂-Pt thin film depending on the Pt concentration.

CONCLUSIONS

Metallic doping is one factor for the TiO₂ anatase phase grain growth. The intensity of the main anatase diffraction peak increased with increasing Pt concentration. The grain sizes estimated from the anatase XRD major diffraction peaks were 15, 20, 35 and 40 nm for the sample with Pt concentrations of 0.01%, 0.05%, 0.085 and 0.1%, respectively. The measured grain sizes using AFM images also increased depending on the Pt concentration. The governing factor to determine the grain size of the TiO₂ thin films is Pt doping.

REFERENCES

1. H.W. Wang, C.F. Ting, M.K. Hung, C.H. Chiou, Y.L. Liu, Z. Liu, K.R. Ratinac, S.P. Ringer, *Nanotechnology*, **20**, 055601 (2009).
2. J. Bai, B. Zhou, *Chem. Rev.*, **114**, 10131 (2014).
3. V. Zoulalian, S. Monge, S. Zrcher, M. Textor, J.J. Robin, S. Tosatti, *J. Phys. Chem. B*, **110**, 25603 (2006).
4. N.B. Chaure, A.K. Ray, R. Capan, *Semicond. Sci. Technol.*, **20**, 788 (2005).
5. H. Yaghoubi, N. Taghavinia, E.K. Alamdari, *Surf. Coating Tech.*, **25**, 1562 (2010).
6. Q. Li, K. Ali, S. Lulia, P. Christos, H. Xu, P. Themistoklis, *Scientific Reports*, **4**, 4522 (2014).
7. W. Zhang, S. Chen, S. Yu, Y. Yin, *J. Crystal Growth*, **308**, 122 (2007).
8. T. Ohno, K. Sarukawa, M. Matsumura, *New J. Chem.*, **26**, 1167 (2002).
9. X.H. Yang, Z. Li, C. Sun, H.G. Yang, C. Li, *Chem. Mater.*, **13**, 3486 (2011).
10. G. Fu, P.S. Vary, C. Lin, *J. Phys. Chem. B*, **109**, 8889 (2005).
11. H. Zhang, G. Chen, *Environ. Sci. Technol.*, **43**, 2905 (2009).
12. D. Morris, Y. Dou, J. Rebane, C.E.J. Mitchell, R.G. Egdell, *Phys. Rev. B*, **61**, 13445 (2000).
13. M. Enachi, M. Guix, T. Braniste, V. Postolache, V. Ciobanu, V. Ursaki, O.G. Schmidt, I. Tiginyanu, *Surf. Eng. Appl. Electrochem.*, **51**, 3 (2015).
14. W.Y. Park, G.H. Kim, J.Y. Seok, K.M. Kim, S.J. Song, M.H. Lee, C.S. Hwang, *Nanotechnology*, **21**, 195201 (2010).
15. D. Eder, M. Motta, A.H. Windle, *Nanotechnology*, **20**, 055602 (2009).
16. H. Tada, F. Suzuki, S. Yoneda, S. Ito, H. Kobayashi, *Phys. Chem. Chem. Phys.*, **3**, 1376 (2001).
17. L. Ravichandran, K. Selvam, B. Krishnakumar, M. Swaminathan, *J. Hazardous Mater.*, **167**, 763 (2009).
18. H. Wang, Z. Wu, Y. Liu, Y. Wang, *Chemosphere*, **74**, 773 (2008).
19. M. Beghi, P. Chiurlo, L. Costa, M. Palladino, M.F. Pirini, *J. Non-cryst. Solids*, **145**, 175 (1992).

ТЪНКИ ФИЛМИ ОТ TiO₂, ПОЛУЧЕНИ ПО ЗОЛ-ГЕЛ МЕТОДА И ДОТИРАНИ С ПЛАТИНА (Pt-TiO₂)

И. Дж. Джиа¹, М. У. Хе², Х. Н. Чен²

¹Училище по машинно инженерство, Тианджински политехнически университет, Тианджин 300387, Китай

²Училище по компютърни науки и софтуерно инженерство, Тианджински политехнически университет, Тианджин 300387, Китай

Постъпила на 3 януари, 2016 г.; коригирана на 12 септември, 2016 г.

(Резюме)

Платината е фиксирана върху повърхността от TiO₂ с помощта на различни методи. Дотирането с платина на зол-гел тънки филми TiO₂ (Pt-TiO₂) става успешно чрез редуциране на хлороплатинова киселина (H₂PtCl₆). Структурата на приготвените композити е изследвана чрез рентгено-структурен анализ (XRD). Физичната морфология на композитите е изследвана с трансмисиона електронна микроскопия (ТЕМ). След закаляване дебелината на филмите е определяна атомен силов микроскоп (AFM).

Droplet characteristic adjustment method based on LEM for 3D electronic printing

M. He, W. Zhu, F. Liu, H. Chen*

School of Computer Science and Software Engineering, Tianjin Polytechnic University, Tianjin 300387, China

Received February 20, 2016; Revised August 30, 2016

The major challenge in 3D electronic printing is the print resolution and accuracy. In this paper, a typical mode - lumped element modeling (LEM) method - is adopted to simulate the droplet jetting characteristic. This modeling method can quickly get the droplet velocity and volume with a high accuracy. Experimental results show that LEM has a simpler structure with sufficient simulation and prediction accuracy.

Keywords: Droplet characteristic adjustment, Lumped element modeling, 3D electronic printing

INTRODUCTION

3D electronic printing has been widely applied to manufacture low-cost electronic products, such as flexible electronics, radio frequency identification (RFID) tags, solar cells, organic light emitting diodes (OLED) and flexible packaging electronic devices, such as medical equipment [1]. A classical implementation of 3D electronic printing is to use a drop-on-demand (DoD) piezoelectric (PZT) inkjet print head to deposit conductive, dielectric and non-conductive ink onto various substrates [2].

A typical DoD piezoelectric inkjet print head for 3D electronic printing is comprised of a number of ink channels that are arranged in parallel [3]. A piezoelectric actuator covers all the ink channels that can generate pressure oscillations inside the ink channel to push the ink droplet out of the nozzle. Nowadays the developments of DoD printing are moving towards higher productivity and quality. Therefore, the adjustable small droplet sizes fired at high jetting frequencies must be implemented.

The printing quality of a DoD piezoelectric inkjet print head is reflected in many respects, such as the jetting direction, the droplet velocity and the droplet volume. The practical applications meeting the various requirements of 3D electronic printing require a higher inkjet performance, while the droplet characteristics of the ink have to be tightly controlled. To improve the droplet jetting performance, several operational issues, such as the residual vibrations and cross talk, should be considered.

To solve such a problem, the researchers have proposed many methods. One of the most typical methods is using numerical techniques to model the DoD piezoelectric inkjet print head [4], which

focuses on the liquid filament evolution of the droplet formation process with known pressure input boundary conditions after solving the nonlinear Navier-Stokes equations. This method provides directly visualized information about the acoustic pressure wave travelling inside the channel [5]. Another typical method is using the analytical modeling method with a higher simulation speed. This method can describe the ink channel dynamics, although the accuracy of the analytical models is lower than that of the numerical models. Based on several assumptions and simplifications, the analytical models can provide a simple and time saving way to control via modeling the droplet generator with sufficient accuracy [6].

In this work, we adopted a typical analytical model – the lumped element modeling method - to simulate the droplet formation process. The advantage of this method is its simpler structure with sufficient simulation accuracy. After setting a series of desired droplet characteristics, a grid search method is applied to determine the parameters of the print head driving waveform.

The rest of this paper is organized as follows: In Section 2, a review of the original lumped element modeling droplet generator is present. The simulation results of the droplet volume and velocity define the most suitable model in Section 3. The prediction process of the droplet characteristics is built in Section 4. Finally, the concluding remarks are summarized in Section 5.

LUMPED ELEMENT MODELING

A classical LEM is presented to simulate the jetting characteristics of a PZT print head, as shown in Fig. 1. An equivalent circuit model is constructed with the aid of the energy storage elements and the ideal dissipative terminal. In this electro-acoustic system, the pressure and voltage are independent variables, while the current and volumetric flow rate

* To whom all correspondence should be sent:
E-mail: perfect_chn@hotmail.com

are dependent variables. The model structure shows that the energy converts from electrical energy to mechanical energy then to fluid/acoustic energy and finally into kinetic energy as described in Fig. 1(b). The droplet generator structure can be characterized by equivalent acoustic mass (representing the stored kinetic energy) and acoustic compliance (representing the stored potential energy), in which the corresponding equivalent circuit models are supported by various fluid mechanisms, as

represented in Fig. 1(a) and 1(c). Furthermore, the piezo-ceramic model is constructed based on the electric fluid/acoustic theory [7]. The neck model is built on the velocity profile function [8]. The nozzle model is constructed in accordance with the end correction for an open tube theory [9]

The equivalent circuit model is shown in Figure 1 the excitation voltage V_{ac} is applied to a piezoelectric ceramic to create mechanical deformation.

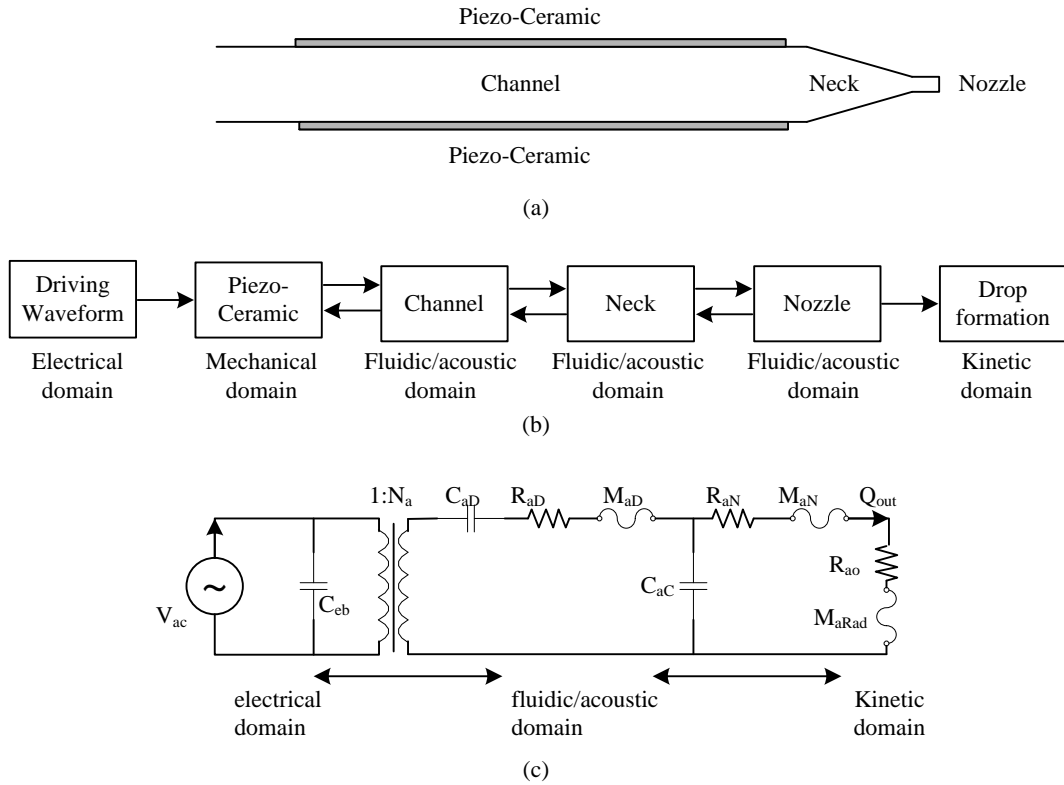


Fig.1. Schematic overview of lumped-element modeling for a PZT print head: (a) Droplet generator structure (b) Model structure (c) Equivalent circuit model.

Table 1. Droplet generator parameters.

	Parameter	Unit	Value
Print head	Channel volume, V_0	pL	166000
	Channel length, L_0	um	7200
	Nozzle radius, a_0	um	13.5
	Neck length, L	um	45
	Piezoceramic thickness, h	um	25
	Free electrical capacitance, C_{eF}	nF	2.8
Ink	Free electrical capacitance, σ	N/m	$45 \cdot 10^{-3}$
	Viscosity, u	$Kg/(m \cdot s)$	15
	Density, ρ_0	Kg/m^3	$1.05 \cdot 10^3$
	Sonic speed, C_0	m/s	1400

The coupling coefficient ϕ_a represents a conversion from the mechanical domain to the acoustic domain. C_{eb} is the blocked electrical capacitance of the piezoelectric material. In the acoustic domain, C_{aD} and C_{aC} represent the acoustic compliance of the piezoceramic and channel. R_{aD} , R_{aN} and R_{aO} are the acoustic resistance due to structural damping, neck tapering and fluid flowing out of the nozzle, respectively. M_{aD} , M_{aN} and M_{aRad} represent the acoustic mass of the piezoceramic neck and nozzle in the proper order, respectively.

The dimensions of the droplet generator and physical properties of the nanosilver ink provided by the LEED-PV Corporation are listed in Table 1 and the calculation formulas of the LEM model parameters are provided in Eq. 1 -9.

$$R_{aN} = \left(2 + \frac{a_0}{r}\right) \frac{\sqrt{2\mu\rho_0\omega}}{\pi r^2} \quad (1)$$

$$M_{aN} = \frac{\rho_0(t + \Delta t)}{\pi r^2} \quad (2)$$

$$\Delta t = 0.85r\left(1 - 0.7\frac{r}{a_0}\right) + 0.85r \quad (3)$$

$$C_{aD} = \frac{\pi r^6(1 - \nu^2)}{16Eh^3} \quad (4)$$

$$M_{aD} = 4\rho_0L / 3\pi a_0^2 \quad (5)$$

$$R_{aD} = 2\xi\sqrt{(M_{aD} + M_{aRad}) / C_{aD}} \quad (6)$$

$$C_{eB} = C_{eF}(1 - \kappa^2) \quad (7)$$

$$R_{aO} = \frac{\rho_0 c_0}{\pi r^2} \left[1 - \frac{2J_1(2kr)}{2kr}\right] \quad (8)$$

$$M_{aRad} = 8\rho_0 / 3\pi^2 a_0 \quad (9)$$

where u is viscosity, w is the wave frequency and a_0/r is the gradients ratio, V_0 is the volume of the cavity, E is the elastic modulus, ν is Poisson's ratio and h is the thickness, ξ is the experimentally determined damping factor [18], J_1 is the Bessel function of the first kind and $k = w/c_0$, κ^2 is the electro-acoustic coupling factor.

SIMULATION

For industry applications in printable electronics fabrication, the print head must work at a certain

status to meet many restrictive conditions. Among these, the most important problem is choosing the appropriate combinations of the driving waveform parameters for the use of conductive inks. However, an exhausting manual selective process inevitably wastes a lot of time. Therefore, the computer-aided methods are urgently needed to search out the appropriate combinations efficiently and robustly.

As mentioned above, the LEM model is chosen to simulate the jetting characteristics of the nanosilver ink. Here, an illustrative example is given to display the effect of predicting the typical combinations of waveform parameters with different dwell times ($T_1 = 3\sim 8\mu s$, $T_2 = 2*T_1$) and the same amplitude (12V). The properties of the nanosilver ink provided by the LEED-PV Corporation have been listed in Table 1. In Fig. 2, the predicted outflow and average velocity curves with various dwell times are depicted. We can observe from Fig. 2(a) that, before the droplets rush out of the nozzle, the depth of the inhaled meniscus is proportional to the dwell time. From Fig. 2(b), the time of the droplet appearing is postponed with the increase of the dwell time. That is, both simulation phenomena consist of a theoretical analysis of the results in [10].

PREDICTION

In this experiment, an illustrative example under the desired conditions is presented to demonstrate the feasibility and effectiveness of the proposed method for predicting the jetting characteristics. The dimensions of the droplet generator and the properties of nanosilver ink are listed in Table 1. In order to reach a high printing resolution and good quality of droplet impact with the substrate, the desired conditions require that the droplet volume is smaller than 14 pL and the droplet velocity is larger than 5 m/s.

Based on the prediction procedure, the predictive values of the drop volume/velocity with various dwell times T_1 and T_2 are listed in Table 2. According to the desired conditions, two combinations of the parameters are found: $T_1 = 5\mu s/T_2 = 13\mu s$ and $T_1 = 5\mu s/T_2 = 7.5\sim 8\mu s$. After a small range search around the predictive values in the actual test, the combination of $T_1 = 4.9\mu s/T_2 = 7.7\mu s$ is finally chosen. The dynamic effect of the jetting characteristics driven by this combination is shown in Figure 2. From this figure, it is clear that the jetting characteristics satisfy the specified desired conditions quite well. Meanwhile, almost no satellite droplets emerge after jetting the main droplets.

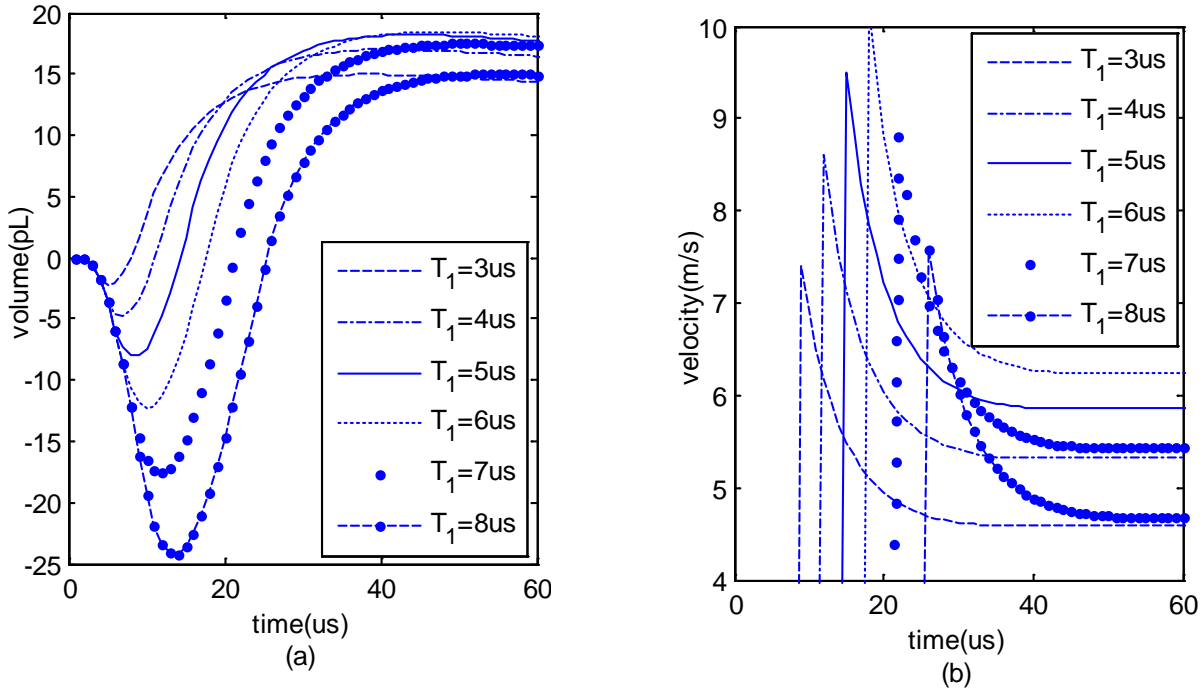


Fig.2. Predictive droplet volume and velocity with a different dwell time $T_2=2*T_1$
 (a) Simulation curves of the outflow change (b) Simulation curves of the droplet average velocity

Table 2. The predictive droplet volume (pL) and velocity (m/s)

T_2 T_1		7	7.5	8.5	9	9.5	10	10.5	11	11.5	12	12.5	13
4	V	11.9	12.7	14.3	14.6	14.9	15.1	15	14.7	14.2	Default	Default	Default
	S	3.95	4.17	4.78	4.91	5.00	4.89	4.71	4.51	4.35	Default	Default	Default
4.5	V	11.7	12.5	15	15.5	15.9	16.2	16	15.7	15.3	14.7	13.9	Default
	S	4.21	4.51	5.16	5.32	5.48	5.60	5.43	5.23	5.01	4.82	4.66	Default
5	V	Default	Default	15.1	15.7	16.3	16.7	16.8	16.6	16.3	15.7	15	14.2
	S	Default	Default	5.31	5.53	5.72	5.87	6.00	5.83	5.63	5.40	5.25	5.09
5.5	V	Default	Default	15.1	15.9	16.5	16.8	16.9	17.1	16.9	16.5	16	15.4
	S	Default	Default	5.24	5.50	5.72	5.93	6.09	6.24	6.01	5.71	5.51	5.37
6	V	Default	Default	Default	Default	15.8	16.3	16.4	16.5	16.5	16.5	15.8	14.95
	S	Default	Default	Default	Default	4.95	5.15	5.33	5.49	5.64	5.44	5.19	4.94
6.5	V	Default	Default	Default	Default	Default	Default	15.5	15.9	16	15.5	15.0	14.3
	S	Default	Default	Default	Default	Default	Default	4.73	4.85	4.95	5.03	4.90	4.69

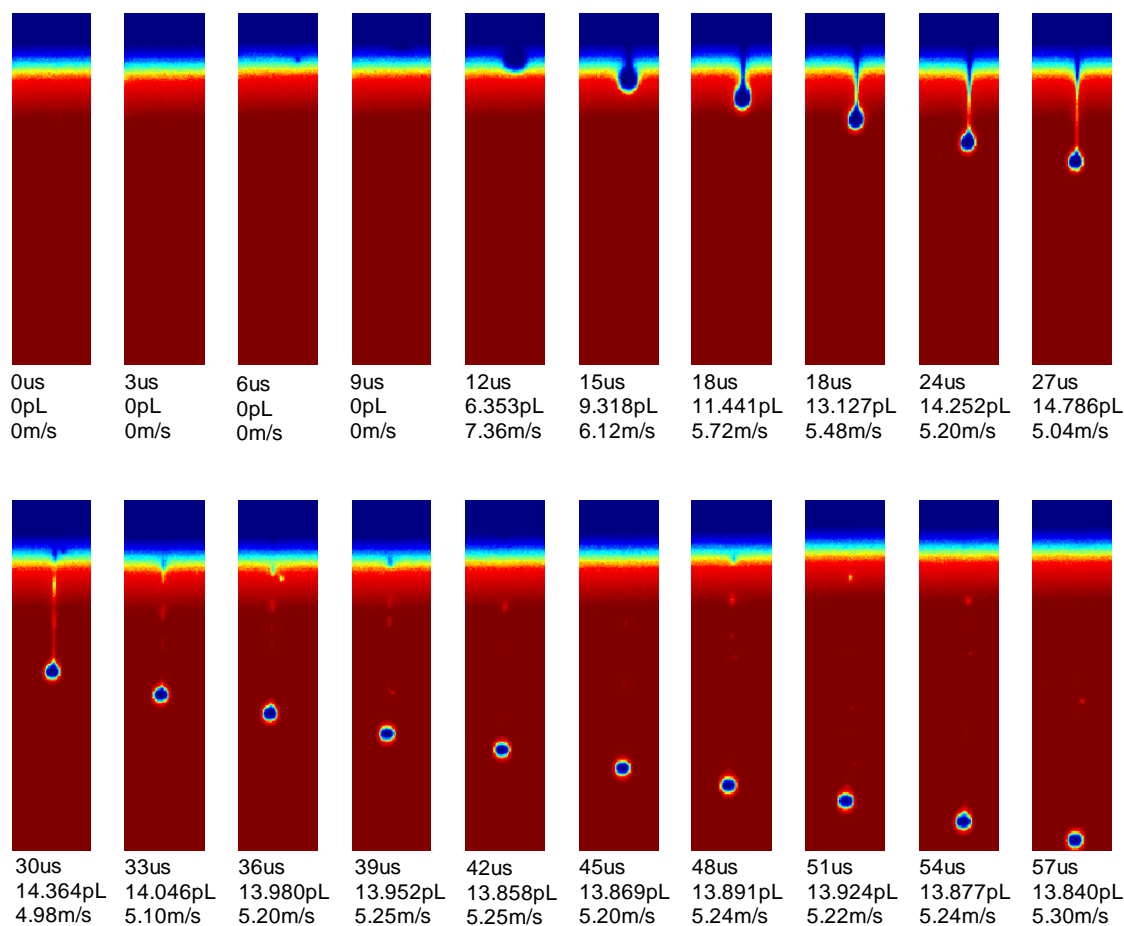


Fig 3. A sequence of pictures of a droplet falling from the nozzle.

CONCLUSION

The lumped element modeling based on the linear model of a piezoelectric ceramic has been successfully used to simulate a piezoelectric droplet generator for 3D electronic printing. In this work, the droplet volume/velocity curves simulated can carry sufficient information to distinguish the nanosilver droplet formation process. The LEM model is also successful in predicting the jetting characteristics under the desired conditions.

REFERENCES

1. J. Hwang, A. Wan, A. Kahn, *Materials Science and Engineering R: Reports*, **64**(1-2), 1 (2009).
2. M. Singh, H.M. Haverinen, P. Dhagat, G.E. Jabbour, *Advanced Materials*, **22**(6), 673 (2010).
3. J.-C. Liou, F.-G. Tseng, *Microelectronic Engineering*, **88**(6), 888 (2011).
4. J. Liu, S.-H. Tan, Y. F. Yap, M. Y. Ng, N.-T. Nguyen, *Microfluidics and Nanofluidics*, **11**(2), 177 (2011).
5. F. Sarrazin, K. Loubère, L. Prat, C. Gourdon, T. Bonometti, J. Magnaudet, *AIChE Journal*, **52**(12), 4061 (2006).
6. X.Q. Xing, D.L. Butler, S.H. Ng, Z. Wang, S. Danyluk, C. Yang, *Journal of Colloid and Interface Science*, **311**(2), 609 (2007).
7. S. Prasad, S. Horowitz, Q. Gallas, B. Sankar, L. Cattafesta, M. Sheplak, in: Proceedings of the 43rd AIAA/ASME/ASCE/AHS Structures, (Structural Dynamics, and Materials Conference, , AIAA, Denver, Colo, USA, April 2002) AIAA Paper 2002-1365.
8. D.T. Blackstock, *Fundamentals of Physical Acoustics*, John Wiley & Sons, New York, NY, USA, 2000.
9. F.M. White, *Fluid Mechanics*, McGraw-Hill, New York, NY, USA, 1979.
10. H. Wijshoff, *Physics Reports*, **491**(4-5), 77 (2010).

МЕТОД ЗА НАСТРОЙКА НА РАЗМЕРА НА КАПКИТЕ ПО LEM-МЕТОДА ЗА 3D ЕЛЕКТРОННО ПЕЧАТАНЕ

М. Хе*, У Жу, Ф. Лиу, Х. Чен*

*Училище по компютърни науки и софтуерно инженерство, Тианджински политехнически университет,
Тианджин 300387, Китай*

Постъпила на 20 февруари, 2016 г.; коригирана на 20 август, 2016 г.

(Резюме)

Главното предизвикателство при 3D-електронното печатане са разделителната способност и прецизността. В настоящата работа е приложен метода LEM (lumped element modeling) за да се симулират характеристиките на капките и струите от мастило. Този метод дава бързо и с голяма точност скоростта на капките и обема им. Експериментите показват, че LEM-методът има проста структура с достатъчна точност на симулирането и предвижданията.

Research on the synthesis and characterization of abiraterone acetate

Y. Liu^{1*}, L. Liu¹; G. Shi¹; J Shi³, W. L. Lai²

¹Xuzhou College of Industrial Technology, Jiangsu, Xuzhou, 221140, China

²Graduate Institute of Environmental Management Tajen University, Taiwan

³The college of natural resource and environment of South China Agricultural University Guangdong Guangzhou 51064, China

Received January 15, 2014; Revised August 27, 2016

Abiraterone acetate is an orally administered, selective inhibitor of the 17 α -hydroxylase and C17,20-lyase enzymatic activities of cytochrome P450 (CYP) 17. The convenient protocol for the synthesis of Abiraterone acetate from dehydroiso and rosterone 3-acetate via a four-step reaction includes converting Ketone carbonyl into hydrazine, an Iodine reaction, cross-coupling and zcetylation. A total conversion of 51-55% for Abiraterone acetate, was accomplished. The structure of Abiraterone acetate was characterized by ¹H NMR, ¹³C NMR, IR, MS, HPLC and elemental analysis. The reaction conditions of the route was studied to reduce the cost and avoid the formation of by-products and make the route suitable for large-scale production.

Keywords: Abiraterone acetate; synthesis ; Structure.

INTRODUCTION

Abiraterone acetate (Zytiga, chemical structure shown Fig.1) is an orally administered, selective inhibitor of the 17 α -hydroxylase and C17,20-lyase enzymatic activities of cytochrome P450 (CYP) 17. CYP17 is required for androgen biosynthesis, with androgen receptor signaling crucial in the progression from primary to metastatic prostate cancer [1-4]. Previously called hormone-resistant or (hormone-refractory prostate cancer) – i.e., prostate cancer not responding to androgen deprivation or treatment with androgen receptor antagonists. In addition, on the Pharmaceuticals market the drug under the trade name Abiratas, Cadila Pharmaceuticals markets the drug as Abretone and Glenmark Pharmaceuticals as Abirapro.

Abiraterone acetate (brand names Zytiga, Abiratas, Abretone, Abirapro) is a steroidal antiandrogen, specifically an androgen synthesis inhibitor, used in combination with prednisone in metastatic castration-resistant prostate cancer (It is a product of the active agent abiraterone and is marketed by Janssen Biotech under the trade name Zytiga.

Abiraterone acetate is a CYP3A4 substrate and hence should not be administered concurrently with strong CYP3A4 inhibitors such as (ketoconazole, itraconazole, clarithromycin, atazanavir,

nefazodone, saquinavir, telithromycin, ritonavir, indinavir, nelfinavir, voriconazole) or inducers such as phenytoin, carbamazepine, rifampin, rifabutin, rifapentine, phenobarbital. It also inhibits CYP1A2, CYP2C9, and CYP3A4 and likewise should not be taken concurrently with substrates of any of these enzymes that have a narrow therapeutic index.

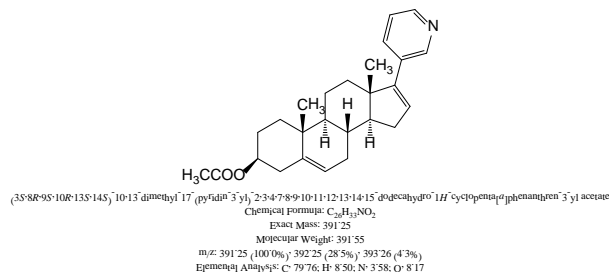


Fig. 1. Chemical structure of Abiraterone acetate.

This article is aimed at the development in the USA of Abiraterone acetate, including its pharmacological properties, although the synthesis of Abiraterone acetate has been discussed together with the problems from a different viewpoint such as the reaction rate, conversion, uncertain properties and derivate product harmful for humans or the environment.

In this research [5-9], dehydroiso and rosterone 3-acetate was used as the starting material with a specific synthetic pathway shown in Scheme 1. The final products were characterized by 1H Nuclear Magnetic Resonance (1H NMR), 13C Nuclear Magnetic Resonance (13C NMR), Infrared Spectroscopy (IR), Mass Spectroscopy (MS) and elemental analysis.

* To whom all correspondence should be sent:
E-mail: liuyu0138@163.com

INSTRUMENTS AND EXPERIMENTS

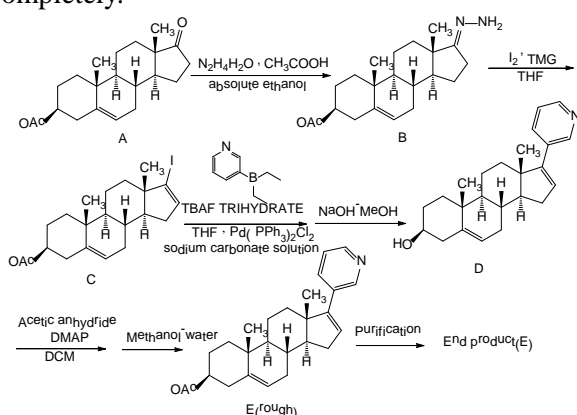
Instruments

A Nicolet 170 SX type infrared spectrometer (KBr tablet); a BRUKER AV - 500 nuclear magnetic resonance instrument (DMSO-d₆+TFA-d); an AGILENT 1200 LC-MSD mass spectrometer and Elementar Vario EL III type element analyzer were employed. Analytical reagents were used in the analysis and for synthesis.

Preparation of different compounds

Preparation of compound B

Anhydrous ethanol (50000 g, 1085.3 mol), compound A (10000 g, 30.26 mol), hydrazine hydrate (2188.75 g, 40.3 mol) and glacial acetic acid (350g, 5.80 mol) were added in the reactor. The reaction temperature was fixed at 20~30°C, the mixture was stirred to a complete dissolution for 60 min (TLC monitoring, VEA: VHex = 2:5, ARf about 0.9, BRf about 0.15, phosphomolybdic acid-a color development reagent), with detection every 15 minutes until the raw material reacted completely.



Scheme 1. Synthesis pathway of Abiraterone acetate.

The mixture was cooled to 0~5°C, the washing process added the DCM (dichloromethane, 65000g) with precooling of the purified water (80000g) at 2~8°C, the organic phase was dewatered by washing stratification in anhydrous sodium sulfate for about 30 min, the dewatering process at the temperature 0~10°C and gas protection by N₂. Washing the filter cake of filtration with a small amount of DCM, the merged filtrate evaporated to dryness under a reduced pressure and removed the DCM (the heated water evaporated at less than 30°C, because B is an unstable intermediate) since the mixture was no obvious liquid in the reactor. After stirring, THF (tetrahydrofuran, 20000g) was immediately added and dissolved for 30 min (and a vacuum drained the residual gas of DCM) a faint yellow solution resulted with the mixture

preserved at 0~10°C and a gas protection by N₂ at the next step given a melting point of 204-206°C.

Preparation of compound C

THF (40000 g, 554.7 mol) and iodine (15000 g, 59.1 mol) were added in the reactor by gas protection of N₂, cooled to -5~5°C, then slowly adding TMG (1,1,3,3-Tetramethylguanidine, 13500 g, 117.2 mol), attention must be drawn to the fact that this process was intensely exothermic and therefore the temperature was maintained under 10 °C. The final mixture was stirred for 10 min and then Compound B and the THF solution were added to the reactor, the temperature was maintained at 5 ~ 5°C and added drop by drop over a period of 6h. The final drops completed the reaction for 20 minutes (the reaction was monitored by TLC ,VEA: VHex = 2:5, A Rf is about 0.15, with phosphomolybdic acid as a color development reagent). Washing filter cake by filtration with a small amount of THF, the merged filtrate evaporated to dryness under reduced pressure and removed the THF at 45~ 55 °C to about a 25-30 L, residue mixture after a reflux reaction for 9h. Following HPLC detection, the diiodide compound concentration was established at less than 0.1 %, evaporated to a dry state under reduced pressure with the THF removed at 45~ 55 °C. Until completely dissolved DCM (36 kg) was added and stirred as a mixture.

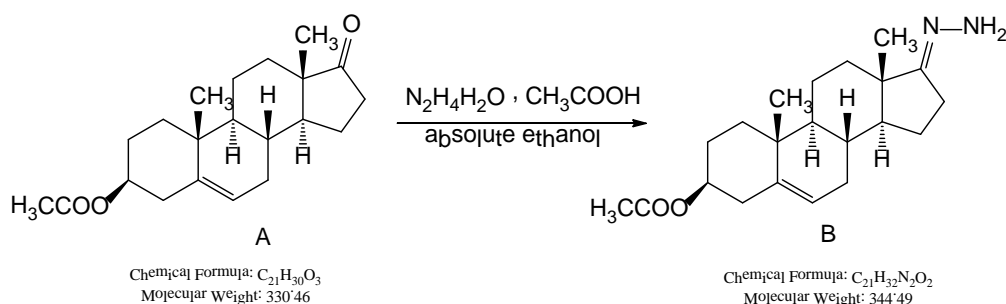
The reaction solution was poured into a precooled 0.6 M of sulfuric acid aqueous solution (50000g, 2~8°C).

The organic layer was washed with purified water twice (40000g * 2), then dried over sodium sulfate. The solvent was concentrated under reduced pressure to 10 L. Anhydrous ethanol (40000g) was added to the mixture, concentrated under reduced pressure at 10~25 °C for 4 h, with precipitation into a white solid, mixing and crystallization for 1h at a controlled temperature of 0~5 °C. Yielding a crude compound C, with 10.5 kg of a light yellow to white powder after washing and stratification, the organic phase obtained after washing the anhydrous sodium sulfate and drying. The filter cake with a small amount of methylene chloride leaching and merging the filtrate, reduced the pressure concentration to about 50 l, adding the anhydrous ethanol (40000g) and concentrated for 4h, with a feed liquid, at the same time continued to concentrate the methylene chloride. Rejection of the filter cake after precooling the ethanol - water (V/V=5:1, 0~5°C) beating time, with two raw intermediates, the light yellow to white powder being about 63 kg. The power was added to the

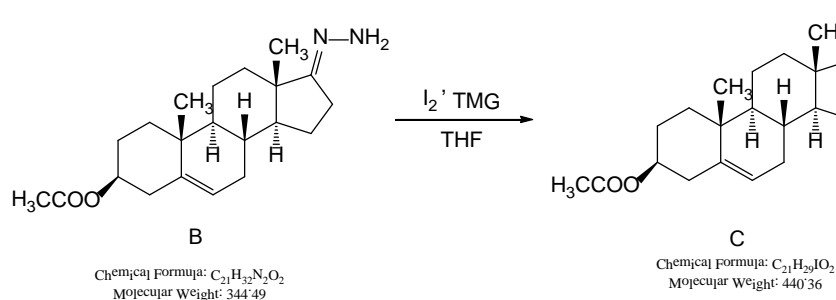
anhydrous ethanol(25000g), heated at 45~50°C, stirred for 60 min and cooled at 0~10°C, crystallizing after stirring for 1h, the solid obtained after filtration was air dried at 45~50°C for 6h to obtain a white powder compound C (10000g), with dry weight loss of less than 0.5%. Step 1 and step 2 yield a total of 71 % with a range: 70% ~ 80%, at a melting point of 172-177°C.

Preparation of compound D

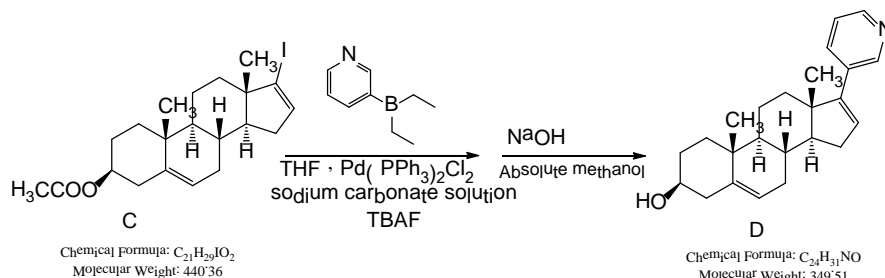
Diethyl(3 - pyridine borane)(3500 g, 3.7 mol), Pd(PPh₃)₂Cl₂(175.4 g, 0.25 mol), TBAF (Tetrabutylammonium fluoride trihydrate, 7870, 24.94 mol) and C (10000 g, 22.71 mol) were stirred with dry THF (35200 g, 488.12 mol) in the reactor at RT(room temperature) for 20min. Then (16.7 %, 31000 g) of sodium carbonate solution were added and heated for a reflux reaction at 65 ~70°C in a water bath, on the surface the reaction mixture become red brown for 75min.



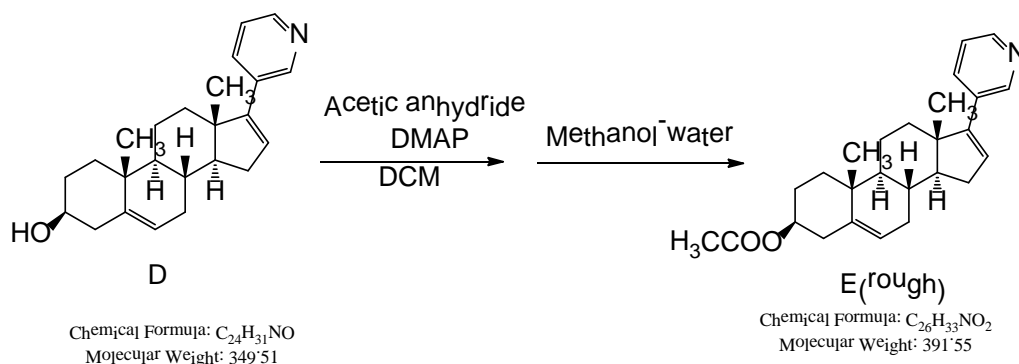
Scheme 2. Synthesis pathway of Compound B



Scheme 3. Synthesis pathway of Compound C



Scheme 4. Synthesis pathway of Compound D.



Scheme 5. Synthesis pathway of Compound E.

The reaction was monitored by TLC for a period of 15 minutes, (VEA: VPE = 1:8, Rf of Borane is about 0.85, Rf of C is about 0.8, phosphomolybdic acid as a color development reagent). After the complete disappearance of compound C the reaction mixture was cooled to 25~35°C adding active carbon, then after stirring for about 30 minutes the mixture was collected by filtration. The organic phase of the mixture was added, 8% of sodium hydroxide methanol solution (22000g) at 25~35°C, the reaction was monitored by TLC over a period of 15 minutes (VEA: VHex = 1:2 and Rf of D is about 0.2, UV detected), after the complete disappearance of compound C, the reaction halts.

The reaction mixture crystallized after being stirred for 1h at 0~5°C. Methanol (14000 g) was added to the filtration cake and stirred for 30 minutes, then purified water (17000g) was added and stirred for 30 minutes. The cake of filtration was washed by water-methanol (v/v=1,31000g). The cake of filtration was washed by precooled THF(0~5°C), the solid obtained by filtration was force air dried at 47~52°C for 6h to gain the white color of the crude solid compound D, the dry weight loss was less than 2%. Crude compound D was added to the THF (20000g), the mixture was stirred and refluxed for 90 minutes cooled and stirred at 0~5°C, after crystallization for 1h the white solid compound D (5400g) was obtained, with a dry weight loss of less than 2% and a melting point of 225-230°C.

Preparation of compound E

DCM(45000 g, 529.8 mol), compound D (5400 g, 15.45 mol), DMAP (4-Dimethylaminopyridine, 200 g, 1.63 mol) and Acetic Anhydride (2500 g, 24.29 mol) were stirred for 16h at 15~35°C, the reaction was monitored by HPLC (compound D less than 0.2%). Activated carbon (120g) was added and stirred for 30 minutes, the liquid of filtration was then washed with saturated sodium bicarbonate water twice. The organic phase was dewatered by stratification of the anhydrous sodium sulfate after

about 30 minutes and the liquid of filtration was then evaporated under a reduced pressure at 20~30°C for a reduced volume of 50L. Methanol (18000 g) was added to the mixture at less than 15°C, evaporated under reduced pressure for 4h, crystallizing into a white solid. At the time of adding the purified water (23000 g) the mixture was stirred crystallizing after 30 minutes. The cake of filtration was dried under reduced pressure for 6h, in order to obtain the white solid rough compound E (5100g), with a dry weight loss of less than 2%.

The solid compound E (rough, 5000g) and active carbon (90g) were added together with acetonitrile (25000g), heated up at 75~80°C, stirred for 60 min, then cooled below 35°C. Then cooled continuously between 0 and 5°C, stirring and crystallizing for 1h, obtaining a solid by filtration and drying under reduced pressure at 45~50°C for 8h to obtain the white solid compound E(4500g), mp.143-147°C.

The HPLC detection condition for the column was C18 (4.5* 250mm, 5μm), the mobile phase consisted of 0.05mol/L ammonium acetate (pH=2.0) the acetonitrile was 5:95, the detection wavelength was 254 nm, flow rate was 1.5mL/min, the concentration of Abiraterone acetate was less than 99.4%, HPLC spectrogram is shown in Fig.2.

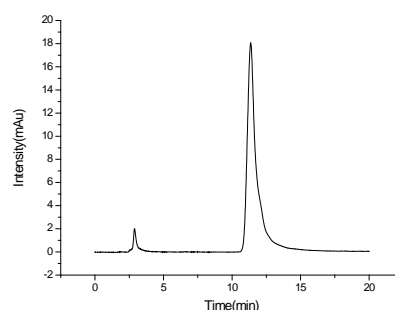


Fig. 2. HPLC spectrogram of Abiraterone acetate.

Compound E (Abiraterone acetate) 1H NMR (400 MHz, $CDCl_3$) δ (ppm): 8.61 (d, $J = 1.5$ Hz, 1H), 8.49 – 8.41 (m, 1H), 7.66 – 7.61 (m, 1H), 7.21

(dd, $J = 7.9, 4.8$ Hz, 1H), 6.00 – 5.97 (m, 1H), 5.41 (d, $J = 5.0$ Hz, 1H), 4.66 – 4.56 (m, 1H), 2.33 (dd, $J = 9.3, 3.6$ Hz, 2H), 2.03 (s, 6H), 1.86 (dd, $J = 15.4, 5.2$ Hz, 2H), 1.80 – 1.70 (m, 2H), 1.63 – 1.53 (m, 3H), 1.08 (s, 3H), 1.04 (s, 3H).

ESI-MS m/z : 392.22[M+H]⁺.

RESULTS AND DISCUSSIONS

In this research, dehydroiso and rosterone 3-acetate as the starting material, reacted with hydrazine hydrate, iodine and Diethyl (3 - pyridine borane). Our attempt to synthesize compound B, was shown in Scheme 2. The Molar ratio of dehydroiso and rosterone-3-acetate and hydrazine hydrate is from 1 to 2, the best molar ratio was 1.42-1.50. The solvent of choice was absolute ethanol its weight ratio was 5, at the same time CH₃COOH was added, at a molar ratio of 0.18. The process for compound C as shown in Scheme 3, molar ratio compound B, iodine and TMG was 1.95 and 3.80, yielding about 75%. The route to Abiraterone acetate commercially available, was obtained for a 52% total yield.

CONCLUSION

The convenient protocol for the synthesis of Abiraterone acetate from dehydroiso and rosterone 3-acetate via a four-step reaction including Ketone carbonyl into hydrazine, an Iodine reaction, cross-coupling and zcetylation has been presented. High purity Abiraterone acetate, can be obtained after purification of the crude product. The total

conversion of Abiraterone acetate was 52%. The reaction conditions of the route were studied in order to reduce the cost and avoid the formation of by-products and make the route suitable for large-scale production.

Acknowledgments: The research and the team were supported by funding of Xuzhou Science and technology innovation, No. KC15H0071.

REFERENCES

- 1.M. Hoy. Sheridan, *Drugs*, **73**(11), 2077 (2013).
- 2.G. Attard, A.H. Reid, T.A. Yap, F. Raynaud, M. Dowsett, S. Settatree, M. Barrett, C. Parker, V. Martins, E. Folkard, J. Clark, C.S. Cooper, S.B. Kaye, D. Dearnaley, G. Lee, J.S. de Bono, *J Clin Oncol* , **26**, 4563(2008).
- 3.G. Attard, A.S. Belldegrun, J.S. de Bono, *BJU Int.*, **96**, 1241 (2005).
- 4.E. Efstathiou, C.J. Logothetis, *Clin. Cancer Res.*, **16**, 1100 (2010).
- 5.G.A. Potter, I.R. Hardcastle, Synthesis of 17-(3-pyridyl)-steroids:GB,2282377A[P], 1995-05-04.
- 6.M.S. Nadia, E. Monika, M.R. Stanley, et al., *J Chem Soc Perkin Trans 1*, **16**, 1847 (2002).
- 7.S. Haidar, R.W. Hartmann, *Arch Pharm*, **335**(11-12), 526 (2002).
- 8.PS. Bury, Process for the preparation of 17- α -vinyl-triflates as intermediates [P], WO2006021777A1, 2005.
- 9.G.A. Potter, I.R. Hardcastle, M.A. Jarman *Org Prep Proced Int*, **29**(1), 123 (1997).

ИЗСЛЕДВАНИЯ И ОХАРАКТЕРИЗИРАНЕ НА АБИРАТЕРОН-АЦЕТАТ

И. Лю^{1*}, Л. Лю¹, Г. Ши¹, Дж. Ши, У. Л. Лаи²

¹Колеж по промишлени технологии, Джиангсу, Ксуджоу 221140, Китай

²Висш институт по управление на околната среда, Университет Тайен, Тайван

³Колеж по природни ресурси и околна среда, Южнокитайски селскостопански университет, Гуандон, Гуанжу 51064, Китай

Постъпила на 15 януари, 2016 г; коригирана на 27август, 2016 г.

(Резюме)

Абиратерон-ацетатът е селективен инхибитор на ензимната активност на 17 α -хидролазата и С17,20-лиазата в цитохром Р450 (СYP) за орална употреба. Подходящият протокол за четири-етапната синтеза на абиратерон-ацетата от дехидро-изо- и ростерон-3-ацетат включва превръщането на кетонова карбонилна група в хидразин, реакция с йод, купелуване и ацетилиране. Постигнато е превръщане от 51-55% по отношение на абиратерон-ацетата. Структурата на абиратерон-ацетата е охарактеризирана чрез ¹H ЯМР, ¹³C ЯМР, ИЧ-, MS-спектроскопия, високо-ефективна течна хроматография и елементарен анализ. Условиата на реакцията по описания маршрут са изследвани с цел да се намалят разходите и да се избегне образуването на странични продукти за постигането на по-едромашабно производство.

Research on the physics-of-the failure model for corrosion damage accumulation under a multi-level stress profile based on the acceleration factor

L. Wang^{1*}, B. Wan²

¹*School of Computer and Information Engineering, Beijing Technology and Business University, Beijing, 100048, PR China*

²*School of Reliability and Systems Engineering, Beihang University, Beijing, 100191, PR China*

Received February 4, 2016; Revised October 19, 2016

Attention is paid in this paper to the problem that the existing physics-of-failure model cannot input and calculate a complex multi-level stress environmental profile when conducting simulation calculations of microelectronic devices' studing reliability. A physical model of corrosion failure is analyzed as an example. We carry out cumulative calculation and improvement using the theory of the accelerated factor, the theory of fatigue damage accumulation and the general function of physics-of-failure model for corrosion damage accumulation under a multi-level stress profile. This model can achieve simulation and prediction of cycle time before failure under a multi-level stress profile. At the end of this paper, an instance of a multi-level stress profile's calculation is provided.

Keywords: Corrosion, Multi-level stress, PoF model

INTRODUCTION

At present, using the technical means of reliability simulation to establish the virtual prototype and calculate the user reliability of microelectronic devices through the simulation of the physics-of-failure model, is one of the most important branches and the future development trend in the field researching the methods of electronic products' reliability design. However, most of the environmental stress parameters of the common physics-of-failure model are becoming uniform. Only a single stress value can be input during calculation. Actually, complex multi-level stress environmental profiles always exist. In this case, the physics-of-failure model cannot be input and calculated. Because of the limitation brought about by this defect, a technical problem appears when simulating and calculating microelectronic devices' for their reliability.

This paper uses a physical model of corrosion failure as an example, predicts a model of multi-level stress damage accumulation and improves the theory, according to the basic theories of accelerated test and factor and theory of fatigue damage accumulation. Meanwhile, the general functional physics-of-failure model for corrosion damage accumulation under a multi-level stress profile and its corresponding mathematical expressions are set up. The model can input complex multi-level stress profiles and calculate the cycle index of damage accumulation as well as time to failure under multi-temperature stress.

PHYSICS-OF-FAILURE MODEL FOR CORROSION

Corrosion failure mechanism

Moisture and impurities can cause the corrosion of the aluminum, aluminum copper alloy or silico aluminum interconnect of the microelectronics components. Due to the low cost and ease of mass production, microelectronic components use a lot of resin for encapsulation, which is moisture permeable and absorptive. Impurities such as a variety of positive and negative ions like Na^+ ions are introduced during the resin material manufacturing process. The ions along with the penetration and absorption in vapour continue to infiltrate into the surface of aluminum or the aluminum alloy interconnects and traverse through the surface passivation film of tiny defects into the metal interconnects inside and cause the interconnects to electrochemically react and then the metal interconnects open or the interconnect resistance increases. The process describes corrosion. In microelectronic components, corrosion of aluminum has two mechanisms: chemical corrosion and electrochemical corrosion [1]~[6].

Chemical corrosion

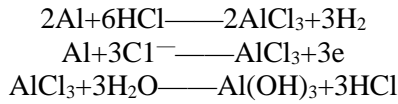
Corrosion of aluminum happens when the microelectronic components are stored in a high temperature and high humidity environment. When exposed to dry air, aluminum forms a layer of Al_2O_3 on the surface and the film will prevent aluminum from being oxidized and the chemical etched. But during the presence of moisture,

* To whom all correspondence should be sent:
E-mail: wangli@th.btbu.edu.cn

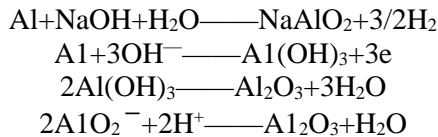
aluminum can form $\text{Al}(\text{OH})_3$ and $\text{Al}(\text{OH})_3$ is soluble in alkali as well as acid.

When the external substances reach the surface of the aluminum material, the chemical reactions are as listed below:

Reactions with an acid substance:



Reactions with an alkaline substance:



Usually, a passivation film on the surface of the chip protects the aluminum. However, in the pad of the wire bonding area, the aluminum metal is exposed on the surface and chemical corrosion frequently occurs in these parts. The corrosion situation of the chip pad is shown in Figure 1.

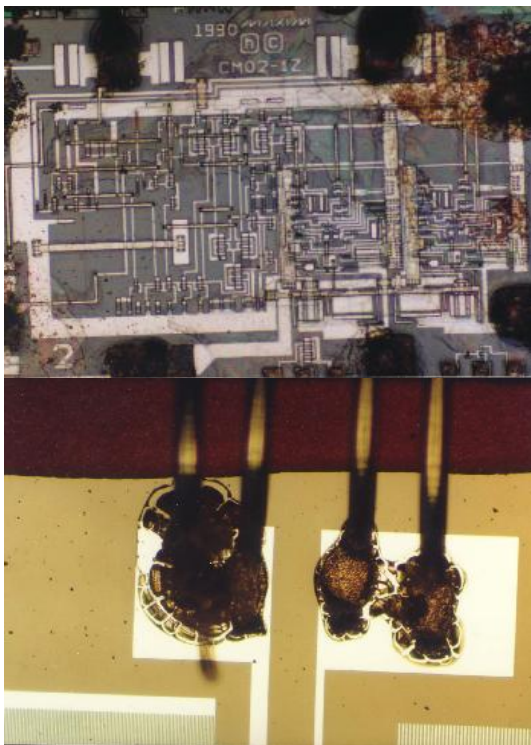
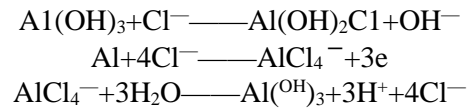


Fig. 1. PAD on the chip is corroded

Electrochemical corrosion

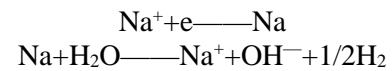
Electrochemical corrosion occurs when the microelectronic components are under exploitation under a high temperature and high humidity environment. According to the positive or negative potential of the aluminum electrode, the electrochemical corrosion is divided into anodic corrosion and cathodic corrosion [7]~[10]. When

the anodic corrosion happens, the aluminum electrode has a positive potential, which attracts negative ions such as Cl^- to start the chemical reactions as follows:



The reaction above reduces the Cl^- absorbed on the anode and the results of the reaction furthers the corrosion of the small amount of Cl^- .

For the cathodic corrosion, due to the negative potential of aluminum, positive ions such as Na^+ , K^+ are attracted to produce chemical reactions as follows:



After the reaction, the concentration of the OH^- increases, the aluminum hydroxide forms and the aluminum is corroded. The electrochemical corrosion of the cathode of the microelectronic components is shown in Figure 2 and Figure 3.

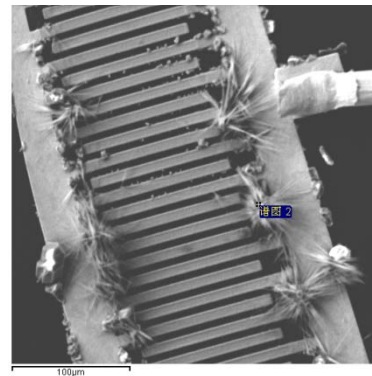


Fig. 2. The electrochemical corrosion of cathode.

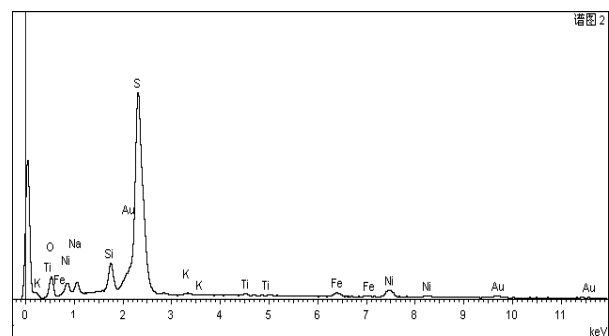
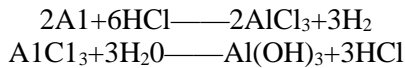


Fig. 3. The ESD of the electrochemical corrosion of the cathode.

The metal in a high humidity environment will obviously corrode. One solution is to use the ceramic sealing packaging which can prevent the corrosion, if the structure is not hermetically sealed, the residue remaining after the plasma or reactive ion sputter etching occurs (such as chlorine) along

with the moisture will corrode the aluminum and attain erosion, even in the absence of an applied electric field:



It is clear that after the formation of $\text{Al}(\text{OH})_3$, the chlorine is not bound, which leads to further corrosion of the exposed aluminum. In the VLSI structure, the metal wires are very close to each other and the electric field between them causes the problem to become complicated.

External lead corrosion

The lead material of a micro electronic device is usually kovar alloy, it is the iron-nickel-cobalt alloy, the linear expansion coefficient of which is similar to that of molybdenum. In addition to the introduction of stress in the mechanical processing and the production of stress corrosion, there is also an electrochemical corrosion reaction during the presence of Cl^- and other impurities, thus the corrosion rate speeds up.

When the water vapor condenses around the external leads and the potential difference exists (such as discrete devices inserted in the printed circuit board), the leakage current travels through the leads continuously, and materials (such as iron) with a high ionization tendency (standard electrode potential to negative) will produce electrochemical corrosion.

As for the silver plating on the external lead, the silver anode will have Ag^+ ions, migrating in the electric field and precipitating at the cathode. Then these will grow like resin on the anode, causing a deterioration in performance, or short circuits.

PoF model of Corrosion

The degradation process of the chemical or electrochemical properties of materials is known as corrosion, which is a time dependent wear-out failure mechanism. From a macroscopic point of view, corrosion will lead to brittle fracture caused by stress, or fatigue crack extension caused by the wear-out; from the microscopic point of view, corrosion can change the electrical properties of the material and its thermal properties. The corrosion rate correlates with the type and dimensions of the materials and the ionic contaminants[11].

The corrosion failure physical model is given by:

$$MTTF = A(\text{RH})^{-n} \exp\left(\frac{Ea}{kT}\right) \quad (1)$$

In the formulation,

A is the constant related to the corrosion area;
RH is the relative humidity;
N is the empirical constant, and generally have values of 3;

Ea is the activation energy, measured by the test;

K is the Pohl Seidman constant;

T is the ambient temperature and the units are degrees Kelvin.

ACCELERATED FACTOR MODEL

The rate of physical and chemical change varies with the temperature, leading to various lifetimes of the products. In the general case, there is a more rapid rate of physical and chemical change under high stress levels, which means a shorter life of the products. Hence, the process of change at a high stress level can be regarded as acceleration of that at a low stress level. The idea of an Accelerated Factor (AF) needs to be put forward, in order to describe the acceleration extent of high stress levels relative to low levels. The accelerated factor, from the accelerated test [12][13][14], is the ratio of the product's lifetime characteristic under different stress levels. It is a parameter used to present the extent of acceleration. While the value of AF is greater than 1, it means that the device's lifetime can be shortened by increasing the stress S. The definition formula is as follows [15][16]:

$$AF = \frac{TF_{op}}{TF_{stree}} \quad (2)$$

Here, TF_{op} is the expected failure time under stress S (normal working conditions) and TF_{stree} under stress S_0 (accelerating stress conditions).

The method of AF damage accumulation converts the multi-level stress of the actual profile to single stress before evaluation with the help of the AF concept. Afterwards, the cycle index of the actual profile will be solved through time to failure under the single failure mechanism and single stress level. Finally, a time to failure for practical working conditions is obtained.

ESTABLISHMENT OF A PHYSICS-OF-FAILURE MODEL FOR CORROSION DAMAGE ACCUMULATION BASED ON THE ACCELERATED FACTOR MODEL

Method for establishing a physics-of-failure model based on an accelerated factor model

The stress θ_0 is selected as a datum plane and the duration of every phase is converted to duration under a datum plane. The overview flow is shown in Figure 4.

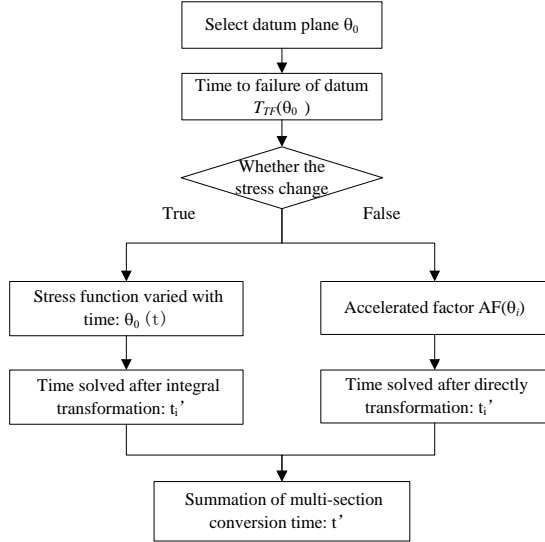


Fig.2. Multi-level stress damage accumulation based on the accelerated factor model.

The specific steps are described below:

1) Calculating the time to failure $T_{TF}(\theta_0)$ under a datum plane θ_0 based on the corresponding physics-of-failure model;

2) According to a model of the failure time, calculating the time to failure under actual working conditions and marking it as $T_{TF}(\theta(t))$;

3) Calculating the acceleration factor according to the formula $AF(\theta(t)) = \frac{T_{TF}(\theta_0)}{T_{TF}(\theta(t))}$;

4) The mission time for one mission cycle can be converted to that of the datum plane through FA.

$$\text{That is } t' = \int_0^T AF(\theta(t)) dt \quad (3)$$

5) Calculating the mission cycle index $N = \frac{T_{TF}(\theta_0)}{t'}$, in accordance with the formula

$$N = \frac{T_{TF}(\theta_0)}{\int_0^T \frac{T_{TF}(\theta_0)}{T_{TF}(\theta(t))} dt} = \frac{1}{\int_0^T \frac{1}{T_{TF}(\theta(t))} dt} \quad (4)$$

Method of accelerating the damage accumulation at a constant stress stage

As shown in Figure 5:

The formula is calculated as:

$$AF(\theta_i) = \frac{T_{TF}(\theta_i)}{T_{TF}(\theta_0)}, \quad (5)$$

$$t_i' = AF(\theta_i) \times (t_{i+1} - t_i), \quad (6)$$

Here, t_i' is the duration that the stress θ_i translated into the datum plane θ_0 within the time

interval $[t_i, t_{i+1}]$; $T_{TF}(\theta_i)$ shows the expected failure time under stress θ_i (normal working conditions) and $T_{TF}(\theta_0)$ under θ_0 (accelerating stress conditions); $AF(\theta_i)$ is the accelerated factor of the stress θ_i and θ_0 .

Method of accelerating damage accumulation at the slowly changing stress stage

The method process is shown in Figure 6.

The formula is calculated as:

$$AF(\theta(t)) = \frac{T_{TF}(\theta(t))}{T_{TF}(\theta_0)} \quad (7)$$

$$t_j' = \int_{t_j}^{t_{j+1}} AF(\theta(t)) dt \quad (8)$$

Here, $\theta(t)$ is the function of stress θ and time t , which can be confirmed according to the known stress profile; $T_{TF}(\theta(t))$ is the expected failure time under slowly changing stress $\theta(t)$; $T_{TF}(\theta_0)$ is on behalf of the failure time under stress θ_0 (specific accelerating stress conditions); and t_j' is the duration that the slowly changing stress $\theta(t)$ translates into a given stress θ_0 within the time interval $[t_i, t_{i+1}]$.

The establishment of a corrosion damage accumulation model based on the accelerated factor

On the basis of a multi-level-stress failure model using the method of AF, the physics-of-failure model and the formula of corrosion PoF model is derived. The specific forms are as follows:

$$N = \frac{T_{TF}(\theta_0)}{\int_0^T \frac{T_{TF}(\theta_0)}{T_{TF}(\theta(t))} dt} = \frac{1}{\int_0^T \frac{1}{T_{TF}(\theta(t))} dt} \quad (9)$$

The final multi-level-stress failure model based on the method of AF can be described as:

$$N = \frac{1}{\int_0^T \frac{1}{A(RH)^{-n} \exp\left(\frac{Ea}{k\theta_H}\right)} dt} \quad (10)$$

EXAMPLE

Figure 7 is a typical profile and the parameters of temperature and time are shown in Table 1.

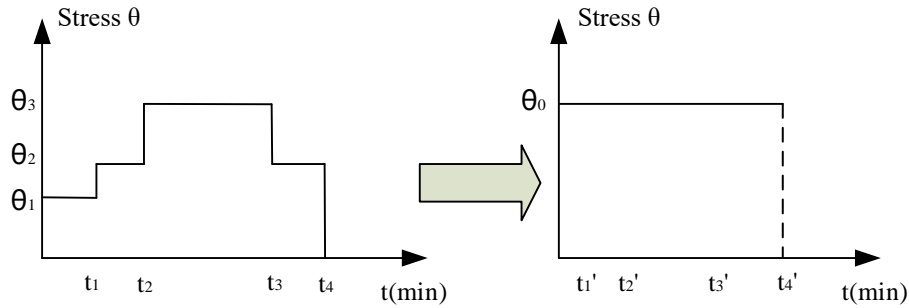


Fig. 3. The condition for the parameter value of stress to remain unchanged.

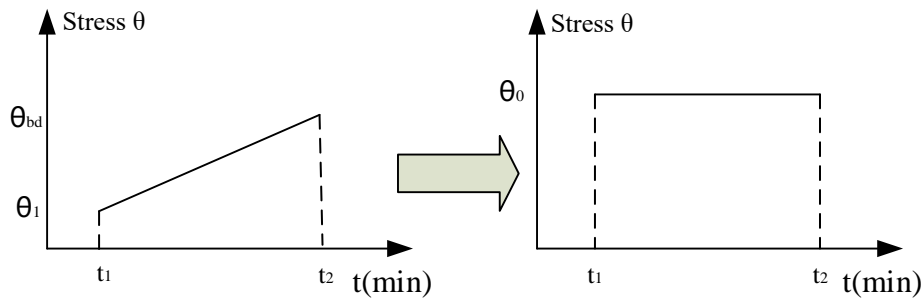


Fig. 4. The condition that the parameter value of stress is slowly changing

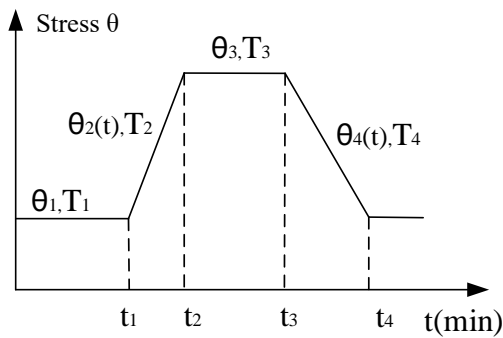


Fig. 7. A typical sectional multi-level stress profile.

Table 1. The parameters of temperature stress

No.	T	t
1	25°C	30min
2	(2t-35) °C	25min
3	75°C	30min
4	(-2t+245) °C	25min

Table 2. Technological parameters

Parameter	value
A	1.3
RH	80%
n	3
k	1.381×10 ⁻²³ J/K
Ea	0.7eV

A certain type of microelectronic device is taken as an example. In accordance with the corrosion

PoF model and formula (1), the device's internal process parameter values can be observed in Table 2.

In accordance with formula (11) and under the profile stipulated in Figure 7 and Table 1, the total cyclic index of damage accumulation of this certain type of microelectronic device in which corrosion failure occurred is N=5043. While the time to failure is TTF=20153h.

CONCLUSIONS

In this paper, the accelerated factor model is applied and the damage accumulation under a multi-level stress profile is calculated based on the physics-of-failure model of corrosion. Meanwhile, the method of accelerating damage accumulation at the constant and slowly changing stress stage is respectively provided. The generalized corrosion damage accumulation model based on the AF is also established. Finally, for the case of a certain type of microelectronic device, the applicability of this model is demonstrated and the total cyclic index before failure and the time to failure of the physics-of-failure model for corrosion damage accumulation under the multi-level stress profile are solved. This paper provides a new theoretical method and solution for more scientific and rational applications of the corrosion failure model in the evaluation of microelectronic devices' reliability and emulation ability.

Acknowledgements: This work was financially supported by Innovation ability promotion project of the Beijing municipal colleges and universities (PXM2014_014213_000033), Major Project of the Beijing Municipal Education Commission of science and technology development plans (KZ201510011011) and the General Project of the Beijing Municipal Education Commission of Science and Technology Development Plans (SQKM201610011009). All support is gratefully acknowledged.

REFERENCES

1. J. Barranco, F. Barrerasb, A. Lozanob, M. Mazaa. *Journal of Power Sources*, **196**, 4283 (2011).
2. L. Hua, C. Yang, *Microelectronics Reliability*, **51**, 2274 (2011).
3. D. Pavlov, *Journal of Power Sources*, **48**, 179 (1994).
4. E. Brambilla, P. Brambilla, C. Canali, F. Fantini, M. Vanzi, *Microelectronics Reliability*, **23**, 577 (1983).
5. R.M. Lum, L.G. Feinstein, *Microelectronics Reliability*, **21**, 15 (1981).
6. R.C. Olberg, J.L. Bozarth, *Microelectronics Reliability*, **15**, 601 (1976).
7. G.J. Andrews, *Microelectronics Reliability*, **30**, 1200 (1990).
8. Y. Kobayashi, T. Wada, *Microelectronics Reliability*, **29**, 1094 (1989).
9. L.C. Tang, *IEEE Transactions on Reliability*, **44**(4), 562 (1995).
10. M.A. Ebrahim, J.J. Higgins, *Applied Mathematics and Computation*, **174**(1), 365 (2006).
11. S.S. Nanson, *Fracture*, **2**, 51 (1966).
12. M.A. Miner, *Journal of the Applied Mechanics*, **67**(12), 159 (1945).
13. L. Wang, X. Wang, J. Xu, H. Zhang, J. Yao, X. Jin, C. Liu, Y. Shi, *Nonlinear Dynamics*, **84**(1), 371 (2016).
14. L. Wang, Z. Liu, C. Wu, *CIESC Journal*, **64**(12), 4649 (2013).
15. L. Wang, C. Gao, X. Wang, Z. Liu. *CIESC Journal*, **68**(3), 1065 (2017).
16. L. Wang, X. Wang, J. Xu, Y. Shi, J. Yu. *Engineering review*, **34**(2), 131 (2014).

ИЗСЛЕДВАНЕ НА НАТРУПВАНЕТО НА КОРОЗИОННИ ДЕФЕКТИ ПРИ МНОГО-СТЕПЕННО НАПРЕЖЕНИЕ С УСКОРЕНИЕ С МОДЕЛА „PHYSICS-OF-FAILURE

Ли Уан^{1*}, Бо Уан²

¹Училище по компютърно и информационно инженерство, Технологичен и бизнес- университет в Пекин, Пекин 100048, Китайска НР

²Училище по системно инженерство, Университет Бейхан, Пекин, Китайска НР

Постъпила на 4 февруари 2016 г.; коригирана на 19 октомври 2016 г.

(Резюме)

В настоящата работа се обръща внимание на факта, че съществуващия „physics-of-failure“ – модел не дава възможност да се изчислят сложни много-степенни напрежения при симулирането на надеждността на микроелектронни уреди. Като пример е анализиран физичен модел за корозионни дефекти. Извършени са кумулативни пресмятания и подобрения с помощта на теорията на ускоряващия фактор и теорията на натрупване на умора в материалите, заедно с модела „physics-of-failure“. Този модел може да постигне симулиране и предсказване на цикъла от време преди разрушаване под многостепенно напрежение. В края на работата е даден илюстративен пример.

Study on the influence of different clearance on the crack of PBX explosive

G. Zhenzhi^{1,2*}, H. Bin¹, G. Zhengming¹, N. Libo¹, C. Lujie¹

¹*Xi'an High Tech Research Institute*

²*NO.96401 Force*

Received March 24, 2016; Revised November 22, 2016

Explosives are widely used in military affairs. Aiming at the characteristics of the explosive component, the paper analyzes the stress intensity factor of the surface crack of the spherical shell and ellipsoidal shell made of explosive material. The results show that the stress intensity factor of the inner surface of the component is larger than that of the outer surface and the stress intensity factor of the surface crack of the explosive component with a cushion layer is larger than that without a cushion. These conclusions provide theoretical guidance for the actual assembly of the nuclear components.

Keywords: PBX Explosive, Crack, Stress Intensity Factor, J-Integral, Clearance Contact.

INTRODUCTION

The JOB-9003 plastic bonded explosive (PBX) is a kind of polymer binder as a continuous phase, an explosive mixed with high-energy particles and two-phase composite materials. It has good detonation and safety characteristics together with excellent mechanical properties. It plays an important role in the development of national defense and modern weapons. The explosive component is composed of a main explosive and a binder.

The main ingredient is Cyclotetramethylene tetranitramine also called octogen (HMX), this is a powerful and relatively insensitive nitroamine high explosive. It is a white crystal and the chemical formula is C₄H₈N₈O₈. Its chemical structure is shown in Fig.1

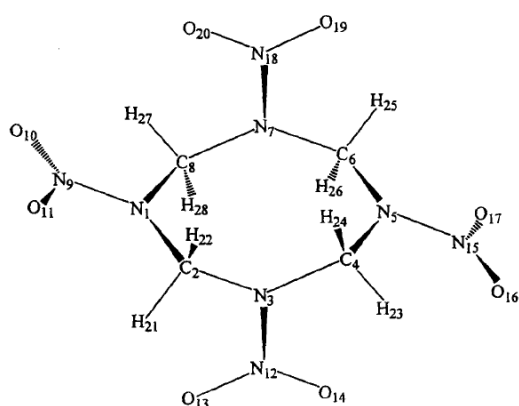


Fig.1. Schematic diagram of the atomic number and optimized geometry of HMX.

The binder is used to ensure the explosives have

plastic properties, appropriate sensitivity and should possess a strong adhesive force, good plasticity and coating performance, while kept at a low glass transition temperature, have good physical and chemical properties and a lower cost. At present, the majority of explosive materials use a polymer binder and its molecular structure is shown in Fig.2.

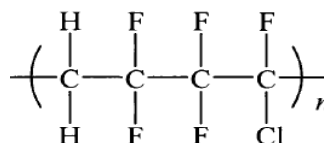


Fig. 2. Molecular structure of the binder

There are many factors affecting the surface cracking of the ellipsoidal explosive. In the process of being formed, processed and used, the explosive parts may be damaged or even generate cracks due to the effect of temperature and mechanical stress, which will cause great loss and influence the original performance. In the long-term the storage of the explosive parts, the bonding surface of the base and the binder is likely to crack under the action of a compressive force or tensile force, as shown in Fig.3 and Fig.4.



Fig. 3.Cracks under the action of a compressive force.

* To whom all correspondence should be sent:
E-mail: happywells@163.com; 542900823@qq.com

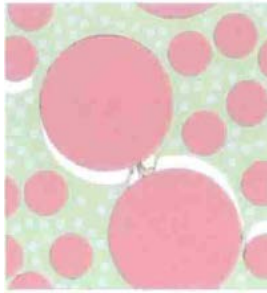


Fig. 4. Cracks under the action of a tensile force.

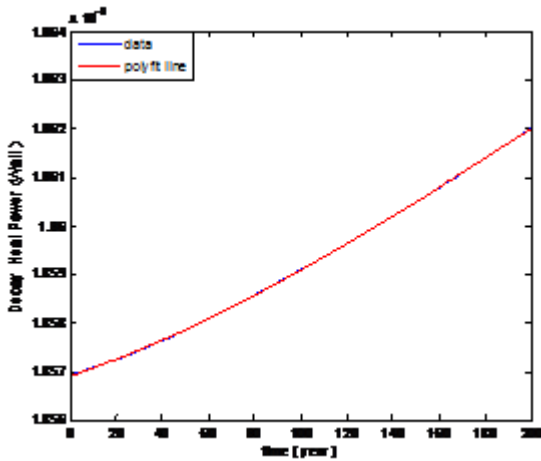


Fig. 5. WgPUecay heat power

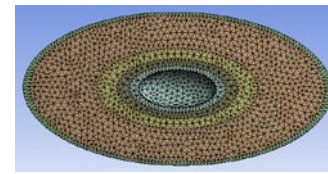
The stress conditions of the explosive parts in the structure of the assembly and the simulation analysis of the nuclear material and the structure of heat, the heat power is shown in Fig. 5. From the figure, we know that in 200 years time, the decay power of plutonium have reached a peak of 2.6887W/Kg. The more the heat released from plutonium, the greater the thermal stress produced by the structure. The heat power produced in this paper is based on the calculation of the peak power of plutonium. According to the storage environment of the parts, the temperature of the component in a ventilated environment is 22~25°C and the convection coefficient of air is $3.8 * 10^{-6} \text{W/m}^2$.

ANALYSIS MODEL AND VERIFICATION CALCULATION

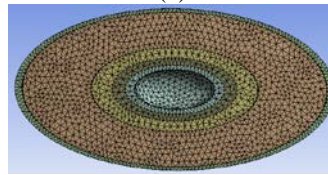
Analysis model

The crack surface at the top of the crack surface on the outer surface of the explosive component is parallel to the crack surface of the top surface of the outer surface of the short diameter parallel explosive component.

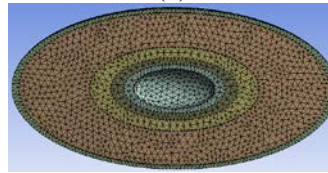
It can be seen from the figure that FEM analysis value and theoretical value is relatively close. The results show that the FEM simulation has a very good effect.



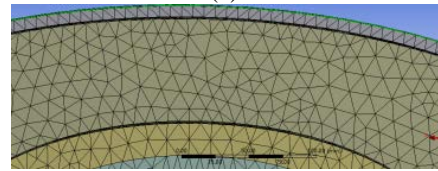
(a)



(b)



(c)



(d)

Fig. 6. Several contact modes on the ellipsoid: (a) Surface contact without clearance; (b) Surface contact with long axis clearance; (c) Surface contact with short axis clearance; (d) Enlarged view with short axis clearance.

Finite element analysis and theoretical calculation analysis

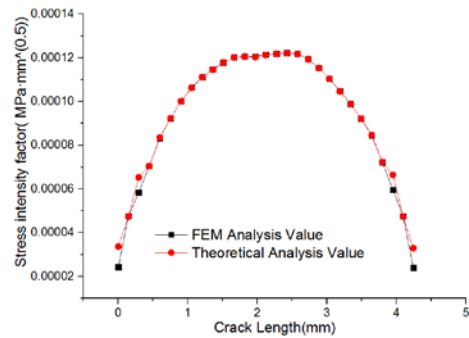


Fig. 7. Crack surface parallel to the short diameter.

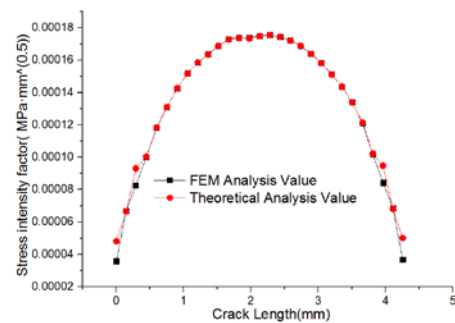


Fig. 8. Crack surface parallel to the long diameter.

CRACK ANALYSIS

Analysis of the inner surface of a crack

The inner surface of the spherical explosive without clearance

It can be seen from the figure that there is a big difference of the crack intensity factor between the spherical parts with a cushion and the spherical parts without a cushion layer. The stress intensity factor of the top of the inner surface of the explosive component with the cushion is close to zero and the value of the stress intensity factor is positive. It shows that the crack is open and the stress intensity factor at the inner surface is less than zero, which shows that the crack is closed. From the section stress contour of the explosive component, we can see that the top of the inner surface of the explosive component without a cushion layer is as high as 171.76MPa and the top of the inner surface with a cushion layer is 144.97MPa. The stress of the surface cushion should be much higher than that without a cushion. The cushion plays a certain role in relieving the stress of the crack of the explosive components.

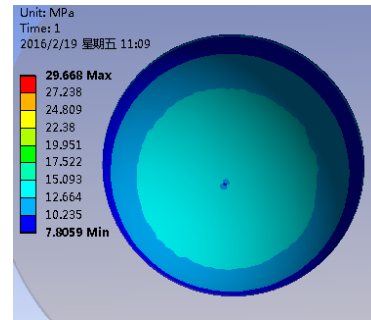


Fig. 11. Contact pressure on the inner surface of the sphere.

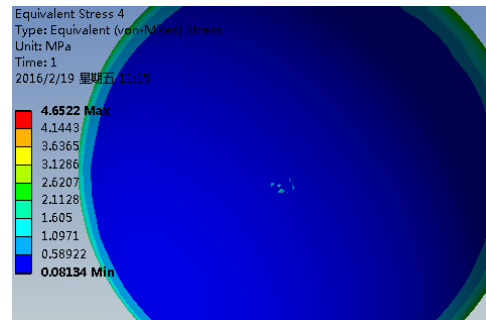


Fig.12. Equivalent stress of the inner surface crack of the spherical component

Crack surface parallels short diameter

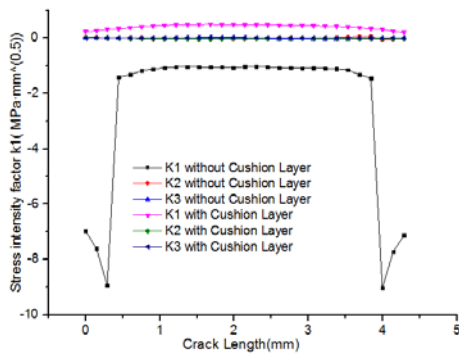


Fig. 9. Stress intensity factors.

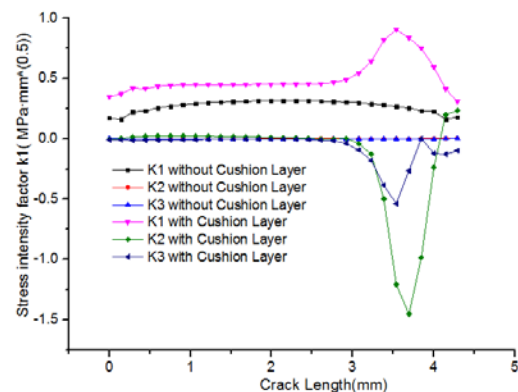


Fig. 13. Stress intensity factor.

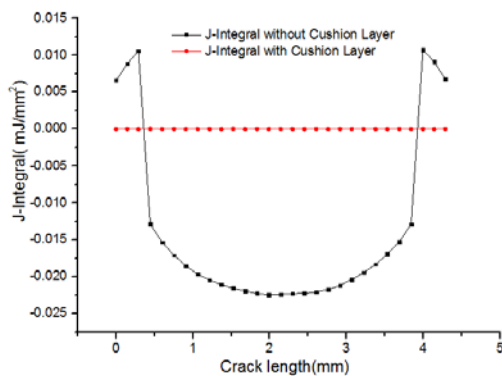


Fig.10. J-integral

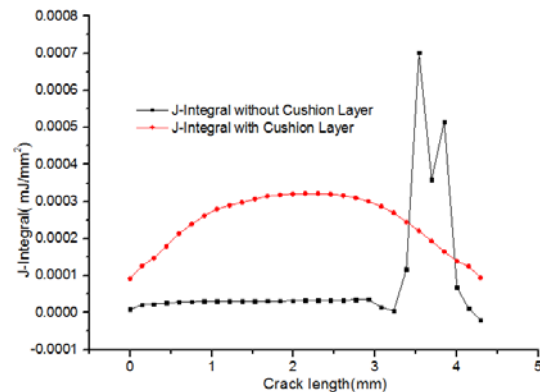


Fig.14. J-integral contrast.

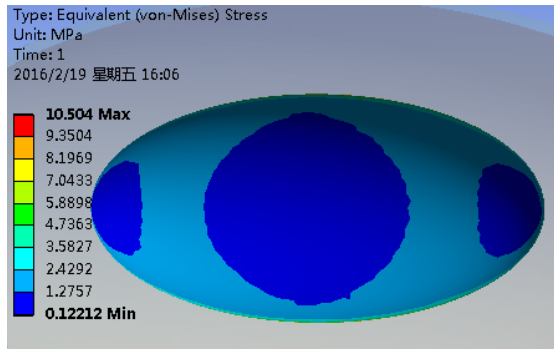


Fig. 15. Inner surface stress without a cushion.

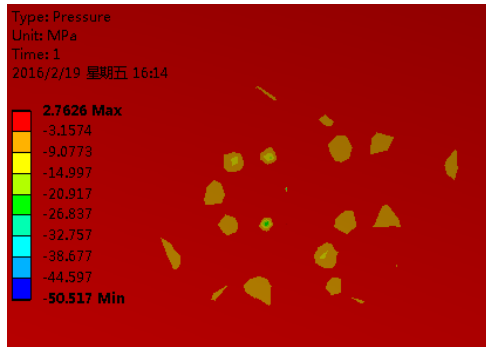


Fig. 16. Inner surface contact pressure with a cushion.

The crack is located on the inner surface of the ellipsoidal explosive without clearance. It can be seen from Fig.15 and Fig.16 that the contact pressure without a cushion of inner surface in general is more than that with a cushion, but in some areas of the crack with a cushion contact the pressure reached -50MPa. From Fig.13 and Fig.14, the stress intensity factor K1 with a cushion is more than that without a cushion. The stress intensity factor with a cushion occurs with mutations at 3.8mm, we can see that the partial stress of the cracks change the surface with a cushion.

Crack surface paralleled to a long diameter

The crack is located on the inner surface of the ellipsoidal explosive without clearance. From Fig.17 it can be seen that the stress intensity factor of the explosives components with a cushion is similar to that without a cushion and the stress intensity factor K1 is more than that without a cushion. As seen from Fig. 20, the maximum stress of the crack reaches 30.157MPa, which is much larger than that without a cushion.

Analysis of the outer surface of the crack

The outer surface of the spherical explosive without clearance

The crack is located on the outer surface of the spherical explosive without clearance. It can be seen from Fig.21 that the stress intensity factor K1

without the cushion is less than zero. According to the definition of K1, the crack is in the closed state. The stress intensity factor K1 is greater than zero with a cushion and the equivalent stress of the crack is shown in Fig.24. It can be seen from Fig.23 and Fig.24 that the equivalent stresses of the outer surface of the PBX component with a cushion and without a cushion are very different.

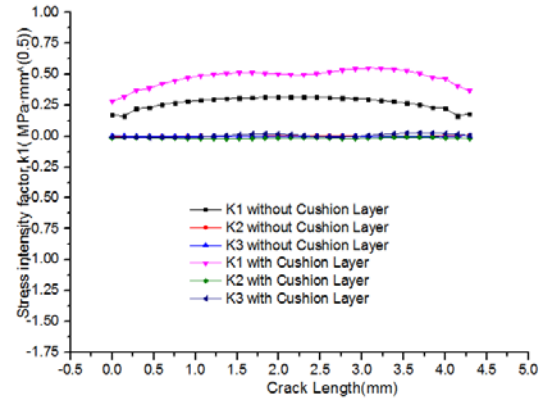


Fig.17. Stress intensity factor

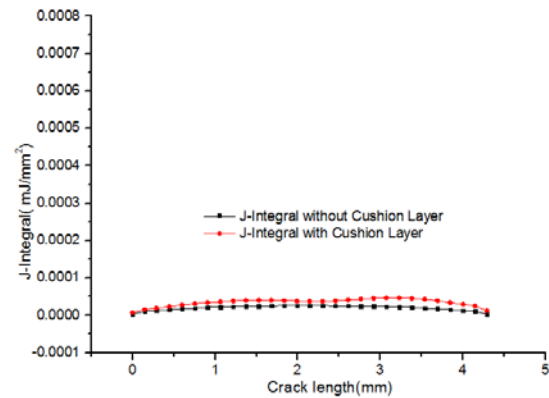


Fig. 18. J-integral.

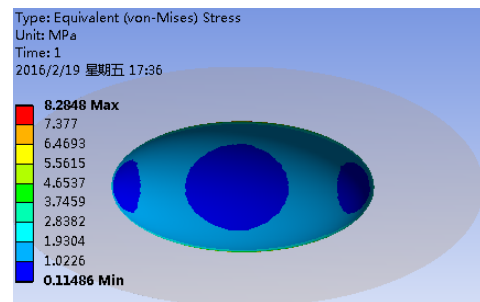


Fig.19. Equivalent stress without a cushion

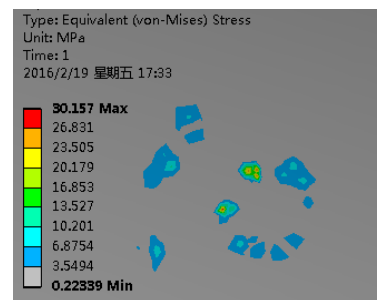


Fig. 20. J-integral with a cushion

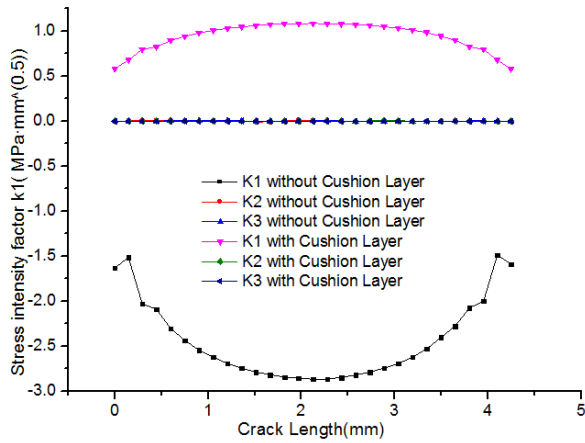


Fig. 21. Stress intensity factor.

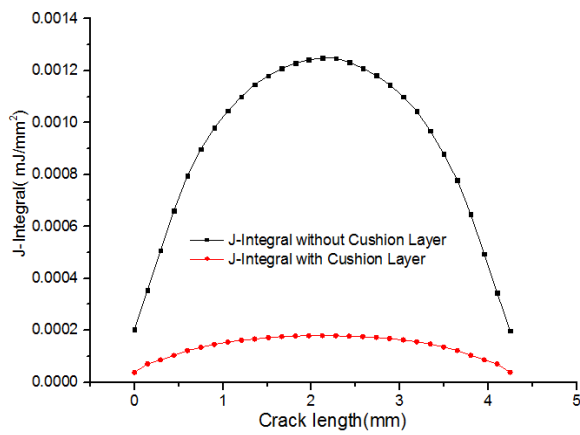


Fig. 22. J-integral.

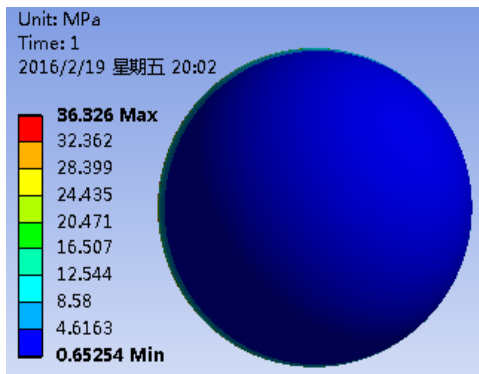


Fig. 23. Contact pressure without a cushion.

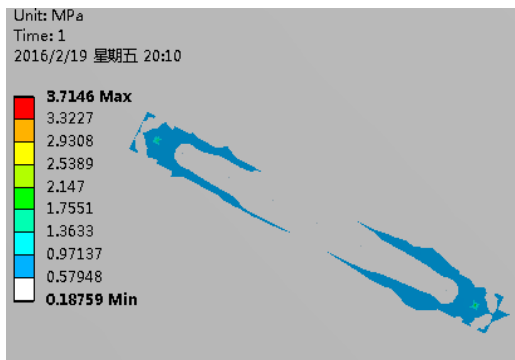


Fig. 24. Equivalent stress with a cushion.

Crack surface parallels a short diameter

The crack is located on the outer surface of the ellipsoidal explosive without clearance. The maximum elastic stress of the ellipsoid without a cushion is 6.3165MPa and at the top of the outer surface of the explosive it was the lowest.

From the stress intensity factor of the crack it can be seen, that the stress intensity factor with a cushion is more than that without a cushion and the J-integral with a cushion is more than that without a cushion, because the J-integral and stress intensity factor K1 are related. As observed in Fig. 27 the maximum equivalent stress of the outer surface is 4.5459MPa and the shape of the elastic stress is the same as the crack shape. The stress intensity factor of the crack is shown in Fig. 25 and the maximum value of the stress intensity factor K1 is concentrated in the middle part of the crack.

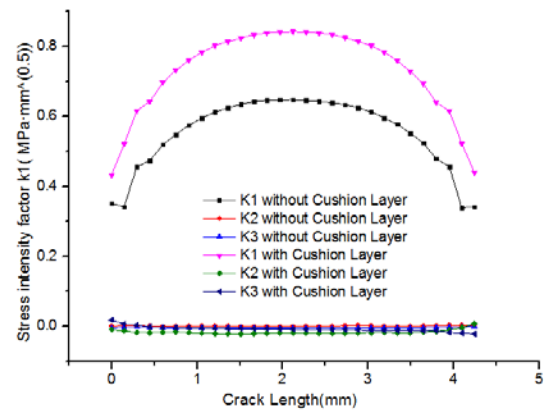


Fig. 25. Stress intensity factor K1.

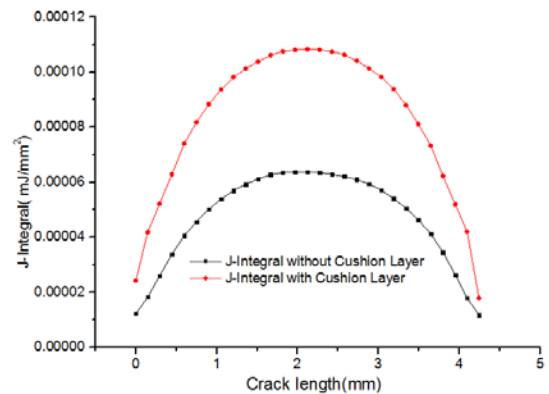


Fig. 26. J-integral.

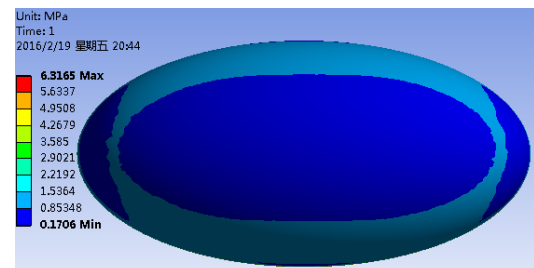


Fig. 27. Elastic stress without a cushion.



Fig. 28. Elastic stress with a cushion.

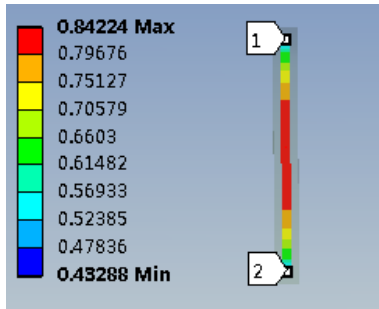


Fig. 29. Stress intensity factor without a cushion.

Crack surface parallels long diameter

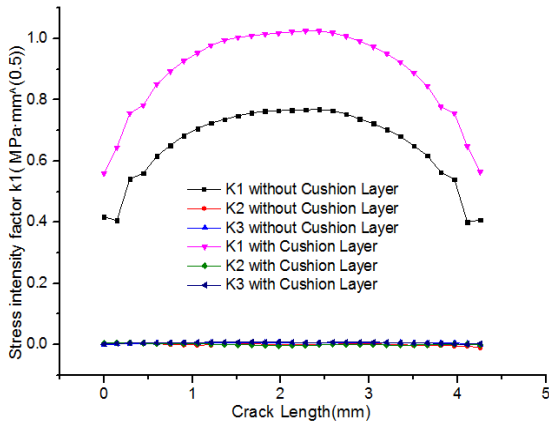


Fig.30. Stress intensity factor.

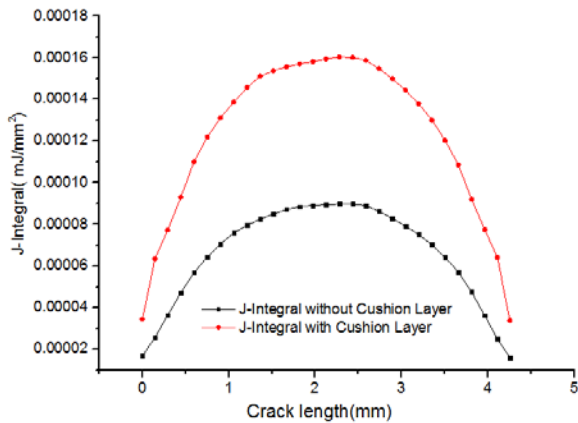


Fig. 31. J-integral contrast.

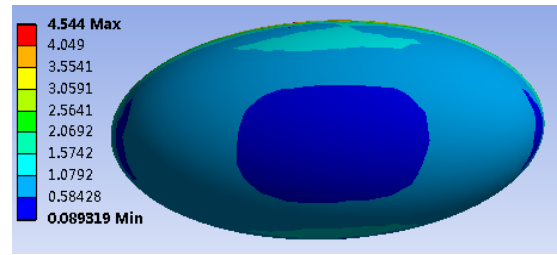


Fig. 27. Elastic stress without a cushion.

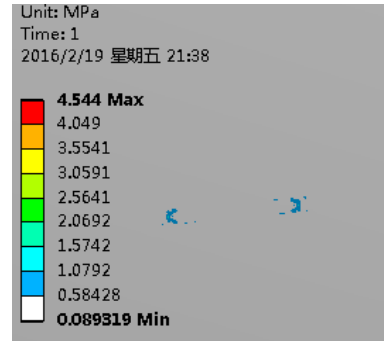


Fig.28. Elastic stress with a cushion.

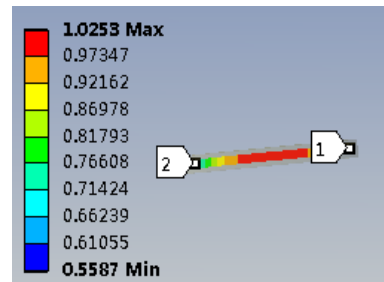


Fig. 29. Stress intensity factor without a cushion.

The crack is located on the outer surface of the ellipsoidal explosive without clearance. The stress value of the crack in the direction of the long diameter is smaller than that of the short diameter. At the same time the stress intensity factors between the crack direction in parallel with the long diameter direction and the short diameter direction are generally the same.

CONCLUSION

1. Under the same condition, the stress intensity factor of the crack in the inner and outer surface is not the same, the stress intensity factor of the inner surface is larger than that of the outer surface, in the middle of the crack, stress intensity factor appears a “broken” phenomenon and the crack in the inner surface occurs as a “break” phenomenon in the 3/4 position of the crack.

2. The stress intensity factor K1 of the crack in the perpendicular direction at the top of the inner surface of the explosive is different and the crack perpendicular to the radial stress intensity factor is greater than the crack parallel to the radial direction.

The two stress intensity factors in the clearance of the explosives components are more obvious.

3. In the proper position of a crack, the stress intensity factor of a crack parallel to a short diameter of the outer surface with a cushion occurs with mutations and the mutations may be caused by the strong strain effect.

4. Without a cushion and sphere the conformal contact and the stress intensity factor is negative, indicating that the crack is in a strong closed state. During the actual engineering, the surface and surface contact state is an ideal state and it will not exist in real life. The crack will not yield a closed state and yet the close state is an ideal result.

5. The stress intensity factor of the inner surface with a cushion is significantly higher than that without a cushion, also the stress intensity factor of the outer surface with a cushion is larger than that without a cushion, but the attenuation stress intensity factor of the inner surface of the explosive is more than that of the outer surface.

6. Under the same conditions, the stress intensity factor of the crack intensity factor of the sphere is larger than that of the ellipsoid.

REFERENCES

1. M.I. Muskhelishvili, Some Basic Problems of the Mathematical Theory of Elasticity [M], Groniagen: Moordhoff, 1953, p. 14,376, 486.
2. A.T. Shitaerman, Contact Problems of the Theory of Elasticity, Gostakhisdat, Leningred, Moscow, Russia, 1949, p. 140, 252.
3. X. Fang, C. Zhang, X. Chen, Y. Wang, Y. Tan, *ActaMech, ActaMech*, **226**, 1657 (2015).
4. J. Jamari, D.J. Schipper, *Tribology Letters*, **21**, 262 (2006).
5. A. Persson, On the stress distribution of cylindrical elastic bodies in contact[D]. Chalmers, Tekniska, Goteborg, Sweden, 1964.
6. M.Ciavarella, P. Decuzzi, *International Journal of Solids and Structures*, 4507 (2001).
7. M.Ciavarella, P. Decuzzi, *International Journal of Solids and Structures*, 4525 (2001).
8. N. Hussain, *International Journal of Engineering Science*, 1149 (1969).
9. H.Nagatani, A.Imou, *Journal of Advanced Mechanical Design, Systems, and Manufacturing*, **6**, 1055 (2008).
10. C.-S. Liu, K. Zhang, L. Yang, *Journal of Computational and Nonlinear Dynamics*, **4**, 106 (2006).
11. A.A. Griffith, *Phil.Trans.Roy.Soc.London[J]*, **A221**, 163 (1921).
12. E. Orowan, *Welding Journal*, **34**, 1575 (1955).
13. G.R. Irwin, *JAM*, **57**, 361 (1957).
14. P. Paris, F. Erdogan, *Laws.J.Basic Eng.*, **85**, 528 (1963).
15. J.R. Rice, *J.Appl.Mech.*, **35**, 379 (1968).

ИЗСЛЕДВАНЕ НА ВЛИЯНИЕТО НА ОТСТРАНЯВАНЕТО НА ПУКНАТИНИ ПРИ РВХ-ЕКСПЛОЗИВИ

Г. Женжи^{1,2}; Х. Бин¹; Г. Женгминг¹; Н. Либо¹; К. Лужие¹

¹. Ксиан Хай-Тек изследователски институт

²NO.96401 Force

Постъпила на 24 март, 2016 г.; коригирана на 22 ноември, 2016 г.

(Резюме)

Експлозивите се използват широко във военното инженерство. В тази работа е разгледано влиянието на интензивността на напреженията при сферична и елипсоидна форма на обвивката на експлозива. Резултатите показват, че напреженията са по-големи от вътрешната страна на обвивката и че напрежението е по-голямо при наличие на амортизатор. Тези резултати позволяват съставянето на теоретично ръководство за реално конструиране на ядрените компоненти.

Numerical analysis of surface cracks of spherical explosive with a cushion

G. Zhenzhi^{1,2*}, H. Bin¹, G.Z. Ming¹

¹*Xi'an High Tech Research Institute*

²*NO.96401 Force*

Received February 30, 2016; Revised October 26, 2016

Explosive components are widely used in military engineering. In view of the characteristics of the crack in the explosive component, the stress intensity factor and the J integral of the PBX component were studied. This paper studies the mechanism of crack damage under different conditions. The results show that the shape of the crack opening at different position of the components is different, together with the crack strength.

The crack intensity factor will be affected by the location of the crack, crack length, crack depth and crack direction. The study of the explosive components provides engineering with theoretical support.

Keywords: PBX Explosive, Crack, Stress Intensity Factor, J Integral, Gap Contact

INTRODUCTION

The explosive components in nuclear structure are an important component of the explosive detonation structure. The main component of the explosives is Octogen (HMX), which is a white crystal with the chemical formula $C_4H_8N_8O_8$. The chemical structure is shown in Fig1.

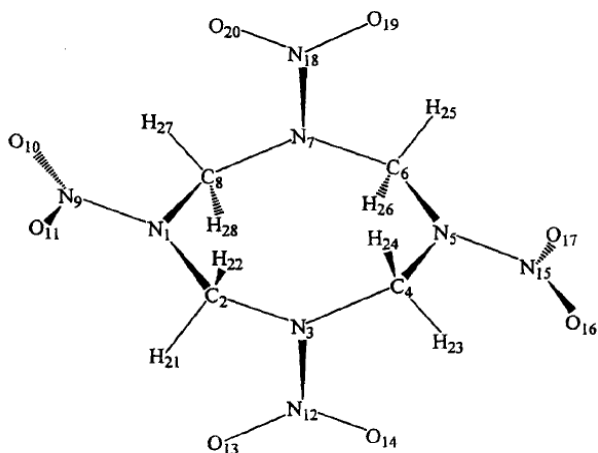


Fig.1. Schematic diagram of the chemical structure

The PBX explosive is formed by the main component and the binder. Under the action of the stress of the structure of PBX, it is easy to crack, which directly affects the performance of the explosive component. Therefore, it is necessary to study the mechanical properties of the explosive component. This article discusses the studies of the law of the crack of the explosive component.

ANALYSIS OF THE INFLUENCE OF THE CRACK ON THE EXPLOSIVE COMPONENTS

Analysis of conforming spherical contact

Study on the interaction of multiple cracks

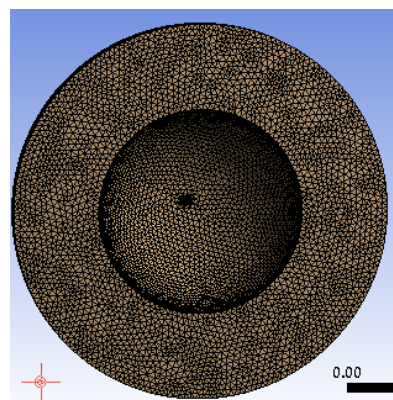


Fig. 1. One crack

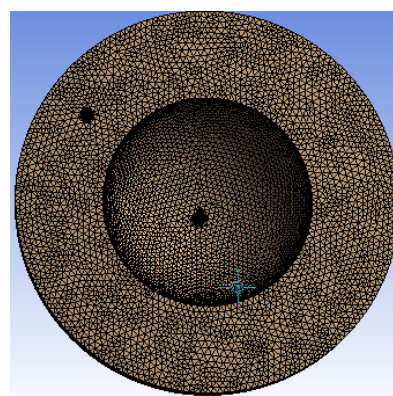


Fig. 2. Two cracks

* To whom all correspondence should be sent:
E-mail: happywells@163.com; 542900823@qq.com

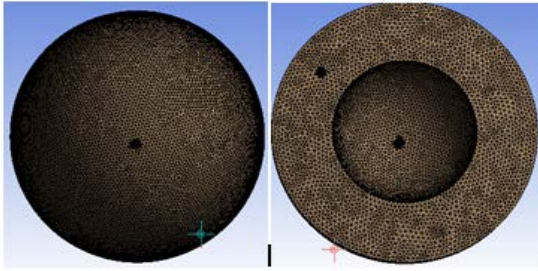


Fig. 3. Three cracks.

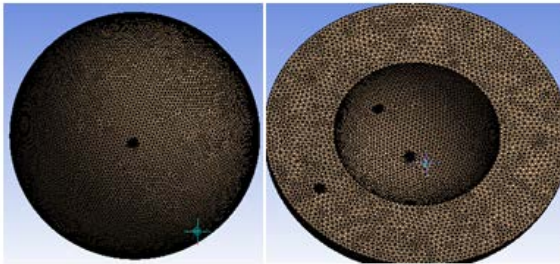


Fig. 4. Four cracks.

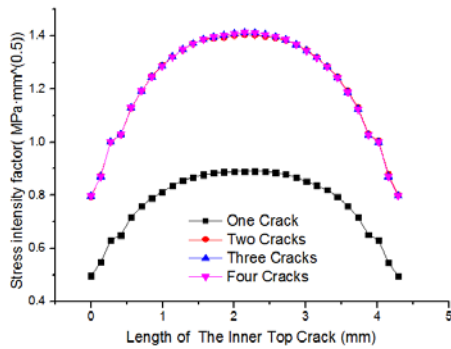


Fig. 5. K1 of stress intensity factor.

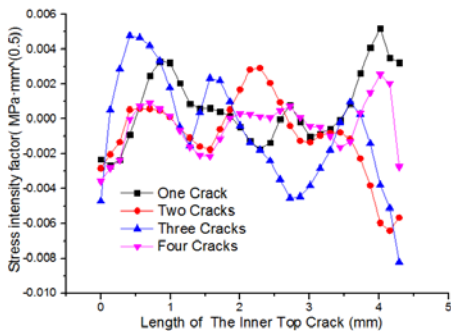


Fig. 6. K2 of stress intensity factor.

Figures 1 to 4, respectively illustrate one to four cracks. It can be seen from the picture, that stress intensity factors are not the same when the surface of an explosive component is subjected to one crack or a plurality of cracks. As observed in Fig.5 to Fig.8, when the explosive component is affected by the two cracks, the K1 influence factor of the crack on the top of the explosive component is different. When the number of cracks increase the stress intensity factor is not significantly different. The stress intensity factor K2 is similar to the

starting position, but the strength of the crack is very different in the end position. At the same time, the stress intensity factor K2 and K3 can be seen to be a wave shape fluctuation from Fig. 6 and Fig. 7. The figures show that the sliding force and tearing force of the crack are more complex. As can be seen in Fig. 8, the J-integral of the crack has the same trend for the stress intensity factor.

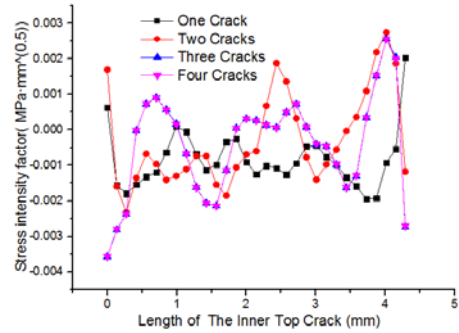


Fig. 7. K3 of the stress intensity factor.

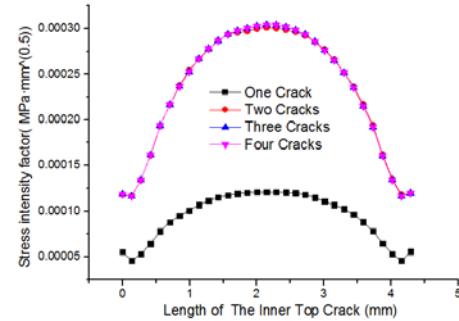


Fig. 8. J-integral

Cracks on the inner surface or outer surface of the explosive without a cushion

It can be seen from Fig.9, that the stress intensity factor at the top of the inner and outer surface is negative, so the crack is in the closed state and is not extended. Observing the stress amplitude, the stress intensity factor of the inner surface is greater than that of the outer surface and illustrates that the force of the inner surface is greater than that of the outer surface.

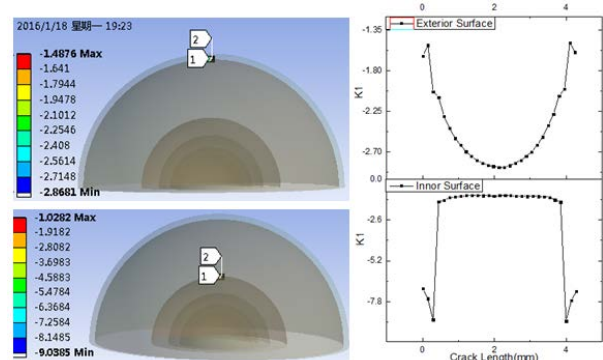


Fig. 9. Cracks on the inner surface or outer surface and the stress intensity factor

The stress intensity factor on the inner surface of the top appeared suddenly changed and the crack stress of the inner surface appeared attenuated at the middle of the crack length. The more closed the joint forces are at both ends of the crack, the more the crack will not occur.

Study on the influence of the crack parameters along with the change in crack length

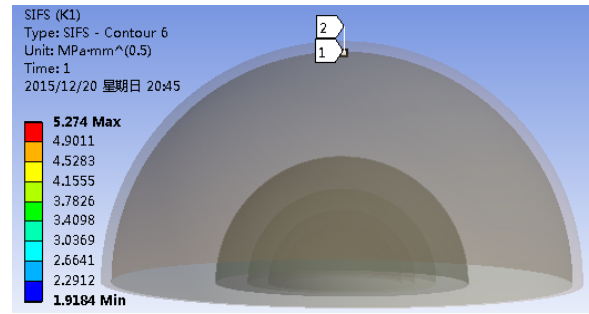


Fig. 10. A crack at the top of the explosive.

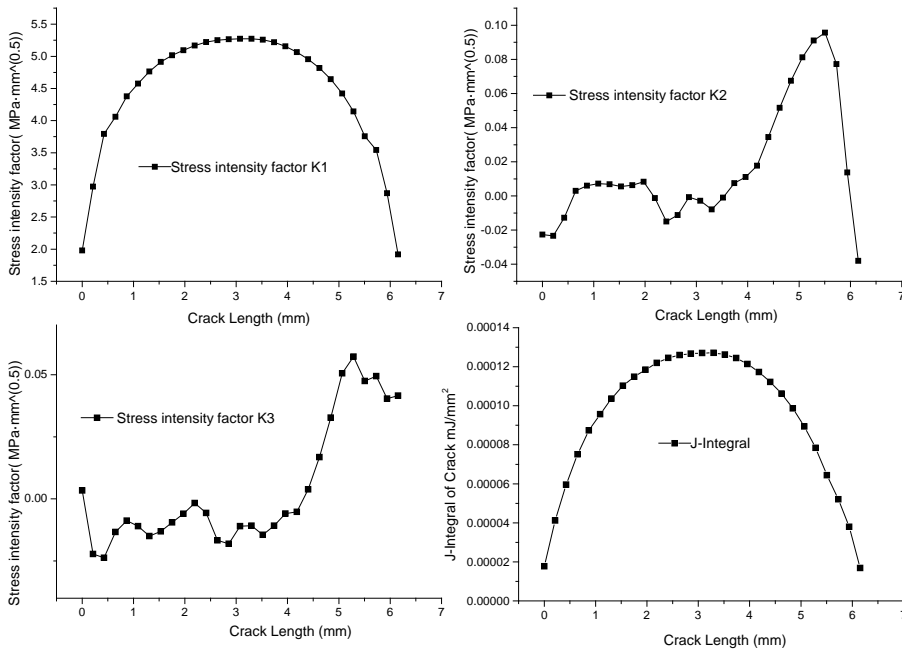


Fig. 11. The major axis radius is 3mm.

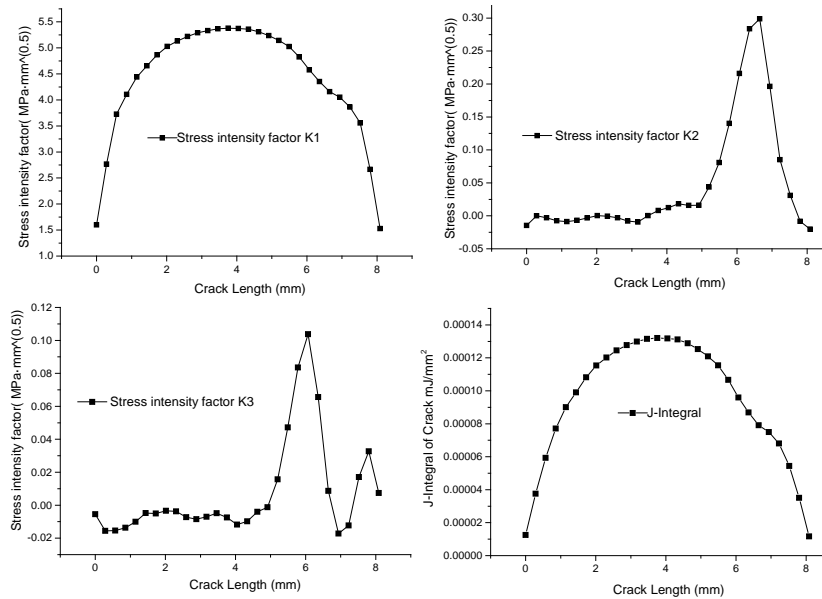


Fig.12. The major axis radius is 4mm.

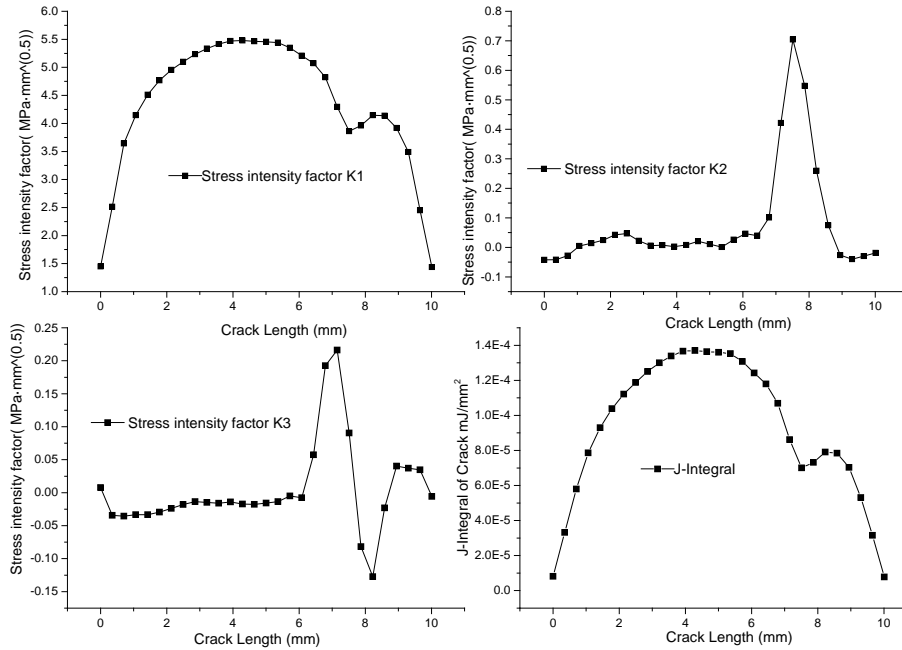


Fig. 13. The major axis radius is 5mm.

The analysis of this section is the case of the outer surface of the explosive component with a cushion layer without a clearance and contact. The crack is located outside the top of the explosive component and the crack length is 3mm, 4mm, 5mm, respectively. Seen in Fig. 11 to Fig.13, the stress intensity factor and J-integral will change along with the length of the crack. With the crack length increasing, the stress intensity factor K1 at some crack positions appear attenuated, meanwhile with the length of the crack increasing the stress intensity factors K2 will increase a lot. The stress intensity factor K3 change is not too obvious and the J- integration curve and the K1 curve are consistent.

of the explosive component, at a depth of the inner surface of the explosive component below 1mm and at a depth of the surface of the explosive component below 2mm.

Analysis of the influence of the crack parameters along with the depth of the inner surface

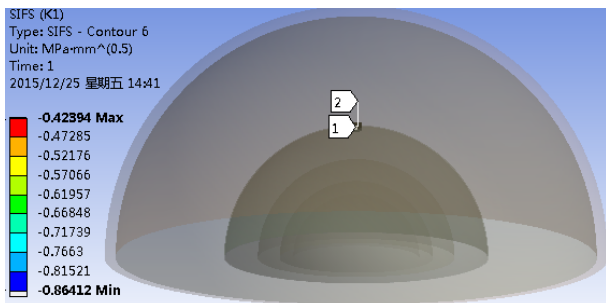


Fig. 14. The location of the crack.

The crack is located at the top of the inner surface of the explosive component without a cushion layer. The locations of the three cracks are as follows: at a depth of the top of the inner surface

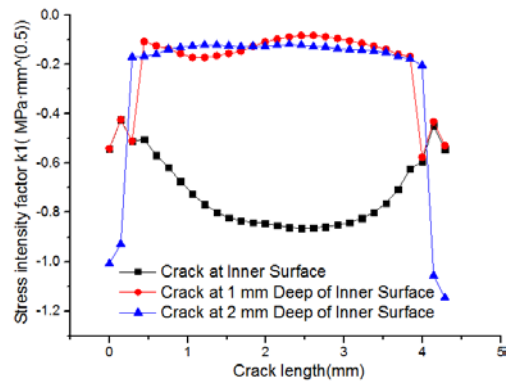


Fig. 15. The stress intensity factor K1 along with the depth.

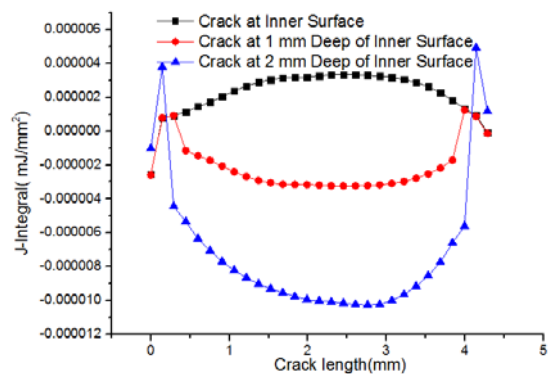


Fig. 16. The J-integral at a different crack depth.

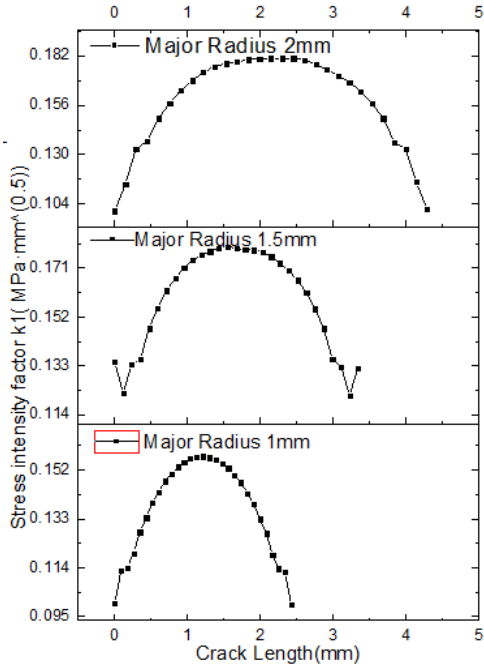


Fig. 17. Stress intensity factor K1.

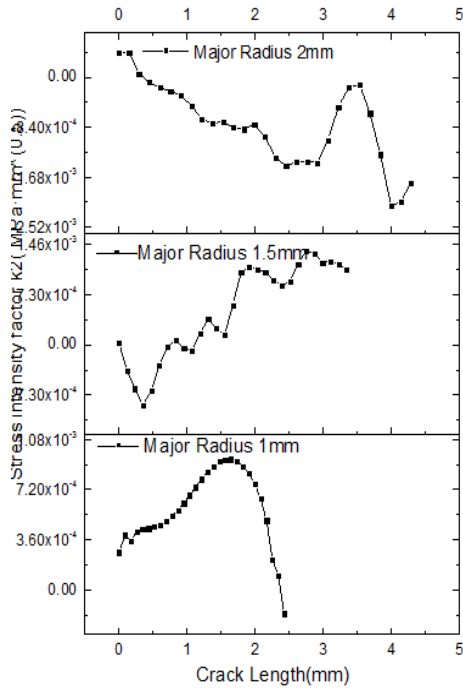


Fig. 18. Stress intensity factor K2

The crack stress intensity factor and J integral are different in three different depths from Fig.15. Generally speaking, the stress intensity of the crack on the surface is greater than the stress intensity factor of the crack at a depth of 1mm and 2mm. As can be seen from Fig.16, the J-integral of the surface crack is greater than that at a depth of 1mm, and the J-integral at the depth of 1mm is greater than that at a depth of 2mm. From Figure 15 and Figure 16 we observe, that the stress of the surface crack is greater than that of the internal crack.

Analysis of the surface crack of a sphere with a clearance contact

Stress intensity factor analysis without a cushion

Effect of the crack length on the stress intensity factor of the inner surface top of the explosive

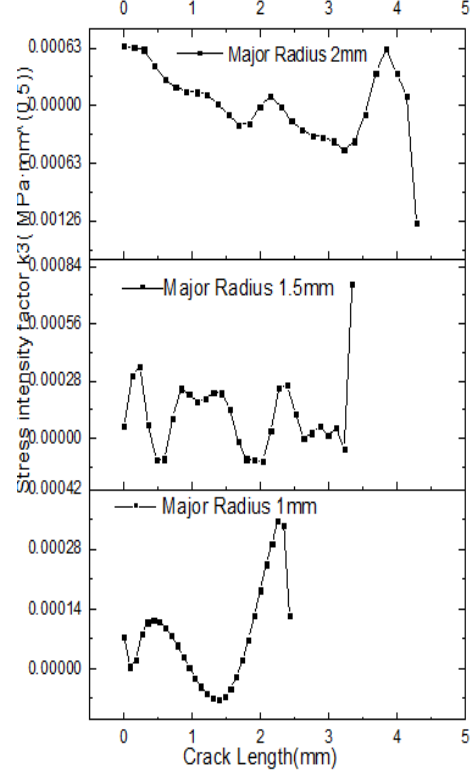


Fig. 19. Stress intensity factor K1.

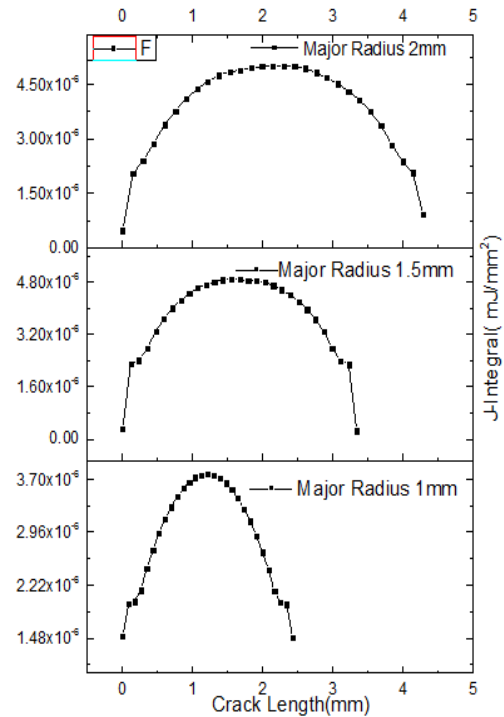


Fig. 20. J-integral.

Effect of crack length on the stress intensity factor of the outer surface top of the explosive

From Fig.21 compared with Fig.21, the stress intensity factors at major radii of 2mm, 2.5mm, 3mm and 3.5mm of the outer surface crack are much larger than those for radii of 1mm, 1.5mm and 2mm. Because there is no cushion on the outer surface to protection the crack, the stress intensity factor of external surface cracks is much larger than that of the inner surface crack. The stress intensity factor of K2 and K3 increases with the increase of crack in length.

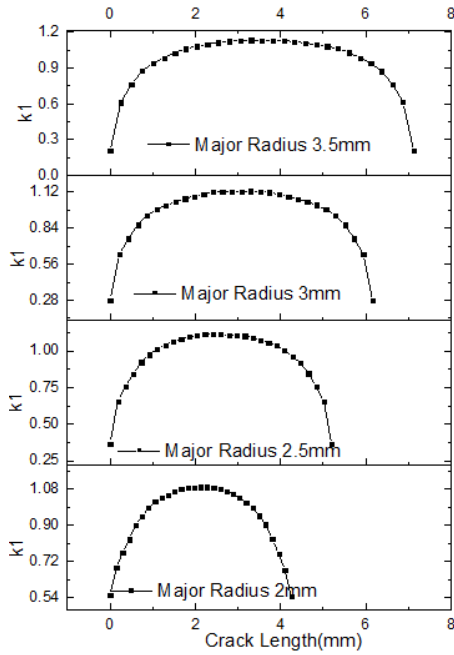


Fig. 21. Stress intensity factor K1.

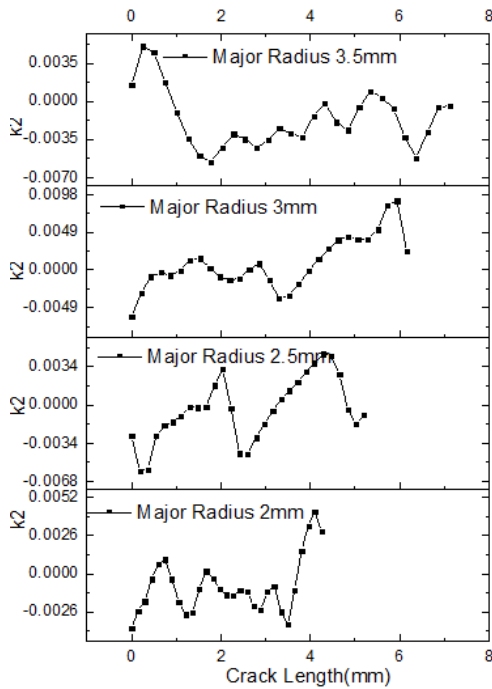


Fig. 22. Stress intensity factor K2.

Analysis of the stress intensity factor of the crack of the inner surface along with the depth

The cracks at four different depths (0mm, 0.5mm, 1mm, 1.5mm) were analyzed in this case. It can be seen that the crack stress intensity factor decreases with the increase in depth of the crack. Especially, when the crack depth is 1mm and 1.5mm, the stress intensity factor attenuation is especially obvious. At the same time, with the increase of depth, the stress intensity factor K2 and K3 also have different degrees of attenuation.

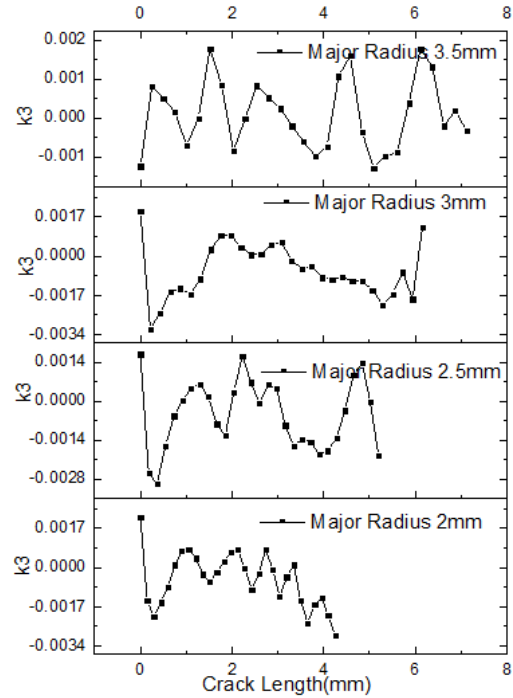


Fig. 23. Stress intensity factor K3.

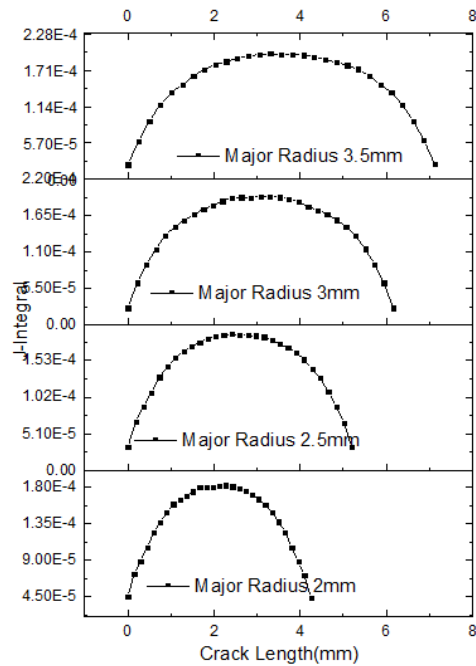


Fig. 24. J-integral.

Analysis of the stress intensity factor of the crack on outer surface along with the depth

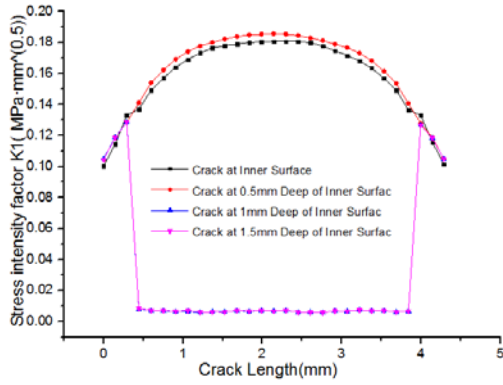


Fig. 25. Stress intensity factor K1.

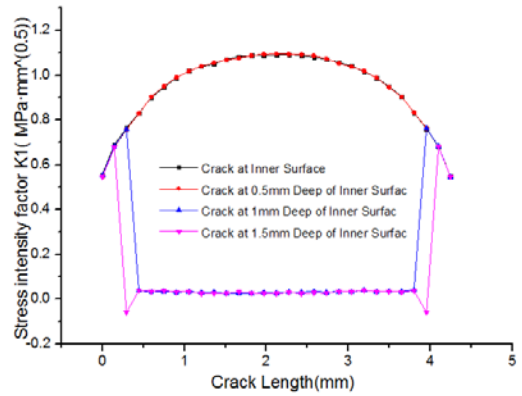


Fig. 29. Stress intensity factor K1.

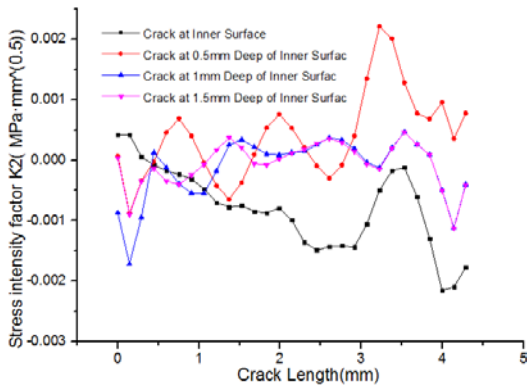


Fig. 26. Stress intensity factor K2.

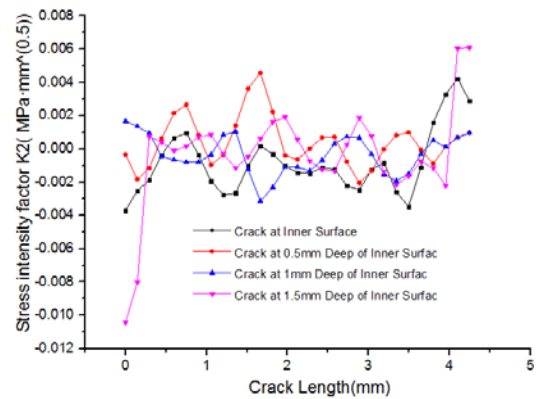


Fig. 30. Stress intensity factor K2.

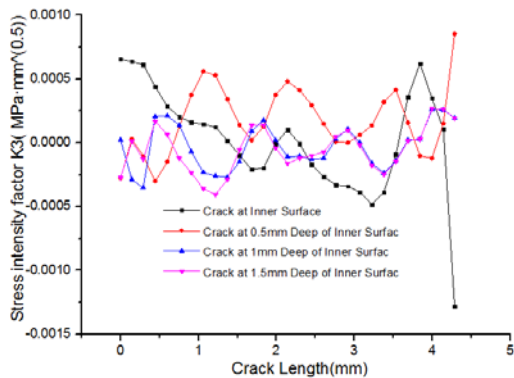


Fig. 27. Stress intensity factor K3.

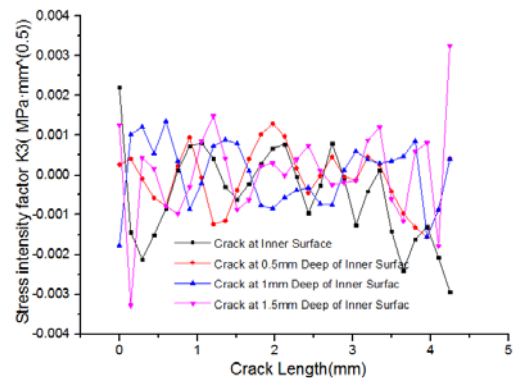


Fig. 31. Stress intensity factor K3.

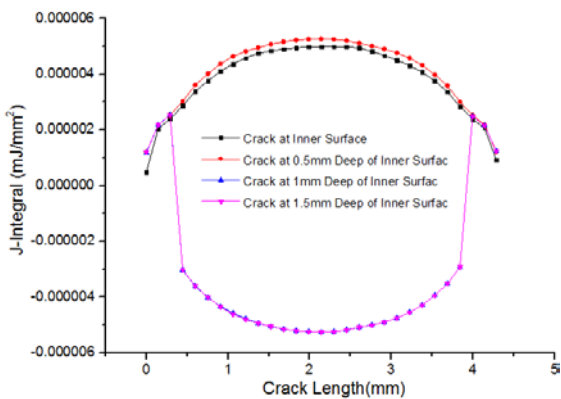


Fig. 28. J-integral

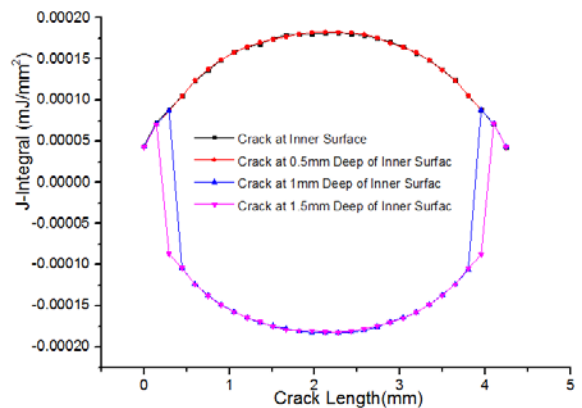


Fig. 32. J-integral.

Compared with the stress intensity factor of the inner surface, the stress intensity factor of the outer surface is very different. First, the stress intensity factor increases, because there is no cushion on the outer surface. When the outer surface of the metal shell is constrained, the stress intensity factor is larger than that of the inner surface; Second, after the depth of the crack below the surface is increased, the intensity factor of the crack is reduced. The stress intensity factor is especially obvious when the crack depth is 1mm and 1.5mm. On the whole, the crack parameters of the outer surface are very similar to the inner surface crack parameters.

Stress intensity factor analysis with a cushion

Analysis of the stress intensity factor of the crack of the outer surface along the depth

The stress intensity factors K1, K2, and K3 are shown in Fig.34 to Fig.36, where the locations are at the outer surface of the top surface depths of below 1 mm, 2 mm and 6 mm of the explosive component crack with a cushion. As can be seen, attenuation suddenly appeared at the stress intensity factor of K1. It can be seen that the deeper the crack is below surface, the smaller the stress intensity factor is. At the same time, it can be seen that the stress intensity factor with the cushion is smaller than that of the stress intensity factor without a cushion given the crack is in the same place.

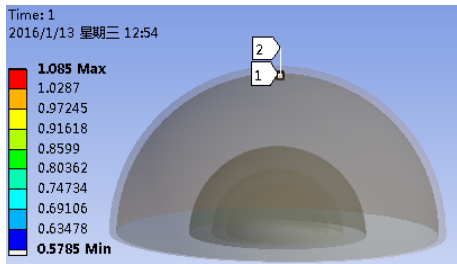


Fig. 33. The crack location.

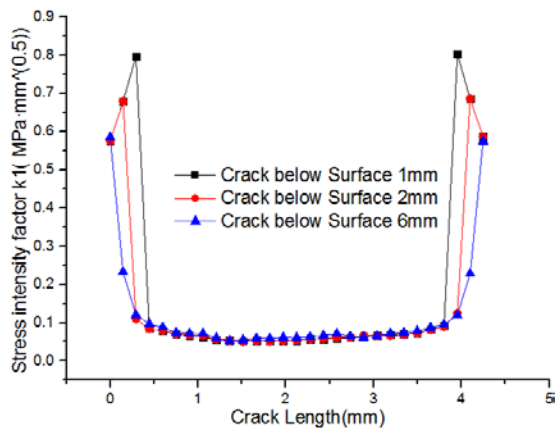


Fig. 34. Stress intensity factor K1.

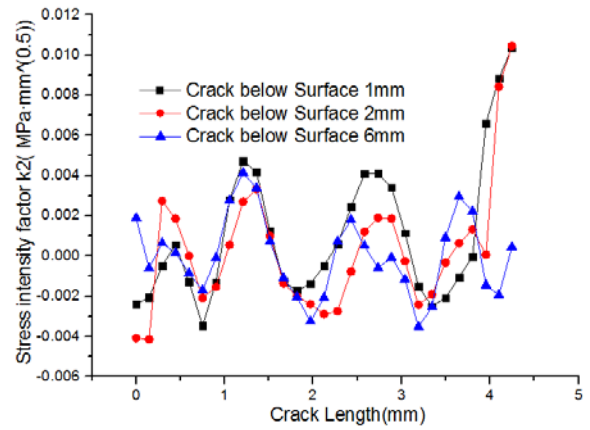


Fig. 35. Stress intensity factor K2

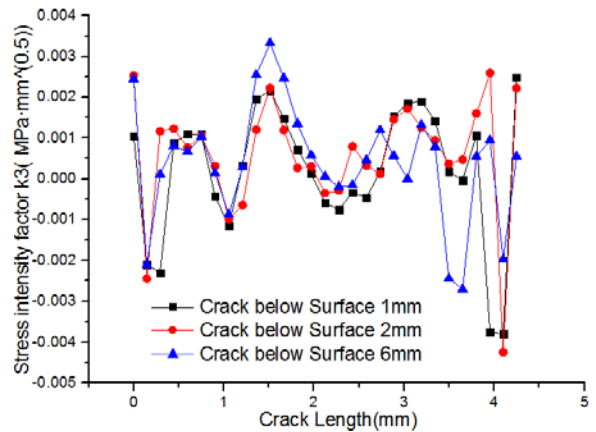


Fig. 36. Stress intensity factor K3

Crack at the bottom of the explosive component near the outer steel shell

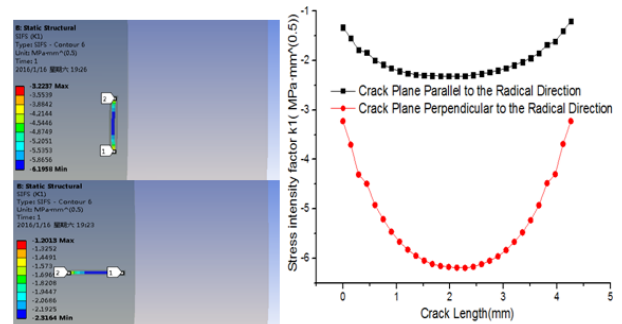


Fig. 37. Two cracks at different directions and the simulation results.

It can be seen that the stress intensity factor is less than zero in two directions, indicating the cracks in the closed state. But the stress intensity factor in both directions vary greatly in size, the stress intensity factor perpendicular to the radial direction is greater than that parallel to the radial cracks. The simulations show that the cracks are perpendicular in the radial direction rather than parallel to the radial cracks and are more susceptible to the effect of the closing force.

A crack at the bottom of the explosive component near a cushion

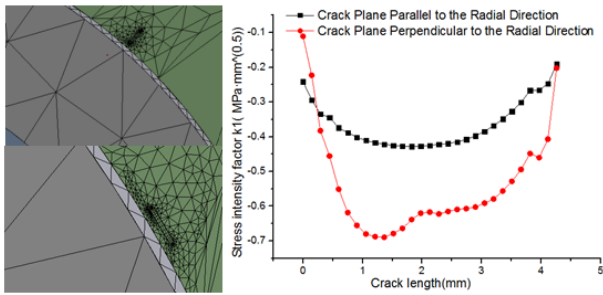


Fig. 38. Two cracks at different directions and simulation results.

The above simulation is the stress intensity factor K1 of the bottom of the explosive component without gap contact. Compare Fig.38 with Fig.37, the stress intensity factor of outer surface crack is much larger than that of the inner surface crack. It can be seen that the cushion has a very good protective effect on the explosive components.

A crack at the bottom of the explosive component near the cushion with a gap contact

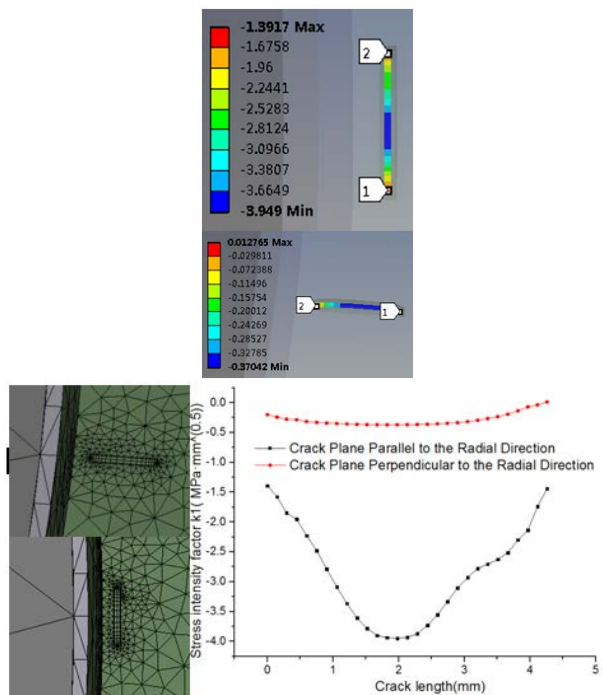


Fig. 39. Two cracks in different directions and the simulation results.

The stress from the crack can be observed with the stress in parallel direction to the radial crack being much larger than the stress perpendicular to the radial crack. Comparing Fig. 38 with Fig.39 shows that the stress of the radial crack is very different for the two contact states. This is the reason that the crack in the radial direction is the

most susceptible to the thermal stress caused by the heat released from the nuclear components. When the initial boundary conditions are set, the bottom surface is fixed in the Y and X directions, so the crack can't be displaced in the plane direction. Since the crack is not moving in the plane direction, the crack is in a closed state.

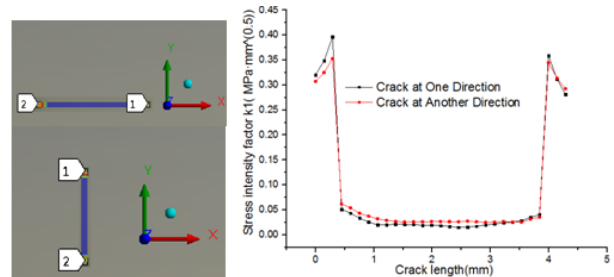


Fig. 40. Two cracks at different directions and simulation results.

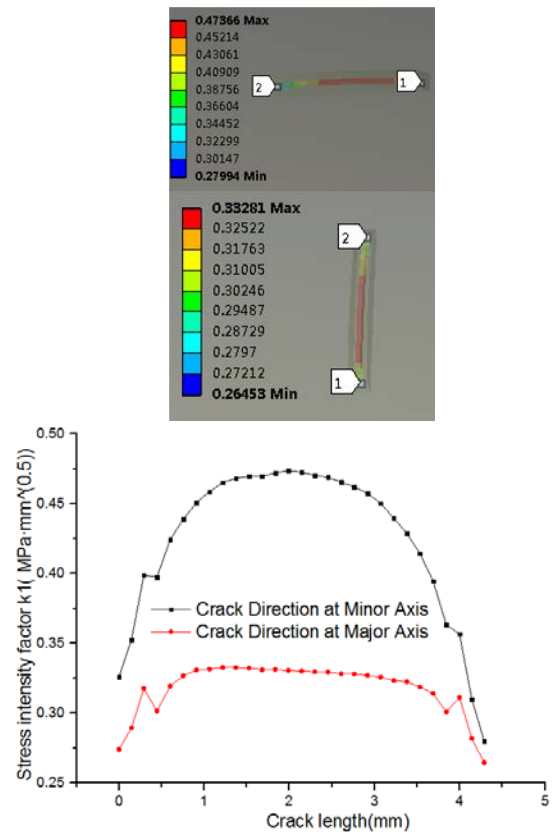


Fig. 41. Two cracks at different directions and simulation results.

A crack at the top of the outer surface of the explosive in two vertical directions

Through the analysis of the external surface crack of the explosive components, it can be seen that the stress intensity factor curve of the two kinds of cracks is similar, which shows that the stress characteristics of the two kinds of cracks on the outer surface are relatively close. It can be seen that the stress intensity factor K1 of the crack on

the outer surface is greater than zero, which indicates that the crack in the outer surface is affected by the opening force. Between 0.4 mm and 4 mm in length, the two kinds of crack intensity factors have a mutation, which shows that the stress is relatively small between 0.4 mm and 4 mm.

A crack at the top of the inner surface of the explosive in two vertical directions

There are differences between the stress intensity factors of the cracks in the two directions at the top of the inner surface. The crack intensity factor in the direction of the short radius is larger than that in the direction of the long radius. This shows that the intensity factor of the crack with a gap is larger than that without a gap. In accordance with Fig. 40 and Fig. 41 the outer surface of the crack occurred mainly due to the simulation of the crack being too long and the stress not enough to support the stress in such a long crack.

CONCLUSION

1 After adding a crack, first the crack stress intensity factor will obviously increase. Continuing to increase the cracks, the stress intensity factor did not change significantly.

2 Under the same condition, the stress intensity factor at the inside and outside surface is not the same. The stress intensity factor at the inner surface is larger than that at the outer surface and the stress intensity factor in the middle of the crack at the outer surface appears a "broken" phenomenon.

3 Once the crack length increases, the crack intensity factor K_I can be mutated. It is shown that the stress of the crack is not enough to support the crack at the corresponding length, so the length of simulation assumes that the crack should shorten.

4 The stress intensity factor K_I of the cracks in the two perpendicular directions at the inner top surface of the explosive with a clearance in contact is different. Generally speaking, the crack stress intensity factor which is perpendicular to the radial direction is larger than that which is parallel to the radial direction.

REFERENCES

1. M. Perl, M. Steiner, *Engineering Fracture Mechanics*, **138**, 233 (2015).
2. M. Perla, V. Bernshtein, *Engineering Fracture Mechanics*, **77**, 535 (2010).
3. J.R. Armitage, Boundary element analysis of thick-walled spherical vessels with surface cracks, Department of Mechanical and Aerospace Engineering Carleton University, Ottawa, Ontario, Canada, 2009.
4. F. Erdogan, J.J. Kibler, *International Journal of Fracture Mechanics*, **5**, 229 (1969).
5. S.-Y. Chen, Experimental and boundary element analysis of Hertzian cone cracking, Purdue University, USA, 1993.
6. A. El Hakimi, P. Le Grogne, S. Hariri, *Engineering Fracture Mechanics*, **75**, 1027 (2008).
7. F.I. Baratta, *Journal of The American Ceramic Society Baratta*, **61**, 490 (1978).
8. Y.-J. Chao, H. Chen, *Int. J. Pres. ves. & Piping*, **40**, 315 (1989).
9. G. Valentin, D. Arrat, *Int. J. Pres. Ves. & Piping*, **48**, 9 (1991).
10. B. Wang, N. Hu, *Engineering Structures*, **22**, 1006 (2000).
11. Y. Murakoshi, Y.S. Biici, A. Atsuml, *Computers & Structures*, **21**, 1137 (1985).
12. M. Perl, V. Bernshtein, *Engineering Fracture Mechanics*, **94**, 71 (2012).
13. X. Fang, C. Zhang, X. Chen, Y. Wang, Y. Tan, *Acta Mech*, **226**, 1657 (2015).
14. J. Jamari, D.J. Schipper, *Tribology Letters*, **21**, 262 (2006).
15. K.E. Koumi, L. Zhao, J. Leroux, T. Chaise, D. Nelias, *International Journal of Solids and Structures*, **51**, 1390 (2014).
16. L. Wanga, X. Liua, D. Lia, F. Liub, Z. Jina, *Medical Engineering & Physics*, **36**, 419 (2014).
17. Z. Liu, J. Shi, F. Wang, Z. Yue, *Acta Mechanica Solida Sinica*, **28**, 35 (2015).
18. C. Liu, K. Zhang, *Transactions of the ASME*, **1**, 160 (2006).
19. Z.-M. Gao, J.-B. Jia, S.-P. He, B. Wang, *Advanced Materials Research*, **588**, 340 (2012).
20. S. Hajdu, *Procedia Engineering*, **69**, 477 (2014).
21. G. Marannano, A. Pasta, A. Giallanza, *Fatigue Frad Engng Mater Structures*, **37**, 380 (2014).
22. J. Zhang, W. Liu, L. Hao, *Polymers & Polymer Composites*, **22**, 347 (2014).
23. V. Kukshal, S. Gangwar, A. Patnaik, *J Materials*, **229**, 91 (2015).
24. V. Kukshal, S. Gangwar, A. Patnaik, *J Materials: Design and Applications*, **0**, 1 (2013).
25. V. Rizov, *Fracture and Complexity*, **8**, 153 (2013/2014).
26. V. Kumar, A. Ghosh, *Theoretical and Applied Fracture Mechanics*, **75**, 22 (2015).

ЧИСЛЕН АНАЛИЗ НА ПОВЪРХНОСТНИ ПУКНАТИНИ ПРИ СФЕРИЧНИ ЕКСПЛОЗИВИ С АМОРТИСЬОР

Г. Женжи^{1,2}, Х. Бин¹, Г.З. Минг¹

¹*Ксиан Хай-Тек изследователски институт*

²*NO.96401 Force*

Постъпила на 30 февруари, 2016 г.; коригирана на 26 октомври, 2016 г.

(Резюме)

Експлозивите се използват широко във военното инженерство. Тук са изследвани характеристиките на пукнатините в експлозивите, факторът на интензивност на напрежението и J-интеграла на РВХ-компонентите. Изследван е механизмът на влияние на пукнатините при различни условия. Резултатите показват, че формата на пукнатината при различно положение на компонентите е различна, заедно със здравината на пукнатината.

Факторът на интензивност зависи от положението на пукнатината, дължината, дълбочината и направлението ѝ.

Research on the mechanism for chemical clogging and its effect on the stability of tailing dam

G. Wang^{1,2*}, Y. Gao¹, Y. Tang¹

¹Kunming University of Science and Technology, 650093 Kunming, China

²Institute of Rock and Soil Mechanics, Chinese Academy of Science, 430071 Wuhan, China

Received March 9, 2016; Revised November 7, 2016

The stability of tailing dam has an important influence on the surrounding ecological environment and the security and property of people. This article, from the micro perspective, analyzes of the water-tailing chemical interactions and process and analyzes its effects on tailing micro structure and dam stability. The experimental results show that ferrous iron in water (PH=9.5-10.3) is constantly in contact with the air and then produces a series of reactions such as oxidation, eventually becomes a clogging substance what mainly include Fe(OH)₃; the chemical clogging substances mainly include Fe(OH)₃, some cements and strong adsorption humus groups that will block the pore channels and absorb the ions or tailings in water to form a larger group that accumulating in porous media and drain mouths will result in poor seepage and affect its permeability; The chemical clogging can reduce the stability of tailing dam. Those researches of chemical process of tailing dam will provide directions references for tailing dam security-research and the improvement of tailing dam water-environment.

Keywords: Tailings dam, chemical clogging, tailing micro structure, stability

INTRODUCTION

Accidents with tailing dam breaching have occurred from time to time in recent years that not only cause enormous economic losses and casualties, but also cause serious environmental pollution and ecological destruction. Studying the mechanism of tailing dam breaching and analyzing the factors influencing dam stability will be of great importance to ensure that the tailing dam will be exploited safely and stably avoiding or reducing the occurrence of probable disasters thereby reducing the inevitable economic losses. A tailing dam is a structure not only storing tailings but also storing tailing water so that water is an important and influential factor as regards dam breach accidents and also an important factor that renders the geotechnical engineering problems more complex. Chemical reactions within the tailing dam, such as the precipitation and crystallization, produce a range of chemical substances that can jam the tailing dam pore channels, for instance sludge plugging, this will influence the dam drainage performance and reduce the safety of the tailing dam. The researches of water-soil interaction, Qiao Juan and Luo Xianqi [1] discussed the water effects on dam breach and made the following conclusion: the water effects on a dam mainly include the

increasing downslope slope strength and reducing slope shear strength; Liu Jifeng [2] researched the change in the laws of slope soil cohesion and the internal friction angle for different water contents and the experiment showed that the internal friction angle (φ) appears to show a downward trend in the form of an exponential function with a water content upward trend and the cohesion appears as a trend first to increase and then to decrease in the form of a Gaussian function with the water content upward; Qin Huali [3] expounded the two ways the water acts on the dam slope and discussed the water effect on the stability of the dam body and its action mechanism; Xing ye [4] and Ma chixiang [5] studied the effect of combining the water-soil coupling interaction with an analysis of tailing dam stability and studying the water-soil coupling interaction of the tailing dam; Zandarina [6], Wang Feiyue [7], Yan Qiong [8] and Hu Jingyou [9] studied the seepage and stress fields of mine granular material and built an equation and calculation model considering tailing dam fluid-solid coupling at different conditions; Zhen Xunzhen [10] built a dam deformation model considering the chemistry, seepage and stress fields coupling and studied in depth the nonlinear compressibility-permeability mathematical model of dam deformation; Feng Xiating [11] built the convection-diffusion-reaction model considering the water-rock system based on the chemical kinetics theory, the solute transport theory and

* To whom all correspondence should be sent:
E-mail: wangguangjin2005@163.com

applied porosity to quantitatively describe the rock microstructure changes caused by the water-rock interaction; Zhang Xingui [12], from the chemical perspective, analyzed the chemical reactions following the water-soil interaction and analyzed the changes in the soil microstructure; Van Gulck [13] studied the mechanism of chemical and biological clogging in the dam porous media through researching the testing column; Rowe and Mclsaac [14] researched the debris-sand clogging phenomenon with solution permeating testing columns.

At present, many researches on stability of tailing dam mainly focus on the dam seepage and the water-soil physical interaction, but researches on water-soil chemical interaction are relatively fewer, So this article analyze the chemical reactions process at the condition of tailing dam specific water-environment, further discussing the clogging mechanism, the main clogging materials and the interactions between sludge plugging and seepage. Researches of chemical process in a dam not only provide directions for tailing dam security-research, but also provide references for improving the tailing dam water-environment and analyzing the chemical action effects on the tailing microscopic structure and the tailing dam stability. Researches of chemical process in a dam not only provide directions for tailing dam security-research, but also provide references for improving the tailing dam water-environment.

RESEARCH AND ANALYSIS ON CHEMICAL CLOGGING MECHANISM

Studying the tailing dam clogging problems, the key is to reveal the conditions, material sources and chemical reaction process of chemical clogging. With the aid of this research, we first collect relevant chemical data about tailing dam and other dam buildings, then forecast the contingent chemical clogging problems, thus providing a theoretical basis for the prevention and control of the engineering problems. Table 1 and table 2 list the main chemical composites of copper-lead-zinc ore tailings and tailing water (PH=9.5-10.3) .

Table 1. Main chemical composites of original tailing (% -mass percentage).

Sample 1 (original tailing)											
Element	Mg	Al	Si	S	K	Ca	Mn	Fe	Cu	Zn	
Content	0.20	9.40	30.4	1.43	3.34	0.27	0.24	3.61	0.01	0.19	
Sample 2 (original tailing)											
Element	Mg	Al	Si	S	K	Ca	Mn	Fe	Cu	Zn	
Content	0.31	7.30	29.3	1.27	4.12	0.18	0.30	4.17	0.03	0.16	

Table 2. Main chemical composites of tailing water (mg/L).

Sample 1 (tailing water)										
Ion	Fe ³⁺	Mg ²⁺	SO ₄ ²⁻	CO ₃ ²⁻	Cl ⁻	Ca ²⁺	Na ⁺	Al ³⁺	K ⁺	Zn ²⁺
Content	0.07	0.15	0.78	7.16	0.01	275	33.7	0.35	57.5	0.04
Sample 2 (tailing water)										
Ion	Fe ³⁺	Mg ²⁺	SO ₄ ²⁻	CO ₃ ²⁻	Cl ⁻	Ca ²⁺	Na ⁺	Al ³⁺	K ⁺	Zn ²⁺
Content	0.10	0.23	0.54	6.14	0.01	210	25.6	0.27	49.6	0.08

Table 3. Main composites of clogging matter (% -mass percentage).

Sample 1 (tailing before clogging)										
Element	Mg	Al	Si	S	K	Ca	Mn	Fe	Cu	Zn
Content	0.25	15.3	27.6	1.32	3.32	10.13	0.34	4.76	0.01	0.11
Sample 2 (tailing before clogging)										
Element	Mg	Al	Si	S	K	Ca	Mn	Fe	Cu	Zn
Content	0.31	2.70	25.2	0.96	3.56	12.85	0.27	5.35	0.04	0.13

From table 1 above, the main chemical composites of copper-lead-zinc ore tailings are Fe, Al, Si, Mg, K, S, but the Cu and Zn are less; Table 2 shows that the main chemical composites of tailing water are Ca²⁺, K⁺, Na⁺, CO₃²⁻ with a relatively smaller content of Mg²⁺, SO₄²⁻, Cl⁻. Analyzing the clogging substances, the main composites are listed in table 3.

From table 3, it is apparent that the matter containing Fe is more and accounts for almost all of the entire matter clogging. Meanwhile we must combine with the analysis of the XRD spectra of the clogging matters. In XRD, in order to confirm the existence of a material, we need to view whether the analysis line and the peak center of XRD line is closer, if closer, we will think the material existing. Combine with figure 1, the analysis line of Fe(OH)₃ is much closer with the peak center of XRD line, so we can determine that the main clogging material is Fe(OH)₃.

Both of Figure 2 and Figure 3 are the pictures of tailing SEM scans and reflect the characteristics of tailing surface. Figure 2 reflects the attached particles on tailing surface, such as sand, silt, clay. Figure 3 reflects the changes of tailing surface characteristics before and after chemical clogging. Before chemical clogging, the tailing surface is smooth and its attachments are less, but after chemical clogging, the tailing surface presents clustered structure and becomes more rough.

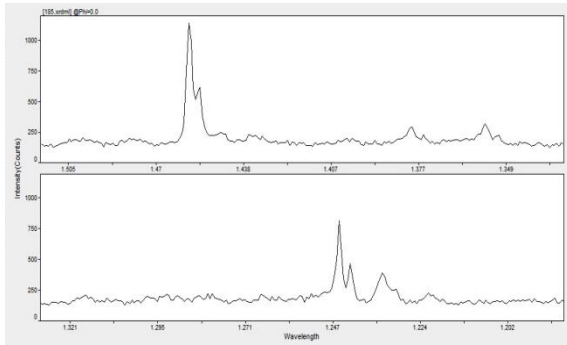


Fig. 1. XRD spectra of clogging matter.

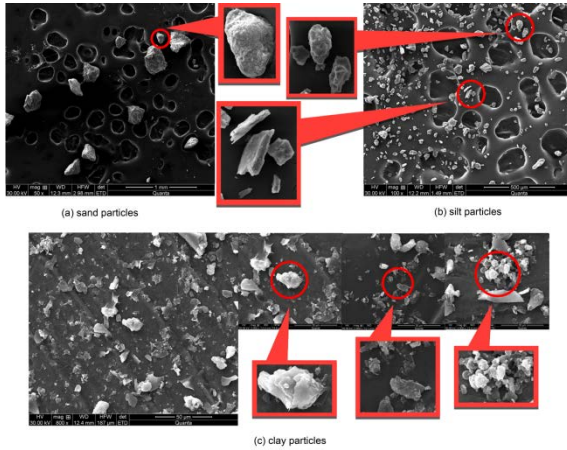


Fig. 2. Tailings SEM scans

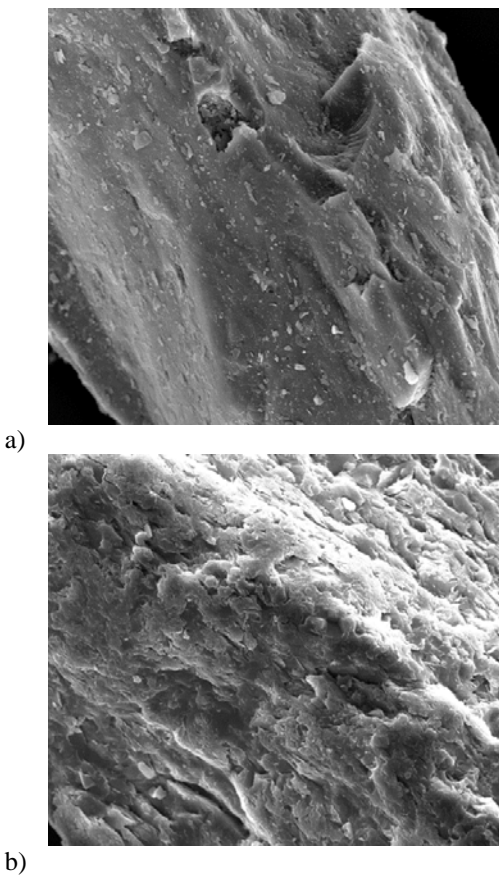
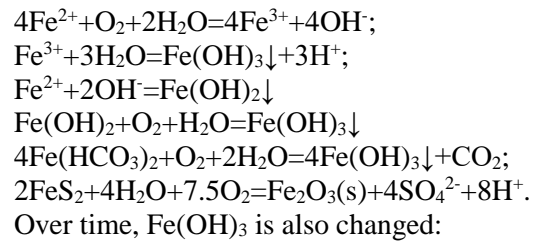


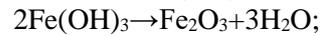
Fig. 3. The microscopic surface of tailing: a) Common tailings; b) Tailings of chemical clogging.

By detecting copper-lead-zinc ore in tailing dam, it was found that the dam is in a good reducing condition so that iron exists mainly in a ferrous form. In accordance with the above analysis of the clogging materials, we know the main component of the clogging material is $\text{Fe}(\text{OH})_3$. Therefore, the mechanism of chemical clogging within the tailing dam is: ferrous iron in water (PH=9.5-10.3) is constantly in contact with the air and produces a series of reactions such as oxidation, eventually becomes a blocking substance with $\text{Fe}(\text{OH})_3$ as the main clogging matter. The clogging substances accumulate in porous media and drain mouths that will result in poor seepage and affect its permeability.

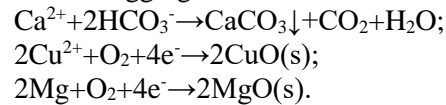
According to the above analysis of copper-lead-zinc ore chemical clogging substance and the wholesome clogging process, the main chemical processes occur in the molybdenum mine tailing dam:



Over time, $\text{Fe}(\text{OH})_3$ is also changed:



In addition to Fe, the tailing water also contains Ca, Cu, Mg and other elements that are in a free state in the dam, when contacting the oxidizing environment, these will generate insoluble materials; condensation cements manufactured by OH^- ions and certain metal cations not only embodying the tailing particles, but also adsorbing other ions in solution that is an important reason for chemical clogging.



In addition the above main chemical reactions, since the tailing dam site are found near mountains, and the tailing water has chemical properties, so some animals and plants die under a cover of tailings, over time, these decomposed and form humus. Humus has a strong chelating effect and can combine organic substances in water by means of Van der waals force, the electrostatic interaction and hydrogen bonding interaction between metal ions and the ion bridge bond, when the water-environment is close to PH=9-10, the plant auxin can combine with humus by the bridge bond roles of some transition metal ions or some common metal ions (Ca^{2+}). The humus in the tailing dam can also combine with clay minerals by Fe^{3+} and Ca^{2+} .

Fulvic acid, the main component of humus, can combine with metal ions and organic matter in a dam by physical and chemical action and form groups with stronger adsorption ability. The whole process of dam chemical clogging can be expressed in the following figure 4:

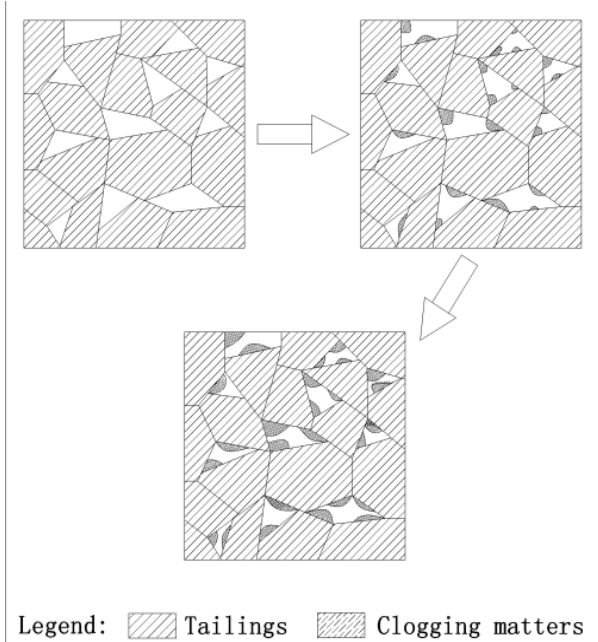


Fig. 4. Porosity changes over time.

From Figure 4 above, with tailings increasing, the chemical matter in the dam is replenished constantly so the chemical reactions taking place will be an ongoing process. The ongoing chemical reactions produce more chemical clogging matter, from the micro structure and the dam pore channels get narrower. Based on the above analysis, the chemical clogging substances mainly include $Fe(OH)_3$, some cements and strong adsorption humus groups that will jam the pore channels and absorb the ions or tailings in water to form a larger group. Tiny particles are the main product as a result of the physical clogging, since the chemical clogging makes the pore channels narrower, the original tiny particles can no longer cross the same channels and the long-term accumulation of fine materials will reduce the dam permeability.

ANALYSIS OF DAM STABILITY

Chemical clogging substances block pore channels by attachment and settlement so that increases the solution flow resistance in porous media and reduces the material migration ability in dam porous media, in addition, it can also change the micro structure of the tailings.

Influence of chemical clogging on the permeability coefficient

According to Darcy the empirical formula [15]:

$$Q = kiAt = k \frac{H}{L} At \quad (1)$$

$$k = \frac{QL}{HA t} \quad (2)$$

L -water permeation through the thickness of the soil; Q -seepage flow; t -seepage time; H -the upper and lower water surface height difference; A- the cross sectional area; k -the permeability coefficient.

Chemical clogging causes the resistance of the tailings water flow in the porous medium to increase resulting in a reduction of the seepage flow Q per unit time, with the seepage time increasing, according to the formula (2), the permeability coefficient k shows a trend to decline in the case of chemical clogging.

Influence of chemical clogging on volume-weight

Because the chemical clogging jams the inner pore channels of the tailing dam, it results in a decrease of the material migration ability in the pore channel and leads to the pore channel within tail ore per unit volume being blocked by the materials that do not migrate in time, causing an increase in the tail ore density per unit volume. In accordance with the above formula, we can come to the conclusion that the tail ore density γ increases in the case of chemical clogging.

The expression for the formula of the gravity density is:

$$\gamma = \rho g \quad (3)$$

ρ -Soil density; g -Soil gravity acceleration

Influence of chemical clogging on the cohesion and internal friction angle

According to the soil test¹⁶, the soil shear strength is expressed as a function of the normal total stress on the shear failure surface in Coulombs and the following general expression is put forward as suitable to evaluate cohesive soil:

$$\tau_f = c + \sigma \tan \varphi \quad (4)$$

τ_f -shear strength; σ -total stress; c -soil cohesion; φ -soil internal friction angle.

By means of Coulomb's law, the indexes which characterize the shear strength of tailing include the tailing internal friction angle and cohesion: the rougher the particle surface is, the higher the density is, so the larger the soil internal friction coefficient $\tan \varphi$ is; the cohesion between tailing particles depends on the connectivity between the

particles and is related to the forces between these and the chemical reactions generated. As can be observed from figure 3, the surface roughness of the tailings increases after the chemical clogging, moreover, the chemical clogging reduces the material migration ability of the porous media, so it also makes the density of the tailings per unit volume increase. Finally, this may cause an increase in the internal friction coefficient $\tan \varphi$ and the combination of both affects the tail ore shear strength.

Influence of chemical clogging on stability of tailing dam

At the scene retrieved tailing samples include mainly the common tailings and the tailings at the clogging location. The saturated infiltration coefficient is measured by taking a constant head permeation test. The cohesion and internal friction angle are measured by a shear strength test. In addition, it also includes other tests, such as: density, volume-weight. The relevant key parameters for the molybdenum starter dam are chosen from similar earth-rock dam survey data¹⁷ and the parameters of the shear strength of the saturated tailings chosen from the literature¹⁸. Other relative parameters get from indoor soil tests. All the needed parameters are shown in the following table 4.

Table 4. Physical and mechanical parameters of the tailings.

Material	γ (kN/m ³)	c(kPa)	φ (°)
Initial tailing dam	24.6	28.18	36.3
Medium tailing	26.4	13.9	31.3
Clogging matter	26.9	15.1	25.2
Fine tailing	26.7	0.64	19.5
Silty tailing	27.6	0.32	14.3

γ -Unit weight; c -Cohesion; φ -Internal friction angle.

Table 5. Stability coefficient of the tailing dam

State	Ordinary	Bishop	Janbu
Bc	1.181	1.357	1.216
Ac	1.047	1.057	1.047

Note: Bc -before clogging; Ac -after clogging

The stability of a tailing dam before and after chemical clogging is analyzed by slide5.0 and the whole tailing dam model is divided into four different materials: starter dam, medium tailing, fine tailing, silty tailing (from left to right) as illustrated in figure 5.

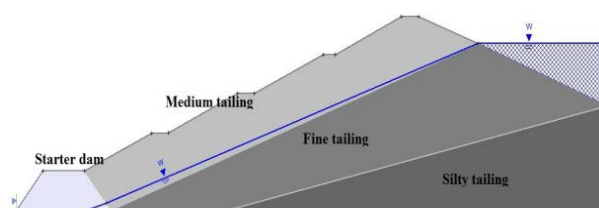


Fig. 5. Calculation section of tailing dam stability.

Clogging occurs mainly in the model corresponding to the position of medium tailing. When analyzing the stability of a tailing dam in the case of chemical clogging, the parameters of medium tailing were replaced by the parameters of clogging materials. The results after analyzing the dam stability are listed in table 5. From table 5, we can study, regardless of the ordinary method, the Bishop simplified method or Janbu simplified method, that the stability coefficient after clogging is smaller than before clogging and also it shows that the chemical clogging can influence the safety and stability of the tailing dam and the trend to reduce the direction.

In fact, chemical clogging occurs in a part of medium tailing area so the actual safety coefficient is higher than for the model, but it is still lower than in the case of chemical clogging.

CONCLUSION

Through the indoor soil test and mathematical model analysis, we study:

- (1) Ferrous iron in water(PH=9.5-10.3) is constantly in contact with the air and produces a series of reactions such as oxidation, eventually becomes a blocking substance with Fe(OH)₃ as the main clogging component.
- (2) The chemical clogging substances mainly include Fe(OH)₃, some cements and strong adsorption humus groups that will jam the pore channels and absorb the ions or tailings in water to form a larger group that accumulate in porous media and drain mouths will result in poor seepage and affect its permeability.
- (3) The surface roughness of the tailings increases after the chemical clogging, moreover, the chemical clogging reduces the material migration ability of the porous media, so it also makes the density of the tailings per unit volume increase. Finally, this may cause an increase in the internal friction coefficient.
- (4) The chemical clogging can reduce the stability of tailing dam.
- (5) Complex chemical environment is the precondition of the chemical clogging, so strengthening monitor on the water environment of

tailing dam will contribute to the study on the stability of tailing dam.

Acknowledgements: The authors acknowledge the collective support granted by the National Natural Science Foundation of China (Grant No 41602307, Grant No 51234004), Key laboratory for open issues (Grant No Z014012), School-enterprise funds (No KKZ4201221008), Yunnan Province Project Education Fund (Grant No KKJD201521003), Yunnan Copper Group School-enterprise funds (Grant No KKZ4201521005, the technology projects of key technologies with the major accident of safety production in 2016 (Grant No yunnan-001-2016AQ).

REFERENCES

1. J. Qiao, X.Q. Luo, *Disaster and Control Engineering*, 39 (2005).
2. J.F. Liu, M.S. Lu, *The Journal of Henan University of Science and Technology (Natural Science Edition)*, 31, 63 (2010).
3. L.H. Qin, C.X. Ma, *METAL MINE*, 116 (2008).
4. Y. Xing, Analysis of the influence of water-soil coupling interaction on the stability of tailing dam, Northeastern University, Shenyang, China, 2009.
5. C.X. M, Analysis of seepage field and research of the principle of water-soil interaction in tailing dam, Northeastern University, Shenyang, 2008.
6. M.T. Zandarin, L.A. Oldecop, R. Rodriguez, *Engineering Geology*, 105, 108 (2009).
7. Y.F. Wang, K.T. Yang, Z.S. Xu, Y.J. Jin, *Rock and Soil Mechanics*, 30, 840 (2009).
8. Q. Yan, S.C. Wu, L. Li, Q.Z. Wang, *METAL MINE*, 5 (2015).
9. J.Y. Hu, L.L. Wu, M.L. Yan, Z. Tang, J.B. Xie, *Journal of Water Resources Architectural Engineering*, 13, 126 (2015).
10. X.X. Zheng, Research of tail deformation coupling model under the action of chemistry-stress-seepage, fuxin, Liaoning Technology University, Liaoning, 2013.
11. Q. Cui, X.T. Feng, Q. Xue, H. Zhou, Z.H. Zhang, *Chinese Journal of Rock Mechanics and Engineering*, 27, 1209 (2008).
12. X.G. Zhang, N.P. Yi, H. Wu, *Geological Journal of China Universities*, 12, 242 (2006).
13. J.F. VanGulck, R.K. Rowe, *Journal of Contaminant Hydrology*, 75, 115 (2004).
14. R.K. Rowe, R. Mclsaac, *Journal of Geo-technical and Geo-environmental Engineering*, 131, 682 (2005).
15. G.X. Li, Advanced soil mechanics, Tsinghua university press, Beijing, 2004.
16. K.G. Zhang, S.Y. Liu, Soil mechanics, China architecture & building press, 2010.
17. T.S. Wo, Y.S. Wang, C.B. Xiao, W.Q. Tian, B.J. Yang, Tailing dam manual, Metallurgical industry press, Beijing, 2013.
18. K.J. Wan, C.X. Yu, J.T. Chen, D.A. Chen, *Resources Environment & Engineering*, 28, 155 (2014).

АНАЛИЗ НА ВЛИЯНИЕТО НА ХИМИЧЕСКОТО ЗАДРЪСТВАНЕ И ПРОСМУКВАНЕ ВЪРХУ СТАБИЛНОСТТА НА ХВОСТОХРАНИЛИЩАТА

Г. Уанг^{1,2*}, И. Гао², И. Танг¹

¹Институт по геомеханика, Китайска академия на науките, 430071 Ухан, Китай

²Университет за наука и технологии в Кунминг, 650093 Кунминг, Китай

Постъпила на 9 март, 2016 г.; коригирана на 7 ноември, 2016 г.

(Резюме)

Устойчивостта на стените на хвостохранилищата има много важно значение за околната среда, ловешкия живот и сигурност. Химичните процеси в хвостохранилището, като утаяване и кристализация произвеждат много химични вещества, които могат да запушат порите на каналите (т.е. задръстване с тиня). По този начин се влияе на режима на източване на хранилището и се застрашава безопасността му. В специфичната хидрохимична обстановка микроструктурите са важен фактор за безопасността на хранилището, а макро-явленията (подаване или скъсване на стената) се отразяват на микро-структурата. В тази работа се анализират химичните ефекти във взаимодействието вода-почва, свързващата роля на микроструктурата, на взаимодействието вода-хвост, както и ефектите върху физични и механични параметри, като коефициента на проникваемост, обемната плътност, кохезия и пр.. В резултат на всичко това се прави анализ за стабилността на хвостохранилището.

Material composition detection using an image segment with an improved artificial bee colony algorithm

L. Sun, X. Liang, Q. Wang, H. Chen*

*School of Computer Science and Software Engineering, Tianjin Polytechnic University,
Tianjin 300387, China*

Received December 21, 2016; Revised October 7, 2016

In the process of material composition detection, image analysis is an inevitable problem. Multilevel thresholding based on the OTSU method is one of the most popular image segmentation techniques. The increase of the number of thresholds increases with the exponential increase in computing time. In order to overcome this problem, this paper proposes an artificial bee colony algorithm with a two-level topology. This improved artificial bee colony algorithm can quickly find the suitable thresholds without the trap of a local optimum. The test results confirm the good performance.

Keywords: Image segment; Artificial Bee Colony; Material Composition Detection

INTRODUCTION

The target of image segmentation is to extract meaningful objects from the image. Segmentation is of major importance and holds an elementary place in image processing for image interpretation. It is useful in the discrimination of an objective from other objects or the background.

In recent years, researchers proposed many methods for image segmentation. Among the existing segmentation techniques, multilevel threshold is a simple but effective tool to isolate the objects of interest from the background, which requires multiple threshold values to achieve segmentation [1]. Several such methods have originally been developed for bi-level thresholds and later extended to multilevel thresholds as described in [2]. However, all of these methods have a common problem, that the computational complexity rises exponentially when extended to multilevel thresholds due to the exhaustive search employed, which limits the multilevel threshold applications.

Recently, to address this issue, several swarm intelligence (SI) algorithms such as powerful optimization tools have been introduced to the field of image segmentation owing to their predominant abilities of coping with complex nonlinear optimizations [3]. Among them, the artificial bee colony algorithm (ABC) is one of the most popular members of the SI family, which simulates the social foraging behavior of a honeybee swarm [4]. Due to its simple arithmetic and good robustness, the ABC algorithm has been widely used in solving many numerical optimizations and engineering

optimization problems. However, when solving complex multimodal problems, the ABC algorithm suffers from the following drawbacks: (1) It is easily trapped into a local minimum in early generation, which leads to a low population diversity in successive generations. (2) With the dimension increasing, the information exchange of each individual is limited to a random dimension, resulting in a slow convergence rate. (3) Due to the random selection of the neighbor bee and dimensions, food sources with higher fitness are not utilized, which influences the global search ability.

In this paper, we propose an improved artificial bee colony algorithm with a two-level topology controlling the information exchange. The experimental results confirm its' good performance.

The rest of the paper is organized as follows. In Section 2 the proposed hierarchical artificial bee colony is presented. Section 3 presents the experimental studies of the improved artificial bee colony algorithm and the other algorithms with descriptions of the involved benchmark functions, experimental settings and experimental results. Its application in image segmentation has been presented in Section 4. Finally, Section 5 outlines the conclusion.

IMPROVED ARTIFICIAL BEE COLONY ALGORITHM

Canonical artificial bee colony algorithm

The artificial bee colony (ABC) algorithm, proposed by Karaboga in 2005 [4] and further developed by Basturk and Akay et al. [5, 6] for real-parameter optimization, simulates the intelligent foraging behavior of a honeybee swarm, as one of the most recently introduced swarm-based optimization techniques.

* To whom all correspondence should be sent:
E-mail: perfect_chn@hotmail.com

The entire bee-colony contains three groups of bees: employees, onlookers and scouts. The employee bees explore the specific food sources; meanwhile passing the food information to the onlooker bees. The number of employee bees is equal to the number of food sources, in other words, each food source is owned by only one bee employee. Then the onlooker bees choose the good food sources based on the information received and then further exploit the food near their selected food source. The food source with a higher quality would have a greater opportunity of being selected by the onlookers. There is a control parameter called “*limit*” in the canonical ABC algorithm. If a food source is not further improved when the *limit* is exceeded, it is assumed to be abandoned by its employee bee and the employee bee associated with that food source becomes a scout beginning to randomly search for a new food source.

Hierarchical Artificial Bee Colony Algorithm with a Two-level Topology (HABC)

In our model, cooperation occurred at two levels, the species level (interaction between the species) and the individual level (interaction within the species). Two hierarchical interaction topologies have been employed in this paper to realize this two-level cooperative mechanism. The first topology (namely the 2-level star topology, is shown in Fig. 1(a)), each individual is influenced by the performance of its own species and all the other species in the ecosystem. In the second topology (namely the 2-level ring topology, as shown in Fig. 1(b)), each individual is influenced only by *n* closest neighbors from its own species and the other *n* species from the ecosystem.

The main steps of the proposed algorithm are summarized as follows: In accordance with the constraints and dimensions of the search problems, the stochastically generated *M* species and each species owns *N* individuals with *D* dimensions. According to the selected topological structure, determine the neighbor individuals of each individual in its own species and the neighbor species of its own species for later information communication. The flow of the proposed artificial bee colony algorithm is shown in Fig. 2.

EXPERIMENTAL STUDY

In this experiment, we compared four variant versions of the Hierarchical Artificial Bee Colony Algorithm with a Two-level Topology and a canonical ABC algorithm.

Table 1 shows the basic statistical results (i.e., the mean and standard deviations of the function values found in 30 runs) of the 30D benchmark test functions—griewank, rastrigin, rosenbrock and ackley. Obviously, the canonical ABC algorithm demonstrates the worse performance as compared to the other four algorithms. The ABC’s variants outperform the canonical ABC algorithm. The ABC algorithm with the star colony and the star swarm is comparatively good amongst these algorithms. The results of the ABC algorithm with the ring colony and the star swarm are also competitive. The two variants of the ABC algorithm with the ring colony and the ring swarm and ABC algorithm with the star colony and the ring swarm yield nearly the same results. This is attributed to the topological structure of the upper level and lower level both with a star scan to improve the convergence rate.

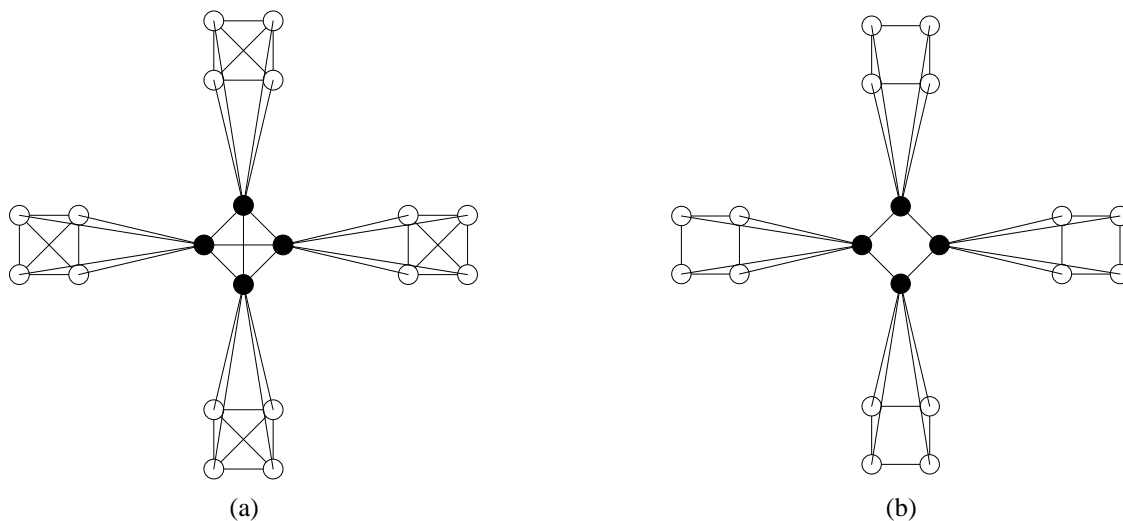


Fig. 1. Two-level interaction topologies: (a) Hierarchical star topological structure (b) Hierarchical ring topological structure.

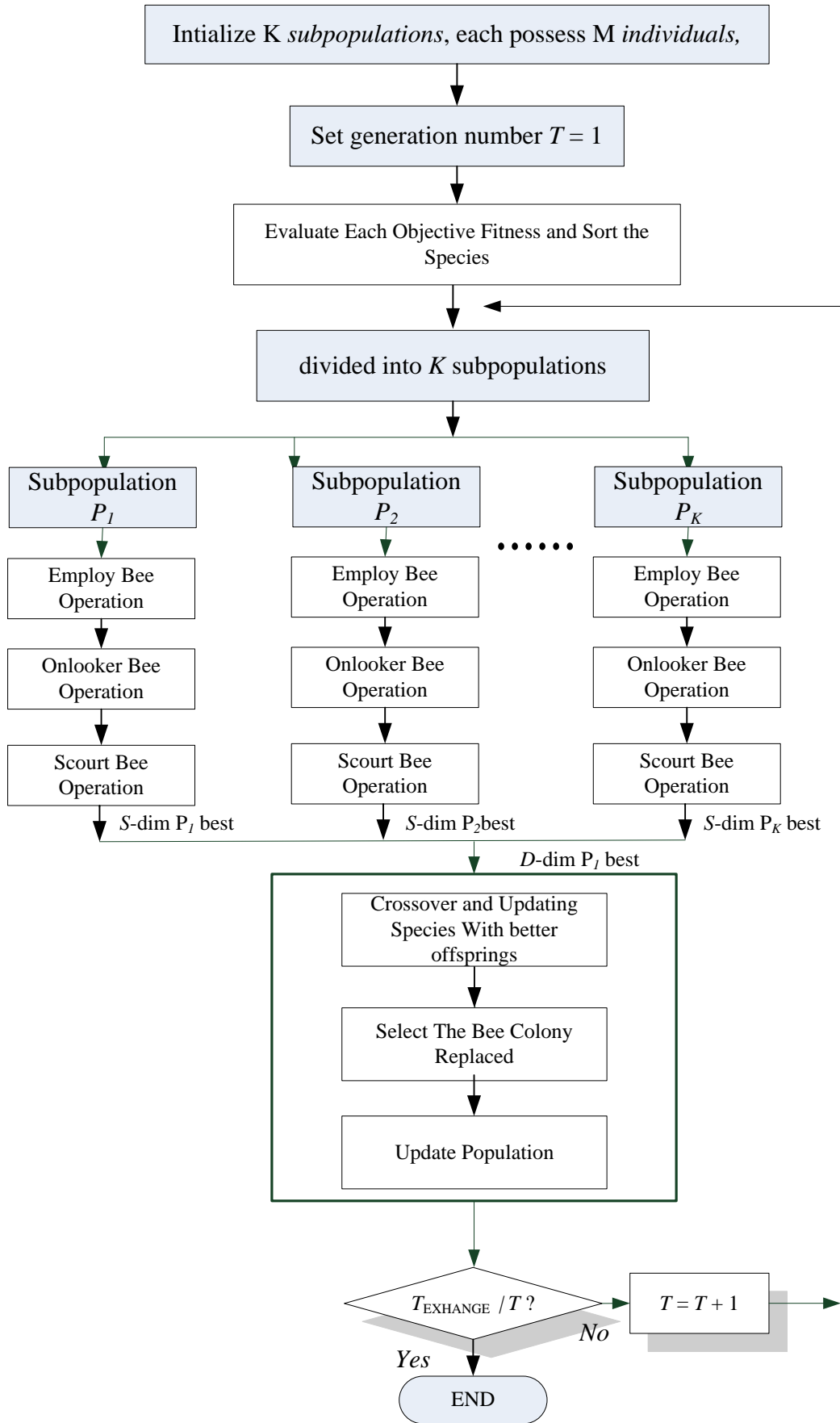


Fig. 2. The flowchart of the proposed artificial bee colony algorithm.

Table 1. Results for all multi-colony algorithms (ring) on benchmark functions.

Function	Criteria	ABC_	colony= ring	colony= star	colony= star	col= ring
	D=30	original	swarm=star;	swarm=star;	swarm=ring	swarm=ring
griewank [-600,600]	Mean	3.5273e-002	2.0072e-002	1.6706e-002	1.8036e-002	2.9307e-002
	Best	2.0460e-002	1.2149e-002	9.9191e-004	4.6484e-003	2.1519e-009
	Worst	1.1344e-001	1.9317e-001	7.5833e-002	1.1030e-001	1.8270e-002
	Std	2.9923e-002	3.0132e-002	6.1813e-003	5.3601e-003	2.0087e-002
rastrigin [-15,15]	Mean	2.3766e+000	1.3091e+001	1.4505e+001	1.5822e+000	7.0624e+001
	Best	7.3355e-001	2.3292e-001	2.1183e+000	3.9955e-001	4.3973e-001
	Worst	8.7333e+000	6.9749e+000	2.4977e+001	7.1948e+000	1.5009e+001
	Std	2.2283e+000	2.3365e+000	6.1069e+000	2.1939e+000	3.8349e+000
rosenbrock [-15,15]	Mean	5.5504e+001	8.0374e+001	2.3365e+001	1.2928e+001	4.5391e+001
	Best	1.0025e+001	1.5002e+001	5.1353e+000	1.8746e+000	1.0252e+001
	Worst	7.5467e+001	1.7651e+002	3.4417e+001	1.9675e+001	6.7366e+001
	Std	2.0495e+001	1.1712e+002	1.1957e+001	1.0906e+001	2.5445e+001
ackley [-32.768,32.768]	Mean	4.6581e-002	3.1423e-001	1.4241e-002	9.0066e-001	3.0116e+000
	Best	5.3002e-003	5.8978e-002	2.0973e-003	4.3395e-002	9.3130e-001
	Worst	9.2545e-002	4.2501e-001	8.3362e-002	3.2369e+000	9.6034e+000
	Std	4.2248e-002	1.7765e-001	3.4167e-002	8.1111e-001	2.1700e+000

Table 2. Objective values and thresholds by the Otsu method.

Image	M-1=2		M-1=3		M-1=4	
	Objective values	Optimal thresholds	Objective values	Optimal thresholds	Objective values	Optimal thresholds
avion	3.4445E4	108,167	3.4583E4	92,146,192	3.4543E4	83,130,174,206
house	2.8486E4	106,178	2.8623E4	86,138,182	2.8576E4	72,116,155,184
lena	1.7784E4	95,156,	1.7764E4	812,129,173	1.7834E4	76,111,143,183
Mean CPU time	1.4427		61.421		2644.543	

Multilevel threshold for image segmentation

The Otsu multi-threshold entropy measure [7] proposed by Otsu has been popularly employed to determine whether the optimum threshold method can provide image segmentation with satisfactory results. Here, it is used as an objective function for the involved algorithms and its process can be described as follows:

Let the gray levels of a given image range over $[0, L-1]$ and $h(i)$ denote the occurrence of gray-level i .

Let

$$N = \sum_{i=0}^{L-1} h(i), P(i) = h(i) / N \text{ for } 0 \leq i \leq L-1 \quad (1)$$

$$\text{Maximize } f(t) = w_0 w_1 (u_0 - u_1)^2 \quad (2)$$

$$\sigma(t) = w_0 \times \sigma_0^2 + w_1 \times \sigma_1^2 + \dots w_N \times \sigma_N^2 \quad (3)$$

$$\delta_0 = \sum_{i=0}^{t-1} (i - u_0)^2 \times P_i / w_0$$

$$\delta_1 = \sum_{i=t}^{L-1} (i - u_1)^2 \times P_i / w_1 \quad \delta = \sum_{i=0}^{L-1} (i - u)^2 \times P_i / w$$

$$w = \sum_{i=0}^{L-1} P_i \quad u = \sum_{i=0}^{L-1} i \times P_i / w$$

Expand this logic to a multi-level threshold

$$f_{12}(t) = w_0 \times \delta_0^2 + w_1 \times \delta_1^2 + w_2 \times \delta_2^2 + \dots + w_1 \times \delta_N^2$$

where N is the number of thresholds. The above function is used as the objective function to be optimized (minimized).

The experimental evaluations for segmentation performance by HABC are carried out on a wide variety of image data sets. These data sets involve a set of popular tested images used in previous studies, namely avion.ppm, house.ppm, and lena.ppm [8]. Table 2 presents the fitness function values, mean computation time and corresponding optimum thresholds (with $M-1 = 2, 3, 4$) obtained by Otsu. Due to that when $M-1 > 4$ the consumption of CPU time is too long to bear, the correlative values are not listed in our experiment. It is noteworthy that the term CPU time is also an important issue in the real-time applications.

As can be seen form Table 3, the proposed algorithm with the ring colony and the ring swarm generally perform close to the Otsu method in terms of the fitness value when $M-1=2,3,4$, whereas the performance of the improved ABC on the time complexity is significantly superior to its counterpart Otsu. In other words, the proposed algorithm consumes less computing time than the traditional one. This is mainly due to the fact that the crossover-based social learning strategy used in the proposed algorithm has a faster convergence speed. Furthermore, the HABC-based algorithm in most cases achieves the best performance among the population-based methods. This can be explained by the HABC two-level ring topology and high convergence rate.

CONCLUSION

In this paper, we propose a novel hierarchical artificial bee colony algorithm with a two-level topology to improve the performance of solving complex problems. The concept and main idea extends the single artificial bee colony algorithm to the hierarchical and cooperative mode by combining the multi-population cooperative co-evolution approach. The proposed algorithm is applied to solve image segmentation. The experimental results show that the proposed algorithm performs well to segment images for material composition detection.

REFERENCES

1. J. Kittler, J. Illingworth, *Pattern Recognition*, **19**, 41 (1986).
2. T. Pun, *Computer Vision Graphics Image Processing*, **16**, 210 (1981).
3. A. Chander, A. Chatterjee, P. Siarry, *Expert Systems with Applications*, **38**, 4998 (2011).
4. D. Karaboga, An idea based on honey bee swarm for numerical optimization, Technical Report-TR06, Erciyes University, Engineering Faculty, Computer Engineering Department, 2005.
5. D. Karaboga, B. Basturk, *Applied Soft Computing*, **8**(1), 687 (2008).
6. D. Karaboga, B. Basturk, in: P. Melin, et al. (Eds.), *IFSA 2007, LNAI 4529, 2007*, p. 789.
7. N. Otsu, *IEEE Transactions on System, Man, and Cybernetics*, **9**, 62 (1979).
8. <http://decsai.ugr.es/cvg/dbimagenes>

ОПРЕДЕЛЯНЕ СТРОЕЖА НА МАТЕРИАЛИ ПО СЕГМЕНТИ НА ОБРАЗИ С ПОМОЩТА НА АЛГОРИТЪМ „ИЗКУСТВЕНА ПЧЕЛНА КОЛОНИЯ

Л. Сун, Х. Лианг, К. Ванг, Х. Чен*

Училище по компютърни науки и софтуерно инженерство, Политехнически университет в Тянджзин 300387, Китай

Постъпила на 21 декември, 2016 г.; коригирана на 7 октомври, 2016 г.

(Резюме)

Анализът на образи е неизбежен проблем при разкриването на строежа на материали. Един от най-популярните методи за сегментирането на образи е многостепенният OTSU-метод. С нарастване броя на степените времето за изчисления нараства експоненциално. За преодоляването на този проблем в настоящата работа се предлага алгоритъма „изкуствена пчелна колония“ с топология на две нива. Този алгоритъм може бързо да намери подходящия брой прагове, почти без попадане в локален оптимум.

Friction stir welding automatic effect on building the microstructure and properties of high nickel steel

L.L. Ping^{1*}, Y.J. Tao²

¹College of Information Engineering, Hebei United University, Tangshan 063009, China

²Hebei Energy Institute of Vocational and Technology 063004

Received March 16, 2014; Revised August 12, 2016

The high nickel steel friction stir welding process of microstructure construction was studied, analyzing the influence of the stability of austenite on the tensile properties of materials. The results show that the austenite grains in the stir zone are more refined and the dislocation accumulation is due more to the rotation speed of the stirring head. During the welding process, the austenite structure of the mixing area is more stable, which improves the strength and elongation of the joint. Therefore, the stability of the retained austenite can be improved and the friction stir welding is an effective method to improve the strength of building materials.

Keywords: friction stir welding, high nickel steel, building materials, austenite

INTRODUCTION

Friction stir welding is a solid state welding technology (FSW), the research and development of the mixing head and the technical conditions promote the application of friction stir welding. During the process of friction stir welding, the material is experiences plastic flow and friction heat is produced, thus friction stir welding can be regarded as a thermo mechanical process, similar to the hot rolling of steel [1]. The thermal mechanical process is accompanied by phase transformation. Therefore, the phase transformation can be controlled by controlling the conditions of friction stir welding, which can improve the mechanical properties of the welding parts. Studies were done of the rotating head speed, welding process and microstructure of the phase change process parameters, welding speed and so on. But the stability mechanism and its influence on the tensile properties of the retained austenite during friction stir welding have not been fully elucidated [2].

Because of its high mechanical strength, good corrosion resistance, low thermal expansion coefficient and high - strength it is widely used in construction, industry, metallurgy and other industries. In addition, due to the martensitic transformation temperature, the high nickel steel (Ms) is low and the phase change process is commonly used to study martensite. Therefore, the high nickel steel material after welding, the microstructure due to phase transformation and its performance will change. The building material of the high nickel steel microstructure changes

automatically mixing the friction welding process studied allowing for an analysis of the influence of the stability of austenite on the tensile properties of materials.

EXPERIMENTAL METHODS

Experimental material was synthesized for vacuum induction furnace smelting and pouring into ingots from high nickel steel, the chemical composition is 24 wt%Ni-0.1%C-bal.Fe. At a temperature of 1073 K the hot rolling process yields plate material with a thickness of 1.6 mm, then the surface oxide is removed and we have automatic friction stir welding as a result. The rotational speed of the rotary head is 400 mm/min, and the rotation speed is 200300 and 400 r/min, respectively. The welding load range is kept within 2000-3000 kg to ensure a constant insertion depth. The material of the stirring head is a hard alloy steel, the diameter of the stirring shoulder is 12 mm, the stirring needle diameter is 4 mm, the length is 1.4 mm and the stirring head dip angle is 3 degrees. The observed direction of the microstructure is the welding direction (WD), which is perpendicular to the horizontal (TD) and normal (ND), as shown in Figure 1. In order to prevent parts welding and rotating hair oxidation, Ar is used as a protective gas, the flow rate is 20L/min.

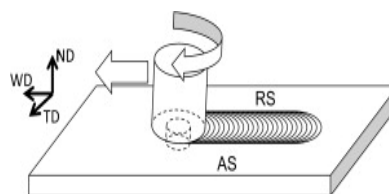


Fig. 1. Schematic diagram of friction stir welding.

* To whom all correspondence should be sent:

E-mail: liu85142012@163.com, liulp@ncst.edu.cn

The welded samples were observed by an optical microscope after cutting, mechanical polishing and solution corrosion in turn. The samples are electronic polishing at 290 K and 20 V in a 900 ml CH₃COOH + 100 ml HClO₄ mixed solution, then with electron backscatter diffraction (EBSD), field emission scanning electron microscopy (FE-SEM) the microstructure and fracture surfaces of the specimens are observed [3]. The geometry and sampling position of the three drawing samples in the mixing area are shown in Figure 2 and the distance between the samples is 2 mm. The sample size of the base material is the same as that of the mixing zone and the sampling method is the same. The tensile test at room temperature is 0.5 mm/min. Before the test, the sample is polished to a thickness of 1 mm, to avoid the influence of the thickness of the test results.

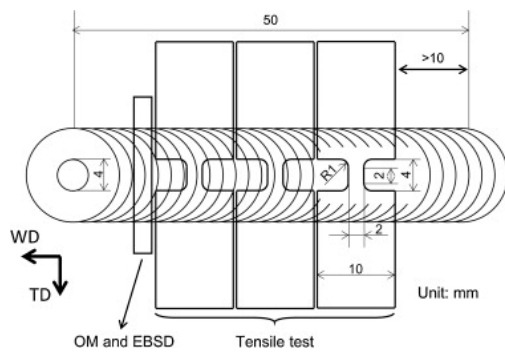


Fig. 2. Geometry and sampling locations of the tensile specimen.

EXPERIMENTAL RESULTS AND ANALYSIS

Microstructure of the base metal

The EBSD analysis in Figure 3 shows the crystal orientation of the high nickel steel base metal as a color map. By comparison with the aid of the standard triangle marked as the color key, the crystal orientation in the lateral (TD) parallel direction are determined. In Figure 3 the BCC and FCC phases are separated by the same position, each color represents the BCC crystalline phase and the FCC phase orientation, the color of the volume fraction of the image area proportion of both the BCC and FCC phases, the proportion of the Analysis and automatic analysis software OIM are given by EBSD. The microstructure of the base metal is composed of martensite and retained austenite. The original austenite grain size is about 30-60 μm, with the length and width of the martensite crystal about 10μm and 2-3μm.

Figure 4 shows the orientation map in the same area of the base metal. The orientation diagram of the BCC and FCC phases in the same position is

given and the maximum intensity is indicated at the bottom of the orientation map. It can be seen that the FCC phase with a high strength are in the [011] orientation and [111] orientation. In addition, it can be observed that the relationship between the crystal degree is [011]/[111], that is, the K-S (Kurdjumov-Sachs) relationship [4].

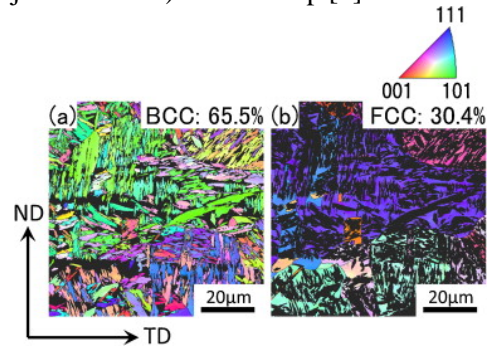


Fig. 3. Diagram orientation of high nickel steel (a) BCC (b) FCC

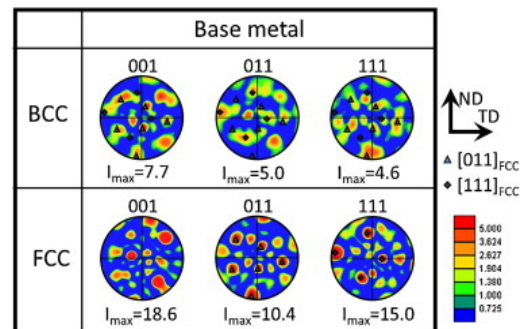


Fig. 4. The diffraction pattern of grain orientation in the same area of the base material.

The joint microstructure

The welding speed is 400 mm/min and the rotation speed is 200, 300 and 400r/min respectively. The friction welding is carried out on high nickel steel and the welding direction is respectively sampled. The optical microscope image is shown in Figure 5. The right side of the figure is the welding direction (AS) and the white dotted line shows the shape of the rotating head. Generally the friction stir welding joints are divided into the base material (BM), stir zone (SZ), heat affected zone (HAZ) and heat affected zone (TMAZ). The mixing zone is deformed under the action of the stirring shoulder or the stirring needle, and the recrystallization phenomenon is obvious. The heat affected zone is affected by the frictional heat and the grain size will obviously grow. The heat affected zone is located in the transition zone between the mixing zone and the heat affected zone. But in this paper, it is difficult to determine the heat affected zone and the heat affected zone, which may be due to the microstructure of the welded

specimens. A large number of black stripes were found in the corrosion images of all the joints, and their morphology was similar to that of the trees. The bright corrosion area of the welded joint obtained by rotating at a speed of 200r/min is the biggest. With the increase of the rotating speed, the corrosion area becomes smaller and smaller. The EBSD diagram (Fig. 6) shows the area corresponding to the austenite phase in the bright corrosion area. In addition, at the speed of 300 and 400r/min in the joint, the small defects can be observed along the cross section of the needle (shown in Figure 5B and C in the white arrow). In order to simplify the comparison of the welded joints, this paper makes a further study of the most obvious characteristics of the micro structure.

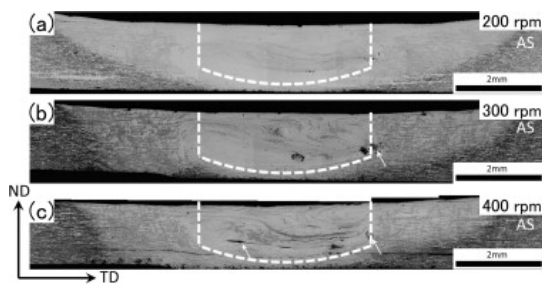


Fig. 5. Optical microscopy: (a) 200r/min (b) 300r/min (c) 400r/min of the joints at different rotation speeds.

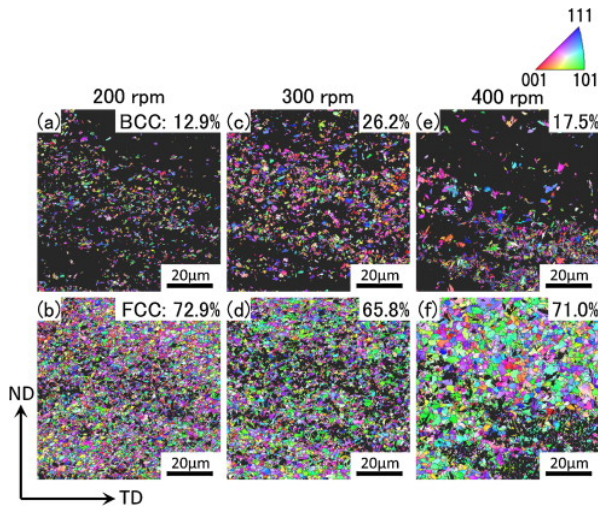


Fig. 6. The crystallization orientation of the joint in the mixing zone. (a,b)200r/min (c,d)300r/min (e,f)400 r/min.

Figure 6 shows the crystal orientation of 0.7 mm at the center of the mixing zone at different rotating speeds. According to the color the crystal orientation can be determined in parallel to the TD. It can be established that the fibrous tissue in the mixing region is composed of BCC grains (martensite) and FCC grains (retained austenite), which is the same as that of the parent material.

However, after friction stir welding, the area of the retained austenite was significantly increased and the austenite grain size was obviously refined. The austenite grain size decreases with the decrease in the rotational speed. In addition, with the decrease of the grain size of the austenite, the martensite grains become smaller. The distribution of the martensite is not uniform, which may be related to the inhomogeneous material flow during friction stir welding.

The orientation map of the mixing zone of the mixing zone at different rotational speed is shown in figure 7-9.

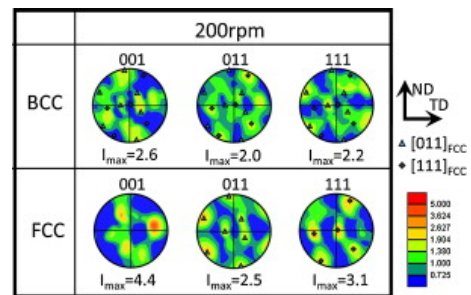


Fig. 7. The orientation of the mixing zone of the 200r/min joint with a rotation speed.

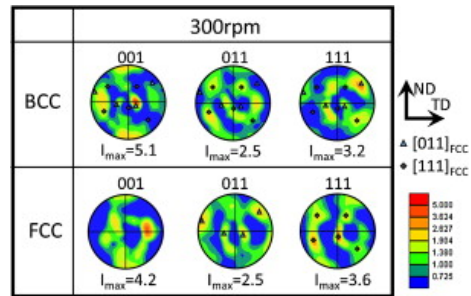


Fig. 8. The orientation of the mixing zone of the 300r/min joint with a rotation speed.

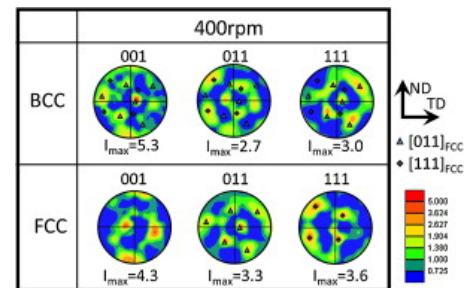


Fig. 9. The orientation of the mixing zone of the 400r/min joint with a rotation speed.

The Figure with a triangle and diamond indicate a strong accumulation phase in the [011] and [111] FCC orientation and the maximum intensity value is given at the bottom of each drawing. According to the density of [011] and [111] in the BCC phase and FCC phase, the relationship between the crystal phase and crystal degree can be observed, which is [011]BCC//[111]FCC and [111]BCC//[011]FCC,

that is K-S (Kurdjumov-Sachs). It is indicated that the martensite is formed by the transformation of austenite during the cooling of the friction stir welding process.

Figure 10 shows the distribution of the grain orientation difference in the parent material and the mixing region of the FCC phase. The small angle grain boundary (LABs) and large angle grain boundary (HABs) of more than 15 degrees are respectively indicated by the red and green lines in the graph. From figure 10A we can establish that the base material contains less LABs and HABs. In contrast, due to the refinement of the austenite, the number of HABs in the stir zone was significantly increased and the LABs were also densely distributed in the austenite grains (Fig. 10b-d). For a quantitative analysis, the average length of the unit area LABs is established and the correlation data of the FCC and BCC phases are given in Figures 11 and 12, respectively. In the figure, VFCC and sigma (1-5) respectively, are the total length of the FCC phase area fraction and 1-5 degrees of dislocation. It can be seen that with the decrease in the orientation difference, the proportion of LABs gradually increased. By comparison of the base metal and the mixing area, we can see that the density of LABs in the BCC phase and FCC phase was significantly increased after welding. The density of LABs in the BCC phase did not show a specific correlation with the rotational speed, but in FCC, the density of LABs decreased gradually (FIG. 11 and 12) with the increase of the rotational speed. The density of LABs was higher in the FCC phase, which indicated that the plastic deformation dislocation accumulated in the process of friction stir welding.

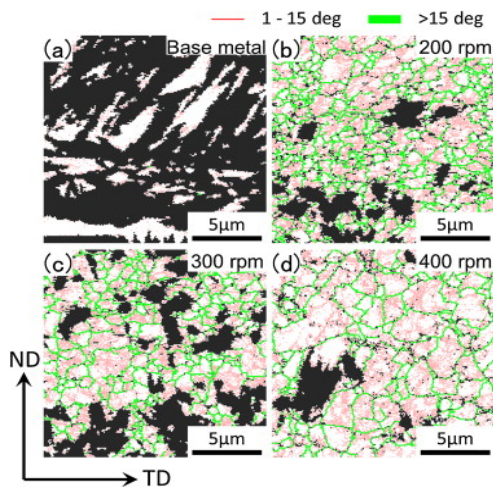


Fig. 10. Grain orientation difference distribution of the base material (a) and stir zone (B, C, d) in the FCC phase.

In the process of friction stir welding, the microstructure of austenite has two changes: grain refinement and LABs increase (FIG. 10). The grain refinement can be realized by recrystallization in the welding process and can be accelerated by the plastic deformation under the high strain rate condition. These two changes should make the austenite tend to be stable, which significantly affects the martensite transformation.

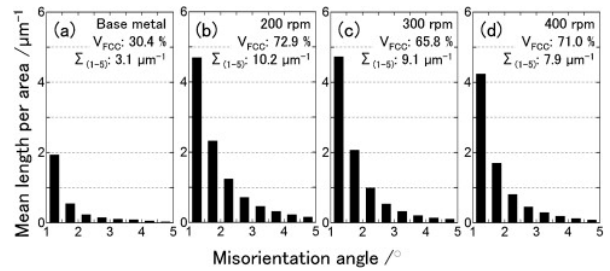


Fig. 11. FCC phase of parent material (a) and stir zone (B, C, d) the proportion of specific bits of the angle histogram.

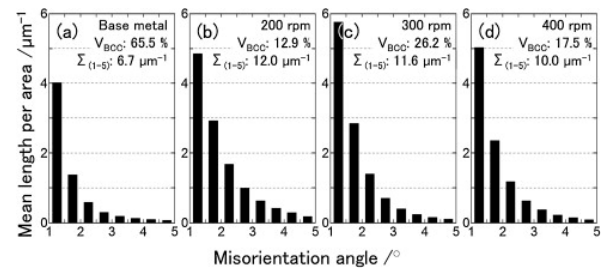


Fig. 12. BCC phase of parent material (a) and stir zone (B, C, d) the proportion of specific bits of the angle histogram.

Tensile properties

Stress - strain curves obtained from 200, 300 and 400 r/min samples obtained by a tensile test at room temperature, respectively. Figure 14 and table 1 provide the ultimate tensile strength of each specimen measured (UTS o max), yield strength (YS: y) and elongation (Ef). It can be seen that the parent material has experienced high work hardening and fracture at a low elongation rate. In general, with the increase of the tensile strength, the elongation of grain refinement in the process of welding is gradually reduced. However, this paper studies the limit of tensile strength and elongation at the same time, as shown in Figure 13.

The stress-strain curve in the concave stir zone shows that the work hardening rate (D /d sigma epsilon) gradually increased. The stress-strain curve of the metastable austenitic stainless steel which has the phenomenon of phase transformation induced plasticity (TRIP) is very similar to that of [5]. Therefore, the tensile property of the stir zone is enhanced and the phase transformation induced

plasticity is shown in the residual austenite of the friction stir welding.

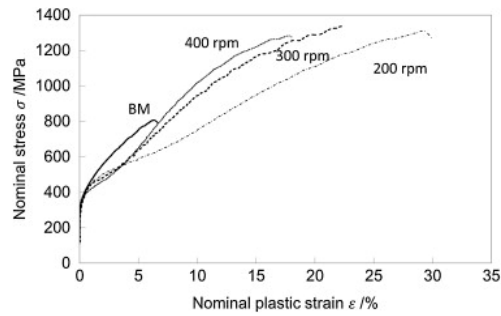


Fig. 13. Stress - strain curves of the samples of the parent material and the mixing zone.

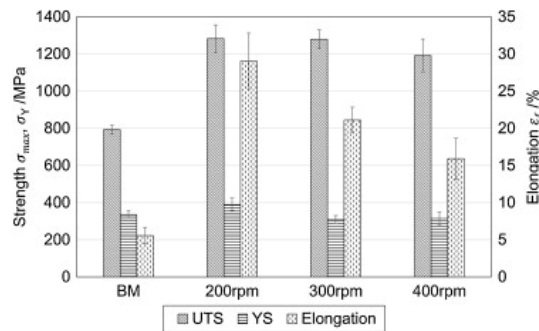


Fig. 14. The tensile properties of the base metal and the mixing zone.

Table 1. Tensile properties of the base metal and the mixing zone.

	Ultimate tensile strength /MPa	Yield strength /MPa	elongation at break /%
BM	793±24	336±20	5.6±1.1
SZ(200r/min)	1283±74	390±35	29.0±3.8
SZ(300r/min)	1279±50	308±22	21.1±1.7
SZ(400r/min)	1192±88	315±35	15.9±2.8

Figure 15 shows the SEM images of the center of the fracture surface of the base metal and the room temperature tensile specimen of the mixing zone. It can be seen that the fracture surface of the base material is flat and smooth (Fig. 15a), which shows that it is shear fractured. The fracture surface of the mixing zone is a ductile surface with a small pit (Fig. 15b-d), so it is a ductile fracture. This change is caused by the phase change of the fracture site. It is showed that the friction stir welding not only increases the strength and elongation, but also changes the fracture mode.

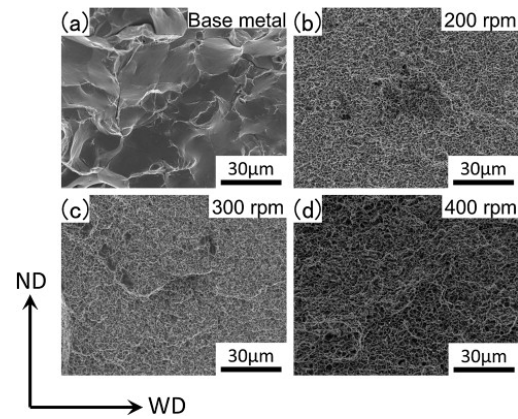


Fig. 15. Fracture surface of a and D (c) in room temperature tensile test specimens.

CONCLUSIONS

In this paper, the microstructure and tensile properties of high nickel steel were studied by automatic friction stir welding. Due to the plastic deformation of the material during the welding process the austenite in the mixing area is more stable. With the reduction of the rotational speed of the mixing head, the austenite grains in the stir zone are more refined and the dislocation accumulation is more significant. During the welding process, the stability of the austenite structure in the stir zone increases the strength and elongation of the joint due to the phase transformation induced plasticity. These results show that the stability of the retained austenite can be improved and the friction stir welding is an effective method to improve the strength of the material.

REFERENCES

1. O. An, H. Anguo, W. Changgui, et al. *Electric welding machine*, **8**, 45 (2007).
2. Y. Mocong, S. Zhonggang, M. Rui, et al. *Materials science and technology*, **1**, 118 (2014).
3. W. Bingjun, Z. Xiwei, et al. *Welding machine mixing aluminum alloy*, **9**, 69 (2013).
4. H. Ground, X. Shaohua, P. Jianhong, et al. *China journal of nonferrous metals*, **9**, 2608 (2012).
5. W. Zhifeng, Z. Aiping, *Foreign metal heat treatment*, **4**, 24 (2004).

ЕФЕКТ НА ТВЪРДО-ФАЗНОТО ЗАВАРЯВАНЕ ВЪРХУ ОБРАЗУВАНЕТО НА МИКРОСТРУКТУРАТА И СВОЙСТВАТА НА ВИСКО-КАЧЕСТВЕНА НИКЕЛОВА СТОМАНА

Л.Л. Пинг^{1*}, И.Дж. Тао²

¹Колеж по информационно инженерство, Обединен университет в Хебей, Тангшан 063009, Китай

²Професионално-технологичен институт по енергетика, Хебей 063004, Китай

Постъпила на 16 март, 2016 г.; коригирана на 12 август, 2016 г.

(Резюме)

Изследван е процесът на твърдо-фазно заваряване върху микроструктурата на никелова стомана и е анализирано влиянието на аустенита върху усукващите свойства на материала. Резултатите показват, зърната аустенит в зоната на заварката са по-фини, а натрупването на дислокации се дължи на повече на скоростта на въртене на заваряващата глава. Структурата на аустенита е по-стабилна по време на заваръчния процес, което подобрява здравината и удължаването на образца. Затова стабилността на запазения аустенит може да се подобри, а твърдо-фазното заваряване да бъде ефективен метод за подобряване на якостта на строителните материали.

Study on the nonisothermal crystallization behavior of polyvinyl alcohol/montmorillonite composite by DSC analysis

J. Song^{1,2}, Z-D. Dai^{1,2}, G. Song³, H.-L. Chen^{4*}

¹Chemistry and Chemical Engineering School of Northeast Petroleum University, Daqing 163318, China

²Heilongjiang Provincial Key Laboratory of Oil & Gas Chemical Technology, Daqing 163318, China

³Communication Training Base of General Staff, Zhangjiakou, Hebei 075100, China

⁴Department of Chemical Engineering and Frontier Research Center on Fundamental and Applied Sciences of Matters, National Tsing Hua University, Hsin-Chu 30013, Taiwan

Received January 25, 2016; Revised September 9, 2016

Polyvinyl alcohol (PVA)/montmorillonite (MMT) composite films were prepared by a solution-casting technique. The nonisothermal crystallization behavior of PVA and PVA/MMT composite have been investigated by differential scanning calorimetry (DSC). It has been found that the uniformly dispersed MMT in the matrix have a great influence on the crystallization behavior of PVA. The Jeziorny method has been employed to analyze the DSC data. The results show that the Jeziorny method can describe this system very well. Comparing with the PVA, the PVA/MMT composite has a higher crystallinity X_t , shorter semicrystallization time $t_{1/2}$ and higher crystallization rate constant Z_c . It can be concluded that MMT acted as an effective nucleating agent and had an effect on the growth of crystallites in the crystallization process of the PVA matrix.

Keywords: polyvinyl alcohol; Montmorillonite; crystallization behavior; DSC analysis

INTRODUCTION

It is well known that montmorillonite (MMT), a kind of inexpensive natural layered silicate, has been widely used to prepare polymer/layered silicate nanocomposites [1-2]. These composites have excellent overall properties and a low gas permeability. Major preparation methods of the polymer nanocomposites include in situ polymerization and the direct blending method (including polymer melt, solution and emulsion blending). In recent years, more and more researchers are interested in direct blending because it is the most direct, most cost-efficient method and is benign for the environment [3-6].

As we know, polyvinyl alcohol (PVA) can dissolve in hot water and there are many hydroxyls existing on its molecular chains. So, it is possible that MMT may be dispersed into the material and has good adhesion to the PVA matrix by simple blending. Furthermore, PVA is a semicrystalline polymer in which high physical interaction exists between the polymer chains, due to hydrogen bonding between the hydroxyl groups.

MMT may affect both the crystallinity and the physical network of PVA, causing variations in both the thermodynamic and kinetic characteristics of crystallization. But studies of the effects of MMT on the crystallization of PVA have not been reported.

In this work, PVA/MMT composite films have been prepared by the solution-casting method. The nonisothermal crystallization behavior of the PVA matrix have been investigated by differential scanning calorimetry (DSC) analysis. The nucleation function of MMT has been observed for the crystallization process of the polymer matrix.

EXPERIMENTAL

Materials

The Polyvinyl alcohol, supplied by Chang Chun Petrochemical Co. Ltd. was 99.5% hydrolyzed. The MMT was provided by the Aldrich Corporation and the organics treated by octadecylamine before use.

Sample Preparation

PVA grains were fully dissolved in deionized water by stirring at 95°C. MMT solution was added, this was dispersed in water for about 30 min in an ultrasonic bath at 90°C. The MMT content of PVA was in wt%. The blend was uniformly mixed by strong stirring and placed in an oven for solvent evaporation at 70°C for about 24 h. Then, the blend solution was ready for film preparation.

The PVA/MMT composite films were obtained by casting the blend solution on glass substrates and drying in an oven at 70°C for 24h and then all the samples were dried for 8h at 70 °C under a vacuum. After being fully dried, the films were

* To whom all correspondence should be sent:
E-mail: msongjun@163.com

peeled off from those glass substrates, the thickness of the obtained films was in the range 0.05–0.1 μm.

Sample Characterization

The melting and crystallization behavior of the PVA/MMT film samples were determined with a Netzsch DSC 200 (Germany) equipped with a cooling system in a nitrogen atmosphere. The instrument was calibrated for temperature and heat enthalpy with pure indium as the standard medium. About 2-5 mg of the sample was sealed in an aluminum pan, heated from room temperature to 230°C at a heating rate of 20 °C/min and held at that temperature for 5 min to eliminate the thermal history. The nonisothermal crystallization process was recorded at a cooling rate of 5°C/min, 10°C/min, 20°C/min and 40°C/min respectively from 230°C to 30°C. The endothermic and exothermic flows were recorded as a function of temperature. The pure PVA sample was treated by the same method for comparison.

RESULTS AND DISCUSSION

DSC analysis is one of the most convenient and accurate techniques for determining the crystallinity of polymers[7-9]. Considering the crystalline essence of PVA, we can safely say that the change of crystallization and melting behaviors of PVA will take place due to the introduction of MMT and the alteration of the interface properties between them, which will affect the final properties of the composite. Owing to the melting point of MMT being much higher than 1400°C, whatever measurements were made by DSC show the properties of the PVA matrix only.

Figure 1 shows the DSC curves of the nonisothermal crystallization of pure PVA and the PVA/MMT composite at the cooling rates of °C/min, 10°C/min, 20°C/min and 40°C/min. The onset temperature (T_0) and the peak temperature (T_p) are listed in Table 1.

It can be seen that with the increase of the cooling rate, the crystallization peaks of the PVA and PVA/MMT composite shift from a high to a low temperature and the peak shapes become wide. This is mainly because the faster cooling rate can degrade the ordered arrangement of the molecular chain during the crystallization process, which makes nucleation lag behind and causes an initial crystallization delay. Finally, the crystallization peaks move from a high to a low temperature. Meanwhile, the faster cooling rate also leads to a worse mobility of the molecular chain. Then the imperfect crystals form, which results in a greater

range of the crystallization temperature and wider crystallization peaks.

Compared with pure PVA, the crystallization temperature of the PVA/MMT composite is higher at any given cooling rate. This phenomenon can be explained by the heterogeneous nucleation effect of the MMT particles. As we know, the homogeneous nucleation of a material occurs spontaneously below the melting point and requires a long time. But the heterogeneous nuclei might be formed as soon as the material reaches its crystallization temperature. Therefore, the heterogeneous nucleation needs less time at the same cooling temperature.

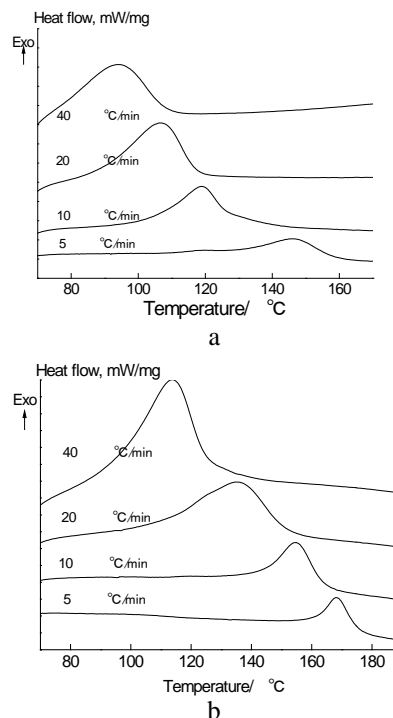


Fig. 1. DSC thermograms of the nonisothermal crystallization for (a) pure PVA and (b) PVA/MMT composite at different cooling rates

To analyze the crystallization process even further, we have calculated the relative crystallinity X_t at any crystallization temperature (T) using the following equation:

$$X_t = \frac{\int_{T_0}^T (dH_c/dT) dT}{\int_{T_0}^{T_\infty} (dH_c/dT) dT} \quad (1)$$

where T_0 is the onset crystallization temperature, T_∞ is the temperature of crystallization termination and dH_c , the enthalpy of the crystallization released during an infinitesimal temperature change dT . In this case, the relationship between X_t and T can be obtained from the DSC data, corresponding to the crystallization peaks in Figure 1. Figure 2 shows the plots of the relative crystallinity versus the crystallization temperature for the PVA and PVA/MMT composite at different cooling rates.

It can be seen from Figure 2 that the crystallization processes of the PVA/MMT composite are over in a shorter time than for pure PVA. It has been known that the crystallization process of the polymer consists of the formation of nuclei and the growth of crystallites. Since MMT can work as crystallization nuclei and help the orderly distribution of PVA chains and crystal sheets, we can safely say that this effects both the formation of nuclei and the growth of crystallites.

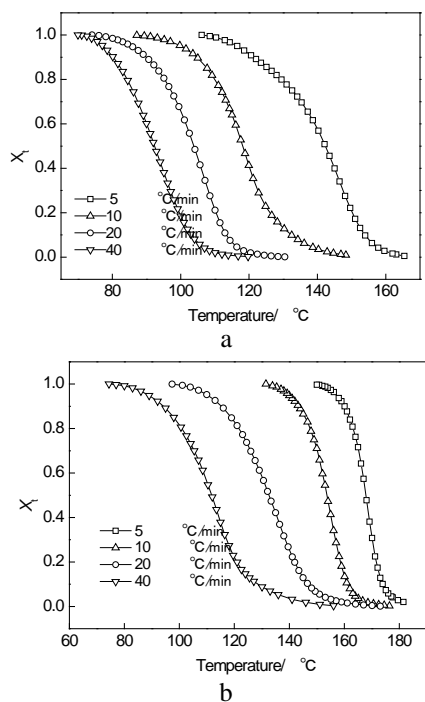


Fig. 2. Plots of X_t versus temperature for crystallization of PVA (a) PVA/MMT (b) composite.

Many researchers use the method of DSC analysis to study the nonisothermal crystallization kinetics of polymers. They start from isothermal analysis and modify it, according to the characteristic of nonisothermal crystallization¹⁰⁻¹¹. Every method has its application area and limitation. In this paper, we use the Jeziorny method¹² to analyze the nonisothermal crystallization kinetics of pure PVA and PVA/MMT composite.

The crystallization process can be expressed by the following Avrami equation:

$$1 - X_t = \exp(-Z_t t^n) \quad (2)$$

where X_t is the relative crystallinity at time t ; n is the Avrami exponent related to the crystallization dimension, mechanism of nucleation and the form of crystal growth; and Z_t is the crystallization rate constant, which describes the nucleation and growth of the crystallites. The logarithmic analytic function of equation 2 is the following equation:

$$\ln[-\ln(1 - X_t)] = \ln Z_t + n \ln t \quad (3)$$

However, the Avrami equation indicates only the relationship of X_t and t , thus we have to convert the measurement temperature to time in accordance with the equation:

$$t = (T_0 - T) / \beta \quad (4)$$

where t is the crystallization time; T_0 is the onset crystallization temperature; T is the crystallization temperature at time t and β is the cooling rate.

According to equation 4, the relationship between the relative crystallinity X_t and the crystallization time t can be obtained as shown in Figure 3.

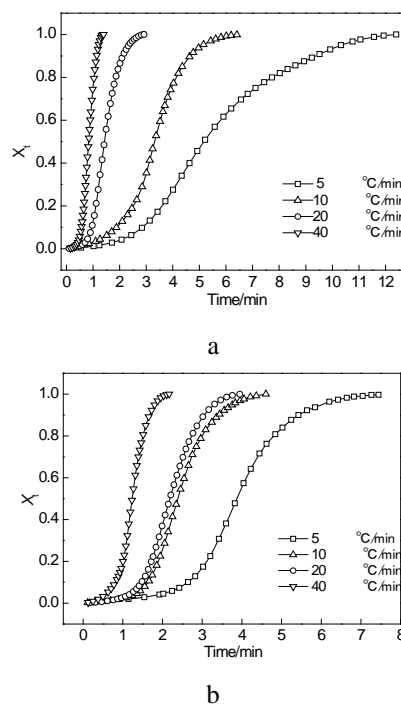


Fig. 3. Plots of X_t versus time for the crystallization of PVA (a) PVA/MMT (b) composite.

The plots of $\ln[-\ln(1 - X_t)]$ versus $\ln t$ for the pure PVA and PVA/MMT composite samples are shown in Figure 4. It is clearly seen from this figure that $\ln[-\ln(1 - X_t)]$ and $\ln t$ show good linear relationships. The meaning is that the Jeziorny method can successfully describe the nonisothermal crystallization kinetics of the PVA and PVA/MMT composite under the given cooling rates.

The values of $\ln Z_t$ and n were obtained from the intercept and slope of these straight lines respectively in accordance with equation 3. Given the characteristics of the nonisothermal crystallization process, the Avrami equation is modified by the Jeziorny method and the constant $\log Z_c$ can be described as the following equation:

$$\log Z_c = \log Z_t / \beta \quad (5)$$

where Z_c is the crystallization rate constant and β is the cooling rate. The calculated results are listed in Table 1.

$t_{1/2}$ is determined by the following equation:

$$t_{1/2} = (\ln 2 / Z_t)^{1/n} \quad (6)$$

where the half time of crystallization ($t_{1/2}$) is the time required to reach 50% of the final crystallization. The values of $t_{1/2}$ are also listed in Table 1.

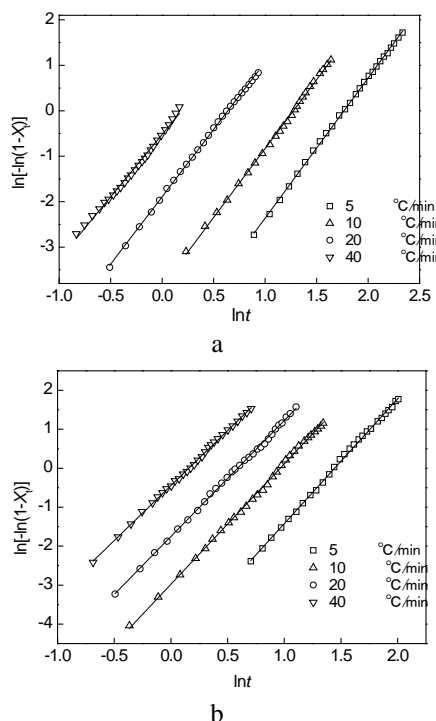


Fig. 4. Plots of $\ln[-\ln(1 - X_t)]$ versus $\ln t$ for crystallization of PVA (a) PVA/MMT (b) composite.

According to Table 2, T_0 and T_p of the PVA/MMT composite was higher than that of pure PVA, indicating that the addition of MMT can effectively increase the crystallization rate. With the increase in the β values, T_0 and T_p shifted to a lower temperature region. The reason is that a high cooling rate can make the system become a part of a low temperature range fast and the low temperature can freeze the mobility of some

segments, which leads to the growth of crystallization.

Obviously, the $t_{1/2}$ values of the PVA and PVA/MMT composite decreased with the increasing β values. Furthermore, the $t_{1/2}$ values of the PVA/MMT composite were smaller than those of pure PVA under the given cooling rates, it showed that MMT acted as an effective nucleating agent for the PVA and it can increase the crystallization rate of the PVA during the nonisothermal crystallization.

The Z_t and Z_c values of the PVA and PVA/MMT composite increased while n decreased with the increase in the β values. Z_t , Z_c , n and ΔH_c of the PVA/MMT composite were higher than that of pure PVA under the given cooling rates, which indicates that the MMT can induce heterogeneous nucleation with a nonisothermal tridimensional growth of the spherulite.

CONCLUSIONS

The crystallization properties of pure PVA and PVA/MMT composite were studied by DSC analysis. The nonisothermal crystallization behavior of PVA/MMT composite was greatly affected by the loading of MMT. The PVA/MMT composite samples were found to have a shorter semicrystallization time $t_{1/2}$, a higher crystallization temperature T_0 and T_p , and crystallization enthalpy ΔH_c than that of pure PVA. The nonisothermal crystallization kinetics of pure PVA and PVA/MMT composite were analyzed by the Jeziorny method. The Avrami constants n and the crystallization rate constants Z_c were compared with the pure PVA. The results showed that the addition of MMT may significantly affect the nucleation and growth of PVA crystallization.

Table 1. Characteristic temperatures and kinetic parameters of nonisothermal crystallization for PVA and PVA/MMT.

	B (°C/min)	T_0 (°C)	T_p (°C)	Z_t	Z_c	n	$t_{1/2}$ (min)	ΔH_c (J/g)
PVA	5	168.12	146.01	0.004	0.336	3.08	4.67	-21.92
	10	148.33	118.91	0.021	0.680	3.03	3.33	-18.82
	20	132.47	106.53	0.151	0.910	2.96	2.19	-14.37
	40	125.84	94.55	0.593	0.987	2.74	1.24	-8.643
PVA/MMT	5	187.22	168.1	0.010	0.397	3.20	3.88	-25.39
	10	177.54	154.8	0.051	0.743	3.09	2.39	-24.62
	20	176.33	135.0	0.174	0.916	2.98	1.43	-19.95
	40	161.14	114	0.641	0.989	2.82	0.84	-16.37

REFERENCES

1. H.Q. Hong, H. He, Z.X. Jia, C. Ding, D.M. Jia, *J Appl Polym Sci*; **102**(4), 3889 (2006).
2. J. Li, C.X. Zhou, G. Wang, *Polym. Test.*, **22**(2), 217 (2003).
3. D.X. Li, D.M. Jia, P. Zhou, *J Appl Polym Sci.*, **93**(1), 420 (2004).
4. Y. Zhu, Z.C. Zhang, X.M. Guan, *Journal of Thermoplastic Composite Materials*, **29**(5), 638 (2016).
5. W.B. Xu, G.D. Liang, H.B. Zhai, *Eur. Polym J.*, **39**(7), 1467 (2003).
6. H.Q. Hong, H. He, D.M. Jia, *Polym Polym Compos*, **16**(2), 131 (2008).
7. T.Z. Zhang, T. Li, N. Erik, *Polymer*, **50**(5), 1206 (2009).
8. P. Li; G. Yang, *Polymers for Advanced Technologies*, **27**(8), 1029 (2016).
9. G.S. Deshmukha; D.R. Peshwea; S.U. Pathaka; J.D. Ekheb, *Thermochimica Acta*, **606**, 66 (2015).
10. Q.X. Zhang, Z.H. Zhang, H.F. Zhang, Z.S. Mo, *J Polym Sci Polym Phys.*, **40**(16), 1784 (2002).
11. G. Xu; K. Min, *Polymer-Plastics Technology and Engineering*, **54**(4), 390 (2015).
12. A. Jeziorny, *Polymer*, **19**(10), 1142 (1978).

ИЗСЛЕДВАНЕ НА НЕИЗОТЕРМИЧНАТА КРИСТАЛИЗАЦИЯ НА КОМПОЗИТИ ОТ ПОЛИ-ВИНИЛОВ АЛКОХОЛ С МОНТМОРИЛОНИТ ЧРЕЗ ДИФЕРЕНЦИАЛНА СКАНИРАЩА КАЛОРИМЕТРИЯ (DSC)

Дж. Сонг^{1,2}, З.-Д. Даи^{1,2}, Г. Сонг³, Х.-Л. Чен^{4*}

¹Училище по химия и химично инженерство, Северо-източен университет по петрола, Дакинг 163318, Китай

²Провинциална лаборатория химична технология на нефта и газа в Хейлунцзян, Дакинг 163318, Китай

³Тренировъчна база Жанцзянку, Хебей 075100, Китай

⁴Департамент по химично инженерство и Център за гранични изследвания по фундаментално и приложно материалознание, Национален университет Цин Хуа, Хсин-Чу 30013, Тайван

Постъпила на 25 януари, 2016 г.; коригирана на 9 септември, 2016 г.

(Резюме)

Композитни филми от поли-винилов алкохол (PVA) с монтморилонит (ММТ) са приготвени чрез леене от разтвор. Кристализацията в не-изотермични условия на PVA и на композитите PVA/ММТ е изследвана чрез диференциална сканираща калориметрия (DSC). Установено е, че равномерно диспергираният ММТ в матрицата има голямо влияние върху кристализацията на PVA. Приложен е Jeziorny-метода за анализа на DSC-данните. Резултатите показват, че този метод описва системата много добре. Сравнението показва, че композитът PVA/ММТ има по-висока степен на кристалност спрямо PVA, по-кратко време на полу-кристализация $t_{1/2}$ и по-висока константа на кристализация Z_c . Може да се заключи, че ММТ действа като ефективен заросиш-образуващ агент и има влияние върху растежа на кристали при кристализацията с матрица от PVA.

Chemical changes and the mechanisms in the sintering process of sea silt

M. Li^{1, 2*}, X. Cong²

¹Hydraulic engineering postdoctoral research station, Hohai University, 210098 Nanjing, China

²School of civil engineering, Huaihai Institute of Technology, 222005 Lianyungang, China

Received January 14, 2016; Revised June 29, 2016

When sea silt that contains more soluble salt is used for the sintering of building materials, its adverse impact is a widespread concern. Lianyungang sea silt in Jiangsu Province is taken as an example. The changes of weight and heat, soluble salt and chlorine content in the sintering process are studied by laboratory experiments. The results show that the ion content of chlorine, sodium and sulfate is higher in the sea silt, the content of SO_4^{2-} reaches a peak of 18‰ at 500 °C, less than 4‰ after 1000 °C; the content of Na^+ decreases dramatically above 600 °C, but remains 0.1 ‰ after 1000 °C; the content of Cl^- decreases sharply above 600 °C and is almost zero at 900 °C. The XRF (X-ray fluorescence diffraction) test of sintering sea silt at 1000 °C shows that chlorine has disappeared and does not exist in a crystalline and glassy ionic state; the possible mechanism of sintering sea silt is dechlorination such that sodium chloride melts to a volatile solution at 800 °C, the sodium chloride gas reacts with the water vapor, carbon or carbon dioxide to yield hydrogen chloride. In this study, the quantitative change of the soluble salt in the sea silt is proved by the change of the sintering temperature. The content of the soluble salt is very low when the sintering temperature is above 1000 °C, which can eliminate the concerns for the sintering materials of sea silt. The transfer and transformation process of sodium chloride was revealed, which suggests that the tail gas treatment should be strengthened in the production of sintering building materials.

Keywords: sea silt, sintering, chlorine, physical, chemical

INTRODUCTION

With the rapid development of the coastal development strategy, the sea sediment production brought about by harbor excavation and waterway dredging increase dramatically, which if abandoned, will seriously affect the appearance of the city and produce the secondary pollution problems of dust and wet mud. More and more sea dredged mud is dumped into the ocean and the selection of the sea dumping site is increasingly difficult, which is a serious impediment to the development of the port and waterway [1]. Sea silt will also bring seawater eutrophication and even result in blocked or even abandoned seawater farms. Another aspect is the ban to use sintered clay bricks and a shortage of alternative raw materials occurs. The way to utilize sea mud is for building materials also by using waste, not to reduce the occupation of cultivated land, thus protecting the environment and providing alternative products for the construction market, with good economic and social benefits [2]. Therefore, it is very important to study the development and utilization of sea silt as a resource.

The feasibility of sea silt sintering building materials has been confirmed [3, 4]. The feasibility

of sintered brick was studied by Salim W, et al. [5] with dredged sea sludge extracted at Kuala Perlis. That local sea silt contains the appropriate brick materials SiO_2 and Al_2O_3 . The scumming degrees of two kinds of sea silt sintered perforated brick with iron tailings and fly ash were studied by Dongyan Han, et al. [6]. It was found that the iron tailings reduce the scumming degree of the sintered bricks and these are more suitable for the admixture. A study of the Xiamen sea silt sintered brick has been made by Zhou Min [7], which shows that the scumming degree is very slight, only in the corners and can even be neglected. The addition of fly ash can effectively reduce the temperature of the scumming. Andrea Mezencevova, et al. [8] have made a study of the strength of a sintered brick using 100% dredged silt and dredged silt adding 50% clay respectively. It was found that two kinds of sintered brick can be used for construction. The compressive strength of the pure sea mud brick is 8.3~11.7 MPa while the compressive strength of sea silt with 50% clay added to the sintered brick is up to 29.4 MPa. In addition to sintering building materials, a very effective water purification and adsorption material that uses the seabed sediments and can remove heavy metals was sintered at 400°C by Dabwan Ahmed H A, et al. [9]. In the sintering process of sea mud, salinity is an important feature. Many researchers worry that sodium chloride has adverse effects including scumming [7, 10].

* To whom correspondence should be sent.
E-mail address: ytlimd@163.com.

Dehydration and desalination technology were used to reduce the salt content in the sea mud [11, 12]. There is also a study showing that the salt content during the sintering process will greatly decrease.

The physical and chemical changes of the sea silt during sintering are presented in this paper, including the change in weight, soluble salt and chloride content and the transfer and transformation mechanism of sodium chloride.

TEST MATERIALS AND METHODS

Materials

The test samples of the sea silt are taken from Oriental Garden of Lianyungang, Jiangsu Province, China. Its main minerals are halloysite, calcite, magnesium chlorite, quartz, albite and glauconite. As shown in Table 1, the characteristics of its main chemical composition are with a slightly low silicon content, high content of potassium, sodium and salt. The content of SiO₂ is slightly low, while the content of Al₂O₃ is middle to high. Table 2 shows that it contains more K₂O and Na₂O that are fusible as well as CaO and MgO that can reduce the refractoriness of clay. It is similar to fusible acid clay in chemical composition. CaCO₃ will break down at 898°C.

Test methods

The method of X-ray diffraction XRD analysis studies the mineral composition together with X-ray fluorescence diffraction XRF used in chemical composition analysis; a German Netzsch simultaneous thermal analyzer (DSC/DTA-TG) STA 449 F3 is used in the thermo-gravimetric analysis; tests of the solubility of salt; the sintered soil samples at different temperatures (including 105, 200, 300, 400, 500, 600, 700, 800, 900, 1000, 1100 °C) were respectively cooled to a room temperature. 10 g of milled powder were weighed and dissolved in 100 ml of deionized water, filtered by filter paper after 48 h and the water samples

diluted 10 times at the end.

The cations (Na⁺, K⁺, Ca²⁺, Mg²⁺) were registered by a Wantong ion chromatograph, automatic sampler and cation chromatographic column at 30 °C, with a flow rate of 0.9 ml/min and an eluent of pyridine dicarboxylic acid system while the anions (Cl⁻, SO₄²⁻, NO₃⁻) were registered by a Wantong ion chromatograph, automatic sampler, conductance detector and eluent generator at 30 °C, with a current of 50 mA, a flow rate of 1.0 ml/min and an eluent of 20 mMol dilute KOH solution.

THERMO GRAVIMETRIC ANALYSES

The thermo-gravimetric analyses curves of sea silt are shown in Figure 1. The quality decreases slowly before 400 °C is reached; it begins to decrease drastically between 400-665 °C; the trend of change begins to decrease between 665-900 °C; the quality changes rarely and remains almost unchanged after 900 °C. Heat is generally generated in the direction of absorption. The heat absorption is very small prior to reaching 400 °C, while the endothermic range increases gradually after 400 °C. There is a significant change in heat fluctuation at 975 °C.

Possible reasons for this phenomenon are the weakly adsorbed water and strongly bound water separated in turn by the increase in temperature and the heat absorption due to the gradual increase in dehydration. At 975 °C a strong endothermic reaction occurs, the reason is that CaCO₃ is possibly decomposed into CaO and CO₂ gas with heat absorption. A large amount of the heat absorption above 1000 °C is related to the heat absorption and phase transformation of the soil when melting.

Table 1. Chemical composition of sea silt

Name	SiO ₂	Al ₂ O ₃	Fe ₂ O ₃	CaO	MgO	K ₂ O	Na ₂ O	SO ₃
Composition content/%	57.10	17.30	11.30	3.10	2.17	4.01	3.10	0.71

Note: detection limit of SO₃ ≅ 30ppm.

Table 2. Physical properties of the main components of sea silt

Component	SiO ₂	Al ₂ O ₃	Fe ₂ O ₃	CaO	MgO	K ₂ O	Na ₂ O	CaCO ₃	Na ₂ SO ₄	K ₂ SO ₄
Melting point/°C	1650	2054	1565	2572	2800	770	1132	825	884	1069
Boiling point/°C	2230	2980	3414	2850	3600	1500	1275	*	1404	1689
Decomposition/°C								898		

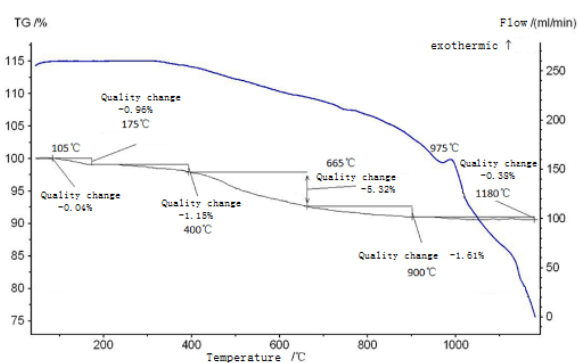


Fig. 1. Thermo-gravimetric analysis curve of sea silt.

CHANGES OF SOLUBLE SALT CONTENT

The changes of soluble salt content are shown in Figure 2.

(a) SO_4^{2-} ions are of a higher content and almost unchanged before 400 °C and increase gradually to a peak concentration of 18‰ between 400-500 °C, the reason is still not clear but the decomposition of some substance containing sulfate is suspected; it decreases gradually after 500 °C, indicating thermal decomposition or a chemical reaction for the molten state of sulfate; it is below 4‰ after 1000 °C.

(b) Overall the content of Ca^{2+} is low, probably because the soluble salt of calcium is very small in quantity especially the formation of micro soluble calcium sulfate in the presence of a large quantity of sulfate. The content of Ca^{2+} is basically unchanged before reaching 400 °C, gradually increasing to its peak of only 0.56‰ at between 400-500 °C and gradually decreasing after 500 °C. Ca^{2+} disappear after 1000 °C, which indicates that Ca^{2+} have reacted with silicon and aluminum to give insoluble alumino-silicate.

(c) The content of K^+ is the lowest and the peak is only at 0.04‰ with a fluctuation in a minimum range before reaching 800 °C. It decreases sharply after 800 °C. As shown in Table 2, the melting point of K_2O is 770 °C. After reaching that temperature, the oxide of potassium melts with the formation of an insoluble alumino-silicate vitreous body reacting with silicon and aluminum.

(d) The content of Na^+ doesn't change basically before 600 °C, but decreases sharply above 600 °C and remains 0.1‰ unchanged after 1000 °C, showing that sodium has reacted with silicon and aluminum to yield an insoluble alumino-silicate.

(e) The content of Mg^{2+} is rare and the highest percentage does not exceed 0.08‰. It fluctuates in the minimum range before 600 °C, is reached and decreases gradually after 600 °C, then the content

becomes zero above 1000 °C, indicating that magnesium has completely reacted with aluminum and silicon to synthesize alumino-silicate crystals.

(f) The content of Cl^- is relatively high. It fluctuates within a small range of 12-14‰ before 600 °C are reached and begins to drastically decrease over 600 °C and drops to almost zero after 900 °C are reached showing the transfer and transformation of chlorine during the high-temperature sintering process, which will be further analyzed as shown below.

THE CHANGES OF CHLORINE CONTENT AND ITS MECHANISM ANALYSIS

Changes of chlorine content

The chlorine content is higher before sintering, but the content of chlorine decreases significantly after sintering^[3], ultimately falling to almost zero. In order to further study the whereabouts of Chlorine, XRF analysis is used to test the content for Chlorine in the sintered sea mud at 1000 °C and the test results are shown in Table 3. From the table, it is obvious that the content of chlorine is zero after the sintering process, which indicates that the chlorine is transferred during the sintering process.

Analysis on the change mechanism of the chlorine content

Basic properties and thermal properties of NaCl

NaCl is soluble in water and with the increase of temperature, the solubility will increase but the change is not obvious. The solubility is 36.0 g at 20 °C. The melting point is 801 °C and the boiling point is 1465 °C.

The thermo-gravimetric analysis curve of sodium chloride is shown in Figure 3. At 54 min, the temperature is 800 °C, the heat absorption peaks and the quality of sodium chloride begins to decrease. It decreases drastically to about 900 °C, with the heat absorption peaking subsequently. This shows that sodium chloride melts with heat over 800 °C and begins to volatilize above 900 °C, with a rapid reduction in quality.

Table 3. Changes of chlorine content in sea silt

Names	The content of chlorine (%)	
	Before	After
Sample 1	2.37	0.000
Sample 2	2.78	0.000
Sample 3	2.19	0.000

* Note: the sintering temperature is 1000°C.

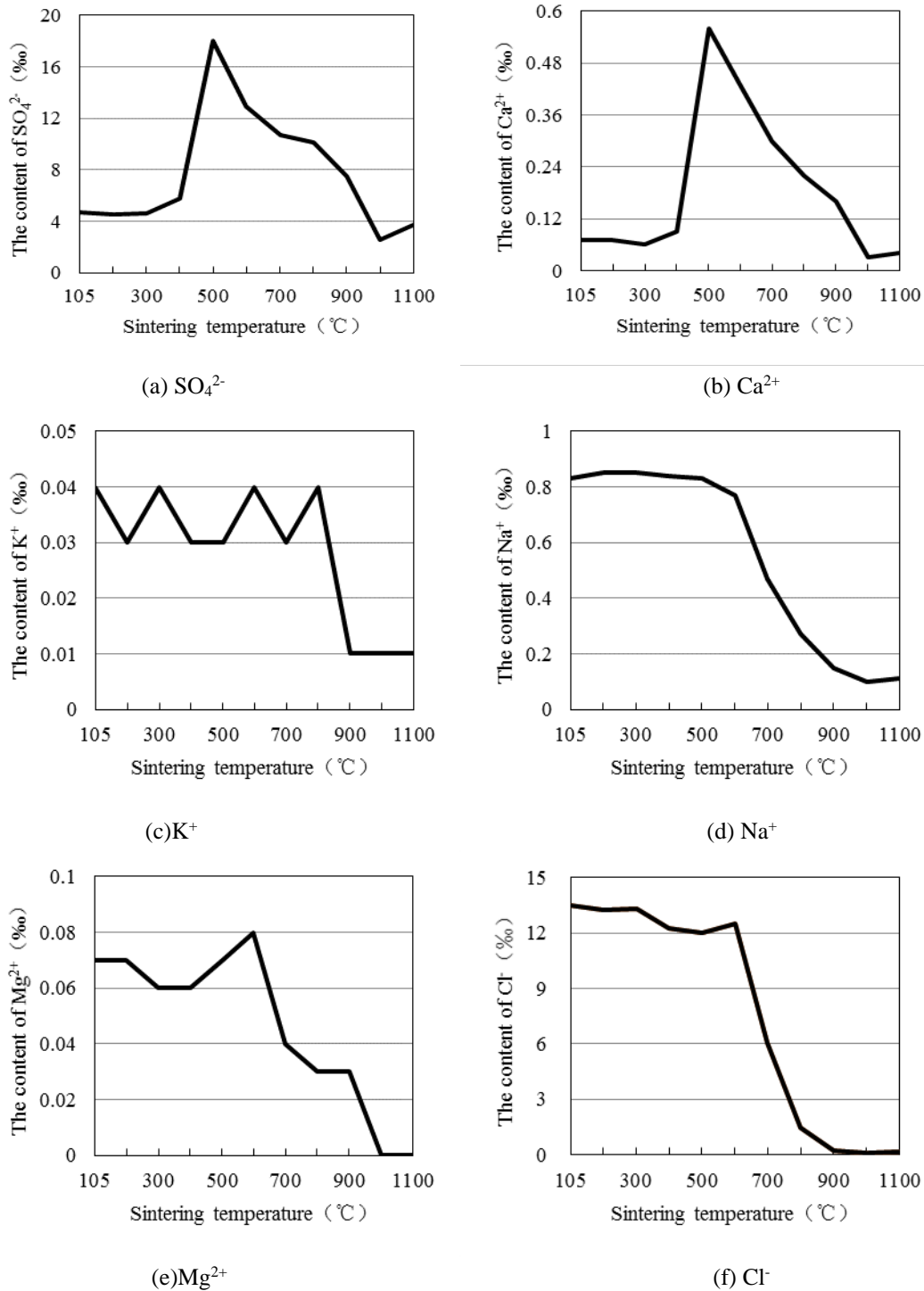
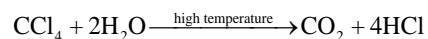
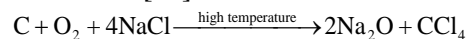


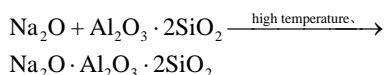
Fig. 2. Changes of soluble salt content with the change of sintering temperature.

Sodium chloride transfer

Under normal temperature and pressure, NaCl doesn't react with water and its melting state also does not react with water at a high temperature. However, four substances of NaCl, the clay components ($\text{Al}_2\text{O}_3 \cdot \text{SiO}_2 \cdot 2\text{H}_2\text{O}$), H_2O and C are indispensable materials to prepare hydrochloric acid and CO_2 or CO directly instead of C participating in the reaction. Therefore, when the

temperature of a coal stove is higher than 800 °C, sea silt in sintering will generate complex chemical changes and produce gaseous HCl, resulting in the heat absorption peak at 800 °C in Figure 3. The main reactions occurring in the sintering process are as follows [13]:





This shows that the element chlorine participates in the reaction to produce HCl gas escaping from the product during the sea silt sintering process. The sintering product will not be of poor quality due to the presence of sodium chloride in the raw materials.

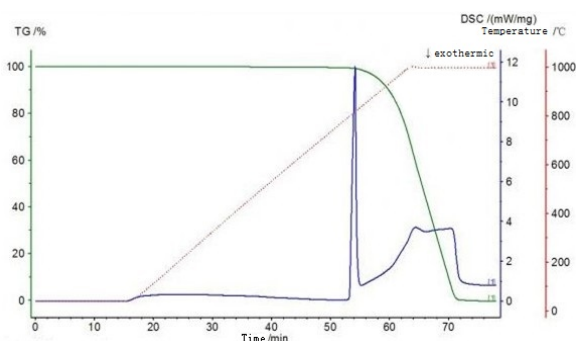


Fig. 3. Thermo-gravimetric analysis curve of sodium chloride

CONCLUSIONS

Through a series of laboratory experiments, the following conclusions can be listed:

(1) With the increase in temperature, the free water, weakly adsorbed water and strongly bound water separate in turn and the heat absorption of dehydration gradually increases. At 975 °C, a strong endothermic reaction occurs the reason is possibly because CaCO_3 is decomposed into CaO and CO_2 gas with the absorption of heat. A large amount of heat absorption above 1000 °C is related to the heat absorption of phase transformation due to the soil melting.

(2) The content of SO_4^{2-} increases to a peak concentration of 18‰ at 500 °C, the reason is still not clear but the decomposition of some substance containing sulfate is suspected; it decreases gradually after 500 °C, indicating the thermal decomposition or chemical reaction of the molten state of sulfate; it is below 4‰ after 1000 °C.

(3) Calcium, sodium, magnesium and potassium react respectively with silicon and aluminum compounds to synthesize an aluminosilicate vitreous body above 500 °C, 600°C and 800°C.

(4) Chlorine has disappeared and does not exist in a crystalline and glassy ionic state when the

sintering temperature is above 1000 °C and the content of soluble salt is very low, which can eliminate the concerns of sintering materials from sea silt.

(5) Sodium chloride melts or becomes a volatile solution at 800 °C, the gaseous chloride sodium reacts with the water vapor, carbon or carbon dioxide to yield hydrogen chloride as the gas escapes.

(6) HCl gas is generated with the transfer and transformation process of sodium chloride, which suggests that the tail gas treatment should be strengthened during the production of sintering building materials.

Acknowledgements: This material is based upon work supported by Natural Science Foundation of China under Grant No.51609093, No.41306114, and Jiangsu Planned Projects for Postdoctoral Research Funds under Grant No. 1601007A.

REFERENCES

- H.Q. Zhang, J. Xie, W. Zhu, Y. Huang, P. Shi, *Marine Science Bulletin*, **23**(6), 54 (2004).
- M. Zhou, *Fujian Construction Science & Technology*, **5**, 33 (2010).
- Z.F. Zhang, M.D. Li, A.G. Tian, B. Gu, *Jiangsu Construction*, **3**, 104 (2015).
- F. Wan, A.G. Tian, *Block-Brick-Tile*, **5**, 11 (2014).
- W.S.W. Salim, S.F. Sadikon, S.M. Salleh, N.A.M. Noor, M.F. Arshad, N. Wahid, *Engineering and Industrial Applications (isbeia)*, 509 (2012).
- H.D. Yan, M.H. Lin, *Advanced Materials Research*, **1616**(450), 115 (2012).
- M. Zhou, *Fujian Building Materials*, **3**, 15 (2010).
- A. Mezencevova, N.N. Yeboah, S.E. Burns, L.F. Kahn, K.E. Kurtis *Journal of environmental management*, **113**, 128 (2012).
- A. Dah, I. Daizo, K. Satoshi, *Journal of Environmental Sciences*, **20**(2), 172 (2008).
- B.W. Gu, A.G. Tian, J. Hu, Z. Xu, *New Building Materials*, **6**, 5 (2008).
- M.D. Li, A.G. Tian, J. Hu, A device for dewatering and desalting of sea silt [P], CN201120473368.1, 2012-7-11.
- M. Gao, A.G. Tian, M.D. Li, B. Gu, *New Building Materials*, **2**, 35 (2013).
- G.S. Yang, *Journal of Foshan Normal College*, **2**, 64 (1984).

ХИМИЧНИ ПРОМЕНИ И МЕХАНИЗМИ НА СИНТЕРУВАНЕТО НА МОРСКА ТИНЯ

М. Ли¹, С. Цонг²

¹*Изследователски пост-докторски център по хидравлично инженерство, Университет „Хохай“, Нанджунг 210098, Китай*

²*Училище по строително инженерство, Технологичен институт „Хуайхай“, Лянунганг 222005, Китай*

Постъпила на 14 януари, 2016 г.; коригирана на 29 юни, 2016 г.

(Резюме)

Морските наноси, използвани за строителни материали имат вредно въздействие върху околната среда. Тинята от езерото Лянунганг в провинция Джиянгу е взета като пример. Промените в теглото, топлината, съдържанието на соли и хлор, натрий и сулфати в процеса на синтеруването на тинята са изследвани експериментално. Резултатите показват, че съдържанието на йоните на хлора, натрий и сулфатите е по-високо в тинята, съдържанието на SO_4^{2-} достига максимум при 18% и 500 °C, по-малко от 4% над 1000 °C; съдържанието на Na^+ намалява драстично над 600°C, но остава 0.1 % над 1000°C; съдържанието на Cl^- рязко намалява над 600 °C и е почти нула при 900 °C. Методът XRF (рентгенова флуоресцентна дифракция) показва, че синтеруваната тиня губи напълно хлоридите при 1000°C и те не се намират нито в кристално, нито в йонно състояние. Възможният механизъм на дехлориране е стапянето на натриевия хлорид до летлива стопилка при 800 °C, като газообразният натриев хлорид реагира с водните пари, въглерода или въглеродния диоксид с получаването на хлороводород. В това изследване се доказват количествените промени при различни температури на синтеруване. Съдържанието на разтворима сол е ниско при температури на синтеруване над 1000 °C, което елиминира опасността за синтеруваните материали от тинята. Установени са пренос и трансформация на натриевия хлорид, което предлага отделяните газове от третирането трябва да се усилят при производството на синтерувани строителни материали.

Preparation and functional properties of maltose ester lactate

Y. Xuexin*

¹*School of Tourism and Cuisine, Harbin University of Commerce, No.138 Tongda Street, Daoli District, 150076 Harbin, China*

Received December 9, 2015; Revised June 17, 2016

First ethyl lactate was prepared from L-lactic acid and ethanol, with L-lactic acid the conversion rate as an index, the effect on the reaction of the molar ratio, reaction time and amount of catalyst were studied. Then maltose ester lactate was prepared from maltose and L-ethyl lactate, with monoester yield as an index, the effect on the reaction of the molar ratio of maltose and L-ethyl lactate, reaction time and amount of catalyst were then studied. The features of products such as: emulsifying and emulsion stability, oil retention were also studied. The results showed that the optimum conditions for the preparation of ethyl lactate is the molar ratio of L-lactic acid and ethanol 2:1, a reaction time of 1h, with the catalyst accounting for 2.5% of the lactic acid amount. The optimum conditions for the preparation of maltose ester lactate is a molar ratio of maltose and L-ethyl lactate of 1:2, a reaction time of 6h and a catalyst amount of 8%.

Keywords: Emulsifier, maltose ester lactate, L-lactic acid, maltose

INTRODUCTION

Since China's accession to the WTO, there are a variety of products that should conform with the international quality standards. In order to satisfy the people's quality requirements and avoid foreign technical barriers to exports, the state requires to implement the international standards for a variety of products. Thus, in the food industry, food emulsifier selection and use heeding the constraints.

Currently the commonly used food emulsifier glycerin fatty acid ester [1], about 53% of the total; soy lecithin and derivatives, accounting for about 20% of sucrose fatty acid esters and sorbitan fatty acid esters Rio 10%, about 6% of propylene glycol fatty acid ester. In addition, xylitol anhydride monostearate, polyoxyethylene stearate and xylitol anhydride and the like. However, in recent years many experiments showed that these emulsifiers are not ideal.

Lately, in bread production, in order to slow down the aging of bread, reduce the gluten strength and improve the machinability of the dough, in order to improve the quality of bread, make color bread, improve smell, taste, shape and better meet the needs of the consumers around the world, bread improvers have been widely introduced.

Bakery products impatiently stored, during the storage process will be acquire mildew and begin to age. In the large-scale production and sales of bread today, especially as the most serious problem is the aging of bread: the bread stored will be a little hard on the skin, the flavor is lost and other changes also

occur. According to the statistics, in 1990 due to the aging of bread the United States losses reached \$ 1 billion. As early as a century ago, the people started to seek solutions, foreign studied developed rapidly in this area. Thus, the French manufactured a bread with a shelf life of up to 92 days; the US military can allegedly increase bread shelf life to three years. Compared with foreign countries, China's bread industry, still experiences significant gaps, aging bread is a serious problem in China's bread industry, generally bread ages in three to five days, due to the short shelf life and intolerant storage, but also bread staling as a constraint to the development of China as an important reason for the bread industry, therefore, how to slow down the aging of bread, our bread industry needs to solve this major issue. Meanwhile, in the baking industry, there are similar problems, to solve this problem, we will promote the development of the baking industry.

In the production and use of the world's food emulsifier class of about 65 [2], the United Nations developed a standard total of 34 species, 58 kinds in the United States, the world's total annual demand is equivalent to about 800 million US dollars, 250,000 tons more than for consumption. In recent years, with the rapid rise of the food industry, emulsifier output ranked first in industrial output, the food additives production and research also has been considerably developed. The food emulsifier is the most important food additive, it not only has the typical surface activity in order to maintain a stable food emulsion state, but also exhibits a number of special features and thus plays an important role in the food industry. More widely applied since 1994 in our country are 30 kinds of food emulsifier varieties that are approved for use.

* To whom all correspondence should be sent:
E-mail: ashleyswift@163.com; yxx310@aliyun.com

This practice started late, but developed rapidly and there are several varieties arrived at following Research and Development. At present, China is capable of producing glycerides, sucrose esters, Span and Tween, propylene glycol, soy lecithin, nearly 30 species, consumption is expected to reach 15,000 ~ 20,000 tons.

L-lactic acid, which is a lactic acid. Lactic acid, its formula is $\text{CH}_3\text{CH}(\text{OH})\text{COOH}$, the scientific name α -hydroxy acid, the molecule contains an asymmetric carbon atom and is therefore optically active (L-, D- and racemic). There are three configurations of lactic acid, L- lactic acid is one kind, one kind of the D- lactic acid, there is a known DL- lactic acid. Lactic acid is an important organic acid, a raw material to it as an additive, preservatives, disinfectants and regulating agents play an important role in the brewing, food, cosmetics, pharmaceuticals, packaging, tobacco and other industries. The study found that the human body is only able to metabolize L- lactic acid, so that only L- lactic acid can be absorbed by the body and the microorganisms without any toxic effects, if too much D- or DL- lactic acid is ingested it will cause the blood rich in D - lactic acid, DL- lactic acid to cause fatigue, metabolic disorders and even poisoning. Therefore, it was suggested to the World Health Organization that D- and DL- lactic acid should not be used in children's foods. Thus, in the food industry L- lactic acid gradually substituted D- Lactic acid as an inevitable trend. Currently L- lactic acid production has just begun, with about 5% of the total production of lactic acid, as production increases, the application will also be expanded.

Starch sugar esters in domestic development is still in its infancy [3], yet we went to further research and develop these. Starch sugar (jelly) as a raw material for ester products, its superior performance and functionality with glycerol esters and such products. I chose maltose and ethyl lactate as the raw material, synthesis of maltose lactate ingestion of the human body, can be hydrolyzed to lactic acid and maltose (broken down into two glucose molecules) that can regulate the body's physiological function, with broad development prospects.

Maltose ester lactate is an important class of thickening with excellent emulsifying properties [4], biodegradation, security, a good surfactant and starch sugar esters. It not only has monoglyceride, sucrose ester emulsification, but also a thickening effect. Especially the emulsion stability of its unique properties, can be used to replace animal and plant gum. It also has more of a role in regulating the body's physiological function, so it

was developed to meet the requirements of the natural, nutritious, low-calorie, multi-functional role people expect. Maltose lactate as the food of industry, the pharmaceutical industry, the cosmetics industry, dispersants, emulsifiers, stabilizers, suspending agents, thickening agents, clouding agents, binders and suds boosters and detergents. The development of maltose lactate can be added as the emulsifier series to a new class of ester products, enriched emulsifier varieties, it has good prospects as a class of products.

L- lactic acid and maltose are good for the health, so these are used as a raw material, this paper describes the process conditions of maltose lactate, providing a theoretical and practical basis for the future development of starch sugar esters.

The synthesis process of maltose lactate is reported rarely and only at the research stage, we have not formed references to sucrose fatty acid ester (SE) and synthetic maltose lactic acid ester transesterification. Transesterification is divided into a solvent and its solvent-free, synthesis experiments were carried out by two methods, the solvent-free starting material can not form a homogenous system, the reaction hardly proceeds, we used selected solvents. The solvents are: methanol, propylene glycol and ethanol. Propylene glycol as a solvent after the reaction takes place is difficult to remove, but maltose was not dissolved in ethanol, so methanol was used as a solvent.

MATERIALS AND METHODS

Synthesis of L- ethyl lactate

Principle of the method

Esterification of L-lactic acid and ethanol in solid ferric chloride as a catalyst may be the mechanism of the process as follows[5] (Fig.1):

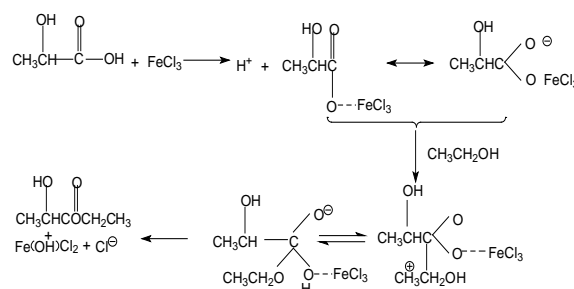


Fig. 1. Synthesis of L-ethyl lactate.

Synthetic methods

A reflux condenser, a thermometer and an electric mixer were installed on a three-necked flask.

First, three-necked flask were added in 100ml of solid iron chloride, L-lactic acid, ethanol, reflux

condenser installed, start the electric mixer stir, and heat up, reflux esterification, and sampled for lactate conversion rate, when a total reflux after a certain time, to join the band agent, installed water separator and reflux condenser, heating was continued reaction, esterification reaction, the esterification side edge excess water separated from the oil-water separator, maintaining evaporated the water carrier and raw materials continue to reflux until no more water separator to separate water droplets when discharged trap layer of water and oil, and heating was continued to maintain boiling, quickly evaporated ethyl acetate, ethanol, mixed with oil recycling to save, and then vacuum distillation to collect the product fractions, analytical testing, the conversion rate calculated by a vacuum pump.

Synthesis of maltose ester lactate

Principle of method

Maltose and ethyl lactate in the catalytic composite catalyst of anhydrous K_2CO_3 and PEG-400 transesterification reaction mechanism is as follows(Fig.2):

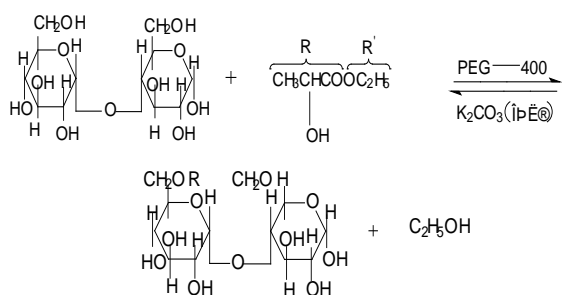


Fig. 2.Synthesis of maltose ester lactate

Synthetic methods

In a three-necked 100mL flask, adding a certain amount of maltose, homemade L-lactate, PEG-400, and a basic catalyst is K_2CO_3 thoroughly mixed together, a high speed stirring, heating. The reaction 6-8 hours, every half hour during the reaction stopper is removed, releasing the resulting ethanol. After completion of the reaction, a basic catalyst is added and tartaric anhydrous K_2CO_3 , pH value reached about 7, the system not only precipitated the crude product as a pale yellow viscous liquid maltose lactate, the yield was calculated.

Analysis method

NaOH standard solution calibration

NaOH standard solution preparation

The solution is 1000mL 0.1mol/L NaOH in a small beaker on the scales quickly weighing 4g of NaOH,

dissolved in 100mL of water and transferred to a 1000mL volumetric flask, then washed with pure water in a beaker three times with 50ml transferred to the capacity of the flask and then diluted to 1000mL, stoppered with a stopper, shaken and posted.

NaOH standard solution calibration

The referencereagent of 0.4-0.5g was accurately weighed with an electronic balance then 250mL of potassium hydrogen phthalate($KHC_8H_4O_4$) was added in a conical flask and dissolved in 20-30mL of distilled water adding 1-2 drops of phenolphthalein indicator to the NaOH solution titrated to a solution prepared from a colorless to reddish appearance, it does not fade for half a minute. Calculate the molar concentration of the NaOH standard solution.

$$C_{NaOH} = \frac{m_{KHC_8H_4O_4} \times 10^3}{M_{KHC_8H_4O_4} \times V_{NaOH}}$$

Wherein:

C_{NaOH} -For calibration of the concentration of NaOH solution (mol / l)

$M_{KHC_8H_4O_4}$ - $KHC_8H_4O_4$ molar mass (g / mol)

$m_{KHC_8H_4O_4}$ - Mass of $KHC_8H_4O_4$ (g)

V_{NaOH} -For calibration of the volume of NaOH solution consumed during titration (ml)

Determination of the L- lactic acid content

Determination of the L- lactic acid density

Dependent on the quality and volume proportional to the pipette the L-lactic acid is 5mL, in the electronic balance the quality is fine, with three sets of parallel experiments, taking the average in accordance with the formula:

$$\text{Density} = \text{Mass} / \text{Volume}$$

Determination of L - lactic acid content (acid-base neutralization titration method)

Taking 5mL of L-lactic acid, this is transferred into a 50mL volumetric flask with a constant volume and shaken. A volumetric flask with 2mL of L- lactic acid is kept in the conical flask with 1-2 drops of phenolphthalein added, the formulated NaOH standard solution after titration appears colorless to reddish and does not fade for half a minute. Write down the number for the volume of NaOH consumed, the three sets of parallel experiments were averaged.

$$\text{L- lactic acid content(\%)} = \frac{\text{Mass of L- lactic acid}}{\text{Mass of sample}}$$

Determination of the L - ethyl lactate acid value

The acid value is: 1g sample and the number of milligrams of free acid is required for KOH[6].

A 1mL amount of the system solution is placed in a pipette then into a Erlenmeyer flask, weighed on an electronic scale and adding to 10mL of distilled water, shaken, dropping 1-2 drops of the cresol red indicator into a standard KOH solution (configuration with NaOH) titrated to a purple color, milli-liters of the KOH solution are consumed. At the same time a blank test is carried out under the same conditions.

Calculated according to the formula:

The acid value is (mg KOH/g)= $N \times V \times 56.1 / W$

Wherein:

V- consumption volume of NAOH solution(ml)

N-Molar concentration of the KOH solution(mol/l)

W- Weight of the sample(g)

56.1- Molar mass of potassium hydroxide

Determination of L-lactic acid conversion rate

Conversion rate(%)= (Total acid number of feedstock - Total acid number of products) / Total acid number of feedstock $\times 100\%$

Determination of the maltose ester lactate yield

Yield(%)=Actual yield / Theoretical yield $\times 100\%$

Determination of the maltose ester lactate features

Oil retention measurement method

Accurately weigh 0.8g of maltose lactate dispersed in 25mL of oil spin at 5000r / min homogeneously for 2min, keep still for 15min, then centrifuge at 500r / min for 15min, afterwards discard the supernatant, access the precipitation weight, while molecular distilled monoglycerides control the experiments, according to the formula[7]:

Hold oil yield(%)=Precipitation mass / Sample mass $\times 100\%$

Determination of the emulsification and emulsion stability

The lactate 1.2g maltose dissolved in 50mL of distilled water is prepared at a certain concentration of the liquid with 50mL of soybean oil added at a speed of 10000r/min homogeneously dispersed for 2min, divided into 2 equal parts, transferred to a 50mL centrifuge tube and centrifuged at 1500r / min for 10 minutes, at the same time completing a control experiment with monoglycerides, calculated

according to the height of the emulsion layer and emulsification as follows:

Emulsification(%) =
Height of emulsion layer / Total height $\times 100\%$

A scale load in a 50mL tube is placed in a water bath at 50°C for 30min successively measuring the volume of the emulsion at every 2.5h. At the same time a single ester is utilized in a controlled experiment.

The emulsion stability is calculated as follows:

Emulsion stability(%)=
Final volume of the emulsion / Initial volume of the emulsion $\times 100\%$

Structural Identification of the product

Removable liquid absorption cell method

The liquid perfusion in a fixed thickness sealed liquid pool or into a removable liquid pool, into the optical path, the whole scan for the determination.

Solid compression method

Weigh the dry solid sample 1 ~ 2mg and 200mg bromine potassium powder in the agate mortar, in the infrared light grinding evenly, pour into the tablet mold in the shop, put the tongue, put the mold on the hydraulic machine and connect Vacuum system, the first pumping 5min, to remove the mixed in the powder of moisture and air, and then pumping the side pressure to 8t, to maintain 5min, remove the vacuum. The mold rotation 1800, and then pressure to 8t, to maintain 2 ~ 3min, remove the mold. With the help of the "sampler", use a hydraulic press to carefully remove the tongue, in the middle of the upper and lower tongue to get a diameter of 1cm, thickness of 0.8mm sheet, put it on the sample box on the back. Then, 200 mg of potassium bromide powder was ground under the same conditions to make a blank potassium bromide sheet and placed on a reference frame. The prepared film is placed on the corresponding optical path of the infrared spectrophotometer, select the appropriate scanning speed, from 4000 ~ 400 cm^{-1} full scan, drawing the infrared spectrum of the sample. The infrared measurement method of the product is the same as above[8].

RESULTS AND DISCUSSION

Determination of the optimum process conditions for the synthesis of ethyl lactate

Process: raw material (catalyst) \rightarrow esterification (the reaction was kept boiling) water removal \rightarrow detected \rightarrow finished product

Determination of the optimum L- lactic acid and ethanol molar ratio

The fixed reaction temperature is 85 °C, the amount of catalyst was 2%, the reaction time is 1h, to change the L- lactic acid and ethanol molar ratios of 1: 1, 1: 1.5,1: 1.8,1: 2,1: 2.5, The conversion rate results are shown in Fig. 3 determined after the synthesis of L- lactic acid

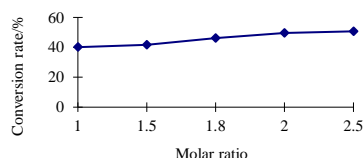


Fig. 3. Effect of the L- lactic acid and ethanol molar ratio on the L- lactic acid conversion rate.

Fig.3. shows that the process parameters for the reaction temperature of 85°C, the amount of catalyst was 2%, the reaction time is under 1h, the conversion of ethyl lactate is mainly affected by the molar ratio of the L- lactic acid and ethanol, the molar ratio is small, the L- lactic acid conversion is low, with an increase of the molar ratio, the L- lactic acid conversion rate also increases, but the molar ratio is more than 1: 2 later, the L- lactic acid conversion rate does not improve up to a 1 molar ratio of the L- lactic acid and an ethanol ratio of 2 is more appropriate.

Determination of the optimal amount of catalyst

The L-lactic acid and ethanol are in a molar ratio of 1: 2, the reaction time was 1h, the reaction temperature is under 85°C, changing the amount of catalyst, the synthesis of L- lactate, measured the amount of catalyst used in amountsfor 0.5% of L- lactic acid, at a 1%, 1.5%, 2%, 2.5% level of conversion of the L- lactic acid, the results are shown in Fig.4.

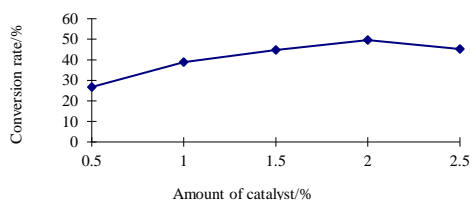


Fig. 4. Effect of the amount of catalyst on the L- lactic acid conversion rate.

The catalyst is generally added to increase the reaction rate and can be seen from Fig.4, it increases with the amount of catalyst, the L- lactic

acid conversion rate gradually increased, but when the catalyst amount used is greater than 2%, the L- lactic acid conversion rate is reduced, the L- lactate synthesis catalyst is about 2%in amount.

Determination of the optimum reaction time

In a molar ratio of L- lactic acid to ethanol is 1: 2, the reaction temperature is 85°C, the amount of catalyst is for the next 2%, the reaction time was changed to 0.5h, 1h, 1.5h, 2h, 2.5h, measuring the L- lactic acid conversion rate, the results are shown in Fig.5.

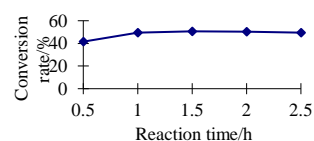


Fig. 5.Effect of the reaction time on the L- lactic acid conversion rate.

Fig.5 shows that, the L- lactic acid conversion rate increases with time, but the conversion rate is not 1h after significant changes in the conversion rate decrease after 2h, a reaction time of 1h is appropriate.

The reaction time is complete and does not have a great influence on the esterification reaction carried out under the same conditions, the reaction time is too long and will lead to reduction of the conversion of L-lactic acid, but also to a deep color of the product, affecting the quality of the product, the appropriate reaction time is 1h.

Identification of the L- ethyl lactate structure

As observed in Fig.6 and Fig.7 the peaks of the L- lactate structures are identified, indicating that this substance is L-ethyl lactate.

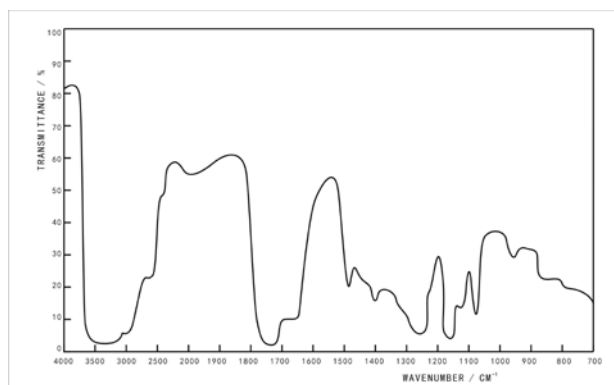


Fig. 6.The L- lactic acid infrared spectrum.

Shown in Fig.6 is the L-lactic acid feedstock infrared spectrum and in Fig.7 the product L-lactate IR spectra for comparison, the product spectrum generatesa methylene (2925cm⁻¹) absorption peak

and a carbonyl peak (1740cm^{-1}) for the ester carbonyl peak, which consists of the carbonyl starting material (1725cm^{-1}), a number moving to a longer wavelength in the direction proven by the reactant converted to the ester product yielding the desired product. (Ethyl lactate and consistent with the spectrum of the standard products).

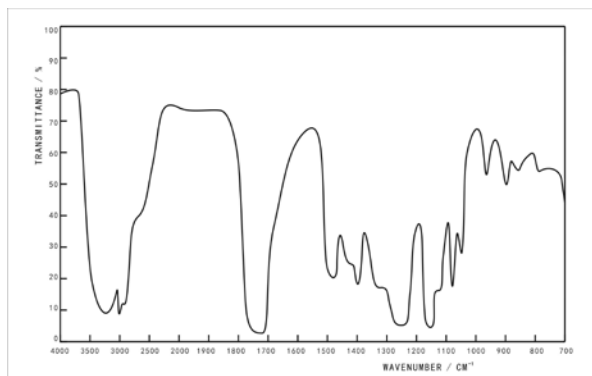


Fig. 7. The L-ethyl lactate infrared spectrum.

Determination of the optimum maltose ester lactate synthesis conditions

Process: raw material (catalyst) → transesterification → neutralization → still → detected → finished.

Determination of the optimum maltose and ethyl lactate molar ratio

In the synthesis of ethyl lactate the maltose reaction temperature is $60\text{ }^{\circ}\text{C}$, the amount of catalyst is 8%, the reaction time was 6h, the change of maltose, the molar ratio of the ethyl lactate and ethyl lactate yields after synthesis were measured in the molar ratios of maltose and ethyl lactate of 1:1, 1:1.5, 1:2, 1:2.5, the results are shown in Fig.8.

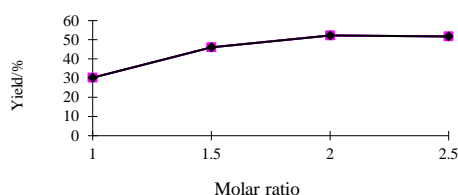


Fig. 8. Effect of the maltose and L-ethyl lactate molar ratio on yield.

Fig.8 shows that the reaction temperature is $60\text{ }^{\circ}\text{C}$, the amount of catalyst is 8%, the reaction time is 6h and the conditions yielding maltose are mainly affected by the lactate and ethyl lactate molar ratio of the maltose impact molar ratio which is small, having a maltose low yield of the lactic ester, given an increase of the molar ratio, the maltose yield of the lactic ester is increased, but a molar ratio of more than 1:2 is registered later, the yield

then declines, thus a mole of the maltose ethyl lactate of 2 is more appropriate: 1 is a control ratio.

Determination of the optimum reaction time

The maltose and ethyl lactate molar ratio is 1:2, the reaction temperature is $60\text{ }^{\circ}\text{C}$, the catalyst dosage is 8% of the synthesised maltose lactate. Synthesis under the above conditions remains unchanged, the reaction times were 5h, 6h, 7h, 8h, for the maltose lactate yields measured, the results are shown in Fig.9.

Shown in Fig.9 are the maltose lactic acid ester synthesis reaction time increases, the yield is not increased, but the reaction time decreased, the product will become darker in color, a reaction time maintained at around 6h is favorable.

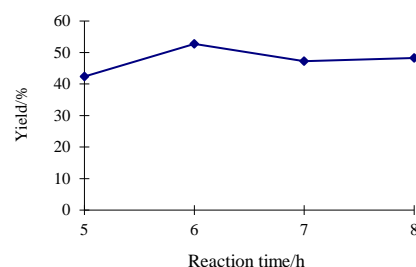


Fig. 9. Effect of the reaction time on the yield.

Determination of the optimum amount of catalyst

The Maltose and ethyl lactate molar ratio is 1:2, the reaction temperature is $60\text{ }^{\circ}\text{C}$, the reaction time is 6h, the conditions change the amount of the catalyst and maltose lactate synthesized, respectively, the amounts of L-lactate catalyst are 6%, 8%, 10%, 12% for the measured maltose yield of the lactic ester, the results shown in Fig.10.

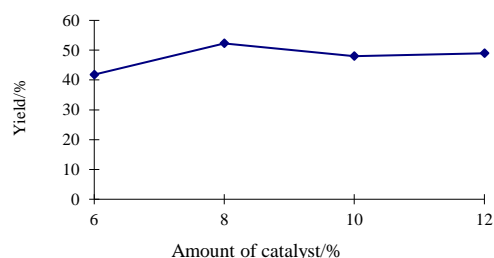


Fig. 10. Effect of the amount of catalyst on yield.

The catalyst added may generally increase the reaction rate of the reaction in the positive direction of the reaction, the excess catalyst will also affect the progress of the reaction and can be seen from Fig.10, it increases with the amount of catalyst, when the catalyst amount exceeds 8%, the maltose yield of the lactate decreased and the additional catalyst causes the product color to deepen,

affecting the quality of the product, such that the appropriate amount of maltose lactate catalyst synthesized is 8% or less.

Effect of the reaction temperature on the synthesis of maltose ester lactate

The temperature requirements for the synthesis of Maltose lactate are very strict, the reaction temperature in the inquiry follow the test:

The maltose and ethyl lactate molar ratio was 1: 2, the reaction time was 6h, the catalyst amount was 8%, the reaction temperature was set at 50 °C, the results of a two-phase reaction system, the raw materials were not dissolved into the solvent, resulting in a yield of less than 10%.

Under the condition of maltose and ethyl lactate molar ratio of 1: 2, reaction time of 6h, catalyst dosage of 8%, the reaction temperature is set at 70 °C, the temperature is too high, resulting in maltose discoloration, the product color is extremely deep, seriously affecting the quality of the product.

Because of these two reasons, the choice of the temperature range is very small, at around 60 °C the yield did not change much, so the reaction temperature was set at 60 °C.

Structural identification of the maltose ester lactate

From the peaks in Fig.11 and Fig.12 the structure of maltose lactate was identified, indicating that this substance is maltose ester lactate.

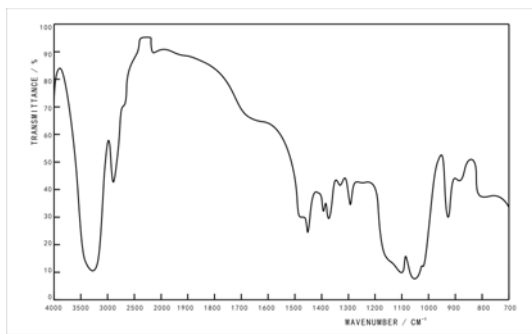


Fig. 11. Maltose infrared spectrum.

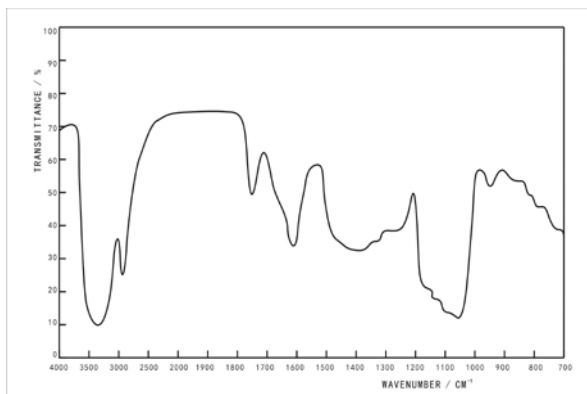


Fig. 12. Maltose ester lactate infrared spectrum.

Fig.11 and Fig.12 present synthesized raw product maltose and maltose lactate apparent from the comparison between the two spectra, the spectrum of the product, the starting material maltose plurality ester carbonyl peak (1740cm⁻¹) and (1580cm⁻¹) of absorption peaks. Very weak carbonyl group (3450cm⁻¹) ester overtone peaks were covered by hydroxy, the reaction proved that the product converted to maltose lactate, the desired product.

Features of maltose ester lactate

Emulsification and emulsion stability of Maltose ester lactate

Emulsifying refers to the lactate maltose binding properties of the oil-water emulsion, the emulsion stability refers to the oil-water emulsion formed together with the ability to maintain stability. Maltose monoglycerides and lactate were measured given emulsification and emulsion stability at the same temperature, the same concentration, as measured and presented in Table 1.

Table 1. Comparison of emulsification and emulsion stability.

Species	Emulsification /%	Emulsion stability/%				
		0.5h	1.0h	1.5h	2.0h	2.5h
Maltose ester lactate	55.00	53.09	53.09	51.22	48.72	48.71
Monoglycerides	40.00	39.14	34.15	32.75	30.89	27.14

Table 1 shows, that maltose lactate has emulsification and emulsion stability, compared with monoglycerides, its emulsifying properties and emulsion stability is greater than for monoglycerides and lactic acid esters, the description of the experiments render emulsification and emulsion stability as standard.

Oil retention of maltose ester lactate

Oil retention refers to the ability to maintain an oil emulsifier, the results in Table 2 present the measured monoglycerides and lactate maltose only holding oil.

Table 2 shows that, compared with monoglycerides, lactic acid ester oil retention by maltose is greater than for monoglycerides,

indicating good oil retention by maltose lactate is desirable.

Table 2. Comparison of oil retention.

Name	Maltose ester lactate	Monoglycerides
Oil retention/%	281.25	187.50

In summary, the laboratory synthesis of maltose lactate in emulsifying, emulsifying stability, oil holdings are similar to monoglycerides or greater than monoglycerides, maltose lactate ester to prove the functional characteristics of the basic meet the requirements, good performance.

CONCLUSIONS

With L-lactic acid and ethanol for the synthesis of L- lactate, the single factor experiment to determine the optimum conditions for the synthesis of ethyl lactate are: a molar ratio of the L- lactic acid and ethanol of 2: 1, a reaction time of 1h, the catalyst accounts for 2% of the L- lactic acid content. While its structure was identified by infrared spectroscopy.

The maltose-step synthesis of L- lactate was synthesized from maltose lactate, through a single factor experiment to determine the optimum conditions for maltose lactate: with a maltose and acetic acid L- ester molar ratio of 1: 2, the reaction time is 6h, the catalyst amount is 8%. While its structure was identified by infrared spectroscopy.

The synthesis of maltose lactate features: emulsifying, emulsion stability, oil retention measured simultaneously using the molecular

distillation of monoglycerides as a control experiment. The results showed that the functional properties of maltose lactate are greater than or equal to those of the monoglycerides.

This experiment proves that the project to prepare maltose lactate either by feature or by practical application of the emulsifiers is basically in line with the requirements of a good performance of the emulsifier. The results will be further applied to maltose lactate to provide basic data.

Acknowledgements: This project was supported partially by the Harbin University of Commerce Ph.D. research project startup (13DW028) .

REFERENCES

1. Z. Wanfu, Food emulsifier, China Light Industry Press, Beijing, 1993, p.63.
2. C. Shixue, Z. Xiqun, T. Guangling, L. Chengxia, D. Guojun, *China Beet Sugar*, **1**, 6 (1995).
3. L. Jiancheng, Jinyizhi, *China Food Additives*, **4**, 43 (1998).
4. L. Jiancheng, Y. Changgui, *Chinese food additives*, **3**, 26 (1998).
5. W. Gang, S. Dun, P. Qiuping, *Harbin Normal University Natural Science Journal*, **13**(6), 63 (1997).
6. X. Baocai, Z. Fuping, Chemicals and Raw Materials Analytical Manual, Chemical Industry Press, Beijing, 2002, p. 14.
7. Z. Qi, C. Yan, *Food Science and Technology*, **3**, 90 (2003).
8. U. Braun, B. Schartel, M.A. Fichera, C. Jaeger, *Polym. Degrad. Stab.*, **92**(8), 1528 (2007).

ПОЛУЧАВАНЕ И ФУНКЦИОНАЛНИ СВОЙСТВА НА МАЛТОЗО-ЛАКТАТЕН ЕСТЕР

И. Ксюексин

Училище по туризъм и готварство, Търговски университет в Харбин, 150076 Харбин, Китай

Постъпила на 9 декември, 2015 г.; коригирана на 17 юни, 2016 г.

(Резюме)

Най-напред се получава етил-лактат от L-млечна киселина и етанол с показател за степента на превръщане, при различни моларни отношения, времена за реакция и количества катализатор. След това малтозо-лактатът се получава от малтоза и L-етил-лактат с показател добива на моноестер. Изследвани са ефекта на времето за реакция, моларното отношение на малтозата и етиловия естер и количеството катализатор. Свойствата на продуктите (емулгиране и стабилност на емулсията, задържането на масло). Резултатите показват че оптималните условия за получаването на етил-лактат са моларно отношение L-млечна киселина и етанол 2:1, време за реакция от 1 час и катализатор 2.5% от количеството на млечната киселина. Оптималните условия за получаването на малтозо-лактатния естер са моларно отношение на малтоза към етилов естер 1:2, време за реакция 6 часа, а количество на катализатора от 8%.

A kind of integrated microfluidic system for rapid pathogenic botrytis cinerea detection

P.F. Xu^{1,2}, N. Yang^{2*}, J. Jia¹, C. Xu¹, J.J. Guo²

¹Engineering and Technology Center for Modern Horticulture, Jiangsu Polytechnic College of Agriculture and Forestry, Jurong, PR China

²School of Electrical and Information Engineering, Jiangsu University, Zhenjiang, PR China

Received February 12, 2016; Revised November 24, 2016

In order to overcome the poor timeliness and low automaticity of the detection of existing botrytis cinerea in fruits and vegetables, an integrated microfluidic system for rapid detection is proposed. In this system, the microelectrode is mounted on the bottom of the microfluidic chip channel and connected to a digital impedance measurement circuit. The magnetic beads whose surface is encased by mouse botrytis cinerea antibody, is controlled by an external Gauss magnetic field to capture botrytis cinerea. Then the combination of botrytis cinerea and the magnetic beads is transferred to a microelectrode array. By constructing a counting circuit based on impedance measurement at the electrode terminals, the amount of botrytis cinerea can be effectively measured. The results show the validity of the system in detecting the amount of botrytis cinerea in fruits and vegetables. In addition, the detection time is only nearly one-fiftieth compared with a traditional laboratory test.

Keywords: Pathogens; formatting; Integrated microfluidic; Rapid detection; Impedance

INTRODUCTION

Gray mold is one of the main diseases which damage the facilities of fruit and vegetable cultivation, mainly infecting the night shade family, cucurbit crops, onion leeks, berries and so on, leading to crop root rotting, withering away, decomposing, stem gangrening and so forth, decreasing the quality, affecting productivity and decreasing by more than 50% the productivity when this is serious. Therefore, highly efficient, rapid, portable botrytis cinerea detection is the key technology to ensure the quality of agricultural production and promotion of the intensive mode of production.

Traditional botrytis cinerea detection methods include the AGAR plate culture method [1]; the direct microscopic counting method [2]; the plate counting method [3]; the light spectrum detection method [4]; the mold rapid test paper method [5] and others. The culture medium is heated in the flame over a long period of time using the AGAR plate culture method, which is not conducive to bacteria recovery and the water is not consistent before and after loading. The plate count method has greatly influences the fungi during the sample treatment process, so it does not reflect the pollution situation accurately. The light spectral detection method is relatively advanced, but the process requires the help of professional laboratory

personnel with complex experimental steps carried out with the aid of expensive equipment. The mold rapid test paper method is simple and easy to operate, cultivating at room temperature, the results are observable in two days, the efficiency is higher, but it is expensive. These defects limit the practical application of the technology in agricultural production it also restricts the development of a high quality and highly efficient horticultural production technology in our country.

In recent years, the micro fluidic technology is an effective method that renders, injection, mixing, reaction and detection linking integrate into a piece of the micron scale chip. The introduction of the system has greatly improved the automation and the objectivity of the fungus detection process, which has caused the wide attention of the scholars at home and abroad [6-9]. However, a complete detection method and detection system of botrytis cinerea matching in fruits and vegetables to the micro fluidic chip does not exist.

On this account, this paper presents an integrated microfluidic system for rapid pathogenic fungus detection based on immunomagnetic capture by the compound microelectrode impedance detection technique.

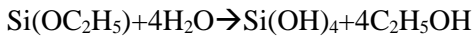
THE IMMUNOMAGNETIC BEAD PREPARATION AND THE ACQUISITION PRINCIPLE OF BOTRYTIS CINEREA

The pathogens' immuno magnetic capture technology uses magnetic beads as carrier for antibody immobilization, via specific binding of the

* To whom all correspondence should be sent:
E-mail: yangning7410@163.com

antibody to antigen, realizing the capture of pathogens, also realizing the enrichment of the object on the solid support surface and then improving the sensitivity of the detection method [10].

The first step of the preparation of an immunomagnetic sample is $\text{Si}(\text{OC}_2\text{H}_5)_4$ (short for TEOS) being hydrolyzed to get $\text{Si}(\text{OH})_4$ under the catalysis of ammonia water. Then a chemical reaction occurs at some active points of the $\text{Si}(\text{OH})_4$ and Fe_3O_4 particle surface, as the combination point on the surface film, obtaining composite magnetic micro spheres ($\text{Fe}_3\text{O}_4@ \text{SiO}_2$). Then using triethoxyaminopropylsilane (short for APTES) as the organic precursor, an Amino modification of the silicon oxide surface of $\text{Fe}_3\text{O}_4@ \text{SiO}_2$ takes place, obtaining $\text{Fe}_3\text{O}_4@ \text{SiO}_2\text{-NH}_2$ composite micro beads (MMPs) in the process of preparation, the main process is shown in the Picture 1.



TEOS

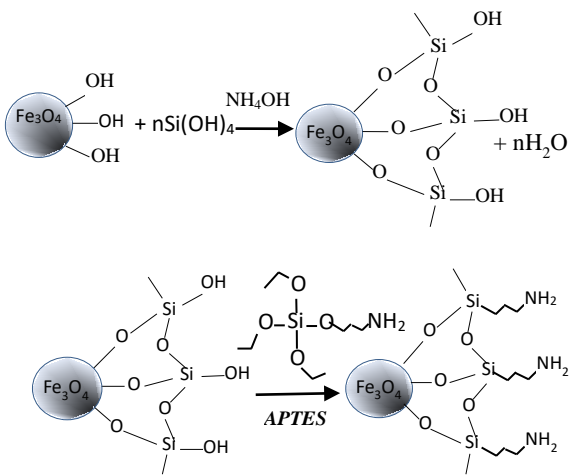


Fig. 1. Preparation principle of $\text{Fe}_3\text{O}_4@ \text{SiO}_2\text{-NH}_2$

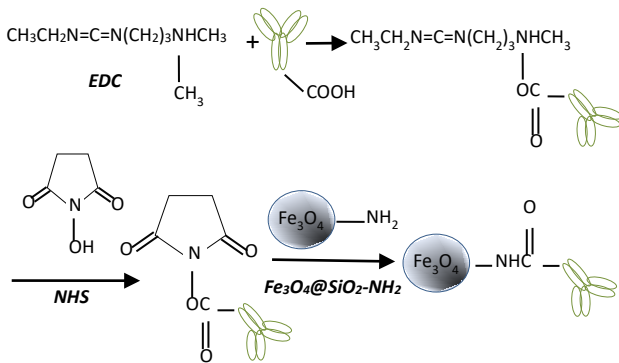


Fig. 2. The preparation principle of IMMPS.

Then activating the carboxyl group of the surface of the mouse's gray mold antibody via an EDC/NHS crosslinking agent, forming intermediate products with the active group and then after being covalently bound to the amino group on $\text{Fe}_3\text{O}_4@ \text{SiO}_2\text{-NH}_2$, obtaining immunocomplex micro beads (IMMPs) in the process of preparation, the process is shown in the Picture 2.

CHIP OPERATING PRINCIPLE

Figure 3 is the principle diagram of an integrated microfluidic system for rapid pathogenic botrytis cinerea detection, which uses chemical crosslinking technology to make pathogens antibody to coat the micron sized magnetic beads, so as to bring beads into the microfluidic chip system, then the microfluidic chip system is placed in a Gauss magnetic field controller (as shown in Figure 4), by controlling the transformation of the magnetic field to drive the magnetic beads. In the process of beads movement, the antibody can effectively capture the pathogen antigen. Then the combination of pathogenic fungus and magnetic beads was brought to the microelectrode array at the bottom of the micro fluidic chip by the Gauss magnetic field controller. After capturing the pathogen antigen, the microelectrode array can measure the impedance change to determine the amount of pathogenic fungus in fruits and vegetables through the impedance measuring circuit.

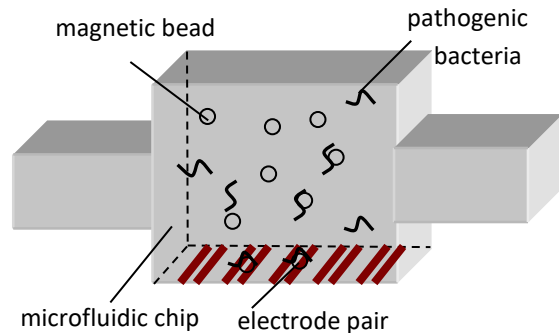
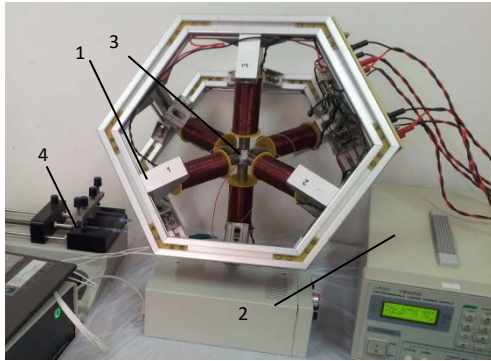


Fig. 3. The principle of rapid detection of pathogenic bacteria.



1. Gauss magnetic field controller; 2. Control power supply; 3. microfluidic chip; 4. driven pump

Fig. 4. Picture of the magnetic field controller.

In order to maximize the detection probability, the electrode array at the bottom of the microfluidic chip is arranged as dense as possible. The electrode pair is closely connected with the detection circuit, and each pair of electrodes has an independent XY address, which can be tested separately.

There are three possible conditions between the electrodes. First, there are no free beads between the electrodes, this is the only ionization medium and the impedance level is low. Second, only the immunomagnetic beads are between the electrodes meaning that the beads do not capture the pathogenic fungus and therefore the impedance level is highest. Finally, the beads capture the free pathogen between the electrodes, under the influence of parallel micro magnetic resistance and fungal cytoplasm resistor, the impedance level reduced to an intermediate value. In order to ensure the sensitivity of the electrode detection, the voltage across the electrodes must always be greater than the bacterial cell membrane breakdown voltage, so the selection is from 0.2V to 1.5V [9]. In this way, the capacitance of the cell membrane can be neglected, which renders the bacteria into a superior conductor. Through the above working principle, a relationship can be established between the concentration and the variation of the impedance of the pathogenic fungus in fruits and vegetables. The equivalent circuit of impedance measurement of the pathogen is shown in Figure 5.

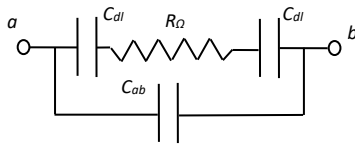


Fig. 5. The equivalent circuit for impedance measurement system

The research electrode and the auxiliary electrode are represented respectively by a and b, then the electrode impedance is calculated as follows:

$$|Z_1| = \sqrt{R_{\Omega}^2 + \frac{1}{(\pi f C_{dl})^2}} \quad (1)$$

$$|Z_2| = \sqrt{\frac{1}{(2\pi f C_{ab})^2}} \quad (2)$$

$$\frac{1}{Z_{total}} = \frac{1}{Z_1} + \frac{1}{Z_2} \quad (3)$$

Where, C_{ab} is the interelectrode capacitance, C_{dl} is the interface between the poles of the electric double layer capacitor, R_{Ω} is the resistance of the fungus and bead complexes, f is the frequency of impedance testing, Z_1 is the impedance of the equivalent circuit of $C_{ab} + C_{dl} + R_{\Omega}$; Z_2 is the impedance of the equivalent circuit of C_{ab} , Z_{total} is the system impedance. The bacteria concentration can be assessed by determining the quantitative relationship between the systematic impedance with the concentration of pathogen.

MICROELECTRODE AND IMPEDANCE DETECTION CIRCUIT

A. The fabrication of a microchannel and microelectrode

The microfluidic chip is produced from poly dimethyl siloxane (PDMS) material. PDMS is evenly mixed with a curing agent in the proportion of 90% and the mixture is injected into the container. The significant number of bubbles produced during the mixing process can be removed by a vacuum-pumping system. The mixture stands at room temperature for about 10 hours until PDMS curing and remolding, so as to form a micro channel based on the microfluidic chip PDMS substrate. the micro channel is used to provide a place to capture the immunomagnetic beads.

The tin indium oxide conductive film is chosen as a substrate. Ultrasonic cleaning is carried out by deionized water, methylbenzene, acetone and alcohol. The water is heated to a temperature of 120°C. The negative photoresist ITO array electrode pattern can be obtained in 4 steps: whirl coating, prebaking, exposure and developing. Afterwards, the microelectrode array (20μm×20μm) is fabricated by means of hard baking, corrosion, removing of the photoresist, scouring, baking and others. Shown in Figure 6 is the microscopic image of the microelectrode array. The overall microfluidic system can be obtained by plasma bonding to the

ITO substrate with a microelectrode array and PDMS chip.

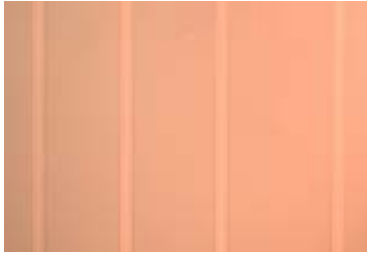


Fig. 6. The microscopic image of microelectrode array

B. Design and fabrication of the impedance detection circuit

For each pair of electrodes, there is a corresponding detection circuit which is used to detect the real part of the impedance. Figure 7 is a simplified schematic of the detection circuit. The detection circuit is used to measure the electrical level between the electrode pairs. The specific steps are the following: first the reference current is injected into one electrode and then passes through the test target and then finally it flows to earth. The test target is a parallel model of the immunomagnetic bead and the aquaculture pathogen. If K1 is closed and K2 is opened, then this state shows that the immunomagnetic bead does not capture the pathogen. If K1 and K2 are closed, then this state shows that the immunomagnetic bead captures the pathogen. The current which is exported from the current supply is converted to a voltage signal through the impedance between the electrodes. The voltage signal is compared with a reference voltage, thus an output signal that reflects the relationship between the electrodes can be obtained.

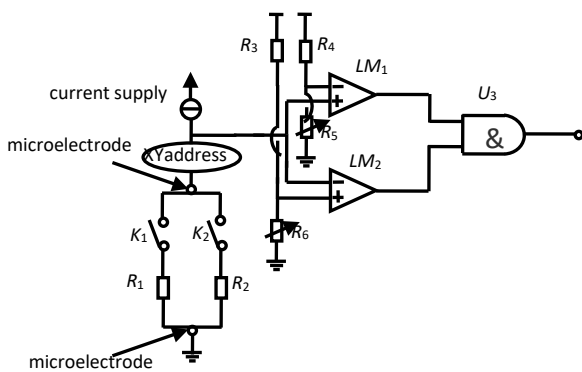


Fig. 7. Impedance detection circuit principle diagram.

In order to enable the detection circuit to accurately measure the amount of the pathogens, the impedance threshold of the pathogens that have fallen into the microelectrode should be measured accurately. The impedance signals that can be obtained through microelectrode measurement are introduced to the logic circuit by ITO lead wire. To ensure the tight joint between the ITO conductive glass and the electronic circuit, this paper adopts silver paste for the welding procedure. The distribution of pathogenic fungi can be observed under a microscope, the different impedance values which correspond to the magnetic beads that carry pathogenic fungi and the magnetic beads that don't carry pathogenic fungi stand idle respectively in accordance with the distribution conditions. The paper uses the *Botrytis cinerea* in strawberries as an example and the average impedance measured by the microelectrode load conditions is 65 kΩ. When magnetic beads don't capture the pathogenic bacteria, the average impedance is 800kΩ. On the other hand when the magnetic beads capture the pathogenic bacteria, it is 200kΩ. According to the values for the impedance, R_5 and R_6 are set effectively, when the magnetic beads capture the pathogenic fungi, the comparator LM_1 and LM_2 output at high levels at the same time so that the gate circuit output digital signal is "1" and its output digital signal is "0" under different conditions.

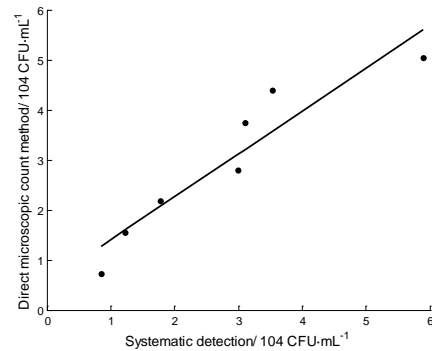


Fig. 8. Regression analysis for the two methods.

The results show that the average relative error of the two detection methods is less than 8%. Compared with the most widely used plate count method, the integrated microfluidic system for aquaculture pathogenic fungus achieved the daily detection accuracy and the detection time was shortened to about 55 minutes, the detection efficiency was raised about 50 times. In addition, the human input and complexity is far lower than for the traditional plate count method during the whole detection process, it greatly improves the

automation level in the detection of the pathogenic fungi in fruits and vegetables.

Table 1. Error comparison of the two detection methods

Sample	Microscopic Count Method CFU·mL ⁻¹	Microfluidic System CFU·mL ⁻¹	Relative Error
1	1.23×10 ⁴	1.56×10 ⁴	-2.68%
2	2.99×10 ⁴	2.79×10 ⁴	6.69%
3	5.89×10 ⁴	5.04×10 ⁴	1.44%

CONCLUSION

A rapid integrated microfluidic detection system is proposed in this paper. The system puts the microelectrode at the bottom of the microfluidic chip channel and it connects with the digital circuit for impedance measurement. The paper uses chemical crosslinking technology to make a pathogenic fungus antibody and coat the magnetic beads also using an external Gauss magnetic field to control the capture of pathogen fungi by magnetic beads. Then the combination of magnetic beads and pathogen fungi is taken to the microelectrode array and the impedance measurement circuit between the microelectrodes will detect the content of the pathogenic fungi. The research results show that the detection system has basically reached the daily detection accuracy and the detection time is shortened to about 55 minutes, the detection efficiency is raised about 50 times and the human input and complexity is far lower than the traditional plate count method during the whole detection process, this greatly improves the process of automation level detection of pathogenic fungi in fruits and vegetables. Thus, research experience was gained in the development of a portable horticultural plants pathogen detection system.

ИНТЕГРИРАНА МИКРОФЛУИДНА СИСТЕМА ЗА БЪРЗО

ОТКРИВАНЕ НА ПАТОГЕНИТЕ *Botrytis cinerea*

П.Ф. Ксу^{1,2}, Н. Ян^{2*}, Дж. Джиа¹, К. Ксу¹, Дж. Дж. Гуо²

¹ Инженерно-технологичен център за модерни хортикултури, Политехничен колеж по земеделие и лесотехника „Джиандзу“, Джуронг, Китайска НР

² Училище по електро- и информационно инженерство, Университет „Джиандзу“, Дженджиян, Китайска НР

Постъпила на 12 февруари, 2016 г.; коригирана на 24 ноември, 2016 г.

(Резюме)

Предложена е микро-флуидна система за бързо откриване на патогените *Botrytis cinerea* в плодове и зеленчуци. В схемата един микроелектрод се монтира на дъното на канал на микро-флуиден чип и се свързва с цифров контур за импедансно измерване. Системата се зарежда с магнитни сфери с имобилизирани антитела от *Botrytis cinerea* (изолирани от мишки) и контролирани от външно магнитно поле за задържането на антителата. Имобилизирани антитела се прехвърлят в микроелектродното пространство. Количеството на *Botrytis cinerea* се определя чрез броящ контур, базиран на импедансно измерване. Резултатите показват приложимостта на системата. Времето за определяне е петдесет пъти по-кратко от необходимото за традиционния лабораторен тест.

Acknowledgements: This work was supported by the Primary Research & Development Plan (Modern Agriculture) of Zhenjiang (NY2015026), Science and Technology projects plan of Jiangsu Polytechnic College of Agriculture and Forestry (2016kj016), Changzhou Sic & Tech Program(CE20155054), China Postdoctoral Science Foundation (2015T80512), Jiangsu Province Higher Vocational College Teachers' Academic Pacesetter High-end Study and Training (2016GRFX022).

REFERENCES

1. J.C. Biffing, D.E. Barlow, R.K. Pirlo, D.M. Babson, L.A. Fitzgerald, S. Zingarelli, L.J. Nadeau, W.J. C-Goodson, J.N. Russell, *International Biodeterioration & Biodegradation*, **95**, 11 (2014).
2. K.J. Griffitt, N.F. Noriea III, C.N. Johnson, D.J. Grimes, *Journal of Microbiological Methods*, **85**, 5 (2011).
3. S. Yagi, T. Nagata, M. Koide, Y. Itoh, T. Koizumi, Y. Azuma. *Beam Interactions with Materials and Atoms*, **183**, 10 (2001).
4. X.Wang, Y. Liu, G.Xie, *The Journal of China Universities of Posts and Telecommunications*, **20**, 8 (2013).
5. L. Yuwei, L. Fengqin, *Chinese Journal of Food Hygiene*, **9**, 6 (1997).
6. N. Yang, R.B. Zhang, P.F. Xu, *Chinese Journal of Scientific Instrument*, **34**, 6 (2013).
7. J.Y. Yoon, J.H. Han, C.Y. Choi, M.Bui, R.G Sinclair. *Transactions of the ASABE*, **52**, 1 (2009).
8. J.P. Lafleur, S. Senkbeil, T.G. Jensen, J.P. Kutter, *Lab on a chip*, **12**, (2012).
9. S. Schreier, G. Dounghawee, D. Triampo, P. Wangroongsarb, R.A. Hartskeerl, W. Triampo. *Acta Tropica*, **122**, 4 (2012).
10. M. Khine, A. Lau, C. I-Zanetti, J. Seo, L.P. Lee, *Lab on Chip*, **5** (2005).

Interference analysis for pesticide residue photometric detection based on integrated microfluidic chip

N. Yang^{1,2}, Z. Li^{1*}, J. Sun¹, P.F. Xu¹, J.J. Guo¹, H.P. Mao^{2*}

¹*School of Electrical and Information Engineering, Jiangsu University, Zhenjiang 212013, PR China;*

²*Institute of agricultural engineering, Jiangsu University, Zhenjiang 212013, PR China;*

Received March 27, 2016; Revised July 25, 2016

In order to improve the accuracy of the photometric detection of pesticide residues performed on integrated microfluidic chip, errors are analyzed and the model is built in photometric detection with different kinds of microfluidic chips. From the point of common, detection error is mainly caused by the temperature and the preparation time. The wavelength which is the causes error has become an impact factor in photometric detection with glass-based microfluidic chip, so the detective wavelength should be optimized. Because of small scale and fixed optical path, the path-length error is unique in glass-based microfluidic chip, which affect the pesticide residue sensitivity of photometric detection system.. Therefore, the relationship between error resulting from fixed optical path and optical path is established and verified by experiments. According to the particularity of photometric detection with paper-based microfluidic, the parameters of the optical wavelength and the color uniformity of different structures were evaluated and the errors analysis were carried out, then the optimal reaction conditions were determined. This research provides theoretical basis for the study of precise photometric detection of pesticide residues with glass-based and paper-based microfluidic.

Keywords: pesticide residues, photometric detection, microfluidic, error model

INTRODUCTION

The data from the state council shows that the number of cancer due to ingestion of food and vegetables with pesticide residues increases by 15% each year [1,2]. Therefore the use of portable equipment to detect residues plays an important role in guaranteeing the safety of food [3,4]. However, precision is the key factor that restricts the development of pesticide residue detection technology.

At present, the detection of pesticide residue is carried out mainly by immunoassay [5~7], sensors [8~10] and quick test card [11~13]. But the testing equipment mentioned above lacks of high sensitivity so it isn't practical for farmers to apply. Photometric detection technology provides the qualitative or quantitative analysis of pesticide residue through testing its light absorption in specific wavelength or a certain range [14]. Microfluidic technology is a new type of technology that puts the basic operating units such as reaction, separation and testing, which were involved in the detection of pesticide residues, into a chip of a few square centimeters (or less) [15,16]. The method combining microfluidic with photometric detection can resolve the problem of low sensitivity of pesticide residue detection.

Domestic and foreign scholars have studied the

error in photometric detection system of pesticide residue. For example, Bera found that, in the process of detection, different ratio of the reactants in the microfluidic chip will produce volume error to different extent, while volume error will affect the accuracy of detection systems [17]. He put forward a simple and feasible method of combining micro molding and enzymatic cross-linking mechanism to make a channel of microfluidic chip, and he also pointed out that the processed error of the channel will have an influence on the test result [18]. Zou found out that the fluctuation of temperature would cause variation of spatial distribution in biochemical reaction, and eventually led to serious error in detection systems [19]. The researcher above shown that it is relatively mature to classify error and research model in photometric detection in the traditional macro scale, the theory of traditional photometry error is not directly applicable in errors caused by fixed optical path in the test condition of micro-nano liter in photometric detection of pesticide residue with integrated microfluidic and the random error existing in paper-based microfluidic chip [20]. For this reason, in this article the error caused by external factors in photometric detection of pesticide residue with microfluidic [21], such as the test temperature and preparation time is discussed. The relationship between error resulting from fixed optical path and optical path is established and verified by experiments.

* To whom all correspondence should be sent:

E-mail: yangn@ujs.edu.cn

AL REACTION AND PHOTOMETRIC DETECTION MECHANISM

The principle of chemical reaction

The reaction principle of enzyme inhibition is that indophenol acetate (C₁₄H₁₁NO₃) can be hydrolyzed into indophenol (C₁₂H₉NO₂) and acetic acid (CH₃COOH). And acetyl cholinesterase (AchE) can catalyze the hydrolysis of indophenol acetate. Indophenol (C₁₂H₉NO₂), the product, is blue. Organophosphate and carbamate in crops will have certain inhibitory effect on acetylcholinesterase (AchE), leading to destroy of the catalysis, hydrolysis and discoloring. The concrete is shown in figure 1:

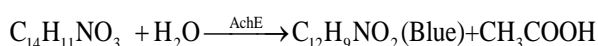


Fig. 1. Principle of chemical reaction

Detection mechanism of absorbance of pesticide residue in glass microfluidic chip

Lambert Beer's law is the theory basis of the detection of pesticide residue in microfluidic chip [22]. This law is also called the basic law of light absorption, which is used to show the relationship among the absorbance of pesticide residues (A), the concentration of a material that can suck light (c) and the thickness of liquid material that can also suck light (l). The relationship among them can be expressed following:

$$A = \alpha \cdot c \cdot l = -\lg T = -\lg (I/I_0) \quad (1)$$

Take parathion pesticide solution as an example to study the formation mechanism of error caused by fixed optical path, in the formula, A is absorbance value when parathion solution is detected in the photometric detection of pesticide residue, α is the absorption coefficient of parathion solution (the light absorption coefficient of parathion solution is $1.736 \cdot 10^4 \text{ L} \cdot \text{cm}^{-1} \cdot \text{mol}^{-1}$), c is the the concentration of pesticide residues in parathion solution, T is transmittance, I_0 is the intensity of the incident light, I is the intensity of transmitted light. The formula (1) shows that the intensity of transmitted light I also can be written in the following form:

$$I = I_0 \cdot 10^{-\alpha \cdot c \cdot l} \quad (2)$$

There are many ways to define the sensitivity of photometric detection system of pesticide residue, and the sensitivity of photometric detection system SEN was defined as the change of intensity of transmitted light caused by the change of unit concentration of components to be tested (Parathion solution), namely ($SEN = |dI/dc|$), the derived process is as follows:

$$\begin{aligned} SEN = |dI/dc| &= I_0 \cdot \ln 10 \cdot (-\alpha \cdot 10^{-\alpha \cdot c \cdot l}) = \\ &= \ln 10 \cdot I_0 \cdot l \cdot \alpha \cdot 10^{-l \cdot \alpha \cdot c} \quad (3) \end{aligned}$$

Take derivative of the sensitivity of photometric detection system of pesticide residue SEN in formula (4) with respect to optical path l , and optical path with maximum sensitivity is:

$$l_0 = 0.434 / \alpha \cdot c \quad (4)$$

The detection mechanism of reflective absorbance of pesticide residue in paper-based microfluidic chip

Since that the paper-based chip is opaque, when the monochromatic light irradiates to the surface of solid, there will be reflection and absorption, according to the theory of KUBELKA-MUNK, reflection of light follows the formula:

$$A_R = K/S \quad (5)$$

In the formula, A_R is reflective absorbance, S is reflective coefficient, K is the linear absorption coefficient. According to the definition of the linear absorption coefficient, the relationship among K , the molar absorption coefficient of light on solid phase (ϵ) and the concentration (C) is as follow:

$$K = \epsilon C \quad (6)$$

So it can be deduced:

$$A_R = C \epsilon / S \quad (7)$$

Reflection coefficient S is only related to the character of interfacial medium of incident light, this part of light intensity can be offset by a blank reference. So there is quantitative relationship existing in the detective signal and concentration of the object to be tasted. If reflection coefficient S remains the same, there is linear relationship existing in A_R and C in a certain concentration range, that is to say, reflective absorbance value is in proportion to the concentration of solution.

THE DESIGN OF TEST SYSTEM

According to the principle of enzyme inhibition reaction and effect of light absorption, a photometric detection system is established. Light is disposed differently because of the different detection mechanism of glass-based microfluidic and paper-based microfluidic.

The design of glass microfluidic detection system

Figure 2 represents schematic diagram of pesticide residue photometric detection system. The test light source 2 was placed on the test area a of microfluidic chip 1, and photosensitive diode 4 under the test area a, to receive the light emitted by the detective light. Spill-resistant cover plates 3 makes microfluidic packaged firmly. Photoelectric detection device will convert light signal into electrical signal, and achieve detecting pesticide

residues through the process of signal acquisition, data collection etc.

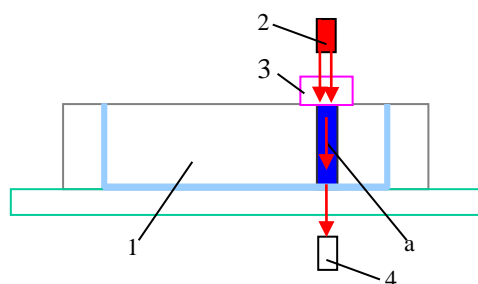


Fig. 2. Schematic diagram of pesticide residue photometric detection system: 1- microfluidic chip, 2- test light source, 3-spill-resistant cover plates, 4- photosensitive diode.

The design of detection system with paper-based microfluidic

Since that paper is not pervious to light, the detection mechanism of reflective absorbance is adopted to detect the pesticide residues. The equipment is same as the one mentioned above and shown in figure 3, in the equipment, paper-based chip 1 was placed on the chip placement agencies 4, and test light source 2 irradiate vertically to the color area b of the chip to make it be irradiated well, and the photosensitive diode 3 also placed vertically in the color area b to receive the reflective light signal. Similarly, the detection of pesticide residues is achieved through the process of signal acquisition, data collection etc.

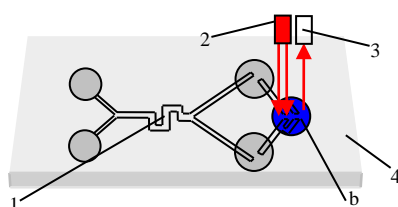


Fig. 3. Schematic diagram of the paper based microfluidic system: 1-paper-based microfluidic chip, 2-test light source,3- photosensitive diode, 4- chip placement agencies

ANALYSIS OF SYSTEM ERRORS IN MICROFLUIDIC

While the system errors are analyzed, both the glass-based microfluidic and the paper-based microfluidic are influenced by the external interference, but there is also interference caused by the chip structure. So, the analysis of common error and the error caused by structure should be done separately in two types of microfluidics.

Analysis of general error

In the process of photometric detection of pesticide residue, both absorbance detection and reflective absorbance detection would be influenced by external interference such as temperature, preparation time etc. So, the interference of error caused by these factors should be analyzed.

Temperature error

Temperature is one of the factors that affects the microfluidic chip based on the chemical reaction, which would lead to differences in color, while color uniformity degree of detection precision is of great significance. In order to achieve the appropriate reaction temperature to obtain chip color uniformity, experiments were carried out. at different reaction temperatures (15°C, 20°C, 25°C, 30°C, 35°C, 40°C, 45°C) with 0 mg/L pesticide reagents in microfluidic chip for enzyme inhibition. The absorbance value was detected at different temperature, and the optimum temperature was determined.

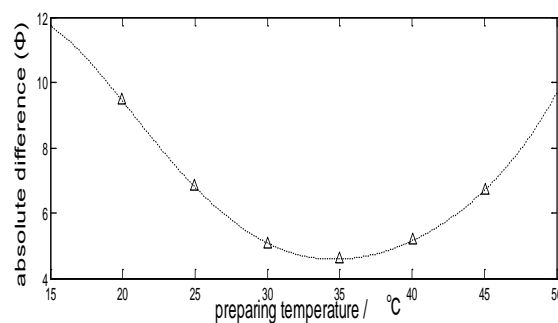


Fig. 4. Absorbance value at different temperature

Preparation time error

Multiple sets of pesticide reagent in multiple concentration are tested at 16°C, with different preparation time (1 min, 6 min, 11 min, 16 min, 21 min, 26 min and 30 min). The average of the results of different concentration of reagent is calculated, and the error between test absorbance and standard absorbance (16°C, 1 min) under different temperature conditions is analyzed.

Figure 5 shows the relationship between preparation time and the error of reflected intensity. In order to reduce the error arising from different preparation time, the compensation formula is

$$M_1 = 0.0001244 T^2 - 0.0062T - 0.0009832$$

where T is prepared time (for preparation?VB)

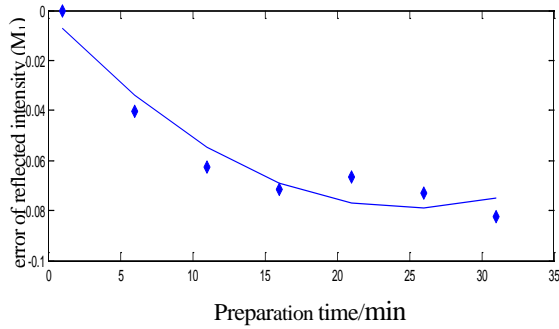


Fig. 5. Relationship between preparation time and absorbance error.

Analysis of errors in glass-based microfluidic system

Error of light wavelength

Light wavelength reflects the relationship between solution concentration and light absorption most veritably. The error of light wavelength is analyzed by color reaction of enzyme inhibition in the detection area in microfluidic chip with five different concentration of parathion solution which are 10^{-4} mol/L、 2×10^{-4} mol/L、 3×10^{-4} mol/L、 4×10^{-4} mol/L and 5×10^{-4} mol/L in experiments.

Table 1 was built based on different absorbance value in the same wavelength, according to the parathion solution with different concentration, and displays the change of the linearity value along with the wavelength in the range of 300-550nm. The better the system linearity is, the higher precision is and the interference of error is less.

Table 1 The value of linearity with wavelength in the range of wavelength 300-550nm.

wavelength	300	350	400	450	500	550
linearity	0.741	0.783	0.861	0.841	0.749	0.698

In the table, when the wavelength is about 300-400nm, the value of linearity in photometric detection system of pesticide residue increases along with the increase of the detective wavelength. But it is not optimized. However, when the wavelength is about 450-550nm, the value of linearity in photometric detection system of decreases along with the increase of the detective wavelength. Eventually, when the wavelength is about 400-450nm, the value of linearity in photometric detection system is obviously higher than that in other scope, and the accuracy is better, with smallest error interference.

Above all, the wavelength of 412nm is chosen as the detective wavelength by experiments, so that the interference of error in photometric detection system of pesticide residues is reduced.

Validation of the error caused by fixed optical path in glass-based microfluidic

After the experiment of light source wavelength, the light-emitting diodes with the wavelength of 412nm are chosen as the light source of photometric detection system for pesticide residues. The model is verified with the example of 10^{-4} mol/L parathion solution, which is the relationship between error caused by fixed optical path and optical path which has been deduced.

In the photometric detection system for pesticide residue, the main sources of error are those caused by transmitted light noise and reference light, while the measuring error caused by the reference light can be neglected. The error caused by transmitted light noise σ_l in photometric detection for pesticide residue can be indicated by the following expressions:

$$\sigma_c = \sigma_l / |SEN| \tag{8}$$

If replace the expressions of the sensitivity of photometric detection system SEN from formula (3) into formula (8), the following expressions of the relationship between error caused by fixed optical path σ_c and optical path l is received.

$$\begin{aligned} \sigma_c = \sigma_l / |SEN| &= \sigma_l / (\ln 10 \cdot I_0 \cdot l \cdot \alpha \cdot 10^{-l \cdot \alpha \cdot c}) \\ &= [\sigma_l / (\ln 10 \cdot I_0 \cdot \alpha)] \cdot 10^{l \cdot \alpha \cdot c} / l \end{aligned} \tag{9}$$

$\sigma_l / (\ln 10 \cdot I_0 \cdot \alpha)$ in formula (9) is believed to be equal to m for convenience due to the fact that σ_l , I_0 , α are all fixed figure. As a result, formula (9) can be simplified as :

$$\sigma_c = \sigma_l / |SEN| = m \cdot 10^{l \cdot \alpha \cdot c} / l \tag{10}$$

It can be seen that $\alpha \cdot c$ is equal to $0.434 / l_0$ from formula (4) (l_0 is the optical path length with maximum sensitivity). So formula (10) can also be expressed as formula (11). The relationship between error caused by fixed optical path in photometric detection σ_c and optical path length l is shown in figure 7.

$$\sigma_c = \sigma_l / |SEN| = m \cdot 10^{(0.434 / l_0) \cdot l} / l \tag{11}$$

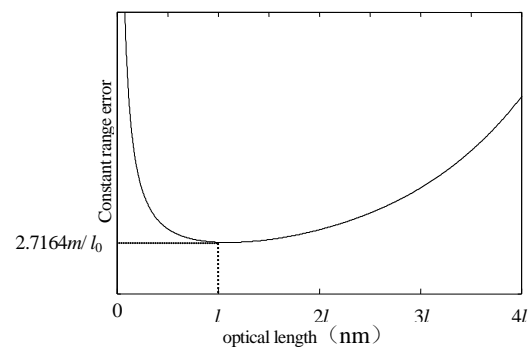


Fig. 7. The relationship between photometric detection error and constant path length in pesticide residues.

Different degree of errors caused by fixed optical path emerges during the detection. The microfluidic chips with the thickness of 0.8 mm, 1.0 mm, 2.2 mm, 2.4 mm, 2.5 mm, 3 mm, 8.5 mm, 9 mm are selected, and photometric detection system of pesticide residues, taking advantages of the chromogenic reaction principle of enzyme inhibition, is used to test the absorbance of pesticide residue in the detection area of the microfluidic chip, measuring absorbance value of parathion solution, the concentration of which is known, and get the measured value of parathion solution indirectly by combining the absorbance value that has been tested with Lambert Beer's law. The error in this optical path is the absolute value of difference between the measured value and the true value of pesticide residues in parathion solution. Figure 8 shows a curve comparison between measured value and the predictive value in formula (11) of error in optical path of any length.

It can be concluded from figure 8 that the curve fitting which involves the error tested by experiments in different optical path length and the predictive error in formula (11) is much better. So this constant error and path length relationship model is basically correct.

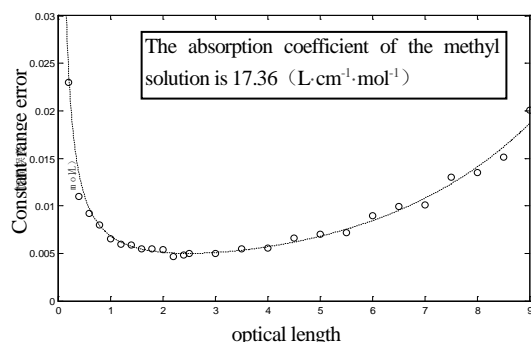


Fig. 8. The path length measurement error and forecast error curve (11)

Analysis of errors in paper-based microfluidic system

Errors of light wavelength

The system uses different wavelengths when testing pesticide residue, because that the mechanism of reflective absorbance detection is adopted. The result of the detection is different along with the different wavelength, so errors in the measurement can be produced.

According to the statement that coloring area in paper-based biosensor (blue) variously absorbs light of different wavelengths, the most sensitive wavelength to the change of pesticide residue concentration is found to be detective wavelength,

which is helpful to reduce experimental error. Therefore, the pesticide reagent of different concentration (0 mg/L, 0.1 mg/L, 0.15 mg/L, 0.2 mg/L, 0.25 mg/L, 0.3 mg/L) is detected in full spectrum in experiments (wavelength: 200nm-1112.428nm). The figure 9 shows the diagram of the relationship between wavelength and illumination intensity.

In the diagram, when the wavelength is 599.753nm, the change rate of the light intensity of different concentrations of pesticides is the largest. It has the better testing linearity, with high accuracy and low error interference, so an appropriate wavelength in this range is chosen as the detective wavelength.

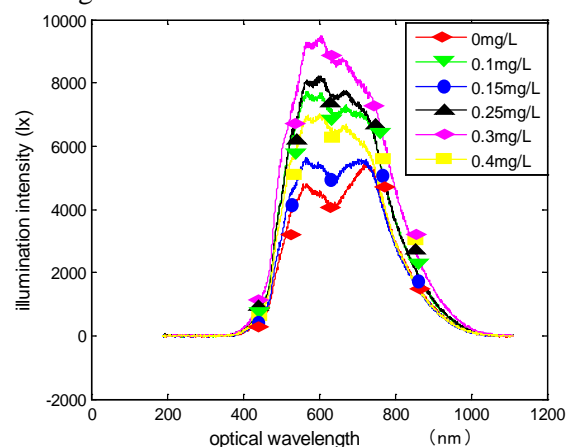


Fig. 9. Illumination intensity of different concentration.

Errors in color uniformity of different structure

Blue material can be produced after chemical reaction, the color uniformity of coloring area is the crucial testing link in paper-based microfluidic system. Uneven distribution of color will result in serious error when photometric detection has been done. So paper-based microfluidic chips of different structure are tested and the color after the reaction is processed in the form of image to determine the error. As shown in figure 10, 11 and 12, in order to compare the color uniformity, the whole color area and local color area enlarged are collected in the form of image with electron microscope and the gray-level histogram is obtained.

For the paper-based microfluidic chips of different structure, it can be concluded that the grayscale average of overall image and focused image, according to the comparison of data, the contrastive formula of color uniformity can be set as follow:

$$\Phi = |A_1 - A_0|$$

Φ is the absolute value of difference after comparing, A_1 is the grayscale average of overall image, A_0 is grayscale average of focus image. The

smaller Φ is, the higher uniformity will be and the errors in detection are smaller.

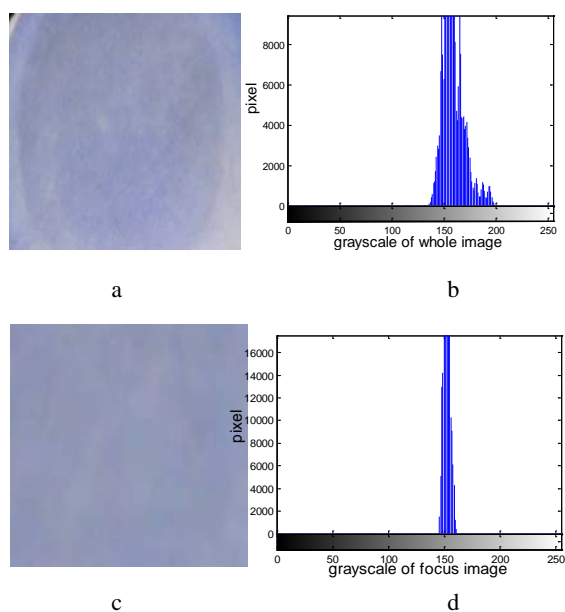


Fig. 10. Bridge structure color uniformity contrast figure: a) picture of whole image; b) gray histogram of whole image; c) picture of focus image; d) gray histogram of focus image.

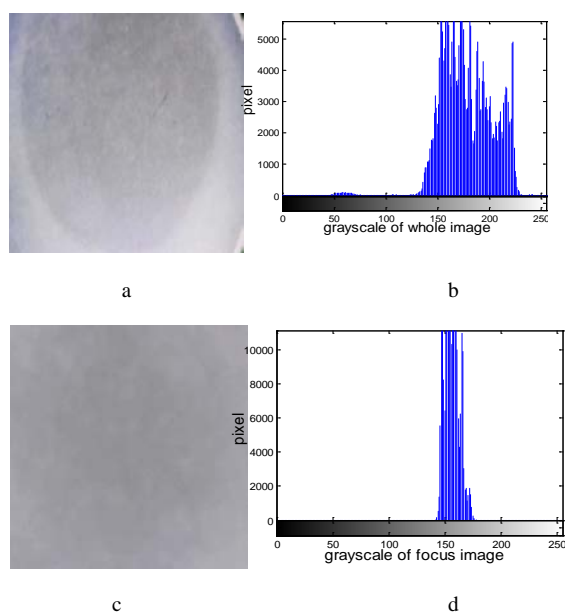


Fig. 11. Y structure color uniformity contrast figure: a) picture of whole image; b) gray histogram of whole image; c) picture of focus image; d) gray histogram of focus image.

Specific experimental data are shown in table 2. The grayscale average of overall image and focus image of bridge structure are 158.563 and 152.512 respectively, the difference is 6.501, and the data of structure Y are 178.274 and 155.686 respectively, with the difference of 22.588. According to the formula, paper-based microfluidic chip of bridge

structure is chosen in photometric detection for pesticide residue, with small difference of the average of color grayscale, uniform color and smaller error.

Table 2. Different structure of the overall image and the focus of the image grayscale average difference contrast table.

structure numerical value	Bridge structure microfluidic	Y structure microfluidic
Average gray value of the whole	158.563	178.274
Average gray value of the focus	152.512	155.686
D-value	6.051	22.588

SUMMARY

The error sources of photometric detection system of pesticide residues performed on microfluidic device have been analyzed. Error analysis has been done, which involves the external factors such as preparation time, temperature, and error analysis model is established. The parameters of the system can be optimized to reduce error sources. The model of the relationship between error caused by fixed optical path and the optical path was analyzed, and the model is verified by experiments from the view of Lambert Beer's law through the study of the formative mechanism of error caused by fixed optical path in glass-base microfluidic system. The results show that error caused by fixed optical path does exist in photometric detection system for pesticide residue, the model of the relationship between error caused by fixed optical path and optical path has been analyzed theoretically. At the same time a method of optimizing the testing data has been put forward for paper-based microfluidic system, reducing the errors in detection of pesticide with paper-based microfluidic chip. In this method, by comparing the testing standards in different cases, errors in light wavelength in detection is analyzed, and the model is established and the parameters of process are optimized, reducing the error in detection system of pesticide residue with paper-based microfluidic.

Acknowledgements: This working was supported by the National Natural Science Foundation of China(31671584), Priority Academic Program Development of Jiangsu Higher Education Institutions(PAPD), Natural Science Foundation of Jiangsu Province(BK20140550), China Postdoc

toral Science Foundation Funded Project (2015 T80512), Development Plan of Zhenjiang to Modern Agriculture(NY2015026) and Changzhou Sci&Tech Program(CE20155054).

REFERENCES

1. Y. Fintschenko, J. Krynitsky, W. Wong. *Journal of Agricultural & Food Chemistry*, **58**, 10 (2010).
2. H. Wang, J. Yu, X. Fei, J.G Zhang. *Guangdong Agricultural Sciences*, **40**, 8 (2013)
3. Y. Lu, S. Song, R. Wang, Z. Liu, J.Meng. *Environment International*, **55**,1 (2015).
4. G .Stefania, M. Comoglio, T. Livio. *Breast Cancer Research Bcr*, **12**, 4 (2010).
5. H. Akhavan-Tafti, D.G Binger, J.J. Blackwood, Y Chen, RS Creager. *Journal of the American Chemical Society*, **135**, 11 (2013).
6. A. Penna, M. Magnan. *Journal of Phycology*, **36**, 6 (2008).
7. M.J. Xie, K. Fukui, M.Horie, Y. Sakihama, K Hashino. *Analytical Biochemistry*, **374**, 2 (2008).
8. V. Tran, S. Reisberg, B. Piro, *Electroanalysis*, **25**, 3 (2013).
9. D.Q. Huo, M.O. Lian, M. Xie, N.I. Bin, M. Zhang. *Chinese Journal of Analysis Laboratory*, **31**, 9 (2012).
10. S.D. Marcos, E. Callizo, E. Mateos, J. Galban. *Talanta*, **122**, 3 (2014).
11. P. Noyrod, O. Chailapakul, W. Wonsawat, S. Chuanuwatanakul, *Journal of Electroanalytical Chemistry*, **719**, 4 (2014).
12. B.M. Del, M.S. De, V. Cebolla, J .Heiland, S. Wilhelm, *Biosensors & Bioelectronics*, **59**, 13 (2014).
13. X. Dai, Q.H. Wu, P.C. Wang, J. Tian, Y. Xu. *Biosensors & Bioelectronics*, **59**, 9 (2014).
14. X. Yu, N. University, Y. Shen, *Chinese Journal of Rare Metals*, **30**, 6 (2006).
15. K. Ren, J. Zhou, H. Wu, *Accounts of Chemical Research*, **46**, 11 (2013).
16. X. Lin, X. Hu, Z. Bai, Q. He, H. Chen. *Analytica Chimica Acta*, **828** , 5800 (2014).
17. N. Bera, S. Majumder, B. Bhattacharya, *Applied Algorithms, Springer International Publishing*, **8321**, 1 (2014).
18. J. He, R. Chen, Y. Lu, L. Zhan, Y. Liu. *Materials Science and Engineering C*, **59**, 53 (2016):.
19. M. Zou, S. Cai, Z. Zhao, L. Chen., Zhao. *Review of Scientific Instruments*, **86**, 4 (2015).
20. Y. Wang, Y.H. Lu, R. Wang, K.X. Xu. *Journal of Tianjin University*, **37**, 10 (2004).
21. N. Yang, R. Zhang, P. Xu, J. Guo, L. Cheng. *Chinese Journal of Scientific Instrument*, **34**, 6 (2013).
22. E. Abraham, C. Hourton-Cabassa, L. Erdei, L. Szabados. *Methods in Molecular Biology*, **639**, 3 (2010).

ИНТЕРФЕРЕНЧЕН АНАЛИЗ ЗА ФОТОМЕТРИЧНОТО ОПРЕДЕЛЯНЕ НА ОСТАТЪЦИ ОТ ПЕСТИЦИДИ С ИНТЕГРАЛНИ МИКРО-ФЛУИДНИ ЧИПОВЕ

Н. Ян^{1,2}, З. Ли¹, Дж. Сун¹, П.Ф. Ксу¹, Дж.Дж. Гуо¹, Х.П. Мао^{2*}

¹ Училище по електро- и информационно инженерство, Университет "Джиандзу", Дженджиян 212013, Китайска НР

² Институт по земеделско инженерство, Дженджиян 212013, Китайска НР

Постъпила на 27 март, 2016 г., коригирана на 25 юли, 2016 г.

(Резюме)

За подобряването на точността на фотометричното откриване на остатъци от пестициди се въвежда микро-флуиден чип и се съставя модел с анализ на грешките. Обикновено грешката на откриване се причинява главно от променлива температура и времето за подготовка на пробата. Дължината на вълната е фактор с основно влияние при фотометричното откриване с микро-чипове на стъклена основа, заради което дължината на вълната трябва да се оптимизира. Поради малките размери и фиксирания оптичен път, грешката от това е единствена при микро-чиповете на стъклена основа, което влияе върху чувствителността на метода. Затова тук е установена грешката при фиксирания оптичен пъти е потвърдена експериментално. Според особеностите на фотометричното определяне с микро-чипове на хартиена основа са определени дължината на вълната и еднаквостта на цвета за различни структури и са анализирани грешките за този случай. В следствие са определени оптималните условия за анализите. Настоящото изследване дава теоретична основа за прецизното фотометрично откриване на остатъци от пестициди с микро-флуидни системи на стъклена или хартиена основа.

Design and evaluation of the microfluidic magnetic isolating method for aquaculture pathogens detection

J.J. Guo^{1,2}, R.B. Zhang^{1*}, N. Yang¹

¹School of Electrical and Information Engineering, Jiangsu University, Zhenjiang, PR China

²School of Electrical and Photoelectronic Engineering, Changzhou Institute of Technology, Changzhou 213002, China

Received January 11, 2016; Revised November 19, 2016

The spread of infectious diseases has a serious impact on the aquaculture industry. But aquaculture pathogens detection in a water environment often relies on traditional laboratory techniques which are difficult to use, time-consuming and lower degree of automation. The paper proposes a magnetic isolating method based on microfluidic chip for aquaculture pathogens detection. We designed a dedicated microfluidic chip with automatic sample injecting, magnetic isolation, and set up the experiment platform based on a microfluidic magnetic isolating system. The optimum magnetic pole current and switching frequency in the microfluidic isolating system were determined and as an example of *Salmonella typhimurium* the performance of the system was experimentally evaluated. The experimental results showed that compared with the passive isolation by barriers, the capture efficiency of the magnetic isolating system increased by 32%, more than 93%, which benefits pathogens efficient separation and high precision detection in the prevention of aquaculture disease.

Keywords: Microfluidic chip; aquaculture pathogens; magnetic isolation; capture efficiency

INTRODUCTION

Nowadays aquaculture diseases have been the biggest barrier to the sustained, rapid and sound development of the aquaculture industry in the world. Among all the causes, many aquaculture pathogens (i.e. *Aeromonas hydrophila*, *Escherichia coli*, *Salmonella typhimurium*) are major factors of aquaculture diseases, which have caused enormous economic loss. Therefore, rapid aquaculture pathogen detection is the key to prevent the occurrence of aquatic product breeding diseases and the quality improvement of aquatic products [1-4]. Compared with pathogens detection technique in the traditional laboratory, The lab-on-a-chip (LOC) devices based on a microfluidic chip is characterized by its high sensitivity, high determination speed, less dosages and high automation [5-9].

The aquaculture water environment are usually diverse and complex, so how to rapidly isolate pathogens from the samples is especially critical to improve subsequent microfluidic detection precision. Conventional pathogens separation methods include filtration, centrifugation, dielectric electrophoresis. Filtration and centrifugation can need multiple procedures, consume a long time and have a difficulty to screen target pathogens. Dielectric electrophoresis is likely to damage the

target pathogens and has a low separation efficiency. The immunomagnetic isolating method applies immunomagnetic nanoparticles (MNPs) coupling pathogen antibodies to capture and separate the target pathogens [10-13]. Nevertheless, The microchip with micro-nano scale structure can cause fluid laminar flow, which cannot bring out the magnetic nanoparticles and target pathogens to sufficiently mix and immunological reaction. In the end the lower isolating efficiency of magnetic nanoparticles can lead to poor detection accuracy.

This paper proposes a microfluidic magnetic isolating method for the aquaculture pathogens detection system and takes *Salmonella typhimurium* for example to experimentally evaluate the proposed method.

A MAGNETIC ISOLATING SYSTEM FOR PATHOGENS MICROFLUIDIC DETECTION

The basic principle

By Maxwell's law the total current is showed as follows [14-15]

$$\oint_L H dl = \sum I \quad (1)$$

In the equation, H is the magnetic field intensity, L is coil winding length, I is the current of electromagnetic coil, Based on equation (1), the intensity of the magnetic field is proportional to the driving current of the electromagnetic coil.

During the process of the magnetic separation of the pathogens, the magnetic field exerts the

* To whom all correspondence should be sent:
E-mail: 474820848@qq.com

magnetic force on MNPs. Meanwhile, the viscous resistance is exerted on MNPs by the microfluid. Therefore, the magnetic force of the single magnetic nanoparticle exerted by the outer magnetic field is:

$$\vec{F}_m = \mu_0 \chi_{\text{eff}} V_p (\vec{H} \cdot \nabla) \vec{H} \quad (2)$$

In the equation: μ_0 is the permeability of vacuum, V_p is the volume of the magnetic nanoparticle, χ_{eff} is the effective magnetic susceptibility of the magnetic nanoparticle.

Based on equations (1) and (2), when other parameters are constant, the magnetic force exerted on the magnetic nanoparticle by the outer magnetic field is proportional to the magnetic field intensity, which is proportional to the drive current of the role coil.

The viscous resistance exerted on single magnetic nanoparticle by the microfluid is:

$$\vec{F}_d = -6\pi\eta r_p (\vec{v}_f - \vec{v}_p) \quad (3)$$

In the equation: η is the fluid viscosity, r_p is the semidiameter of the magnetic nanoparticle, v_f is the fluid velocity, v_p is the speed of the magnetic nanoparticle.

Based on Newton's second law :

$$m_p \frac{d\vec{v}_p}{dt} = \vec{F}_m + \vec{F}_d + F_g \quad (4)$$

In the equation: m_p is the mass of the magnetic nanoparticle, F_g is the sum of the magnetic nanoparticle's gravity and buoyancy.

Due to the minuteness of the magnetic nanoparticle, F_g is far less than the magnetic force and the viscous resistance and can be ignored.

$$\vec{F}_m + \vec{F}_d = 0 \quad (5)$$

According to the equation (5), the magnetic force balances with the viscous resistance exerted by the microfluid. The capture and separation of pathogens with MNPs are affected by the magnetic force F_m .

Based on the Navier-Stokes equation of the incompressible fluid while in laminar flow

$$\rho_f \frac{\partial \vec{v}_f}{\partial t} + \rho_f (\vec{v}_f \cdot \nabla) \vec{v}_f = -\nabla P + \eta \nabla^2 \vec{v}_f + c \vec{F}_m \delta(f) \quad (6)$$

In the equation: ρ_f is the fluid density, P is the pressure intensity of the microfluid, c is the concentration of the magnetic nanoparticles, $\delta(f)$ is the periodic function varying with the magnetic field frequency f .

Based on equation (6), the capture and separation of pathogens with MNPs are affected by the magnetic field frequency and the concentration of MNPs.

The magnetic capture efficiency of pathogens can be defined (Capture efficiency, CE),

$$CE = \frac{C_m}{C_0} \times 100\% \quad (7)$$

In the equation: C_m is the concentration of pathogens after magnetic isolation, C_0 is the initial concentration of pathogens.

the capture efficiency can quantitatively evaluate the performance of the magnetic isolating method of microfluidic detection system.

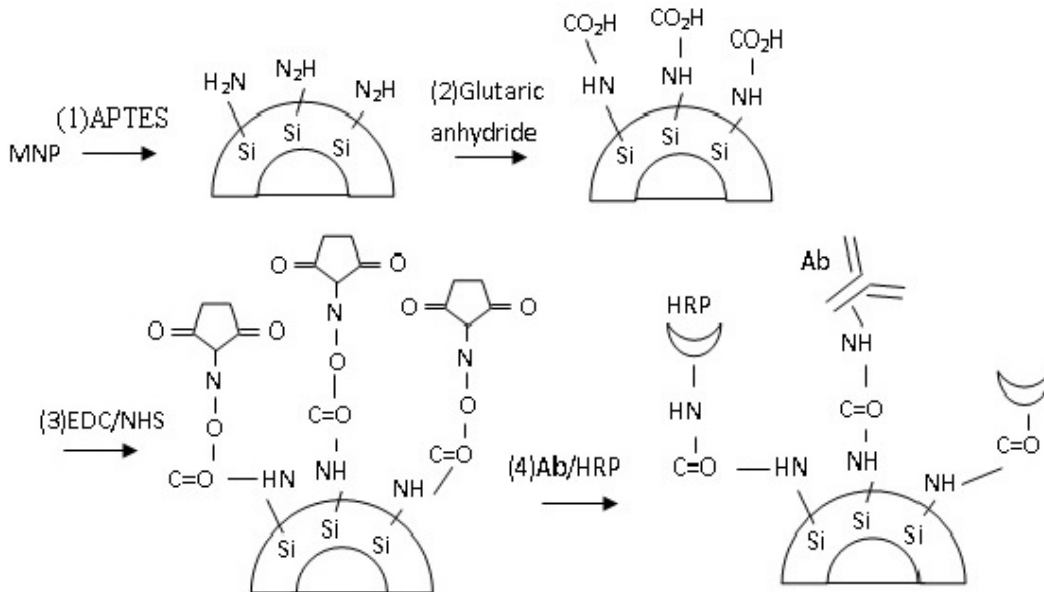


Fig. 1. Functionalization scheme of magnetic nanoparticles.

Functionalization of the magnetic nanoparticles

This experiment used the magnetic nanoparticle with 10nm silica shell and 160nm iron oxide core. As a proof of the immunoreaction principle, 180nm magnetic nanoparticles were functionalized with anti-*Salmonella typhimurium* Ab and horse radish peroxidase (HRP) to generate Ab-HRP-MNPs. The scheme for the MNPs immune-functionalization is shown in Fig.1. Treatment of the magnetic nanoparticles with (3-aminopropyl) triethoxysilane (APTES) produced a self-assembled monolayer containing surface amino groups that were converted to carboxyl groups by reaction with glutaric anhydride. The carboxyl groups were activated by sequential reactions with 1-ethyl-3-(3-dimethylamino-propyl) carbodiimide (EDC) and N-hydroxysuccinimide (NHS). The resulting NHS groups were used for chemical conjugation of anti-*S. typhimurium* Ab and HRP enzyme to generate Ab-HRP-MNP [16].

Design of a microfluidic chip

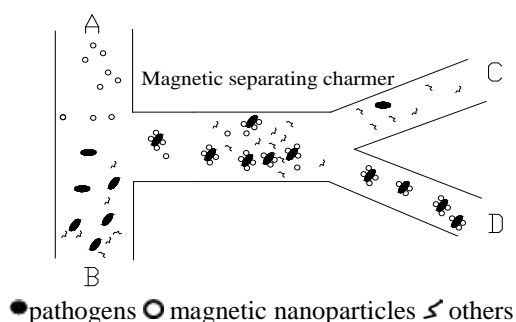


Fig.2. Structure model of the microfluidic chip

As shown in figure 2, A is the inport of immunomagnetic nanoparticles and B is the inport of pathogens. Immunomagnetic nanoparticles and pathogens are simultaneously injected into the magnetic separating chamber by an injector pump. C is the impurity outlet and D is the detection outlet after magnetic separation. The microfluidic chip adopts port on-off method to realize the flow control of the sample fluid. Port A and B adopts the injector pump to run and stop the flow. Outlet C and D adopt manual clips with teflon catheter to control the on-off flow. The material of the chip is polydimethylsiloxane (PDMS), which is bonded to a glass substrate. The micro channel volume on the chip is 8.2×10^{-3} mL.

The magnetic separating chamber is mainly used for the complete mixture of magnetic nanoparticles and pathogens, which cause specific immune-response under the action of an external magnetic field to realize the capture and separation of the

pathogens. The inadequate separation will yield great errors of subsequent detection.

Experimental platform

Fig.3 is the photo of the overall experimental platform. The microfluidic chip is set on the +Z iron core terminal of the magnetic field generator, which is in the center of the generator. The Microinjector is connected to an injection pump (0.098 μ m/pace, flow accuracy of CVs < 1%). The pathogen samples and MNPs solution (particle size 180 nm, concentration 10 mg/mL) are injected into the microfluidic chip through the port A and B. The outlet C is connected to the impurity collecting tube and the outlet D is connected to the sample collecting tube after the magnetic separation.

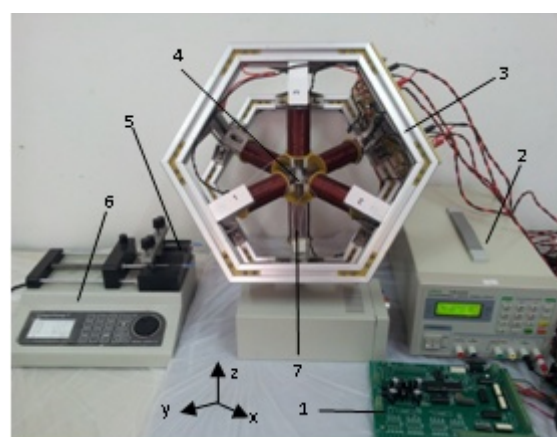


Fig.3. Photo of the microfluidic magnetic isolating system:1-Power controlled panel,2-DC stabilized supply power, 3-Magnetic field generator, 4-Microfluidic chip, 5 - Microinjector, 6 - Injection pump, 7 - test tube.

The magnetic field generator is driven by role currents from six iron core coils and generates parallel magnetic fields in six positive and negative directions. The magnetic induction intensity in each direction at the center of the magnetic separation chamber can be adjust between 0~65mT. The power control board can manage the DC stabilized power supply (YB3205, 0-5A) by a program supplying power in all directions. the X-Y-Z magnetic field were varied to realize magnetic separation of the pathogens.

The size of applied magnetic nanoparticles is 180 nm in the experiments and their surface is conjugated with *Salmonella typhimurium* specific antibodies which can have specific binding with *Salmonella typhimurium* and produce the magnetic nanoparticles/ pathogens compounds.

Separated pathogens are collected into the test tube and adopted the plate counting method to count the pathogens colony. The magnetic capture

efficiency of pathogens is calculated to verify the effect of the separation of the chip.

Experimental procedure

Water environment of aquaculture usually has a lower pathogens content in unit volume, so the pathogens detection needs to adopt the vacuum pump with special membrane ($<0.45\mu\text{m}$) to enrich pathogens, and need to rinse and dilute to earn pathogens samples. The standard detection method applies plate counting method. The sample is applied to the color culture medium, and put into the oscillation incubator with constant temperature (37°C , $200\text{r}/\text{min}$) to conduct a 48h enrichment culture. In the end the concentration of the pathogen samples is obtained by the pathogens colony counting.

Salmonella typhimurium is used as the target pathogens, while *Escherichia coli* and *Staphylococcus aureus* are used as interference pathogens in the experiment. The pathogens strain is provided by the Food Engineering Experiment Center of Jiangsu University in China. Three kinds of strains are blended into pathogens solution through phosphate buffer solution (PBS) and series of concentration samples are obtained after gradient dilution. The plate counting method is adopted to obtain the concentration of pathogens in standard samples. Three kinds of pathogen samples are blended into the synthetic samples of the pathogens in aquaculture according to a certain concentration ratio. We mix 0.1mL of *Salmonella typhimurium* samples with 0.9mL of *Escherichia coli* and *Staphylococcus aureus*. Synthetic samples of *Salmonella typhimurium* with series of concentrations are obtained after a $10^1\sim 10^8$ gradient dilution.

Four magnetic poles of the X-Y plane of the magnetic field generator are driven to produce parallel magnetic field to magnetic separating chamber of chips. Then the samples are disturbed with MNPs movement to speed up immunological reaction to produce MNPs/pathogen compounds, which is shown in Fig.2. After a certain period of time, the magnetic pole in the X-Y direction stops and the magnetic pole in the -Z direction starts to attract the beads wrapped pathogens cells to the underside of the separation chamber. The B port is replaced by PBS buffer injection washing separation chamber and the magnetic pole in the -Z direction stops releasing MNPs/pathogen compounds to realize the separation of pathogens from samples. Samples from the output D are taken to test tube to carry out plate colony counting and

The magnetic capture efficiency of the pathogens is calculated using equation (7).

WORKING PARAMETERS OPTIMIZATION OF THE MAGNETIC SEPARATION SYSTEM

The main parameters of the microfluidic magnetic separation system include the magnetic pole current and magnetic frequency.

The synthetic sample of 1mL *Salmonella typhimurium* (2.8×10^3 CFU/mL) and 1mL of MNPs solution are injected into the microfluidic chip. Different parameters are adopted to detect the magnetic capture efficiency and determine the system's optimal working parameters.

Based on equation (1) and (2), the magnetic capture efficiency is connected with the magnetic force of the magnetic nanoparticles. When the magnetic pole current increases, the magnetic field intensity increases and so does the magnetic force of the magnetic nanoparticles. When the magnetic field intensity meets or exceeds its saturation level, the magnetic force no longer increases. Therefore, the experiments adopt 7 kinds of magnetic current (0.5~3.5A) to detect magnetic capture efficiency. As observed in Fig.4, the results show that when the magnetic pole current is more than 3A, the change of the magnetic capture efficiency is not obvious, which the magnetic nanoparticles reach magnetic saturation. The magnetic force of the magnetic nanoparticles exerted by the magnetic field is a maximum. Thus, the optimum magnetic pole current of the system is 3A.

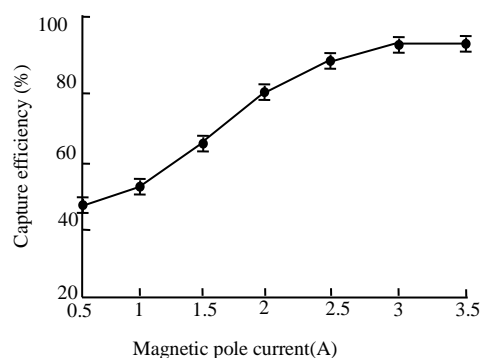


Fig. 4. Capture efficiency VS. Magnetic pole current.

Based on equation (6), the switching frequency of the magnetic field varied to disturb the flow of the sample fluid, which improve the immunological reaction of magnetic nanoparticles and pathogens and thus increase the magnetic capture efficiency. When the switching frequency is too low, the disturbance of the magnetic force is too slow and the magnetic capture efficiency is not high. The capture efficiency increases with the increase of the magnetic switching frequency. When the frequency

is too high, the magnetic nanoparticles lag the disturbance of the magnetic force owing to the action of the viscous liquid resistance. At the same time, the magnetic nanoparticles can't be fully released owing to the action of the rapidly changing magnetic force. So the magnetic field with the further increase of the magnetic switching frequency will lead to the decline of the magnetic capture efficiency. The experiments adopt 7 kinds of magnetic switching frequency (1~4 Hz). As observed in Fig.5, the results show that when the magnetic frequency is over 3Hz, the magnetic capture efficiency starts to decline significantly. So the optimal magnetic frequency is 3Hz.

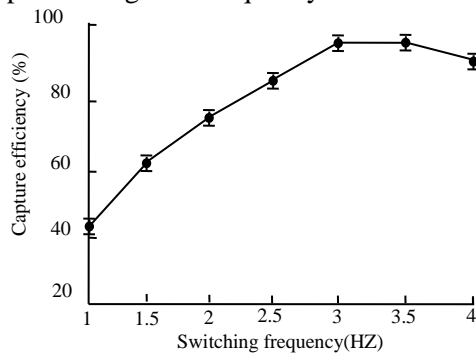


Fig.5. Capture efficiency vs. switching frequency.

RESULTS AND DISCUSSION

The performance of the microfluidic magnetic separation system mainly include the capture efficiency, the separation speed and the degree of automation.

We use the above optimum parameters of the system to analyze the results of the magnetic separation of the samples with different concentrations. The pathogen sample (1 mL *Salmonella typhimurium* 3×10^8 CFU/mL) is taken as detection target. Meanwhile, two kinds of interfering pathogens with different concentrations is added and mixed. After gradient dilution, 7 kinds of target pathogens detection samples are obtained. The target detection sample and 1 mL magnetic nanoparticles solution are injected into the microfluidic chip at the same time and the magnetic separation detection is conducted under the condition of the optimum parameters. A quantitative relationship between the magnetic capture efficiency and the target pathogens concentrations in samples is obtained, as shown in Fig.6.

The results illustrates that when the target pathogens concentration is within the range from 3×10^2 CFU/mL to 3×10^6 CFU/mL, the capture efficiency of target pathogens is over 93% on

average. When the concentration of target pathogens is over 3×10^6 CFU/mL, the magnetic capture efficiency of the system is below 93%. Thus, the magnetic separation method has a high capture efficiency to pathogens with both a high concentration (10^6 CFU/ml) and a low concentration (10^2 CFU/mL).

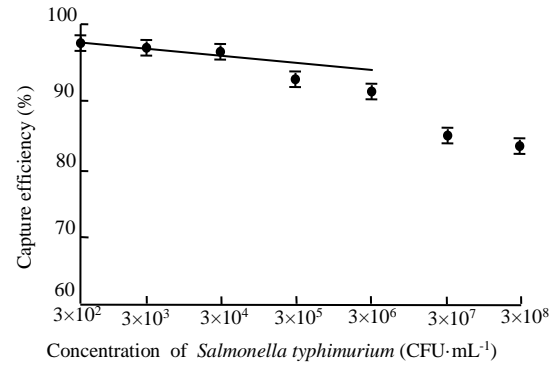


Fig. 6. Capture efficiency vs. the concentration of *Salmonella typhimurium*.

In order to analyze and verify the performance of the designed microfluidic magnetic separation system, after adding interfering pathogens to conduct detection 6 groups of target pathogens samples with random gradient concentration within the range from 4×10^2 CFU/mL to 4×10^7 CFU/mL are injected into the system. Passive microfluidic chips mentioned in the document [15] are adopted to conduct comparison and analysis of pathogens separation.

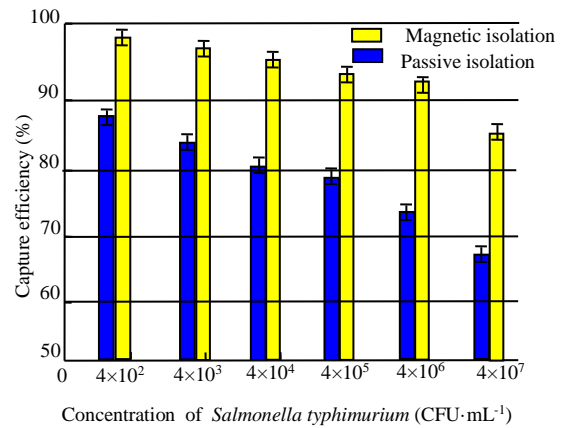


Fig. 7. compared analysis for the proposed method and passive isolation method

Fig.7 is the comparison histogram of *Salmonella typhimurium* capture efficiency with two kinds of methods. As shown in Fig 7, compared with the passive separation method, the target pathogens capture efficiency of the magnetic separation method increases about 32% and realizes the high efficiency separation of the aquatic microfluidic pathogens concentration. It is also convenient to

improve subsequent detection accuracy and efficiency of pathogens.

CONCLUSIONS

This paper integrates magnetic separation on a microfluidic chip, and establishes a microfluidic magnetic isolating system for aquaculture pathogens detection. Compared with the passive capture separation method, the capture efficiency of the proposed method increases by 32% and realizes the high efficiency isolation of the aquatic pathogens. It is also convenient to improve the subsequent detection accuracy of the pathogens. The proposed method will provide prospective references for the research of aquaculture disease by early warning and prevention.

Acknowledgements: This working was supported by National Natural Science Foundation of China (61673195), Jiangsu Province Agricultural Independent Innovation Project (CX(14)2092), and Jiangsu Province Common Universities Graduate Research and Innovation Program (CXLX12_0662), Changzhou Sci&Tech Program (CE20155054), National Undergraduate Innovative Practice Project(201611055005).

REFERENCES

1. A.Adams, K.D.Thompson. *Aquaculture Research*, **42(s1)**, 93 (2011).
2. W. Shuqin, W.Yajun, *China Fisheries*,**8**, 9 (2010).
3. H. Sharma, R. Mutharasan, *Sensors and Actuators B: Chemical*, **183**, 535(2013).
4. F.J.H Hol, C. Dekker, *Science*, **346**, 1251821 (2014).
5. A.M. Foudeh, T.F. Didar, T.Veres, *Lab on a Chip*, **12**, 3249 (2012).
6. Y. Yang, S. Kim, J. Chae, *Microelectromechanical Systems, Journal of*, **20**, 819 (2011)..
7. S. Agrawal, K. Paknikar, D. Bodas, *Microelectronic Engineering*, **115**, 66(2014).
8. A. Van Reenen, A.M. De Jong, *Lab on a Chip*, **14**, 1966(2014)..
9. G.H. Lee, S.H. Kim, K. Ahn, *Journal of Micromechanics and Microengineering*, **26**, 013003 (2015).
10. R. Wang, Y. Ni, Y. Xu, *Analytica chimica acta*, **853**, 710 (2015).
11. L. Malic, X. Zhang, D. Brassard, *Lab on a Chip*, **15**, 3994(2015).
12. D. Das, M.F. Al-Rjoub, R.K. Banerjee, *Journal of biomechanical engineering*, **137**, 051008 (2015).
13. A. Munir, Z. Zhu, J. Wang, *Sensors and Actuators B: Chemical*, **197**, 1 (2014).
14. X. Han, Z. Wang, Q. Cao, *IEEE Transactions on Applied Superconductivity*, **26**,1(2016).
15. G. Jianjiang, Z. Rongbiao, Y. Ning, *Transactions of the Chinese Society for Agricultural Machinery*, **46**, 155 (2015).
16. S. Mun, S.J. Choi, *BioChip Journal*,**9**:;10 (2015).

ПРОЕКТИРАНЕ И ОЦЕНКА НА МЕТОД С МИКРО-ФЛУИДНА ИЗОЛАЦИЯ ЗА ОТКРИВАНЕ НА ПАТОГЕНИ В АКВАКУЛТУРИ

Дж.Дж. Гуо^{1,2}, Р.Б. Джан^{1*}, Н. Ян¹

¹Училище по електро- и информационно инженерство, Университет "Джиандзу", Дженджиян 212013, Китай

²Училище по електро- и фотоелектронно инженерство, Технологичен институт в Чанджоу, Чанджоу 213002, Китай

Постъпила на 11 януари, 2016 г., коригирана на 19 ноември, 2016 г.

(Резюме)

Разпространението на инфекциозни болести има сериозно въздействие върху аквакултурната промишленост. Откриването на патогените във водна средачесто зависи от традиционни лабораторни методи, при които включват изолация и продължителни операции, при ниска степен на автоматизация. Тук се предлага метод с магнитна изолация за откриването на патогени в аквакултури, основан на микрофлуиден чип. Ние проектирахме микрофлуиден чип с автоматично впръскване на пробата, магнитна изолация и устройство за експериментална платформа. Определени са оптималния полярен магнитен поток и превключващата честота в изолационната система и като пример експериментално е изследвана културата *Salmonella typhimurium*. Опитните резултати показват, че в сравнение с пасивната изолацияна бактериите ефективността на улавяне им нараства с 93%, което благоприятства ефективното отделяне на патогените и високата точност при откриването им при предпазването на аквакултурите от заболявания

Optimization of fermenting conditions for antioxidant activity and yield of polysaccharides from mushroom solid fermentation

Z. Yuan, P. Yan*, D. Jing

School of Municipal and Environment Engineering, Harbin Institute of Technology, Harbin, 150001, China

Received January 23, 2016; Revised August 6, 2016

In order to establish a simple procedure for producing edible mushrooms with a high polysaccharides yield, antioxidant and hydroxyl radical scavenging activity, experiments were conducted to optimize the fermentation conditions for the mushroom, as well as the fermentation time. The results showed that mushrooms can grow on this medium and produce abundant polysaccharides which have the capacity for antioxidant and hydroxyl radical scavenging, which also provide a theoretical and practical way to a large-scale production of *Pleurotuseryngii* with a high polysaccharides yield, high antioxidant and hydroxyl radical scavenging activity under an optimum fermenting time of 20 days' cultivating.

Keywords: polysaccharids, solid mushroom fermentation

INTRODUCTION

Mushrooms are able to convert lignocellulose biomass waste into human food and also produce medicinal and nutritional products which have many health benefits [1-3]. *Pleurotuseryngii* is an edible mushroom native to the Mediterranean regions of Europe, the Middle East and North Africa, but also grown in many parts of Asia [4]. It may naturally contain chemicals that stimulate the immune system [5]. Dietary intake of *Pleurotuseryngii* may function as a natural cholesterol lowering dietary agent [6].

Polysaccharides such as *Ganoderma lucidum* polysaccharides [7], lentinan [8] and *Pleurotuseryngii* polysaccharides [9], from edible mushrooms have been reported as antioxidants in recent years. In this study, *Pleurotuseryngii* was fermented on a solid medium of kelp waste, a main oceanic nonproductive in related industries. The microparticles obtained from the incubation were investigated for antioxidant activity and hydroxyl radical scavenging activities.

The results showed that the *Pleurotuseryngii* can grow on the solid medium and produce polysaccharides. Meanwhile, the assays showed that an antioxidant activity and hydroxyl radical scavenging capacity of the microparticles obtained from *Pleurotuseryngii* incubation were significantly higher than those of the kelp waste without fermentation. The assays showed that antioxidant activity and hydroxyl radical scavenging capacity under the optimum conditions were significantly higher than those without optimization. It would be a beneficial pathway to recycle kelp waste by the fermentation of *Pleurotuseryngii* to produce

potential natural antioxidants.

MATERIALS AND METHODS

Mushroom strains and solid fermentation

The kelp waste material was obtained from factories engaged in sodium alginate production in Weihai, China. The mushroom *Pleurotuseryngii* was preserved in our Lab and initially incubated on a potato dextrose agar PDA medium (fresh potato 20%, glucose 2% and agar 1.5%) in a Petri dish at 25°C for 10 days. Agar plugs, 10 mm in diameter with young mycelia were punched out by a puncher and inoculated into 370 ml tissue culture bottles containing 50 g kelp waste with additive glucose and wheat bran.

The medium without fermenting mushrooms was used as negative control and the antioxidant BHT was used as positive control. Each treatment had three replications and each replication included three parallel tissue culture bottles. Uniform design and DPS software were employed to optimize the yield of polysaccharides from *Pleurotuseryngii* and the second-order regression model with five-factor five-level design was established. The factors and levels considered in the experiment are listed in table 1 and the test schemes were elaborated in table 2.

The experiments were conducted by the test schemes, the optional conditions were chosen and the verification experiment was then conducted under the optimum conditions. Single factor experiments were conducted respectively according to the relationship between the fermenting time and the yield of mushroom polysaccharides, antioxidant activity, as well as the hydroxyl radical scavenging activity. The EC₅₀ value is the effective

* To whom all correspondence should be sent:
E-mail: 43359998@qq.com

concentration at which hydroxyl radicals were scavenged by 50% and obtained by interpolation from regression analysis.

Treatment of the experimental samples

A ferment powder suspension, hot water extracts, the polysaccharides solution and BHT solution was prepared for positive control. After fermentation for 20 days, the kelp waste product was dried and shattered into microparticles (160~200 mesh), then suspended in distilled water. The prepared concentration of this powder suspension is 50mg/mL.

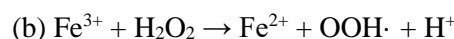
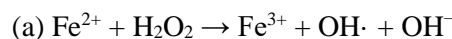
A water bath (100 °C) for 2 hours was applied to extract the soluble part of the product which contained polysaccharides and other soluble substances. After precipitation and lyophilization, it was dissolved in distilled water with a hot water extraction of 50mg/mL.

Fourfold volumes of ethanol (95%) were added to the hot water extraction, centrifuged at 6,000 rpm for 30 min, left at 4°C overnight and the polysaccharides were obtained after precipitation and lyophilization. The polysaccharides were also re-dissolved (50mg/mL) in distilled water for further study. Finally, BHT control experiments which is known as an antioxidant were carried out

under the same conditions. All the chemicals used in the study were of analytical grade.

Assays for hydroxyl radical scavenging activity

Fenton's reagent is the most common reaction producing HO·, which was developed in the 1890s by Henry John Horstman Fenton. Ferrous iron (II) is oxidized by hydrogen peroxide to ferric iron (III), a hydroxyl radical and a hydroxyl anion. Iron (III) is then reduced back to iron (II), a peroxide radical and a proton by the same hydrogen peroxide.



Adding griess reagent to Fenton's reagent system, there is a maximum absorbance peak at 550 nm. In a definite concentration range, the light absorption of Fenton's reagent system is positively related to the concentration of HO·. Thus, the light absorption OD value will reduce when the inhibitor HO· exists in the system, which can test the hydroxyl radical scavenging activity of the substance. The formula is listed below as formula (1), where OD_c is the absorbance without samples and OD_u is the absorbance in the presence of the samples of the ferment products. Hydroxyl radical scavenging activity (%) = [(OD_c - OD_u) / OD_c] × 100 (1)

Table1. Factors and Levels to be optimized.

Factor	Code	Level				
		1	2	3	4	5
Water content (%)	X1	50	55	60	65	70
Bran content (%)	X2	5.0	5.5	6.0	6.5	7.0
pH value	X3	0	0.25	0.5	0.75	1
Glucose content (%)	X4	0	0.04	0.08	0.12	0.16
Temperature (°C)	X5	15	20	25	30	35

Table2. Test schemes of the fermentation.

Numerical	code				
	X1	X2	X3	X4	X5
N1	4	3	5	3	1
N2	3	5	3	5	1
N3	1	2	3	4	5
N4	1	4	4	4	2
N5	4	4	1	4	2
N6	2	5	2	2	4
N7	2	1	5	5	3
N8	2	2	2	2	1
N9	5	1	3	1	2
N10	5	3	2	5	5
N11	5	5	4	3	3
N12	3	1	1	3	4
N13	4	2	4	2	4
N14	1	3	1	1	3
N15	3	4	5	1	5

Assays for antioxidant activity of the microparticles

The chemical kits used for total antioxidant capacity (T-AOC) were purchased from Nanjing Jiancheng Bioengineering Institute (Nanjing, China). The measurement was followed by the manufacture's instruction.

T-AOC was described as the following equation:

$$T-AOC (U/mg) = [(As - Ao) / 0.01 / 30] \times Vt / Ms. (2)$$

Where As is the absorbance of the sample, Ao is the absorbance without the sample, Vt (ml) is the total volume of the reaction mixture and Ms (mg) is the mass of the sample.

RESULTS AND DISCUSSION

Optimization of the solid fermentation conditions from *Pleurotuseryngii*

Pleurotuseryngii can vigorously grow on the solid medium, as shown in Figure 1.



Fig.1. *Pleurotuseryngii* fermented on a kelp waste medium.

Uniform design and DPS software were employed to optimize the yield of polysaccharides from *Pleurotuseryngii*. Then a regression equation prediction model was established see formula (3) below, whose correlation coefficient $R=1$ and the residual path coefficient =0.99994 a residual path coefficient

$$=0.00805, p=0.0254 \leq$$

regression equation was significant with a good fitting degree.

$$\hat{y} = 1.582 + 0.635X1 - 0.584X3 - 0.628X4 - 0.007X1 * X1 - 0.015X3 * X3 - 0.572X4 * X4 - 0.008X5 * X5 + 0.016X1 * X3 + 0.017X1 * X4 + 0.007X1 * X5 - 0.038X2 * X3 + 0.161X3 * X4 - 0.005X3 * X5 (3)$$

The selected optimum solid fermentation conditions for the growth rate are shown in table 3. According to the optimization of the growth rate for *Pleurotuseryngii*. optimum conditions of the fermentation were: water content 70%, the PH value 5.0, the bran content 1. 0%, and the glucose content 0.16%, the temperature of the solid fermentation condition was 25.9°C. The maximum predicated growth rate for *Pleurotuseryngii* was 4.78mm/day. The verification experiments were conducted completed under the optimum conditions, which gave a growth rate of 4.93 mm/d. The fitting degree of 97.0% indicated a close agreement of the values predicted by the models and the values in the verification experiments.

Optimization of the fermentation time for a yield of mushroom polysaccharides, antioxidant activity and hydroxyl radical scavenging activity

After fully fermentation, the relationship between the fermentation time and the yield of mushroom polysaccharides, the antioxidant activity and the hydroxyl radical scavenging activity were investigated respectively. The results are shown in tables 4 to 6.

As is in table 4, the antioxidant activity affected by the fermentation time reached the top value 20 days after the bottles had fully grown mushrooms. Table 5 shows the yield of polysaccharides reached the top on that day too.

Table 6 shows that 15 days after fully grown, the hydroxyl radical scavenging activity was highest as EC_{50} was the lowest.

Table3. Optimal fermenting conditions

Optimal parameters		Results	
Water content (W_c , %)	70	Predictive value (mm/day)	4.78
PH value (P_H , 1)	5.0	Actual value (mm/day)	4.93
Bran content (B_c , %)	1.0	Fitting rate (%)	97.0
Glucose content (G_c , %)	0.16	Traditional growth rate(mm/day)	3.15
Temperature(T_F , °C)	25.9	Multiple of the increase(%)	58.1

Table 4. Antioxidant activity affected by fermenting time.

Fermenting time	Antioxidant activity(U/mg)
Kelp waste medium	0.252
0 day after fully grown	0.263
5 day after fully grown	0.327
10 day after fully grown	0.339
20 day after fully grown	0.387

Table 5. Yield of polysaccharides affected by the fermentation time

Fermenting time	Yield of polysaccharides(mg/g)
Kelp waste medium	59.49
0 day after fully grown	88.79
5 day after fully grown	100.64
10 day after fully grown	107.89
20 day after fully grown	123.83

Table 6. Hydroxyl radical scavenging activity affected by the fermentation time

Fermenting time	EC ₅₀ (U/mg)
Kelp waste medium	122
0 day after fully grown	30.55
5 day after fully grown	17.44
10 day after fully grown	19.28
15 day after fully grown	12.83
20 day after fully grown	14.35

Hydroxyl radical scavenging activity

The hydroxyl radical scavenging activity of the microparticles suspension, hot water extracts and polysaccharides obtained from solid fermentation, the kelp waste medium and BHT solution are shown in Figures 2 to 4.

The hydroxyl radical scavenging activity of the obtained samples from *Pleurotuseryngii* incubation (T in figures 2 to 4), BHT (C1) and the kelp waste alone(C2) were control tested. The Data was presented as the mean of three independent experiments ± SD.

The formula is listed below as formula (3), where OD_c is the absorbance without samples and OD_u is the absorbance in the presence of the samples of the fermentation products.

$$\text{Scavenging effect} = (\text{OD}_c - \text{OD}_u) / \text{OD}_c \quad (3)$$

In accordance with figures 2 to 4, a dose-dependent increase of the hydroxyl radical scavenging activities of the microparticles is apparently exhibited. The hydroxyl radical scavenging activity of the microparticles suspension was less than BHT but more than the kelp waste medium without fermentation. But the hot water extracts (figure 3), especially the

polysaccharides (figure 4) drawn from the fermentation products had much more hydroxyl radical scavenging activity than the BHT and kelp waste medium without fermentation.

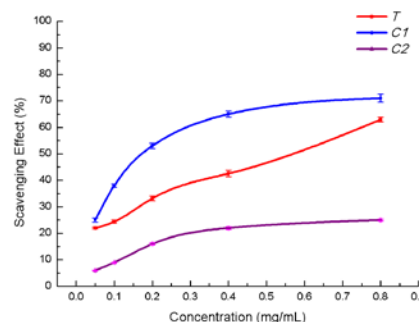


Fig.2. Hydroxyl radical scavenging capacities of the powder suspension (T) obtained from *Pleurotuseryngii*

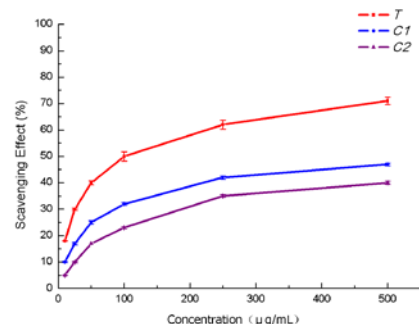


Fig.4. Hydroxyl radical scavenging capacities of the hot water extracts (T) obtained from *Pleurotuseryngii*

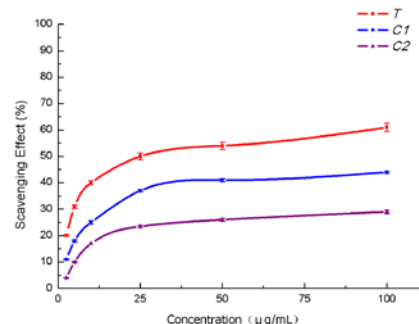


Fig.5. Hydroxyl radical scavenging capacities of the polysaccharides (T) obtained from *Pleurotuseryngii*

Compared with the data for hydroxyl radical scavenging, among the fermented powder suspension, the hot water extraction, the polysaccharides solution and BHT solutions (as positive control), *Pleurotuseryngii* solid ferment products have a high hydroxyl radical scavenging activity, which also increased with the higher concentration of polysaccharides which exist in both the suspension and extracts solution at different concentrations.

Antioxidant activity of the microparticles

As shown in table 7, the antioxidant activity of the mushroom sample, microparticles suspension obtained from *Pleurotuseryngii* fermentation was 0.141U/mg, which was slightly lower than that of the kelp waste without *Pleurotuseryngii* fermentation as control 2 and the BHT solution as control 1. The antioxidant activity for the hot water extracts obtained from fermentation products was 0.530U/mg, which was significantly higher than that of the kelp waste without *Pleurotuseryngii* fermentation and the BHT solution. The antioxidant activity for the polysaccharides obtained from fermentation was 1.433U/mg, significantly higher than that of the kelp waste without fermentation and the BHT solution, which means the hot water extracts and polysaccharides have more antioxidant activities.

Table 7. Antioxidant activity(U/mg)

Sample	Results
Powder suspension	0.141
Hot water extract	0.530
polysaccharides	1.433
BHT	0.218
Kelp waste medium	0.174

CONCLUSIONS

In this work, the *Pleurotuseryngii* can grow on the solid medium and produced polysaccharides. It was shown that the antioxidant activity and the hydroxyl radical scavenging capacity of the microparticles obtained from *Pleurotuseryngii* incubation were significantly higher than those from the kelp waste without fermentation. Likewise the assays showed that the antioxidant activity and hydroxyl radical scavenging capacity under the optimum conditions were significantly higher than those without optimization. A dose-dependent increase of the hydroxyl radical scavenging activities of the microparticles was apparently exhibited. The hydroxyl radical scavenging activity

of the microparticles suspension was less than for BHT but more than for the kelp waste medium without fermentation. But the hot water extracts, especially the polysaccharides drawn from the fermentation products had a much higher hydroxyl radical scavenging activity than BHT and the kelp waste medium without fermentation. After optimization of the fermentation time, the optimum fermentation time was chosen, which can affect the yield of polysaccharides, the antioxidant activity and hydroxyl radical scavenging activities. Thus, each component of the fermentation investigated of the antioxidant activity and hydroxyl radical scavenging activities obviously have encouraging results. It would be a beneficial pathway to recycle the kelp waste by fermentation of *Pleurotuseryngii* to produce potential natural antioxidants.

REFERENCES

1. B.Z.Zaidman, M. Yassin, J. Mahajna, S.P. Wasser *Appl. Microbiol. Biotechnol.*, **67**, 453(2005).
2. P.Y. Mark, J.H.Won, Y.H. Kim, J.W.Choi, H.J.Park, K.Y. Lee, *Journal of Ethnopharmacol.*, **101**, 120 (2005)
3. M. Shamtshyan, V. Konusova, Y. Maksimova, A. Goloshchev, A. Panchenko, A. Simbirtsev, N. Petrishchev, N. Denisova, *Journal of Biotechnol.*, **113**, 77(2004)
4. Archived, May 18, 2006, at the Wayback Machine.
5. H. Nozaki, S. Itonori, M. Sugita, K. Nakamura, K. Ohba, A. Suzuki, Y. Kushi, *Biochemical and Biophysical Research Communications*, **373**(3), 435(2008)
6. N. Alam, K.N. Yoon,; J.S. Lee,; H.J. Cho,; M.J. Shim, T.S. Lee, *Saudi Journal of Biological Sciences*, **18**(4), 403 (2011).
7. B.S. Sanodiya, G.S. Thakur, R.K. Baghel, G.B. Prasad Bisen, *Current Pharmaceutical Biotechnology*, **10**(8), 17 (2009).
8. J.J. Zhang. R. Duan, K. Xu, Z.L. Li, *Journal of Fisher Science*, **29**, 10 (2010).
9. C.L. Hurd, P.J. Harrison, K. Bischof, S.C. Lobban, *Seaweed Ecology and Physiology*, Cambridge University Press, United Kingdom, 2014.

ОПТИМИЗАЦИЯ НА УСЛОВИЯТА ЗА ТВЪРДО-ФАЗНА ФЕРМЕНТАЦИЯ НА ГЪБИ ВЪВ ВРЪЗКА С ТЯХНАТА АНТИОКСИДАНТНА АКТИВНОСТ И ДОБИВА НА ПОЛИЗАХАРИДИ

Дж. Юан, П. Ян*, Д. Джън

Училище по социално и екологично инженерство, Технологичен институт в Харбин, Харбин 150001, Китай

Постъпила на 23 януари, 2016 г. ; коригирана на 6 август, 2016 г.

(Резюме)

Проведени са експерименти за установяване на оптималните условия за добиване на едливи гъби с висок добив на полизахариди и на антиоксиданти отсртаняващи хидроксилните радикали. Резултатите показват, че могат да растат и да произвеждат обилно полизахариди с горепосочените свойства. Тези резултати дават възможност за мащабиране на процеса и за промишлено прилагане на тази твърдо-фазна ферментация с гъбите *Pleurotus eryngii* при оптимално време от 20 дни.

Using point cloud data for tree organ classification and real leaf surface construction

Ting Yun^{1,2,5}, Bangqian Chen², Weizheng Li³, Yuan Sun⁴, Lianfeng Xue^{1,5*}

¹*School of Information Science & Technology, Nanjing Forestry University, 210037 Nanjing, China.*

²*Danzhou Investigation & Experiment Station of Tropical Crops, Ministry of Agriculture/Rubber Research Institute, Chinese Academy of Tropical Agricultural Sciences, Danzhou 571737, China*

³*Advanced Analysis and Testing Centre, Nanjing Forestry University, 210037 Nanjing, China.*

⁴*College of Forestry, Nanjing Forestry University, 210037 Nanjing, China.*

⁵*Joint Center Sustainable Forestry Studies in Southern China, Nanjing Forestry University, 210037 Nanjing, China*

Received December 18, 2015; Revised September 17, 2016

Terrestrial Laser Scanning (TLS) enables easy and fast Point Cloud Data (PCD) acquisition from objects, and it has been widely used in complex scene survey. However, trees have seriously irregular and complex morphology, and scanning process always be influenced by external environment variation and have occlusion effect, so quantifying the 3-D morphology structure and assessing parameters of forest stands by TLS is challenging. In order to solve these problems, we applied computer technique to improve Terrestrial Laser Scanning (TLS) performance in forestry measurement. Here, new PCD feature vectors, including shape, orientation, normal vector distribution and normal vectors of tangent plane, was proposed, and Supervised Locally Linear Embedding (SLLE) algorithm and Gaussian Mixture Model (GMM) were adopted for the feature dimensionality reduction and PCD classification as well. Hence, the algorithm efficiency was improved and various tree organs could be automatically identified. Moreover, a leaf modeling method using polynomial fitting method and Moving Least Squares (MLS) were presented to depict real foliage silhouette and eliminate ghost points, yielding accurate reconstruction of complex foliage surface. As detailed experimental comparison stated, the recognition rate remained higher than 87.51 % while our classification method was applied to different tree PCD, and accurate 3D morphological reconstruction of leaf models have similar leaf area versus manually LI-3000C measurement results. Thus, our method show promise in further exploration of utilizing TLS as an effective tool for forestry parameter retrieval.

Keywords: Terrestrial Laser Scanning (TLS), Point Cloud Data (PCD), Tree organ classification, Leaf surface reconstruction.

INTRODUCTION

The forest has an irreplaceable status and role in regulating the earth's environment for human survival and slowing down and even curbing the global environmental degradation trend. Moreover, forest measurement science and forestry information research have become an important issue in recent years, we have to face the task that exploring the fine measurement of forest trees and providing an effective way to improve the accuracy and efficiency of forestry data collection for forestry surveying.

In recent years, quite a few methods of analyzing plant structure and measuring plant parameters was proposed, which could be divided into two types.

Firstly, tree measurement method based on the image processing and computer graphics theory is designed to calculate ecological parameters of the plants. Image recognition methods [1,2] was adopted to analyse numerous leaf images in order

to classify different plant species. 3D reconstruction model of plant was utilized to characterize tree structures, light interception within the canopy and leaf photosynthetic capacity [3,4,5]. Moreover, a multitude of computer software, including YPLANT [6], Arbaro [7], VegeSTAR [8] and Speedtree [9] were designed for bio-simulation.

Secondly, laser scanning shows incomparable advantages in tree measurement in recent years. Many researchers selected Terrestrial laser scanner to obtain spatial explicit points representing target trees, and proposed a plethora of methods on basis of scanning data to retrieve ecological parameters. These achievements include developing PCD feature histograms to reflect plant geometrical information [10], reflecting changes in the deep oxidation state of the xanthophylls cycle from TLS return intensity [11], presenting voxel-based method with line quadrat direction to retrieve the biophysical characteristics of the forest canopy [12,13] and modeling laser-vegetation interactions probabilistically based on Poisson gap model [14], and so on. Besides, airborne laser scanning (ALS) offers an opportunity to conduct large scale surveying of vegetation at great resolution than has

* To whom all correspondence should be sent:

E-mail: 18951080592@163.com, xuelianfeng@njfu.edu.cn

previously been available. Commercially-available equipments, such as aircraft and drones, loaded laser scanners and was manipulated by engineers to rapidly generate point-cloud data of vegetation. Corresponding algorithm were proposed for a broad range of forestry and environment management applications, such as forest biomass estimation [15], delineation of individual tree crown [16], aboveground biomass and carbon storage evaluation [17,18] and tree species recognition [19].

Although a number of researches have done considerable work on agricultural and forestry measurement, three challenging questions still remained in forestry parameters acquisition from scanning data. 1) How do we extract and distinguish every leaf from the flourishing tree's PCD with enormous variation in leaf inclination angle and azimuth angle? 2) The scanning data exists noise and deviation caused by occlusion effect and external environment interferences [20]. How do we eliminate deviation and design appropriate algorithm to construct real foliage data? 3) The presentation of scanned leaf is in the discrete points and not 3D surface model. How do we design a reasonable algorithm realizing the transformation from scanned point to leaflet surface.

Based on the above issues, here, two meaningful works have been done on basis of PCD. Firstly, original feature vector composed by normal vector, normal vector distribution and normal vectors of tangent plane was proposed, and supervised manifold learning method was designed to process these feature vectors for principal component analysis and dimensionality reduction. Then, Gaussian Mixture Model (GMM) and Expectation-Maximization (EM) method were adopted to the processed features in order to realize PCD classification and automatically recognize tree organs. Secondly, we established polynomial equations to fit leaf boundaries based on PCD, and manipulated MLS algorithm to eliminate noise points caused by external interference. Then, Delaunay triangulation method was introduced to generate numerous triangle meshes composing real leaf surface.

MATERIALS AND METHODS

Data collection by TLS

Our experimental trees were chose on the campus of Nanjing Forestry University ($32^{\circ}08'N, 118^{\circ}81'E$), including many well-isolated individual trees such as Michelia trees and Sakura trees. Assuming that the shape of target tree crowns

is ellipsoidal, each scan was obtained in azimuthally symmetric location and target tree located in the centre of the experimental plot. Every TLS placed in turn at different lateral side and kept several meters away from target tree. After TLS scanning procedure finished, every scan of different angle was finally integrated into a single coordinate system through registration process to acquire full coverage of objective trees.

Extraction of PCD feature

The features we employed include color, shape and orientation information. For every point $p_i = (x_i, y_i, z_i)$ in point cloud P , $P \subset R^3$, its surrounding finite space is defined the set of k nearest points $p_j = (x_j, y_j, z_j)$ with the mean being $\bar{p}_j = (1/k) \sum_{j=1}^k p_j$, The covariance matrix C_p of point p_i is defined by $C_{p_i} = \frac{1}{k} \sum_{j=1}^k (p_j - \bar{p}_j)^T (p_j - \bar{p}_j)$. Let $e_i = \{e_i^0, e_i^1, e_i^2\}$ be the eigenvector and $\lambda_i = \{\lambda_i^0, \lambda_i^1, \lambda_i^2\}$ be the corresponding eigenvalue of C_{p_i} and $\lambda_i^0 \leq \lambda_i^1 \leq \lambda_i^2$. e_i^0 corresponding to the minimum λ_i^0 approximates the normal vector at point p_i .

Next, we computed the covariance matrix of normal vector about this neighborhood using equation (1), where \bar{e}_i denotes the mean normal vector of the 3D points in the neighborhood $\bar{e}_i = (1/k) \sum_{j=1}^k e_j^0$.

$$V_p = \frac{1}{k} \sum_{j=1}^k (e_j^0 - \bar{e}_i)(e_j^0 - \bar{e}_i)^T \quad (1)$$

Consequently, Eigenvalue Decomposition on this covariance matrix V_p was performed to get three eigenvalues l_i^0, l_i^1, l_i^2 of V_p . For isotropic spatial distributions (corresponding to fruits), always $l_i^0 \approx l_i^1 \approx l_i^2$; for predominantly linear distributions (branches), $l_i^0 \geq l_i^1 \approx l_i^2$; and for roughly planar distributions (leaves), $l_i^0 \approx l_i^1 \geq l_i^2$.

Next, we calculated local tangent space feature of every point cloud. Assuming that the set of data points are sampled from a d -dimensional affine subspace, i.e.,

$$p_j = c_i + Q_i \theta_j + \varepsilon_j \quad (1 \leq j \leq k) \quad (2)$$

where $\varepsilon_j \in R^3$ represents noise vector, $\theta_j \in R^d$ is projection coordinates about p_j on the local tangent space, $\Theta_i = [\theta_1, \theta_2, \dots, \theta_k]$ and $d \leq 3$. $c_i \in R^3$

is the origin coordinates of the tangent space and $Q_i \in R^{3 \times d}$ is a matrix which forms an orthonormal basis of the affine subspace. The problem of linear manifold learning amounts to seek c_i, Q_i, θ_j to minimize the reconstruction error, i.e.,

$$\min_{c_i, Q_i, \theta_j} \sum_{j=1}^k \|p_j - c_i - Q_i \theta_j\|_2^2 = \min_{c_i, Q_i, \theta_j} \|p_j - c_i - Q_i \Theta\|_2^2 \quad (3)$$

The matrix of p_i neighborhood is also denoted as $X_i = [p_1, p_2, \dots, p_k]$, and we extract local information by calculating the eigenvectors and eigenvalue of the correlation matrix $(X_i - \bar{p}_i t^T)^T (X_i - \bar{p}_i t^T)$, where $\bar{p}_i = \frac{1}{k} \sum_{j=1}^k p_j$, t is a k -dimensional column vector of all ones. i.e.,

$$X_i \left(I - \frac{1}{k} t t^T \right) X_i^T = U_i \Lambda_i U_i^T \quad (4)$$

where $U_i = [u_i^1, u_i^2, \dots, u_i^k]$ is orthogonal matrix, and the diagonal elements of the diagonal matrix Λ_i are monotone decreasing, so the local tangent space information for the sample point p_i is calculated:

$$\begin{cases} c_i = \frac{1}{k} X_i t \\ Q_i = [u_i^1, u_i^2, \dots, u_i^d] \\ \Theta_i = Q_i^T X_i \left(I - \frac{1}{k} t t^T \right) \end{cases} \quad (5)$$

From the above derivation, we can calculate the column vector u_i^m which is corresponding to the smallest diagonal element of Λ_i , and u_i^m is also the normal vectors of local tangent space on p_i .

We represented the features of a given point p_i using the color information (r_i, g_i, b_i) , normal vector e_i^0 , normal vector distribution l_i^0, l_i^1, l_i^2 and normal vectors of tangent plane u_i^m to form 12-dimensional feature vector $c_{p_i} = \{r_i, g_i, b_i, e_i^0, l_i^0, l_i^1, l_i^2, u_i^m\}$ for each point in the cloud. Consequently, these features were taken into the supervised manifold learning method to extract the principal component for realizing dimensionality compression.

Feature optimization by supervised LLE

Sam [21] proposed nonlinear dimensionality reduction algorithm by Locally Linear Embedding (LLE), which include unsupervised LLE and supervised LLE algorithms. Here, supervised LLE was introduced to deal with PCD features for improving algorithm efficiency.

Specific steps of the SLLE are as follows: Firstly, we separated whole PCD into training samples and testing samples, The features of

training samples denote as $C_{q \times H}$. Through the LLE projection we can get $Y_{t \times H}$, where q is original dimension of training samples, t is output dimension of training samples, H is the numbers of training samples; Let C' be the set of testing samples, and choose one test sample c_{H+1} , $c_{H+1} \in C'$. c_{H+1} is taken into the matrix $C_{q \times H}$, then the matrix size of $C_{q \times H}$ becomes $q \times (H+1)$. Afterwards, try to finding K nearest neighbors of c_{H+1} in testing samples. The Dijkstra distance is used as a similarity measure, but for the testing samples, the priori category information cannot be taken into account. Secondly, find weight coefficients of c_{H+1} and its k -nearest neighbor points, which satisfy the following conditions:

$$\min \varepsilon_{\Pi}(W) = \left| c_{H+1} - \sum_{j=1}^k w_j^{H+1} c_{H+1,j} \right|^2, \quad \text{where}$$

$\sum_{j=1}^k w_j^{H+1} = 1$. $c_{H+1,j}$ ($j=1, 2, \dots, k$) are the neighbor points of the c_{H+1} , w_j^{H+1} is the weight coefficients between c_{H+1} and $c_{H+1,j}$. Thirdly, the LLE algorithm is used to find low-dimensional embedding features of the testing samples, which preserve the geometries inalterability in a low-dimensional space. Through the SLLE transform, training samples and testing samples of PCD are projected into the low dimensional space with the invariance of main characteristics, the original features c_{p_i} of point p_i reduce to low-dimensional vectors \mathfrak{Z}_{p_i} .

PCD classification based on GMM

Our tree PCD data set was manually labeled as two semantic classes (branch and leaf). Using a portion of the data, Gaussian Mixture Model (GMM) classifier was used to classify tree PCD.

A Gaussian mixture model is a weighted sum of A component Gaussian densities as given by following equation.

$$p(\mathfrak{Z}_p | \lambda) = \sum_{i=1}^A \omega_i g(\mathfrak{Z}_p | \mu_i, \sigma_i) \quad (6)$$

where \mathfrak{Z}_p is processed PCD features. $g(\mathfrak{Z}_p | \mu_i, \sigma_i)$, $i=1, \dots, A$, are the component Gaussian densities. Each component density is a Gaussian function of the form, with mean vector μ_i and covariance matrix σ_i , and ω_i is the weight coefficient of each class. The expansion formula of g is:

$$g(\mathfrak{Z}_p | \mu_i, \sigma_i) = \frac{1}{(2\pi\sigma_i)^{d/2}} \exp \left\{ -\frac{1}{2} (\mathfrak{Z}_p - \mu_i)' \sigma_i^{-1} (\mathfrak{Z}_p - \mu_i) \right\} \quad (7)$$

The mixture weights satisfy the constraint that $\sum_{i=1}^M \omega_i = 1$. The mean vectors, covariance matrices and mixture weights from all component densities parameterize GMM. These parameters are collectively represented by the notation, $\lambda = \{\omega_i, \mu_i, \sigma_i\}$, $i = 1, \dots, A$. Then the Expectation Maximization (EM) algorithm is proposed to maximize the likelihood $p(\mathfrak{S}_p | \lambda)$ of the data \mathfrak{S}_p drawn from an unknown distribution. Specific formula is expressed as follows:

$$\lambda^* = \arg \max_{\lambda} \prod_{j=1}^n \sum_{k=1}^A \omega_k g(\mathfrak{S}_{pj}, \lambda_k) \quad (8)$$

where n represents the number of whole PCD. The output of the SLLE, GMM and EM generated an integrated classification for scanning points based solely upon their feature vectors.

Foliage surface reconstruction

TLS scanned data always be interfered by plant swaying in the wind and perspective occlusion. This section addressed accurate leaf boundary detection and 3D leaf surface reconstruction on basis of discrete points.

Foliage boundary depiction

TLS rangefinder system was based upon the principle of time-of-flight measurement of short infrared laser pulses. A rotating polygon mirror wheel realizes the line scan measurement and the frame scanner mechanism relies on rotating the optical head together with the fast line scan mechanism. Both the vertical scan and tilt scan covering the whole field of tree can produce global scan with a line scan angle. Thus, the tree PCD obtained by TLS show linear characteristics and can be represented by linear function $y_i = k_i x_i + b_i$ on horizontal (X-Y) plane. After each scan line equation was obtained, we can easily determine the endpoints of every scanning line, which represent the edge points of scanned foliage. These edge points at left and right sides can be denoted as $P_{Ledge} = \{(x_{l1}, y_{l1}, z_{l1}), (x_{l2}, y_{l2}, z_{l2}), \dots, (x_{ln}, y_{ln}, z_{ln})\}$, $P_{Redge} = \{(x_{r1}, y_{r1}, z_{r1}), (x_{r2}, y_{r2}, z_{r2}), \dots, (x_{rn}, y_{rn}, z_{rn})\}$, respectively. Under the guidance of polynomial fitting, we firstly proposed fitting algorithm to locate the true leaf boundary points based on each half-side edge points. To the end points $P_{Ledge} = \{x_l, y_l, z_l\}$, the magnitudes of y_l was taken as input parameters to calculate the corresponding fitting x'_l and z'_l values. Polynomial fitting was adopted to find the polynomial coefficients

$v^x(x_l, y_l)$ with term number n' that make the data x'_l close to x_l , i.e., $x'_l \approx x_l = v_1^x y_l^{n'} + v_2^x y_l^{n'-1} + v_3^x y_l^{n'-2} + \dots + v_{n'-1}^x y_l + v_{n'}^x$, where x'_l is calculated value to substitute x_l . Likewise, Polynomial fitting was also used to obtain fitted z'_l substituting initial z_l . The specific formula is as follows: $z_l \approx z'_l = v_z^z(y_l) = v_1^z y_l^n + v_2^z y_l^{n-1} + v_3^z y_l^{n-2} + \dots + v_{n-1}^z y_l + v_n^z$. Thus, smooth outer contour of each foliage could be delineated when the fitted boundary points $P'_{edge} = \{x'_l, y_l, z'_l; x'_r, y_r, z'_r\}$ are connected in sequence.

Leaf surface fitting based on MLS

In this step, we smoothed and re-sampled data for each leaf point cloud using the Moving Least Square (MLS) method [22]. The algorithm fitted a 2D manifold to the 3D point cloud data and re-sampled the points to place them on the estimated surface. The method also provided surface normal and curvature estimates and up-sampled or down-sampled the point set appropriately. After MLS fitting processing, foliage scanned point $p_i = (x_i, y_i, z_i)$ was transformed into $p'_i = (x_i, y_i, z'_i)$.

Delaunay triangulation was applied to convert every point p'_i into smooth leaf surface as triangular mesh.

As shown above, we extended method to deal with foliage silhouette delineation and smooth surface reconstruction on basis of PCD. Our method is intuitive and well suited for processing deviations caused by leaf jitter in wind and perspective occlusion. Visually important aspects of foliage appearance such as posture and smooth boundary be easily captured and described. Next, the experiments were conducted to demonstrate the effectiveness of our approach.

RESULTS AND DISCUSSION

Every target trees including Michelia tree and Sakura tree on our campus was scanned from three side-lateral locations with a middle sampling resolution and three markers were used as reference to align the three scans. Then, the ground points were removed and each individual tree was isolated for analysis.

Plant organs classification

After applying our algorithm to TLS point cloud data of an individual tree, we obtained a promising classification result as shown in Fig 1.

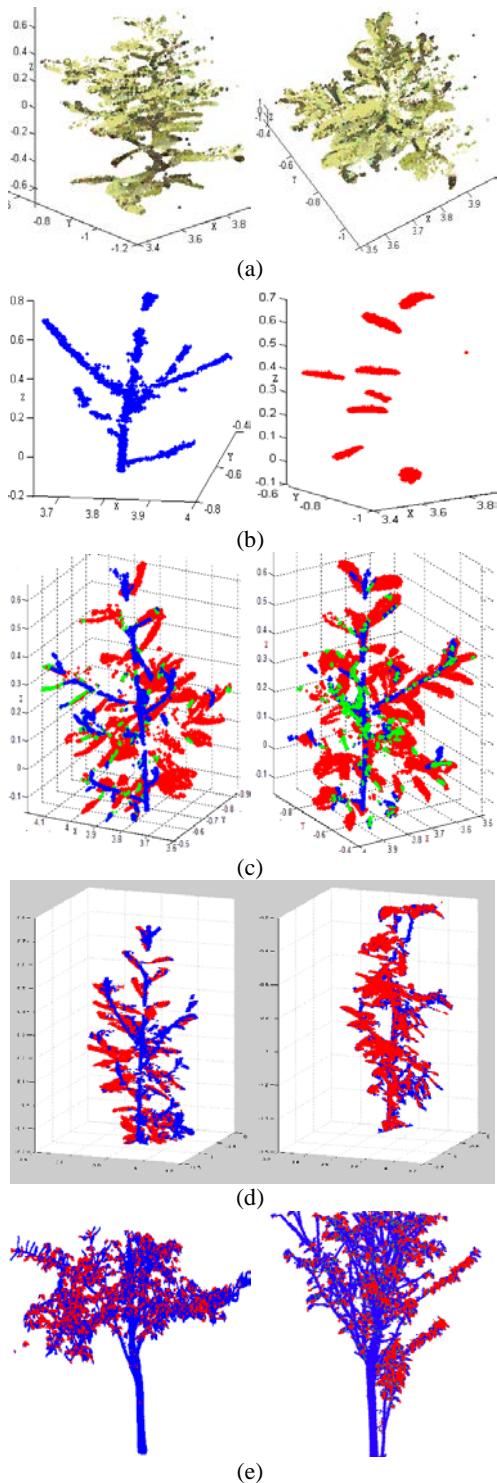


Fig. 1. Visualization of final classification of different components being to an individual tree. (a) Original point cloud data of Michelia tree. (b) Partially selected PCD was manually labeled as two classes (branch and leaf), which was taken as training samples of SLLE and used in GMM. (c) Preliminary classification with linear class points in blue color (i.e., branches and stems), surface class points in red color (i.e., leaves and shoots) and undetermined class points in green color. (d) Adjusted classification of Michelia tree after adapting algorithm parameters. (e) Final classification of Sakura tree after correcting misclassified points by our method.

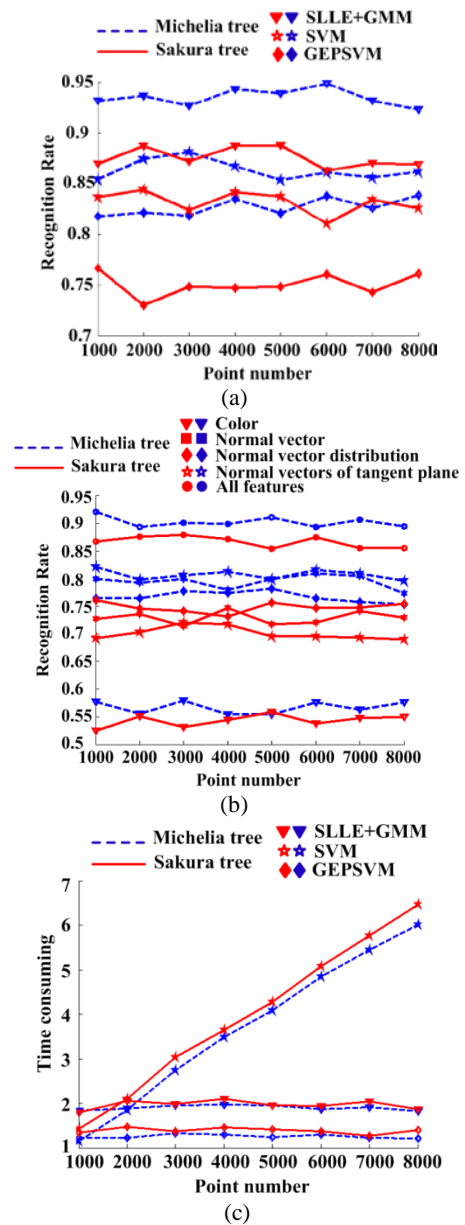


Fig. 2. Comparison with various algorithms and feature sets. (a) Recognition rates of different classifiers. (b) Recognition results using different feature sets. (c) Computation time of different classifiers.

The misclassification of minor points was occurred while leaves and shoots were misclassified as linear class due to perspective occlusion. Besides, small branches shaded by surrounding leaves always be misclassified as planar class. However, for most of scanned data, our method can identified photosynthetic and non-photosynthetic components using color, orientation and geomantic information. These salient features make the proposed method robust to lighting and inevitable color changes as the plant matures. Thus, obtaining better non-destructive measurements of foliage from tree PCD are realized for convenient leaf area estimate.

Consequently, we conducted a comparison with different classifiers and feature sets. Fig. 2 (a) shows that our SLLE + GMM classification method achieved a significant improvement in tree organ recognition. There are 92.38 % and 87.51 % recognition rate on the Michella tree and Sakura tree, respectively. The result is higher than other similar algorithms such as SVM and GEPSVM²³, which is shown in Fig. 2(a). Color, normal vector, normal distribution and normal vectors of local tangent plane of PCD features were respectively adopted to address the recognition rate of our method. It is clearly visible from Fig. 2(b) that all feature combination gives the highest recognition rate, with an average recognition rate of higher than 85.01 %. Due to the interference of external environment light, the minimal average recognition rates depending upon the color features only achieve average 50.27 %. In terms of time consuming, our algorithm takes similar time with GEPSVM method, but less time than other semi-supervised SVM classification methods, which is shown in Fig. 2 (c).

Plant leaf reconstruction

In order to test validation of our leaf surface construction algorithm, we preliminarily measure real Michelia leaf by LI-3000C portable area meter, which can displays and stores plant parameters such as: individual leaf area, accumulated area, leaf length and width. The practical experiment conducted by our student was shown in Fig 3(a).

Consequently, 3D watershed algorithm was designed to separate each leaf from whole leaf PCD and the classification results were shown in Fig 3(b).

We randomly chose some classified foliage data for 3D reconstruction, and Fig. 4 illustrates tree leaves modeling process on basis of PCD. Fig 4(a) shows classified scanned points of one leaf, where the green points are the original scanning PCD with noise and deviation and show linear arrangement along laser beam emitting angle. The linear equation was adopted to fit each scan line that likes blue lines in Fig 4(a). Preliminary leaf silhouette was labeled by the endpoints of each line. Then, we focused on the half side endpoints of every blue line and adopted polynomial curve fitting method to draw two fitting surfaces, and the x_i and z_i magnitude of these points were modified to define smooth and real leaf boundary through the intersection algorithm of these two surfaces. The process was shown in Fig 4(b). After the detection of leaf boundary, we discarded outlier points outside the leaf silhouette, and then the Least

Squares (LS) estimation and Moving Least Squares (MLS) method were adopted to the residual foliage points for eliminating deviation caused by wind. Fig. 3(c) is the result of foliage surface fitting through the LS method (blue color) and the result of the MLS method (red color). The comparison between LS and MLS methods were carried out in Fig. 4(d), where original scanning points, fitted results by LS approach and by MLS approach were shown by green, blue and red color, respectively. Due to the global convergence performance, the LS method cannot reflect local curvature of the leaf surface. MLS can achieve partial optimal solutions of the equations, so the MLS surface fitting scheme can describe the local geometric information of foliage. Seen from the Fig. 4(e), the MLS method gives a better result than the LS method as MLS fitted results are closer to the original topological properties of real foliage surface. Finally, after leaf silhouette extraction, Fig. 4(f) gives polygon-based representations and curled meshes of leaf surface. Then the transform from discrete scanning points into 3D leaf surface was realized and visualization of Michelia and Sakura leaf by our method were achieved.

We compared the area of our reconstruction leaf model with the precise measurement value by LI-3000C. Specific comparison data was shown in Table 1. For the experimental leaves such as Michelia and Sakura tree with different size and curvature, measured results from LI-3000C and our method got similar value, which proved our method is versatile and effective enough to apply for a much larger variety of plant leaf modeling.

Table 1. Leaf area estimation from meter and our 3D model.

	Number of tetrahedron composing leaf model	Area of the reconstruction leaf model	Leaf area using LI-3000C	Deviation between two methods
Michelia leaf	Mesophyll (3212)	61.13 (cm ²)	63.03 (cm ²)	3.02 %
	Vein (487)			
Sakura leaf	Mesophyll (879)	14.93 (cm ²)	15.72 (cm ²)	5.03 %
	Vein (148)			

CONCLUSION

In recent years, TLS has been used for forestry parameter measurement, but the topology structure of tree is irregular. The scanning results always be interfered by external environment, such as wind and illumination variation, so deviation often exists in the scans and results in failing to capture

accurate 3D structural information of forest stands. Meanwhile, TLS using LiDAR popular tools is capable of producing 3D PCD about scanning trees, but extracting structural and biophysical parameters directly from discrete PCD is a problem to be solved.

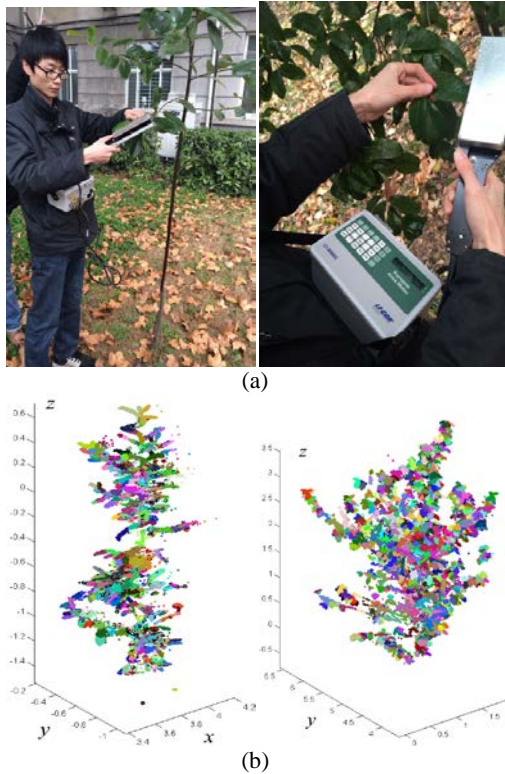


Fig. 3. Schematic to illustrate the (a) practical experiment using LI-3000C portable area meter and (b) separation of each leaf using 3D watershed method from scanned data.

In this paper, we have used computer graphics and vision theory to quantitatively identify the tree structure and accomplished the foliage surface reconstruction from discrete PCD. The main contributions of our research were as follows:

1) We demonstrated the feasibility of recovering fine-scale plant structure in 3D point clouds using features extraction and pattern recognition theory. The proposed feature extraction method employs a combination of color, shape, normal vector distribution and normal vectors of tangent plane to model the local neighborhood about given 3D point in terms of its spatial distribution. Consequently, the dimensionality of PCD features reduced by SLLE were brought into the GMM and EM classifiers, which enabled us to label each point as the fruit (isotropic distribution), leaf (planar) or branch (linear). Our experiment results on different tree PCD show that our method can automatically detect tree leaves and branches with high accuracy.

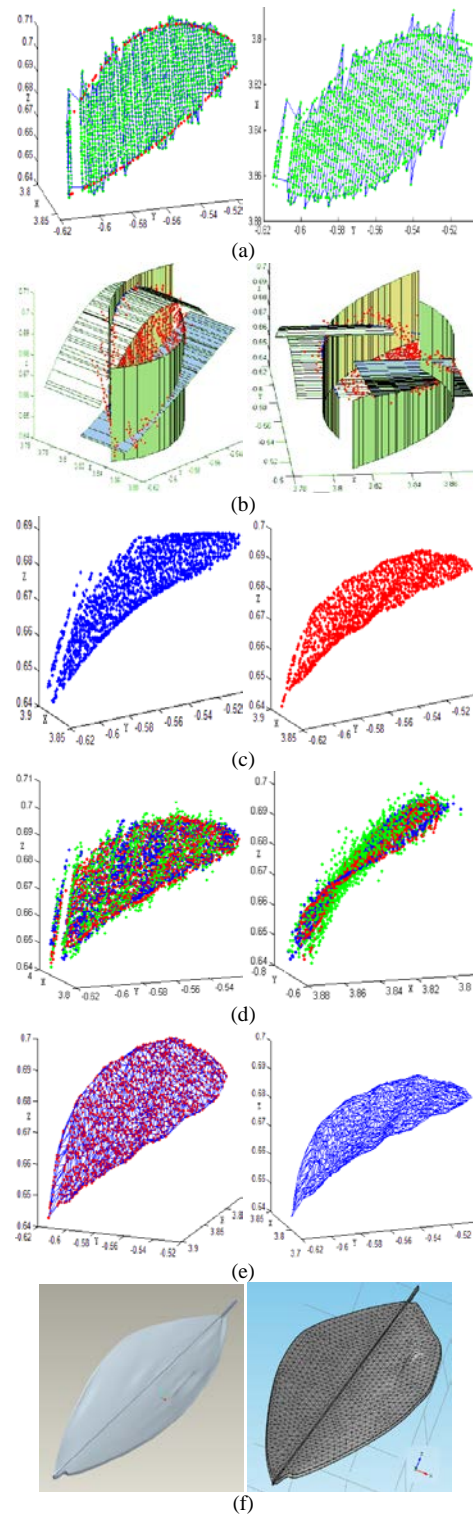


Fig. 4. Different stages of foliage surface reconstruction through our method. (a) Original scanned points of one leaf, which shows linear arrangement on X-Y plane. (b) Smooth edge points generated through the binary polynomial fitting. (c) The points with blue and red color are the fitted results through LS and MLS, respectively. The points in green color are the original scanned points. (d) Visualization results through LS and MLS processing from different viewpoints. (e) Triangulation based on the LS and MLS fitted points. (f) Final construction model of 3D foliage surface using our method.

2) In the multi-location scanning process of TLS, foliage jittering in the wind and perspective occlusion always occurred to lead to inadequately representation of target object surfaces. Thus, scanned PCD can not reflect integrated information of real canopy leaves. In our work, the bilateral edge points of foliage elements were extracted through calculation of bilateral endpoints of spatial lines, which were arranged along with the scanning angle of TLS increasing. Based on these extracted edge points, polynomial curve fitting method was adopted to obtain two fitting surfaces with original Y magnitude. Consequently, the intersection algorithm of this two fitting surfaces was proposed to determine smooth foliage silhouette. For the inner points of leaf surface, MLS approach was designed to remove deviation caused by tree joggling in wind and preserve the localized biologic deformation characteristics. Finally, Delaunay triangulation algorithm was designed to realize the transform from the discrete PCD into real leaf surface.

In brief, this paper used the latest measurement technology (TLS) to extend the traditional approaches of tree index acquisition. The main contributions include combining pattern recognition theory to identify different plant organs and accurate leaf surface reconstruction based on the computer graphics technique. After this subject study, we can provide more useful information about canopy structure and enhanced the capability of terrestrial LiDAR for characterizing forest canopies. With further development of our methods for extracting biophysical and ecological parameters from TLS data sets, long-term forest ecosystem monitoring will benefit from our techniques assuring data for sustainable forest management practices.

Acknowledgements: The authors would like to thank the support from National Natural Science Foundation of China (31300472), Natural Science Foundation of Jiangsu Province (BK2012418), Opening Project Fund (RRI-KLOF201501) of Key Laboratory of Rubber Biology and Genetic Resource Utilization, Ministry of Agriculture. Meanwhile, we appreciate for the experimental devices provided by National Basic Research Program of China (973 Program, (2012CB416904) and Priority Academic Program Development of Jiangsu higher education Institutions. Above all, we tender the anonymous reviewers our deepest thanks for your great help in this paper.

REFERENCES

1. B. Yanikoglu, E. Aptoula, C. Tirkaz, *Machine Vision and Applications*, **25**(6), 1369 (2014).
2. F. Fotopoulou, N. Laskaris, G. Economou, S. Fotopoulos, *Pattern Analysis and Applications*, **16**(3), 381 (2011).
3. R.N. Lati, S. Filin, H. Eizenberg, *Precision Agriculture*, **14**(6), 586 (2013).
4. J.A. Prieto, G. Louarn, J.P. Pena, H. Ojeda, T. Simonneau, E. Lebon, *Plant Cell Environ*, **35**(7), 1313 (2012).
5. J. Fan, Y. Fan, T. Dong, L. Ji, *Science China Information Sciences*, **56**(9), 1 (2013).
6. A.B. Iandolo, R.W. Pearcy, L.E. Williams, *Australian Journal of Grape and Wine Research*, **25**, (2013).
7. S. Chaivivatrakul, L. Tang, M.N. Dailey, A.D. Nakarmi, *Computers and Electronics in Agriculture*, **109**, 109 (2014).
8. R. Giuliani, E. Magnanini, F. Nerozzi, E. Muzzi, H. Sinoquet, *Agricultural and Forest Meteorology*, **128**(1-2), 17 (2005).
9. J. Gumbau, M. Chover, I. Remolar, C. Rebollo, *Computers & Graphics*, **35**, 2, 364 (2011).
10. S. Paulus, J. Dupuis, A.-K. Mahlein, H. Kuhlmann, *BMC bioinformatics*, **14**(1), 1 (2013).
11. T.S. Magney, S.A. Eusden, J.U. Eitel, B.A. Logan, J. Jiang, L.A. Vierling, *New Phytologist*, **201**(1), 344 (2014).
12. G. Zheng, L.M. Moskal, *IEEE Transactions on Geoscience and Remote Sensing*, **50**, 10, 3958 (2012).
13. G. Zheng, L.M. Moskal, *IEEE Transactions on Geoscience and Remote Sensing*, **50**(10), 3970 (2012).
14. K. Zhao, M. García, S. Liu, Q. Guo, G. Chen, X. Zhang, Y. Zhou, X. Meng, *Agricultural and Forest Meteorology*, **209-210**, 100 (2015).
15. C. He, M. Convertino, Z. Feng, S. Zhang, *PloS one*, **8**(10), 920 (2013).
16. L. Jing, B. Hu, T. Noland, J. Li, *ISPRS Journal of Photogrammetry and Remote Sensing*, **70**, 88 (2012).
17. C. Godwin, G. Chen, K.K. Singh, *Landscape and Urban Planning*, **136**, 97 (2015).
18. C. Hopkinson, L. Chasmer, A.G. Barr, N. Kljun, T.A. Black, J.H. McCaughey, *Remote Sensing of Environment*, **181**, 82 (2016).
19. M. Dalponte, H.O. Ørka, L.T. Ene, T. Gobakken, E. Næsset, *Remote Sensing of Environment*, **140**, 306 (2014).
20. J.-F. Côté, R.A. Fournier, G.W. Frazer, K.O. Niemann, *Agricultural and forest meteorology*, **166**, 72 (2012).
21. S.T. Roweis, L.K. Saul, *Science*, **290**(5500), 2323 (2000).
22. P. Breikopf, H. Naceur, A. Rassineux, P. Villon, *Computers & Structures*, **83**(17), 1411 (2005).
23. R. Khemchandani, S. Chandra, *IEEE Transactions on pattern analysis and machine intelligence*, **29**(5), 905 (2007).

ИЗПОЛЗВАНЕ НА ТОЧКОВИ ДАННИ В ОБЛАК ЗА КЛАСИФИКАЦИЯТА НА ОРГАНИТЕ И РЕАЛНИЯ СТРОЕЖ НА ЛИСТАТА НА ДЪРВЕТА

Тин Юн^{1,2,5}, Банкиан Чън², Уайджън Ли³, Юан Сун⁴, Лянфън Сю^{1,5*}

¹ Училище по информатика и технологии, Университет по горско стопанство, Нанджун, Данджоу 571737, Китай

² Изследователска и изпитателна станция за тропически култури, Данджоу 571737, Китай

³ Център за анализи и изпитания, Университет по горско стопанство, Нанджун, Китай

⁴ Колеж за горско стопанство, Университет по горско стопанство, Нанджун, Китай

⁵ Център за изследвания за устойчиво горско стопанство в Южен Китай, Университет по горско стопанство, Нанджун, Китай

Постъпила 18 декември, 2015 г.; коригирана на 17 септември 2016 г.

(Резюме)

Наземното лазерно сканиране (TLS) позволява лесното и бързо събиране на точкови данни в облак (PCD) от различни обекти и се използва масово. Дърветата обаче имат съществено не-регулярна и сложна морфология и сканирането винаги ще бъде повлияно от външни промени и ефекти на включване. Затова количественото определяне на 3D морфологията и оценката на параметрите в горите чрез TLS е предизвикателство. За да решим този проблем, ние приложихме компютърна техника за подобряване на наземното лазерно сканиране (TLS) за измервания в горска среда. Предложени са нови PCD-вектори, включително форма, ориентация, нормално разпределение на векторите и нормалните вектори в равнината на тангентите и алгоритъм за контролирано локално линейно включване (SLLE). Гаусов смесен модел (GMM) е възприет за намаляване размерността на задачата, както и PCD-класификацията. Така ефективността на алгоритъма е подобрена и различни органи на дърветата се идентифицират. Освен това, методът за моделиране на листата използва полиномиална апроксимация и с „подвижните най-малки квадрати“ (MLS) се описват истинските силуети на листата, избягват се случайни петна, водейки доточна реконструкция на сложната повърхност на листата. Подробните експерименти показват, че разпознаемостта остава по-висока от 87.51 %, като нашият метод е приложен за различни PCD на дърветата, а точната 3D-морфологична реконструкция на листата дава подобна площ на ръчно определените по LI-3000С-методика. Така нашият метод дава обещаващи резултати за използването на TLS като ефикасно средство за намиране на параметри на растенията.

BULGARIAN CHEMICAL COMMUNICATIONS

Instructions about Preparation of Manuscripts

General remarks: Manuscripts are submitted in English by e-mail or by mail (in duplicate). The text must be typed double-spaced, on A4 format paper using Times New Roman font size 12, normal character spacing. The manuscript should not exceed 15 pages (about 3500 words), including photographs, tables, drawings, formulae, etc. Authors are requested to use margins of 3 cm on all sides. For mail submission hard copies, made by a clearly legible duplication process, are requested. Manuscripts should be subdivided into labelled sections, e.g. **Introduction, Experimental, Results and Discussion, etc.**

The title page comprises headline, author's names and affiliations, abstract and key words.

Attention is drawn to the following:

a) **The title** of the manuscript should reflect concisely the purpose and findings of the work. Abbreviations, symbols, chemical formulas, references and footnotes should be avoided. If indispensable, abbreviations and formulas should be given in parentheses immediately after the respective full form.

b) **The author's** first and middle name initials, and family name in full should be given, followed by the address (or addresses) of the contributing laboratory (laboratories). **The affiliation** of the author(s) should be listed in detail (no abbreviations!). The author to whom correspondence and/or inquiries should be sent should be indicated by asterisk (*).

The abstract should be self-explanatory and intelligible without any references to the text and containing not more than 250 words. It should be followed by key words (not more than six).

References should be numbered sequentially in the order, in which they are cited in the text. The numbers in the text should be enclosed in brackets [2], [5, 6], [9–12], etc., set on the text line. References, typed with double spacing, are to be listed in numerical order on a separate sheet. All references are to be given in Latin letters. The names of the authors are given without inversion. Titles of journals must be abbreviated according to Chemical Abstracts and given in italics, the volume is typed in bold, the initial page is given and the year in parentheses. Attention is drawn to the following conventions:

a) The names of all authors of a certain publications should be given. The use of “*et al.*” in

the list of references is not acceptable.

b) Only the initials of the first and middle names should be given.

In the manuscripts, the reference to author(s) of cited works should be made without giving initials, e.g. “Bush and Smith [7] pioneered...”. If the reference carries the names of three or more authors it should be quoted as “Bush *et al.* [7]”, if Bush is the first author, or as “Bush and co-workers [7]”, if Bush is the senior author.

Footnotes should be reduced to a minimum. Each footnote should be typed double-spaced at the bottom of the page, on which its subject is first mentioned.

Tables are numbered with Arabic numerals on the left-hand top. Each table should be referred to in the text. Column headings should be as short as possible but they must define units unambiguously. The units are to be separated from the preceding symbols by a comma or brackets.

Note: The following format should be used when figures, equations, *etc.* are referred to the text (followed by the respective numbers): Fig., Eqns., Table, Scheme.

Schemes and figures. Each manuscript (hard copy) should contain or be accompanied by the respective illustrative material as well as by the respective figure captions in a separate file (sheet). As far as presentation of units is concerned, SI units are to be used. However, some non-SI units are also acceptable, such as °C, ml, l, etc.

The author(s) name(s), the title of the manuscript, the number of drawings, photographs, diagrams, etc., should be written in black pencil on the back of the illustrative material (hard copies) in accordance with the list enclosed. Avoid using more than 6 (12 for reviews, respectively) figures in the manuscript. Since most of the illustrative materials are to be presented as 8-cm wide pictures, attention should be paid that all axis titles, numerals, legend(s) and texts are legible.

The authors are asked to submit **the final text** (after the manuscript has been accepted for publication) in electronic form either by e-mail or mail on a 3.5” diskette (CD) using a PC Word-processor. The main text, list of references, tables and figure captions should be saved in separate files (as *.rtf or *.doc) with clearly identifiable file names. It is essential that the name and version of

the word-processing program and the format of the text files is clearly indicated. It is recommended that the pictures are presented in *.tif, *.jpg, *.cdr or *.bmp format, the equations are written using "Equation Editor" and chemical reaction schemes are written using ISIS Draw or ChemDraw programme.

The authors are required to submit the final text with a list of three individuals and their e-mail addresses that can be considered by the Editors as potential reviewers. Please, note that the reviewers should be outside the authors' own institution or organization. The Editorial Board of the journal is not obliged to accept these proposals.

EXAMPLES FOR PRESENTATION OF REFERENCES

REFERENCES

1. D. S. Newsome, *Catal. Rev.–Sci. Eng.*, **21**, 275 (1980).
2. C.-H. Lin, C.-Y. Hsu, *J. Chem. Soc. Chem. Commun.*, 1479 (1992).
3. R. G. Parr, W. Yang, *Density Functional Theory of Atoms and Molecules*, Oxford Univ. Press, New York, 1989.
4. V. Ponec, G. C. Bond, *Catalysis by Metals and Alloys* (Stud. Surf. Sci. Catal., vol. 95), Elsevier, Amsterdam, 1995.
5. G. Kadinov, S. Todorova, A. Palazov, in: *New Frontiers in Catalysis* (Proc. 10th Int. Congr. Catal., Budapest, 1992), L. Guzzi, F. Solymosi, P. Tetenyi (eds.), Akademiai Kiado, Budapest, 1993, Part C, p. 2817.
6. G. L. C. Maire, F. Garin, in: *Catalysis. Science and Technology*, J. R. Anderson, M. Boudart (eds), vol. 6, Springer-Verlag, Berlin, 1984, p. 161.
7. D. Pocknell, *GB Patent 2 207 355* (1949).
8. G. Angelov, PhD Thesis, UCTM, Sofia, 2001.
9. JCPDS International Center for Diffraction Data, Power Diffraction File, Swarthmore, PA, 1991.
10. *CA* **127**, 184 762q (1998).
11. P. Hou, H. Wise, *J. Catal.*, in press.
12. M. Sinev, private communication.
13. <http://www.chemweb.com/alchem/articles/1051611477211.html>.

CONTENTS

<i>The Institute of Chemical Engineering at the Bulgarian Academy of Sciences – 30 years recap</i>	5
<i>70th Anniversary for Professor Venko Beschkov, DSc</i>	7
<i>Professor Christo Boyadjiev's 80 years anniversary, 60 years in science</i>	9
<i>M. Mileva, Y. Raynova, I. Kindekov, D. Krastev, K. Idakieva, In vitro investigation of the antioxidant properties of Cancer pagurus hemocyanin</i>	11
<i>G.L. Huang, H. Gao, C. Yi, D. Huang, J. Han, Study on the synthesis of 2,3,4,6-O-tetraacetyl-α-D-glucopyranosyl bromide</i>	17
<i>R. Rehman, T. Mahmud, R. Ejaz, A. Rauf, L. Mitu, Sorptive removal of Direct Blue-15 dye from water using Camellia sinensis and Carica papaya leaves</i>	20
<i>M. Vadivel, S. Shobana, S.A. Narayan, L. Mitu, J. Dhavethu Raja, M. Sankarganesh, Optimization of process conditions and characterization of ethylene-propylene-diene rubber with bismaleimide</i>	26
<i>A. Firdos, A.R. Tariq, M. Imran, I. Niamat, F. Kanwal, L. Mitu, Antioxidant potential of black pepper extract for the stabilization of sunflower oil</i>	31
<i>B. Purevsuren, Ya. Davaajav, J. Namkhainorov, Z. I. Glavcheva-Laleva, V. Genadiev, I. K. Glavchev, Pyrolysis of animal bone, characterization of the obtained char and tar and application of bone tar for crosslinking of epoxy resin</i>	34
<i>T. Hr. Radoykova, S. K. Nenkova, I. V. Valchev, Monomeric phenolic compounds from hydrolyzed waste lignocellulosic materials</i>	40
<i>S. N. Chaulia, Synthesis, spectroscopic characterisation and biological activity studies of Co(II), Ni(II), Cu(II) and Zn(II) metal complexes with azo dye ligand derived from 4,4'-diaminodiphenylether and 5-sulpho salicylic acid</i>	46
<i>N. Ismail, R. Joshi, J. Engstler, J. J. Schneider: Improved hydrogen storage capacity of CNTs synthesized in presence of iron catalyst using arc discharge method in air atmosphere</i>	62
<i>R. Sadoudi, D Ali Ahmed, M. Trache, A Kecili, Studies of the physico-chemical characteristics and fatty acid composition of commercially available Algerian frying edible oils</i>	68
<i>A.R. Rezvani, H. Janani, F. Rostami-Charati, B.W. Skelton, Synthesis of a new five-coordinate ternary copper (II) complex: crystal structure and spectral studies</i>	74
<i>R. K. Bandi, A. Waghmare, R. M. Hindupur, H. N. Pati, A simple, efficient and scalable synthesis of substituted bis-arylchloromethanes</i>	79
<i>R. Şimşek, M.G. Gündüz, C. Şafak, Ö. Kökpınar, M. Aydın, Free radicals properties of some gamma-irradiated organic compounds</i>	82
<i>S. Sajjadifar, M. A. Zolfigol, N. Javaherneshan, G. Chehardoli, Comparison between acetic acid and propanoic acid as a solvent/catalyst in the indolenines synthesis: an approach without any indole by-product</i>	87
<i>O. Ismail, A. S. Kipcak, İ. Doymaz, S. Piskin, Thin-layer drying kinetics of nectarine slices using IR, MW and hybrid methods</i>	92
<i>İ. Kara, Ö. Yalçinkaya, Evaluation of persistence of gunshot residue (GSR) using graphite furnace atomic absorption spectrometry (GFAAS) method</i>	101
<i>E. Grigorova, M. Khristov, I. Stoycheva, B. Tsyntsarski, D. Nihtianova, P. Markov, Effect of activated carbons derived from apricot stones or polyolefin wax on hydrogen sorption properties of MgH₂</i>	109
<i>I. Petrova, V. Shikov, V. Gandova, K. Mihalev, D. I. Dimitrov, Spectrophotometric and thermodynamic study on the co-pigmentation interaction between strawberry anthocyanins and quercetin in model systems</i>	115
<i>S. S. Nalimova, I. E. Kononova, V. A. Moshnikov, D. Tz. Dimitrov, N. V. Kaneva, L. K. Krasteva, S. A. Syuleyman, A. S. Bojinova, K. I. Papazova, A. Ts. Georgieva, Investigation of the vapor-sensitive properties of zinc oxide layers by impedance spectroscopy</i>	121
<i>Bl.V. Itoua, D.S. Ogunniyi, P. Ongoka, L. Petrov, Effect of fumaric acid on the properties of alkyd resin and palm oil blend</i>	127
<i>Q.-Z. Zhang, J.-L. Liu, F. Yang, X.-P. Hao, C.-Y. Ke, Q. Pan, X.-L. Zhang, Density functional theory based study of the heat of polymerization of olefins</i>	134
<i>L. Raicheva, G. Radeva, S. Nenkova, R. Nikolov, Adsorption characteristics of activated carbon obtained from residual hydrolyzed lignin</i>	139
<i>Y. Xin, H. Wang, F. Chen, Synthesis and anti-plant pathogenic fungal activity of novel benzofuran-2-carboxamide derivatives</i>	145
<i>YuJiao Tu, Haizhi Wu, Determination of metal ions by ultrasound-assisted hollow fiber liquid-phase microextraction technique</i>	151
<i>Jing Liu, Xingyu Zeng, Dongxing Zhou, Yunrong Zhao, Xianhui Pan, Environmental safety assessment on chlorination by-products in brine discharged from desalination plant</i>	157
<i>Yu-Jian Lu, Xin-Ming Wu, Yu Guan, Song-Lin Zhang, Jin-Liang Wang, Jiu-Xia Zhao, Wen-Yu Hanq Zhi-Qiang Shen, Optimization of cell culture for H9N2 subtype AIV and establishment of high-yield cell strain</i>	161

<i>LanQing Wei, XinYan Jiang, JinAn Shi, WenZhou Zhao, XiaoPeng Shao, QiBing Chen, Ying Sun</i> , Study on dust-catching and inhibiting microorganism ability of <i>Jacaranda mimosifolia</i> under the same condition of compare experiment	171
<i>Yonggang Zeng, Wenyuan Li, Jin Huang, Zhengwen Huang, Jin Wang, Jin Qian, Ao Yuan, Tingting Du, Yaqi Hu, Dagang Li</i> , Study on new rural domestic sewage treatment technology based on CASS and VBF	176
<i>The 4th Asia-Pacific Conference on Engineering Technology (APCET 2016)</i>	183
<i>Z. Yuan, P. Yan</i> , Hydroxyl radical scavenging activity of microparticles prepared from solid fermentation by edible-medicinal fungi	185
<i>Y.J. Jia, W.X. Su, Y.B. Hu, H.N. Chen</i> , Pt doped TiO ₂ (Pt-TiO ₂) sol gel thin films	190
<i>M. He, W. Zhu, F. Liu, H. Chen</i> , Droplet characteristic adjustment method based on LEM for 3D electronic printing	193
<i>Y. Liu, L. Liu; G. Shi; J Shi, W. L. Lai</i> , Research on the synthesis and characterization of abiraterone acetate	199
<i>L. Wang, B. Wan</i> , Research on the physics-of-the failure model for corrosion damage accumulation under a multi-level stress profile based on the acceleration factor	204
<i>G. Zhenzhi, H. Bin, G. Zhengming, N. Libo, C. Lujie</i> , Study on the influence of different clearance on the crack of PBX explosive	210
<i>G. Zhenzhi, H. Bin, G.Z. Ming</i> , Numerical analysis of surface cracks of spherical explosive with a cushion	217
<i>G. Wang, Y. Gao, Y. Tang</i> , Research on the mechanism for chemical clogging and its effect on the stability of tailing dam	228
<i>L. Sun, X. Liang, Q. Wang, H. Chen</i> , Material composition detection using an image segment with an improved artificial bee colony algorithm	234
<i>L.L. Ping, Y.J. Tao</i> , Friction stir welding automatic effect on building the microstructure and properties of high nickel steel	239
<i>J. Song, Z-D. Dai, G. Song, H.-L. Chen</i> , Study on the nonisothermal crystallization behavior of polyvinyl alcohol/montmorillonite composite by DSC analysis	245
<i>M. Li, X. Cong</i> , Chemical changes and the mechanisms in the sintering process of sea silt	250
<i>Y. Xuexin</i> , Preparation and functional properties of maltose ester lactate	256
<i>P.F. Xu, N. Yang, J. Jia, C. Xu, J.J. Guo</i> , A kind of integrated microfluidic system for rapid pathogenic botrytis cinerea detection	264
<i>N. Yang, Z. Li, J. Sun, P.F. Xu, J.J. Guo, H.P. Mao</i> , Interference analysis for pesticide residue photometric detection based on integrated microfluidic chip	269
<i>J.J. Guo, R.B. Zhang, N. Yang</i> , Design and evaluation of the microfluidic magnetic isolating method for aquaculture pathogens detection	276
<i>Z. Yuan, P. Yan, D. Jing</i> , Optimization of fermenting conditions for antioxidant activity and yield of polysaccharides from mushroom solid fermentation	282
<i>Ting Yun, Bangqian Chen, Weizheng Li, Yuan Sun, Lianfeng Xue</i> , Using point cloud data for tree organ classification and real leaf surface construction	288
<i>INSTRUCTIONS TO THE AUTHORS</i>	297

СЪДЪРЖАНИЕ

<i>М. Милева, Ю. Райнова, Ив. Киндеков, Д. Кръстев, К. Идакиева, In vitro</i> изследване на антиоксидантните свойства на хемоцианин от рак <i>Cancer ragurus</i>	16
<i>Г. Л. Хуанг, Х. Гао, С. Ыи, Д. Хуанг, Дж. Хан,</i> Изследване на синтеза на 2,3,4,6- <i>O</i> -тетраацетил- α -D-глюкопиранозил бромид	19
<i>Р. Рехман, Т. Махмуд, Р. Руаз, А. Рауф, Л. Миту,</i> Сорбционно отстраняване на багрилото директно синьо-15 от вода използвайки листа от <i>Camellia sinensis</i> и <i>Carica papaya</i>	25
<i>М. Вадивел, С. Шобана, С.А. Нараян, Л. Миту, Дж. Дхавеетху Раджа, М. Санкарганеш,</i> Оптимизация на условията на процеса и охарактеризиране на каучук от етилен-пропилен-диен с бис-малеинимид	30
<i>А. Фирдос, А.Р. Тарик, М. Имран, И. Ниамат, Ф. Канвал, Л. Миту,</i> Антиоксидантен потенциал на екстракт от черен пипер за стабилизирането на слънчогледово масло	33
<i>Б. Пуревсурен, Я. Давааджав, Дж. Намхайноров, З. И. Главчева-Лалева, В. Генадиев³, И. К. Главчев,</i> Пиролиза на животински кости, характеризиране на получените въглен и катран и прилагането на костен катран за омрежване на епоксидна смола	39
<i>Т. Х. Радойкова, С. К. Ненкова, И. В. Вълчев,</i> Мономерни фенолни съединения от отпадъчни хидролизни лигноцелулозни материали	45
<i>С.Н. Чаулия,</i> Синтеза, спектроскопско охарактеризиране и биологична активност на Co(II), Ni(II), Cu(II) и Zn(II) метални комплекси с лиганди от азо-багрило, получено от 4,4'-диаминодифенилетер и 5-сулфосалицилова киселина	61
<i>Н. Исмаил, Р. Джоши, Й. Енгстлер, Й.Й. Шнайдер,</i> Подобен капацитет на въглеродни нанотръби (cnt) за складиране на водород при дълго изпразване във въздух в присъствие на железен катализатор	67
<i>Р. Садуди, Д. Али Ахмед, М. Траче, А. Кецили,</i> Изследване на физико-химичните характеристики и състава от мастни киселини на търговски алжирски хранителни растителни масла	73
<i>А. Реза Резвани, Х. Джанани, Ф. Ростами-Чарати, Б.У. Скелтън, Н. Надери, Дж. Асгарпанах,</i> Синтеза на нов третичен мед (II) комплекс: кристална структура и спектрални изследвания	78
<i>Р. К. Банди, А. Вагмар, Р.М. Хиндупур, Х.Н. Пати,</i> Проста, ефективна и мащабирана синтеза на субституирани бис-арил-хлорометани	81
<i>Р. Шимшек, М. Г. Гюндюз, Дж. Шафак, Й. Кьокпинар, М. Айдын,</i> Свойства на свободните радикали на някои гама-облъчени органични съединения	86
<i>С. Саджадифар, М.А. Золфигол, Н. Джавахернешан, Г. Чехардоли,</i> Сравнение между оцетната и пропановата киселина като разтворител/катализатор в синтезата на индоленини: подход без индолови странични продукти	91
<i>О. Исмаил, А.С. Кипчак, И. Доймаз, С. Пишкин,</i> Кинетика на сушене на тънки слоеве от нектарини при ig , mw и хибридни методи	100
<i>И. Кара, О. Ялчинкая,</i> Оценяване на трайността на остатъци от изстрели (GSR) с атомно-абсорбционна спектрофотометрия в графитна пещ (GFAAS)	108
<i>Е. Григорова, М. Христов, Б. Цинцарски, И. Стойчева, Д. Нихтянова, П. Марков,</i> Ефект на активни въгленни, получени от кайсиеви костилки или полиолефинов восък върху сорбционните свойства по отношение на водород на MgH_2	114
<i>И. Петрова, В. Шиков, В. Гандова, К. Михалев, Д. И. Димитров,</i> Спектрофотометрично и термодинамично изследване на ко-пигментационни взаимодействия между антоциани от ягоди и кверцетин в моделни системи	120
<i>С. С. Налимова, И. Е. Кононова, В. А. Мошиников, Д. Ц. Димитров, Н. В. Кънева, Л. К. Кръстева, Ш. А. Сюлейман, А. С. Божинова, К. И. Папазова² А. Ц. Георгиева,</i> Изследване на измерени по метода на импедансна спектроскопия на чувствителните към изпарения свойства на слоеве от цинков оксид	126
<i>Бл. В. Итуя^{1*}, Д. С. Огуний², П. Онгока¹, Л. Петров³,</i> Влияние на фумаровата киселина върху свойствата на смеси на алкидна смола и палмово масло	133
<i>К.-Ж. Жанг, Дж.-Л. Лю, Ф. Янг, С.-П. Хао, К.-Ю Ке, С. Пан, Кс.-Л. Жанг,</i> Изследване на топлината на полимеризация на олефини с помощта на теорията на плътностния функционал (DFT)	138
<i>Л. Райчева, Г. Радева, С. Ненкова, Р. Николов,</i> Адсорбционни характеристики на активен въглен получен от отпадъчен технически хидролизиран лигнин	144
<i>Я. Син, Х. Уанг, Ф. Чен,</i> Синтеза на нови бензофуран-2-карбоксамидови производни и тяхната активност спрямо патогенни гъбички	150
	301

Ю Джиао Тю, Хайжи Вю, Определяне на метални йони чрез ултразвук-подпомагана течна-микроекстракционна техника с кухи ВЛАКНА	156
Джинг Лю, Ксингю Зенг, Донгжинг Жу, Юнронг Жао, Ксианхой Пан, Екологична оценка на безопасността на вторични продукти на хлориране в саламура, изхвърлена от инсталация за обезсоляване	160
Ю-Джиан Лю, Ксин-Мин Ву, Ю Гуан, Сонг-Лин Жанг, Джин-Лиан Ван, Джиу-Ксиа Жао, Вен-Ю Хан, Жи-Цян Шен, Оптимизация на клетъчна култура на H9N2 подтип на AIV и установяване на клетъчен щам с висок добив	170
Ланцин Уей, Синйен Дзян, ДзинАн Шай, Уънджоу Джиао, СяоПън Шао, Цибин Чън, Ин Сун, Проучване на прахоулавянето и способността за инхибиране на микроорганизми на <i>Jacaranda mimosifolia</i> при еднакви условия на експеримент за сравнение.....	175
Юнган Дзън, Уънюан Ли, Дзин Хуан, Джануън Хуан, Дзин Уан, Дзин Циен, Ао Юан, Тинтин Ду, Яци Ху, Даган Ли, Проучване на нова технология за обработка на селски битови отпадни води на базата на CASS и VBF	182
4- ^{та} конференция на Азиатско-тихоокеанския регион по инженерна технология (APCET 2016),	183
3. Юан, П. Ян, Способност за остраняване на хидроксилни радикали от микрочастици, получени при твърдо-фазна ферментация на едливи медицински гъби	189
И. Дж. Джиа, М. У. Хе, Х. Н. Чен, Тънки филми от TiO ₂ , получени по зол-гел метода и дотирани с платина (Pt-TiO ₂)	192
М. Хе, У. Жу, Ф. Лиу, Х. Чен, Метод за настройка на размера на капките по LEM-метода за 3D електронно печатане	198
И. Лю, Л. Лю, Г. Ши, Дж. Ши, У. Л. Лаи, Изследвания и охарактеризиране на абиратерон-ацетат	203
Ли Уан, Бо Уан, Изследване на натрупването на корозионни дефекти при много-степенно напрежение с ускорение с модела „physics-of-failure”	209
Г. Женжи; Х. Бин; Г. Женгминг; Н. Либо; К. Лужие, Изследване на влиянието на отстраняването на пукнатини при РВХ-експлозиви	216
Г. Женжи, Х. Бин, Г.З. Минг, Числен анализ на повърхностни пукнатини при сферични експлозиви с амортисьор	227
Г. Уанг, И. Гао, И. Танг, Анализ на влиянието на химическото задръстване и просмукване върху стабилността на хвостохранилищата	233
Л. Сун, Х. Лианг, К. Ванг, Х. Чен, Определяне строежа на материали по сегменти на образи с помощта на алгоритъм „изкуствена пчелна колония“	238
Л.Л. Пинг, И.Дж. Тао, Ефект на твърдо-фазното заваряване върху образуването на микроструктурата и свойствата на виско-качествена никелова стомана	244
Дж. Сонг, З.-Д. Даи, Г. Сонг, Х.-Л. Чен, Изследване на неизотермичната кристализация на композити от поли-винилов алкохол с монтморилонит чрез диференциална сканираща калориметрия (DSC)	249
М. Ли, С. Цонг, Химични промени и механизми на синтеруването на морска тиня	255
И. Ксюексин, Получаване и функционални свойства на малтозо-лактатен естер	263
П.Ф. Ксу, Н. Ян, Дж. Джиа, К. Ксу, Дж.Дж. Гуо, Интегрирана микрофлуидна система за бързо откриване на патогените <i>Botrytis cinerea</i>	268
Н. Ян, З. Ли, Дж. Сун, П.Ф. Ксу, Дж.Дж. Гуо, Х.П. Мао, Интерференчен анализ за фотометричното определяне на остатъци от пестициди с интегрални микро-флуидни чипове	275
Дж.Дж. Гуо, Р.Б. Джан, Н. Ян, Проектиране и оценка на метод с микро-флуидна изолация за откриване на патогени в аквакултури	281
Дж. Юан, П. Ян, Д. Джън, Оптимизация на условията за твърдо-фазна ферментация на гъби във връзка с тяхната антиоксидантна активност и добива на полизахариди	287
Тин Юн, Банкиан Чън, Уайджън Ли, Юан Сун, Лянфън Сю, Използване на точкови данни в облак за класификацията на органите и реалния строеж на листата на дървета	296
ИНСТРУКЦИЯ ЗА АВТОРИТЕ	297